2 1 JUN 2000

ProQuest Number: 10183049

ProQuest 10183049

AN INVESTIGATION INTO THE FLOW

STRUCTURE OF A GENERALISED

OPEN CHANNEL INTAKE

Christopher BOWLES

Thesis submitted in partial fulfilment of the requirements for the
Doctor of Philosophy Degree in Civil Engineering
in the Department of Civil and Structural Engineering
Nottingham Trent University

September 1999

Above: Small scale, run-of-the-river, low head hydropower plant in the Netherlands.

Right: Two-dimensional graphic showing a three-dimensional view of a computational mesh which represented a generalised intake structure of 15 degree intake angle. The image is viewed from the downstream end of the model looking upstream. The coloured particles formed part of an animated tracking routine.
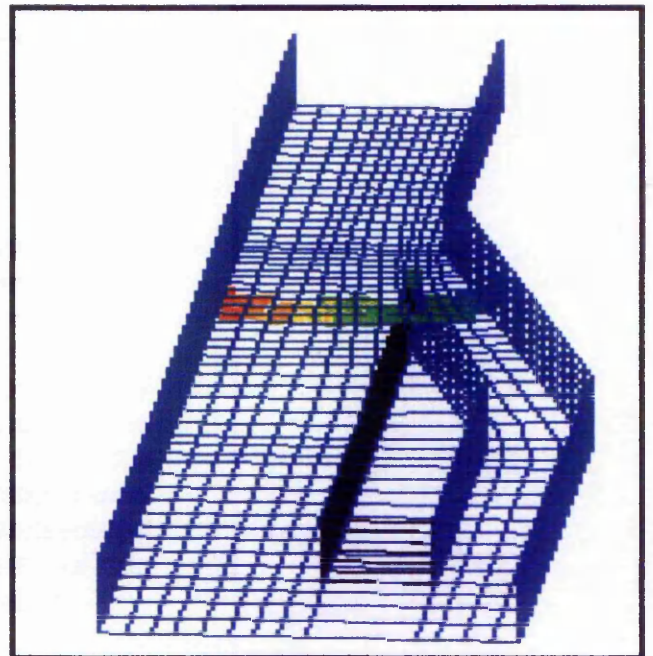
ABSTRACT

BOWLES, C. B., 1999. An investigation into the flow structure at a generalised open channel intake.

Open channel intake structures occur in many different applications such as navigable water courses, irrigation, power station facilities for cooling or steam production and run-of-the-river hydropower facilities. All these applications suffer from problems such as energy losses due to asymmetric flow patterns and the commonly associated problem of sedimentation.

The flow structure and the associated energy losses at a generalised open channel intake structure are investigated using three-dimensional numerical and physical modelling techniques. Intake angles of 15, 30 and 45 degrees with flow split ratios (intake channel flow / main channel flow) ranging from 0.5 to 3.0 and Reynolds numbers ranging from 1×10^5 to 3×10^5 are investigated. A predictive hypothesis for the position and shape of the dividing streamplane is presented and tested with reasonable correlation. The hypothesis can be applied to channel width ratios of 0.5 (intake channel / main channel) with a plane, smooth, rectangular cross sectional area. The flow structure is also described using flow visualisation techniques in the physical model and streamline plotting, velocity vector and velocity profile graphics. A study is also undertaken to describe the turbulent kinetic energy in the flow domain. Predictions near the bed of the flow domain are poor in all analyses with improved results with depth towards the surface. Areas of secondary circulation cells, flow reversal and stagnation zones are identified by numerical and physical models.

Validation of the numerical code is undertaken using three dimensional velocity and root mean square velocity data collected using the Acoustic Doppler Velocimeter (ADV). Calibration of the ADV is undertaken and the results closely match the manufacturers stated calibration data. The numerical code used is a finite volume method solving the Reynolds Averaged Navier Stokes equations and the k-ϵ turbulence model. Validation of the code indicated that it was suitable for the investigation of the flow structure in this instance but failed to predict completely areas of high velocity gradients or flow reversal.

KEY WORDS: intake flow structure, validation, CFD, Acoustic Doppler Velocimeter, energy losses, run-of-the-river hydropower.

CONTENTS

6

MODELLING OF INTAKE FLOWS

6

FIGURES

13

14

16

TABLES

TABLES

18

1

INTRODUCTION

1.1   GENERAL

Diversion flows are found in an assortment of natural and man made environments including natural river bifurcations, meander cut-offs and side diversion channels such as water intakes and irrigation headworks. It is with regard to side diversion channels that this thesis is concerned. Diversion flows are also associated with branching arteries within living cardiovascular systems. It is reasonable, when analysing fluid in motion, to consider that the fluid is operating under ideal conditions, be it that the surface which is in contact with the water is smooth or fluid properties do not affect its behaviour. However, realistically this is never the case.

The mechanics of the flows in these situations are complex and not well understood, exhibiting non-uniform three-dimensional flow patterns which include zones of flow division, separation and reversal and streamwise vortices. There will always be, to some degree, associated energy losses within the system of flow. A common contributory source to energy losses is that due to friction. Such factors will inhibit the capacity of the fluid to operate to its full potential. In the case of a lateral hydropower intake adjacent to a flowing river, the capacity of the hydropower station to operate to its optimum efficiency depends on the ability of the hydraulic engineer to design an intake channel and structure which produces minimal energy losses in the flow. The associated energy losses can be extremely onerous and are therefore of great interest to the hydraulic engineer.

1.1.1 Problem Description

This study evolved from a very broad overview of problems associated with small scale, low head, run-of-the-river hydropower generation. Initially several problems were identified which were subsequently investigated in further detail. Numerous sites were visited in England and a research visit to the United States of America, sponsored by the Royal Academy of Engineering, was undertaken. The findings of these visits will be summarised by the following sections.

Site Visits in England

Site visits were undertaken to Belper Mill, Duffield Mill and Borrowash Mill on the River Derwent in Derbyshire, Davyhulme on the Manchester Ship Canal and Glenridding in Cumbria. Potential sites have also been visited at Colwick Sluices and Beeston Weir on the River Trent in Nottinghamshire. In addition to these specific site visits, meetings have been conducted with developers and suppliers in the industry. Meetings have been held with Gilkes Hydro of Kendal, Cumbria, Norweb Power Generation, Manchester, Derwent Hydropower, Derbyshire and Bridgestone Rubber Dams, London. In every instance these developers and suppliers have highlighted typical problems associated with small scale, low head, run of the river hydropower. This initial study indicated that there were four main problems :-

- Energy losses.
- Sedimentation at intakes.
- Fish passage at hydropower developments.
- The effects to navigation at hydropower developments.

Site Visit to the United States of America

A research trip of five weeks in duration was undertaken to the United States of America (USA) in March 1996. This involved visiting small scale, low head, hydropower sites across seven States in the USA. Twelve sites in Maine, ten sites in New York, two sites in Iowa, one site in Kansas, three sites in Utah, two sites in Montana, one site in Oregon and two sites in California were visited. In addition meetings were held with developers and researchers at Voith Hydro, Pennsylvania (equipment suppliers), Georgia Institute of Technology, Atlanta, Georgia (research), Iowa Institute of Hydraulic Research, Iowa (research), Washington County Water Conservation District, St George, Utah (developers) and Redding Hydro, Redding,

California (developers). The USA could be considered to be approximately fifteen years ahead of England in terms of development of small scale hydropower. Development of this natural resource in the USA was instigated in the 1970's as a result of the oil embargoes which were enforced at that time. The instigation of the development of this resource in England has occurred on a much smaller scale as a result of a different incentive, the Government's Non Fossil Fuel Obligation (NFFO 1994).

The research visit to the USA highlighted identical problems to those presently being experienced in England, with many of the problems having not yet been solved. Figure 1.1 shows energy losses occurring at a small scale run-of-the-river hydropower intake in Maine, U.S.A. Notice the vortex formation that was present just upstream of the intake. This is a typical cause of energy losses and in this case was costing the developer up to 30% loss in power production.
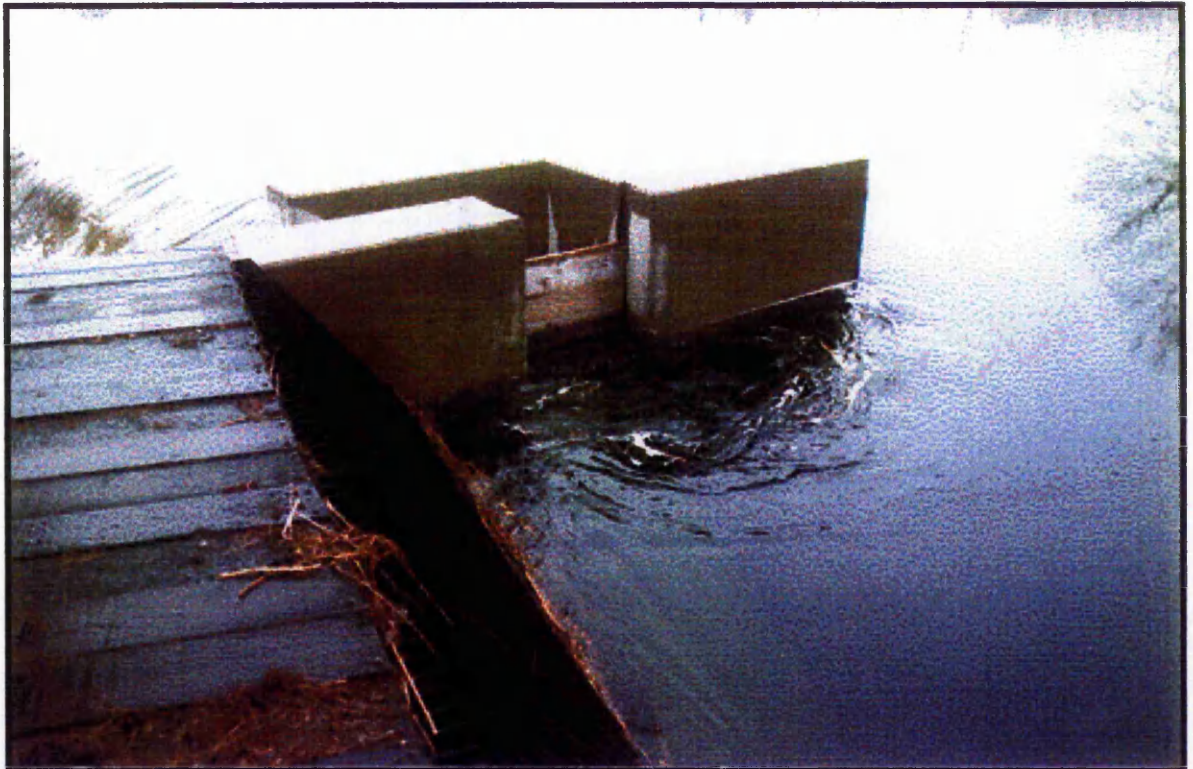
Figure 1.1   Energy losses occurring at an intake at a site in Maine, USA

Of all the problems highlighted by the preliminary research it was found that the most significant both in England and the USA, was the problem of energy losses at intakes. In addition to the obvious loss of power production, flow asymmetry can also

cause structural problems to turbine blades and turbine mountings due to vibrations and cavitation. It is specifically with regard to energy losses therefore that this thesis is concerned.

The problem of energy losses at intakes are a result of the flow patterns induced by the sudden change in flow direction that gives rise to a complex three dimensional flow structure that is characterised by strong secondary circulation, dramatic pressure variations and depth varying flow features. Parameters which affect these features include :

Main channel Reynolds Number, $Re_d = \dfrac{U_1 . D}{\nu}$ 1.1

where U_1 is the mean velocity at the main channel inlet, D is the flow depth and ν is the kinematic viscosity.

Discharge Ratio, $Q_r = \dfrac{Q_I}{Q_M}$ 1.2

where Q_I is the flow rate in the diverted inlet channel and Q_M is the total flow rate in the main channel.

Diversion Angle, θ

where θ is the angle at which the diverted inlet channel is offset from the main channel.

Aspect Ratio, AR = D/W   1.3

where W is either the width of the main channel or inlet channel.

Main Channel Bed Roughness, which can be defined by a local roughness Reynolds number, $k_s^+ = \dfrac{(k_s / D).\mu_\tau}{\nu}$, where k_s/D is the equivalent non dimensional sand grain

(1.5) roughness height and μ_τ is the shear velocity equal to $\sqrt{\dfrac{\tau_0}{\rho}}$, where τ_0 is the magnitude of the wall shear velocity and ρ is the density of the fluid.

The parameters that were specifically covered by the scope of this thesis were the Reynolds number, the discharge ratio, the diversion angle and the aspect ratio. The effects of the roughness of the bed and walls were not considered by this thesis.

For further details on sedimentation problems at intakes the reader is referred to Neary *et al.* (1994), and for further details on fish passage the reader is referred to Sotiropoulos (1996).

1.1.2 Applications of Intakes

Run of the River Hydropower Generation

The focus of this research was with regard to intakes for run-of-the-river hydropower generation. It is with reference to this application that energy losses are a vital consideration. Figure 1.2 shows an aerial view of a run of the river intake arrangement. This site is located in the Netherlands and it can be observed that the impoundment of the flow is minimal. Notice also the relatively short forebay and tailrace which is typical of such an installation. Careful design of the forebay is required to minimise energy losses.
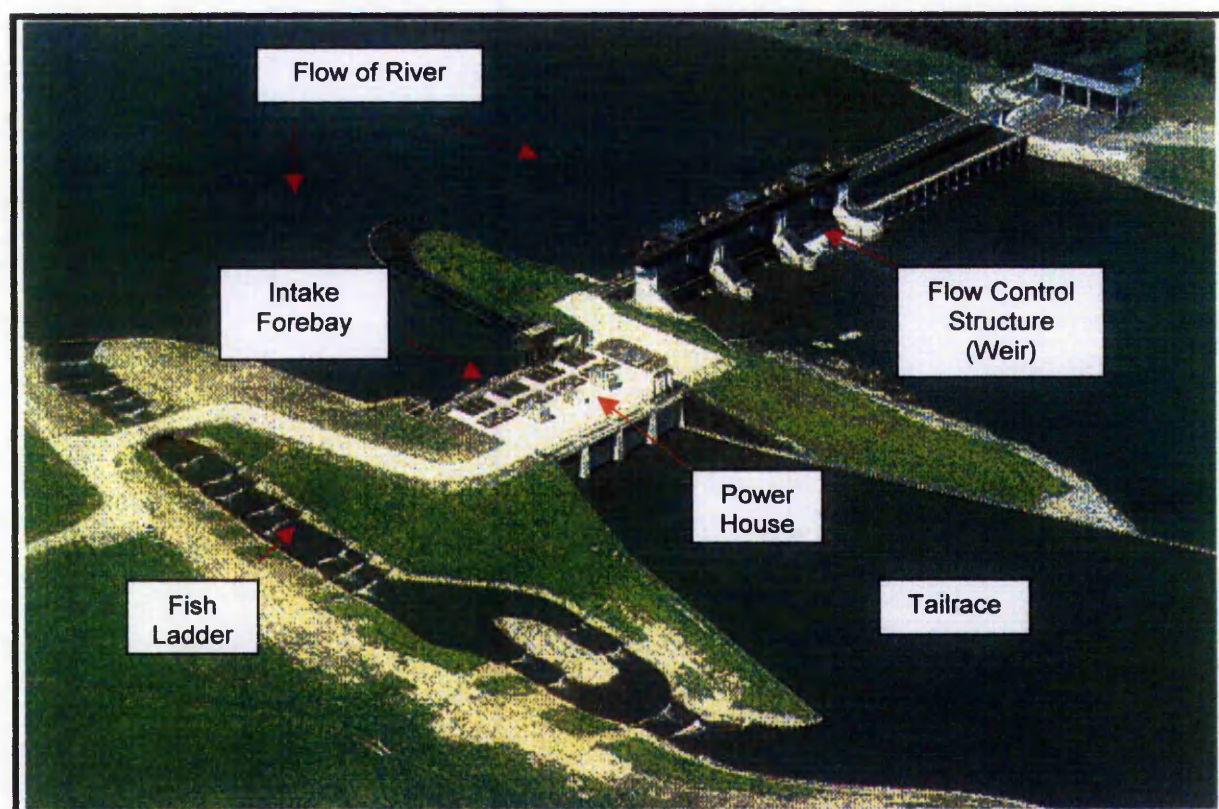
Figure 1.2   Run of the river site in the Netherlands.

Finding two identical intakes of the thousands of run of the river projects is difficult. The wide diversity of existing intakes underlines the unique aspects of hydroelectric design. No two projects face exactly the same design opportunities and constraints. Sites differ and designs must respond to a broad range of potential environmental and operational factors. However, in spite of their wide diversity, all intakes share the following common purpose :

'Delivery of the required flow over the desired range of headwater elevations with optimum hydraulic efficiency '.

Figure 1.3 shows a schematic diagram to represent the important features of a run of the river hydropower site. The research described by this thesis uses a generalised arrangement as shown by Figure 1.3.

Other Uses of Intakes

Hydraulic intakes are also found in other hydraulic engineering applications. Intake design should be considered in irrigation engineering when abstracting water from existing watercourses. Similar problems are experienced with irrigation intakes as with run of the river hydropower intakes. Siltation problems are frequently experienced at irrigation intakes requiring regular dredging of channels. Head loss due to energy losses at intakes may also limit the conveyance of irrigation channels.

Intakes to fossil fuel powered electricity generating stations are used to provide water for the generation of electricity by steam turbines and for cooling purposes. The accumulation of sediment at the entrance of the intake can cause blockage and excessive movement of the sediment into the diversion. This can cause the malfunctioning of the travelling screens and can completely obstruct the intake bays at lower water stages. The entrained sediment can be detrimental to the cooling system by accelerating the erosion of its various components and increasing maintenance costs. Thus sediment problems at such intakes may be more onerous than energy losses specifically although the two problems are associated.

Navigation of craft in watercourses may be affected by intake design. The alteration of the flow field in response to installation of intakes and the effect upon navigation in the watercourse should be considered during the design process. Similarly any

changes to the siltation regime of the watercourse may have an effect upon navigation.
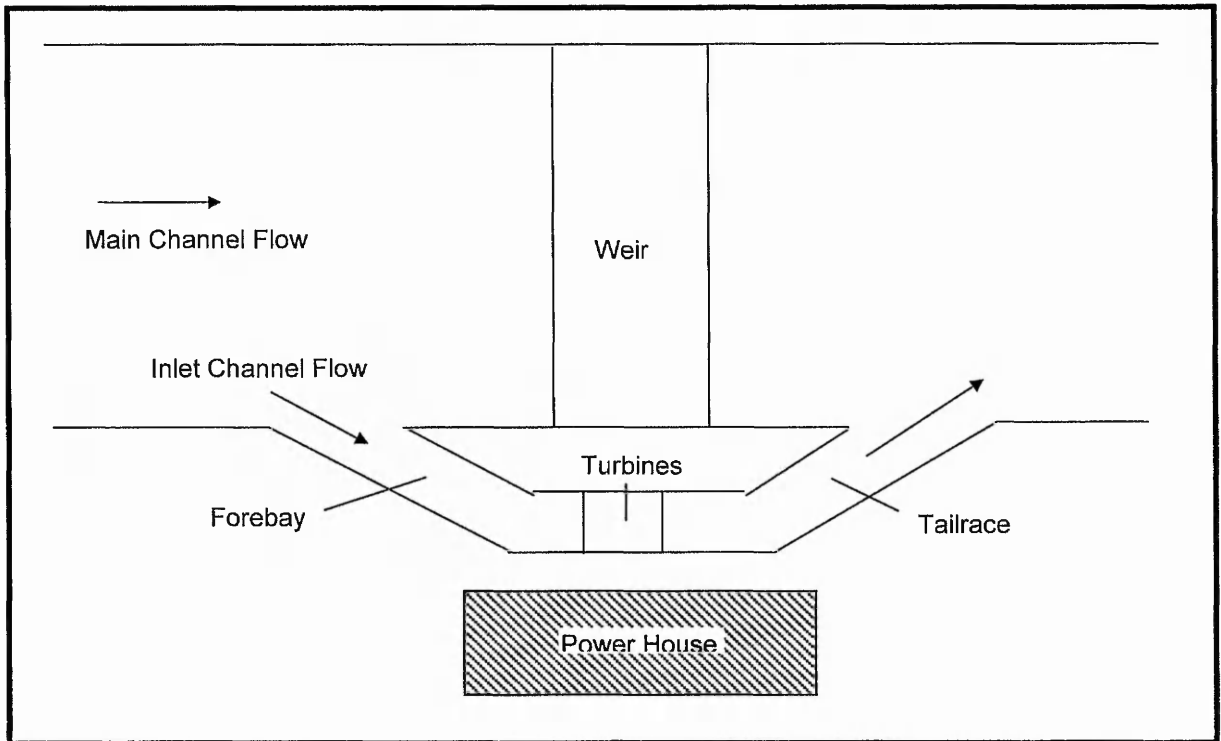
Figure 1.3   A schematic diagram for a generalised run of the river hydropower site.

The preceding pages have identified the problem with which this thesis is concerned and have also introduced the industrial applications where the problem of energy losses at intakes occur. The specific application of the thesis of energy losses at run-of-the- river hydropower intakes has also been introduced. The following sections of this chapter present an outline of the thesis, introduce the techniques by which the subject will be investigated, present the objectives of the thesis and finally the original contribution to knowledge of the thesis.

1.2   OUTLINE OF THESIS

Figure 1.4 shows a flow diagram to outline the structure of the thesis.

The following sections give a brief overview of the most important sections of the thesis.
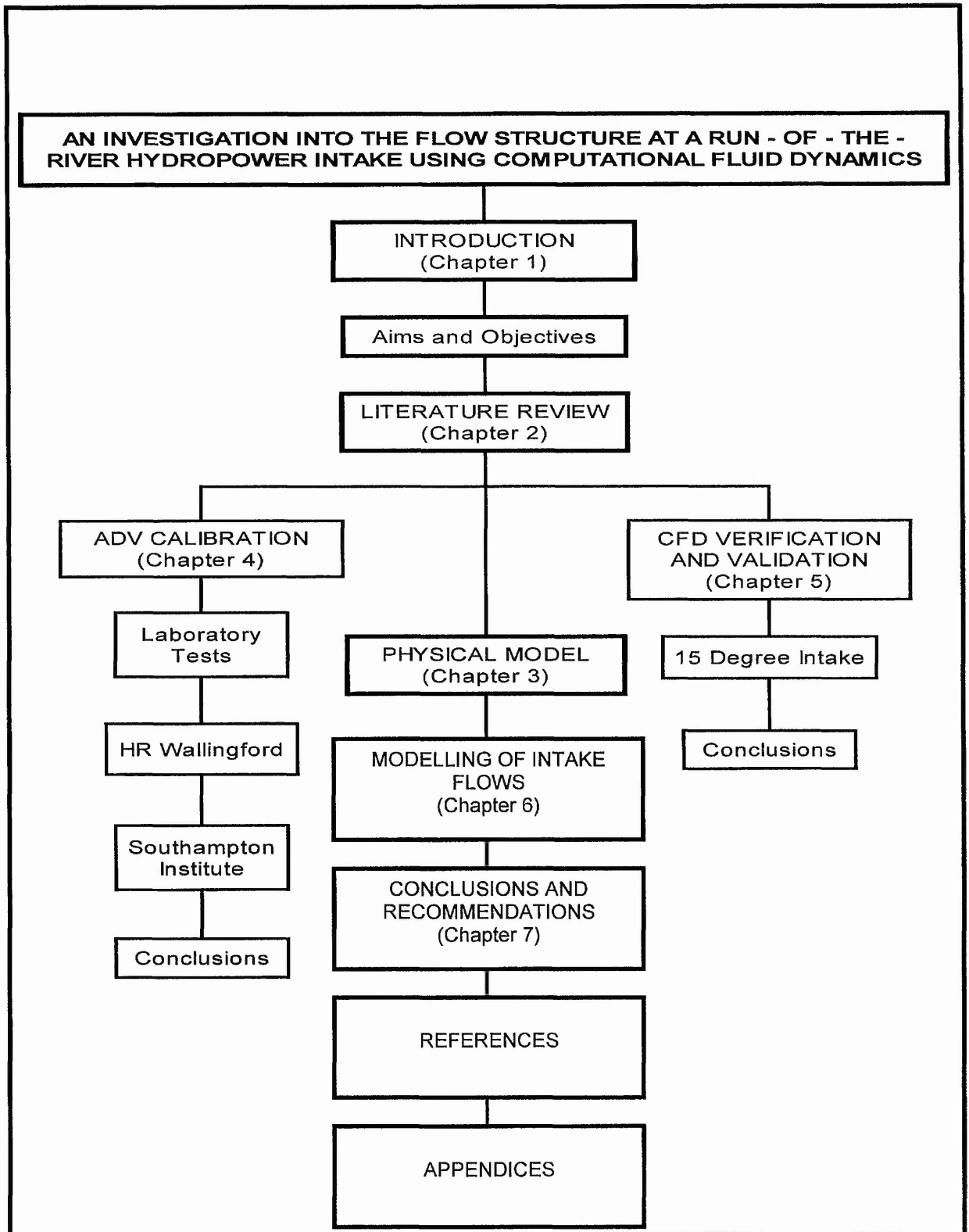
Figure 1.4   Outline of Thesis.

1.3   PHYSICAL MODEL AND MEASUREMENT EQUIPMENT

An overview of the physical modelling and the measurement equipment used in the investigation is given here. The reader is referred to chapter 3 for further details.

1.3.1 Physical Modelling

A physical model was constructed, as part of the investigation, in the hydraulics laboratory of the Department of Civil and Structural Engineering. The model was contained within a tank measuring 7.8m long by 1.2m wide by 1.5m deep and was designed to represent a generalised run of the river intake in which the intake angle could be varied between 15 and 30 degrees to the main channel. The model was designed using the Froude Law of similarity such that the dimensions of the model could realistically represent a prototype situation. Water was delivered to the model via a centrifugal pump capable of delivering flows of up to 150 l/s, through a 200mm diameter plastic pipe to inlet baffles in the tank. Measurements of flow in the model were determined using, an orifice plate positioned in the inlet pipe connected to an electronic manometer, a sharp crested weir placed in the main and inlet channels and the velocity area method with velocity meters. A flow staightening device was included at the inlet to the model. The model was constructed from marine grade ply in order to prevent rotting. The surface of the ply was also painted using gloss paint. The Manning's friction coefficient n, for the model was assumed to be equal to 0.012. A schematic diagram of the model arrangement is shown in Figure 1.5.

The model was used to investigate the flow structure at the generalised intake with changes in Reynolds number, intake angle, depth of flow and flow split ratio, Qr. The effects of friction on the flow structure at the intake was not investigated in this study. Measurements of velocity vectors, turbulent intensity, turbulent kinetic energy and the kurtosis of the velocity measurements taken in the model were used to validate and verify the computational analyses which were carried out as part of the investigation.
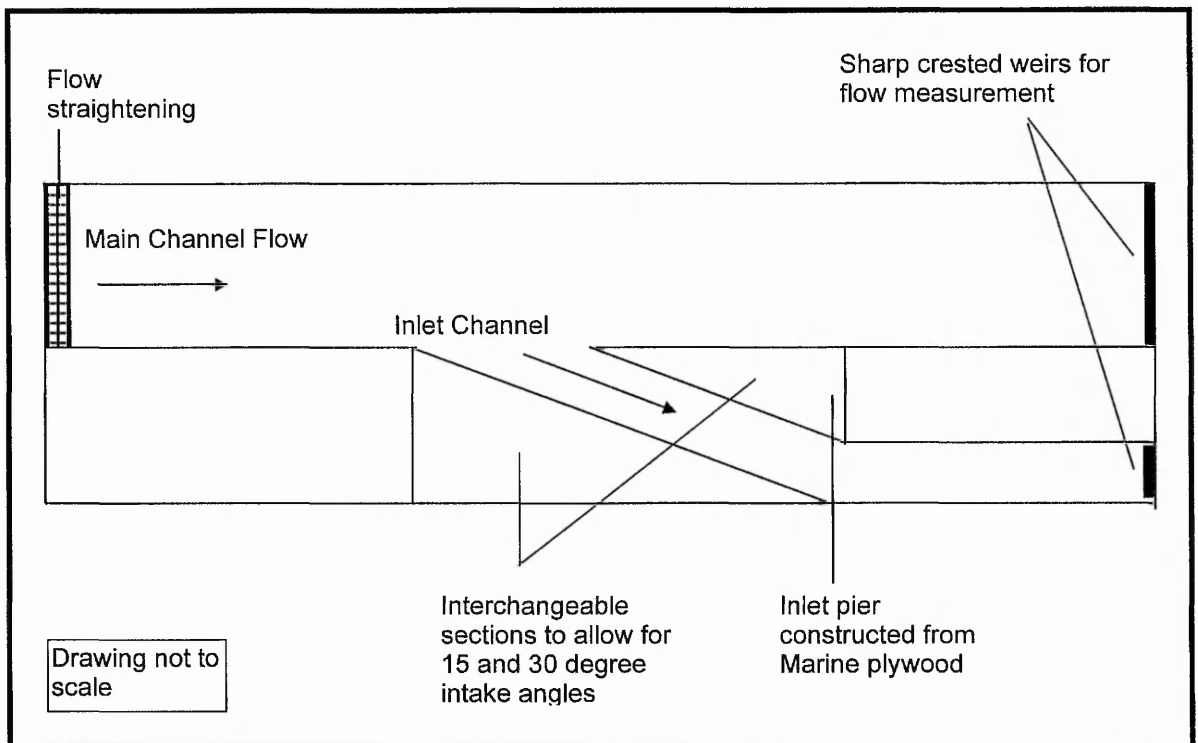
Figure 1.5   Schematic plan of physical model arrangement.

For greater detail of the physical model the reader is referred to the Appendix A, Drawings CB/1/11/96 and CB/2/11/96 and chapter 3.

1.3.2 Measurement Equipment

Velocity measurements in the model were undertaken using two methods; the Acoustic Doppler Velocimeter and a propeller current meter.

Propeller Meter

The propeller current meter is one of the most universally used instruments for velocity determination. The principle is based upon the relationship between the velocity of the water and the resulting angular velocity of the impeller rotor blade. By placing the current meter at a point in the flow and counting the number of revolutions of the impeller during a measured time interval, the velocity of the water at that point can be determined. The number of revolutions of the impeller is obtained by various means depending on the design of the meter but normally this is achieved by an electric circuit through the contact chamber. Contact points or a reed switch in the chamber are designed to complete an electric circuit at selected frequencies of

revolution, normally once per revolution. From the switch a twin conductor cable carries the electric pulses generated by each revolution of the impeller to a counter device. In all types of design the electrical impulses produce a signal which registers a unit on a counting device. Intervals of time are measured by a stopwatch or by an automatic timing device. With all propeller meters, a velocity formula relating to the number of revolutions per second, is supplied by the manufacturer. One problem with the propeller meter is that it is not possible to detect the angle of the velocity vector in the flow. The meter will only measure the velocity in the direction in which the impeller is pointing. For physical modelling purposes, the impeller is usually much smaller than for river flow measurement.

The Acoustic Doppler Velocimeter

The Acoustic Doppler Velocimeter (ADV) is an electronic piece of apparatus that measures fluid velocity in three components. The ADV uses acoustic sensing techniques to measure flow in a remote sampling volume. The measured flow is undisturbed by the presence of the probe. Data are recorded at an output rate of 25 Hertz (Hz). The 3-D velocity range is ± 2.5 m/s. The instrument consists of three modules: the measuring probe, the conditioning module and the processing module (see Figure 1.6). The measurement probe is attached to the conditioning module which contains low noise electronics enclosed in a waterproof housing.
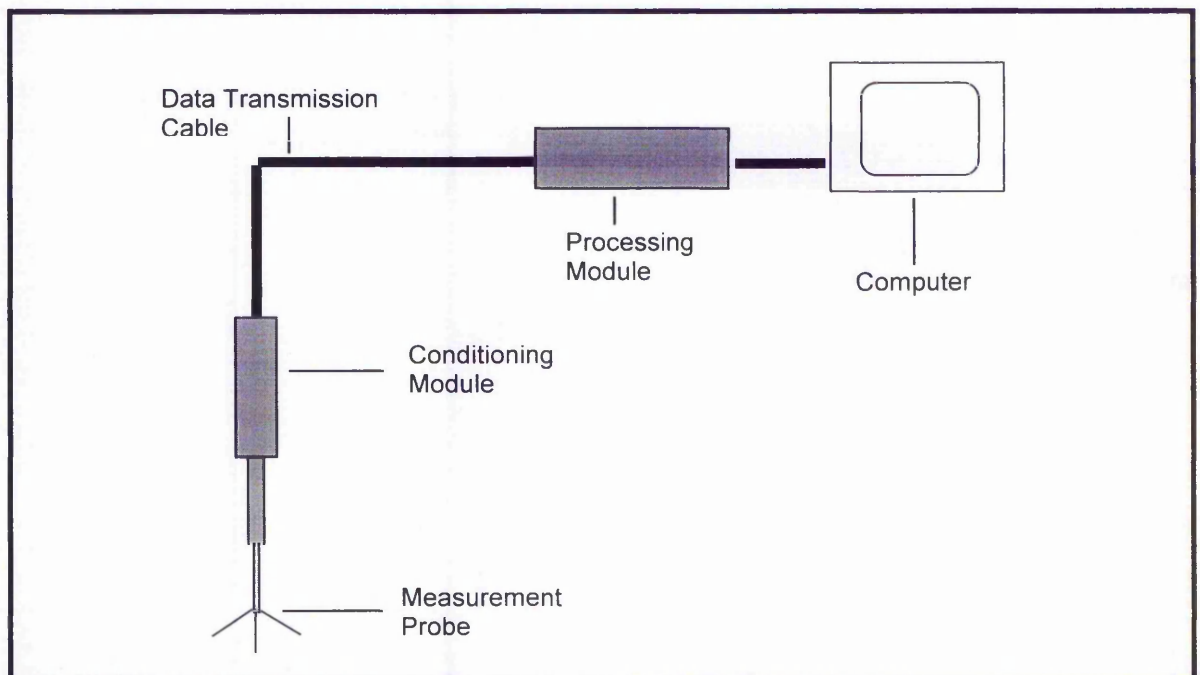
Figure 1.6   Schematic diagram of ADV modules.

The acoustic sensor consists of one transmit transducer and three receive transducers. The receive transducers are mounted on short arms around the transmit transducer at 120^0 azimuth intervals. The acoustic beams are orientated so that the receive beams intercept the transmit beam at a point located approximately 50mm below the sensor. The interception of these four beams, together with the width of the transmit pulse, define the sampling volume. This volume is 3-9mm long and approximately 6mm in diameter. All three receivers must be submerged in the liquid to be measured to ensure correct velocity measurements. Figure 1.7 shows a schematic elevation of the ADV probe and Figure 1.8 shows a photograph of the probe.
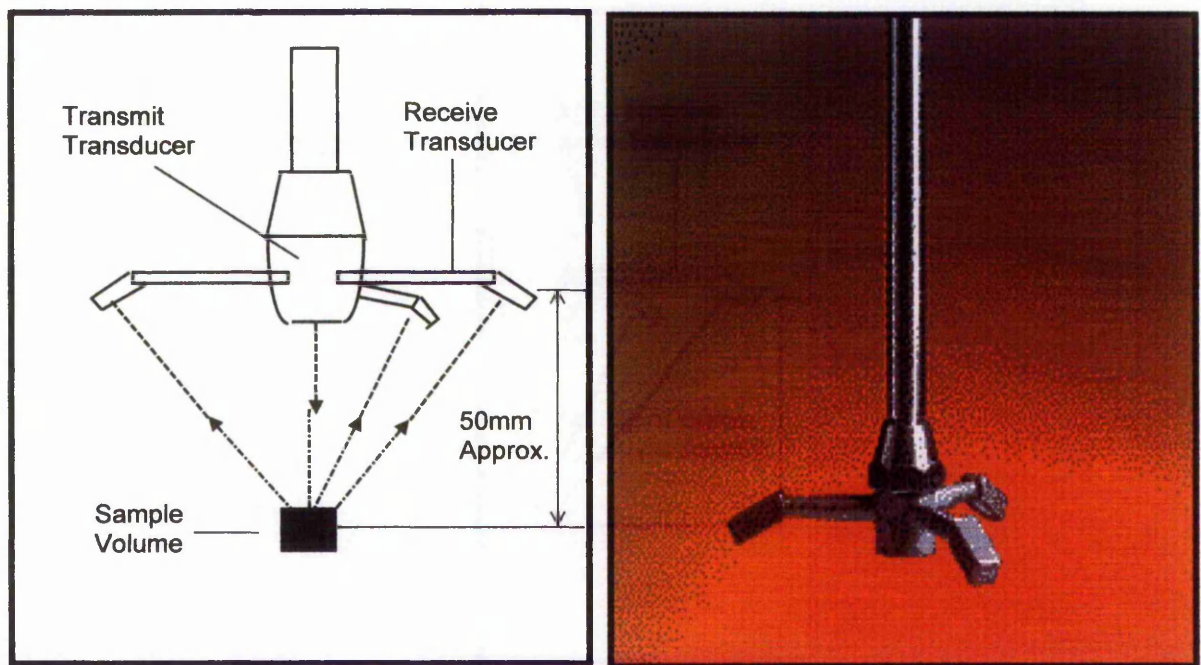
Figure 1.7 Schematic diagram of ADV probe.   Figure 1.8 Photograph of ADV probe.

The analogue output from the ADV is analysed using post processing software and data such as the 3D velocity components, the root mean square (RMS) of the velocity, the skewness and kurtosis of the data, the signal to noise ratio (SNR) and the correlation (COR) of the data can be viewed through the graphical user interface (GUI). Examples of the GUI are shown by Figures 1.9 and 1.10.
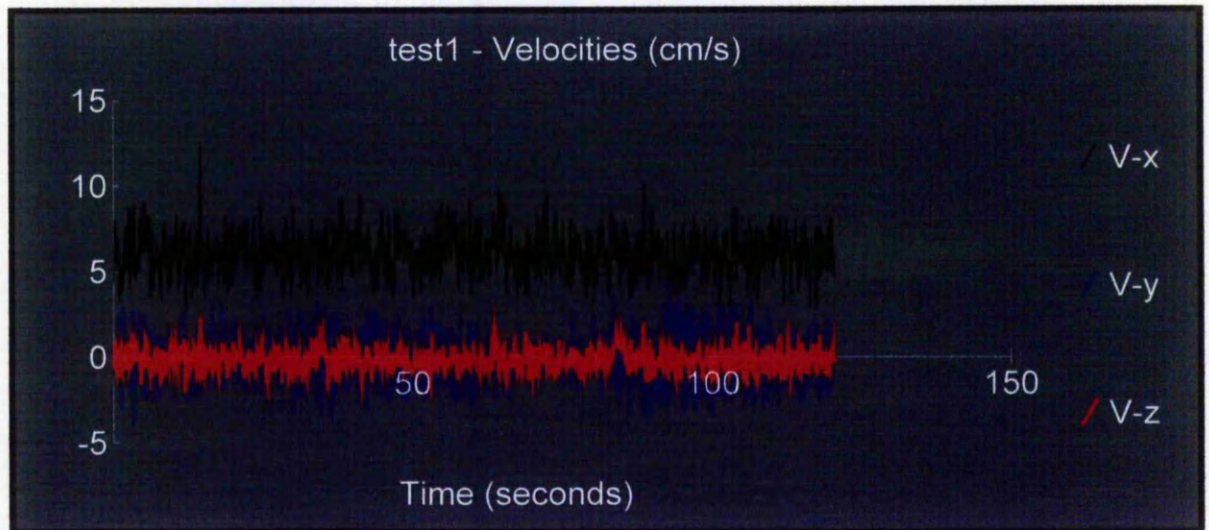
Figure 1.9   Velocity data.

Figure 1.10   SNR and COR data.

1.4   COMPUTATIONAL MODEL

The computational model used in this study is called SSIIM and was developed by Dr Nils Olsen of the University of Trondheim. SSIIM is an acronym for Sediment Simulation In Intakes with Multiblock option. The program is designed for use in river, environmental, hydraulic and sedimentation engineering. The program solves the Navier-Stokes equations with the k - epsilon turbulence model on a three-dimensional, non-orthogonal structured grid (see Figures 1.11 and 1.12).

The Navier Stokes equation for non-compressible and constant density flow can be modelled as :

$$\frac{\partial U_i}{\partial t} + U_j \frac{\partial U_i}{\partial x_j} = \frac{1}{\rho} \cdot \frac{\partial}{\partial x_j} (-P \delta_{ij} - \rho.\overline{u_i u_j})$$　　　1.5
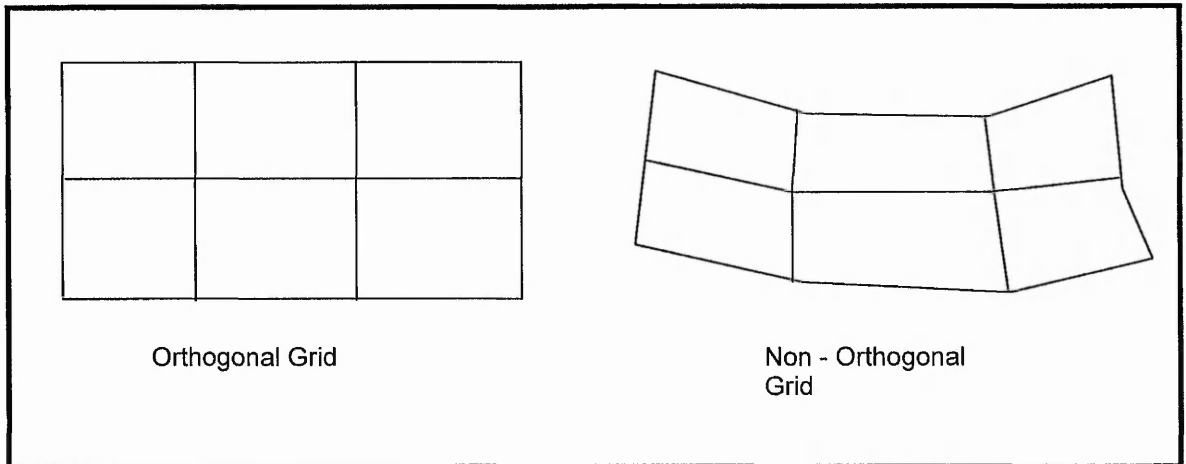
Figure 1.11　Orthogonal and non orthogonal grid.

A control volume method is used for the discretisation, in conjunction with the Power Law (POW) scheme or the Second Order Upwind (SOU) scheme for discretisation of the convective terms in the Navier Stokes equation. The Semi Implicit Method of Pressure Linked Equations (SIMPLE) method is used to solve the pressure coupling in the Navier Stokes equations. The modification to the SIMPLE method called the SIMPLEC method is also available as an option. The solution is implicit including the boundaries of the grid which gives the velocity field over the geometry.
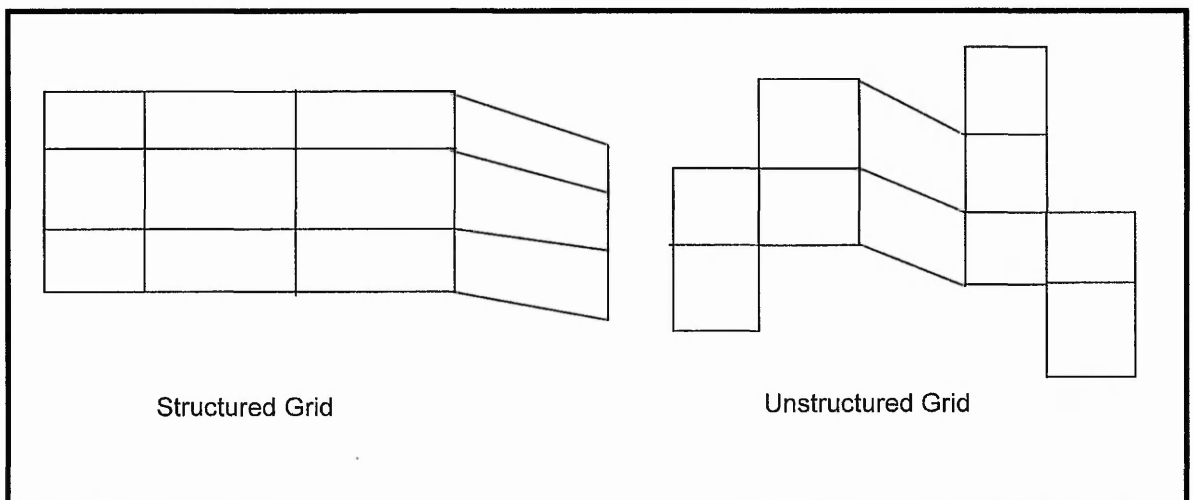
Figure 1.12　Structured and unstructured grids.

The initial free water surface is generated by a standard one dimensional backwater calculation. The friction loss is generated by Manning's formula. It is also possible for

the user to specify the free water surface. Wall laws for rough boundaries are used as described by Schlichting (1979).

The model has a user interface with capabilities of presenting graphical plots of velocity vectors and scalar variables. The plots show a two dimensional view of the three dimensional grid. Three plots showing the geometry in plan, in cross section and in longitudinal profile are available. In addition it is possible to simulate particle animation for visualisation purposes.

The model includes several utilities which make it easier to input data. The most commonly used data can be given in dialog boxes. Several of the modules in the program can be run simultaneously. This exploits the multi-tasking capabilities of the operating system which SSIIM runs under, IBM's OS/2 Warp. There is an interactive grid editor with elliptic and transfinite interpolation. Grids and some of the input data can be changed during the calculation. This can be useful for convergence purposes or when optimising the geometry with respect to the flow field. An example of the GUI is shown by Figure 1.13.

Some of the most important limitations of the program are listed below :-
- The program neglects non-orthogonal diffusive terms.
- The program neglects stress terms for elements that are not at the boundary
- The grid lines in the vertical direction have to be completely vertical.
- Internal walls cannot be used within two cells from a multiblock connection.
- Kinematic viscosity and density of the fluid are equivalent to water at 20^0 C.
- Fully turbulent flow is assumed.
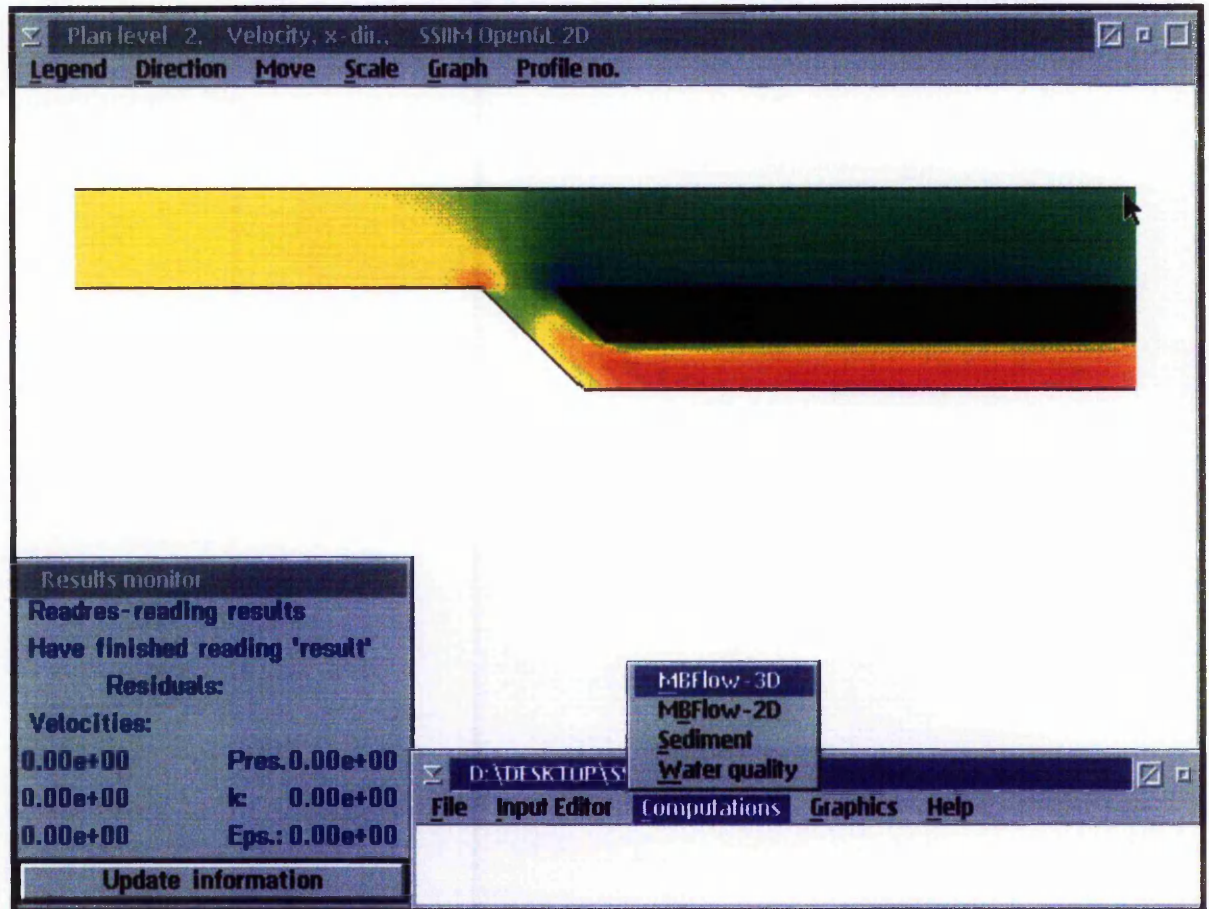
Figure 1.13   Sample GUI from SSIIM.

SSIIM can also be used for sediment transport analyses. The velocities calculated in the flow field by the model are used when solving the convection-diffusion equations for different sediment sizes. This gives the trap efficiency and sediment deposition pattern. However, within the constraints of this thesis, the sediment transport capabilities of the model are not used or tested.

1.5   AIMS, OBJECTIVES AND ORIGINAL CONTRIBUTION TO KNOWLEDGE

1.5.1   Aims

The aims of the investigation are to :-

• Provide new data for the nature and pattern of open channel, free surface, intake flow splits using physical and computational modelling.

• Provide engineering design guidelines for the prediction of various parameters associated with the flow structure at a generalised intake of small scale run of the

river hydropower, to improve the efficiency by optimising the design of the associated civils works.

1.5.2 Objectives

The objectives employed to achieve the aims are :-

- Familiarisation with the previously conducted research by a thorough literature review into calibration of the Acoustic Doppler Velocimeter (ADV), validation of numerical models and the flow structure at open channel diversions.

- The design and construction of a physical model suitable for the study of the flow features at an intake structure.

- Provide an assessment and validation of a recently developed 3D numerical model for its suitability to investigate intake flow.

- Provide an assessment and calibration of a recently developed Acoustic Doppler Velocimeter (ADV) for measuring 3D fluid velocities.

1.5.3 Original Contribution to Knowledge

The areas of original contribution to knowledge contained in this thesis are :-

- Calibration of the Acoustic Doppler Velocimeter (ADV) independently of the manufacturer.

- Validation and verification of the 3D numerical code independently of its' author and an assessment of the suitability of the code to predict the flow structure at open channel diversions.

- Provide new, previously unavailable data of the flow structure at a generalised open channel diversion.

- Provide a direct comparison of a relatively new computational predictive tool to actual physical measurements.

- Prediction of the position of the 3D dividing streamplane in a generalised intake structure for intake angles ranging from 15 to 45 degrees based upon computational analyses with validation by physical measurements.

- Prediction of the turbulent kinetic energy for the generalised intake based upon computational analyses with validation by physical measurements.

2

LITERATURE REVIEW

2.1   INTRODUCTION

Chapter 1 has given the reader an insight into the problem that has been investigated by this thesis. At this point it is appropriate to re-iterate the parameters which affect energy losses at intakes. Energy losses occur as a result of the flow patterns induced by the sudden change in flow direction that gives rise to a complex three dimensional flow structure that is characterised by strong secondary circulation, dramatic pressure variations and depth varying flow features. The parameters which affect these features include:

- Main channel Reynolds Number.
- The discharge ratio.
- The diversion angle.
- The aspect ratio of the channel.
- The main channel bed roughness.

This literature review therefore deals primarily with previous research that has been undertaken with regard to identifying and quantifying the effects of the above parameters. It also provides a critical review of the previous research undertaken, highlighting shortfalls and problems with the findings. Reference will be made to the research highlighted by this chapter in subsequent chapters of this thesis. Minor literature reviews have also been undertaken with regard to the other subsections of this research study, namely ADV calibration and CFD validation. This information is contained within chapters 4 and 5 respectively.

Three examples can be presented here which typify the problems associated with intakes when poor hydraulic design has taken place. Yildiz and Kuzum (1994) investigated the problems associated with poor intake design on the Seyhan river in Turkey. In 1992 the Syhan II hydroelectirc plant started operating producing 4.5MW instead of the planned 7.5MW. The efficiency of the turbines was tested by GEC Alsthom Neypric Minihydro and compared well with results obtained from turbine model results. Therefore a further physical model was constructed, to test the hydraulic design of the power plant.

The intake to the plant consisted of three channels separated by wing walls which passed flow to three bulb turbines. It was found that the shape and angle of the wing walls to the main channel flow were causing re-circulation and eddy regions at the entrance to the intake. This, in turn, caused uneven flow to enter the turbines resulting in loss of power production and inevitable excessive wear to the turbines. It was found that only one of the turbines was operating to its' design performance with the other two operating well below. The researchers found that by changing the shape and angle of the intake wing walls in the physical model, the efficiency of the turbines could be vastly improved. The findings of the physical model study were applied to the prototype and significant improvements in power production were observed.

Cabelka (1950) undertook an extremely similar physical model study at a low head hydropower plant in Czechoslovakia. He found that excessive re-circulation was occurring at a 90 degree intake to the hydropower plant which was causing a loss in power production of 300 000 kWh per annum. The yearly output of the plant between 1911 and 1920 averaged 3.3 million kWh and the design output was 5.9 million kWh. Cabelka's physical model study and his subsequent recommendations to improve the intake angle and shape, increased the output of the plant by approximately 50%.

Cabelka also investigated the possibilities of improving the design of new low head hydropower plants built near weirs and proposed that "the axis of the intake into the turbine should be turned about the turbine axis to suit the flow of the river and every part of the structure built into the water flow should be streamlined. Such an arrangement would greatly facilitate the correct hydraulic design of the intake and

outflow from the turbines. The water flow in a power station to such design would be considerably more favourable and the hydraulic losses thereby considerably reduced and the efficiency of the turbines increased". Cabelka made the observation that if the weir was situated in a bend of the river, the power plant should be built on the outside bank to prevent, or at least decrease, the build up of sediment in the intake. He stated that the shape of the separating weir between the weir and the intake should correspond with the extreme streamline flow existing during the major part of the year. The projection of the front part of the separation pier upstream should be as small as possible and should be proportional to the height of the overfall in the adjacent weir section, so that the flow from the upstream section to the intake is continuous and the hydraulic losses are kept to a minimum.

Cabelka commented that the proposed layout of new low head hydraulic power plants presents several advantages from the hydraulic point of view and also from the economic aspect both in terms of erection and operation. These advantages are: uniform and undisturbed intake of water and outflow from the turbines resulting in small hydraulic losses and good turbine efficiency; a decreased rate of clogging by sediment carried by the stream, resulting in lower maintenance costs; and lower initial costs. Cabelka made these comments in 1950 and as will be shown by this thesis, it is unfortunate that frequently his advice was subsequently not followed.

Bowles in 1995 undertook a research study visit to the USA (see also chapter 1) in which he found that several of the sites that he visited had problems with energy losses at the intakes. A significant example (Figure 1.1), was that of a site in Maine where a re-circulating eddy region was causing a loss of power production of up to 30%.

This literature review presents a summary of the present knowledge into the flow structure at intakes with reference to low head, small hydropower. The evolving descriptions or such diversion flows are then presented based upon a rigorous literature survey undertaken by the author. These descriptions are divided logically into the following sections: field observations and laboratory experiments; observations by biomedical researchers; theoretical model descriptions; and finally, numerical model descriptions. A concise summary of this research is then presented in the conclusions to the chapter.

2.1.1 Flow Structure of Diversion Flows

Flow structures and certain features of the structure have been identified by numerous researchers in recent years. These have mainly comprised researchers working in the fields of sediment transport processes (Neary 1992, 1993, Neary *et al.* 1994, Hager 1984, Ramamurthy & Satish 1988) to list a few. Researchers involved in studying blood flow in arteries have also identified relevant structures (Karino *et al* 1979, Bharadvaj *et al.* 1982, Cho *et al* 1985, Lee & Chu 1992,).

The findings of Neary are summarised by Figure 2.1.
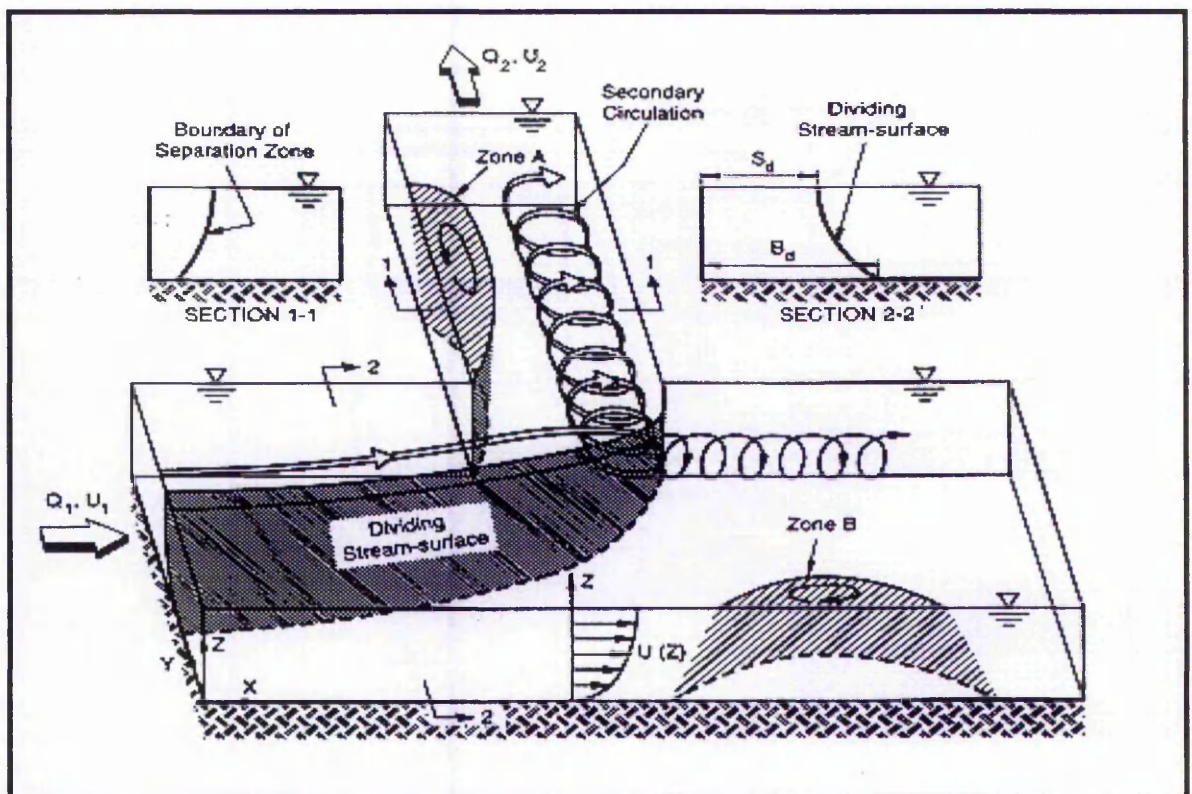
Figure 2.1   Three dimensional flow patterns in a 90 degree rectangular diversion. (from Neary, 1994)

Neary describes the flow structure exhibited above as follows:

"As the flow approaches the intake, it is accelerated laterally by the suction pressure at the end of the branch channel. This causes the main flow to divide so that a portion enters the branch channel with the remainder continuing downstream in the main channel. The portion withdrawn by the branch is delineated by a curved shear

layer surface, denoted as the dividing stream surface. Due to the streamwise curvature of the dividing stream surface, the diverted flow experiences an imbalance between the transverse pressure gradient and shear and centrifugal forces that initiates a clockwise secondary motion cell. This secondary motion interacts with the separation bubble along the inner wall of the branch channel (Zone A) resulting in a very complex three dimensional flow. Flow curvature may also induce a counter-clockwise secondary motion cell in the main channel downstream of the junction region. Furthermore, a separation bubble may form along the outer wall of the main channel (Zone B) depending on the cross sectional shape and the discharge ratio. This rarely occurs at water intakes with relatively low discharge ratios, but is quite common in branching arteries and natural river bifurcations".

There is a significant pressure variation present across the face of the entrance to the inlet channel. A low pressure point is located at the upstream corner with a high pressure point located at the downstream corner of the intake entrance. These high and low pressure regions are associated with high and low water surface elevations respectively but these are not usually significant for the range of flow conditions encountered at water intakes. The high pressure region is usually referred to as the stagnation region where the dividing streamplane usually ends and where downflow and secondary circulation cells can often occur.

The dividing streamplane and zones A and B are not uniformly distributed over the flow depth with the lower portion of the streamplane near the bed extending further into the main channel than the portion of the streamplane near to the surface of the flow. These are signified by Bd and Sd respectively in Figure 2.1. Zone A decreases in size form the water surface to the bed whereas Zone B, if present, increases in size towards the bed.

Neary illustrated the energy losses with regard to a 90 degree intake. The flow features and structures are extremely similar for other intake angles although Zone B is not observed. It was part of the objectives of this study to highlight and illustrate these findings for intake angles ranging from 15 to 45 degrees. Although much of the literature referenced here refers to 90 degree intake angles the principles that are outlined can be applied to other intake angles. Attention is particularly focussed to literature that deals with similar parameters identified by this study, namely the

effects of Reynolds Number, discharge ratio, diversion angle and aspect ratio.

2.2   EVOLVING DESCRIPTIONS OF DIVERSION FLOWS

The first known description of a diversion flow was illustrated by Leonardo Da Vinci in approximately 1507 and is shown by Figure 2.2.
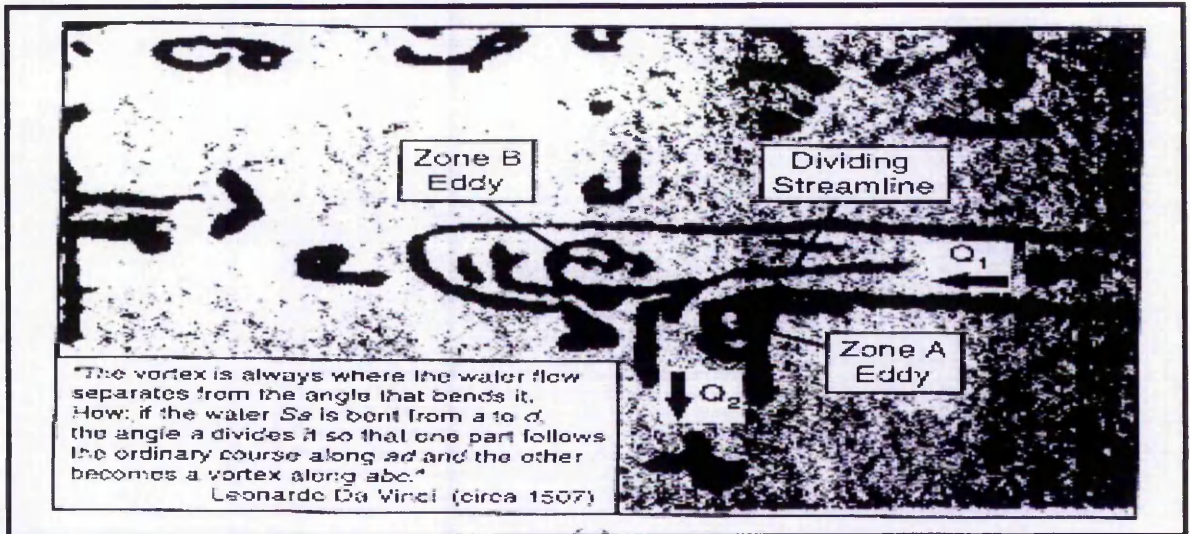
Figure 2.2   The early conceptual model of Leonardo Da Vinci.

Da Vinci's investigation was two-dimensional and the image clearly showed the dividing streamplane that is typical of dividing flow. Also illustrated are the eddy zones A and B. Da Vinci's illustration was copied and developed by numerous researchers in the following centuries including Francesco Cardinali in 1828 who developed Da Vinci's work and which resembles the findings of recent researchers. His depiction of dividing flow is shown by Figure 2.3.
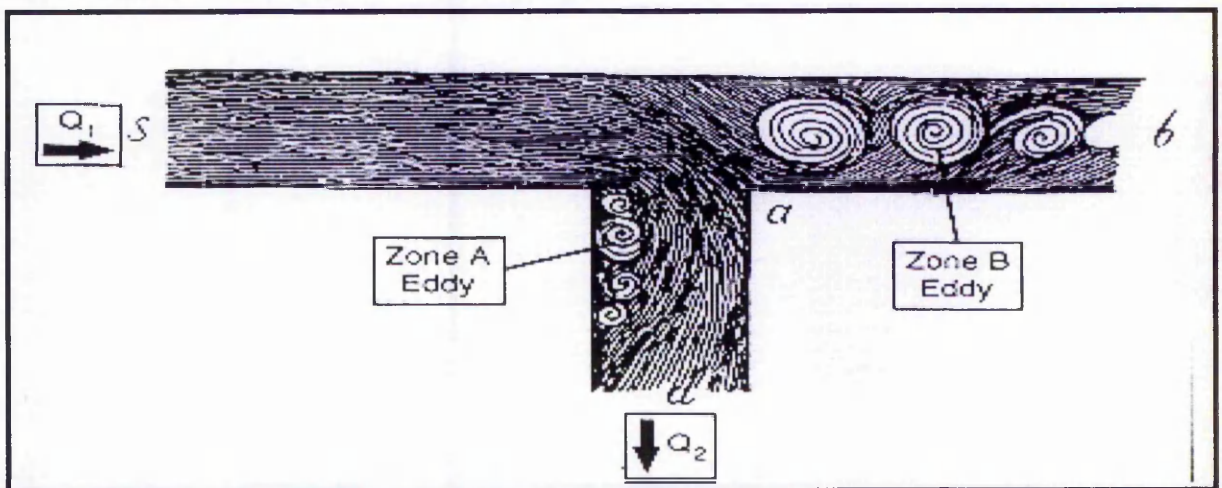
Figure 2.3   Conceptual model of Francesco Cardinali .

The following sections of this review show how the early ideas of Da Vinci and Cardinali were developed to the present day findings. The review is sub-divided into sections; field and laboratory investigations, theoretical models and numerical simulations. Reference is also made to the finding of biomedical researchers. Biomedical researchers have investigated situations with low Reynolds Numbers and closed conduits in contrast to environmental hydraulic engineering situations where high Reynolds numbers and open channels are prevalent. However the flow features that have been identified by both disciplines are remarkably similar.

2.2.1 Field and Laboratory Observations

A large proportion of the investigations into the flow structure at lateral intakes has been undertaken by engineers interested in sediment transport into intake structures. These engineers have found that large amounts of bed load sediment was transported into the intakes which suggested a three dimensional flow structure in which the dividing streamplane near the bed extends further into the main channel than near the surface. The description of the flow pattern has evolved over the last 40 years with observations of prototype intakes and experimental investigations.

Linder (1952) reported experimental investigations in which the proportion of sediment entering the intake channel was related to the intake angle. He reported that the proportion of the main channel sediment entering the intake channel decreased with intake angles from 30 to 120 degrees then increased slightly with angles up to 150 degrees. These findings were obviously related to the position of the dividing streamplane although he did not specifically identify its position. He also identified the occurrence of a helicoidal flow pattern "initiated by the difference between the centrifugal force at the surface and that at the bed level".

Avery (1989) reported flow patterns and streamlines based on physical observation on flows into a 90 degree diversion in which he highlighted flow separation and recirculation. He isolated stagnation points S1 and S2 depicted by Figure 2.4.

Figure 2.4   Streamlines at a 90 degree intake (from Avery, 1989).

Vanoni (1975), Bondurant and Thomas (1952) and Abdel (1949) also made physical observations and experimental invetigations which developed the initial theories of Da Vinci.

Despite the evidence of three dimensionality given by field observations, the most comprehensive experimental studies of diversion flows were concerned mainly with backwater characteristics and energy losses which depended largely upon two dimensional descriptions of the recirculating eddies observed in the main and branch channels. Taylor (1944) investigated the division of the flow at a lateral intake which he stated was dependent upon the backwater characteristics of the two branch channels and the dynamic conditions existing at the junction. He made physical measurements of the flow split at a 90 degree intake but made no comparison to theory. He assumed that the main and inlet channels were not controlled by gates but merely by the characteristics of the branches themselves. He also assumed that the branch channels were of the same cross sectional area. He used the notation illustrated in Figure 2.5 for the variables. The quantities flowing in each channel and the corresponding depths were represented as a function of the following seven factors: The intake angle θ; the three depths y_1, y_2, y_3; any two of three quantities, say Q_3 and Q_2; and the velocity with which the stream enters the branch. Taylor

stated that for any given intake angle θ, it was possible by dimensional analyses to reduce the remaining six variables to four.
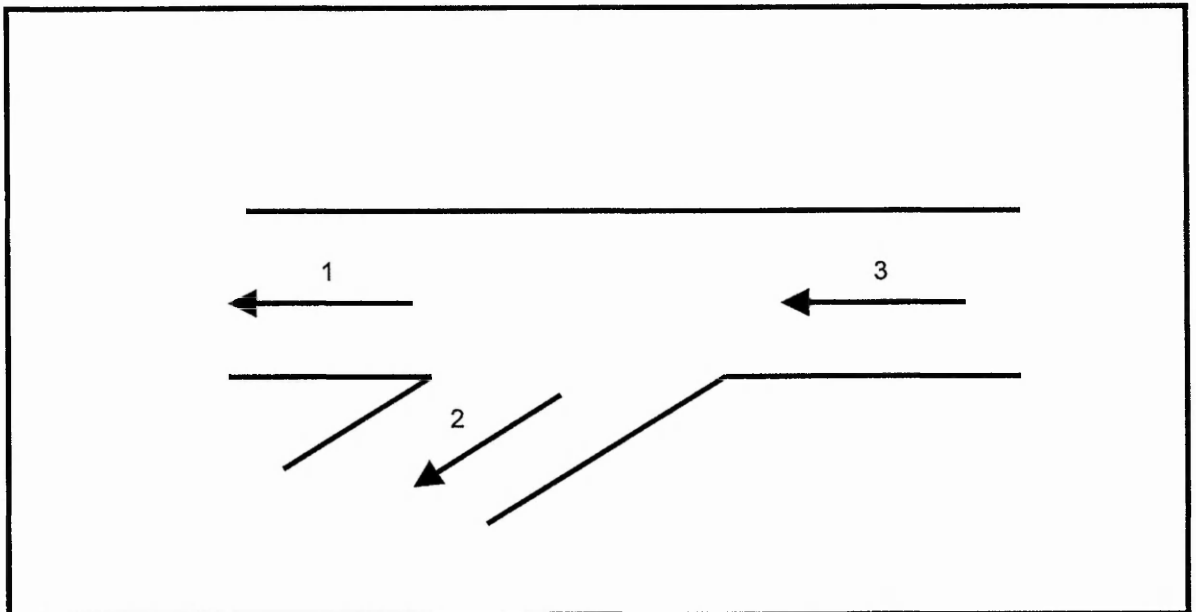
Figure 2.5   Notation used by Taylor.

They were : $\dfrac{Q_2}{Q_3}, \dfrac{y_3}{y_2}, \dfrac{y_1}{y_2}$ and $\dfrac{(V_3)^2}{2.g.y_3} = k_3$ 2.1

Where: y = depth, Q = flow, V = depth averaged velocity.

Figure 2.6 shows the experimentally determined data for a channel division in which $\theta = 90^0$.
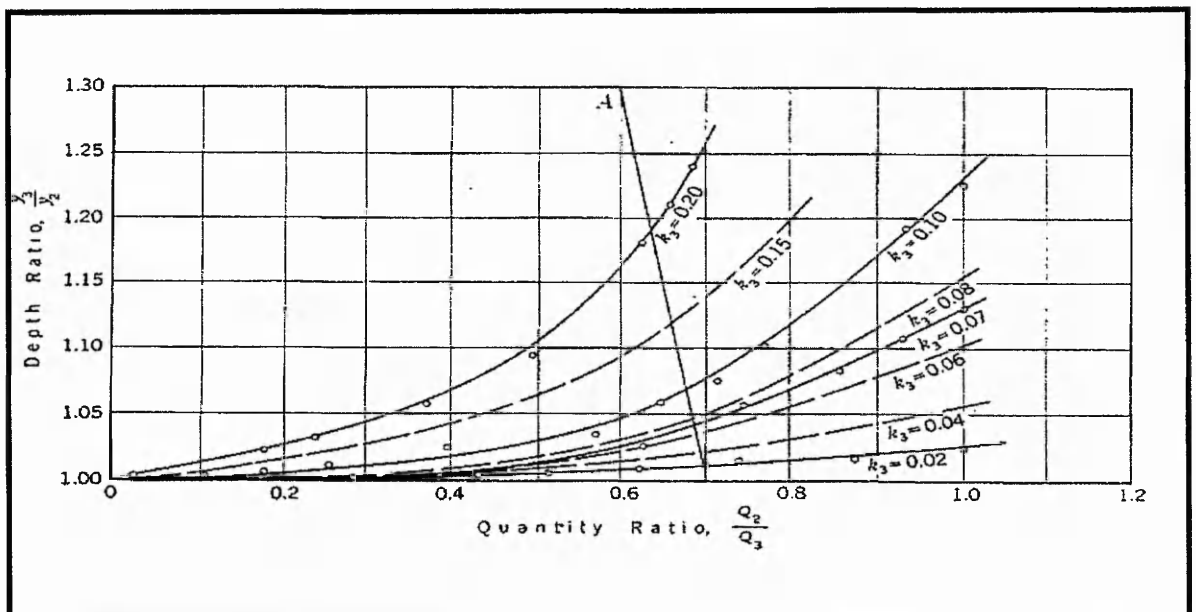
Figure 2.6   Characteristic of stream division in which $\theta = 90$ (from Taylor, 1944).

Figure 2.7 shows the relationship that Taylor found to exist among the three depths within the range of the values of k_3 considered.
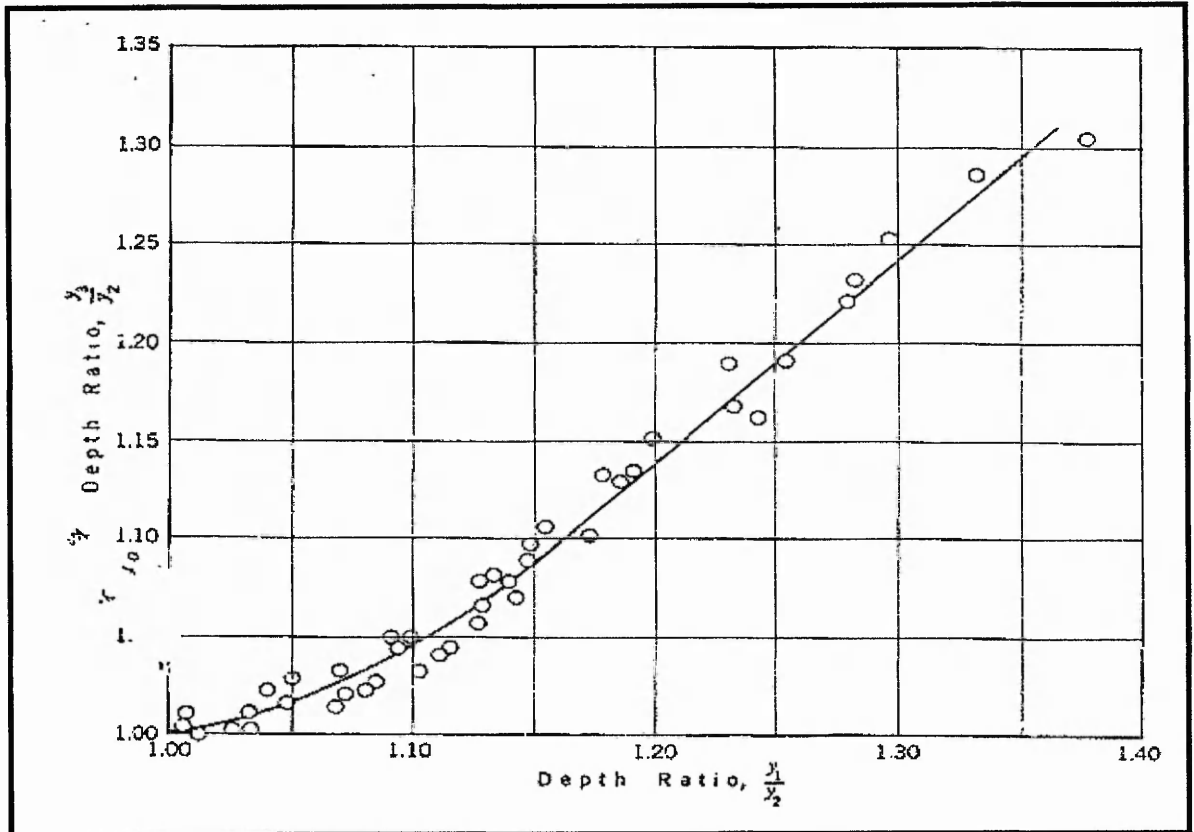
Figure 2.7   Relationship between depths in a 90^0 stream division (from Taylor, 1944).

Using these graphs, Taylor assumed a flow split Q_2 / Q_3 say 0.5, from which the depths y_1 and y_2 could be fixed. The ratio of y_3 to y_2 was then determined using Figure 2.7. It was possible by choosing various values of Q_2, to obtain a curve between Q_2 / Q_3 and y_3 / y_2. For the assumed conditions this curve appears as A in Figure 2.6. The locus of the points of intersection of curve A and the k_3 curves gave all the possible combinations of the variables. The value of k_3 with which Q_3 entered the branch was then determined. The curve A was then re-plotted in terms of the numerical values of y_3 and factor k_3 using rating curves for the channels which Taylor constructed and his graph of k_3 against y_3 (see Figure 2.8) onto which curve B was plotted.

The correct value of k_3 had to satisfy not only curve B but also the relationship for k_3 . This was found by plotting the relationship for k_3 and obtaining the intersection with

curve B. This gave the correct values of k_3 and y_3 were then back substituted to obtain the flows in the main and inlet channel.
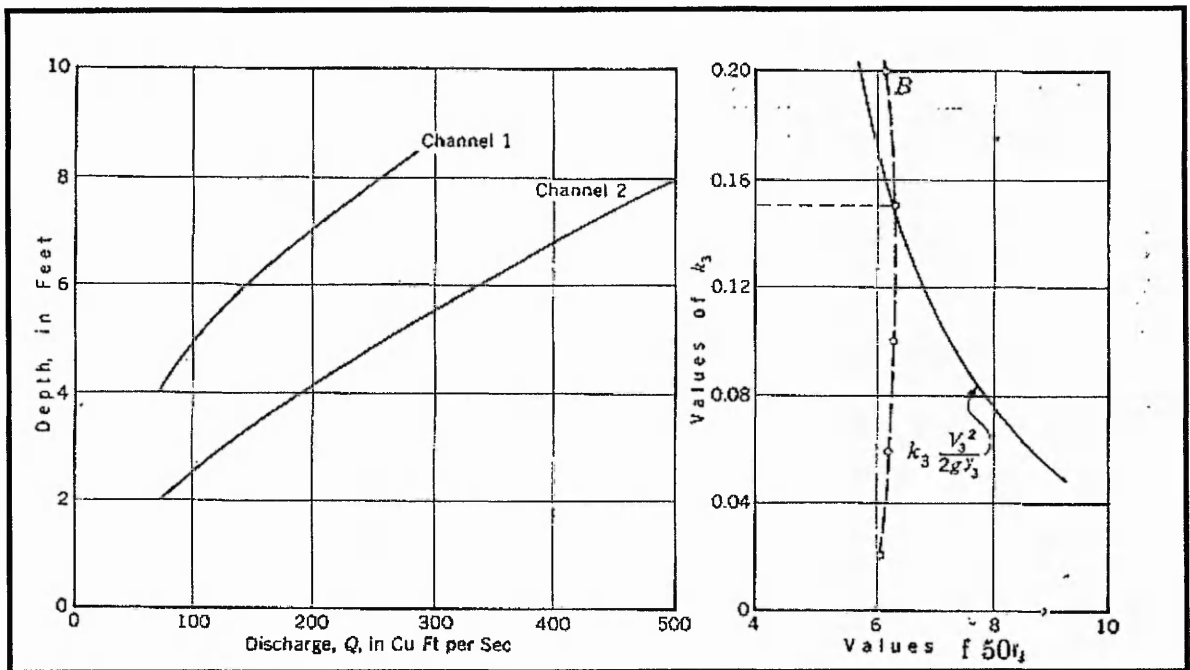
Figure 2.8   Rating curves and factor graph (from Taylor, 1944)

A major problem with Taylor's interpretation was that a factor in the derivation was the depth. Frequently it is impossible to measure the depth in the channel to significant accuracy. The study was also limited because he assumed that the inflows to the branches were not controlled by gates, and he only considered a 90 degree intake angle. These situations rarely occur in hydraulic engineering.

Ramamurthy and Satish (1990) studied the solution to the general case of dividing flow through right angled junctions for all branch flow conditions. Thus the discharge ratio Q_2 / Q_1 is expressed in terms of the Froude number F_1 and the depth ratio Y_1 / Y_2. Note that Ramamurthy and Satish used a different notation to Taylor. Figure 2.9 shows the experimental situation and the notation used.

A derivation using the momentum equation was used by Ramamurthy and Satish to produce the following formulae which express the Froude number in the main channel downstream of the branch, F_2, in terms of F_1 and R_q and R_y where:

$$R_q = \frac{Q_2}{Q_1}, R_y = \frac{Y_1}{Y_2}, \frac{Q_3}{Q_1} = 1 - R_q \qquad 2.2$$

Figure 2.9   Dividing flow in open channels (from Ramamurthy and Satish, 1990).

$$\frac{1-R_q}{40}.F_1^4 + \left(\frac{1}{6}+\frac{5}{6}R_q - R_q^2 R_y\right)F_1^2 + \frac{R_y^2-1}{2R_y^2} = 0 \qquad 2.3$$

$$\frac{F_2^{\frac{4}{3}}}{1+2F_2^2} = \frac{F_1^{\frac{4}{3}} R_q^{\frac{4}{3}}}{1+2F_1^2\left[\frac{1}{6}+\frac{5}{6}R_q + \frac{F_1^2}{40}\left(1-R_q\right)\right]} \qquad 2.4$$

Ramamurthy and Satish produced a graph of F_1 in terms of R_1 where k = 0.83, where:

$$k = \frac{5}{6} - \frac{\left(F_1^2\right)}{40} \qquad 2.5$$

This is shown by Figure 2.10. They also collected experimental data to compare to their theoretical solutions. Tables 2.1 and 2.2 show that they obtained fair agreement with both their own data and that of Sridharan (1966). Ramamurthy and Satish method accommodated control gates and did not require the measurement of flow depths in the branch channel but it only considered 90 degree intake angles. It was also only a two dimensional study. However, their method had much wider

applications than previous studies because there were no restrictions to the nature of the flow in the branch channel.
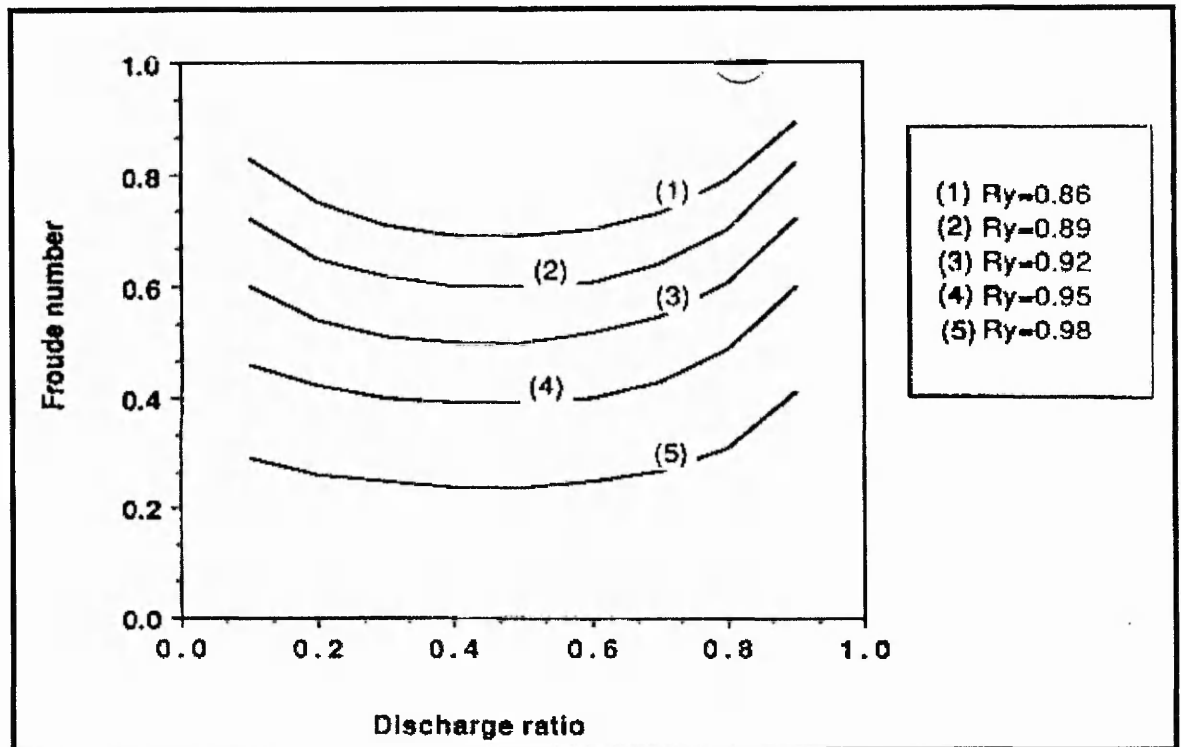
Figure 2.10 F_1 in terms of R_y (k=0.82) (from Ramamurthy and Satish, 1990).

R_q	Y_1 (m)	F_1	Y_2 (m) Calculated	Y_2 (m) Measured	Error (%)
0.15	0.077	0.48	0.082	0.082	-1
0.16	0.079	0.47	0.084	0.083	-1
0.25	0.088	0.39	0.092	0.093	0
0.36	0.094	0.36	0.098	0.098	0
0.40	0.101	0.32	0.105	0.104	-1
0.50	0.108	0.29	0.111	0.110	-1
0.57	0.113	0.27	0.116	0.116	0
0.65	0.119	0.25	0.121	0.120	-1
0.72	0.123	0.24	0.125	0.125	0
0.84	0.131	0.22	0.132	0.131	-1
0.53	0.143	0.94*	0.187	0.190	2
0.48	0.147	0.92*	0.190	0.188	-1
0.43	0.150	0.89*	0.191	0.189	-1
0.42	0.174	0.71	0.204	0.203	-1
0.40	0.179	0.67	0.207	0.208	1

Table 2.1   Comparison of experimental data of Y_2 and predicted values (after Ramamurthy and Satish, 1990).

*F_1 = values exceed the limit of applicability , F_1 < 0.75.

R_q	Y_1 (m)	F_1	Y_2 (m) Calculated	Y_2 (m) Measured	Error (%)
0.380	0.038	0.57	0.042	0.045	6
0.277	0.048	0.48	0.052	0.053	3
0.472	0.041	0.65	0.047	0.053	12
0.354	0.054	0.57	0.059	0.063	5
0.525	0.045	0.75	0.053	0.055	3
0.207	0.061	0.50	0.065	0.067	3
0.413	0.049	0.70	0.057	0.058	2
0.253	0.063	0.56	0.069	0.072	4
0.486	0.056	0.68	0.064	0.066	2
0.500	0.055	0.75	0.065	0.067	3
0.313	0.064	0.60	0.071	0.074	3
0.377	0.068	0.61	0.076	0.079	4
0.152	0.077	0.51	0.083	0.087	5
0.454	0.063	0.69	0.074	0.076	3
0.257	0.077	0.57	0.085	0.088	3
0.318	0.080	0.59	0.086	0.091	2
0.183	0.088	0.51	0.094	0.096	2
0.756	0.057	0.98	0.074	0.073	-1
0.392	0.082	0.65	0.093	0.095	2
0.372	0.113	0.66	0.093	0.097	5
0.077	0.099	0.48	0.105	0.110	5
0.423	0.081	0.74	0.095	0.099	4
0.184	0.099	0.54	0.108	0.111	3
0.222	0.116	0.53	0.126	0.128	2
0.528	0.092	0.76	0.110	0.109	-1

Table 2.2   Comparison of experimental data (after Sridharan, 1966) of Y_2 and predicted values. (after Ramamurthy and Satish, 1990).

Law and Reynolds (1966) were the first researchers to study intake angles other than 90 degrees. In their work, they showed experimentally that, given a constant width of several channels, the limit curve corresponding to free overfall conditions followed a simple pattern for different angles of intersection. They were also the first to investigate secondary flow features, studying the formation of re-circulating eddies at diversions. These eddies formed within the separation zones located in the branch and main channel. They were visualised in the bottom flow of the branch channel by injecting potassium permanganate onto the white channel bed. In the main channel they were visualised by using white chalk powder seeded onto the flow's surface. Any differences that may have existed between the flow patterns at the surface and those at the bed were either thought to be insignificant or were ignored. Sketches of the re-circulating eddies in the branch and main channels are shown by Figure 2.11.

The subscript 'b' denotes the location downstream in the branch channel. No subscript indicates the location in the main channel upstream of the diversion.
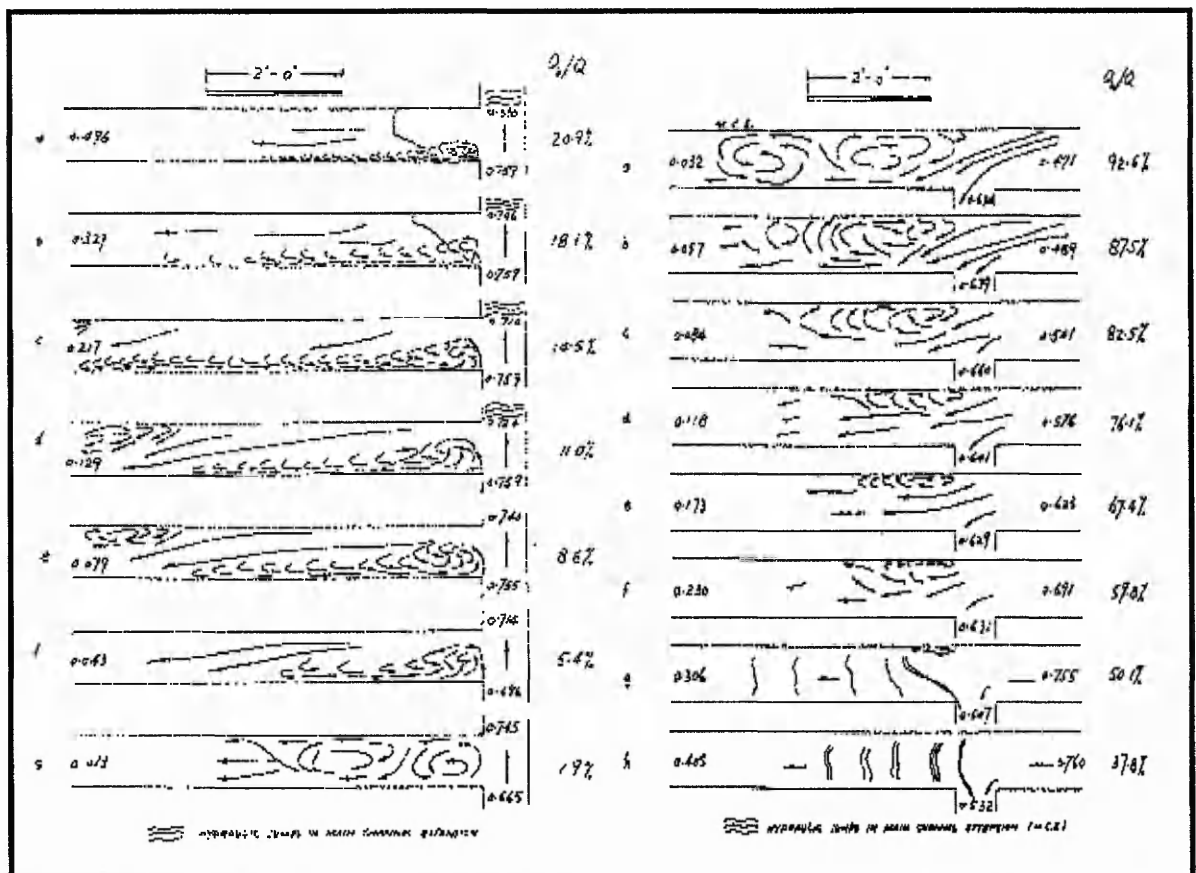
Figure 2.11 Development of recirculation regions in the branch (left) channel and main channel (right) extension (from Law and Reynolds, 1966).

The illustrations shown by Figure 2.11 indicate that the formation and the size of the recirculation region were dependent upon the discharge ratio. For discharge ratios in the range 0 to 0.43 recirculation was observed in the branch only. Above 0.43, recirculation regions began to form in the main channel, downstream of the diversion. Beyond 0.5 recirculation regions were only found in the main channel.

The size of the recirculation region was observed to increase with decreasing discharge ratios. Conversely, the size of this region in the main channel was observed to increase with increasing discharge ratios. From these observations Law and Reynolds were able to make a crude estimate of the contraction coefficient in the branch channels for their theoretical analysis. They derived their theoretical analysis again using the momentum and energy equations and using mean Froude numbers based on the mean velocities and mean depths:

$$F = \frac{F_b}{\left[\left(\frac{Q_b}{Q}\right)\cdot\left(1+\frac{2}{c}F_b^2\right)^{\frac{3}{4}}\right]}$$

2.6

and

$$\left(\frac{Q_m}{Q}\right)\left(\frac{F}{F_m}\right) \approx \frac{3}{4}F^2\left[1-\left(\frac{Q_m}{Q}\right)^2\right]$$

2.7

Where subscripts b refers to the branch channel, m refers to the main channel downstream of the branch and no subscript refers to upstream of the branch channel. It is noticed that the first of these two equations contains a coefficient c which refers to a contraction coefficient which Law and Reynolds approximated from observations and the values are shown by Table 2.3.

Range of F applicable	Effective width of delivery	Contraction coefficient, c	Range of Qb / Q
$0.1 \leq F \leq 0.5$	1	1	$0 \leq Q_b / Q \leq 1.0$
$0.5 \leq F \leq 0.8$	1/8	0.125	$0 \leq Q_b / Q \leq 0.2$
$0.5 \leq F \leq 0.8$	½	0.500	$0.2 \leq Q_b / Q \leq 0.4$
$0.5 \leq F \leq 0.8$	1	1	$0.4 \leq Q_b / Q \leq 1.0$

Table 2.3   Contraction coefficients for the flow in a branch channel (after Law and Reynolds, 1966).

Law and Reynolds compared their theoretical derivation to experimental data as shown by Figures 2.12 and 2.13.
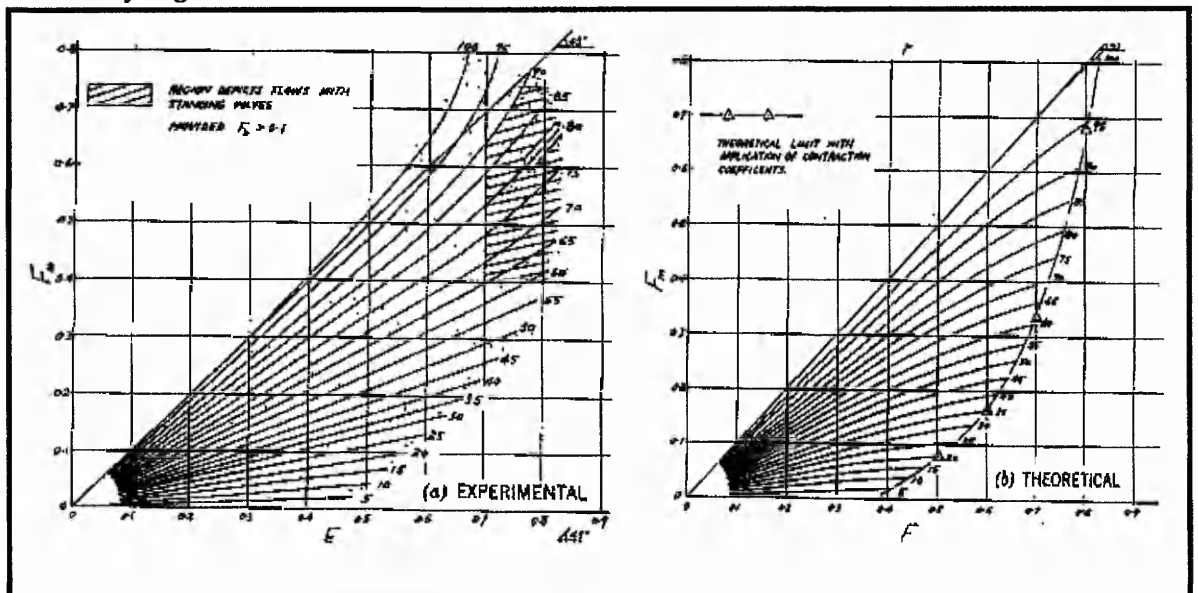
Figure 2.12   Values of F versus F_m with isolines of Q_m/Q(%) (from Law & Reynolds, 1966).
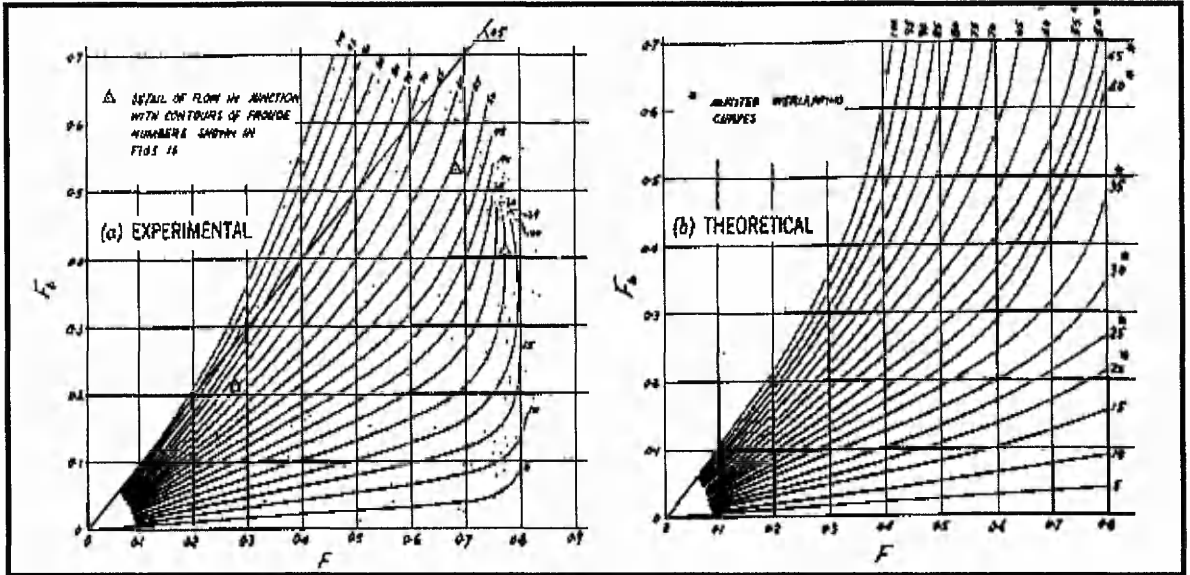
Figure 2.13   Values of F versus F_b. (from Law & Reynolds, 1966).

All the previous studies only considered the problem in two dimensions. Lakshmana *et al* (1968) were the first researchers to expand the study of secondary features by including an examination of the dividing streamplane in the main channel. They observed that the surface streamlines entered the branch with a reasonably smooth curvature while the bed streamlines turned sharply into the branch at the downstream corner of the junction. The surface streamlines were observed by means of confetti, and the bed streamlines by using small pieces of woollen thread. Measurements of the distance at which the streamlines extended into the main channel were taken 150mm upstream of the junction, perpendicular to the channel. Measurements of the surface streamlines were denoted S_d and those for the bed streamlines, B_d, as shown by Figure 2.14.
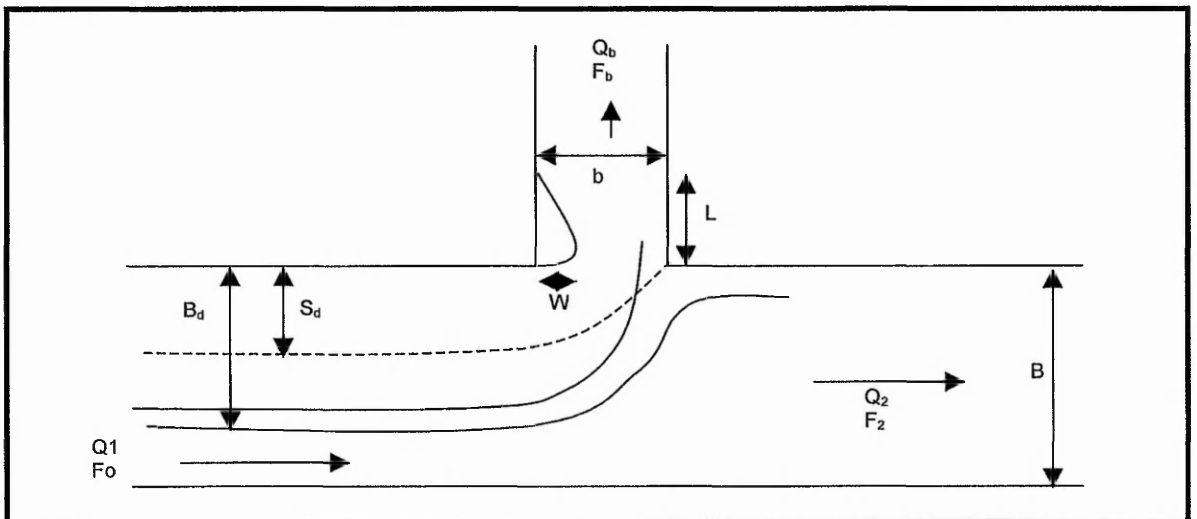
Figure 2.14   Definition sketch for division of flow.

The observations of Lakshmana *et al.* are summarised by Figure 2.15 which shows S_d and B_d for various discharge ratios, which are indicated by the numbers adjacent to the data points. The dividing streamline measurements are normalised by the main channel width, B. The figure shows that the proportion of near bed flow diverted from the main channel was much greater than the proportion of surface flow.
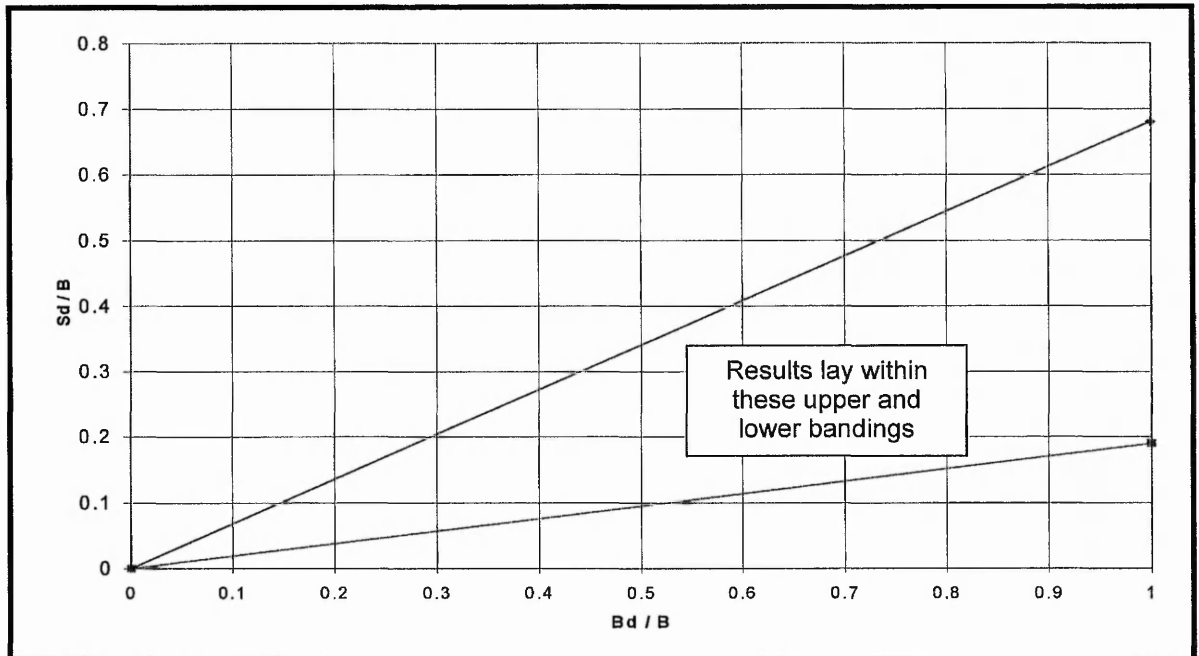
Figure 2.15   Effect of discharge distribution on surface and bed dividing streamlines (after Lakshmana *et al.*, 1968).

They found that most of the observations were contained between two limits which corresponded to B_d equal to 1.5 to 5.5 times S_d. separate plots were also made for variations of S_d / B, B_d / B and Q_b / Q_1 with F_2 taking F_b as the third parameter. The plot for Q_b / Q_1 is shown by Figure 2.16. It can be seen that a reasonably good trend was obtained from the data without much scatter. Using the results from which Figure 2.16a was plotted and using the results of two other analyses for B_d / B and S_d / B, cross plots were constructed to compare the extent of surface and bed diversions and an example is shown by Figure 2.16b. This figure shows that except for low F_2 values, B_d / B was larger than S_d / B. For low F_2 values, all three quantities B_d / B, S_d / B and Q_b / Q_1 were high as most of the water was diverted into the branch in such cases.

Lakshmana *et al.* also conducted a more detailed study of the separation zone in the

branch channel than Law and Reynolds. Test cases included main channel Froude numbers, F_2 ranging between 0 and 0.5. Empirical relationships were derived
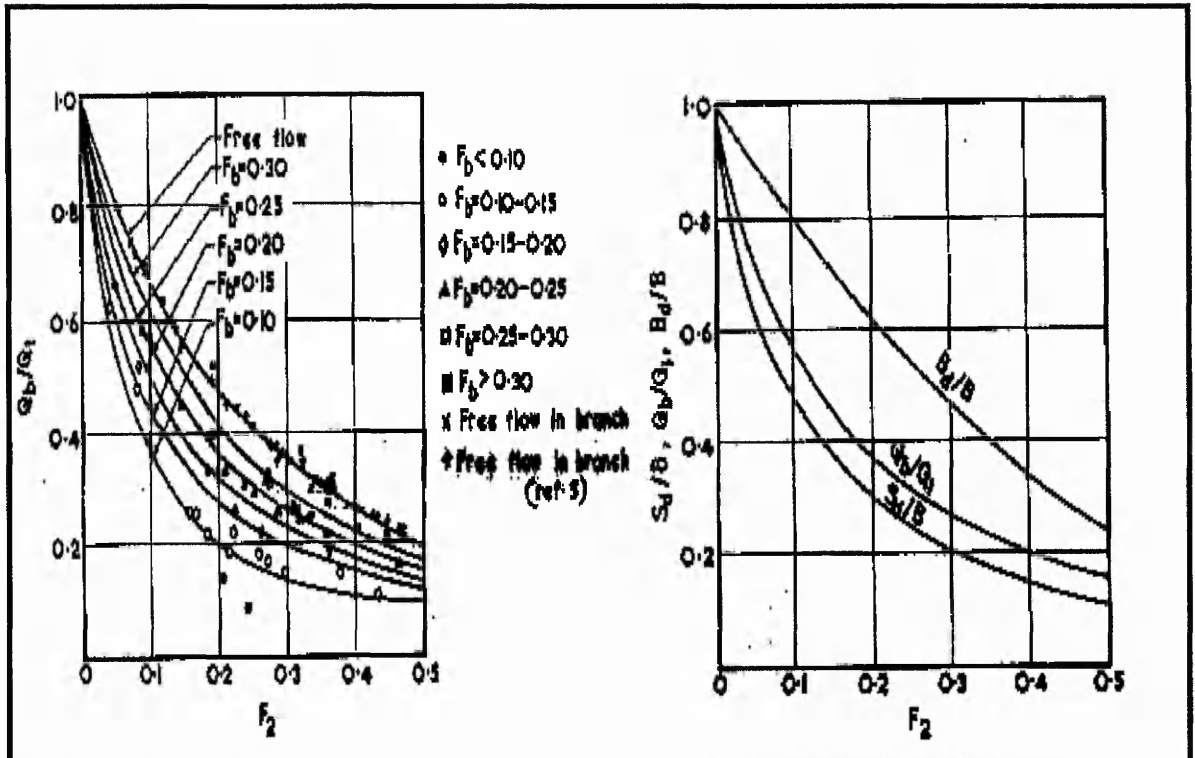
Figure 2.16a Effect of F_b and F_2 on division of flow.   2.16b Effect of F_2 at F_b = 0.25 on B_d / B, S_d / B and Q_b / Q_1 (from Lakshmana et al., 1968).

between the size of the separation zone and the Froude numbers downstream in the main and the branch channels, denoted by F_2 and F_b. They observed that the size of the return flow zone increased clearly with a decrease in F_b. They also attempted to correlate experimentally the parameters of the return flow (contraction coefficient C_c and L / b) with the flow conditions in the main and branch channels. F_2 and F_b were chosen as the parameters because they gave at least as good a correlation as any other and because they were used to correlate other parameters previously described. Figure 2.16 shows the variation of the coefficient of contraction and the variation of the length of the return flow zone with F_2.

It can bee seen from Figure 2.16 that there was considerable scatter of the data obtained. However trends were observed by Lakshmana et al. denoted by the curves plotted on the graphs. The coefficient of contraction was a maximum for a free flow in the branch channel for a given value of F_2, and decreased as F_b decreased. For F_2 round 0.5 and for low values of F_b, nearly 80% if the branch channel width was

covered by the return flow zone. Many of the experimental observations made by Lakshmana *et al.* were useful but only for 90 degree intakes. They observed depth variations of the dividing streamplane into the main channel, S_d / B_d that ranged from 0.1 to 0.5. Thus the discharge ratio was derived using the following formula:

$$\frac{Q_2}{Q_1} = \left[\frac{F_2}{w.F_b} + 1\right]^{-1}$$

2.8

Where $w = W_2 / W_1$ the ratio of the width of the branch channel to the main channel.

Razvan (1989) presented three dimensional observations of the dividing streamplane at a 90 degree intake. His interpretation is shown by Figure 2.17.
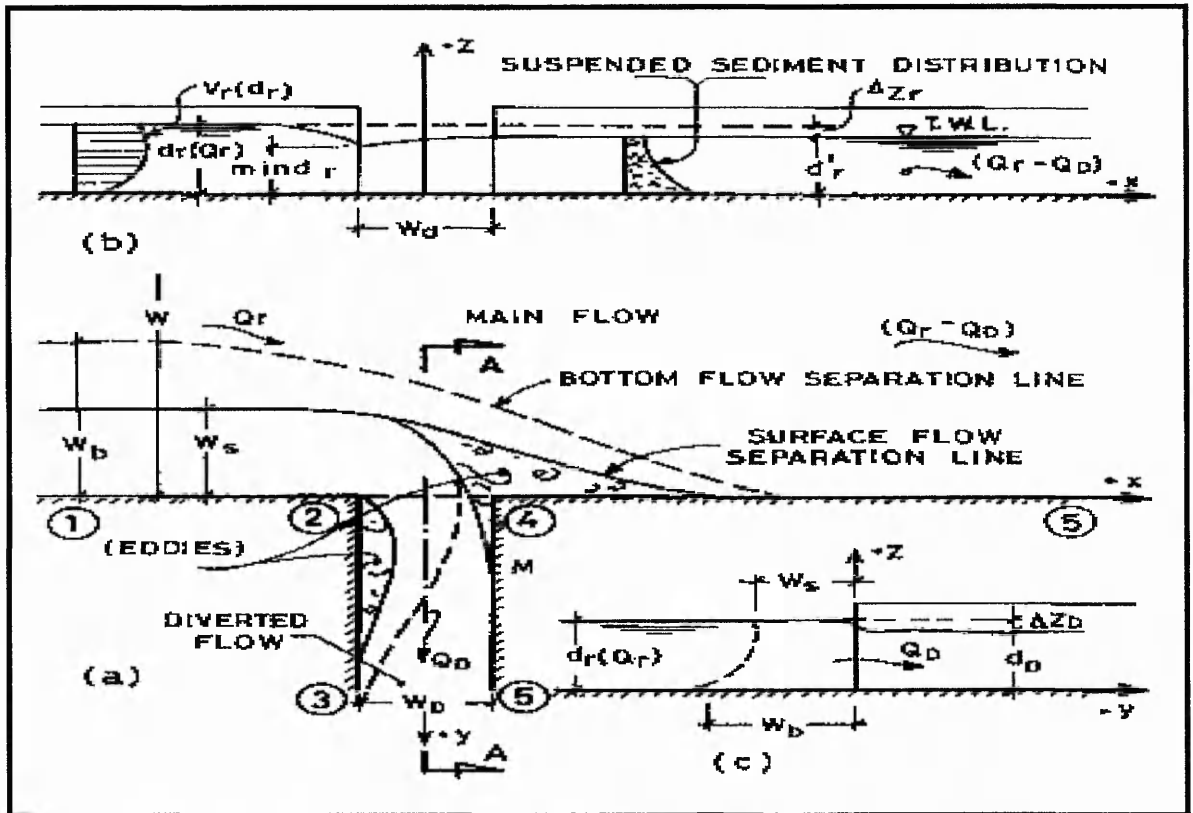
Figure 2.17   Flow pattern at a schematic diversion (from Razvan, 1989).

Here Razvan represented the diversion rate, K_D as:

$$K_D = \frac{Q_D}{Q_r}$$

2.9

He stated that K_D was a function of the main channel Froude number and the ratio of the widths of the diversion channel to the main channel. This was in agreement with previous researchers.

For his experimental observations Razvan was able to plot the sketches shown by Figure 2.18 which relates the diversion rate to the main channel Froude number.
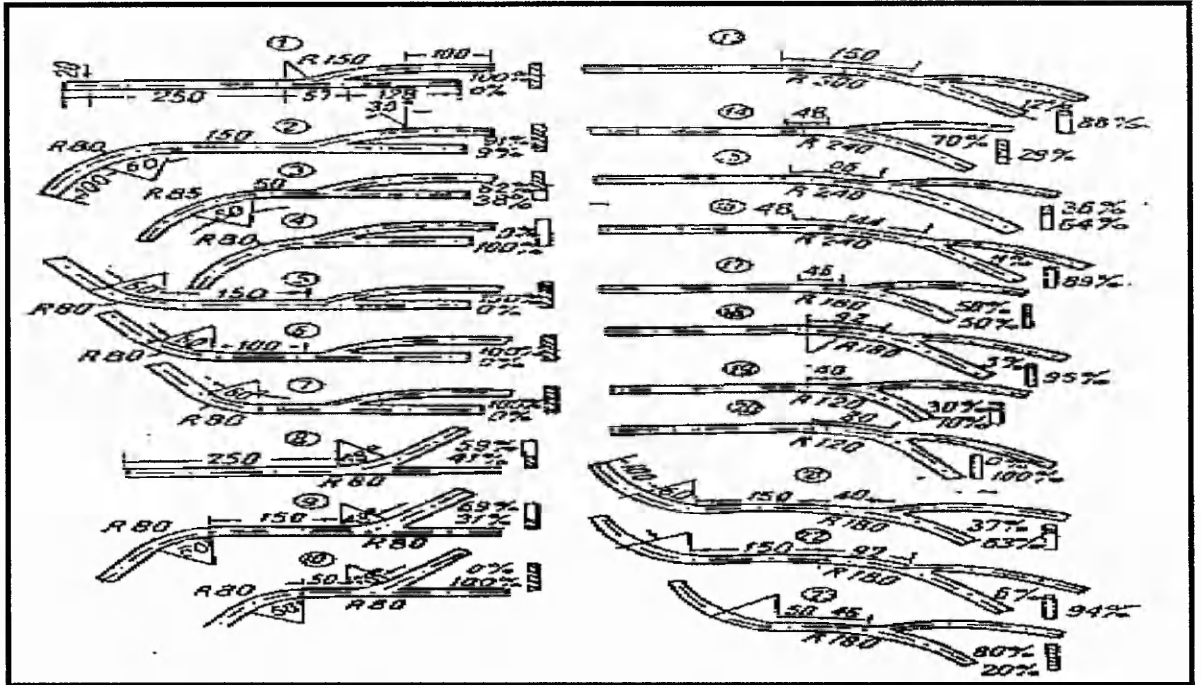
Figure 2.18   The maximal diversion rate (from Razvan, 1989).

Razvan's study was not particularly detailed but represented a good qualitative analyses of flow into a 90 degree intake.

Levi (1947) formulated theoretical equations for the position of the dividing streamplane based on a two-dimensional anlaysis. With reference to Figure 2.17 he derived the following equations for the position of the streamplane:

$$x = -0.5.W_D . \frac{1}{\sin \phi} + \frac{(a-1)q}{\pi . V_2} .F_1(-X)$$

2.10

$$y = \frac{(a-1)q}{\pi . V_2} .F_2(-X)$$

Where ϕ was the intake angle and F_1 and F_2 were functions which were tabulated by Levi.

Cioc (1962) undertook a similar study to Levi to predict the dividing streamplane and the diversion rate. A relation of the diversion rate K_D as a function of the widths ratio, W_D / W_r was derived and this was confirmed experimentally as shown by Table 2.4.

W_D / W_r	2.00	1.00	0.20	0.10
K_D (potential flow)	0.83	0.62	0.18	0.10
K_D (with vortex zone)	0.8	0.42	0.12	0.06

Table 2.4   Experimental results (after Cioc, 1962).

Ofitserov (1952) derived expressions for the positions of the relative widths of the surface and bed dividing streamline as a function of the diversion rate, K_D :

$$\frac{W_s}{W_r} = 0.05 + 1.7K_D$$
$$\frac{W_b}{W_r} = 1.02K_D - 0.04$$

2.11

Where W_s, W_b and W_r are the dimensions referred to in Figure 2.17. For very small diversion rates, $K_D < 0.04$, the flow pattern as represented by Figure 2.17 becomes irrelevant and a slow circulation occurs at the diversion channel entrance. From experimental results it was confirmed that an increased entrance width W_D, is accompanied by an increased diversion of bottom currents.

More recently Neary and Odgaard (1993) reported experimental observations on the three-dimensional flow features at a 90 degree intake. They found that the degree of three-dimensionality of the diversion flow depended on the velocity ratio, U_2 / U_1 and the main channel bed roughness, where U_1 is the bulk channel velocity at the main channel inlet and U_2 is the bulk velocity at the branch channel exit. The effects of main channel bed roughness were observed by comparing two dimensional streamline plots at three different flow depths as shown by Figure 2.19. Neary and Odgaard reported depth variation ratios for a smooth bed ($S_d / B_d = 0.60$) and a rough gravel bed ($S_d / B_d = 0.46$) that they found were to be independent of the velocity ratio, shown by Figure 2.20.
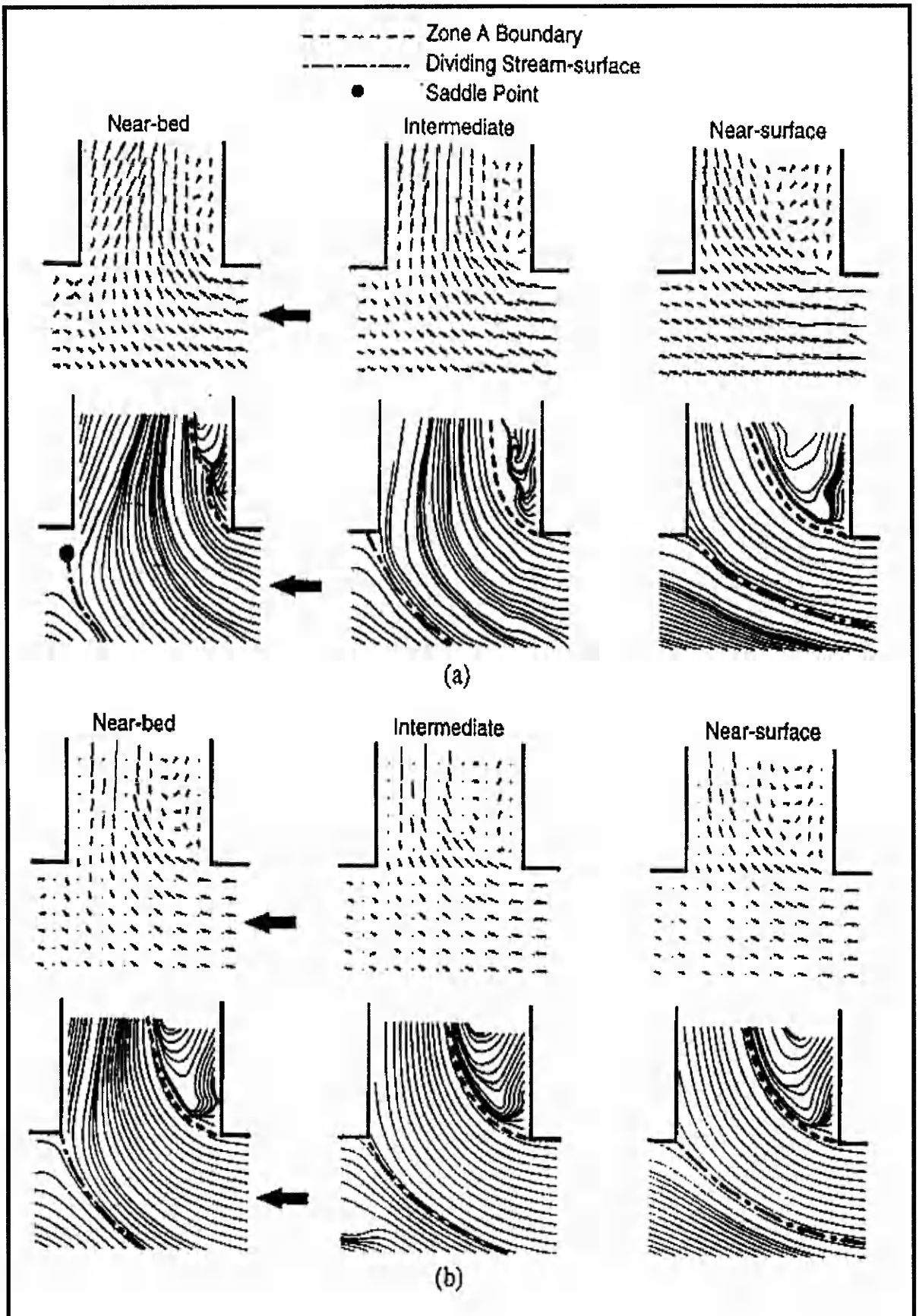
Figure 2.19   Streamline plots U_2 / U_1 = 0.6 (a) rough bed (b) smooth bed (from Neary and Odgaard, 1993).
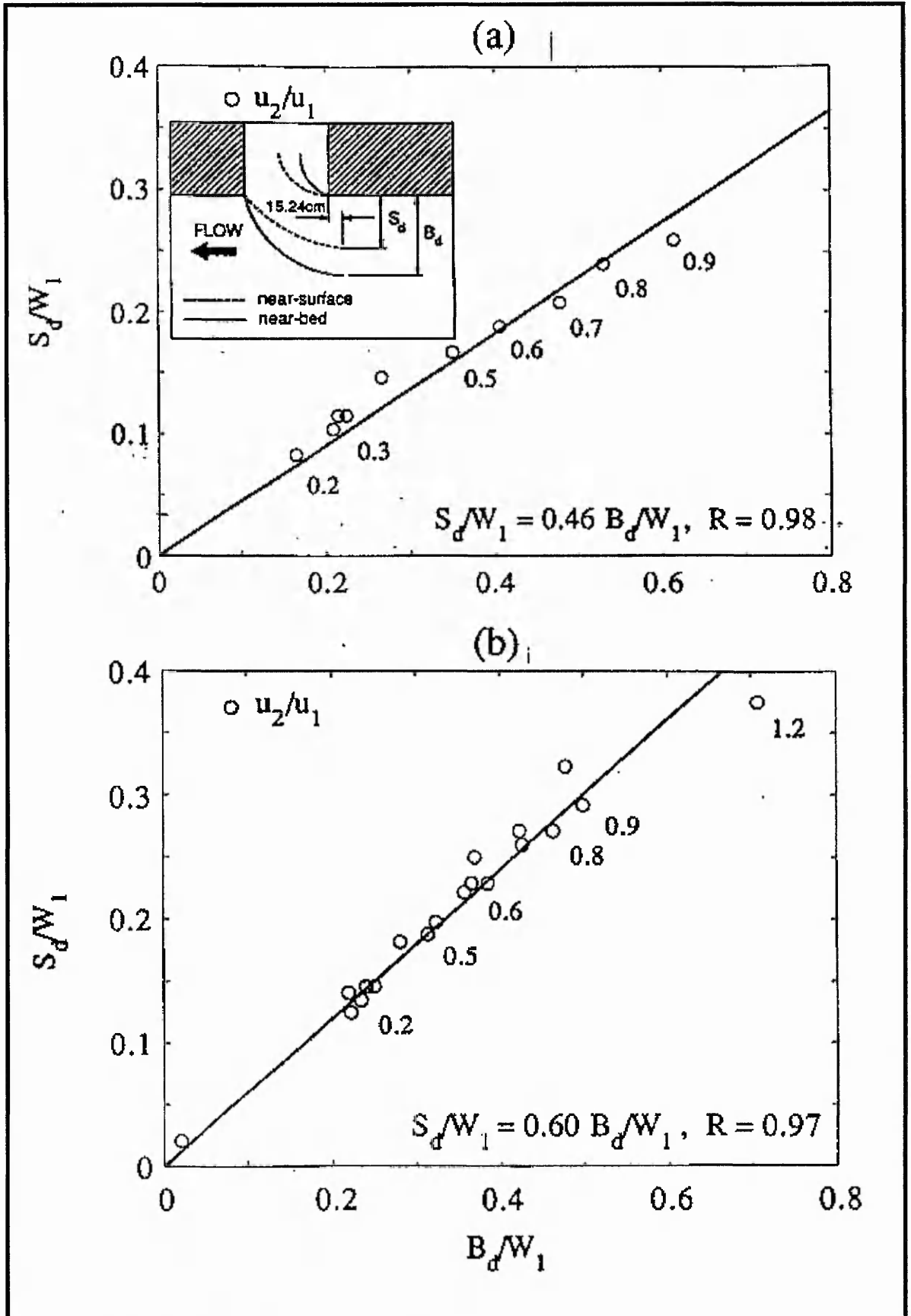
Figure 2.20   Depth variation ratios (a) rough bed (b) smooth bed (from Neary and Odgaard, 1993).

2.2.2 Observations by Biomedical Researchers

Medical researchers have been investigating flow splits for the last 20 years. They have identified specific three-dimensional flow features associated with the localisation of atherosclerotic lesions and the deposition of platelet thrombi in arterial branches. The most detailed descriptions of three-dimensional separation of diversion flows have come from visualisation experiments of modelled arterial branches.

Karino *et al.* (1979) studied flow patterns in glass models of 3mm diameter 90 degree T-junctions with square or rounded corners, which represented idealised models of branching vessels in the human or animal vasculature. They assumed laminar, conduit flow (Reynolds numbers 15 to 420) which was typical of blood flow but many of the observations they made can be compared to open channel, turbulent flow. To visualise the flow they used small, coloured polystyrene spheres in a suspension of aqueous glycerol and time delayed photography. Figure 2.21 shows a selection of the observations they made with Reynolds numbers and mean inlet velocities. The solid lines in the diagrams represent the paths of the sphere in or close to the middle plane of the conduit, the dashed lines represent the paths which are far out of the middle plane. This shows how the spheres crossed the mainstream from vortex A to vortex B. R and S are the respective reattachment and separation points and the numbers indicate the particle velocities in mm/s.

From Karino *et al.*'s initial observations they developed a graph shown by Figure 2.23 to relate the critical Reynolds number for vortices A, B and C against the relative flow rate through the main tube. The solid lines represent data obtained from the square T-junction, the dashed lines from the rounded T-junction. Figure 2.24 shows the particle velocity distribution through the T-junction that Karino *et al.* studied. It is interesting to note the qualitative comparison that can be made with the results of Neary and Sotiropoulos (1996) who predicted the laminar flow through a similarly shaped open channel junction using computational analyses (see Figure 2.36)
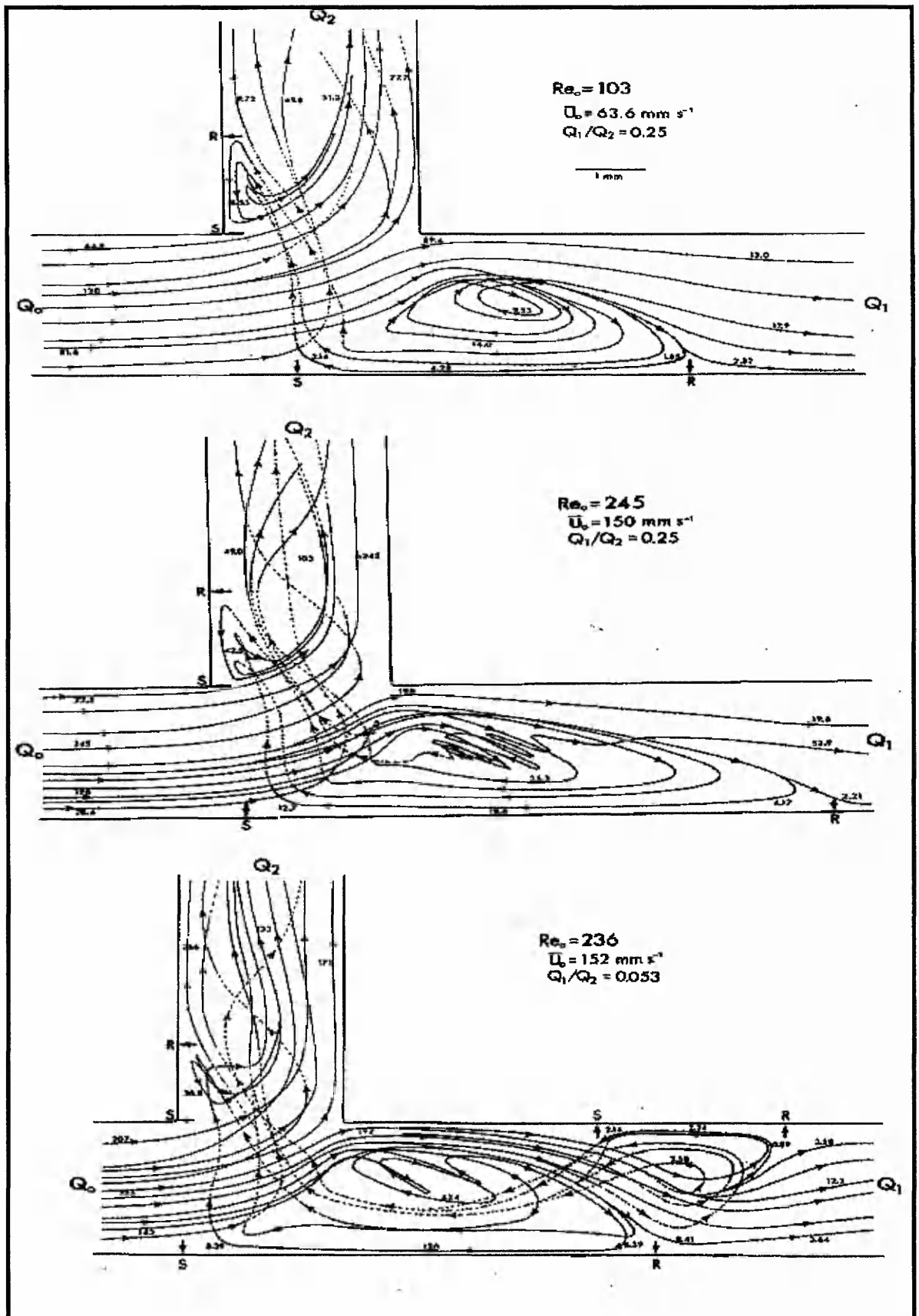
Figure 2.21   Blood flow observations (from Karino *et al.* , 1979).
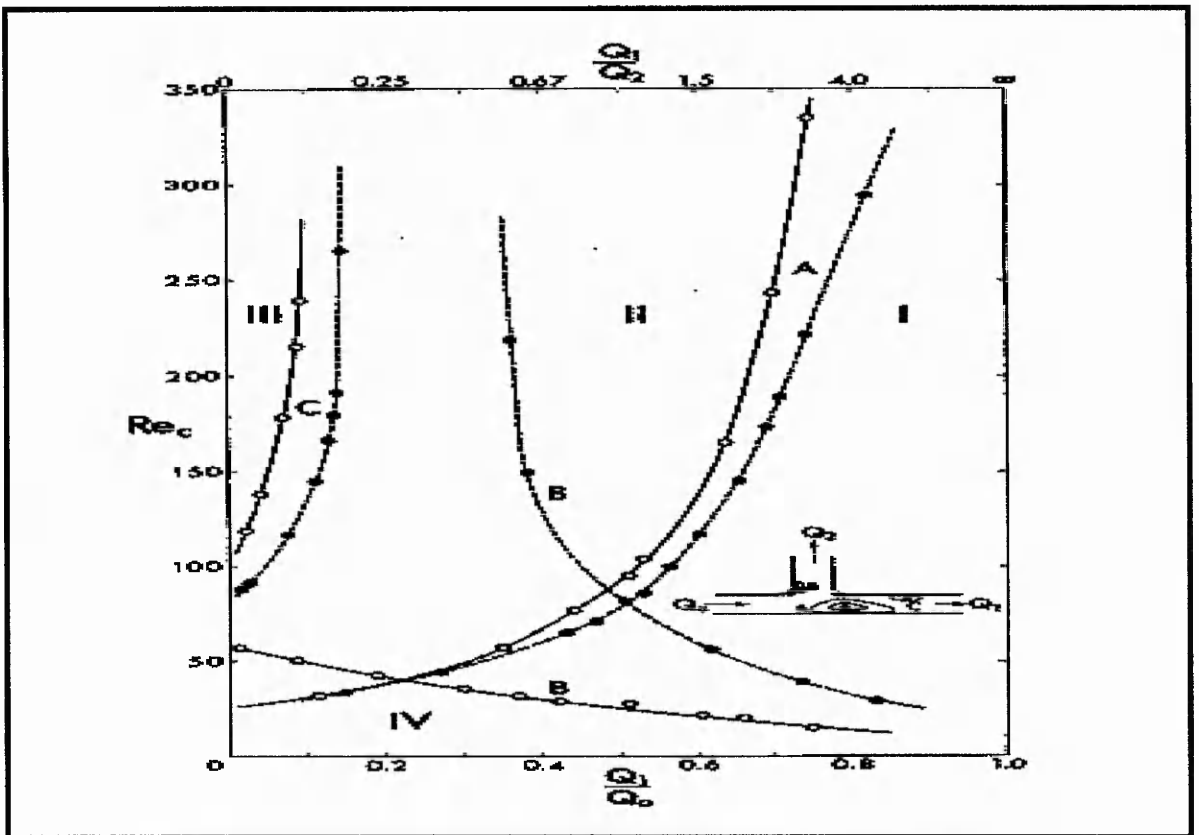
Figure 2.22   Measured critical Reynolds number for vortices A, B and C against the relative flow rate (from Karino *et al.,* 1979).
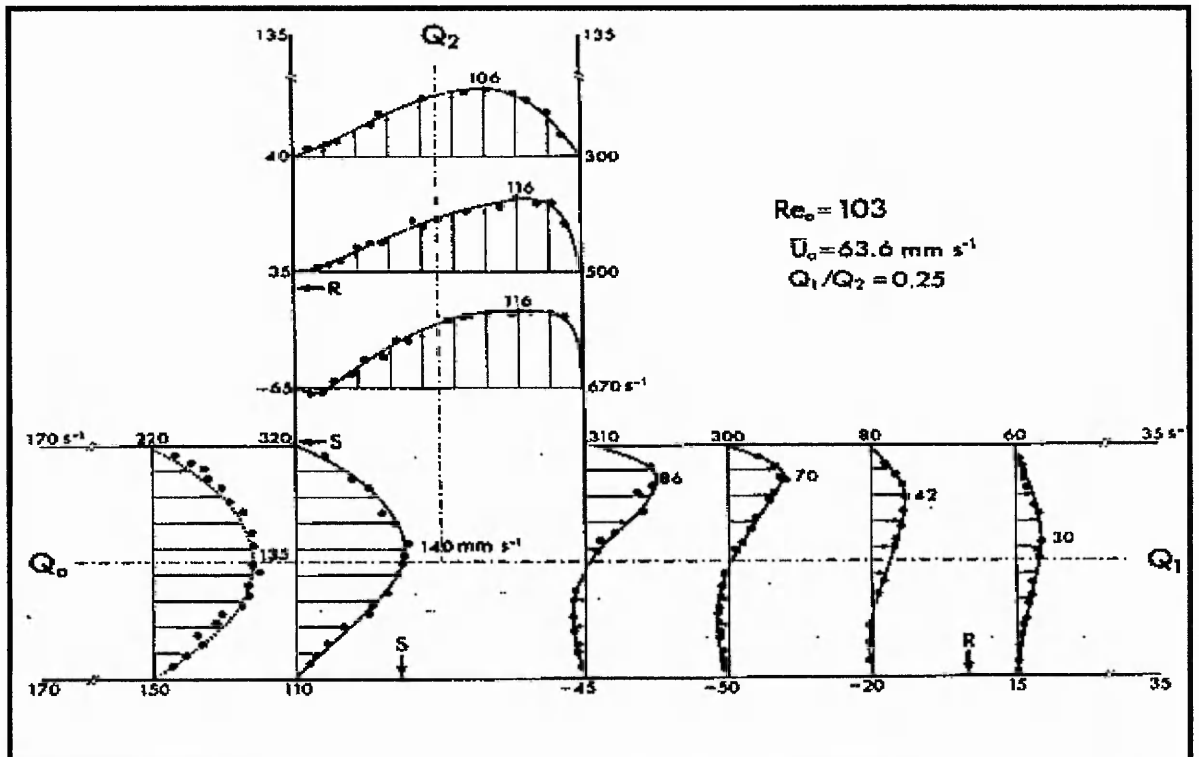
Figure 2.23   Particle velocity distribution through the T-junction (from Karino *et al.,* 1979).

Bharadvaj *et al.* used flow visualisation techniques in a glass model of a human carotid bifurcation, over a range of upstream Reynolds numbers and flow division ratios to reveal the complex flow field in which secondary flows play an important role. They observed separation regions occurring at the outer corners of the branching. Figure 2.24 shows their schematic representation of the flow field at the human carotid bifurcation based upon model observations.
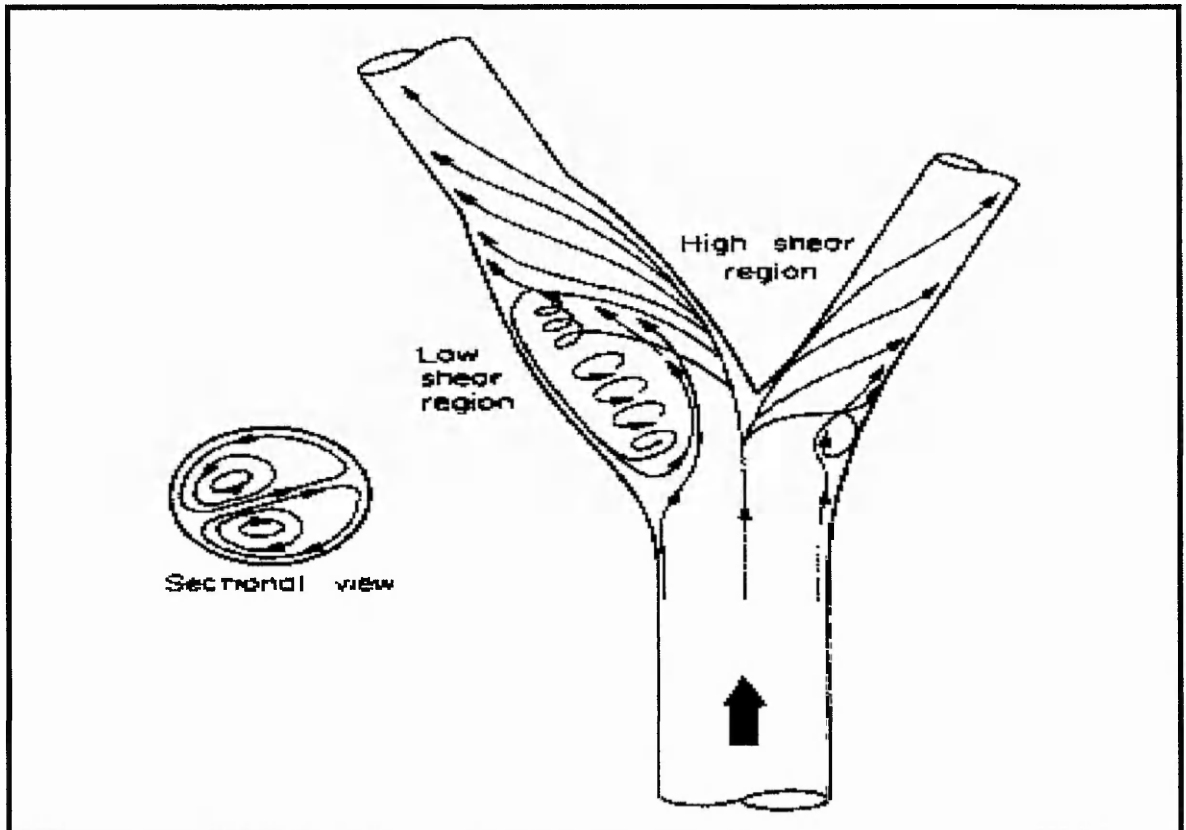
Figure 2.24   Schematic representation of the flow field at the human carotid bifurcation (from Bharadvaj, 1982).

Lee and Chiu (1992) used CFD to compute the flow field of a two dimensional aortic bifurcation and compared their results to experimental data. They examined models under conditions of steady flow and pulsing flow. 90 degree T-junctions were again studied but they also applied their computational model to other bifurcation angles. Figure 2.25 shows sample results of the prediction of the streamline patterns and the pressure contours at a 90 degree T-junction. Notice the low pressure region at the upstream corner to the branch and the high pressure region at the downstream corner. Figure 2.26 shows similar predictions for the flow at an aortic bifurcation.
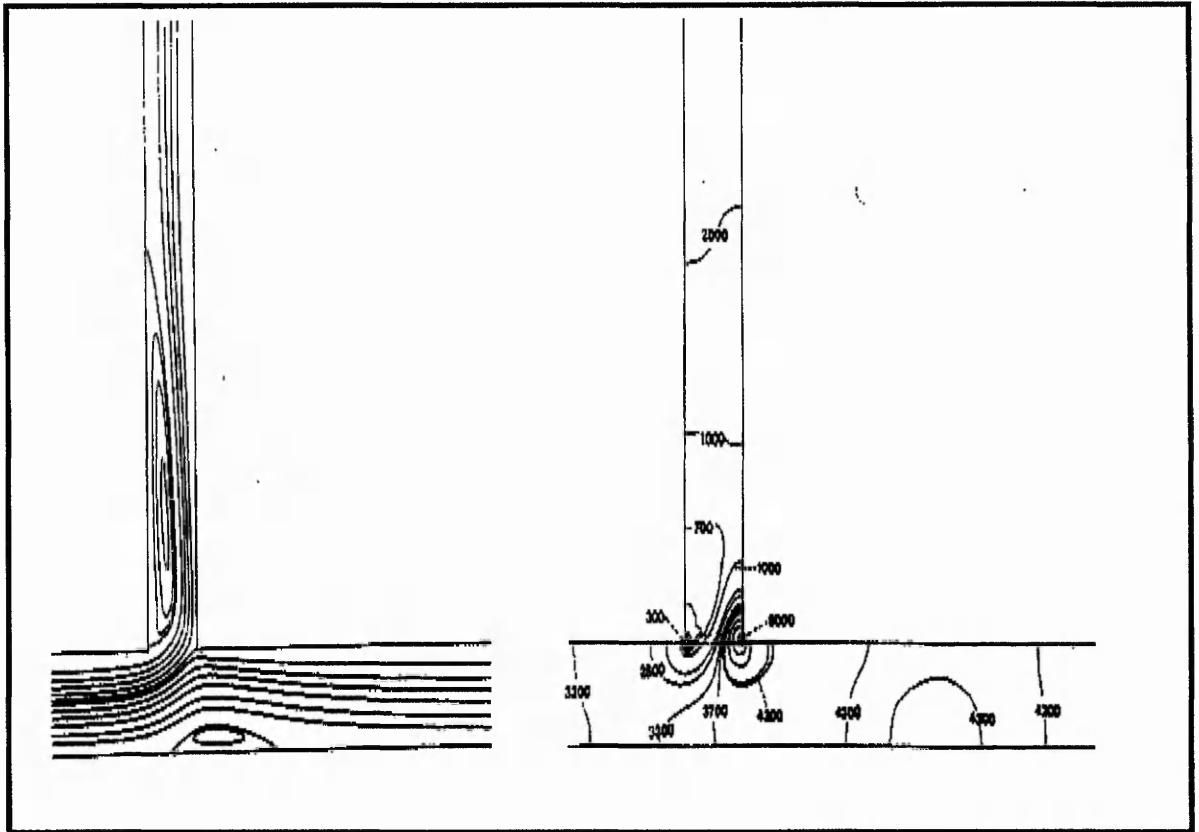
Figure 2.25   Streamlines (a) and pressure contours (b) of a T-junction (from Lee & Chiu, 1992).
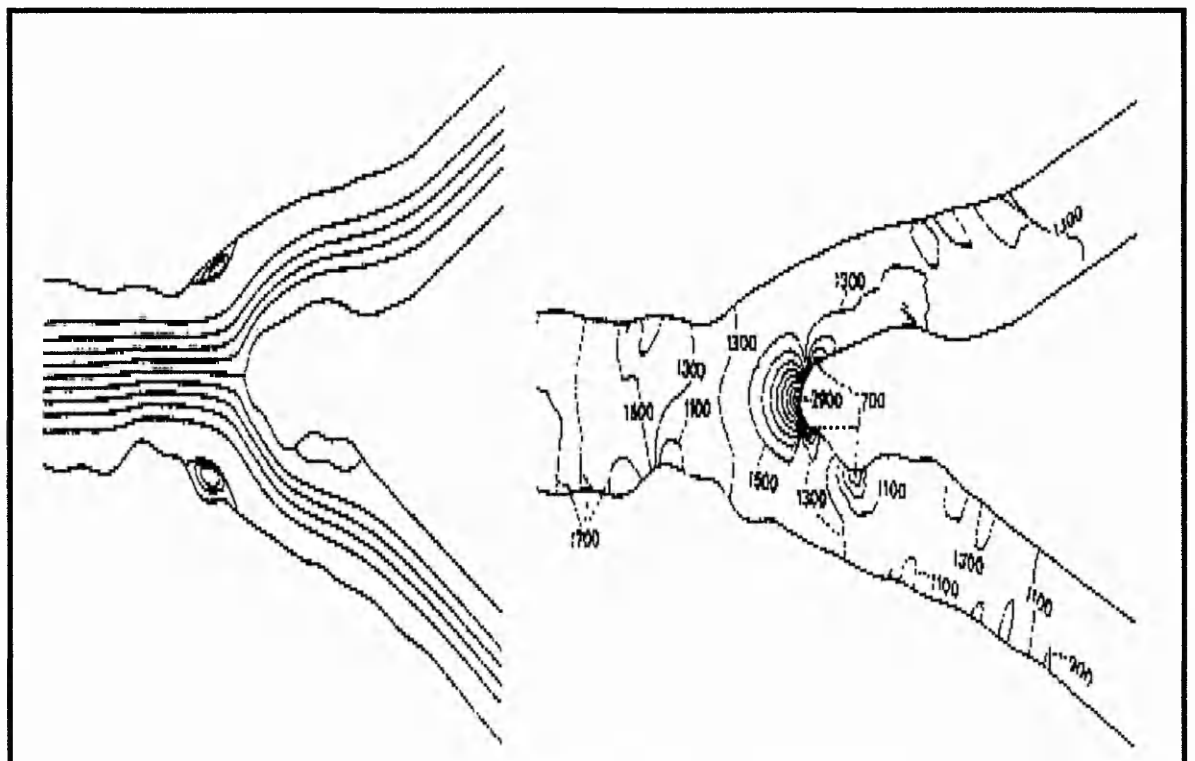
Figure 2.26   Streamlines (a) and pressure contours (b) of an aortic bifurcation (from Lee & Chiu, 1992).

Cho *et al.* (1985) carried out an investigation of branch flow ratio, angle and Reynolds number effects on the pressure and flow fields at arterial branch models. They primarily looked at intake angles of 30 and 60 degrees and measured the pressure change across the branching channel. The range of Reynolds numbers corresponded to laminar blood flow and they were able to plot graphs of the pressure change with the diversion ratio m_3 / m_1 (where subscripts 3 and 1 represent the main channel upstream of the branch and the branch respectively) based upon their experimental measurements. Figure 2.27 shows the effect of branch angle on the pressure change with different Reynolds numbers representing laminar flow.
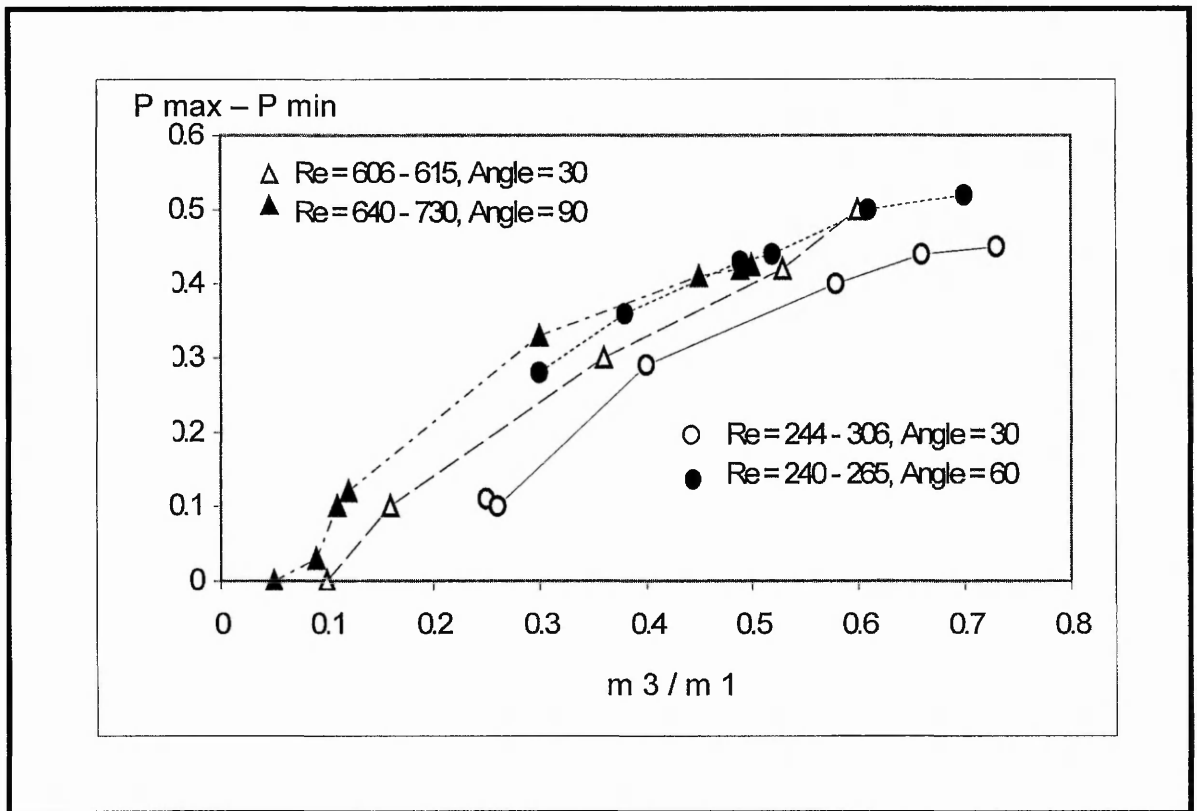
Figure 2.27 Effect of branch angle on the dimensionless pressure rise coefficient for fixed Reynolds numbers (after Cho *et al.,* 1985).

The qualitative assessment of the finding of biomedical researchers is extremely interesting and it is possible to make comparisons with open channel, water flow. However, quantitatively it is not possible to compare the results that they obtained to open channel, water diversions since in every instance laminar, conduit flow, typical of arterial flow was assumed. In addition the density and viscosity of the fluid used in the experimental analyses represented blood and not water.

2.2.3 Theoretical Model Descriptions

Past researchers have applied control volume analyses with mass, momentum and energy conservation laws to predict specific features of diversion flows, including the size of the separation zone downstream of the inlet to the diversion channel (see Figure 2.1) and the extension of the dividing streamplane.

Law and Reynolds (1966) obtained a relationship between the discharge ratio, Q_2 / Q_1 and the depth ratio of the branch to main channel, d_2 / d_1. They assumed that the depths upstream and downstream of the junction in the main channel were equal. Also the solution required knowledge of the contraction coefficient, μ, which had to be obtained experimentally.

Ramamurthy and Satish (1988), through a similar analysis, developed a relationship between the discharge ratio and the main channel Froude number downstream of the junction, F_3. Unlike Law and Reyonld's analyses their analyses could be applied to diversions with different branch to main channel width ratio, W_2 / W_1. However, it still required introducing a contraction coefficient, which was derived using the analogy between the division of flow in a branch channel and that in a two dimensional lateral conduit outlet fitted with a barrier wall.

Hager (1984) formulated a simple model which derived the contraction coefficient entirely from a theoretical basis. Hager observed experimental tests of the flow patterns for different discharge ratios with lateral intake angles less than 90 degrees. His observations are shown by Figure 2.28. Hager used the control volume approach to derive his equations shown by Figure 2.29. P_s approximately corresponds to the energy head at the inflow section 1:

$$P_s = P_1 + \frac{Q^2}{2.g.b^2} \qquad\qquad 2.12$$

He then applied the momentum equation to the control volume specified in Figure 2.29 in the inflow direction which lead to:
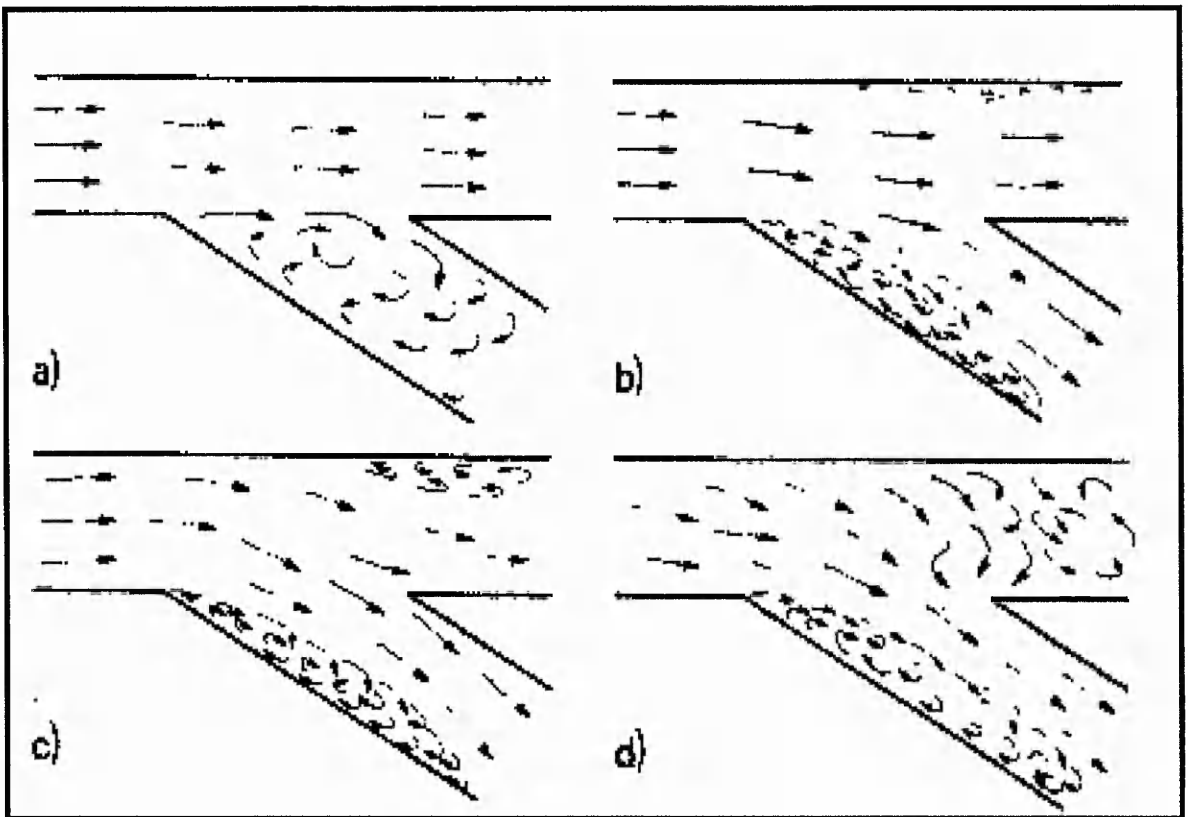
Figure 2.28 Hager's qualitative observations for flow split ratios of (a) 0, (b) 1/3, (c) 2/3, (d) 1(from Hager, 1984).
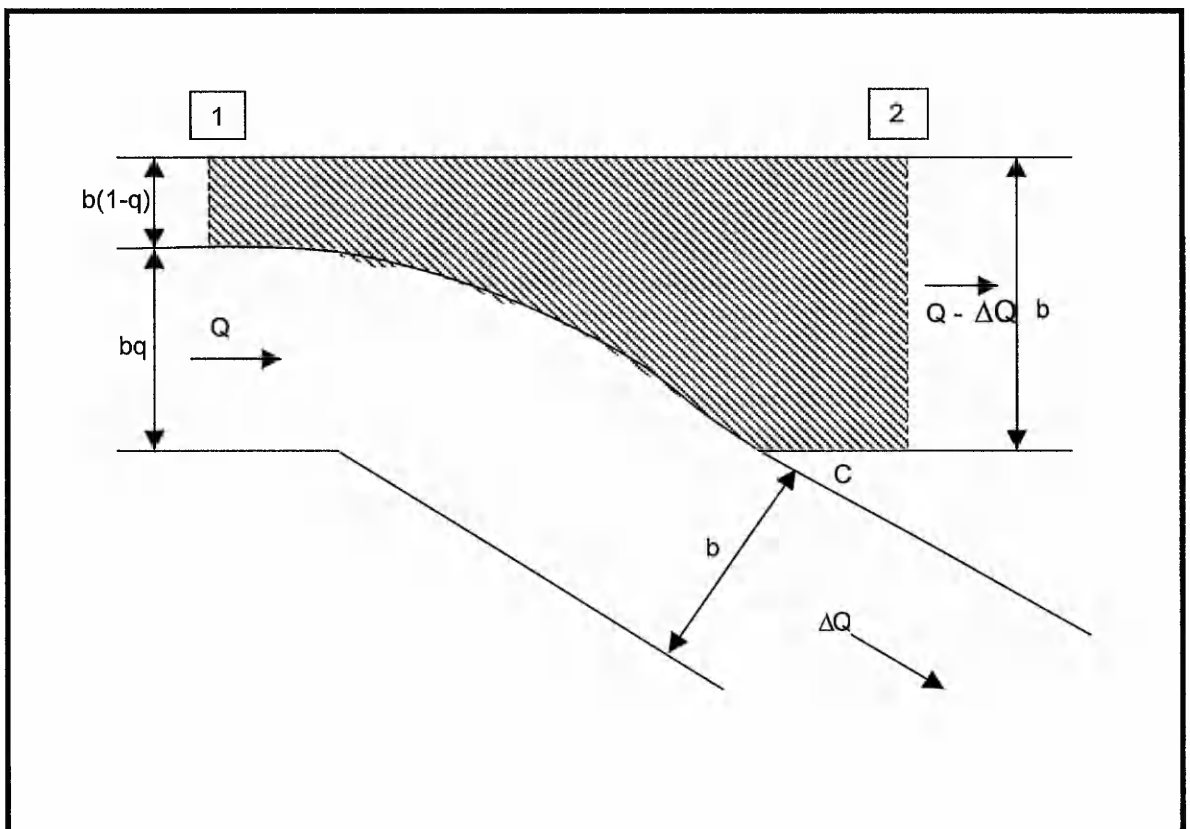
Figure 2.29 Control volume for Hager's theorem (after Hager, 1984).

$$P_1.b(1-q) + \frac{[Q(1-q)]^2}{g.b(1-q)} + P*b.q = P_2.b + \frac{[Q(1-q)]^2}{g.b} \qquad 2.13$$

Where $q = \Delta Q / Q$ and $P*$ denotes the averaged reduced pressure head on the dividing streamplane approximately given by:

$$P* = (P_1 + P_2) / 2 \qquad 2.14$$

Combining equations 2.13 and 2.14 gives:

$$\Delta P = \frac{Q^2}{g.b^2}\left[(1-q^2) - (1-q) - q/4\right] \qquad 2.15$$

Using the energy equation (Bernoulli) between positions 1 and 2:

$$P_1 + \frac{(Q-\Delta Q)^2}{2.g.b^2(1-q)^2} = P_2 + \frac{(Q-\Delta Q)^2}{2.g.b^2} + \Delta H \qquad 2.16$$

Where ΔH is the local energy loss. This is usually represented in terms of the velocity head:

$$\Delta H = \xi_t \cdot \frac{Q^2}{2.g.b^2} \qquad 2.17$$

Where ξ_t denotes the loss coefficient of the main channel. Combining equations 2.16 and 2.17 now gives:

$$\Delta P = \frac{Q^2}{2.g.b^2}\left[\xi_t + (1-q)^2 - 1\right] \qquad 2.18$$

Therefore using equations 2.15 and 2.18:

$$\xi_t = q\left(q - \tfrac{1}{2}\right) \qquad 2.19$$
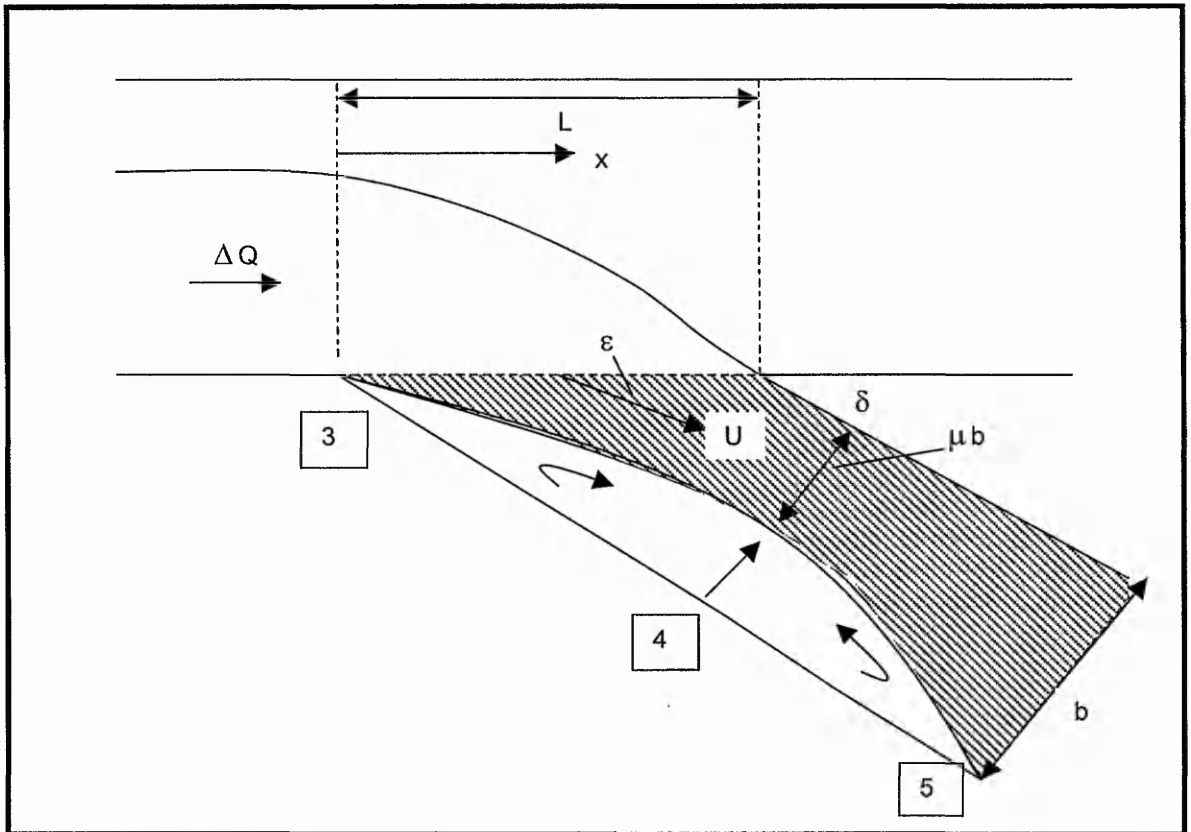
Figure 2.30   Control volume for lateral branch (after Hager, 1984).

Experiments conducted by Hager showed that the average outflow angle $\varepsilon = \delta/4$. Application of the momentum equation in the direction of the inlet channel gives:

$$b\,(P_1 + P_s)/2 + \frac{Q.\Delta Q.\cos(3\delta/4)}{g.b} = P_4.b + \frac{\Delta Q^2}{g.\mu.b} \qquad 2.20$$

Accounting for equation 2.12 the pressure differential becomes:

$$P_1 - P_4 = \frac{\Delta Q^2}{g.b^2}\left[\frac{1}{\mu} - \frac{\cos(3\delta/4)}{q} - \frac{1}{4.q^2}\right] \qquad 2.21$$

Hydrostatic pressure distributions were assumed at positions 3 and 4. $\Delta H_{3-4} = 0$ and with the application of the energy equation between positions 3 and 4 gives:

$$(P_1 + P_s)/2 + \frac{Q^2}{2.g.b^2} = P_4 + \frac{\Delta Q^2}{2.g.\mu^2 b^2} \qquad 2.22$$

From which Hager obtained:

$$P_1 - P_4 = \frac{\Delta Q^2}{2.g.b^2}\left(\frac{1}{\mu^2} - \frac{3}{2.q^2}\right)$$

2.23

Eliminating $(P_1 - P_4)$ from equations 2.21 and 2.23 gave a quadratic relationship for $1/\mu$:

$$\frac{1}{\mu^2} - \frac{2}{\mu} - \frac{1}{q^2} + \frac{2.\cos(3\delta/4)}{q} = 0$$

2.24

The maximum width of the separation zone, H is:

$$H = W_2(1-\mu)$$

2.25

Equation 2.24 can be extended to include different widths of main channel and inlet channel:

$$\left[\frac{1}{\mu}\right]^2 - 2\left[\frac{1}{\mu}\right] + 2\left[\frac{w}{q}\right].\cos\left[\frac{3\delta}{4}\right] - \left[\frac{w}{q}\right]^2 = 0$$

2.26

Where $w = W_2 / W_1$.

The solution can be obtained by the relationship:

$$\left[\frac{1}{\mu}\right] = \frac{-b + \sqrt{b^2 - 4ac}}{2a}$$

2.27

Where

a = 1.0

b = -2.0

$$c = 2\left(\frac{w}{q}\right)\cos\varepsilon - \left(\frac{w}{q}\right)^2$$

2.28

The contraction coefficient thus depends on both δ and q.

The momentum equation was now applied between position 4 and 5 in the direction of the intake and assuming hydrostatic pressure distribution gives:

$$P_4.b + \frac{\Delta Q^2}{g.\mu.b} = P_5.b + \frac{\Delta Q^2}{g.b}$$ 2.29

Using the energy equation for the same control volume gives:

$$P_4 + \frac{\Delta Q^2}{2.g.\mu^2.b^2} = P_5 + \frac{\Delta Q^2}{2.g.b^2} + \Delta H$$ 2.30

Where:

$$\Delta H = \xi_I . \frac{Q^2}{2.g.b^2}$$ 2.31

ξ_I was the loss coefficient for the inlet channel. From equations 2.29 and 2.30:

$$\xi_I = q^2 \left(1 - \frac{1}{\mu}\right)^2$$ 2.32

Or:

$$\xi_I = 1 - 2q.\cos(3\delta / 4) + q^2$$ 2.33

Hager then compared his theoretical derivations to experimental results. He measured the loss coefficient in the main channel, ξ_t and compared this to the theoretical value derived from equation 2.19. He also compared his results to those of other researchers shown by Figure 2.31a, namely Gardel and Rechsteiner (1970) (dashed line), Miller (1979) and Ito et al. (1973) (dotted line). Hager's experimental data is represented by the solid squared and open squared symbols. His theoretical data is represented by the solid line. Figure 2.31b shows a plot of the range of ξ_t for arbitrary branch geometry, the centre line of which can be represented by:

$$\xi_t = \tfrac{4}{5} q(q - \tfrac{1}{2})$$ 2.34

Deviations from the curve were usually less than +/- 0.05 which is shown by the shaded region.
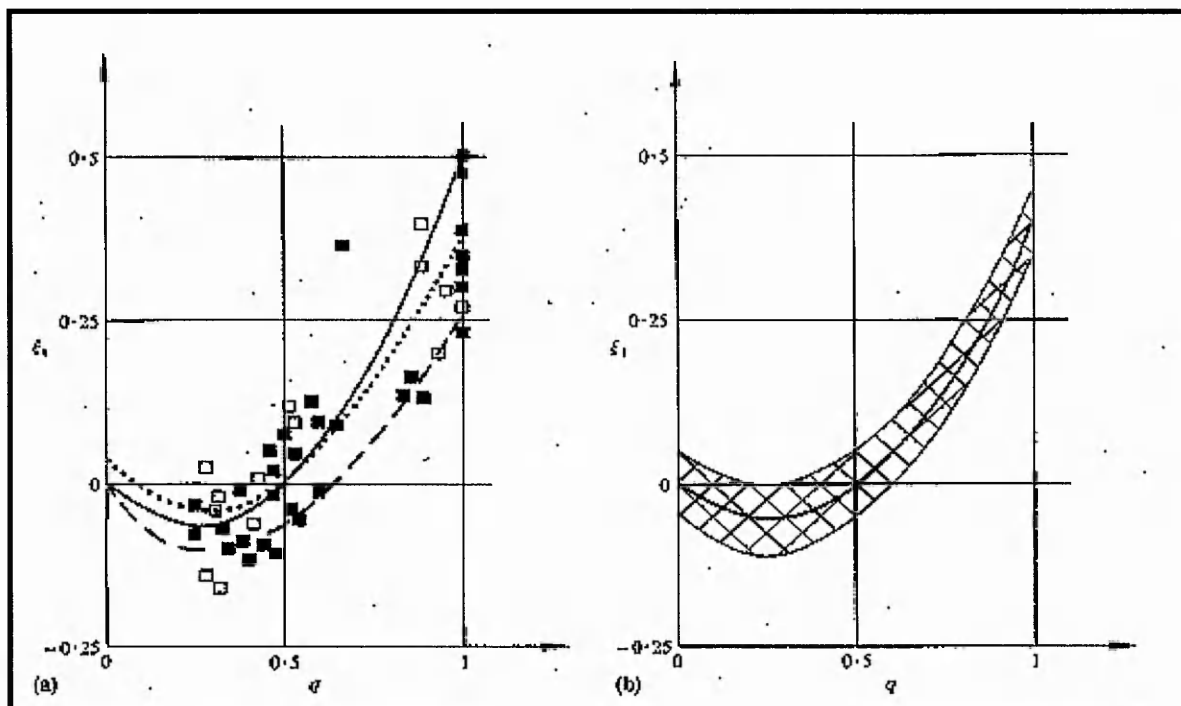
Figure 2.31   (a) Comparison between theoretical and experimental data for ξ_t, (b) ξ_t for arbitrary branch geometry (from Hager, 1984).

Figure 2.32a shows the graphical representation of equation 20 for different intake angles. Figure 2.32b shows Hager's theoretical results for the loss coefficient in the intake channel, ξ_l , for a 45 and 90 degree intake angles, compared to the results of Gardel and Rechsteiner (solid circles), Miller (dashed line) and Ito *et al.* (solid triangles). It can be observed that the comparison of results was acceptable.

Hager also noticed that the loss coefficient in the intake channel could be reduced considerably by rounding the edges of the intake. Ito *et al.* measured quantitatively that ξ_l could be lowered to about 50% from a sharp edge intake when choosing r = b/2 where r denotes the radius of curvature of the intake edge. This is a design tool which is often used in practice.
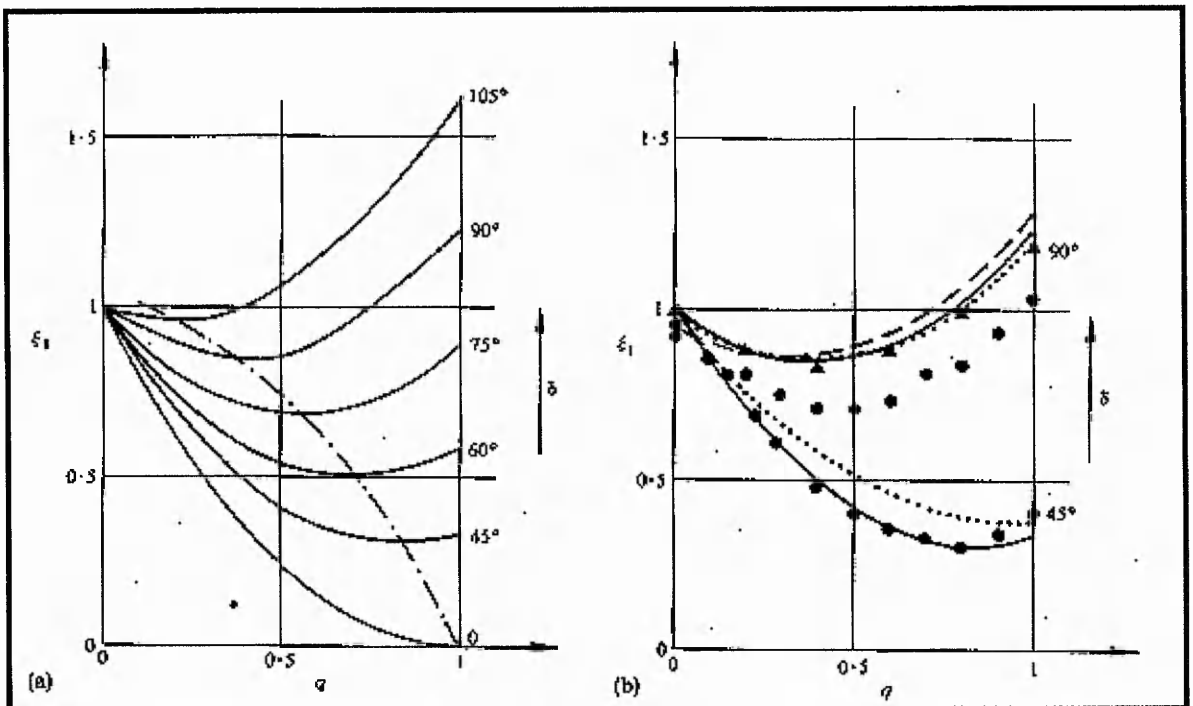
Figure 2.32   (a) Plot of theoretically derived loss coefficient in the intake channel. (b) Comparison of theoretical derivation of ξ_l to experimental data for a 45 and 90 degree intake angle (from Hager, 1984).

In all the preceding descriptions of theoretical models, the researchers only considered two-dimensional flow. Neary (1992) extended Hager's two dimensional anylsis to a *quasi* three dimensional analysis by including continuous functions for the vertical main and inlet channel velocity profiles. Neary defined the maximum width of the separation zone, H was determined by the relationship:

$$H = W_2 (1-\mu).$$ 2.35

Where W_2 was the width of the inlet channel. He then divided the flow depth into a designated number of strata, n, of thickness, d / n, where d = depth of flow. For each stratum, the velocity profiles at sections 1 and 2, in the main channel and inlet channel respectively, were integrated as follows:

$$Q(z)_{1,2} = \int_{(i)d/n}^{(i+1)d/n} u(z)_{1,2} W_{1,2}.dz$$ 2.36

The discharge ratio at each stratum, q_i was then computed as:

$$q_i = \frac{Q_{2,i}}{Q_{1,i}} \qquad\qquad 2.37$$

S_i, μ_i, and H_i were then calculated using equations 2.26, 2.35 and:

$$S = W_1 \cdot q \qquad\qquad 2.38$$

Where S = the distance that the dividing streamplane extends into the main channel and W_1 = width of the main channel.

A sample graph of Neary's results is shown by Figure 2.33, comparing Neary's modified theory to that of Hager's and with experimental measurements.
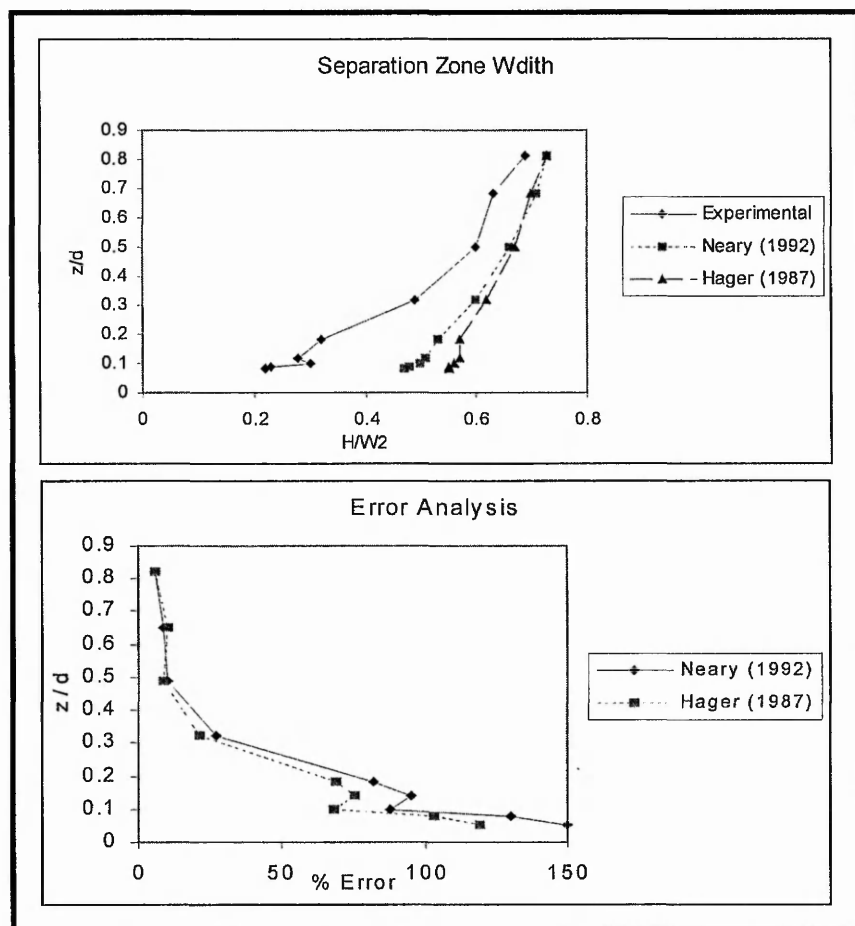
Figure 2.33   Comparison of theoretical model predictions with experimental results from Neary and Hager (after Neary, 1992 and Hager, 1987).

The approach of Neary however, had limited success, because it failed to account for vertical flow exchange driven by secondary circulation. The results from Neary's analysis stressed the importance of secondary circulation in diversion flows and also emphasised the need for three-dimensional numerical modelling of diversion flows. However, again, Neary considered only 90 degree intakes.

2.2.4 Numerical Model Descriptions

Numerical model descriptions of the types studied by this thesis have mainly consisted of two-dimensional calculations for studying branch flows in human cardiovascular systems and have been outlined in section 2.2.2 (Chen and Lian, 1992; Lee and Chiu, 1992; Hayes *et al.*, 1989; Leipsch *et al.* 1982). These studies have indicated interesting qualitative similarities with diversion flow such as those in this study but since most of the biomedical studies have involved laminar, conduit, blood flow, no quantitative insights have been presented for open channel numerical diversion predictions. The only truly three dimensional numerical study to have been conducted on open channel flow was by Neary (1995).

Laminar flow calculations were reported by Leipsch *et al.* (1982) using a finite difference method on a staggered mesh, Hayes *et al.* (1989) who employed a finite element method and by Lee and Chiu (1992) who used a finite volume multiblock approach. All the studies were validated using the experimental results of Leipsch *et al.* all the accuracies obtained were comparable despite the numerical methods, order of accuracy, grid refinement or treatment of the computational meshes. The largest errors were found within the recirculation region along the branch channel wall.

The numerical scheme that Leipsch *et al.* used consisted of an implicit hydrid differencing scheme which improves stability by transforming to a first order accurate scheme if the cell Reynolds number exceeds two. They used a non-uniform staggered computational mesh which had blanked out nodes outside the flow domain. Pressure velocity coupling using a marker and cell type pressure Poisson method satisfying the continuity equation while suppressing odd-even coupling at the pressure nodes. Their grid was 44 x 34 cells in the x and y directions. The

computational model main channel was 9.2m long and the branch channel was 5.5m long. The mesh of Hayes *et al.* was a finite element non-staggered mesh with 140 x 14 triangular elements for the main channel and 98 x 14 elements for the branch channel. They were the only group to examine the effect of the position of the downstream exit and found that this had a negligible effect on the results.

The multiblock technique (described in more detail in chapter 4) was used by Lee and Chiu to divide the main and branch channels into two simple sub domains. This was used in conjunction with an explicit finite volume method using the second order upwind scheme for convection terms and central differencing for diffusion terms in the Navier Stokes equations. More details on these schemes can be found in chapter 4. A non staggered grid was also used. 146 x 62 grid nodes were employed for the main channel with 62 x 62 grid nodes for the branch channel and this arrangement achieved grid independence.

Chen and Lian investigated turbulent flow simulations as did Issa and Oliveira (1994) using the high Reynolds number k-ε turbulence model with wall laws for the boundaries. Validation for both studies was achieved using the experimental results of Popp and Sallet (1982).

Chen and Lian used a finite difference method with the SIMPLE algorithm on a staggered grid; the order of accuracy of their solution is not known. The computational domain was a single block by using a method called the changing loop variable method. This avoided storing grid nodes outside the solution domain. This complicated coding but reduced the computational storage requirements. The results that they obtained compared well to the experimental results of Popp and Sallet. However they did not consider three dimensional effects and therefore at higher discharge ratios the predictions deviated considerably from the experimental measurements. Velocity measurements for Reynolds numbers of 38 000 and two discharge ratios, 0.38 and 0.81 were compared. Sample velocity profiles in the x direction are shown by Figure 2.34 which show the predicted results of Chen and Lian (solid line) with the experimental results of Popp and Sallet (dotted line). It can be observed that the correlation was reasonable.

The only three dimensional turbulent flow simulations of diversion flows have been

carried out recently by Issa and Oliveira and Neary *et al.* (1995). Issa and Olivera
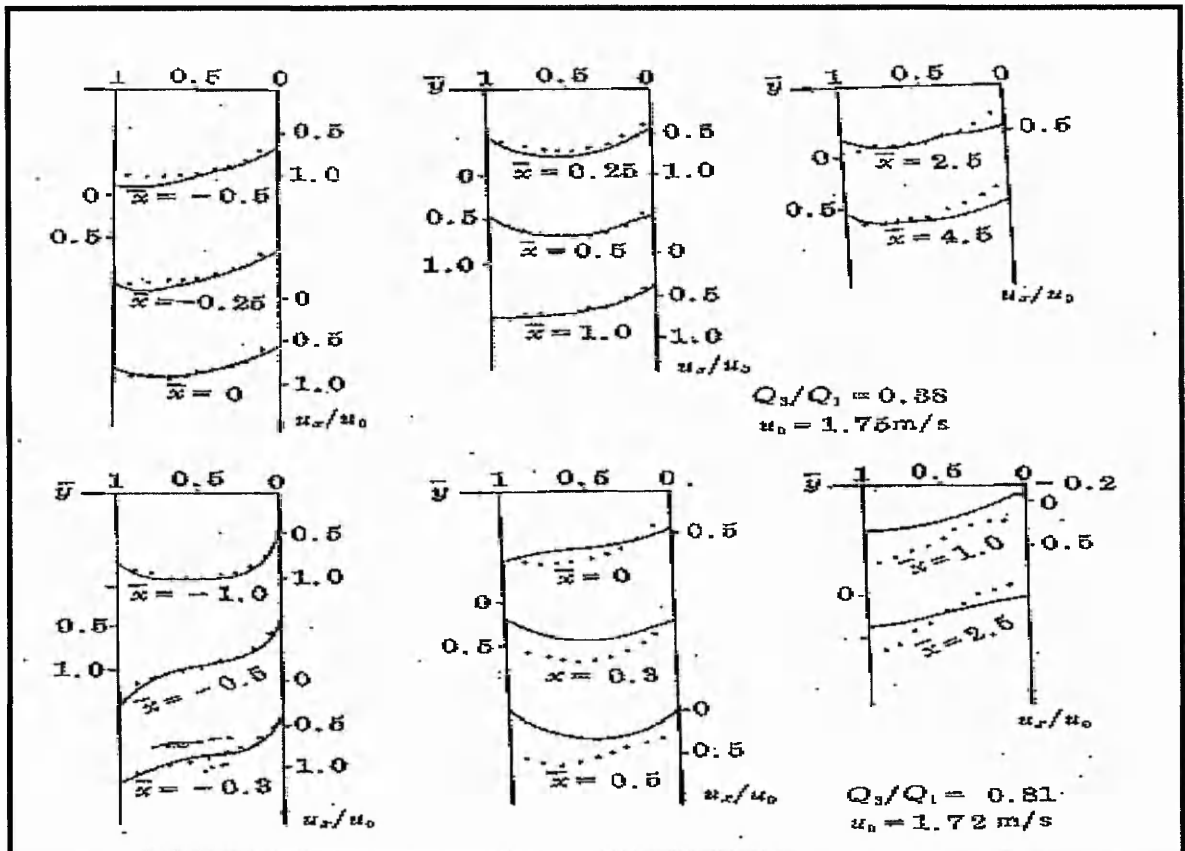
Figure 2.34   Predictions of Chen and Lian (from Chen and Lian, 1992) compared to the experimental results of Popp and Sallet (from Popp and Salet, 1982).

used the SIMPLE algorithm with a finite volume discretisation on a non-staggered mesh. They avoided grid nodes outside the solution domain by using a method similar to Chen and Lian called 'indirect addressing'. Comparisons of their predictions with the results of Popp and Sallet were reasonable, but they used the first order accurate upwinding scheme for the convection terms and their grid dependency study was insufficient. This gave rise to doubts of their results and it is also unfortunate that they did not report the complex three-dimensional features of the flow diversion.

Neary *et al.* (1995) solved the Reynolds Averaged Navier Stokes in orthogonal curvilinear coordinates. They used the near wall k-ω turbulence model (Wilcox 1994). Calculations were carried out for a 90 degree rectangular diversion and the results were compared to   experimental measurements. The computed solutions were further analysed to highlight the complex three-dimensional separation and

limiting streamline patterns. They found that the bed solid boundary and the side walls induce a complex three-dimensional flow which included: a depth varying dividing streamplane in the main channel; a depth varying flow separation and reversal zone in both the main and inlet channel; and transverse circulation currents which sweep near bottom flow into the zones of flow reversal.

The numerical model that Neary used was based on one developed by Sotiropoulos and Patel (1992). The governing equations were discretised on a non-staggered computational grid using the second order accurate central finite difference approximations for the diffusive terms and the first order accurate upwind differencing scheme for the convective terms.

Neary examined laminar flow in a 90 degree intake and compared his predictions to that of Popp and Sallet (1983) in order to validate his model. The computational mesh used is shown by Figure 2.35.
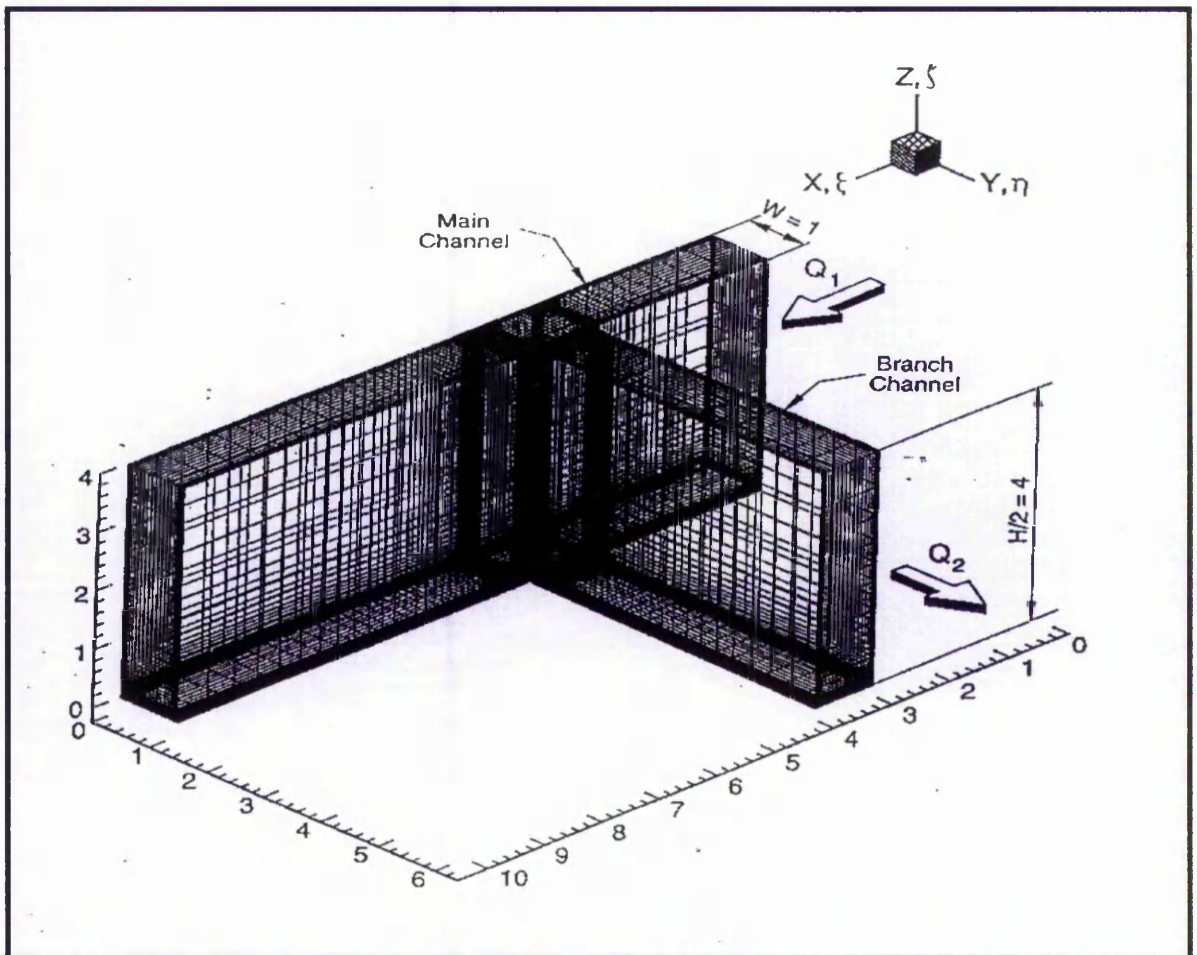
Figure 2.35   Computational mesh (from Neary *et al.,* 1995).

Neary also compared his laminar flow predictions to the experimental results of Leipsch *et al.* (1982) and a sample of these results is shown by Figure 2.36.
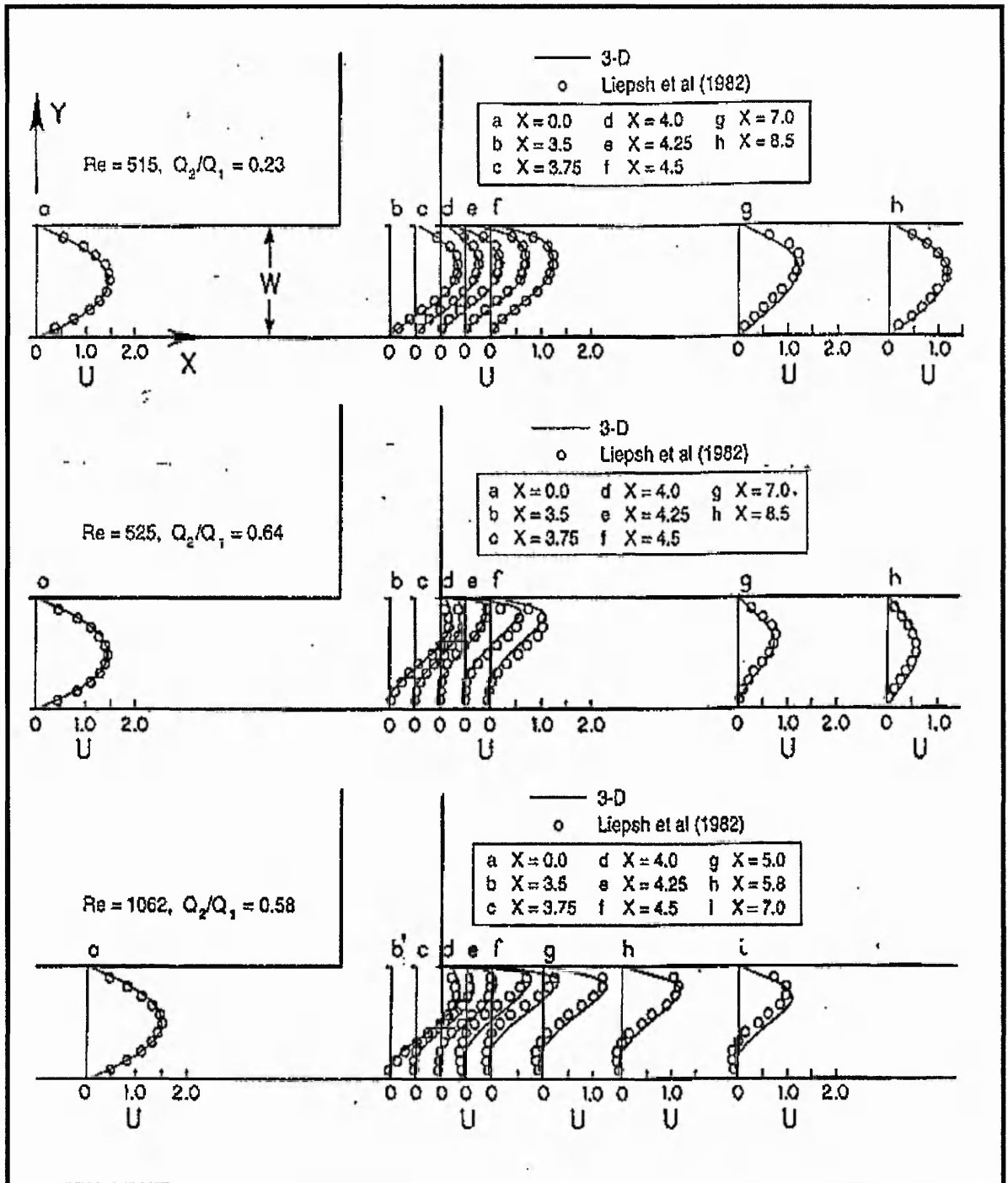
Figure 2.36   Comparison between predicted (Neary) and measured (Leipsch *et al.*, 1982) velocity profiles (from Neary *et al.*, 1995).

It can be observed that Neary obtained a very good agreement for this laminar flow case. Neary developed his study to visualise the flow pattern at the intake using computational streamlines. Figure 2.37 shows samples of these results.
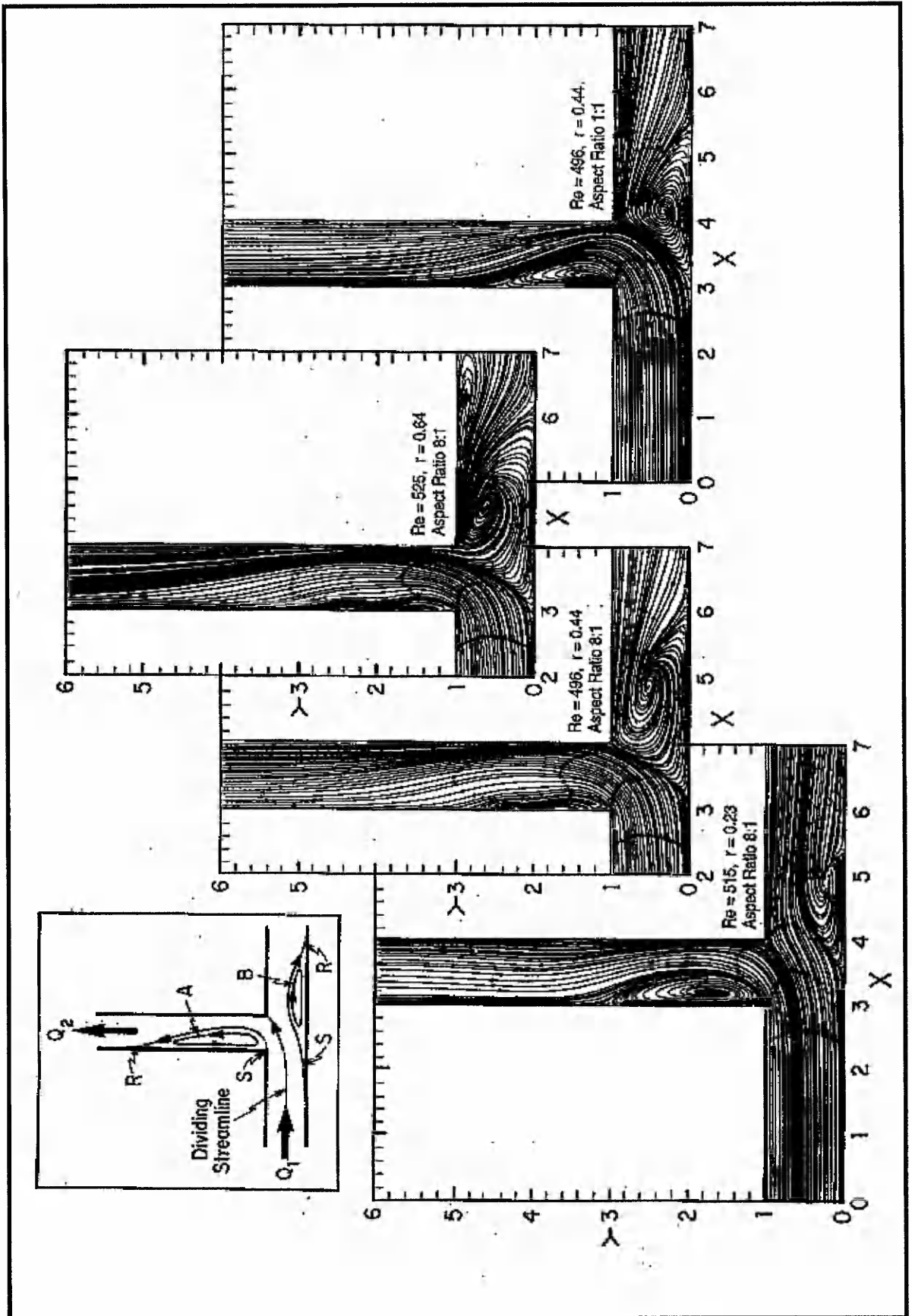
Figure 2.37   Laminar flow streamline plots through a 90 degree intake (from Neary and Sotiropoulos, 1996)

The particle trajectories shown by Figure 2.37 closely resemble those reported by Karino *et al.* (1979) for flow through 90 degree circular pipe junctions, but this was the first time that this complicated flow feature had been observed for rectangular diversions. Neary further illustrated this with three dimensional particle traces as shown by Figure 2.38.

(a)

(b)
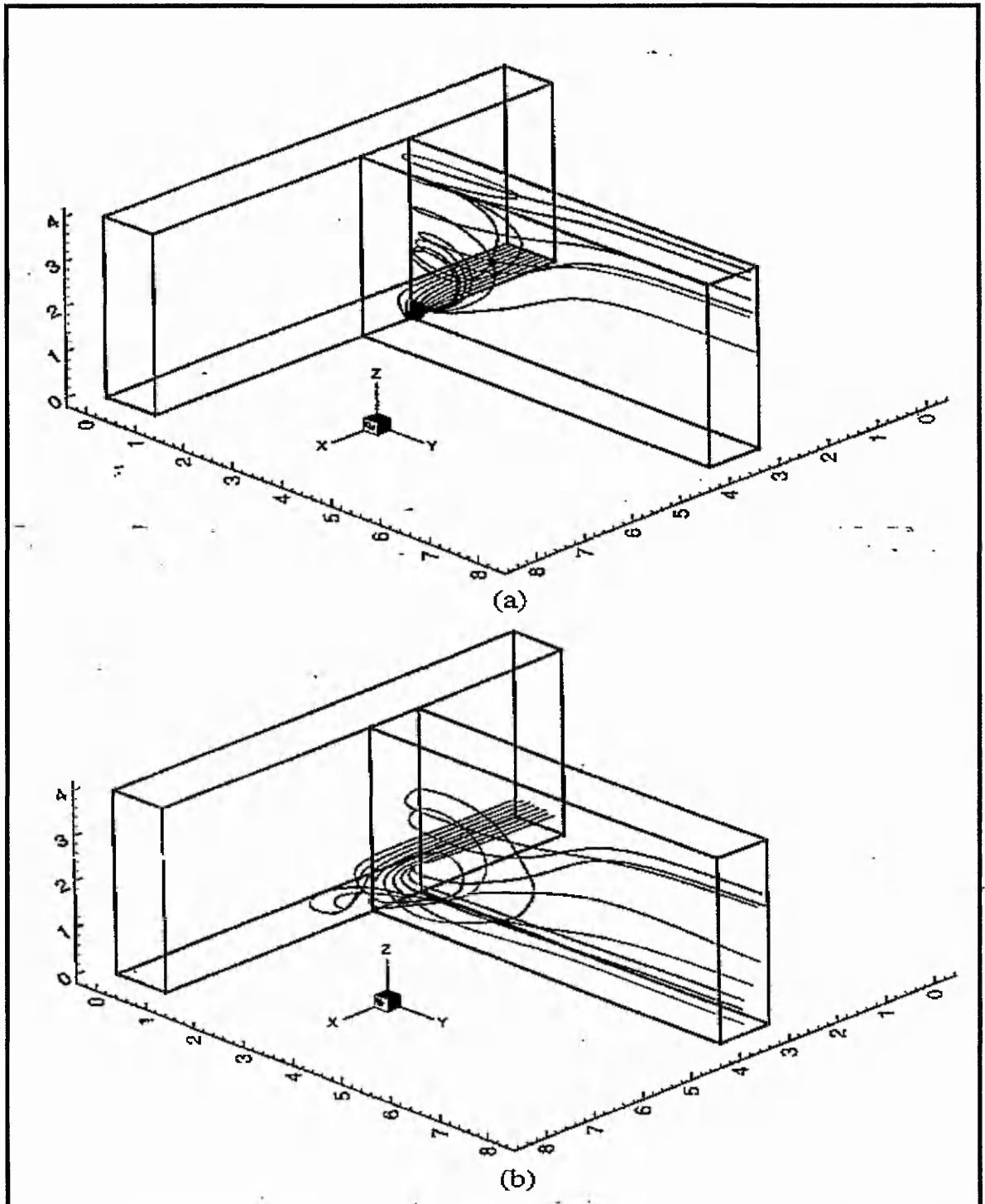
Figure 2.38   Three dimensional particle traces of the flow through a 90 degree diversion (from Neary and Sotiropoulos, 1996).

Particles were computationally released upstream of the junction at two horizontal planes, one near the bed (z=0.01m) and one at an intermediate level (z=0.40m). These plots demonstrated the complexity of the flow in the vicinity of the junction and clarify the relationship between the limiting streamline patterns, vortices and three-dimensional separation. It was shown that all particles released near the bed entered the branch channel, were captured in an area of re-circulation and swirled upwards towards the surface. This upward spiralling motion was fed by the focus, F_s, on the bed of the inlet channel. Even more complicated flow patterns were observed when particles were released at an intermediate plane. Several of these actually got swept past the inlet channel into another re-circulation region then exit, travelled upstream and then entered the inlet channel where they were captured by another re-circulation region.

Neary developed his study to investigate turbulent flow in a 90 degree intake. He compared his results to experimental measurements taken in an earlier investigation by himself. Neary presented comparison velocity profiles a sample of which are shown by Figure 2.39.

Neary found that his model had the tendency to predict more skewed profiles than the measured profiles, particularly in the inlet channel, which was evident in all the cases he tested. His results showed increasing discrepancies beyond the inlet channel centreline where the transverse velocity gradients induced by the diversion become more pronounced. The predicted profiles generally over estimated the measurements. Predicted profiles in the inlet channel were significantly more skewed than the measured profiles and became increasingly more skewed downstream. Faster redevelopment of the measured profiles than those predicted was observed and Neary suggested that some kind of turbulence relaxation effect was present for these flows that was not fully modelled. He also suggested the most likely explanation was increased turbulence diffusion due to Reynolds stresses anisotropies.

Serious discrepancies were observed between predictions and measurements within the separated flow region in the inlet channel. This behaviour suggested that either the secondary motion was not predicted accurately using an isotropic turbulence model or measurement errors had occurred in the velocities or bulk parameters e.g.

the discharge ratio.
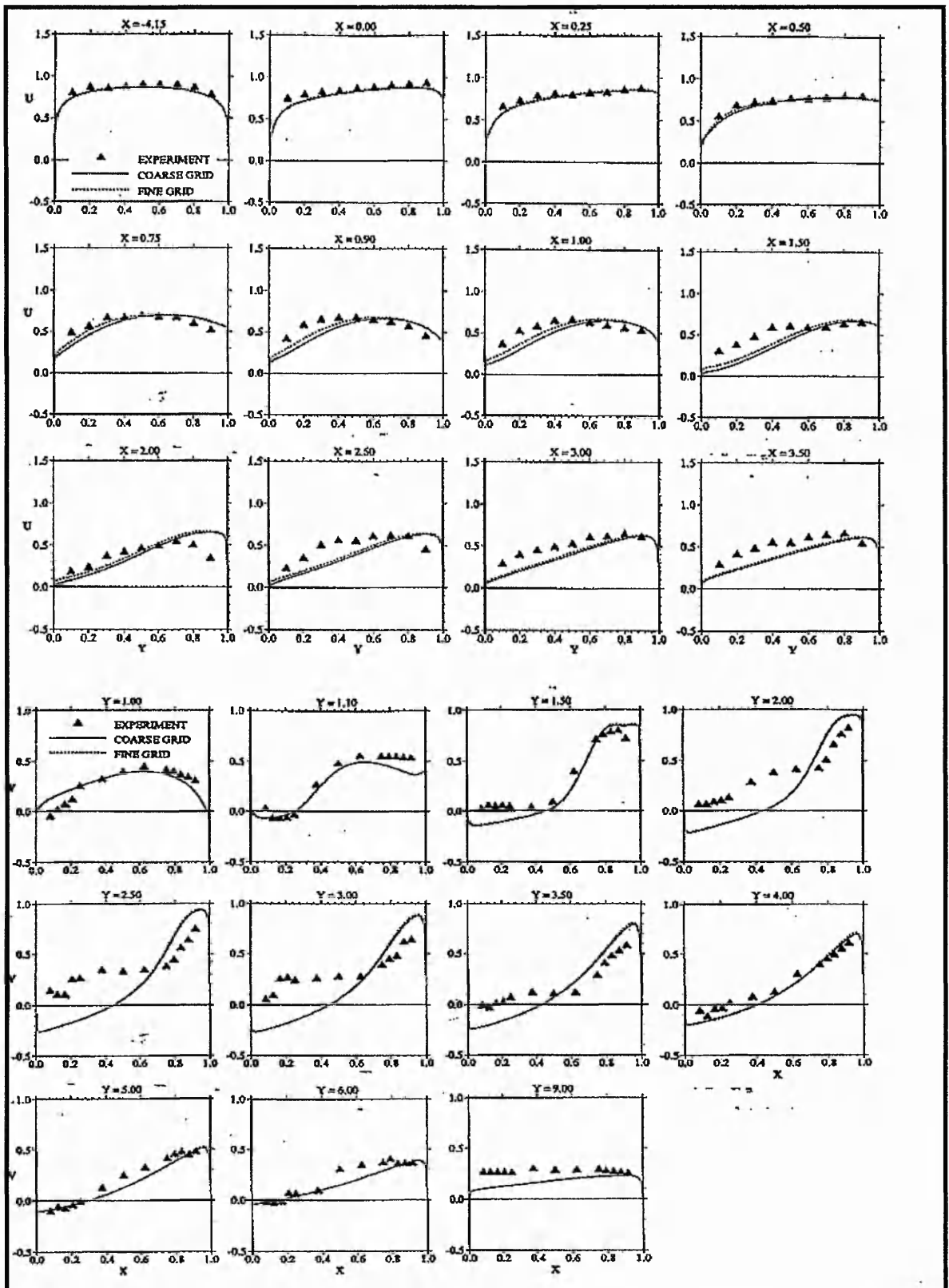
Figure 2.39   Comparison between predicted and measured velocity profiles in the main and inlet channels of a 90 degree diversion (from Neary, 1995).

2.3   CONCLUSIONS

The preceding sections have highlighted, comprehensively, the research that has been undertaken in the field of diversion flows. Particular attention has been attributed to the factors affecting energy losses at intakes. The need to elucidate energy losses occurring at diversions has demanded increasingly more accurate three-dimensional descriptions of these flows. This study was instigated by the need for improved methods for predicting energy losses due to flow asymmetry at lateral intakes angles other than 90 degrees. Physical modelling techniques have been predominantly used for these studies but they are expensive, excessively time consuming and introduce scaling effects that cause discrepancies between model and prototype. The three-dimensional features associated with intake flows have been identified using physical modelling techniques but theoretical models have been restricted to two-dimensional predictions which have failed to capture the three-dimensional phenomena. The future lies with CFD modelling since, with recent advances and the availability of powerful, yet relatively inexpensive PC based numerical codes, the ability to study and identify three-dimensional features is readily available to the hydraulic engineer.

Table 2.5 summarises succinctly the research that has been undertaken into diversion flows from 1944 to date. In total the author of this study has located 30 groups of researchers who have been relevantly involved over this 55 year period. It can be observed from Table 2.5, that the research has predominantly involved the study of 90 intake angles. Although the flow features present at 90 degree intake angles are similar to those present at other intake angles, subtle differences exist, that will be presented during the course of this thesis. Thirteen groups of researchers have examined flow structures at intake angles other than 90 degrees, all of which have focussed on mainly physical or experimental observations and occasionally theoretical predictions. There are presently no records of any researchers studying intake angles other than 90 degrees using numerical techniques. Four groups of researchers have studied 90 degree intake angles using numerical techniques, including Neary and researchers associated with him have modelled 90 degree intakes extremely successfully and their findings have been utilised to predict sediment transport and deposition problems at these intakes. The column relating to the author does not necessarily represent published material.

In undertaking this study the author has endeavoured to ensure the most accurate prediction possible using the code that was available and experimental modelling techniques. The model however, did not take account of free surface effects observed for open channel flows which are commonly modelled by invoking kinematic and dynamic boundary conditions at the free surface. This study uses the findings of Taylor 1944, who found that for uniform open channel diversion flow, for discharge ratios between less than 0.45 and Froude numbers less than 0.4, there was less than a 2% variation of flow depth in the vicinity of the diversion. Therefore it was a reasonable assumption to neglect backwater effects at the diversion which could be modelled by taking account of the free water surface using kinematic and dynamic boundary conditions at the free surface.

In addition secondary circulation cells are induced by anisotropic turbulent Reynolds stresses. Stress induced cells may interact with the skew induced cells generated by the mean flow either by adding vorticity directly to the skew induced cell, or indirectly by modifying the vertical velocity gradient. Reynolds anisotropies would also cause a faster decay of the skew induced vorticity as it travels downstream. All these phenomena will not be correctly modelled by the isotropic turbulence model that was used in this study. Other, minor short comings will be discussed by subsequent chapters.

DIVERSION FLOW FEATURE	Abdel 1949	Avery 1989	Bharadvaj 1982	Bondurant 1952	Bowles 1999	Cardinali 1822	Cho 1985	Cioc 1962	Da Vinci 1507	Gardel 1970	Hager 1984	Issa 1994	Ito 1973	Karino 1979	Lakshmana 1968	Law 1966
Field observations	✓	✓			✓	✓	✓	✓	✓	✓	✓	✓	✓	✓	✓	✓
Experimental observations	✓				✓	✓	✓			✓	✓	✓	✓	✓	✓	✓
Theoretical model descriptions			✓		✓				✓		✓					✓
Numerical model descriptions					✓											
Dividing streamline – 2D		✓		✓	✓		✓	✓	✓	✓	✓		✓		✓	✓
Separation and recirculating eddies – 2D		✓	✓	✓	✓	✓	✓	✓		✓	✓		✓		✓	
Depth varying dividing streamplane	✓				✓										✓	
Secondary circulation cells			✓		✓							✓				
Depth varying zones of separation and recirculation – 3D					✓									✓		
Near bed singularities											✓					
Coherent 3D separation			✓		✓	✓			✓		✓	✓		✓	✓	✓
2D Flow visualisation					✓		✓	✓			✓	✓		✓		✓
90 Degree intake angle		✓	✓		✓		✓	✓			✓	✓		✓		✓
Multiple intake angle	✓	✓		✓			✓	✓		✓	✓					✓
Flow split ratio – 2D			✓													
Biomedical observations			✓													
Laminar flow	✓		✓					✓						✓		✓
Turbulent flow	✓	✓	✓	✓	✓	✓	✓	✓	✓	✓	✓	✓	✓	✓	✓	✓

DIVERSION FLOW FEATURE	Leipsch 1982	Levi 1947	Linder 1952	Miller 1979	Lee 1992	Neary 1993	Neary 1994	Neary 1995	Popp 1983	Ramamurthy 1990	Razvan 1989	Sotiropoulos 1992	Sridharan 1966	Taylor 1944	Vaononi 1975
Field observations	✓		✓				✓	✓	✓		✓				
Experimental observations	✓		✓	✓		✓	✓	✓	✓	✓	✓		✓	✓	✓
Theoretical model descriptions		✓						✓		✓	✓				
Numerical model descriptions	✓				✓			✓				✓			
Dividing streamline – 2D	✓	✓	✓	✓	✓	✓	✓	✓	✓	✓	✓		✓	✓	✓
Separation and recirculating eddies – 2D	✓	✓	✓	✓	✓	✓	✓	✓	✓	✓	✓		✓	✓	✓
Depth varying dividing streamplane			✓			✓	✓	✓	✓			✓			
Secondary circulation cells						✓	✓	✓	✓			✓			
Depth varying zones of separation and recirculation – 3D	✓				✓	✓	✓	✓	✓						
Near bed singularities							✓	✓			✓				
Coherent 3D separation								✓			✓				
2D Flow visualisation											✓				
90 Degree intake angle	✓	✓	✓		✓	✓	✓	✓	✓	✓			✓	✓	✓
Multiple intake angle			✓	✓			✓								
Flow split ratio – 2D			✓		✓			✓							
Biomedical observations	✓														
Laminar flow	✓		✓	✓		✓		✓		✓					
Turbulent flow		✓	✓	✓		✓	✓	✓	✓	✓	✓	✓	✓	✓	✓

Table 2.5   Summary of research undertaken in the field of diversion flow.

3

PHYSICAL MODELLING

3.1   INTRODUCTION

The design of a physical model was undertaken in order to study the different relationships between various parameters of the flow into an intake structure. The model represented a generalised configuration for the intake structure of a small scale, low head, run - of - the - river hydropower station. The parametric relationships studied using the physical model were as follows:

- The relationship between the discharge ratio, Qr in the model and the flow entering the intake structure, Qi with respect to intake angles of 15^0 and 30^0. The model was constructed to allow a range of main channel flows and depths to be tested.

- The relationship between the position of the dividing streamplane in the model with respect to intake angles of 15^0 and 30^0, Reynolds number and discharge ratio, Qr.

- The relationship between the turbulent intensity in the model with respect to intake angles of 15^0 and 30^0, Reynolds number and discharge ratio, Qr.

- Flow visualisation of the turbulence conditions present at the intake structure with respect to intake angles of 15^0 and 30^0, Reynolds number and discharge ratio, Qr. Presence of eddies, re-circulation and vortex shedding were identified.

- The effects of flow straightening systems in the model inlet.

The physical model was constructed in the large channel facility of the Hydraulics laboratory of the Department of Civil and Structural Engineering of Nottingham Trent University. The overall dimensions of the facility are 7.8m long by 1.2m wide by 1.5m deep.

Figures 3.1 and 3.2 show photographs of the physical model viewed looking upstream and downstream. The intake angle of the physical model was 15^0. For further details the reader should refer to Appendix A, drawings CB/1/11/96 and CB/2/11/96. The purpose of the physical modelling was to provide validation data for CFD analyses on the intake configuration.

Figure 3.1   Physical model viewed looking upstream.
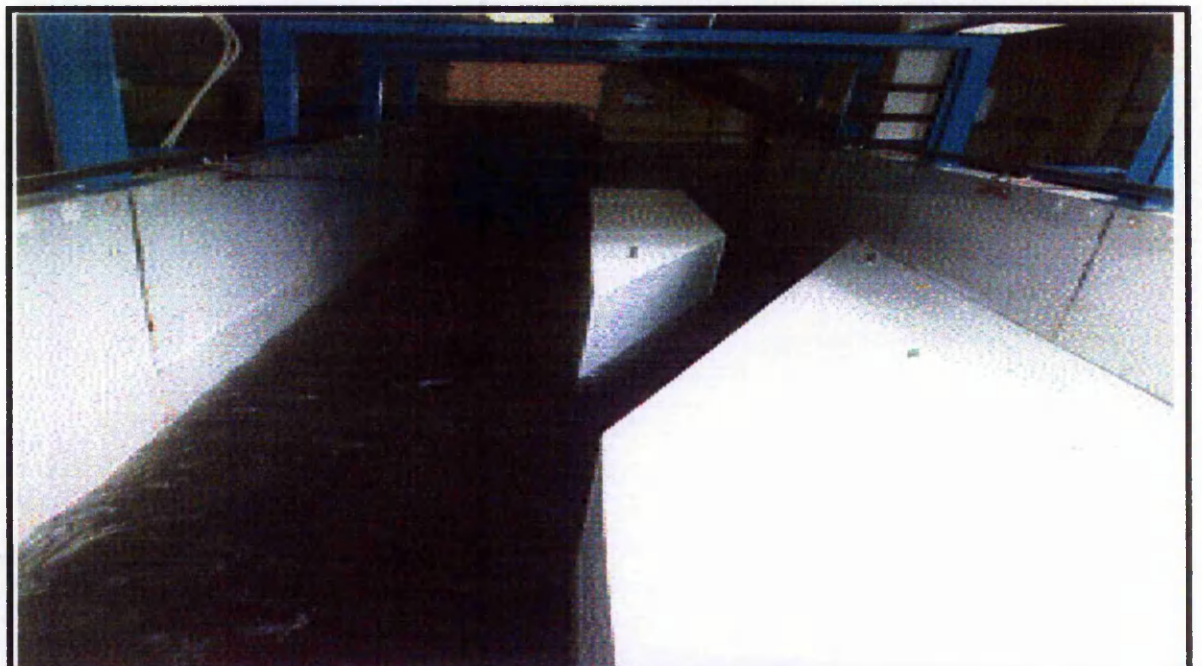
Figure 3.2   Physical model viewed looking downstream.

3.2   MODEL DESIGN

3.2.1 Intake Structure

The model was constructed from marine grade plywood and finished with a gloss paint surface to minimise rotting. This surface gave a Manning's friction coefficient of approximately 0.012. The model was designed using the Froude Scaling Law of Similarity, (Novak and Cabelka 1989).

Model Scaling

Physical models have been used in hydraulic research for many years. It is possible to estimate the size of the prototype that the physical model may represent. To behave in a similar manner to a prototype, physical models should obey certain laws of similtude. To simulate the hydraulics at structures in an open channel it has been widely established that the Froude number should be equal for the model and the prototype. The scale of the physical model to represent a typical low head , small scale, run-of-the-river hydropower site was 1 : 10.

Froude Number (inertia/gravity), $F_r = \left(\dfrac{V^2}{L.g}\right)^{\frac{1}{2}}$ 3.1

Where :-   V = Velocity

                     L = Characteristic Length

                     g = Acceleration due to Gravity

Thus for open channel flow :-

$$F_r^2 = \frac{Q^2.B}{g.A^3}$$ 3.2

Where :-   Q = Flow

                     B = Width of Channel

                     A = Cross Sectional Area of Channel

The geometric scale or length ratio, L_r, between model and prototype is defined by :-

$$L_r = \frac{L_P}{L_m}$$ 3.3

where subscripts $_m$ and $_p$ refer to the model and prototype respectively.

The flow of water into an intake structure is driven by gravity forces and other forces may be neglected if the model is large enough for fully turbulent flow to develop. For fully turbulent flow in this type of model, the Reynolds Number must be greater than 5000, where the Reynolds Number is defined as :-

$$R_e = \frac{\rho.R.V}{\mu}$$ 3.4

Where :-

ρ = Density of Water

R = Hydraulic Radius = A / P

P = Wetted Perimeter

V = Velocity

μ = Dynamic Viscosity

The ratios between the model and prototype of the various parameters of interest are determined from Froude scaling. The scale multipliers according to Froude scaling are :-

Parameter	Scale Multiplier (prototype / model)
Length	L_r
Area	L_r^2
Volume	L_r^3
Time	$t_r = L_r^{0.5}$
Velocity	$V_r = L_r^{0.5}$
Discharge	$Q_r = L_r^{2.5}$
Force	L_r^3

Thus at a scale of 1 :10, the model main channel width of 600mm could represent a prototype main channel width of 6.0m, with flow of up to 16 m^3/s. Similarly a model intake width of 300mm corresponds to a prototype intake channel width of 3.0m. This represents a small, run - of - the - river site. The flow in the model was turbulent in all situations with a Reynolds Number greater than 5000.

Model Construction

Drawing CB/1/11/96 Appendix A, shows a general layout of the physical model. The model was designed to represent a generalised intake structure of rectangular cross section to simplify the analyses of the relationships between the parameters significantly affecting the flow structure at the inlet. The model was constructed such that two intake angles of 15 and 30 degrees could be investigated. A schematic diagram of the physical model is given by Figure 1.5.

An independent traversing system was designed and constructed for the model (see drawing CB/2/11/96, Appendix A). The purpose of this system was to provide a mounting and positioning method for the ADV in the tank. It was necessary to make this independent of the tank due to vibration that was present in the tank walls. The vibrations of the tank were caused by the operation of the pump and vibrations in the delivery pipe.

The main and inlet channel bed were constructed using 22mm thick "Wysaform" sheeting. This was a waterproofed wood ply material and was more durable than marine ply that was used for the construction of the walls of the main and inlet channels. The interchangeable sections of the model, indicated by details A, B and C of drawing CB/1/11/96, were also constructed form marine ply. Silicone sealant was used to provide flexible waterproofing at all joints.

The inlet to the whole model incorporated a flow straightening device. It was found upon initial operation of the model that the flow entering the model was extremely turbulent with large areas of flow reversal and re-circulation. A flow straightening device was therefore incorporated and this was positioned at the inlet to the model. The design and testing of the flow straightening device is covered by section 3.3 of this chapter. The device consisted of 50mm thick of coarse man made geotextile material (in the past known as "horsehair") in combination with 150mm thickness of honeycomb material. The honeycomb material was factory manufactured from high strength cardboard and resin impregnated. It was also coated with a coat of gloss paint. The cell size of the honeycomb was 17mm in diameter.

3.2.2 Flow Measurement by Weirs

Flow measurement in the physical model was undertaken in a number of ways. The inflow into the model was measured using an orifice plate and this is covered by section 3.2.3. Flow measurement in the inlet and main channels of the model was undertaken using sharp crested weirs, a vertical gate and using the ADV. This section covers the flow measurement using the weirs and vertical gate.

Sharp Crested Weir

A suppressed sharp crested weir was used in the main channel of the physical model to measure the flow. This is shown diagrammatically by Figure 3.3. Figure 3.4 shows a photograph of the weir as constructed in the physical model.
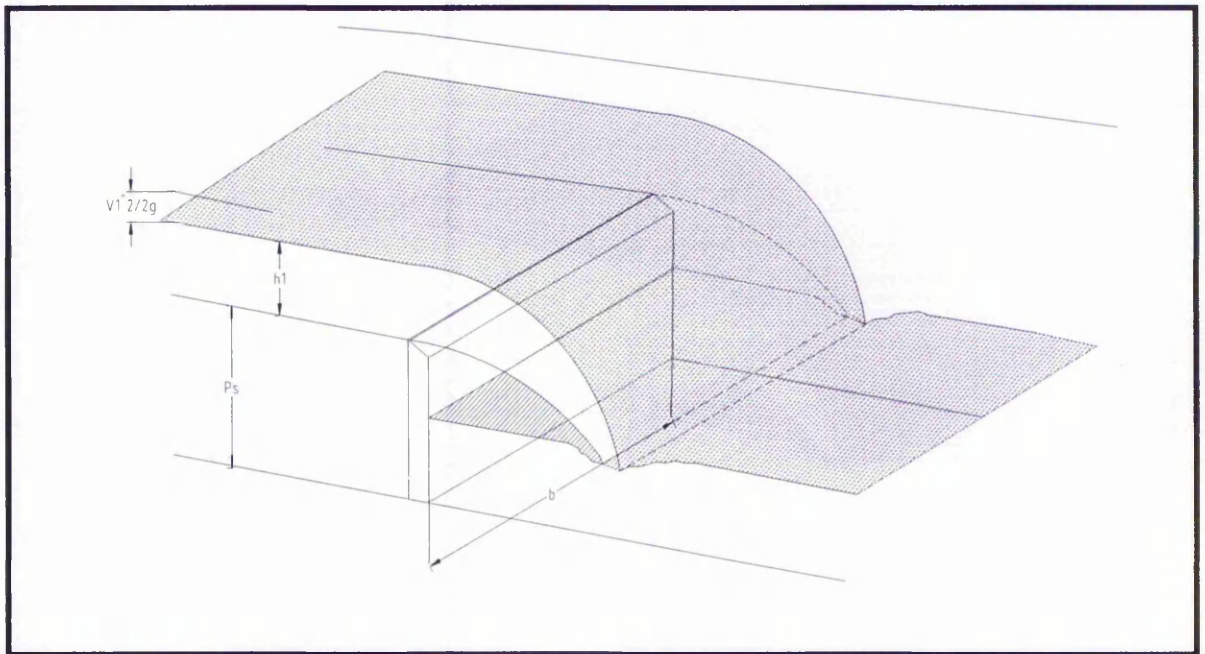
Figure 3.3   Suppressed Weir.

The operation of the weir is based on the depth of flow over the crest and therefore a relationship between the head above the crest h and the discharge Q can be derived using Bernoulli's equation. An idealised relationship between depth and discharge is obtained. This relationship is then modified by use of a coefficient of discharge C_d, to take account of the differences between ideal and real flows, since the actual flow over a weir is complex, involving three dimensional velocity patterns as well as viscous forces.

Figure 3.4   Suppressed weir used in the physical model.

Uncertainties for Rectangular Weir

The term "uncertainty" is defined as "an estimate characterising the range of values within which the true value of the measured lies" (British Standards Institute, 1989) and must not be confused with the term "accuracy". Uncertainty is the property of the measurement undertaken rather than the instrument used to make the measurement, which is termed as accuracy and is often used by the manufacturer of the device. The extent of the uncertainty for each measurement is dependent upon the errors in temperature, density, pressure and installation of the meter.

The calculations for the uncertainties for a rectangular weir are set out in BS 3680: Part 4A : Clause 11 and are explained below.

1.   Uncertainty due to discharge coefficient, X_{ce} :

$$X_{ce} = \pm 1.5\,\% \ \text{for } h/p < 1.0$$
$$X_{ce} = \pm 2.0\,\% \ \text{for } 1.0 < h/p < 1.5$$
$$X_{ce} = \pm 3.0\,\% \ \text{for } 1.5 < h/p < 2.5$$

2.   Uncertainty due to effective width, X_{be} :

$$X_{be} = \pm \frac{100\sqrt{\left[(e_b^2 + e_{kb}^2)\right]}}{b} \qquad\qquad 3.5$$

e_b = uncertainty in measured width

e_{kb} = 0 (as clause 11.6)

b = width of channel

3.   Uncertainty due to effective head, X_{he}

$$X_{he} = \pm \frac{100\sqrt{\left[e_h^2 + e_{h0}^2 + e_{kh}^2 + (2S_h)^2\right]}}{h}$$ 3.6

e_h = uncertainty in measured head

e_{h0} = uncertainty in gauge zero

e_{kh} = 0 (as clause 11.6)

S_h = standard deviation in head

h   = head above weir

4.   Total Uncertainty is discharge reading, X_Q :

$$X_Q = \pm \sqrt{(X_{ce}^2 + X_{be}^2 + X_{he}^2)}$$ 3.7

N. B. All uncertainties are expressed as a percentage.

Example Calculation

1.   h = 106mm

    p = 300mm   h/p = 106 / 300 = 0.35

                h/p < 1.0

    Therefore $X_{ce} = \pm\textbf{1.5\%}$

2. e_b = 1.0mm

    e_{kb} = 0

    b = 600mm (main channel)

$$X_{be} = \pm \frac{100\sqrt{(1.0)^2}}{600} \quad \Rightarrow X_{be} = \pm\textbf{0.17\%}$$

3. e_h = 0.1mm

    e_{h0} = 0.1mm

    e_{kh} = 0

    S_h = 0.05mm (based on 10 successive head readings)

    h = 106mm

$$X_{he} = \pm \frac{100\sqrt{\left[0.1^2 + 0.1^2 + (2\times0.05)^2\right]}}{106} \Rightarrow X_{he} = \pm0.16\%$$

Therefore the total uncertainty in discharge measurements is :

$$X_Q = \pm\sqrt{\left[1.5^2 + 0.17^2 + 0.16^2\right]}$$

$$X_Q = \pm1.52\%$$

Design of Weir Plate

The rectangular thin plate weir is a general classification in which the rectangular notch is the basic form and the full width weir is the limiting case. Triangular notch weirs also exist. However, for simplicity and for the flow conditions in the physical model, a full width weir was designed for the main channel. For the inlet channel a full width weir was initially designed but this was subsequently replaced by a vertical gate (see later in this section).

The design of the full width weir was carried out in accordance with BS 3680 : Part 4A : 1981 – *Measurement of liquid in open channels Part 4A. Method using thin plate weirs.* Figure 3.5 illustrates the form of the full width weir. Since the width of the weir was also the width of the respective channels, i.e. the main and inlet channels, a suitable height of weir needed to be determined. This was accomplished by designing different sized weirs and calculating the range of flows that each weir could accurately measure.

Figure 3.5   Full width weir (BS 3680, 1981)

Discharge calculations were established from the Rehbock formula proposed in 1929, measuring discharge as a function of the effective head h_e and was of the form:

$$Q = 2/3 \, C_d \, b \, h_e^{2/3} \sqrt{(2g)} \qquad\qquad 3.8$$

Where : $C_d = 0.602 + 0.083 \, h/p$

                  $h_e = h + 0.0012$ – effective head

Practical implications for use of the Rehbock formula are listed as below :

- h/p shall not be greater than 1.0;
- h shall be between 0.03 and 0.75m;
- b shall not be less than 0.30m;
- p shall not be less than 0.10m.

Incorporating the restrictions above, the design flows for a 0.10, 0.20, and 0.30m high weir were investigated for both the main and minor channels (0.60m and 0.30m in width respectively). The tabular and graphical results of the designs are shown by Tables 3.1 and 3.2 and Figure 3.6 and 3.7. From the results obtained, a weir plate of height 0.30m was fabricated and installed. This was due to the fact that it could measure a larger range of flows than the 0.10m and 0.20m high weirs. The weir was installed vertically

h (m)	p (m)	h/p	h_e (m)	C_e	Q (l/s)
0.000	0.300	0.000	0.001	0.602	0.044
0.050	0.300	0.167	0.051	0.616	12.641
0.100	0.300	0.333	0.101	0.630	35.916
0.150	0.300	0.500	0.151	0.644	67.033
0.000	0.200	0.000	0.001	0.602	0.044
0.050	0.200	0.250	0.051	0.623	12.783
0.100	0.200	0.500	0.101	0.644	36.705
0.150	0.200	0.750	0.151	0.664	69.194
0.000	0.100	0.000	0.001	0.602	0.044
0.050	0.100	0.500	0.051	0.644	13.209
0.100	0.100	1.000	0.101	0.685	39.072

Table 3.1   Data for discharge over a rectangular weir – main channel.

h (m)	p (m)	h/p	h_e (m)	C_e	Q (l/s)
0.000	0.300	0.000	0.001	0.602	0.044
0.050	0.300	0.167	0.051	0.616	6.320
0.100	0.300	0.333	0.101	0.630	17.958
0.150	0.300	0.500	0.151	0.644	33.516
0.200	0.300	0.667	0.201	0.657	52.554
0.250	0.300	0.833	0.251	0.671	74.858
0.300	0.300	1.000	0.301	0.685	100.312
0.000	0.200	0.000	0.001	0.602	0.022
0.050	0.200	0.250	0.051	0.623	6.391
0.100	0.200	0.500	0.101	0.644	18.353
0.150	0.200	0.750	0.151	0.664	34.597
0.200	0.200	1.000	0.201	0.685	54.766
0.000	0.100	0.000	0.001	0.602	0.022
0.050	0.100	0.500	0.051	0.644	6.604
0.100	0.100	1.000	0.101	0.685	19.536

Table 3.2   Data for discharge over a rectangular weir – inlet channel.
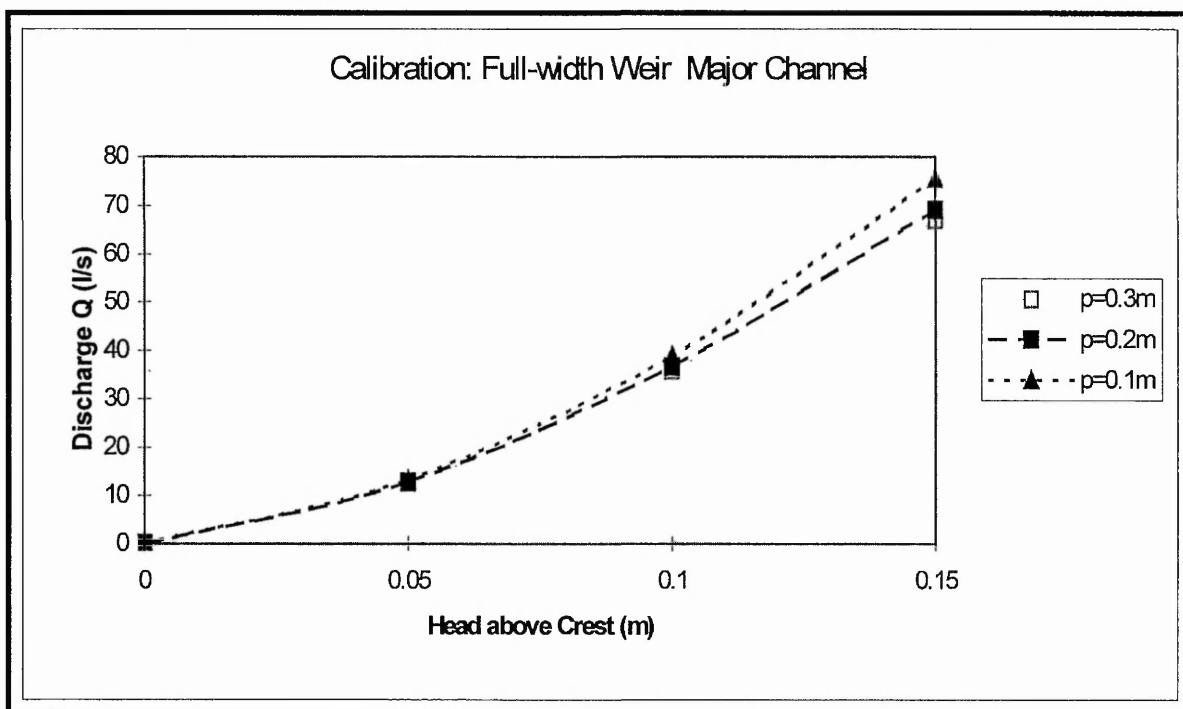
Figure 3.6   Calibration for full width weir in main channel.

and perpendicular to the walls of the channel, the intersection of the weir plate with the walls and floor of the channel were watertight and firm and the weir was capable of withstanding the maximum flow without damage of distortion. These are criteria specified by BS 3680.

Calibration: Full-width Weir Minor Channel
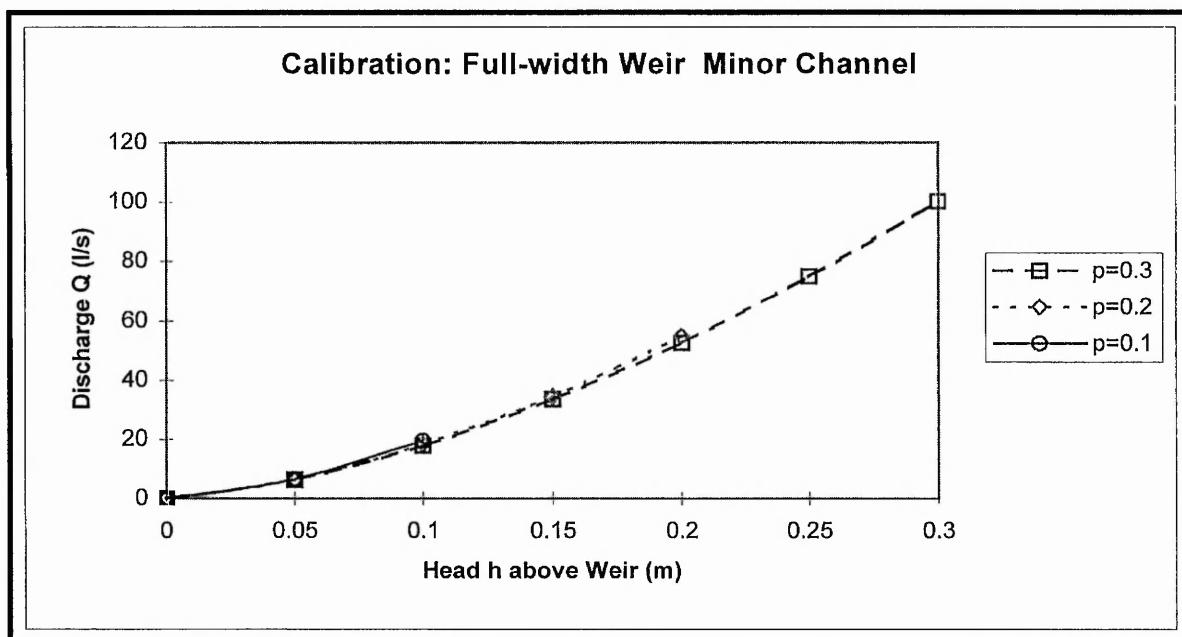
Figure 3.7   Calibration for full width weir in minor channel.

Calibration equations for the main and inlet weirs with a crest height of 0.30m are as follows :-

Main channel :	$y = 4.629\,x^2 - 0.726x - 4.002$	3.9
Inlet Channel :	$y = 1.858\,x^2 + 2.0128 - 4.419$	3.10

Vertical Sluice Gate

Initially a rectangular full width weir plate was installed in the inlet channel of the physical model. This model set up was used during the flow split measurements to determine the flow split ratio, Q_r of an uncontrolled intake configuration. Subsequently a control system was required to the inlet channel in order to vary the flow split ratio during the investigation of the flow structure at the intake. For this model application a vertical sluice gate provided the simplest method of discharge control.

Uncertainties for Vertical Sluice Gate

No specific details relating to uncertainties for vertical sluice gates are given in the British Standards. However BS ISO TR 5168 : 1998, *Fluid Flow, Evaluation of Uncertainties*, and BS 5844 : 1980, *Flow Measurement, Liquids in Open Channels, Uncertainty Estimation*, give general guidelines on uncertainties for flow measuring

devices. In addition the parameters involved in the uncertainty estimation for the sharp crested weirs are comparable to the parameters involved with the vertical sluice gate. The discharge equations for the sharp crested weir and the vertical sluice are functions of a discharge coefficient, C_d, the width of the measuring structure, b, and the measured heads, h_e, y_G and y_1 respectively. It is therefore reasonable to assume that the uncertainty involved with each of these parameters will be similar for each measuring device. A sample calculation is given in section 3.2.2 for the uncertainty estimation for the sharp crested weir. Based on the figures given in the sample calculation a total uncertainty in discharge measurements of +/- 1.5% is obtained for the sharp crested weir. Therefore, using the previous assumptions a total uncertainty in discharge measurements of +/- 1.5% can similarly be applied to the vertical sluice gate.

Design of Vertical Sluice Gate

The vertical sluice gate was designed and installed in the inlet channel to provide a method of controlling the flow split ratio, Q_r in the physical model. A calibration curve was plotted for the vertical sluice gate based on the equations for a vertical sluice gate:

$$C_d = \frac{C_c}{\sqrt{1+(C_c \cdot y_G / y_1)}}$$
3.11

where $\qquad C_c = 0.61$ for $0 < (y_G / E_{S1}) < 0.5$

and $\qquad Q = b.C_d.y_G.\sqrt{2.g.y_1}$

Table 3.3 and Figure 3.8 show the results of this calibration.

The required opening of the sluice gate to give the inlet discharge, Q_l, was calculated based on an iterative process. The flow split ratio, Q_r was known, the total and the main channel discharge were known, Q_t and Q_m respectively, and the depth in the main channel, y_1 was known.

Qr	Qt	Qm	Depth over Weir	Qi	Sluice Opening	Qr (actual)
	(l/s)	(l/s)	(mm)	(l/s)	(mm)	
0.50	22.00	14.60	55.10	7.40	15.50	0.507
0.50	35.00	23.30	75.20	11.70	24.00	0.502
0.50	47.00	31.30	91.40	15.70	31.70	0.502
0.50	58.00	38.60	104.90	19.40	38.70	0.503
0.50	68.00	45.30	116.40	22.70	44.80	0.501
1.00	22.00	11.00	45.60	11.00	23.60	1.000
1.00	35.00	17.50	62.20	17.50	37.00	1.000
1.00	47.00	23.50	75.60	23.50	49.10	1.000
1.00	58.00	29.00	86.90	29.00	60.20	1.000
1.00	68.00	34.00	96.50	34.00	70.10	1.000
1.50	22.00	8.80	39.10	13.20	28.70	1.500
1.50	35.00	14.00	53.60	21.00	45.30	1.500
1.50	47.00	18.80	65.20	28.20	60.40	1.500
1.50	58.00	23.20	75.00	34.80	74.20	1.500
1.50	68.00	27.60	84.10	41.40	88.00	1.500
2.00	22.00	7.30	34.50	14.70	32.20	2.014
2.00	35.00	11.60	47.20	23.40	51.10	2.017
2.00	47.00	15.60	57.60	31.40	68.40	2.013
2.00	58.00	19.30	66.40	38.70	79.60	2.005
2.00	68.00	22.30	73.00	44.70	97.20	2.004
2.50	22.00	6.30	31.20	15.70	34.70	2.492
2.50	35.00	10.00	42.70	25.00	55.20	2.500
2.50	47.00	13.40	52.00	33.60	74.20	2.507
2.50	58.00	16.80	60.50	42.20	93.30	2.512
2.50	68.00	19.40	66.60	48.60	107.50	2.505
3.00	22.00	5.50	28.40	16.50	36.70	3.000
3.00	35.00	8.70	38.90	26.30	58.60	3.023
3.00	47.00	11.70	47.50	35.30	78.80	3.017
3.00	58.00	14.50	54.80	43.50	97.30	3.000
3.00	68.00	17.00	61.00	51.00	114.40	3.000

Table 3.3   Calibration of vertical sluice gate.
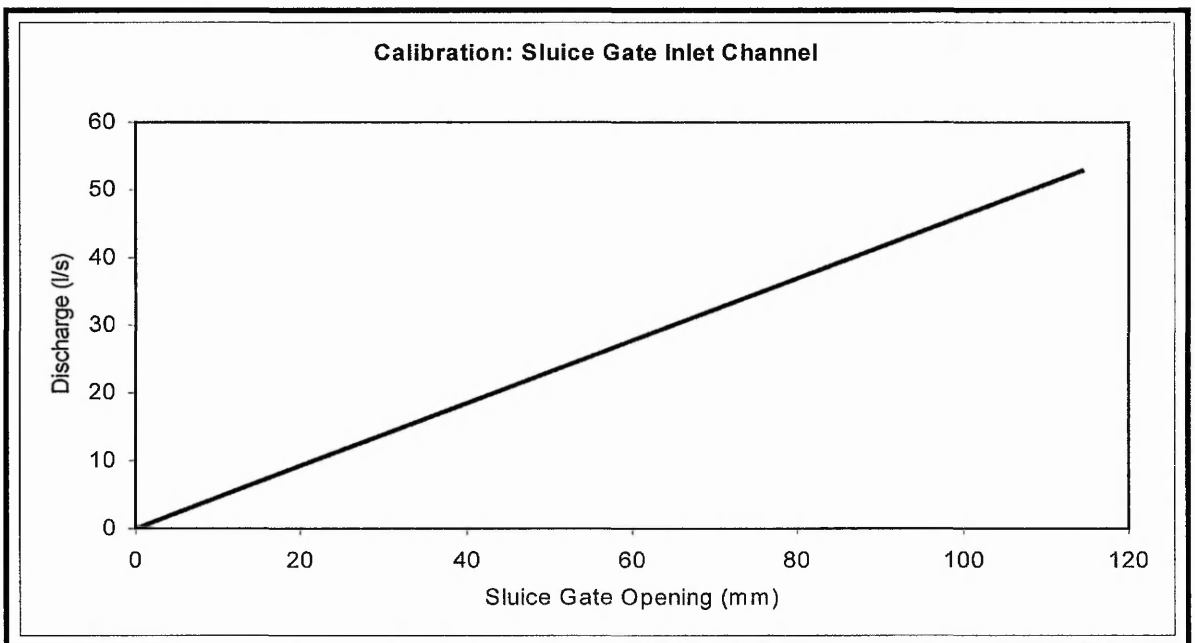
Figure 3.8   Calibration of vertical sluice gate.

Figure 3.9 shows a photograph of the vertical sluice gate installed in the physical model.

Figure 3.9   Vertical sluice gate in the physical model.

3.2.3 Flow Measurement by Orifice Plate

The total inflow into the physical model, Q_t, was measured using an orifice plate positioned in the delivery pipe to the model. The orifice plate is a common and widely used measuring device in pipelines running full. In its simplest form it consists of a thin sheet of metal with a concentric hole through which the fluid passes. The plate is inserted into the pipeline between two flanges and pressure tappings are positioned at a predetermined position to record the pressures on each side of the plate.

The position of the tappings vary and this effects the value of the coefficient of discharge. Provided that a standard position of tappings are used then inaccuracies in differential pressure readings will be negligible. The standard position of tappings include radius tappings, also known as d and d/2 tappings because of their respective positions from the orifice plate, corner tappings and flange tappings which are equidistant from the orifice plate. The differential pressure on both the upstream and downstream side of the plate are measured, from which the discharge can be calculated.
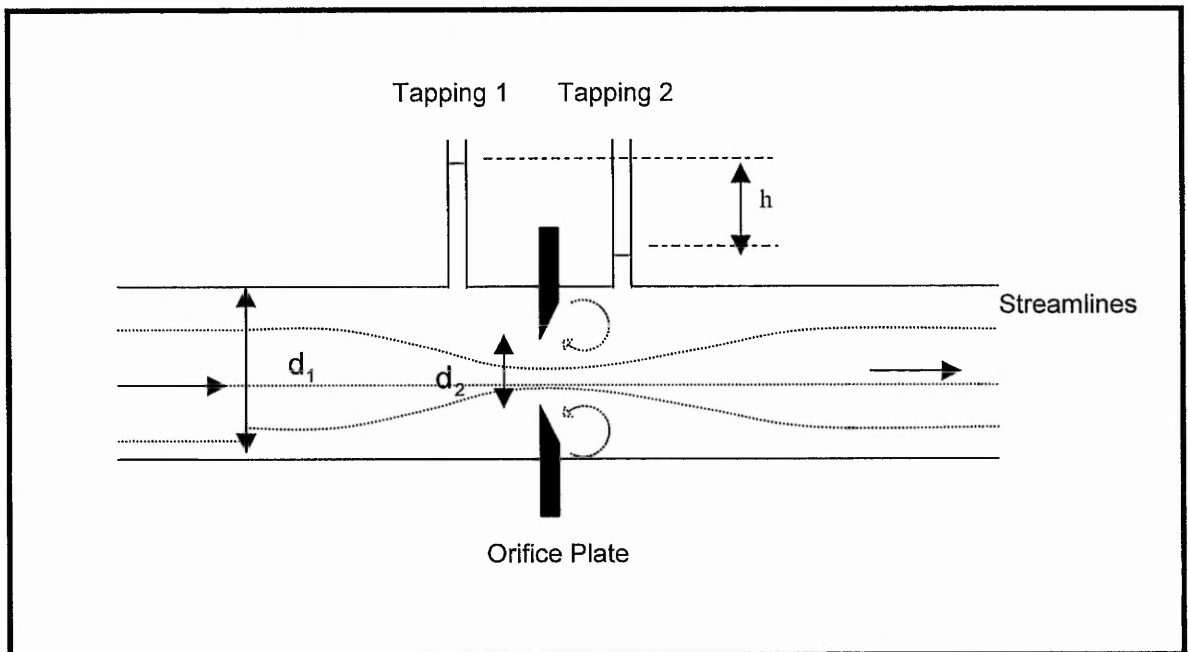
Figure 3.10   A simple orifice plate.

Design of the Orifice Plate

Design of the orifice plate was carried out in accordance with the specifications set out in *British Standards BS 1042 Section 1.1 : "Specifications for square edged orifice plates, nozzles and venturi tubes inserted into circular cross section conduits running full"*. It was necessary to design an orifice plate that was capable of measuring the range of flows which were encountered in the physical model. The corresponding flow range was 0 – 65 l/s.

The specifications for an orifice plate set out by BS 1042 are summarised below:

Clause	Specification
8.1.7.1	The diameter of the orifice $\geq$ 12.5mm $0.20 \leq$ diameter ratio $\beta \leq 0.75$.
8.2.1.3	Flange tappings must be a distance of 24.5mm +/- 0.5mm from the orifice plate – upstream and downstream $(\beta > 0.6)$.
8.2.1.7	Tappings upstream and downstream will have the same diameter.
8.3.1	$Re_D \geq 1260\beta^2 D$ (NB: D is diameter of pipe)

Table 3.4   BS 1042 Specifications for orifice plate.

The diameter of the orifice plate designed was 150mm with an inlet pipe diameter of 202.6mm. This gave a corresponding β = 0.74, therefore satisfying clause 8.1.7.1. A flanged tapping arrangement was used to measure the differential pressure.

Discharge Formula

The preferred discharge formula used by BS 1042, as opposed to the equation derived previously is of the form:

Mass flow rate,

$$q_m = \frac{C_d}{\sqrt{(1-\beta^4)^2}} \cdot \frac{\varepsilon.\pi.d^2}{4} \sqrt{2.\Delta P.\rho} \qquad\qquad 3.12$$

(CLAUSE 5.1 BS 1042 SECTION 1.1)

Volumetric flow rate,

$$Q = \frac{q_m}{\rho} \qquad\qquad 3.13$$

Where:

q_m = mass flow rate, kg / s

ε = expansibility factor (negligible, assume = 1)

ΔP = differential pressure: $P_1 - P_2$, N/m^2

ρ = density of fluid (assumed to be 1000 kg/m^3)

Calculation of Flow Range

Using equations 3.12 and 3.13, a direct relationship of flows can be established. Consider a volumetric flow rate, Q of 0.040m^3/s, then:

$$q_m = Q\rho = 0.040 \times 1000 = 40 \text{ kg/s}$$

Rearranging equation 3.13 gives:

$$\Delta P = \left| \frac{4.q_m\sqrt{(1-\beta^4)}}{C_d.\varepsilon.\pi.d^2} \right|^2 \cdot \frac{1}{2\rho} \qquad\qquad 3.14$$

ΔP is expressed in N/m^2. The pressure difference across the orifice plate was measured using a digital manometer (see next section). The manometer outputs

readings in terms of millibars (mb) and hence the preceding equation must be divided by 100 to give ΔP readings in mb. Hence:

$$\Delta P = \left| \frac{4.q_m \sqrt{(1-\beta^4)}}{C_d.\varepsilon.\pi.d^2} \right|^2 . \frac{1}{200\rho} \qquad\qquad 3.15$$

Table A.7 of BS 1042 Section 1.1 gives typical values for the coefficient of discharge associated with orifice plates. The corresponding value of C_d with a β ratio of 0.74, flanged tappings with $Re_D = 3 \times 10^5$ was found to be 0.6025. Note that for $Re_D = 1 \times 10^6$, $C_d = 0.6005$, however, a Reynolds Number as high as this corresponds to a much higher flow rate than is desirable and hence the chosen value of 0.6025 is reasonable.

Therefore:

$q_m = 40$ kg/s

$C_d = 0.6025$

$d = 0.150$m

$\beta = 0.74$

$\rho = 1000$ kg/m^3

$$\Delta P = \left| \frac{4 \times 40 \times \sqrt{(1-0.74^4)}}{0.6025 \times 1 \times \pi \times 0.150^2} \right|^2 . \frac{1}{200 \times 1000}$$

$\Delta P = 49.41$ mb

Therefore a differential pressure reading of 49.4 mb corresponded to a flow rate of 0.04 m^3/s or 40 l/s through the inlet pipe.

Table 3.5 and Figure 3.11 show the ratings for the orifice plate used in the physical model. Figure 3.12 shows a photograph of the orifice constructed into the model.

Volumetric Flow Rate, Q (m³/s)	Mass Flow Rate, q_m (kg/s)	V (m/s)	Re_D	Pressure Difference (mb)
0.005	5	0.155	31360	0.771
0.010	10	0.310	62720	3.085
0.015	15	0.465	94079	6.942
0.020	20	0.620	125439	12.342
0.025	25	0.775	156799	19.284
0.030	30	0.931	188159	27.769
0.035	35	1.086	219518	37.796
0.040	40	1.241	250878	49.367
0.045	45	1.396	282238	62.480
0.050	50	1.551	313598	77.136
0.055	55	1.706	344958	93.334
0.060	60	1.861	376317	111.075
0.065	65	2.016	407677	130.359
0.070	70	2.171	439037	151.186
0.075	75	2.326	470397	173.555
0.080	80	2.482	501756	197.467
0.085	85	2.637	533116	222.922
0.090	90	2.792	564476	249.919
0.095	95	2.947	595836	278.459
0.100	100	3.102	627196	308.542

Table 3.5   Flows and differential pressure for 150mm diameter orifice plate.
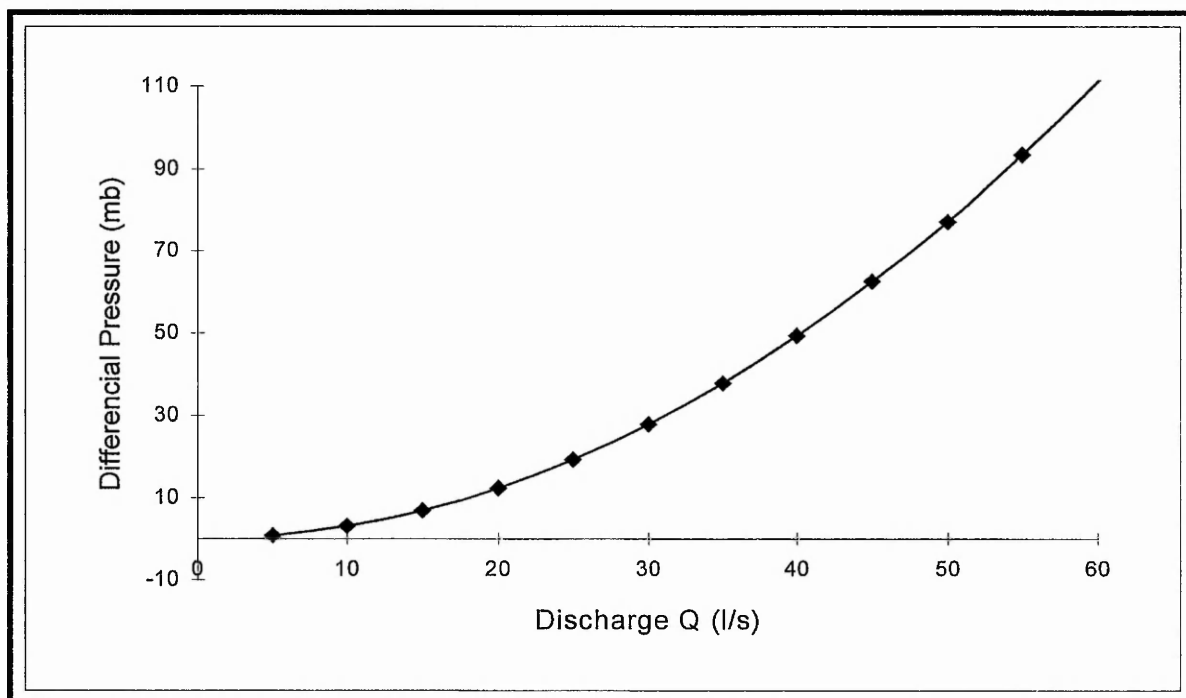
Figure 3.11   Calibration chart for 150mm diameter orifice plate.

The calibration equation for the orifice plate was:

$$y = 0.0309 \, x^2 - 0.0003 \, x \qquad\qquad 3.16$$

Where y = differential pressure and x = discharge.

Uncertainties for an Orifice Plate

International Standards Organisation (ISO) 5168 provides guidelines for the determination and calculation of the uncertainty for discharge measurements using an orifice plate. However, the uncertainty can be assumed to be sufficiently accurate with a value of +/- 1% (Kent, 1956) provided that:

- The flow approaching the meter is normal, i.e. the velocity distribution in the pipe of sufficient length upstream of the meter is not disturbed by bends or other fittings.
- The flow is reasonably steady.
- The viscosity of the fluid is low.
- The head or fall of pressure across the orifice is not greater than 4% of the absolute pressure.
- The orifice has a good square edge.
- The flange tappings do not project into the pipe and are located within +/- 5% of the specified position.
- The pressure is correctly transmitted to the meter and not impaired by leaks or by false heads due to moisture locks or unequal density in the two limbs.

For the application of the orifice plate in the physical model all of the above criteria were satisfied giving an approximate uncertainty of +/- 1%.
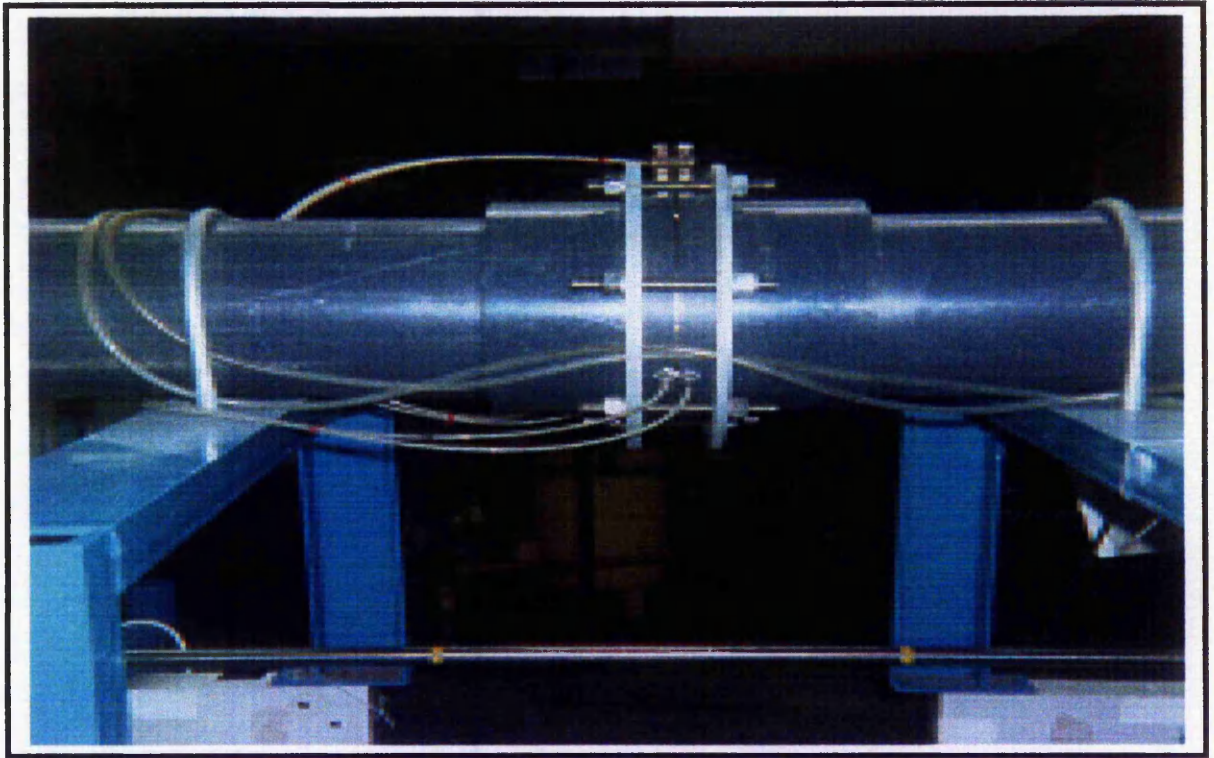
Figure 3.12   Orifice plate in the physical model.

3.2.4 Electronic Manometer

For the purposes of measuring the differential pressure across the orifice plate an electronic manometer was used. The manometer manufactured by Digitron was initially calibrated to check to the manufacturers calibration. The manometer was capable of measuring absolute and differential pressures and calibrations for both functions were tested although only the differential pressure was measured across the orifice plate. The Digitron manometer was connected with two plastic tubes to tappings on either side of the orifice plate through which the differential head across the orifice plate was measured. The differential head measured across the orifice plate leads to a measurement for the differential pressure based on the following relationship:

$$\Delta P = \rho_w.g.\Delta h \qquad\qquad 3.17$$

where: ΔP = Differential pressure (in Pascals (N/m^2))

ρ_w = Density of water

Δh = Differential head.

The manometer was calibrated by attaching two plastic tubes to the instrument which were in turn connected to two reservoirs holding water. The two reservoirs were elevated at different heads relative to each other, which were measured and recorded. The corresponding differential pressure was measured by the manometer. Comparisons of differential pressure measured by the manometer and calculated from the measured head are shown by Table 3.6 and Figures 3.13 and 3.14 shows the comparison in terms of percentage error of the measured differential head from the calculated differential head.

Differential Head (m)	Calculated Differential Pressure (mB)	Measured Differential Pressure (mB)	Measured Differential Pressure (mB)	Measured Differential Pressure (mB)
0.0	0.0	0.0	0.0	0.0
0.5	49.0	48.7	48.3	45.2
1.0	97.9	99.4	95.4	95.8
1.5	146.8	147.6	146.5	145.5
2.0	195.8	200.0	195.6	199.0
2.5	244.8	241.0	240.0	237.0
3.0	293.8	283.0	283.0	280.0
3.5	342.7	333.0	334.0	325.0
4.0	391.7	381.0	382.0	374.0
4.5	440.7	431.0	431.0	426.0
5.0	489.6	475.0	474.0	468.0

Table 3.6   Measured and calculated differential pressures.

The calibration of the manometer was represented with a straight line relationship as shown above with the equation of the line:

$$y = 0.953x + 2.418 \qquad\qquad R^2 = 0.999 \qquad\qquad 3.18$$

This represents a reasonably linear, direct relationship between the measured and calculated differential pressures. Figure 3.14 shows that the manometer measures to an uncertainty of +/- 5%. It appears that a rogue reading was obtained during one of the tests (red dotted line) at approximately 60 mBar. This result has therefore been discounted.
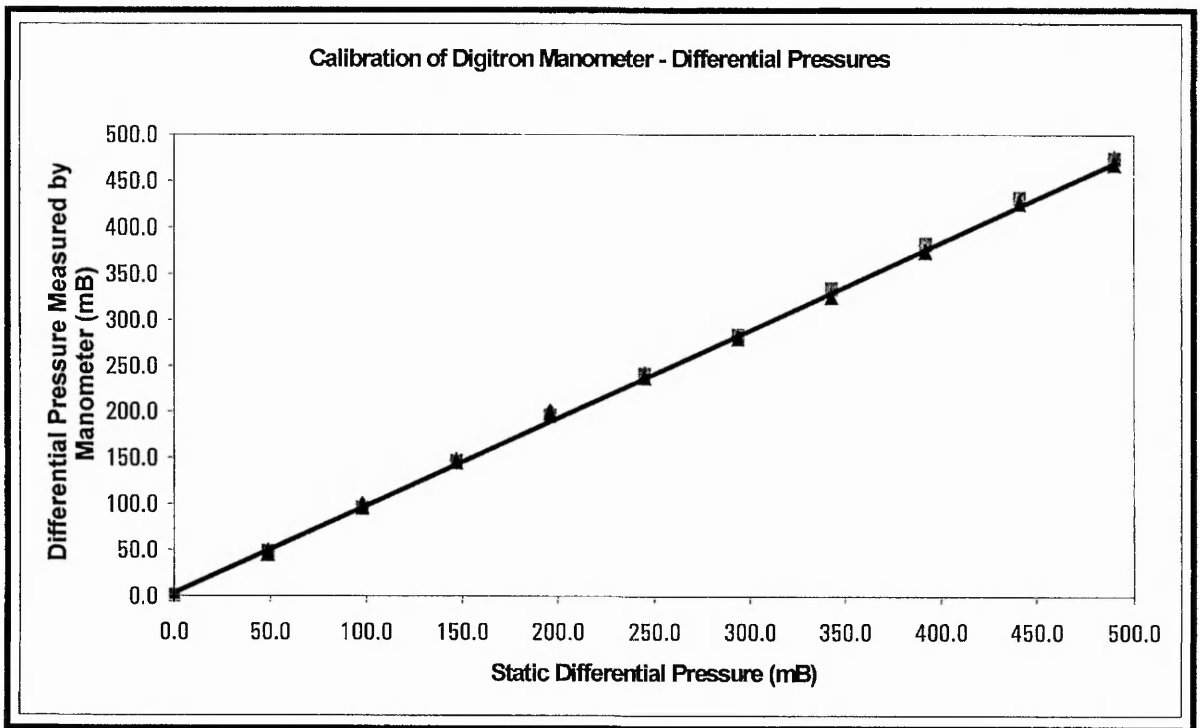
Figure 3.13   Calibration graph of electronic manometer.
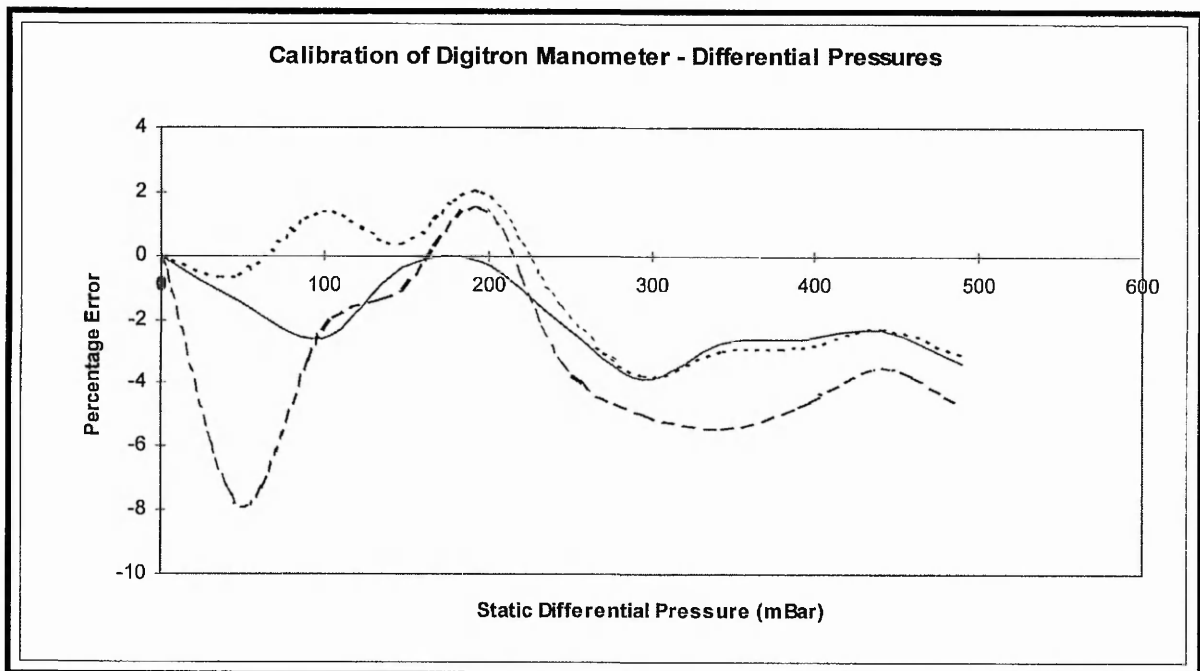
Figure 3.14   Percentage errors in measured differential pressures.

3.3   FLOW STRUCTURE AT THE ENTRANCE TO THE MODEL

The design of the flow straightening device was completed and the flow structure at the entrance to the model was then investigated using the ADV. Velocity profiles were measured 1.0m downstream of the entrance to the model, at three points in the cross stream direction; 150mm from the right wall of the channel, 150mm from the left wall of the channel and at the centreline of the channel. The flow and depth were 58 l/s and 395mm respectively. These profiles are shown by Figure 3.15. Similarly profiles of TKE were measured at the same position. Profiles of TKE with depth are shown by Figure 3.16.

Figure 3.15 shows the variation of velocity in the streamwise direction with depth at three positions across the channel. It can be observed from the profiles that the velocity across the channel did not exhibit the characteristics that are typical of a fully developed flow. Under fully developed flow conditions it would be normal to find the greatest magnitude of velocity at the centreline of the channel. However from Figure 3.18 it can be seen that generally the greatest velocities occurred near the right wall of the channel and the lowest velocities occurred near the left wall of the channel. In addition the shape of the velocity profile was not typical of a velocity profile derived from Boundary Layer Theory (Chow,1959 and Hamill, 1995).

There are various reasons to explain the results shown by Figure 3.18. Uniform flow was not fully achieved at the entrance to the model and the flow was also highly turbulent. The intake channel was located 3.0m downstream of the entrance to the model and therefore this obviously had some effect on the flow pattern entering the model. Flow was drawn towards the intake causing higher approach velocities towards the right wall of the main channel as shown by Figure 3.20.

The presence of non-uniform flow at the entrance to the model was not a critical problem. However this did influence the ability of the computational model to predict the flow structure successfully and it was necessary to create inflow data files to specify the velocity distribution at the entrance to the model rather than use the default, fully developed, velocity distribution. Ideally a fully developed flow in the physical model would have been favourable but this rarely occurs in prototype situations and therefore was not considered to be onerous.
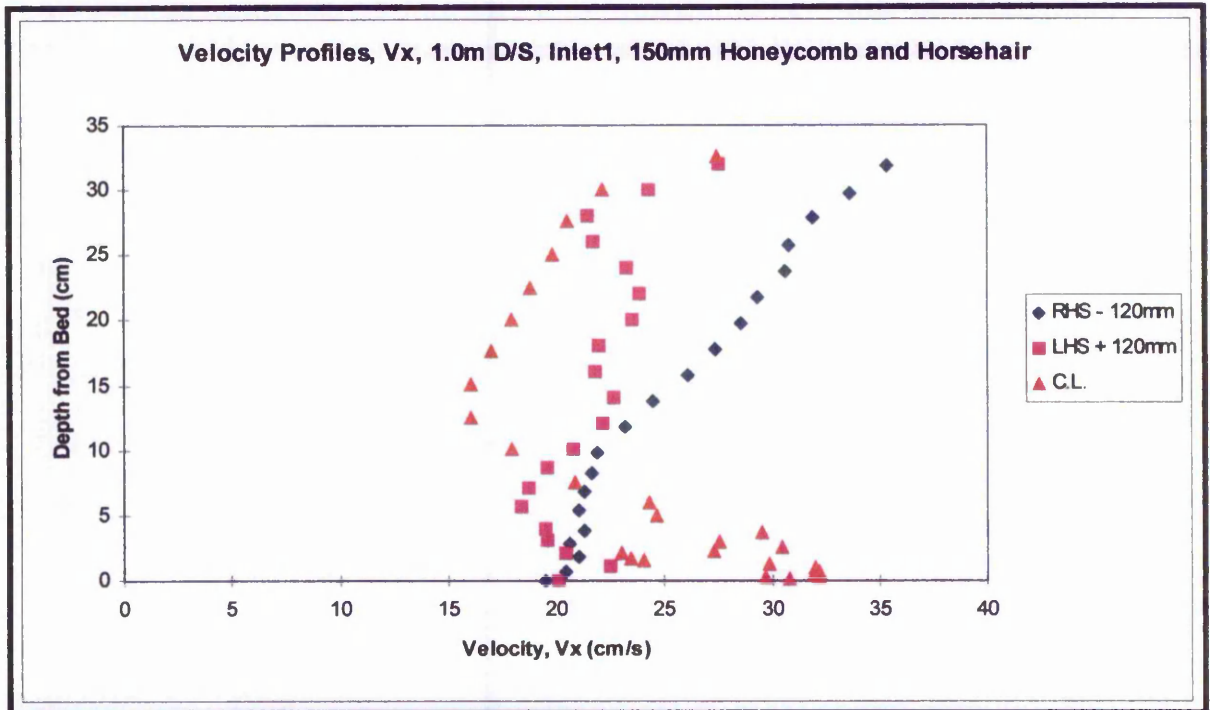
Figure 3.15   Velocity profiles at the inlet.
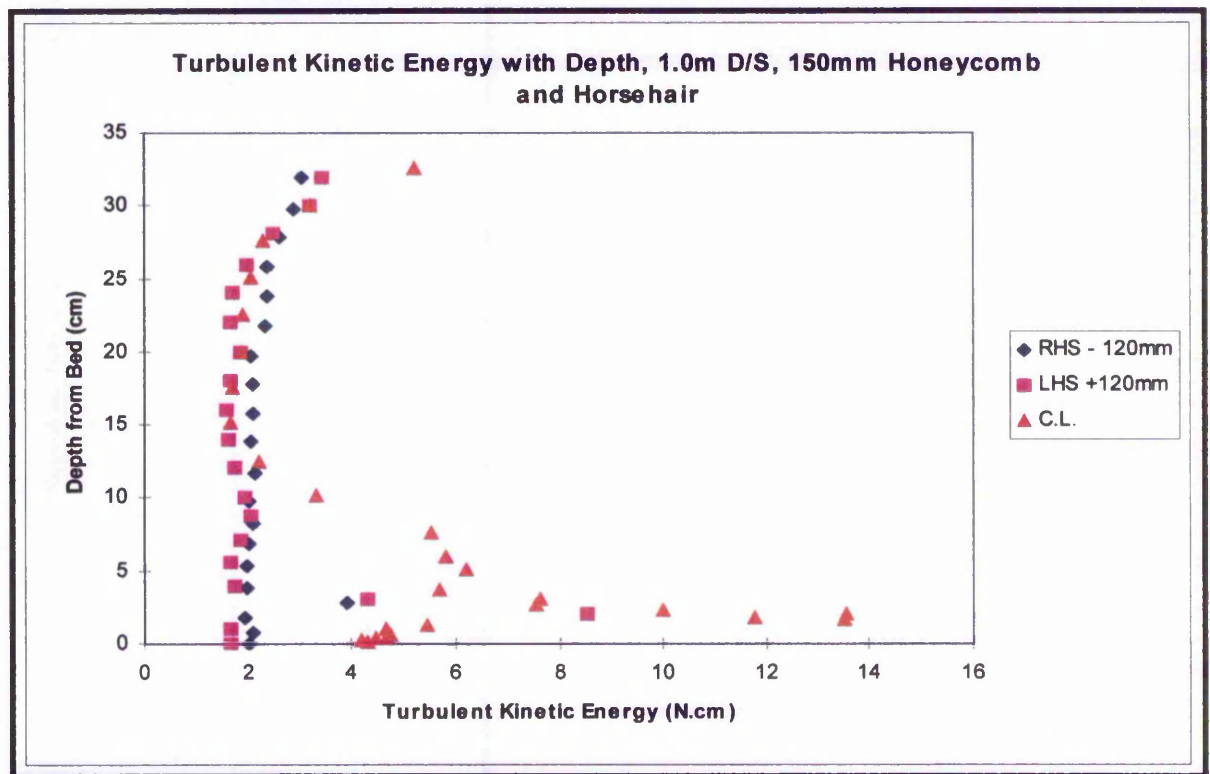
Figure 3.16   Turbulent kinetic energy profiles at the inlet.

Non uniform flow entering model entrance due to close proximity of intake and the highly turbulent nature of the flow

Flow pattern more representative of fully developed flow downstream of intake.

Significantly greater velocities particularly for greater flow split ratio.

Drawing not to scale
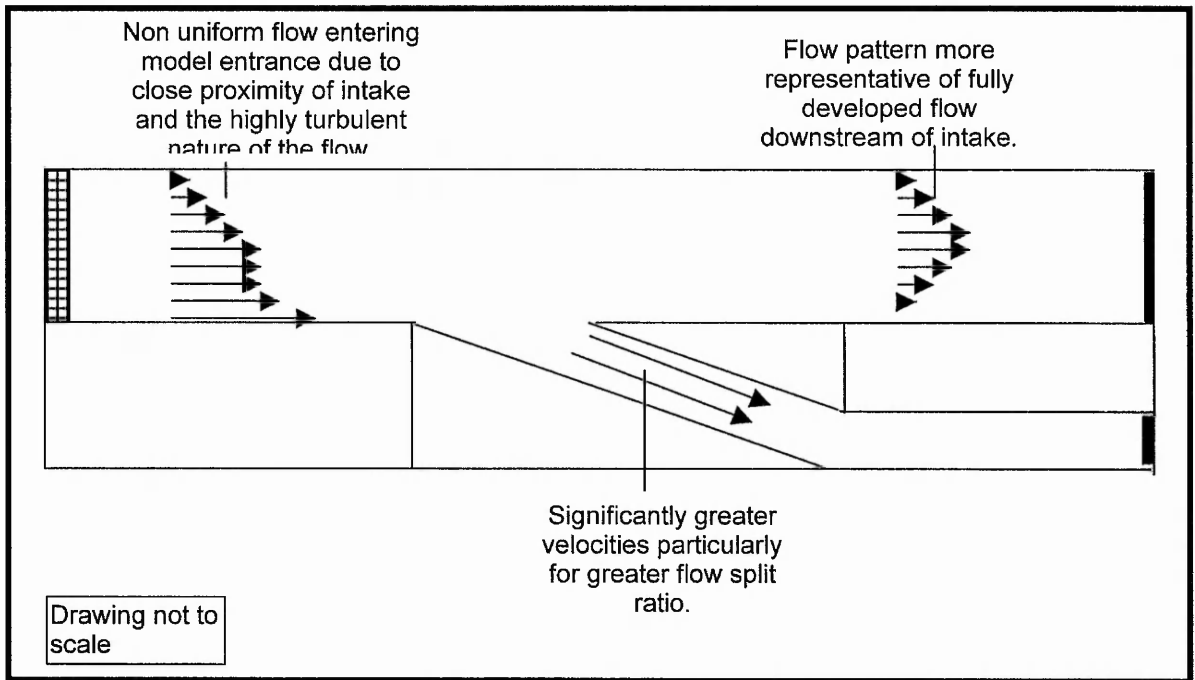
Figure 3.17   Diagrammatic representation of flow pattern in the physical model.

4

ADV CALIBRATION

4.1   INTRODUCTION

The Acoustic Doppler Velocimeter (ADV) is a relatively high precision instrument that measures mean velocity and higher order statistics of fluid flow in three directions. The measurements are insensitive to water quality which allows for a wide range of applications. ADVs are used in laboratories, wavebasins, rivers, estuaries and oceanographic research. The development of the ADV was initiated under contract by the United States Army Engineer Waterway Experiment Station (WES) in 1992 to satisfy the need for an accurate current meter that can measure 3D dynamic flow in physical models.

The ADV uses acoustic sensing techniques to measure the velocity characteristics of seeding particles suspended in and following, the mean bulk flow as they pass through a remote sampling volume. It is non-intrusive and direction sensitive. It is a simple, inexpensive yet valuable diagnostic technique especially in large scale modelling of fluid flow. Data are available at an output range of 25 Hz. The 3-D velocity range is +/- 2.5 m/s, and the velocity output has no zero offset.

The instrument consists of three modules: the measuring probe, the conditioning modules and the processing module which contains low noise electronics enclosed in a waterproof housing. The acoustic sensor consists of one transmit transducer and three receive transducers. The receive transducers are mounted on short arms around the transmit transducer at 120^0 azimuth intervals. The acoustic beams are orientated so that the receive beams intercept the transmit beam at a point located approximately 55mm below the sensor. The intersection of these four beams, together with the width of the transmit pulse, define the sampling volume. The

volume is 3 to 9mm long and approximately 6mm in diameter. Figure 4.1 shows a diagram of the ADV modules and Figures 4.2 and 4.3 show a schematic diagram and a photograph of the ADV probe.
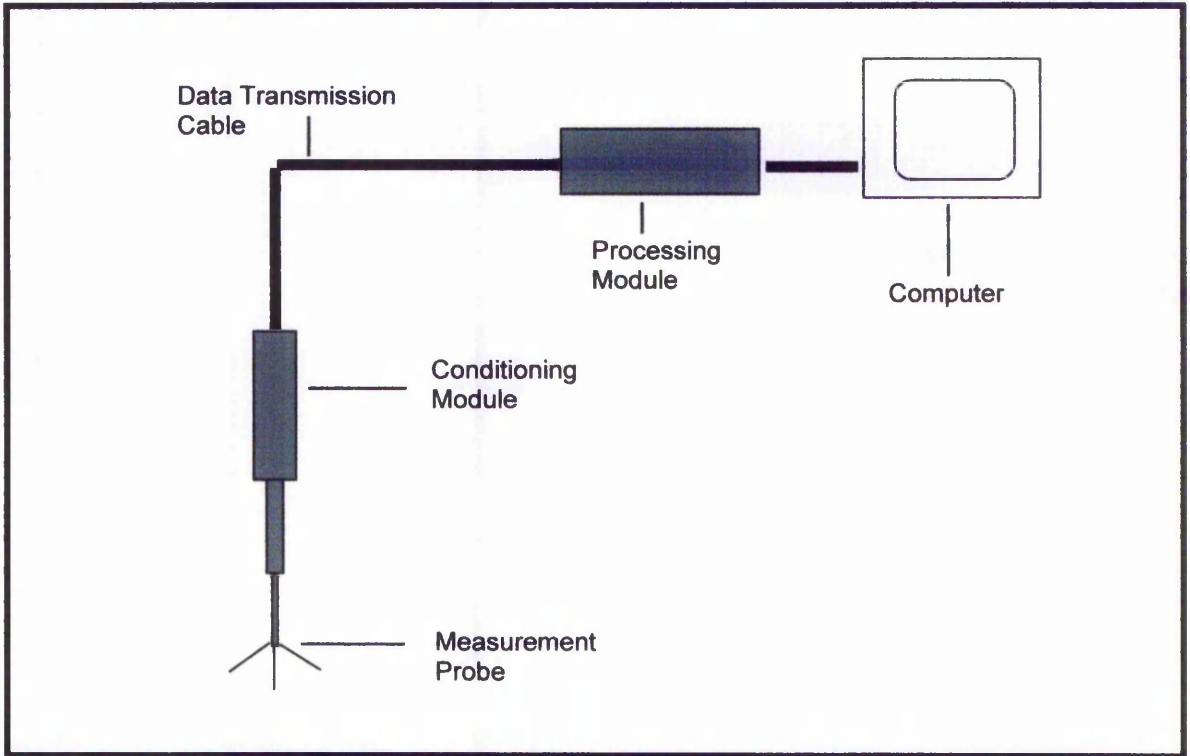
Figure 4.1   Schematic diagram of ADV modules.
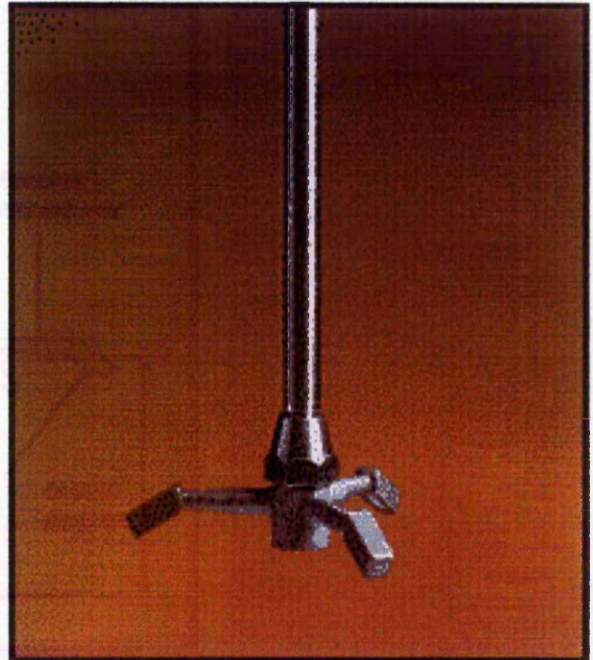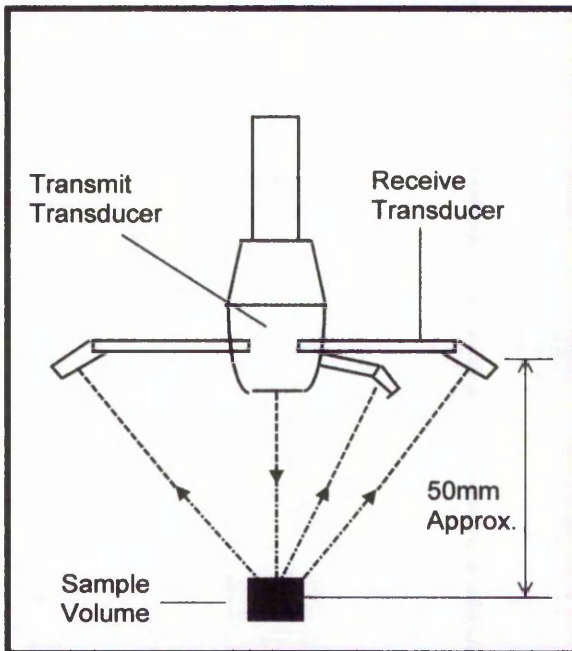
Figure 4.2 Schematic diagram of ADV probe.   Figure 4.3 Photograph of ADV probe.

The conditioning module contains all of the sensitive analogue electronics that permit the detection of the weak backscattered signals. Digital signal processing and system control is performed by a single circuit card that fits into a 16 bit IO slot of an IBM compatible computer. This card contains a signal processor that can perform the required computations for real time estimation of 3 axis velocities at output rates up to 25 Hz. Electrical power for the signal conditioning module and for driving the transmit transducers is derived from the computer power bus so that no external power supply is needed.

The system operates by transmitting short acoustic pulses along the transmit beam. As the pulses propagate through the water, a fraction of the acoustic energy is scattered back by small particles suspended in the water (e.g. suspended sediments, artificial seeding, etc.) The three receivers detect the "echoes" originating at the sampling volume, which are Doppler shifted due to the relative velocity of the flow with respect to the probe. The Doppler shift observed at each receiver is proportional to the component of the flow velocity (V_1, V_2 and V_3) along the bisector of the receive and transmit beams. Doppler shifts measured at the three receivers thus provide estimates of flow velocity along three different directions, which are then combined geometrically to obtain three orthogonal components of the water velocity vector, V.

The ADV measures the three orthogonal components of the velocity vector within a common sampling volume defined by the interception of the transmit and receive beams. The system uses pulse-to-pulse coherent Doppler techniques (Miller and Rochwarger 1972), (Zrnic 1977) and (Lhermitte and Serafin 1984). The manufacturers claim to achieve short term velocity errors of 1-10 mm/s at rates up to 25 Hz, even in highly variable flow conditions with peak velocities as high as 2.5m/s. The processing algorithms are self adaptive to avoid pulse-to-pulse interference when operating close to the surface or to a solid boundary.

The ADV used in this study was purchased by the Department of Civil and Structural Engineering of The Nottingham Trent University (TNTU) in March 1996 at a cost of £12 000. It was purchased from HR Wallingford, equipment sales who acted as the UK agents for the manufacturers, Sontek. The ADV is presently also manufactured by another company, Nortek form Norway who act as suppliers of the ADV to Europe. HR Wallingford are still the UK agents for Nortek. Sontek continue to operate

from San Diego, California and supply ADVs to the USA and the rest of the World. It is estimated that there are currently 400 ADVs in use around the World.

To the authors knowledge there have been only two calibration exercises carried out independently of the manufacturers, Sontek or Nortek. Dr William H. Snyder carried out rigorous calibration tests to challenge the manufacturer's calibration in September 1997 (Snyder 1997) whilst undertaking research in Stratified Flow Tanks at the University of Surrey. However, Dr Snyder's calibration research has not been officially published in any journal or conference proceedings (at the time of writing of this thesis). In addition the author of this thesis has published data regarding the independent calibration of the ADV (Bowles *et al* 1997). Further calibration tests have been performed by the author since August 1997 and it with regard to the independent calibration of the ADV that this chapter is concerned.

4.2   MANUFACTURER'S CALIBRATION

The manufacturer's calibration of the ADV was undertaken in two steps. First, the exact probe geometry was determined. Although designed to a specification of 30^0, the three angles between the transmit transducer, sampling volume and receive transducers will vary slightly from probe to probe. The small variations in angle must be included in the calibration and each probe has its own calibration table. The data was generated during factory testing and can be expressed as a transformation matrix, T between the measured velocity V_l with components V_1, V_2 and V_3 and the earth referenced velocity vector V with orthogonal components V_x, V_y and V_z :

$$V = \begin{bmatrix} \sin\phi_1 \cos\theta & \sin\phi_1 \sin\theta & \cos\phi_1 \\ \sin\phi_2 \cos(\theta + 2\pi/3) & \sin\phi_2 \sin(\theta + 2\pi/3) & \cos\phi_2 \\ \sin\phi_3 \cos(\theta + 4\pi/3) & \sin\phi_3 \sin(\theta + 4\pi/3) & \cos\phi_3 \end{bmatrix} * V_i$$

where ϕ_i represent the three calibration angles and θ is the rotation around the z-axis (heading). Rotation around the x and y – axes (pitch and roll) was disregarded. The system was calibrated by running the probe three times in a towing tank, each time with a different carriage velocity. Detailed analysis of the full set of equations showed that this technique provided estimates of the calibration angles that were accurate to

within 0.1^0 (Lohrmann *et al* 1994). This method did not require a high precision mounting fixture and was robust with respect to small pitch and roll angles (<5^0).

The geometry of the probe does not change unless it is physically damaged. Damage to the probe arms can normally be detected by inspection. However, the software supplied with the ADV contains a program called ADFCHECK which detects bent or twisted probe arms which are no longer focussed on the sampling volume. If damage has occurred to a probe arm the signal strength from the damaged arm will display significantly reduced signal strength compared to the signal strength from the undamaged receiver arms. For very small deformations that cannot be detected by a reduction in signal strength there may be a small effect on the calibration. However, it is claimed by the manufacturer that the geometry of the probe arms and the implementation of the signal processing, prevent a significant impact on the calibration. Small deformations in the receiver arm only result in very small errors in the horizontal velocity. An example given by the manufacturer claimed that the calibration error is less than 1% even if the change in angle as a result of deformation is as large as 5%.

ADFCHECK can be used to detect almost any problem associated with the ADV. Graphical output of signal strength using ADFCHECK can be analysed to detect the following problems.
- Probe not connected correctly. This is recognised by a flat response in all receivers after the initial transmission of a signal.
- Signal conditioning module not connected.
- Weak scattering. This is caused by a lack of scattering particles in the water and can be rectified with the addition of artificial seeding material.
- Malfunctioning transmitter.
- One or more receiver not working properly. The signal from each receiver should have the same strength at the sampling volume.
- Damaged probe. This can be detected if the peak strength in one receive transducer is offset along the horizontal axis.
- Excessive noise level. This is usually due to external electromagnetic interference but may also be due to water condensation on the receiver electronics inside the signal conditioning module. Excessive noise can be reduced by coiling the cable

between the processing module and the computer and by keeping the electronics dry by placing a bag of dessicant inside the conditioning module.

- High signal levels past the boundary. If the signal level does not fall off rapidly past the boundary peak but continues to exhibit high signal levels, the standard deviation in the velocity data may be larger than necessary. This can be resolved by covering the boundary below the probe with rubber matting or similar acoustically absorbing material.

Figure 4.4 shows a diagram of the output from the ADFCHECK program.
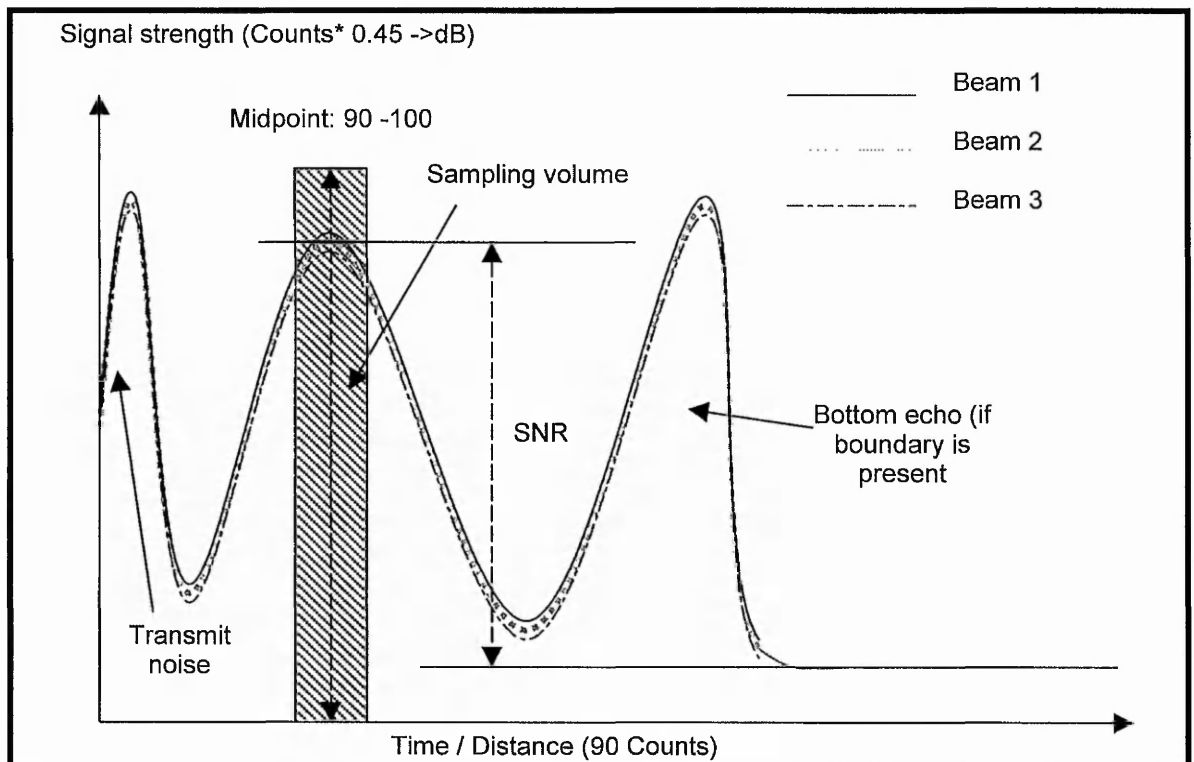
Figure 4.4   Output from the program ADFCHECK.

The second part of the calibration was involved in the normal data collection procedure. Before each run, the speed of sound is calculated based on site specific temperature and salinity values. The speed of sound can vary from 1440 m/s in cold, fresh water to 1540 m/s in warm, salt water. Without calibration, a nominal speed of sound of 1490 m/s could lead to errors as large as 3.3%. with routine calibration prior to each use, the error due to the speed of sound is limited to about 0.2% if the operator knows the temperature to within 1^0C.

4.2.1 Manufacturer's Test Results

The first evaluation of the ADV system was conducted at WES (Kraus *et al* 1994), where tests were conducted in a spillway model, 2D and 3D wave basins, a ship navigation model and a circular channel. In these tests the velocity measurements gathered using the ADV were compared to measurements gathered using other devices including a Laser Doppler Velocimeter (LDV) and pitot tubes. The manufacturers found that the ADV was successful in all the comparisons with other velocity sensors. The tests also demonstrated the versatility and ease of use of the ADV. The ADV could be set up to record measurements in minutes rather than hours as is often the case with LDV. It could also be used in many different applications from small scale models to large river networks. It successfully recorded measurements in a wide variety of flow regimes including breaker zones in wave basins and hydraulic jumps in a spillway model.

Most comparisons were made based on statistical analyses of mean, standard deviation and power spectra as opposed to instantaneous velocities. However, a comparison of instantaneous velocities was made with an LDV in a 2D wave basin. A 2D Dantec LDV was aligned visually with the ADV so that both instruments recorded measurements in the same sampling volume. The LDV and ADV sampled at 50 Hz and 25 Hz respectively.

Good visual agreement in terms of shape and the peaks of the oscillatory signals was obtained from the two instruments. Regression analyses were performed on the data sets giving a slope of the straight line of 1.03 and a y intercept of 0.11 cm/s.

Towing tank tests were also conducted at North West Research Associates Inc. (NWRA) in Bellevue, Washington, USA. The towing tank at NWRA was 9.75m long, 0.91m wide and 0.91m deep. The ADV was mounted to a carriage which travelled along the top of the channel driven by an electrical engine whose speed was accurately known. The standard deviation of the measured speed of the carriage was calculated to be 0.2% over the range 1 to 250 cm/s.

The purpose of the towing tank tests was to verify the linearity of the ADV velocity measurements. The velocity vector was computed from the three co-ordinate

velocities by using a transformation matrix as described previously. The matrix incorporated the relative position and orientation of the four acoustic transducers and if the system is linear, the manufacturers claimed that the matrix can be determined empirically by calibrating the system at one speed. They claimed that the system will remain constant provided that the physical dimensions and geometry of the probe remain unchanged.
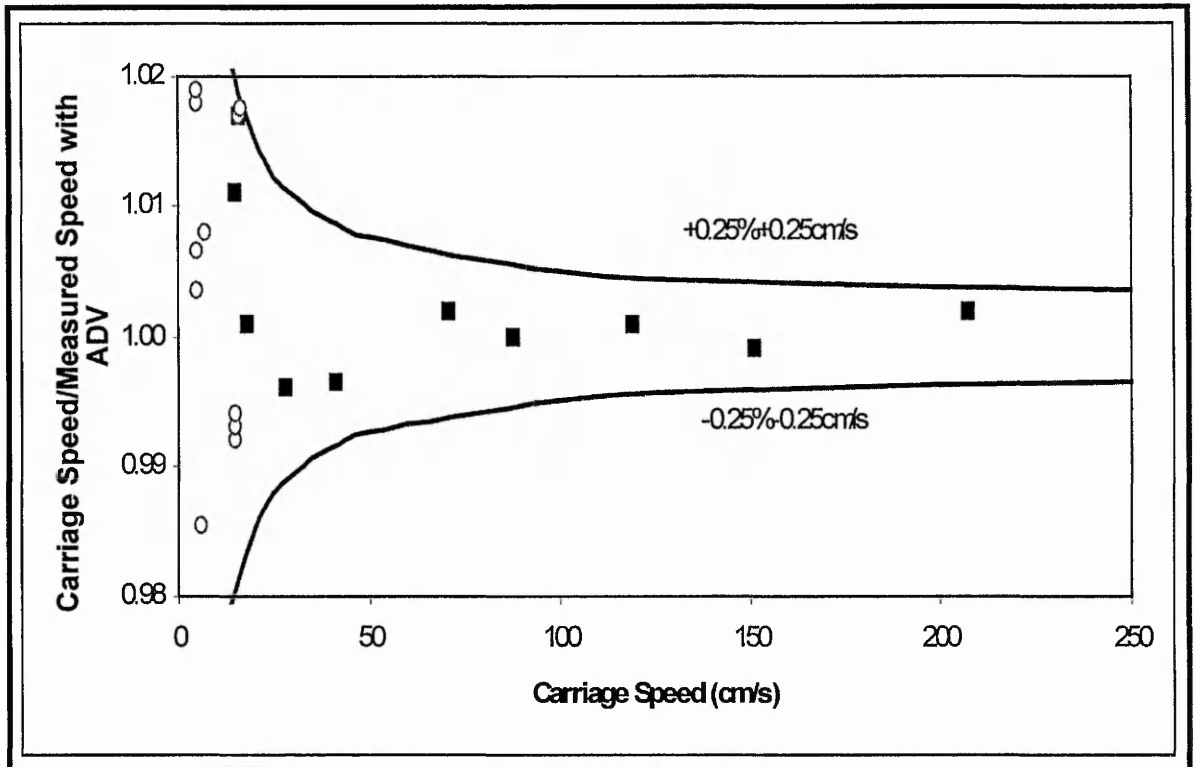
Figure 4.5   Manufacturer's ADV Calibration (from Lohrmann *et al.* 1994)

Figure 4.5 shows the ratio between carriage speed and the velocity component in the streamwise direction for carriage speeds from 10 to 250 cm/s. The graph shows that the output output was linear to better than 0.25% over the range from 15 to 250 cm/s. Below 15 cm/s, the tests at NWRA (square markers) showed that there was a bias towards the lower velocities. This was due to a hardware problem which was corrected and later tests (round markers) indicated that the ADV was accurate to within +/- 0.25% +/- 0.25 cm/s.

Tests have also been conducted by the manufacturer for the ability of the ADV to capture turbulent kinetic energy and Reynolds stress measurements within the bed boundary layer. Doppler noise (sometimes called short term error) is an inherent part of all Doppler based backscatter systems. It is related to the random distribution of

particles that contribute to the acoustic echo. The magnitude of Doppler noise is a function of the signal strength and the flow conditions and in many cases it may be greater than the fluctuating signal of the velocity that represents the turbulent kinetic energy. Important aspects of Doppler noise that should be noted are :

- Doppler noise can be reduced by averaging over independent measurements.
- The noise from two independent channels is uncorrelated.
- Doppler noise is white in the spectrum.

The first point is extremely important since it means that the effects of Doppler noise is reduced as the averaging period increases.

The measured velocity component, U, comprises three parts; the mean velocity, $\overline{U}$ and a fluctuating part that contains the turbulent energy, U ' and the Doppler noise, U_d. Thus:

$$U = \overline{U} + U^i + U_d \qquad\qquad 4.1$$

and

$$\overline{U^i + U_d} = 0, \qquad\qquad \overline{(U^i + U_d)^2} = \overline{U^{i2}} + \overline{U_d^2} \qquad\qquad 4.2$$

The third expression states that the time averaged product between the natural fluctuations and the Doppler error (noise) is zero. This is an important aspect of the noise and allows the calculation of quantities that are smaller than the Doppler noise such as turbulent kinetic energy. In oscillatory flow the turbulence level can be estimated by analysing the energy level of the saturation range in the velocity spectrum. Because Doppler noise is white it can be identified as a "noise floor". It is characterised by a flattening of the spectrum as the Nyquist frequency (f_N) is approached. This occurs at 12.5 Hz in the case of the ADV with a sample rate of 25 Hz.
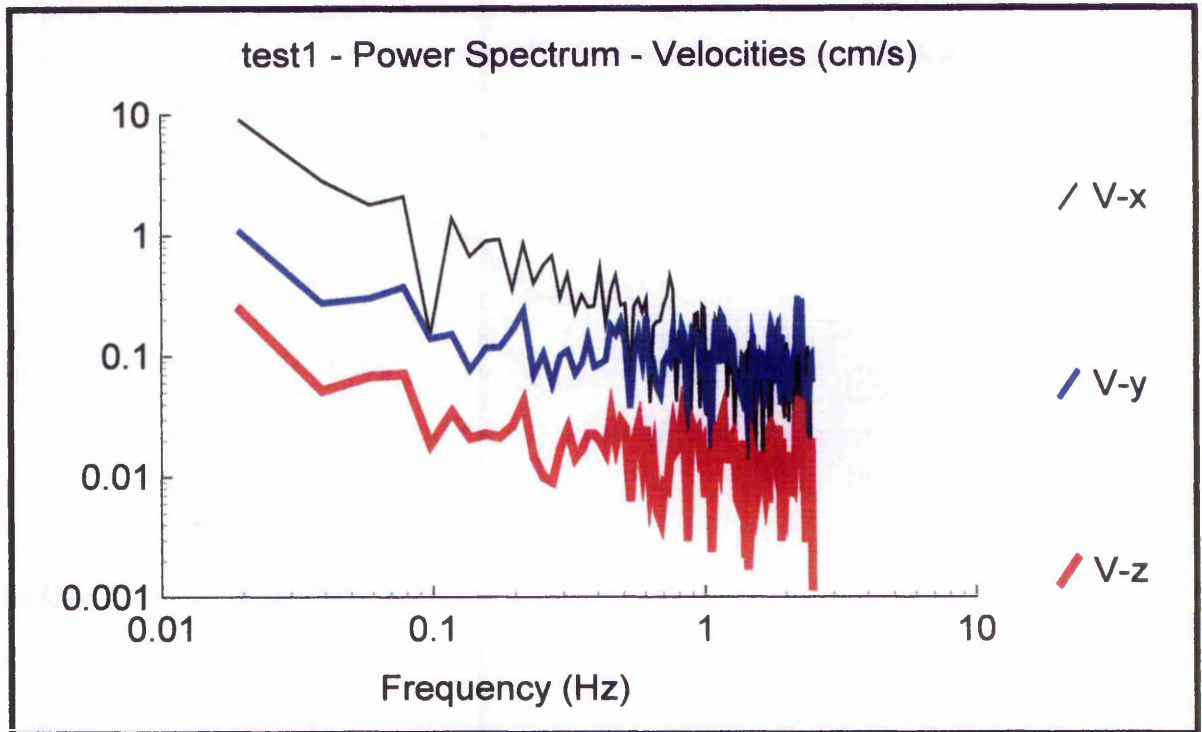
Figure 4.6 Typical power spectrum for the ADV. The Doppler noise was higher for the horizontal components (Vx and Vy) than for the vertical components (Vz).

The power spectrum shown in Figure 4.6 is a Fast Fourier Transformation (FFT) (Press *et al* 1989) of the velocity time series. For time series vector **V** containing n = 2^m samples, the FFT vector **F** contains j = 1 + 2^{m-1} elements which satisfy the equation :

$$F_j = \frac{1}{n} \sum_{k=0}^{n-1} V_k \cdot e^{2\pi(j/n)ki}$$

4.3

The amplitude of **F** is independent of the sampling period and rate. A pure sign wave with amplitude 1.0, such as $f(t) = \sin\left[2\pi \frac{t}{T}\right]$, will have a resulting FFT amplitude of 0.5 at frequency 1/T.

The amplitude of the measured signal is shown with frequency. Fourier Series and Fourier Integrals allow the transformation of time domain waveforms to the frequency domain and vice versa. The Nyquist Frequency is the highest frequency that can be defined by the sampling rate. The rule governing sampling is referred to as the Nyquist sampling theorem (Ramirez 1985). This states that the sampling rate must

be at least twice the frequency of the highest frequency component in the waveform being sampled. In other words, there must be at least 2 samples per cycle for any frequency component which is to be defined. If there are fewer, the sampling rate is less than twice the highest frequency component, then aliaising will occur.

Aliaising occurs when the measured phase difference between the two acoustic pulses transmitted and received by the ADV exceeds 180^0. The ADV cannot distinguish between a phase difference of 181^0 and -179^0; as a result the velocity recorded in the ADV file will change sign, producing a dramatic spike in the velocity data, known as a velocity ambiguity. The ADV uses the measured phase difference to determine flow velocity. The phase difference is proportional to the Doppler shift associated with acoustic signals reflected off moving scatterers in the sampling volume. The aliaising of the velocity data biases the average velocities and makes instantaneous velocity measurements uncertain.

It can be observed from Figure 4.6 that the flattening of the spectrum occurs between 5 – 10 Hz. For the vertical velocity, the noise floor is negligible below the Nyquist frequency and this is the component of choice in the case of isotropic turbulence.

To summarise, the manufacturer's claim that the ADV can be used to measure mean velocity components in fluid flow to an uncertainty of +/- 0.25% +/- 0.25 cm/s in the velocity range of 1 – 250 cm/s. The ADV can also measure turbulent kinetic energy in excess of the Doppler noise and / or indirectly estimate the energy as long as the saturation range in the spectrum can be resolved.

4.3   INDEPENDENT CALIBRATION

4.3.1   Introduction

The manufacturer's claims for the calibration of the ADV have been documented in the previous section. The author has undertaken a thorough literature review of subjects associated with the ADV. It was found that there were numerous examples of literature describing applications of the ADV but no official publications described any form of checks on the manufacturer's claims whatsoever. An internal university report by Dr Snyder of the University of Surrey (Snyder 1997) was identified which described and presented results of calibration tests but Dr Snyder's research has not officially been published to date. It was therefore decided that an independent calibration was required to verify the manufacturer's claims. To this end calibration research has been presented by the author (Bowles *et al* 1997), (Bowles 1996), (Bowles 1997). The following sections describe these and subsequent calibration tests and present the results.

Four sets of calibration tests have been carried out since the initial purchase of the ADV in March 1996. The first was undertaken in an Armfield flume in the Hydraulics Laboratory of the Department of Civil and Structural Engineering at TNTU. The second set of tests were undertaken in the Towing Tank Facility at HRW. The third and fourth sets of tests were undertaken at the Towing Tank Facility at Southampton Institute, UK. For all of the tests, seeding was required to the tanks since there was insufficient particulate matter present in the still body of water in the tanks. Towing tank tests have been previously undertaken using the ADV by the designers (Lohrmann *et al.*, 1994), (Cabrera and Lohrmann, 1994) but in all tests the sizes of the facilities were much smaller than were used in the calibration tests presented here.

4.3.2   Tests at the Hydraulics Laboratory, TNTU

A relatively simple towing tank test was carried out in the Armfield flume in the Hydraulics Laboratory at TNTU. The flume was 11 metres long by 300 mm wide by 400 mm deep. The ADV was attached to a carriage running along rails on the top of

the flume. Clean tap water was introduced to the flume by high pressure hose. Figure 4.7 shows a photograph of the test rig.
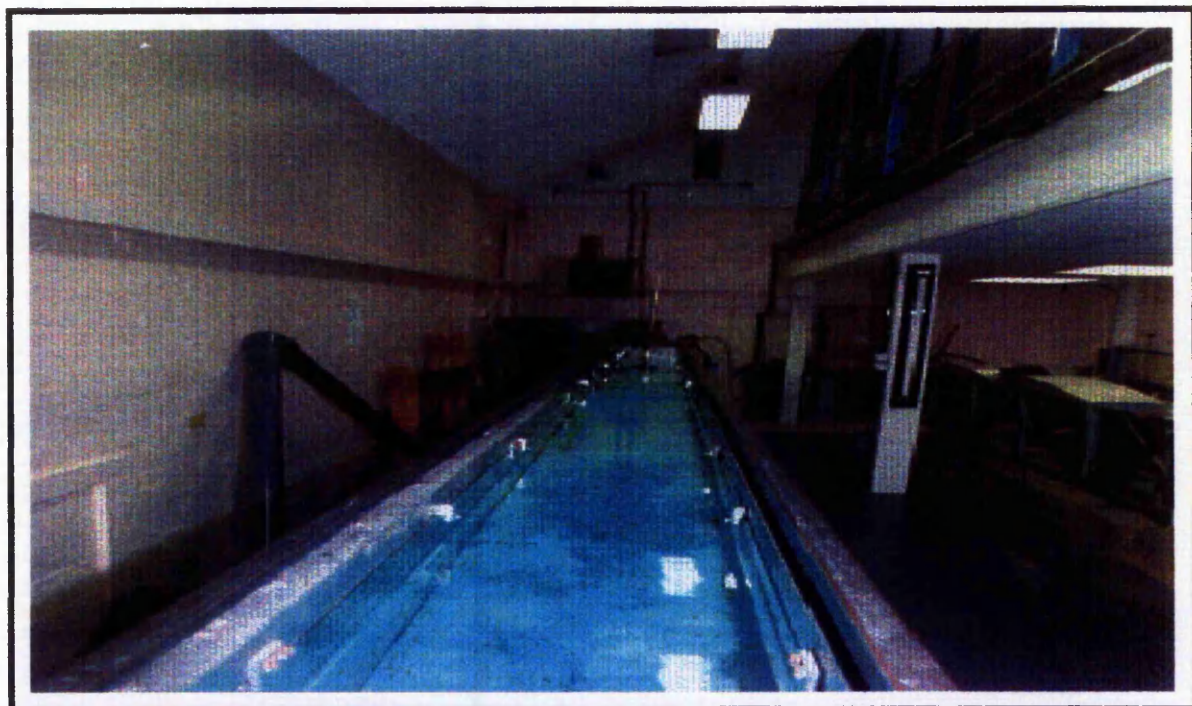
Figure 4.7　　The Armfield Flume at TNTU.

An initial test was carried out in the flume to investigate if seeding was required. The ADV was pushed manually through the flume following a period of stabilisation of the water in the flume and measurements were recorded. This was undertaken to ascertain the scattering characteristics of the particulate matter present in the still body of water. There is a functional relationship between the signal strength and Doppler noise. If the signal strength is too weak, as may be the case in quiescent basins or in stationary flumes, the Doppler noise becomes high and the introduction of small particles (seeding) may be required. To ensure that this information is available both during the data collection and during post processing, the software displays and stores the Signal to Noise Ratio (SNR) of the scattered signal. The noise level, N, is measured at the beginning of each measurement sequence and it is close to the noise level of the ADV. The signal strength, I, is measured each time the receivers measure the velocity and the SNR is defined as :

$$SNR = 10 \, Log_{10}\left[\frac{I}{N}\right] \qquad\qquad 4.4$$

Doppler noise varies with SNR. An SNR of 15 dB is usually sufficient to obtain reasonably low noise data at a sampling rate of 25 Hz, whereas a ratio of about 5 dB is sufficient to obtain good quality data at 1 Hz.

For the flume tests described here an SNR of 2-3 dB was obtained. A methodology for seeding was therefore required. A series of seeding tests were subsequently carried out in the flume (see section 4.3.3). A burette was used to introduce the seeding material upstream of the ADV probe. Seeding material of varying concentrations was delivered to the burette at varying rates via gravity. The seeding was tested with two positions of the burette in relation to the ADV in the streamwise direction and vertically in relation to the probe. Video recording was also taken to observe the flow pattern of the seeding material, dyed blue using methylene blue, as it passed around the probe. PVC powder in suspension with water was used for the seeding material. Figure 4.8 shows an electron microscope image of the PVC particle which appear as spherical balls.   Figure 4.9 shows a video image of the dyed seeding material passing around the probe.
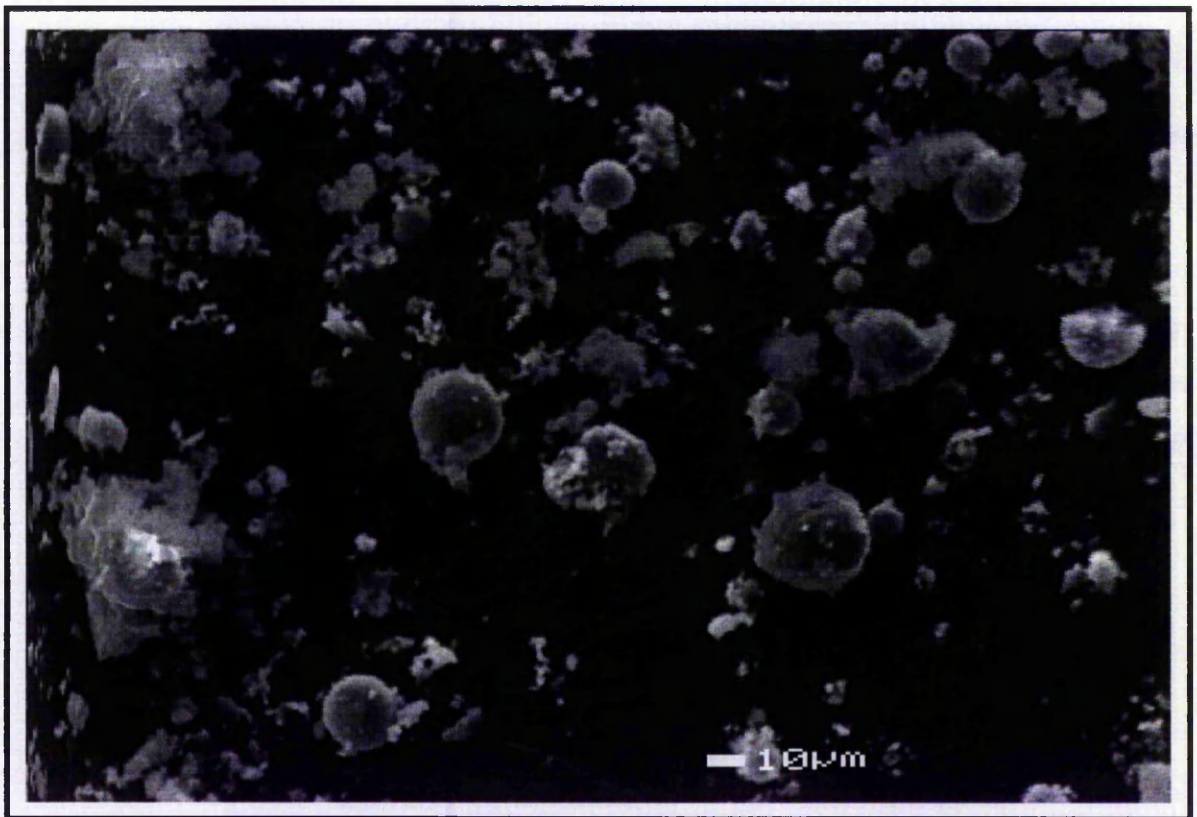
Figure 4.8   Electron microscope image of the PVC particles.
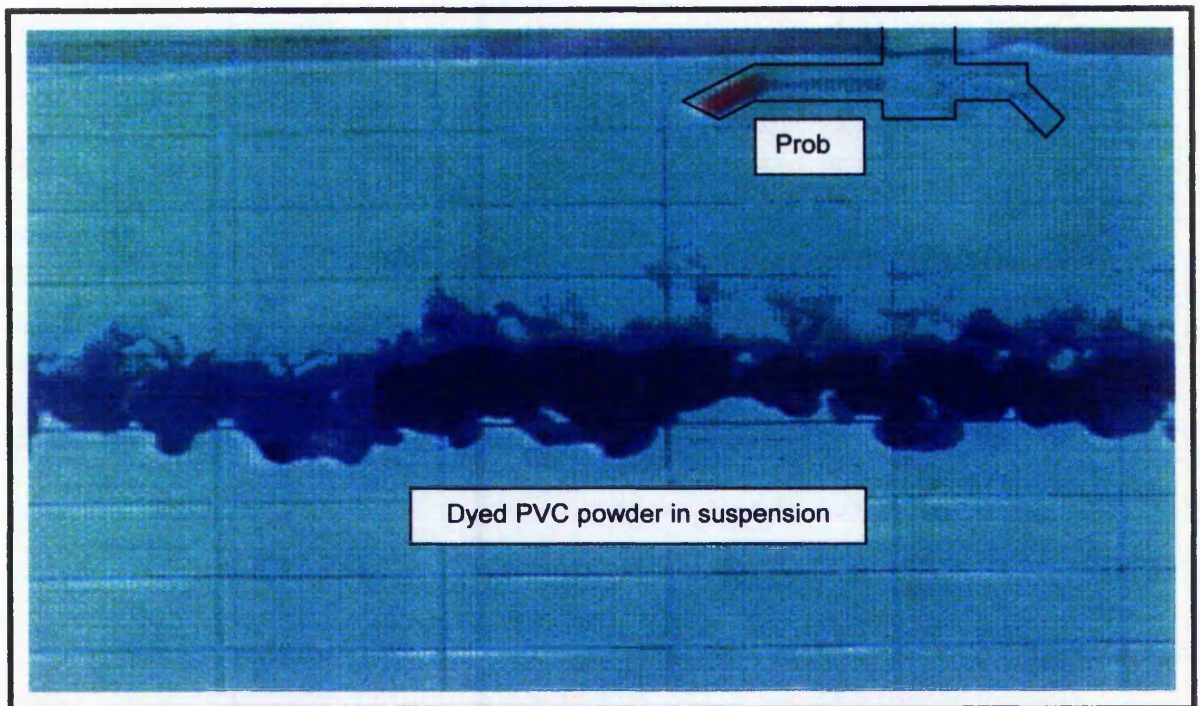
Figure 4.9   Video image of the dyed PVC powder in suspension with water passing around the ADV probe.

Analyses of the test results and observation of the seeding material as it passed around the probe indicated the most suitable arrangement for successful seeding. This was found to be with a concentration of PVC powder with water of 15 g/l, applied at a delivery rate of 1.5 ml/s. The seeding burette was positioned at 670mm in front of the ADV probe, with the tip of the burette operating at an elevation of 10mm above the sampling volume. The supplier of the PVC powder was EVC (UK) Ltd., The Heath, Runcorn, Cheshire. The catalogue number of the powder was EVC MP 8058 PVC. (See also section 4.3.3)

Towing tank tests were subsequently undertaken in the flume by recording the time taken for the carriage holding the ADV, to travel a pre-determined distance, to enable the velocity of the carriage to be calculated. The velocity of the carriage was then compared to the velocities measured by the ADV and this is presented in Table 4.1. Figure 4.10 shows the linearity between the measured velocities by the ADV and the velocity of the carriage. It can be observed from Table 4.1 that the percentage errors were excessive, with maximum errors as large as 15.9%. However the linearity of the ADV calibration was reasonable as shown by Figure 4.10. The equation of the trendline is shown as y = 0.98x which is very near to a direct linear relationship of

1:1. The correlation coefficient of 0.958 also indicated the close linear relationship that existed.

ADV - Vx (cm/s)	Velocity of Carriage (cm/s)	Carriage - ADV (cm/s)	% Error	SNR (dB)
17.76	20.2	2.44	12.08	24.2
11.21	13.3	2.09	15.71	12.2
27.06	27.7	0.64	2.31	25.6
27.67	26.2	-1.47	-5.61	24.8
23.21	23.1	-0.11	-0.48	20.8
13.07	15.7	2.63	16.75	12.9
31.53	35.3	3.77	10.68	33.0
17.79	19.3	1.51	7.82	12.8
16.42	16.6	0.18	1.08	27.1
22.17	24.7	2.53	10.24	14.7
40.27	38.9	-1.37	-3.52	20.2
16.05	19.1	3.05	15.97	23.2
23.87	24.3	0.43	1.77	27.6
43.83	39.9	-3.93	-9.85	24.9
12.81	14.7	1.89	12.86	34.5
12.94	14.4	1.46	10.14	22.4
38.17	38.2	0.03	0.08	27.0

Table 4.1   Errors between the carriage velocities and the velocities measured using the ADV.
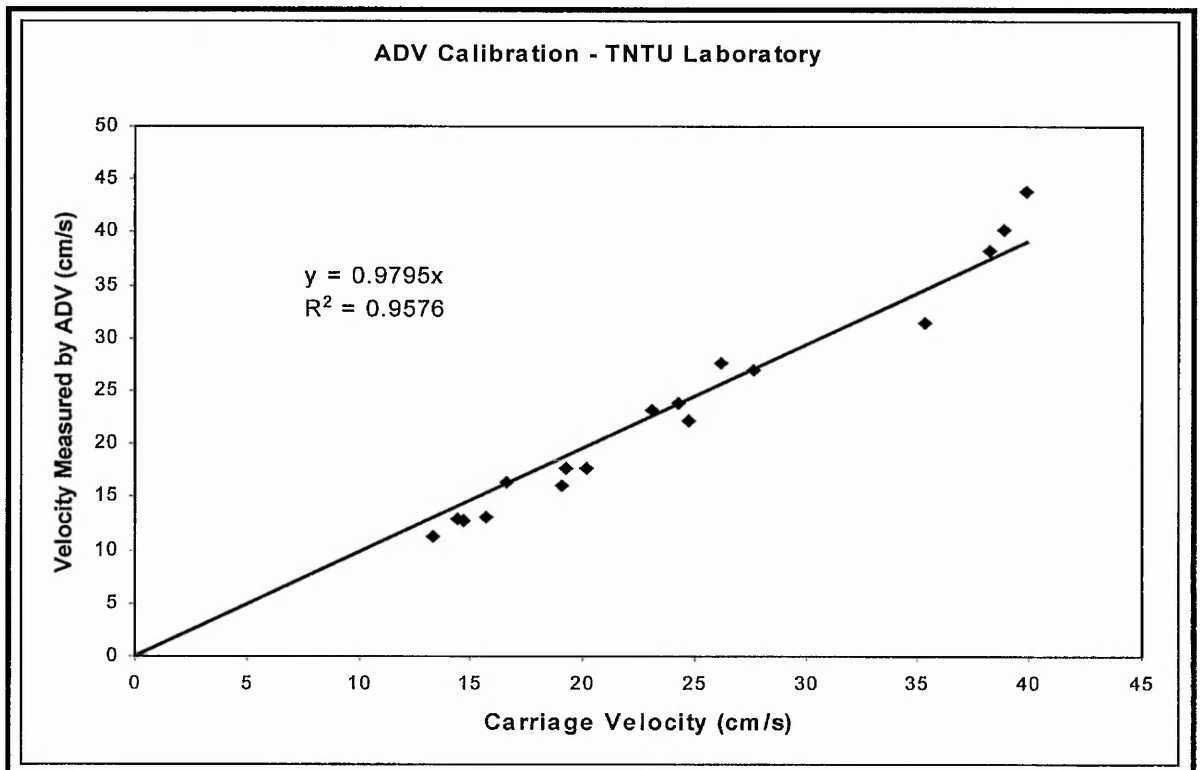
Figure 4.10   Basic calibration test for the ADV

A mean SNR of 22.8 dB was obtained from the measured results, with a minimum of 12.2 dB and a maximum of 34.5 dB. This showed that the errors obtained were not due to insufficient seeding of the body of water. The manufacturer's state that a minimum of 5 dB SNR is required for the measurement of mean flow velocities.

The correlation coefficient (COR), expressed in percentage, was in excess of 80% for all measurements. The COR is a quality parameter resulting from the ADV Doppler calculations. A perfect COR of 100% would suggest that all particles within the sampling volume were moving in precisely the same manner. Low COR may result from a number of factors: highly turbulent flow, the presence of large individual particles (or bubbles), a low SNR, or interference from boundaries. The manufacturer's recommend rejection (or at least scrutiny) of all data with COR's less than 70%. In the results presented in this Chapter, the post processing software, WinADV (see Chapter 1) was used to filter out such data. Very few samples were however rejected with COR's seldom less than 70%.

The results of this preliminary towing tank test at TNTU caused concern and subsequently the facility at HRW was used to undertake a more rigorous test.

4.3.3   Test at HR Wallingford Limited, Oxfordshire, UK.

A towing tank test was undertaken at the facility at HRW. This towing tank is 78 m long by 2m wide by 2m deep and is the largest facility of its kind in the UK. A carriage holding the ADV runs along the top of the tank at a known velocity. It was necessary to fabricate a mounting attachment for the ADV to the carriage and it was also necessary to modify the seeding arrangement. Figure 4.11 shows a photograph of the facility at HRW.

An initial visit was undertaken to HRW in November 1996 when a preliminary test was carried out in the tank to ascertain if there was a requirement for seeding the water body. The test showed that the largest SNR measured was 2-3 dB.
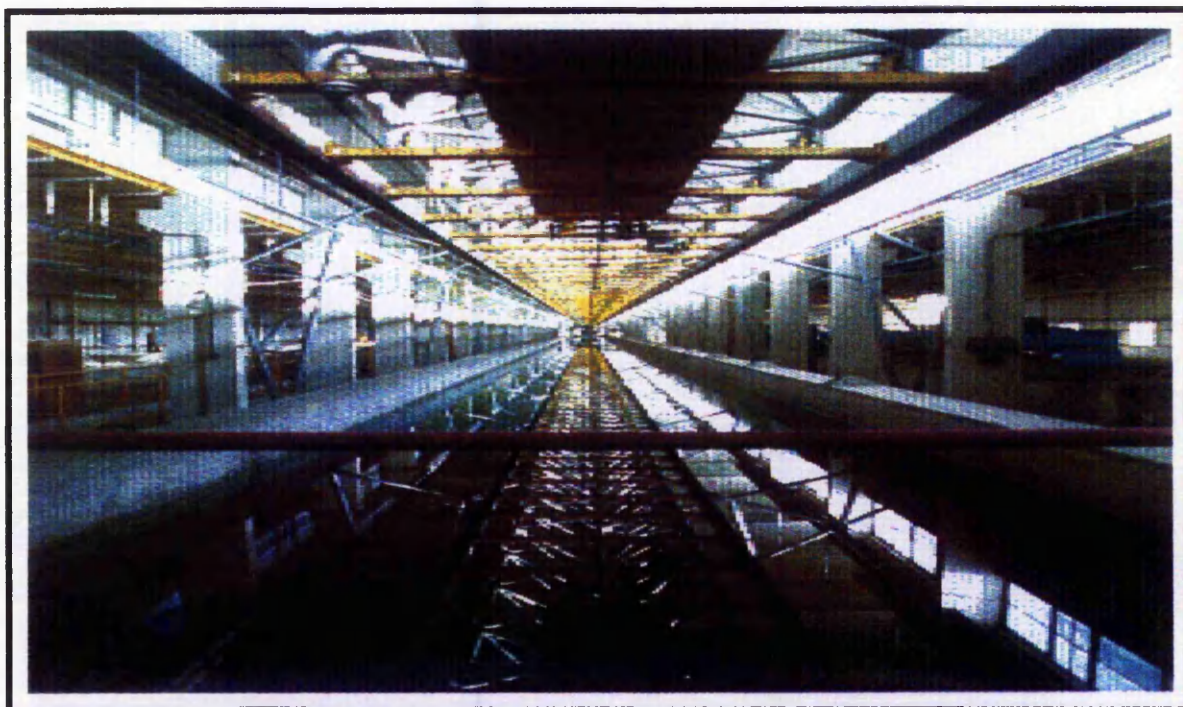
Figure 4.11   Towing Tank at HRW.

Seeding Tests at HRW

The ADV was mounted onto the carriage of the towing tank temporarily using electrical tape. One run was then carried out over 78m of the tank. The carriage velocities used were :-

- 0.1 m/s
- 0.2 m/s
- 0.3 m/s
- Carriage stationary
- 0.5 m/s
- Carriage stationary
- 1.0 m/s backward through the channel.

The standard deviation of the measured velocity of the carriage was quoted as 0.2% by the operators of the facility at HRW. The carriage velocity is calibrated regularly and it was found that the carriage came up to speed within 10 metres in all cases. The test lasted for approximately 310 seconds. Recordings were made by an observer using a lap top computer, sitting in the carriage of the tank. Carriage velocities were recorded from a control booth at the end of the tank. Table 4.2 summarises the results of the test.

Velocity of Carriage (cm/s)	Velocity Measured by ADV (Vx) (cm/s) (Filtered Data) (cm/s)	Average COR (Filtered Data) (%)	Average SNR (Filtered Data) (dB)	Velocity Measured by ADV (Vx) (cm/s) (Unfiltered Data) (cm/s)	Average COR (Unfilt. Data) (%)	Average SNR (Unfilt. Data) (dB)
20	19.71	71.22	7.02	16.85	41.37	2.28
30	0	0	0	23.26	38.62	3.84
0	0.28	74.62	6.57	2.28	40.34	5.45
50	21.3	74.33	3.58	24.08	32.91	3.13
0	0.14	74.67	5.89	0.81	42.15	1.95
100	0.06	76.59	4.74	13.31	31.22	3.06

Table 4.2   Velocity of carriage compared to velocity measured by the ADV.

Table 4.2 shows that the results obtained were poor. Two sets of ADV data for the velocity in the x-direction (streamwise) are given. One set consists of filtered data the other of unfiltered data. The filtering process was carried out by WinADV. The filtering criteria was the COR. When filtering occurred, any signal having a COR less than 70% is discarded for further calculations. Thus it can be seen from the column headed Average COR (filtered data) that 5 out of 6 of the data sets have a COR in excess of 70%. One set of data had a COR of 0 which was because the data set was of particularly poor quality with no data having a COR greater than 70%. Therefore in this case all the data was filtered out.

It should be noted also that the SNR obtained were very poor, especially in the unfiltered data set with a maximum of 5.45 dB being achieved. The significance of this was highlighted by the resulting velocities that were obtained, with gross errors occurring in some cases.

Figure 4.12 illustrates the time series graph of velocities in three components for the test from WinADV. The steps in the time series graph correspond to the changes in velocity of the carriage and are labelled accordingly in m/s. Several features of this graph should be noted. First, as the ADV was turned on (t=0s), the vertical velocity increased (predominantly negatively) from zero to a value of approximately −0.5 cm/s, while the carriage remained stationary. Figure 4.13 shows a time series for the first 10 seconds of the test. This negative vertical velocity was due to the energy output by the transmitter; a net downward force is exerted on the fluid due to non

linear effects of the pressure field. As the carriage was started the vertical velocity returned quickly to zero then increased to a value of about -0.97 cm/s. This latter effect was not due to the non
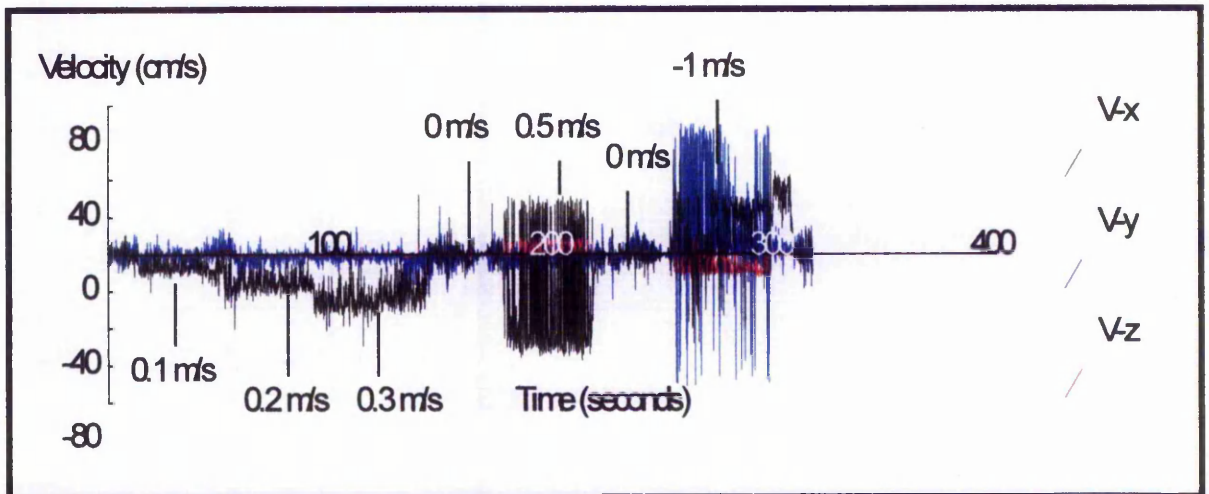
Figure 4.12   Time series graph of velocities during seeding trials.

linear pressure field because new fluid was encountered continuously. The steady state value of the indicted vertical velocity was induced by the head of the probe itself.
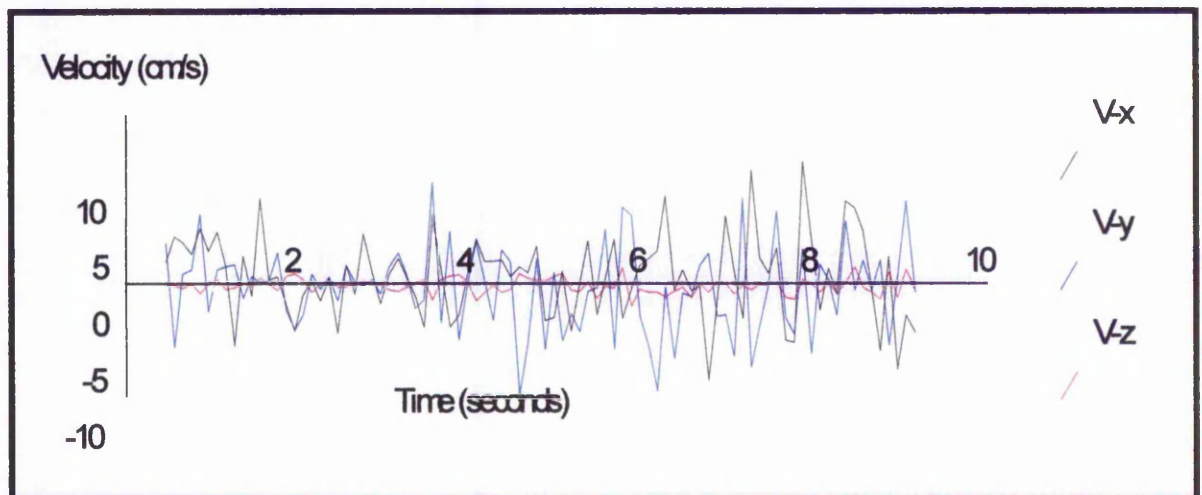
Figure 4.13   Time series for first 10 seconds of test (carriage stationary).

Third, the noise on the signal is Doppler noise (or White noise), which is inherent in the ADV system, related to the random distribution of particles that contribute to the back scattered echo. This noise appears as turbulent intensity if the signals are not

averaged. In the present case this can be observed from the fluctuation of the signals in Figure 4.14 despite the carriage being stationary. The rms values are $v_x'/U = 3.5\%$, $v_y'/U = 3.8\%$, $v_z'/U = 0.8\%$. These values are typical but generally reduce with an increase in COR and SNR. The values improve with increase in seeding material. Note also that the vertical component of turbulence is much smaller than the horizontal components. This is also an inherent characteristic of the ADV system (see Figure 4.6, typical power spectrum for the ADV).

As a result of the preliminary test at HRW seeding tests were conducted in the Hydraulics Laboratory of TNTU.

Seeding Tests at TNTU

Seeding tests were undertaken in February 1997 in the Armfield Flume (see section 4.3.2) at TNTU. Initially 4 control tests were undertaken with no seeding. 17 further test were undertaken with varying seeding dosing rates, velocity of carriage and position of the burette. Table 4.3 shows the results of the 4 control test with no seeding applied to the fresh tap water in the tank.

Velocity of Carriage (cm/s)	Velocity Measured by ADV (Vx) (cm/s) (Filtered Data) (cm/s)	Average COR (Filtered Data) (%)	Average SNR (Filtered Data) (dB)	Velocity Measured by ADV (Vx) (cm/s) (Unfiltered Data) (cm/s)	Ave. COR (Unfilt. Data) (%)	Ave. SNR (Unfilt. Data) (dB)
26.2	1.17	73.75	8.44	8.69	53.98	3.23
42.3	0	0	0	14.49	51.02	2.57
13.7	12.03	71.47	5.10	8.05	55.03	2.75
17.5	0.05	77.19	6.65	0.11	53.99	2.62

Table 4.3   Control tests with unseeded water.

The results indicate gross errors in the measured velocity. It may be concluded that the errors are due to low SNR proving that the tap water required seeding.

17 subsequent tests were undertaken in the flume. Table 4.4 summarises the results of the test that were carried out. The results show that a much closer correlation was obtained between the velocity of the carriage and the velocity measured by the ADV. Similarly the SNR that was obtained from the test was substantially higher than in the

unseeded tests, with a minimum SNR of 12.2 dB and a maximum of 34.5 dB. The improved SNR and COR occurred as a result of the introduction of seeding.

Test No.	Horiz. Burette Position in front of ADV (mm)	Vertical Burette Position in relation to ADV (mm)	Dosing Rate (ml/s)	Velocity of Carriage (cm/s)	Velocity Measured by ADV (Vx) (cm/s)	Ave. SNR (dB)	Ave. COR (%)
1	330	+10	1.2	20.2	17.8	24.2	87.3
2	330	+10	1.5	13.3	11.2	12.2	78.8
3	330	+10	1.6	27.7	27.1	25.6	82.1
4	330	+10	1.8	26.2	27.7	24.8	82.6
5	330	-25	1.5	23.1	23.2	20.8	81.9
6	330	-25	1.3	15.7	13.1	12.9	79.0
7	330	-25	2.0	35.3	31.5	33.0	83.7
8	330	-25	1.4	19.3	17.8	12.8	77.6
9	670	-25	0.5	16.6	16.4	27.1	88.8
10	670	-25	2.1	24.7	22.2	14.7	76.9
11	670	-25	2.3	38.9	40.3	20.2	78.8
12	670	-25	2.0	19.1	16.1	23.2	86.1
13	670	+10	2.0	24.3	23.9	27.6	86.7
14	670	+10	2.6	39.9	43.8	24.9	78.4
15	670	+10	0.6	14.7	12.8	34.5	91.8
16	670	+10	0.6	14.4	12.9	22.4	85.8
17	670	+10	2.4	38.2	38.2	27.0	79.8

Table 4.4   Seeding test results.

Further analysis of the results are shown by Figures 4.14, 4.15 and 4.16.
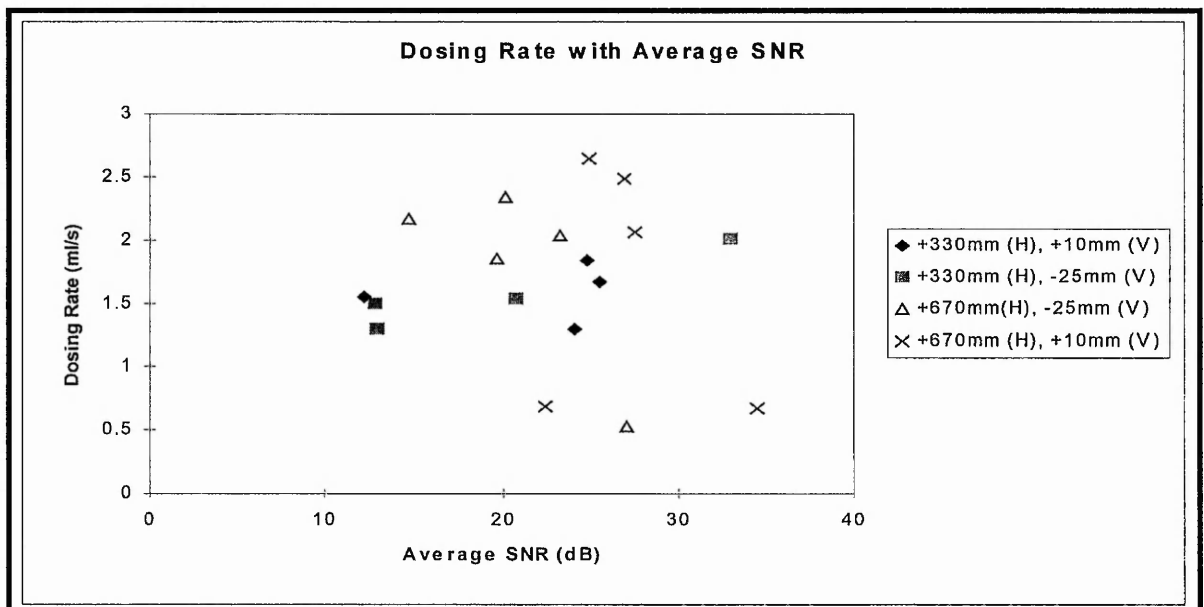
Figure 4.14   Dosing rate with average SNR.
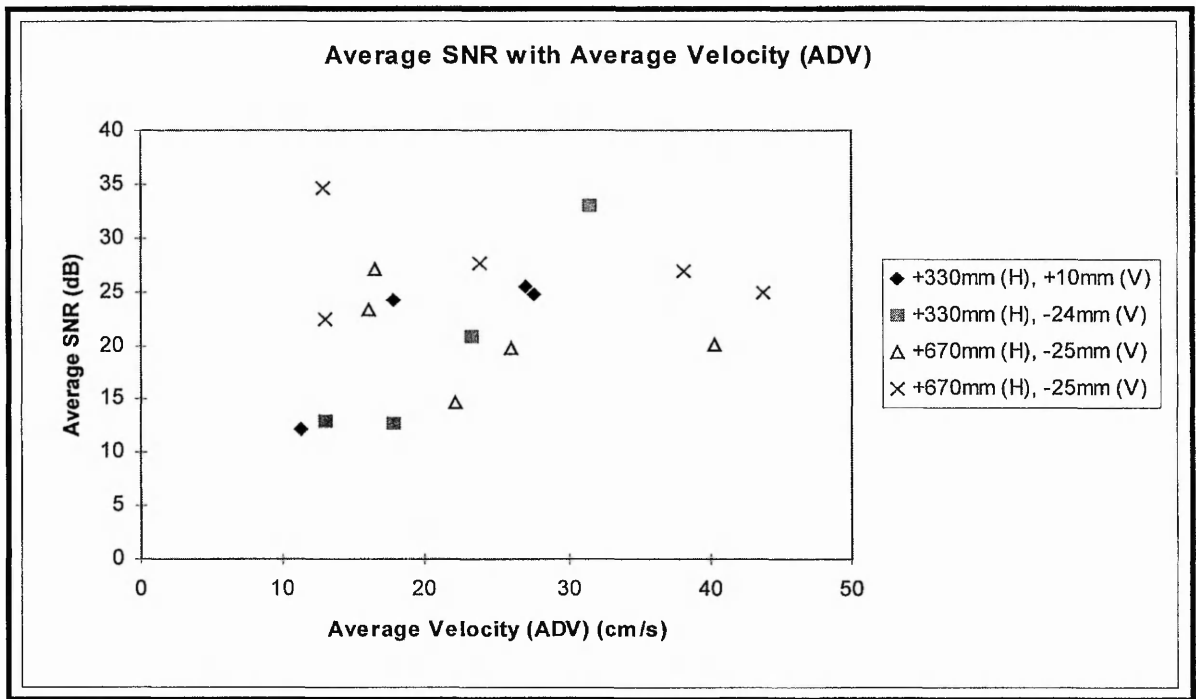
Figure 4.15   Average SNR with mean velocity (Vx).

Figure 4.14 shows the dosing rate with the average SNR. A minimum of 12.2dB was obtained at a dosing rate of 1.54 ml/s. A maximum SNR of 33.0 dB was obtained at a dosing rate of 0.68 ml/s. The maximum SNR was obtained at a relatively low dosing rate, however it should be observed from the graph that the trend shown was that high SNR's were generally obtained at dosing rates in excess of 1.5 ml/s. The graph also indicates that generally, a burette seeding position of 670mm in front of and 10mm above the ADV was favourable.

Figure 4.15 shows the variation of SNR with the mean velocity measured using the ADV. Larger SNR's were obtained throughout the spread of velocities with the burette seeding position 670mm in front of the ADV. In addition lower SNR's were observed at higher velocities.

The conclusion to the seeding tests were that the following operating conditions should be used:

- Seeding rate of PVC in suspension with water of 1.5 ml/s.
- Seeding concentration of 15 mg/l.
- Burette position of 670mm in front of the ADV with the tip of the burette operating at an elevation of 10mm above the sampling volume.

Delivery of Seeding Material

Apparatus was constructed to attach the ADV to the carriage of the towing tank facility at HRW and a method of delivering the seeding material to the apparatus was required. A 12 volt car windscreen washer pump initially operated well at the desired flow rate but seized after 1.5 hours. Seeding of the tank was required over a full eight hour period of testing and therefore this was not the correct solution to the problem.

It was found that the most appropriate method of delivery of the seeding material was by gravity feed from a reservoir elevated at a head above the burette. A series of further seeding tests were carried out using a burette nozzle diameter of 0.6mm with a seeding reservoir at varying elevation above the burette. Seeding material was passed from the reservoir to the burette via flexible polythene pipe. The head loss through the delivery pipe was assumed to be negligible. The flow rate was calculated by measuring the time taken for a known volume of seeding material to discharge. Figure 4.17 illustrates the results of this test.
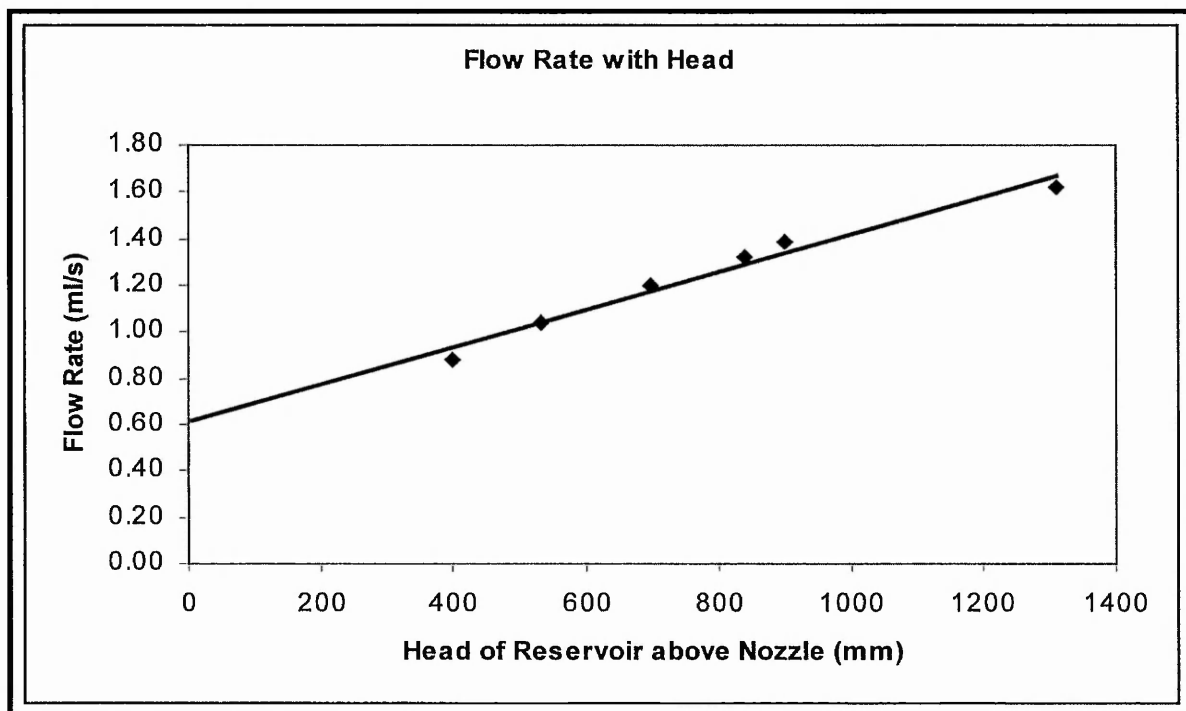
Figure 4.16   Seeding flow rate with head of reservoir.

Figure 4.16 shows a linear relationship and the elevation of the seeding reservoir above the burette was 1.1m to achieve a flow rate of 1.5 ml/s with a burette nozzle size of 0.6mm.

An adjustable holder for the ADV was subsequently designed and this was constructed in the laboratories of TNTU. The holder was designed to allow yaw (rotation in the horizontal plane) and pitch (rotation in the vertical plane) of the ADV probe. The fabrication details of the holder are shown in drawing CB/1/11/96 in Appendix B. Figure 4.17 shows a photograph of the ADV and holder attached to the towing tank carriage.
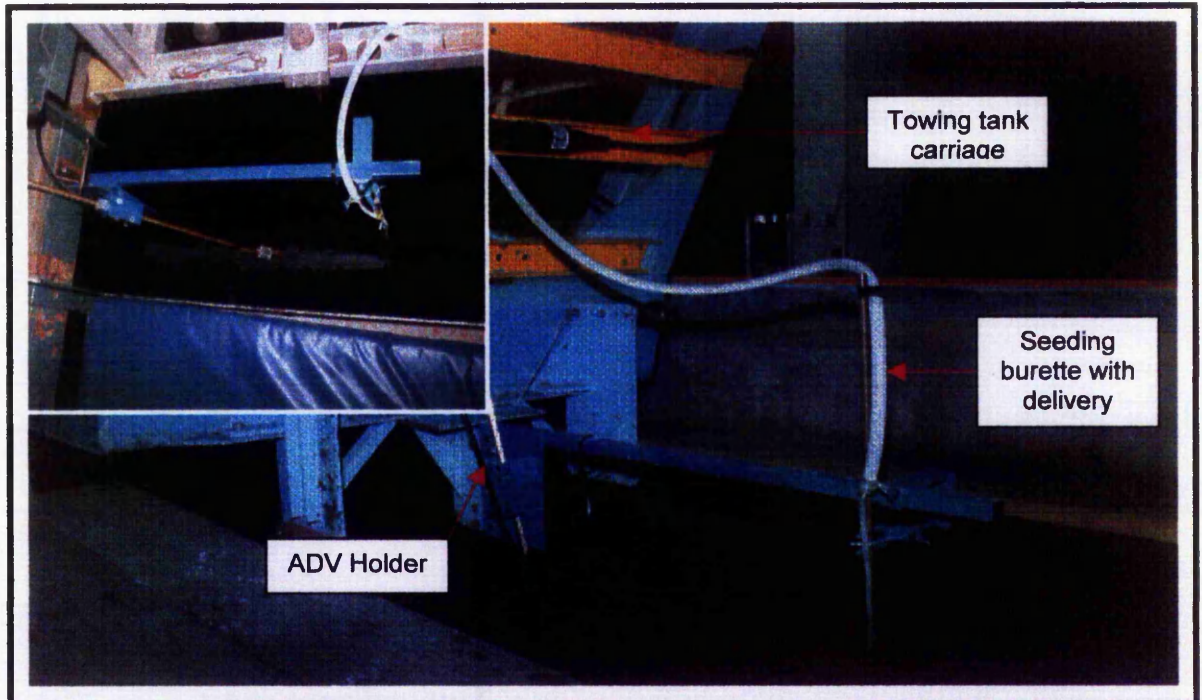
Figure 4.17   ADV holder attached to carriage (inset showing ADV from above and plume of seeding material).

Results of Towing Tank Tests at HRW.

The towing tank test at HRW was undertaken on 14 March 1997. 48 tests in total were completed during the day using velocities from 5 cm/s to 60 cm/s. 36 tests were completed with the orientation of the ADV probe in the streamwise direction (Vx). 8 tests were completed with the probe orientated at 90 degrees yaw to the streamwise direction and 4 test were completed with the probe orientated at 15 degrees pitch (to the vertical) in the streamwise direction.

Table 4.5 shows the results of the first set of 36 tests. 8 of the tests were discarded due to gross errors. The minimum SNR that was obtained was 7.66 dB which was in excess of the manufacturer's recommendation of 5dB for the measurement of mean velocities. However, analysis of the percentage errors between the carriage velocity

and the resultant velocity as measured by the ADV, indicated that there were excessive errors. The minimum error that was obtained was 8.1% with a maximum error of 17.7%.

Test No.	ADV Vx	ADV Vy	ADV Vz	ADV Resultant Velocity	Carriage Velocity	Carriage - Resultant	% Error	SNR
	(cm/s)	(cm/s)	(cm/s)	(cm/s)	(cm/s)	(cm/s)		(dB)
1	3.42	2.13	1.15	4.19	5	0.81	16.20	7.66
1c	3.99	0.90	1.28	4.29	5	0.71	14.28	14.19
2a	4.19	0.91	1.15	4.44	5	0.56	11.22	16.34
2b	4.02	0.92	1.05	4.26	5	0.74	14.89	14.64
2c	2.58	3.33	0.62	4.26	5	0.74	14.84	13.1
2c	2.88	2.73	0.70	4.03	5	0.97	19.41	12.31
3b	6.06	5.79	0.16	8.38	10	1.62	16.17	20.6
3c	6.48	5.33	0.47	8.40	10	1.60	15.96	19.91
3c	7.91	2.63	1.04	8.40	10	1.60	16.00	20.75
3d	6.69	4.56	1.11	8.17	10	1.83	18.28	19.83
4	18.28	1.70	0.85	18.38	20	1.62	8.11	17.19
5	17.56	2.89	0.75	17.81	20	2.19	10.94	19.13
6	22.60	9.46	0.24	24.50	30	5.50	18.33	16.6
7	25.22	4.70	0.95	25.67	30	4.33	14.43	20.33
8	23.41	7.86	0.49	24.70	30	5.30	17.67	13.89
9	23.96	6.76	0.64	24.90	30	5.10	16.99	20.25
10	27.47	0.21	1.27	27.50	30	2.50	8.33	25.12
11	43.85	5.40	0.19	44.18	50	5.82	11.64	12.59
12	45.67	2.54	0.33	45.74	50	4.26	8.52	14.42
13	42.08	8.57	0.55	42.95	50	7.05	14.11	13.38
14	42.62	7.92	1.03	43.36	50	6.64	13.28	13.18
15	41.69	9.66	1.33	42.82	50	7.18	14.37	12.59
16	44.75	23.23	2.86	50.50	60	9.50	15.83	12.11
16	48.19	14.13	1.62	50.24	60	9.76	16.26	12.11
17	49.55	11.72	1.32	50.93	60	9.07	15.11	12.12
18	51.73	8.72	1.04	52.47	60	7.53	12.55	12.32
19	50.08	11.58	1.52	51.42	60	8.58	14.29	11.21
20	49.25	12.44	1.43	50.82	60	9.18	15.31	13.53

Table 4.5   Towing tank test at HRW, ADV aligned in streamwise direction (zero pitch and yaw).

Further analysis of the results is presented by Figure 4.18 which shows that although there appears to be excessive errors, a reasonably linear relationship existed between the data. A regression coefficient of 0.99 with a linearity close to 1:1 was obtained.

Table 4.6 shows the results of the towing tank test with the ADV probe at 90 degrees yaw. It is clear from Table 4.6 that errors were again excessive. The signs indicated in the table show the direction of travel of the ADV through the tank.

Velocity Measured by ADV with Calibration Velocity

$y = 1.1688x - 0.6296$
$R^2 = 0.9831$
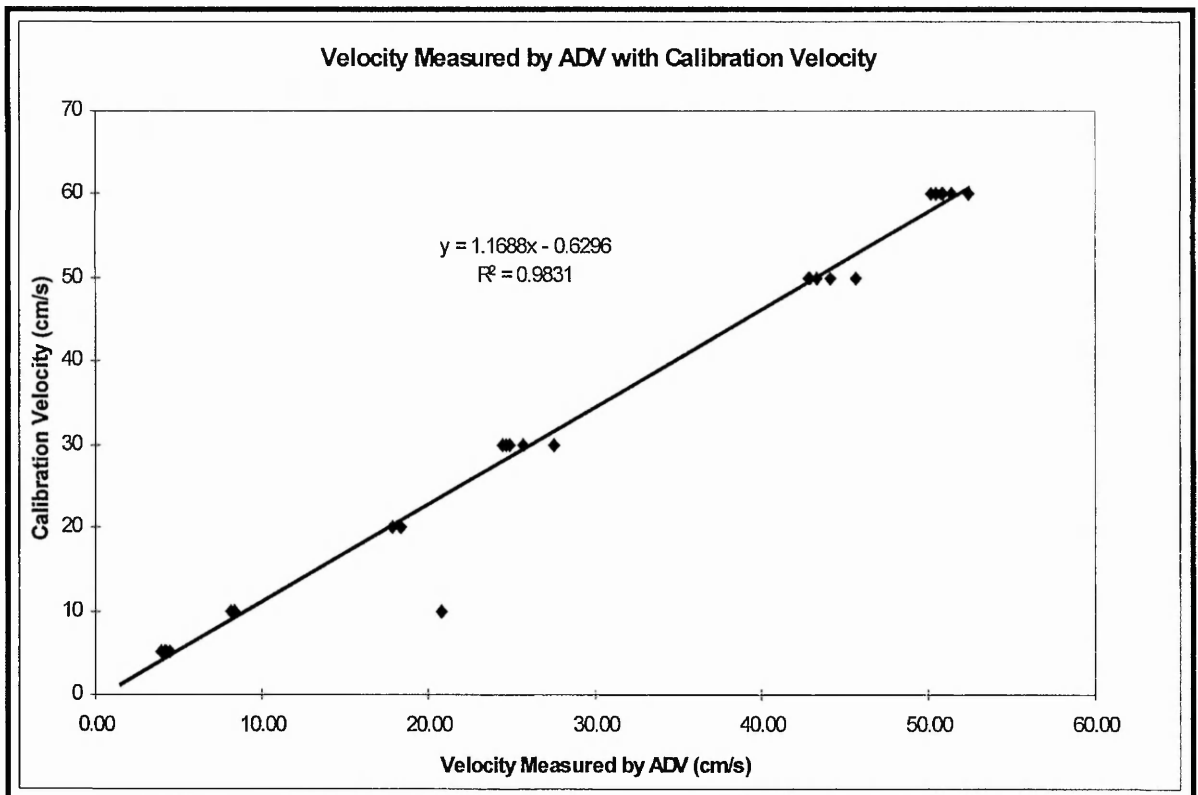
Figure 4.18   Linearity of towing tank test at HRW, ADV aligned in streamwise direction (pitch and yaw zero).

Test No.	ADV Vx (cm/s)	ADV Vy (cm/s)	ADV Vz (cm/s)	Resultant Velocity (cm/s)	Carriage Velocity (cm/s)	Carriage - Resultant (cm/s)	% Error	SNR (dB)
21	-23.29	-23.48	4.83	33.42	60	26.58	44.3	13.07
22	39.22	-2.83	14.36	41.86	60	18.14	30.2	11.67
23	-16.89	5.84	13.39	22.33	60	37.67	62.8	12.33
24	14.88	-0.65	7.77	16.80	20	3.20	16.0	9.22
25	5.56	2.95	12.00	13.55	20	6.45	32.3	9.60
26	48.05	2.97	6.64	48.60	30	-18.60	62.0	7.50
26	17.95	-1.64	9.27	20.27	30	9.73	32.4	7.97

Table 4.6   Towing tank test at HRW, ADV aligned at 90 degrees yaw, zero pitch.

Errors were similarly large with the ADV aligned at 15 degrees pitch, zero yaw, with errors in the order of 15-18% as shown by Table 4.7.

No.	ADV Vx	ADV Vy	ADV Vz	Resultant Velocity	Carriage Velocity	Carriage Resultant	% Error	SNR
	cm/s	cm/s	cm/s	cm/s	cm/s	cm/s		dB
27	32.3	-11.3	4.8	34.6	30	-4.6	15.2	12.98
28	-22.2	-6.1	-8.7	24.7	30	5.3	17.8	10.92

Table 4.7   Towing tank test at HRW, ADV aligned at 15 degrees pitch, zero yaw.

Conclusions from Towing Tank Tests at HRW

The design of the seeding mechanism performed satisfactorily with SNR's in excess of 10 dB in almost all cases. This seeding mechanism was therefore used in all subsequent towing tank tests.

It was clear from the towing tank tests undertaken at HRW that the ADV velocity factory calibration was unacceptable. These results may be considered as reasonable in a highly turbulent flow, however this was not the case in the towing tank. This fact will be discussed in more detail in later sections. Analyses of the tests was not totally rigorous since no account was taken of the effect of velocity range or sample rates on the results. These subjects were considered in detail in later tests. In consequence of these tests at HRW the ADV was subsequently returned to the suppliers, HRW Equipment Sales for checking.

4.3.4 Towing Tank Tests at Southampton Institute, UK.

The ADV was returned from HRW Equipment Sales and subsequently towing tank tests were undertaken at Southampton Institute (SI), UK. It was necessary to change to the facility at Southampton due to the excessive costs incurred with the use of the facility at HRW. The facility at SI is similar in operating principle to the facility at HRW although on a slightly smaller scale. The tank is approximately 60m long by 3m wide by 1.5m deep. A photograph of the facility is shown by Figure 4.19.

Results of Towing Tank Tests at Southampton Institute.

Two days of testing were undertaken at SI. The first visit took place on 1 July 1997. The second visit which took place in May 1998 will be covered later in this section. In total 96 tests were undertaken at Si in July 1997; 51 with the ADV aligned in the streamwise direction (zero pitch and yaw), 30 with the ADV aligned in the cross

stream direction (90 degrees yaw, zero pitch) and 15 with the ADV aligned at 90 degrees yaw and 30 degrees pitch.

Figure 4.19   Towing Tank facility at Southampton Institute.

In addition sampling rates of 5, 15 and 25 Hz were tested. The 10MHz acoustic signal frequency used by the ADV can be sampled at rates ranging from 0.1Hz to a maximum of 25Hz. At sample rates less than 25 Hz the ADV performs internal "ensemble" averaging of multiple samples and outputs the data at the chosen rate. This averaging reduces the variance of individual measurements, including Doppler noise but also reduces the higher frequency content of the fluctuating velocity signals.

The velocity range was fixed at +/- 100 cm/s since this was the maximum velocity at which the ADV was to be tested. The ADV system provides a number of different velocity ranges to improve the accuracy of the system in different applications. With all Doppler measurements, there is an inherent random error referred to previously as Doppler noise. By setting the ADV to lower velocity ranges, the Doppler noise is reduced, although the system cannot then resolve large velocities. Higher velocity ranges have a higher level of instrument generated noise, although they are able to resolve larger velocity levels. The advice of the manufacturer is to always use the smallest velocity range that will not be exceeded when taking measurements with the

ADV. Higher velocities can still measure low flows, although the data will have a higher noise level.

The ADV has no minimum detectable velocity because the ADV has no potential for zero drift (due to the Doppler principle). However, the ADV specifications state that the maximum zero bias is 0.25 cm/s. Because of the nature of the ADV Doppler processing. There are maximum velocity levels beyond which the ADV cannot make accurate measurements. These levels are a function of the velocity range specified in the ADV software. The maximum velocity that can be measured is different for vertical (along the axis of the transmitter) and horizontal (perpendicular to the axis of the transmitter) velocities. Maximum velocity limits for the different ADV range setting are shown below (Nortek 1996).

ADV Velocity Range Setting (+/- cm/s)	Maximum Horizontal Velocity (+/- cm/s)	Maximum Vertical Velocity (+/- cm/s)
3	30	8
10	60	15
30	120	30
100	300	75
250	360	90

Table 4.8 shows the results of the towing tank test with the ADV aligned in the streamwise direction (zero yaw and pitch). Notice from this table that the errors measured were vastly improved from the results of the test at HRW. The error between the resultant velocity measured using the ADV and the carriage velocity ranged from a minimum of 4.7% to a maximum of 6.7%, where the resultant velocity was calculated as:

$$R^2 = V_x^2 + V_y^2 + V_z^2 \qquad\qquad 4.5$$

It should also be noted that the SNR was in excess of 20 dB and the COR was in excess of 91%.

Figure 4.20 shows the basic calibration check for the ADV produced from the tabulated results. The graph shows that the linearity of the ADV calibration was extremely good with a gradient of the least squares line of 0.94 very close to a 1:1 relationship. Similarly a correlation coefficient of 0.99 shows excellent linear agreement. It was clear however, that there appeared to be a bias in the errors. The

mean of the errors was 5.5% with a standard deviation from the mean of 0.75%.

	Carriage Velcocity	Vx-Avg	Vy-Avg	Vz-Avg	Error	% Error	COR	SNR	AMP
	(cm/s)	(cm/s)	(cm/s)	(cm/s)	(cm/s)		(%)	(dB)	
TEST5	60.6	56.94	-1.48	-1.97	3.66	6.4	92.18	41.89	158.43
TEST6	60.5	57.01	-1.89	-2.26	3.49	6.1	91.95	33.58	139.42
TEST7	60.52	57.28	-2	-2.39	3.24	5.7	93.01	31.77	134.88
TEST9	14.33	13.35	0.01	-0.32	0.98	7.3	92.86	15.48	97.34
TEST10	14.44	13.84	0.01	-0.4	0.6	4.3	92.23	15.86	96.89
TEST11	14.52	13.81	-0.11	-0.31	0.71	5.1	91.14	22.06	111.64
TEST12	21.89	20.9	-0.46	-0.75	0.99	4.7	97.63	26.7	122.1
TEST13	21.99	20.97	-0.44	-0.77	1.02	4.9	97.39	24.03	116.88
TEST14	21.98	20.96	-0.45	-0.8	1.02	4.9	97.36	24.2	116.28
TEST15	26.26	25.04	-0.33	-1.09	1.22	4.9	98.04	35.78	142.88
TEST16	26.26	25.14	-0.34	-1.14	1.12	4.5	97.91	33.06	137.22
TEST17	26.3	25.02	-0.44	-1.07	1.28	5.1	97.8	32.18	134.49
TEST18	30.93	29.45	-0.6	-1.17	1.48	5.0	97.53	26.7	121.75
TEST19	30.91	29.62	-0.58	-1.23	1.29	4.4	97.34	26.2	120.93
TEST20	30.89	29.61	-0.56	-1.24	1.28	4.3	97.12	25.13	118.43
TEST21	36.13	34.6	-0.79	-1.59	1.53	4.4	97.56	48.45	172.67
TEST22	36.07	33.64	-0.72	-1.45	2.43	7.2	97.4	45.05	165.1
TEST23	36.06	34.44	-0.75	-1.46	1.62	4.7	97.1	34.29	140.75
TEST24	40.91	38.92	-1.27	-1.61	1.99	5.1	96.85	31.41	134.04
TEST25	41.04	39.06	-1.09	-1.64	1.98	5.1	96.84	44.43	164.34
TEST26	40.9	38.89	-0.73	-1.64	2.01	5.2	96.8	49.1	174.18
TEST27	45.97	43.79	-1.29	-1.72	2.18	5.0	96.52	45.46	166.39
TEST28	45.97	43.61	-1.41	-1.61	2.36	5.4	96.3	37.05	147.16
TEST29	45.95	43.87	-1.31	-1.88	2.08	4.7	96.26	49.79	177.11
TEST30	46.01	43.73	-0.72	0.03	2.28	5.2	96.2	26.04	120.89
TEST31	50.59	47.66	-0.85	0.03	2.93	6.1	96.13	24.71	117.46
TEST32	50.63	48.15	-0.76	0.02	2.48	5.2	95.7	23.49	114.62
TEST33	50.64	47.46	-0.8	0.04	3.18	6.7	95.7	23.29	113.82
TEST34	55.61	52.8	-0.87	-0.02	2.81	5.3	94.8	22.51	112.35
TEST35	55.63	52.87	-0.87	-0.02	2.76	5.2	94.55	22.11	111.08
TEST36	55.61	52.75	-0.97	-0.02	2.86	5.4	94.14	20.29	107.52
TEST37	60.66	57.01	-0.94	-0.16	3.65	6.4	92.26	20.02	106.89
TEST38	60.67	57.07	-0.91	-0.14	3.6	6.3	92.27	19.85	106.17
TEST39	60.67	57.2	-0.93	-0.16	3.47	6.1	92.73	19.55	105.13
TEST40	69.92	66.28	-0.57	-0.71	3.64	5.5	82.51	28.38	126.99
TEST41	70.12	66.18	-0.77	-0.47	3.94	6.0	88.46	32.76	137.18
TEST42	70.18	66.22	-0.38	-1.1	3.96	6.0	89.99	50.75	179.03
TEST43	80.83	75.77	-1.13	-0.63	5.06	6.7	92.34	33.71	139.4
TEST44	80.76	76.05	-1.3	-0.41	4.71	6.2	92.83	29.56	128.75
TEST45	80.72	76	-1.35	-0.33	4.72	6.2	93.4	27	123.13
TEST46	90.9	85.6	-1.52	-0.24	5.3	6.2	93.28	27.28	124.12
TEST47	90.96	86.09	-1.51	-0.26	4.87	5.7	92.65	26.03	121.19
TEST48	90.9	86.22	-1.46	-0.27	4.68	5.4	92.54	26.19	121.57
TEST49	101.13	95.16	-1.64	-0.58	5.97	6.3	93.3	24.85	118.12
TEST50	101.23	95.38	-1.63	-0.63	5.85	6.1	92.82	23.01	114.52
TEST51	101.43	95.75	-1.66	-0.58	5.68	5.9	92.44	22.06	111.96

Table 4.8   Towing tank test at SI, ADV aligned in streamwise direction (zero yaw and pitch)
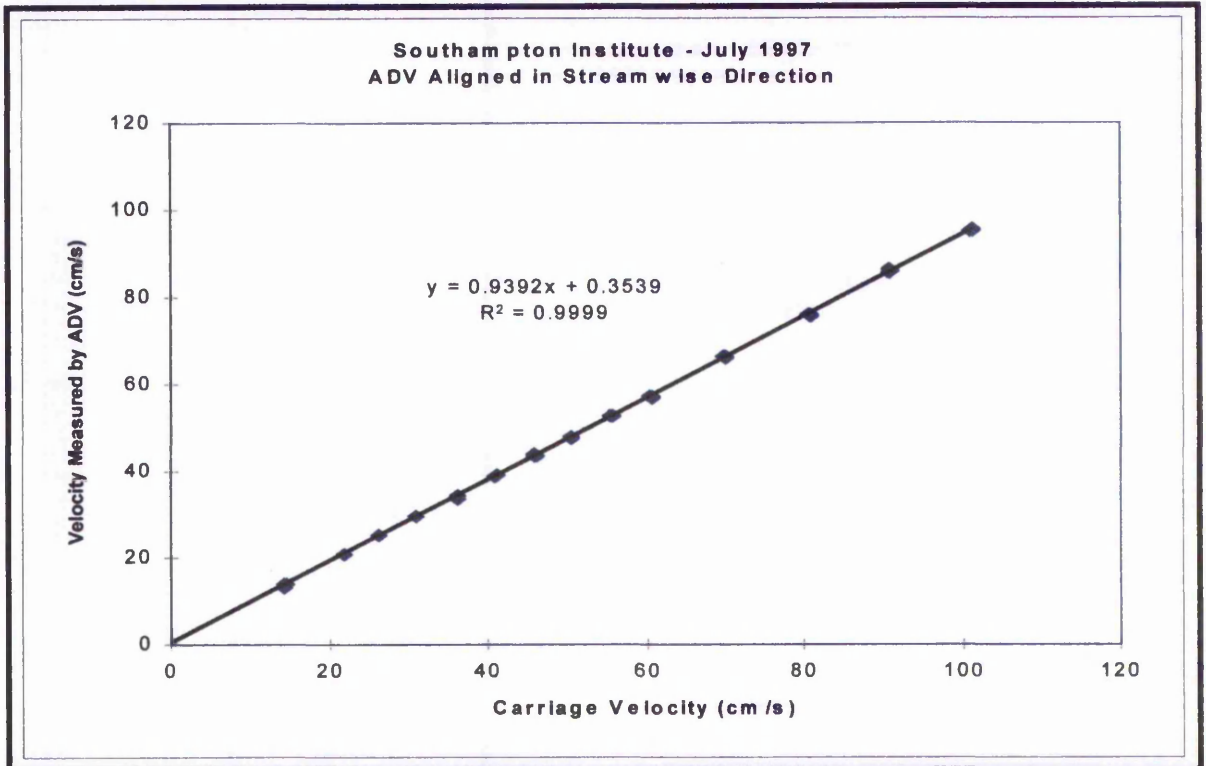
Figure 4.20   Basic calibration check at SI, ADV aligned in streamwise direction (zero yaw and pitch).

The effect of the sampling rate used on the measurement of mean velocities was also investigated. Figure 4.21 shows the linearity of the ADV calibration with sampling rate.
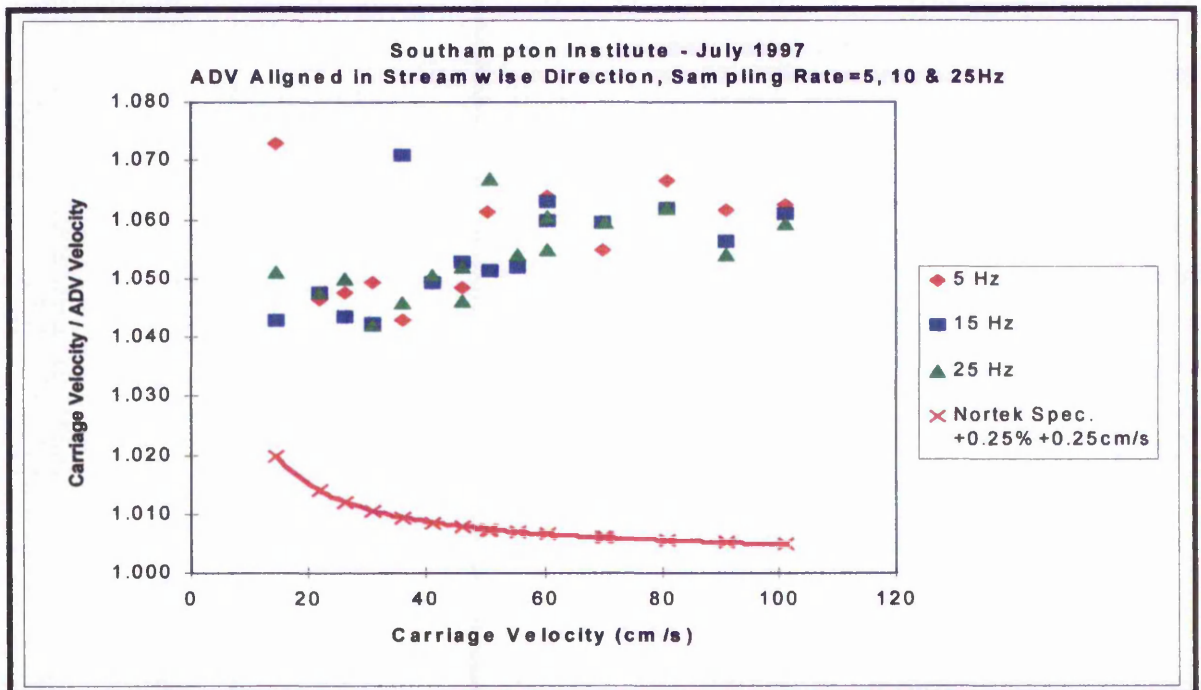
Figure 4.21   Linearity of ADV calibration, ADV aligned in streamwise direction (zero yaw and pitch).

Figure 4.22 illustrates no noticeable effect of the sampling rate on the accuracy of the ADV. The spread of results however, appears to reduce with increasing velocity. The solid (red line) indicated on the graph represents the manufacturer's claimed accuracy. It should be noted that the measured errors lie clear of the claimed error bounds by the mean error bias quoted previously of approximately 5.5%.

The received signal pattern recorded in this set of tests was investigated and a comparison was made to the previous test at HRW. The time series output from the ADV was compared between the two tests. Figure 4.22 shows a time series from a typical test at HRW. Figure 4.23 shows a time series from a typical test at SI.
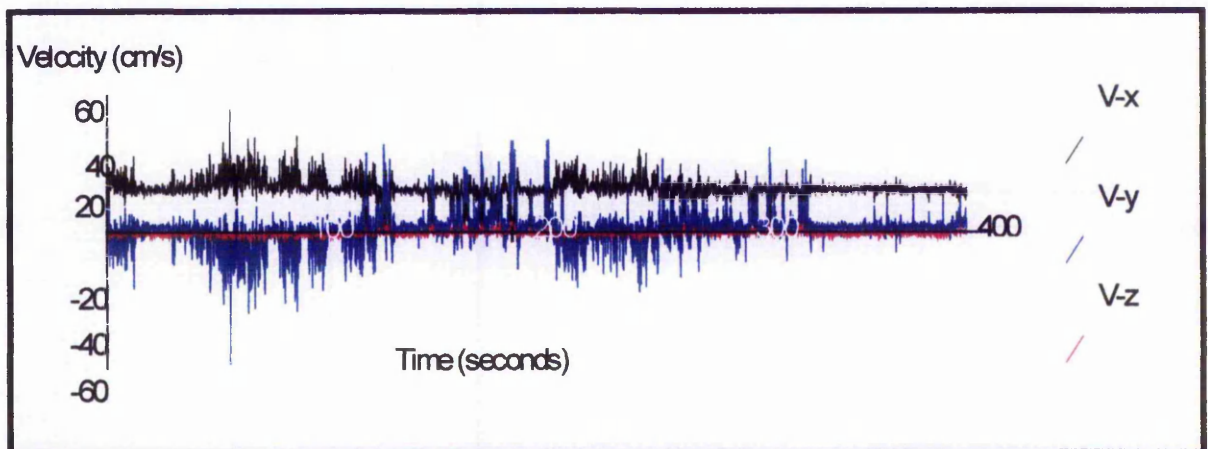
Figure 4.22   Time series of signal output from a typical test at HRW.
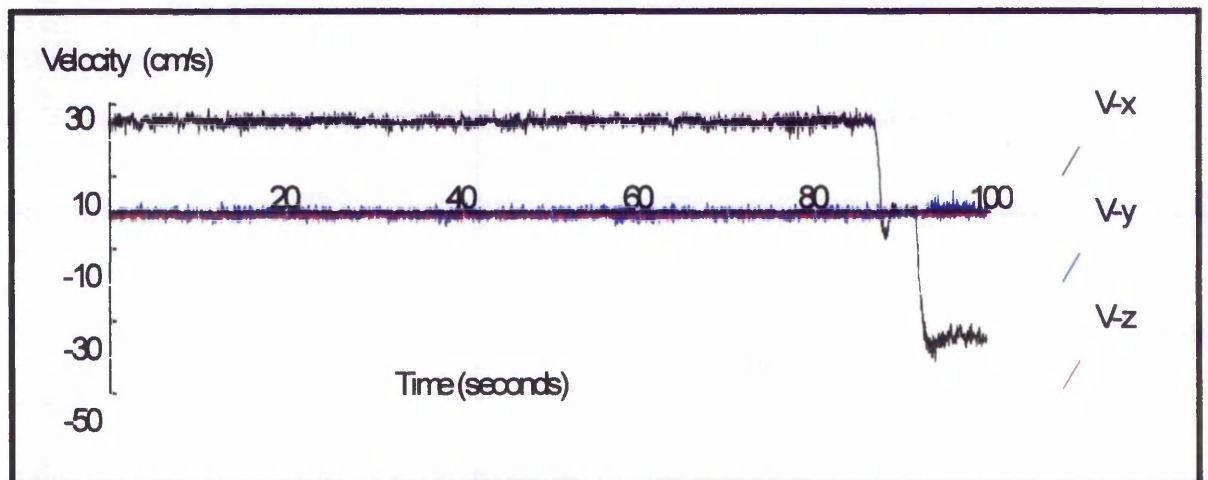
Figure 4.23   Time series of signal output from a typical test at SI.

It can be seen from Figure 4.23 that the signal received from the x component receiver for velocity is much "cleaner" than the corresponding signal from Figure 4.22. The turbulence levels in the signals in Figure 4.22 are considerably greater

than in Figure 4.23. The rms values of turbulence intensity from Figure 4.22 are in the order of v_x'/U = 85% in comparison with v_x'/U = 5% from Figure 4.23. The sampling rate for both graphs was 25 Hz, the velocity range was +/- 100 cm/s. The mean Vx for Figure 4.22 and Figure 4.23 were 18.3 cm/s and 19.2 cm/s respectively. The sudden drop in the Vx signal in Figure 4.23 was due to the towing tank carriage stopping. Further clarification of these results is shown by the SNR and COR Figure 4.24 and 4.25.
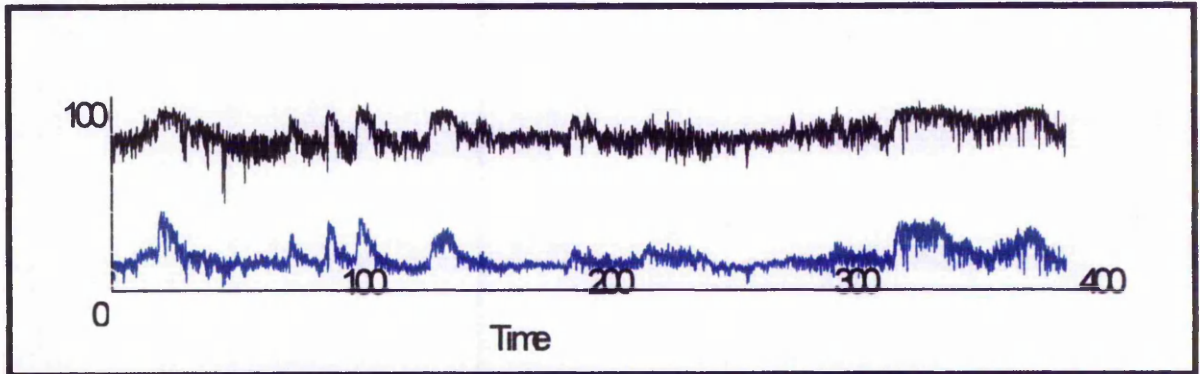
Figure 4.24   SNR (lower line) and COR for a typical test at HRW.
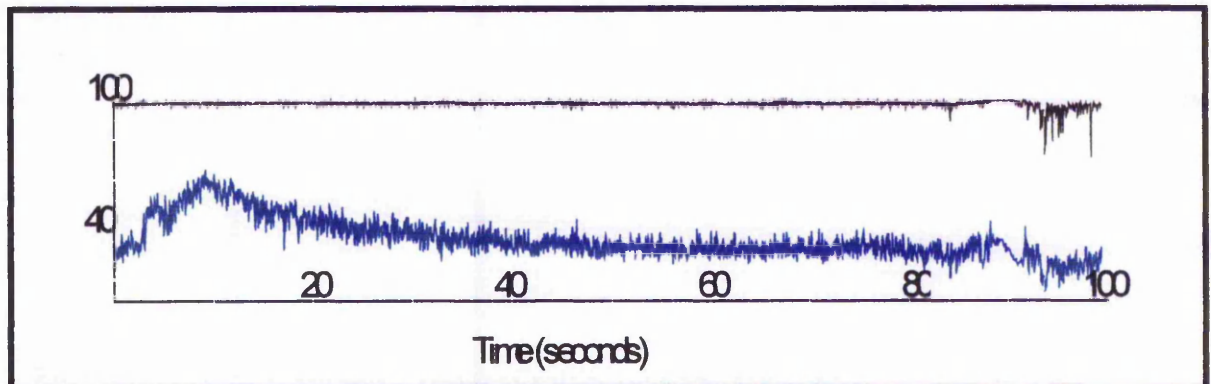
Figure 4.25   SNR (lower line) and COR for a typical test at SI.

Figure 4.24 shows the COR fluctuating to a greater extent than in the SI test shown by Figure 4.23. The levels of COR were generally higher at SI than at HRW although the seeding rates and the facility were similar. Additionally the fluctuations in the SNR signal were again present at HRW as shown by Figure 4.24, in comparison to the relatively stable SNR signal at SI shown by Figure 4.25. The sudden rise and then the gradual fall in the SNR signal at SI was probably due to the higher concentration of seeding material at the beginning of the tank. For each test the seeding delivery to the tank would start prior to movement of the carriage and hence a build up of seeding material at this position occurred. It should also be noted that in general the

SNRs were higher at SI than HRW. This could have been due to more particulate matter being present in the tank at SI than at HRW prior to the introduction of seeding material.

It is difficult to isolate the causes of the difference in turbulence levels observed in Figures 4.22 and 4.23. Similarly it is difficult to explain the fluctuations of the SNR and COR in Figure 4.24 in comparison to the stable signals recorded in Figure 4.25. It was certain however, that there was a fault in the operation of the ADV during the tests at HRW and that this was rectified by HRW Equipment Sales prior to the testing at SI. This fault probably caused the anomolies observed in the preceding graphs.

Further analysis can now be made with towing tank tests at SI with the ADV aligned in the cross stream (90 degrees yaw) direction and aligned at 30 degree pitch.

Table 4.9 shows the results of the ADV calibration at 90 degree yaw. A very similar calibration line was obtained for this set of tests to the previous set with the ADV aligned at zero yaw. A close linear relationship existed between the velocity magnitude, measured using the ADV and the carriage velocity with the equation of the linear regression line $y = 0.98x + 0.42$ and the correlation coefficient, 0.99. It is therefore more useful to show the linearity Figure 4.26 in the presentation of results.
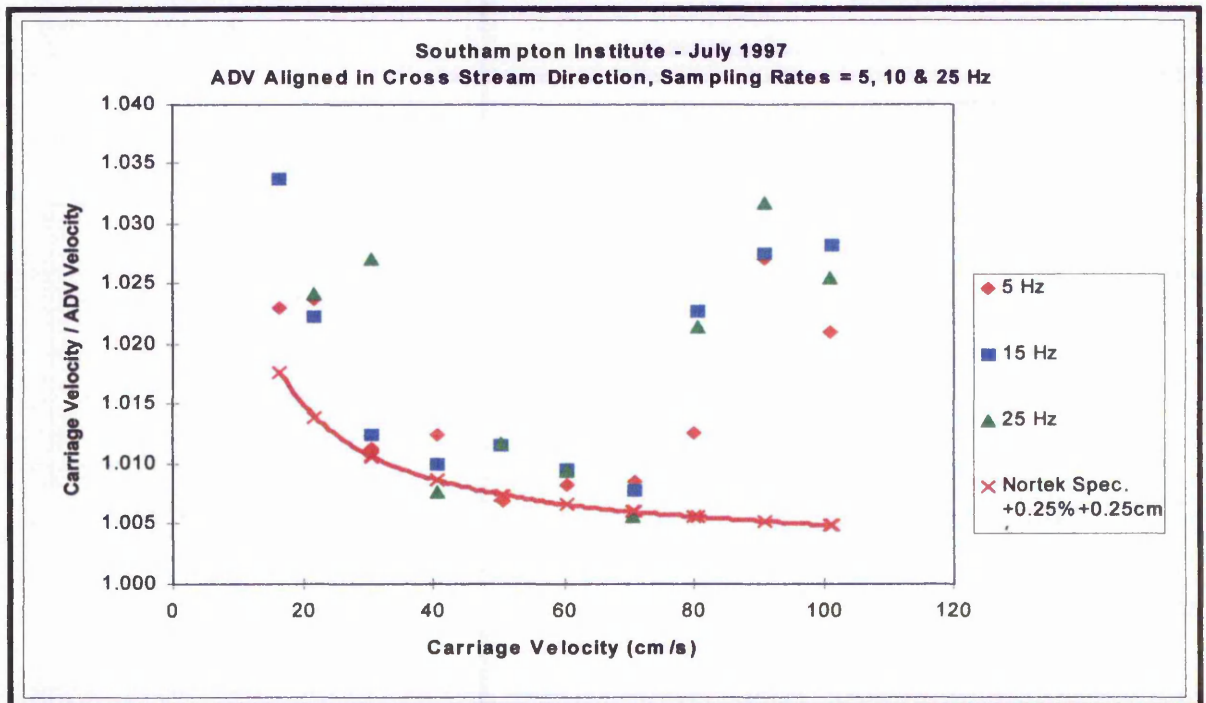
Figure 4.26   Linearity of ADV calibration, ADV aligned in cross stream direction (90 degree yaw, zero pitch).

	Vx-Avg	Vy-Avg	Vz-Avg	Carriage V	Result. V	Error	% Error	COR	SNR	AMP
	(cm/s)	(cm/s)	(cm/s)	(cm/s)	(cm/s)	(cm/s)		(%)	(dB)	
TEST52	-0.06	16.04	0.2	16.41	16.04	0.37	2.30	96.9	18.97	105.11
TEST53	-0.03	15.93	0.24	16.47	15.93	0.54	3.38	98.41	21.49	110.64
TEST54	-0.01	15.83	0.25	na	15.83	na	0.00	98.29	20.89	109.59
TEST55	-0.14	21.34	0.36	21.85	21.34	0.51	2.37	97.9	19.66	107.05
TEST56	-0.13	21.36	0.37	21.84	21.36	0.48	2.23	97.76	19.33	106.28
TEST57	-0.16	21.34	0.38	21.86	21.34	0.52	2.42	97.37	18.9	104.63
TEST58	-0.19	30.35	0.5	30.7	30.35	0.35	1.14	97.17	18.15	103.53
TEST59	-0.13	30.17	0.5	30.55	30.17	0.38	1.24	96.4	17.06	101.01
TEST60	-0.14	29.76	0.51	30.57	29.76	0.81	2.71	97.09	18.54	104.11
TEST61	-0.26	40.22	0.66	40.73	40.23	0.50	1.25	94.5	15.7	97.52
TEST62	-0.27	40.32	0.64	40.73	40.33	0.40	1.00	95.46	16.64	99.37
TEST63	-0.33	40.46	0.67	40.78	40.47	0.31	0.77	95.41	16.45	99.27
TEST64	-0.32	50.2	0.8	50.56	50.21	0.35	0.70	95.71	16.82	100.46
TEST65	-0.33	49.96	0.79	50.55	49.97	0.58	1.17	94.8	16.18	98.97
TEST66	-0.29	49.91	0.79	50.5	49.92	0.58	1.17	94.84	16.06	99.02
TEST67	-0.31	60.05	0.86	60.55	60.06	0.49	0.82	94.77	16.12	98.83
TEST68	-0.4	59.98	0.86	60.56	59.99	0.57	0.95	93.72	15.46	96.95
TEST69	-0.32	60.03	0.85	60.6	60.04	0.56	0.94	94.33	15.89	97.95
TEST70	0.21	70.25	0.05	70.85	70.25	0.60	0.85	94.77	34.53	141.31
TEST71	-0.19	70.2	0.65	70.75	70.20	0.55	0.78	93.87	41.04	156.77
TEST72	-0.38	70.27	0.68	70.67	70.27	0.40	0.56	94.49	44.71	163.97
TEST73	-0.27	79.05	0.97	80.05	79.06	0.99	1.26	93.93	51.32	180.34
TEST74	-0.01	78.96	1.06	80.76	78.97	1.79	2.27	93.82	25.05	119.25
TEST75	0.07	79.04	1.08	80.74	79.05	1.69	2.14	94.25	24.09	117.03
TEST76	-0.48	88.59	1.53	91.01	88.60	2.41	2.71	93.42	22.71	114.15
TEST77	-0.48	88.58	1.53	91.04	88.59	2.45	2.76	92.95	21.91	111.62
TEST78	-0.58	88.2	1.53	91.01	88.22	2.79	3.17	93.01	20.93	110.01
TEST79	-0.58	99.07	1.23	101.16	99.08	2.08	2.10	92.73	20.88	109.88
TEST80	-0.59	98.51	1.27	101.3	98.52	2.78	2.82	91.58	19.67	106.75
TEST81	-0.64	98.63	1.25	101.16	98.64	2.52	2.55	92.03	20.4	107.45

Table 4.9   Towing tank test at SI, ADV aligned in cross stream direction (90 degree yaw and zero pitch).

Figure 4.26 should now be compared to Figure 4.21. In conjunction with Table 4.9 it can be seen that the errors are reduced to a mean of 1.7% with a standard deviation from the mean of 0.9%, with the ADV aligned at 90 degrees yaw. Examination of Figure 4.26 shows that the results of the test lie much nearer to the manufacturer's error bounds than the test with the ADV aligned at zero yaw.

A final test at SI was undertaken with the ADV aligned at 90 degrees yaw and 30 degrees pitch. The errors increased again to a mean of 2.3% with a standard deviation from the mean of 1.7%. Table 4.10 shows the results of this set of tests.

	Vx-Avg	Vy-Avg	Vz-Avg	Carriage V	Resultant V	Error	% Error	COR	SNR	AMP
	(cm/s)	(cm/s)	(cm/s)	(cm/s)	(cm/s)	(cm/s)		(%)	(dB)	
TEST82	-0.97	19.77	10.4	22.76	22.36	0.40	1.79	95.82	34.88	141.78
TEST83	0.9	20.11	7.5	22.81	21.48	1.33	6.18	96.91	44.12	162.93
TEST84	1.45	20.93	5.63	21.96	21.72	0.24	1.09	97.76	50.8	178.13
TEST85	0.78	27.85	10.13	30.28	29.65	0.63	2.14	94.46	31.96	135.32
TEST86	0.98	26.19	12.66	30.27	29.11	1.16	4.00	94.53	26.99	122.44
TEST87	1.21	24.64	14.96	30.24	28.85	1.39	4.81	95.17	22.58	112.5
TEST88	0.27	42.4	24.78	50.39	49.11	1.28	2.60	93	22.14	111.16
TEST89	0.19	41.79	24.35	50.46	48.37	2.09	4.33	92.55	21.67	110.07
TEST90	0.19	42.95	25	50.36	49.70	0.66	1.34	91.67	20.14	106.5
TEST91	1.6	62.65	35.37	70.64	71.96	-1.32	-1.84	90.54	18.84	103.81
TEST92	1.91	62.36	35.34	70.62	71.70	-1.08	-1.51	90.56	18.07	102.68
TEST93	1.71	62.75	35.35	70.65	72.04	-1.39	-1.93	90.47	18.07	102.68
TEST94	3.93	78.31	45.77	91.07	90.79	0.28	0.31	91.92	18.29	102.54
TEST95	4.08	78.33	45.72	91.07	90.79	0.28	0.31	91.18	18.12	102.47
TEST96	3.96	78.18	45.58	91.04	90.58	0.46	0.50	91.01	17.29	101.21

Table 4.10   Towing tank test at SI, ADV aligned at 90 degrees yaw and 30 degrees pitch.

Conclusions from first tests at SI

To summarise the tests at SI, mean errors in the calibration of 6% in the x direction and 2% in the y direction were observed. It is not clear why the errors should be different in the x and y directions but it is probable that it is related to the factory calibration method and the transformation matrix, T, which is used in the calibration process. ADFCHECK was run prior to testing proceeding at SI and the graphical output of this test is shown by Figure 4.27. The results from SI however, were a vast improvement on those from HRW.

Figure 4.27 indicated that the three channels of the ADV were operating correctly. The SNR of each of the emitted signals was approximately equal although the SNR of the reflected signal received in the x channel was approximately 15% lower than the SNR of the reflected signal of the two other receivers. Correspondence with the manufacturer's confirmed that this did not have a significant effect on the errors obtained.

It was observed that the sampling rates appeared to have no influence on the error in the measurement of the mean velocities, although the exact effect of sampling rate on turbulence levels was not fully ascertained. This subject was investigated more

closely on the next day of testing at SI (see next section).

A report of the tests at HRW and SI was sent to the manufacturer's, Sontek. The ADV was subsequently returned to Sontek for recalibration. The second day of testing was undertaken after the ADV was returned by Sontek.
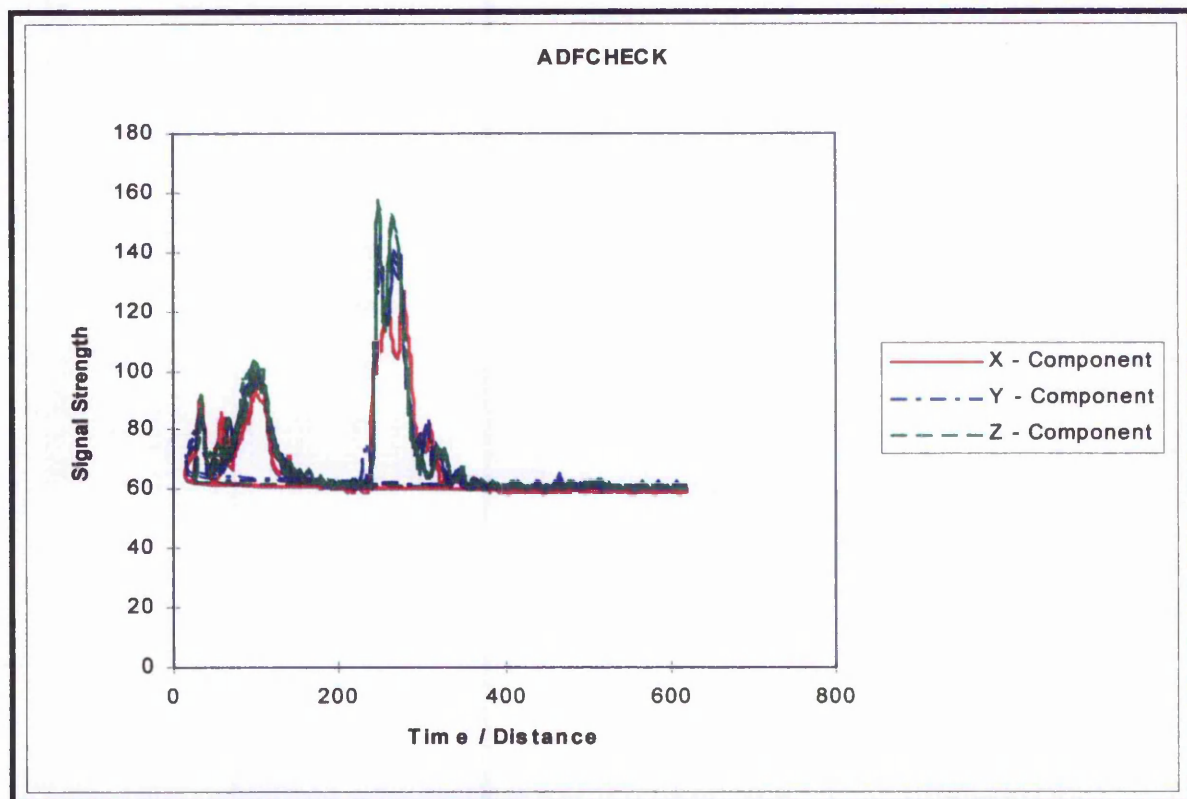
Figure 4.27   SNR from ADFCHECK.

Second Day of Towing Tank Tests at SI

The ADV was sent to Sontek, USA, for recalibration and subsequently returned to TNTU. A second day of testing was organised at SI and was undertaken in May 1998. 72 tests in total were completed in the day. The testing programme is shown in Table 4.11. In addition, 1 control test was undertaken to ascertain the SNR in the tank prior to seeding. It was found that in similarity with previous towing tank tests an average SNR of 3 dB was obtained which is lower than the recommended minimum, confirming that seeding was necessary. The SNR of the remaining test were monitored closely to maintain a SNR in excess of 15 dB. It was found that the SNR rarely dropped below 20 dB. The COR was also monitored and any data which dropped below a COR of 70 % was filtered out using WinADV. The majority of the data did not drop below 70 % COR.

Figure 4.28 shows the linearity of the ADV with the carriage velocity. Measurements were taken using three sampling rates of 5, 15 and 25 Hz. The results of the previous

Yaw (Degrees)	Pitch (Degrees)	Sample Rate (Hz)	Velocity Range (+/- cm/s)	No. of Tests
0	0	5	100	7
0	0	15	100	7
0	0	25	100	7
90	0	25	100	7
0	0	25	3	3
0	0	25	10	3
0	0	25	30	3
0	0	25	100	3
0	0	25	250	3
0	15	25	100	9
0	30	25	100	7
			Temperature (Degrees C)	
0	0	100	5	1
0	0	100	10	1
0	0	100	15	1
0	0	100	20	1
0	0	100	25	1
0	0	100	30	1
			Salinity (ppm)	
0	0	100	10	1
0	0	100	20	1
0	0	100	30	1
0	0	100	40	1
0	0	100	50	1
0	0	100	60	1
TOTAL	NUMBER	OF	TESTS	71

Table 4.11   Testing programme for SI (2).

test at SI are also shown on the same graph for comparison. The velocity range was set on +/- 100 cm/s. The specifications quoted by Nortek of +/- 0.25 % +/- 0.25 cm/s , are shown as a solid curve on the graph. It can be seen that in this test 7 points fell within the specifications and in general the results were an improvement from the results of the previous tests at SI in July 1997. The mean of the velocity error in the streamwise direction (Vx) in July 1998 was 7% in comparison to a mean of 2% in May 1998. Clearly the recalibration of the ADV by Sontek had made a significant difference to the results. Similar improvements were observed in the Vy and Vz components.

A calibration check was also carried out on the cross stream (Vy) and vertical components of velocity (Vz).Figures 4.29 and 4.30 show calibration tests undertaken
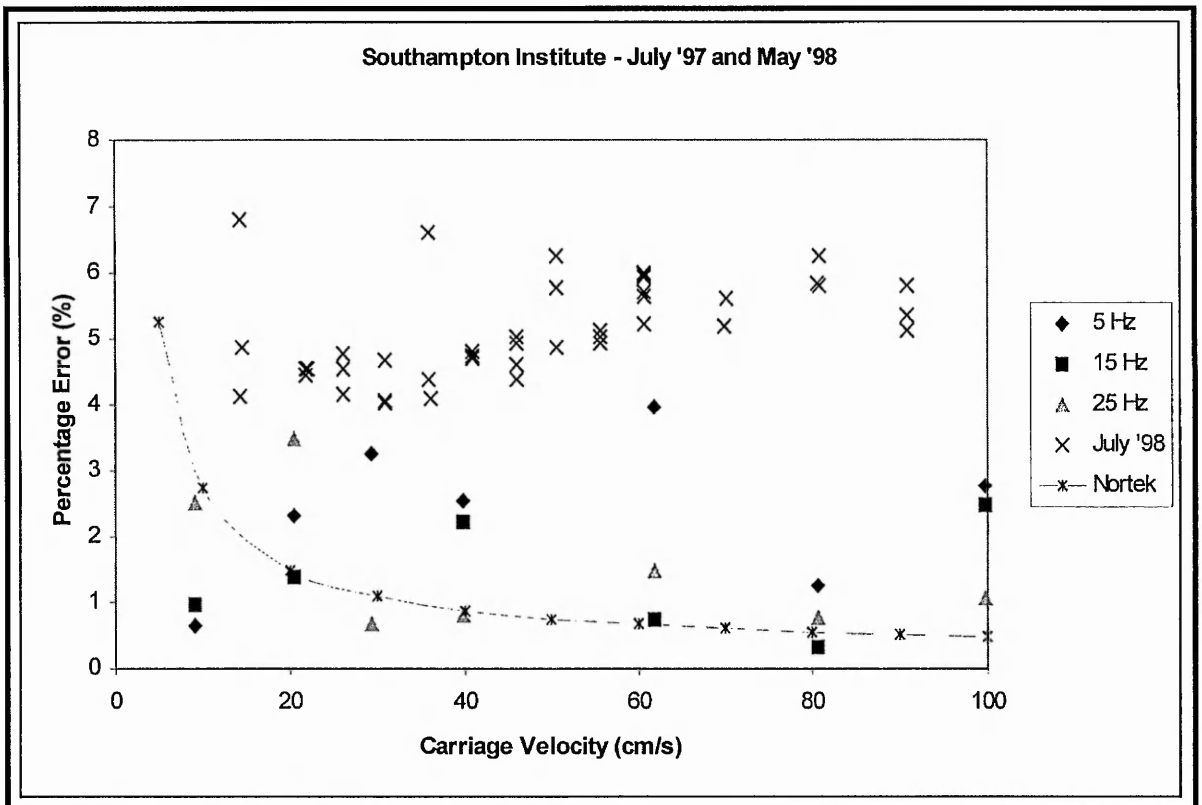
Figure 4.28   Linearity of ADV test at SI
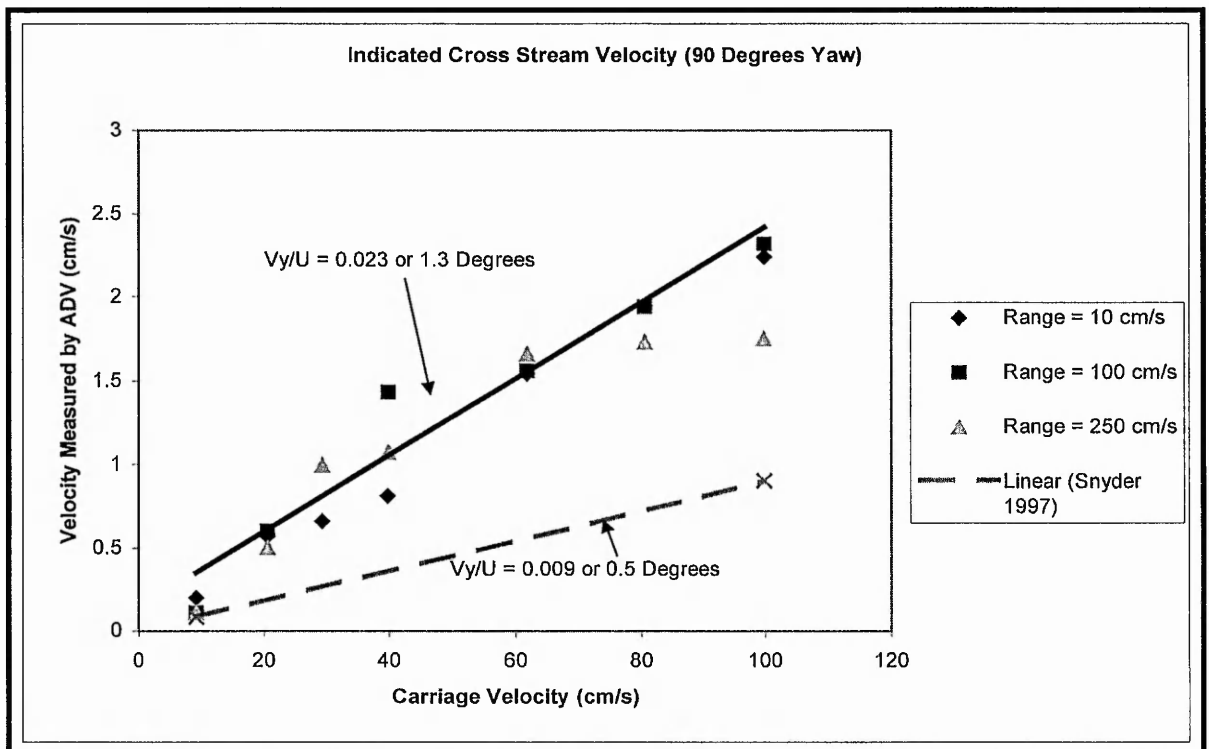
Figure 4.29   Indicated cross stream velocity (Vy).
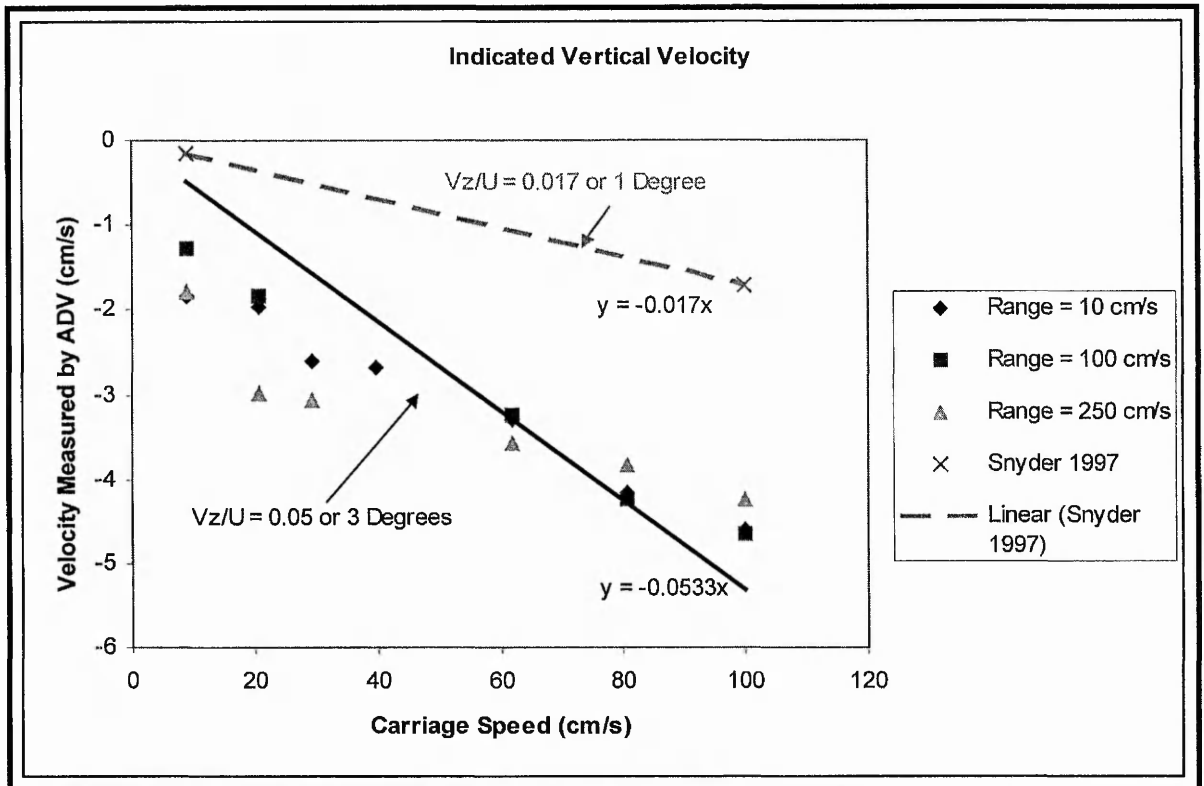
Figure 4.30   Indicated vertical velocity (Vz).

on Vy and Vz components respectively. The results of Snyder (1997) are also plotted on these graphs (blue dashed line). Snyder found that in the cross stream direction (Vy) data recorded at +/- 2 cm/s was influenced by high turbulence in the tank that was used for the tests. The tank that was used in the tests of Snyder was considerably smaller than the facility at SI and hence turbulence in the tank was more of a problem to Snyder. The facility at SI is intended for testing of model ship hulls and includes a wave making facility. To reduce the time taken for dissipation of waves, baffles have been constructed into the walls of the facility at SI which greatly assisted in the reduction and dissipation of turbulence. Snyder found that measurements in the Vy direction were subject to errors of 0.5^0 and 0.1^0 when towing in the forward and backward directions respectively. The results of the test at SI showed a discrepancy of 0.8^0 from the results of Snyder. The angle calculated from the tests at SI was 1.3^0 which is within the ability of the operator of the ADV to align the probe. Also the angle seemed to be independent of velocity range setting.

A greater discrepancy was observed with Snyder in the Vz direction as shown by Figure 4.30. Snyder found that measurements in the Vz direction were subject to errors of 1.0^0 as opposed to an angle of 3^0 measured at SI. A negative vertical

velocity was indicated by the ADV when the carriage was stationary as discussed earlier. This motion is induced by the pressure field generated by the transmitter of the probe. With slight movement of the carriage, the probe encounters new fluid continuously so that the induced vertical velocity goes to zero. Again, the angle seems to be independent of velocity range setting.

Figure 4.31 shows the yaw response of the ADV (rotation of the ADV about its vertical axis). Yaw response measurements were undertaken at a nominal carriage velocity of 19.96 cm/s and at a velocity range setting of 100 cm/s. The probe was rotated though the vertical axis at increments of 10^0. However, difficulty was experienced in measuring this angle accurately in the facility and therefore the accuracy of the angles measured was probably +/- 3^0. The velocity components (Vx and Vy) fit reasonably well to a sinusoid as shown by Figure 4.31. The deviations from the curve are probably predominantly due to the errors in measurement of the horizontal angle.
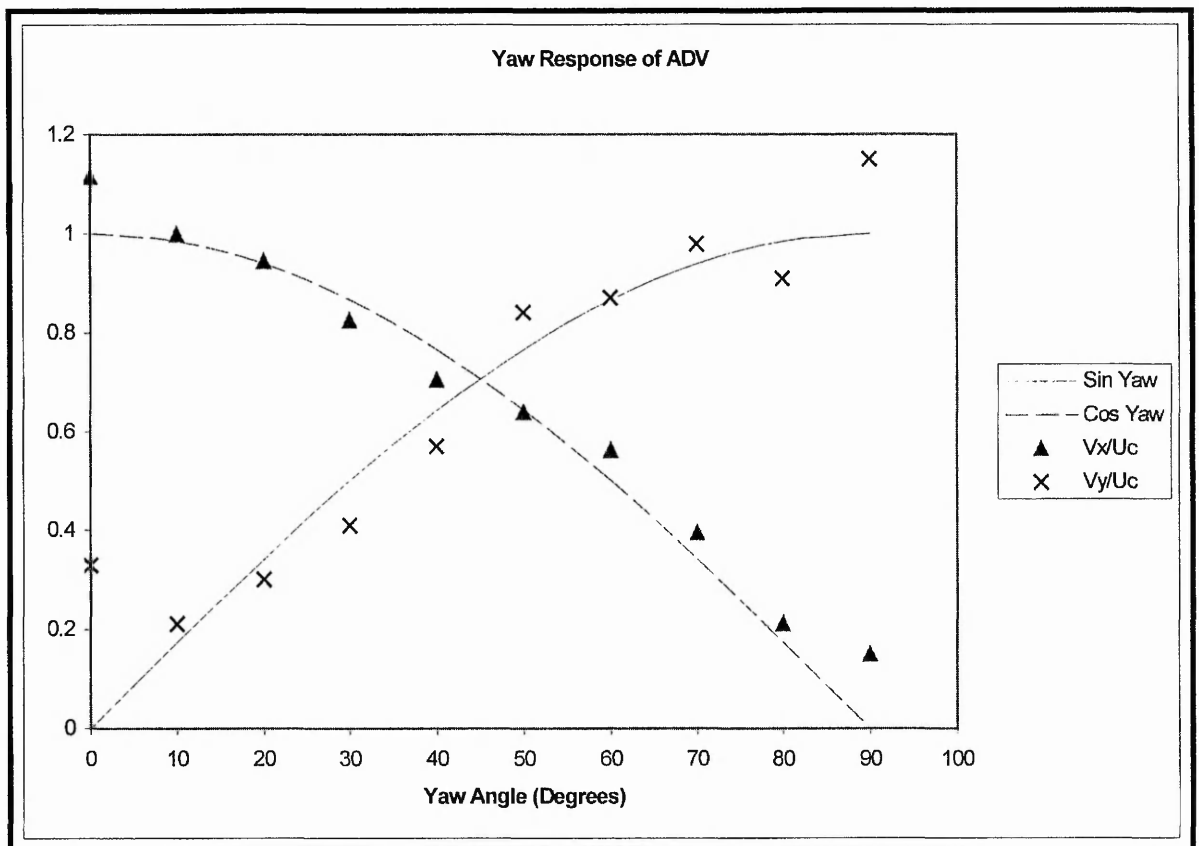
Figure 4.31   Yaw response of the ADV.

Figure 4.32 shows the Reynolds number effects of the probe. The fluid medium and the size of the probe were fixed and therefore Reynolds number effects could only be tested by towing the probe at different velocities. The probe was orientated at 90 degrees yaw and zero pitch. It can be seen that the results are in good agreement with the manufacturer's claimed accuracy with 5 out of the 7 tests within the specifications. It appeared that in general the ADV performed better in the y direction than in the x direction.
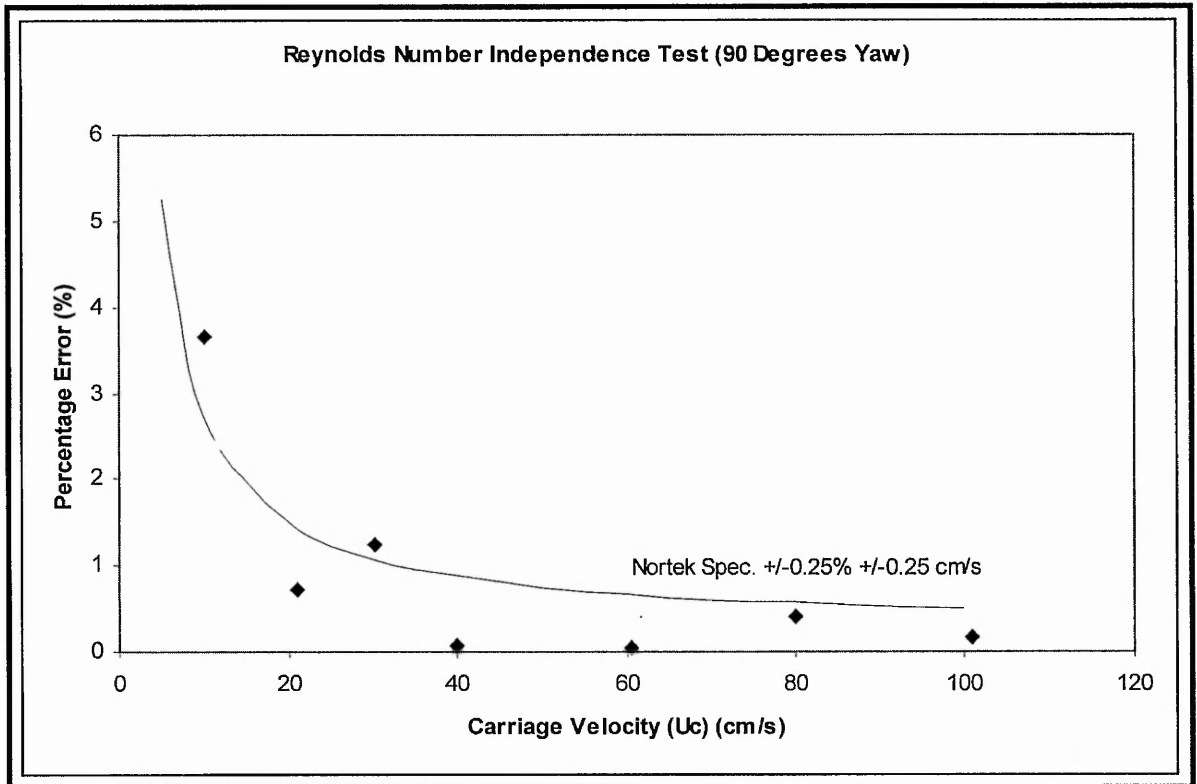
Figure 4.32   Performance of the ADV in the y direction.

Figure 4.33 shows the performance of the ADV with regard to velocity range setting. For this test three carriage velocities of 20.6, 39.8 and 60.0 cm/s were used in conjunction with velocity range settings of +/- 3, 10, 30, 100 and 250 cm/s. The graph shows that generally the range setting had little effect on the accuracy of the measurements taken. However two rogue results were recorded with carriage velocities of 39.8 and 60.0 cm/s with the ADV set on a velocity range setting of +/3 cm/s. The maximum horizontal velocity that can be measured with a velocity range setting of +/- 3 cm/s is 30 cm/s (as discussed previously). The measured velocity exceeded this allowable maximum and this was therefore the likely explanation for the gross errors obtained. It was unusual to find that this did not occur with the +/3

cm/s velocity range setting with a carriage velocity of 20.6 cm/s.
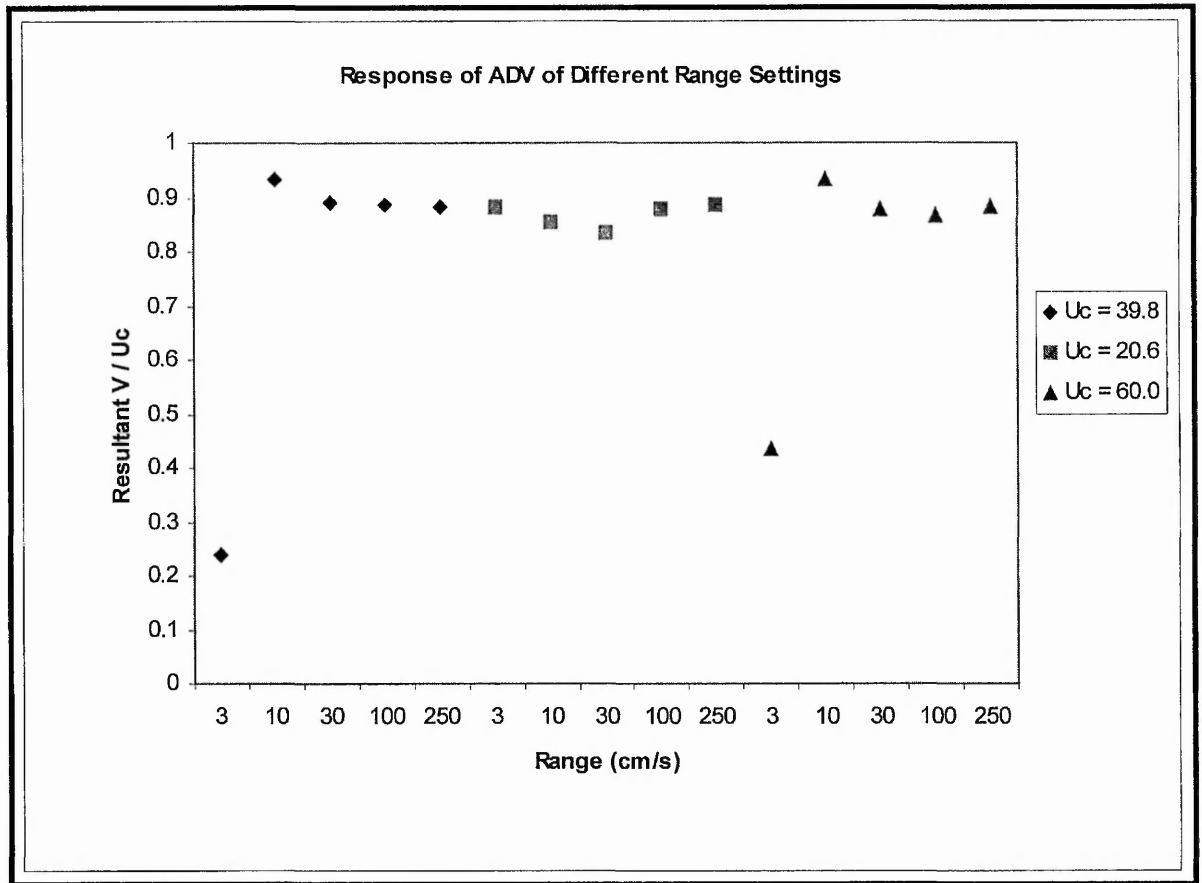
Figure 4.33   The effect of velocity range setting on the measurement of mean velocities.

Two final tests were undertaken at SI to examine the effect of the calibration issues of salinity and temperature on the measurement of mean velocities. Salinity and temperature are used to calculate the speed of sound in water, which is obviously a component of the acoustic Doppler calculations. For the first test the carriage velocity was fixed at 21.05 cm/s with a velocity range setting of +/- 100 cm/s and measurement runs were undertaken varying the input of the temperature at 5, 10, 15, 20, 25 and 30 ^{0}C. The measured temperature of the body of water in the towing tank was 17.5 ^{0}C. Figure 4.34 shows the results of the test and it can be clearly seen that the best accuracy obtained occurred at a temperature of approximately 18 ^{0}C. At this point on the graph the percentage error was almost 0%. This result confirmed that the calibration of the ADV with regard to temperature was acceptable and within the manufacturer's claimed specification.

Similarly Figure 4.35 shows the results of the tests for salinity. Again the carriage velocity was fixed at 21.05 cm/s and the salinity value input into the ADV software was varied at 10, 20, 30, 40, 50 and 60 parts per million (ppm). A sample of the water contained in the towing tank was taken and was subsequently analysed for salinity in
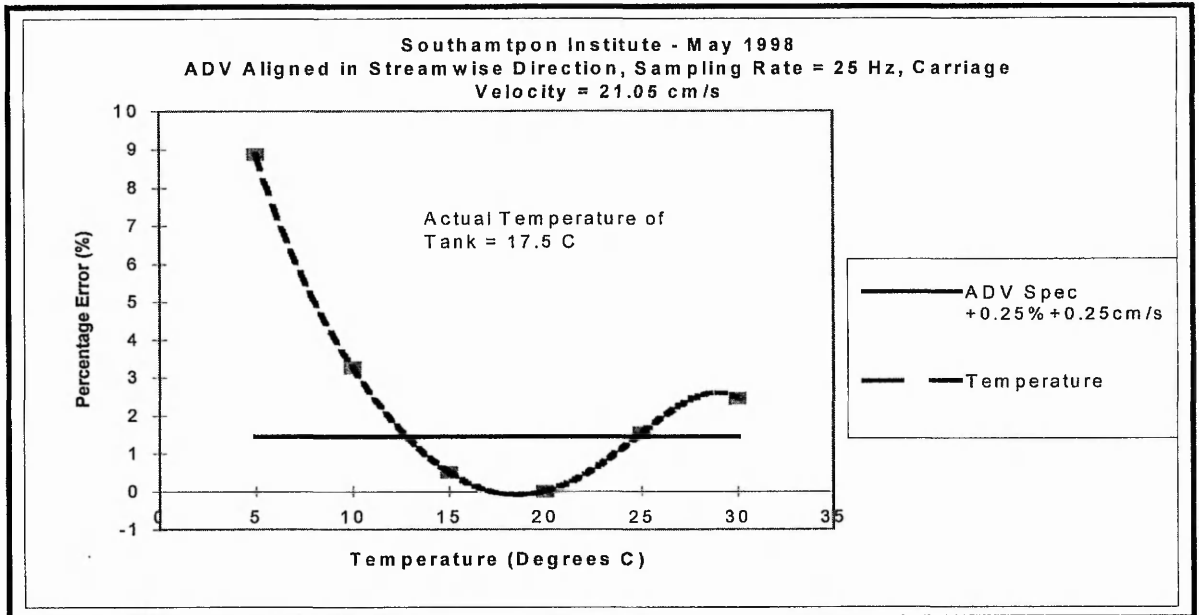
Figure 4.34   Temperature check on the ADV.

the laboratory at TNTU. The actual salinity of the water from the towing tank was found to be approximately 10 ppm. Unfortunately no tests were recorded with salinities set lower than 10 ppm in the ADV software but it can be observed that the percentage error of 0.7% was obtained at a salinity setting of 10ppm. This measurement also falls within the specification of the manufacturer.
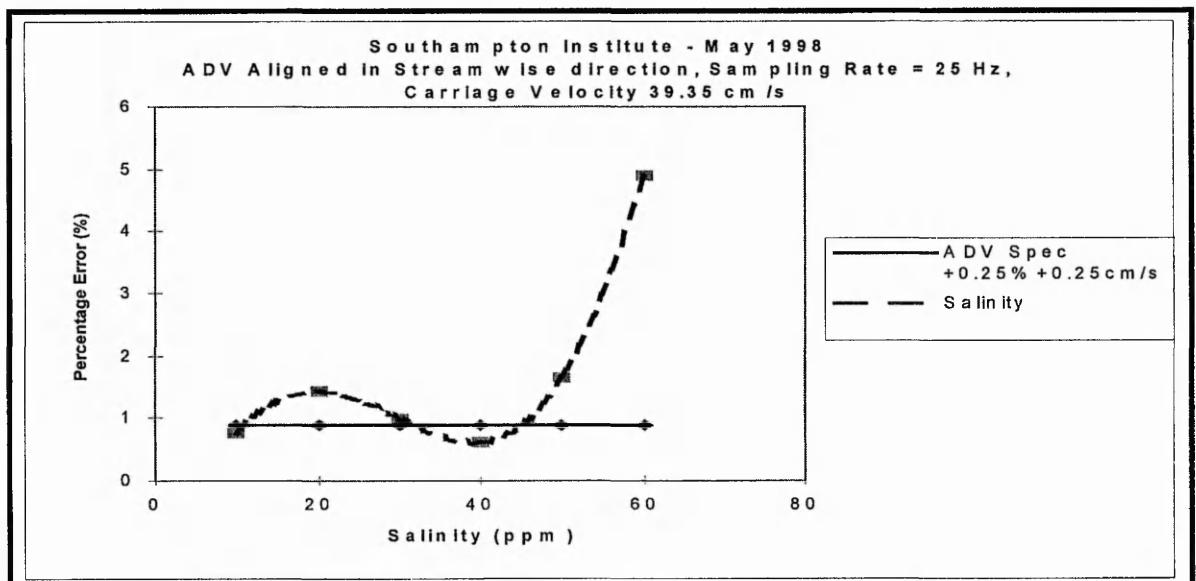
Figure 4.35   Salinity check on the ADV.

4.4   CONCLUSIONS TO THE TOWING TANK TESTS

The preceding sections have described in detail the full range of tests that were undertaken from the time when the ADV was first purchased by TNTU to the final test at SI in May 1998. It has been shown that the initial tests were very problematic with large errors measured in the ADV. Two main problems were encountered during the calibration period:

- The ADV had a serious fault within the system. The exact nature of the fault was not accurately identified although it appears that it may have been due to a connection error at some point within the system. However, the problem was intermittent and did not affect all data recorded. The problem was eventually rectified by the suppliers of the ADV. Data recorded prior to the identification of this problem was analysed and any corrupted data was discarded. Analyses of the data were undertaken by examining the SNR, Amplitude and COR data of each test. Corrupted data was identified by a significant drop in the signal response of one or more of the receiving channels. Data recorded after the recalibration of the ADV by Sontek in August 1997 was not corrupted (this formed the majority of the data recorded and presented in this thesis).

- The ADV initially purchased in March 1996 also had errors in the factory calibration. Eventually the manufacturer was convinced that the recorded calibration errors of 7% in the x direction and 2% in the y direction were valid. When the ADV was returned in September 1997 after factory recalibration, the calibration errors were vastly improved. Calibration errors of 2% in the x direction and 1% in the y direction were subsequently recorded. A conference paper has been produced based on these results (Bowles *et al* 1997) and the author has subsequently had numerous correspondence with researchers from around the World who have similarly undertaken their own calibration checks. A simple, reasonably accurate calibration check has been devised and published on the Internet by the author and the Supervisory team (see Appendix C) of this research study. The calibration check can be undertaken in any laboratory with an hydraulic flume (Armfield flume or similar).

In addition to the above points the following were also identified:

- Ultimately the study showed that the measured accuracy of the horizontal velocity to close to the stated bounds of the manufacturer of +/- 0.25% +/- 0.25 cm/s. Some of the tests lay within these bounds. For many purposes (including the applications involved with this research study) the range of accuracy is acceptable, as the instrument does not need calibration and is not subject to drift.

- A downward velocity of about 1 cm/s was indicated by the ADV when it was stationary and this was due to the non linear effects of the pressure field generated by the transmitter. This indicated vertical velocity disappeared at horizontal velocities in excess of 2 cm/s. More serious was an apparent downward motion induced by the probe itself. The vertical velocity was always negative (down into the tank, away from the surface) and had a value of approximately 5% of the horizontal velocity indicating a streamline deflection of approximately 3^0.

- The inherent Doppler noise limits the turbulence levels that may be observed. The level of turbulence appeared to be independent of the velocity of flow and increased with a lowering of the SNR and with increased velocity range setting of the instrument. In one set of tests the vertical component of turbulence (rms) was approximately 0.2 cm/s.

- Yaw tests were conducted which showed a reasonable cosine response at a nominal velocity of 20 cm/s. Pitch tests were not successful however and it was found that at pitch angles of 15^0 gross errors in velocity measurement were recorded. This correlates with the findings of Lohrmann *et al* (1994) who stated that the factory calibration method using the transformation matrix **T** (see section 4.2), is robust to small pitch and roll angles ($<5^0$). This angle was exceeded in the pitch tests showing that the method was not robust to angles in excess of 5^0.

- The measurement of mean velocities appeared to be independent of sampling frequency and velocity range (provided that the manufacturer's guidelines for velocity range were followed, see section 4.3.4). The effect on turbulence measurements however was simple to quantify. In areas of highly turbulent flow the maximum sampling rate of 25 Hz should be used in order to capture the relevant rms data. At lower sampling rates the effects of Doppler noise was more

onerous since the influence of Doppler noise was increased with reduced averaging.

4.5 SAMPLING RATE AND TIME PERIOD TESTS

4.5.1 Introduction

It is important when using the ADV to ascertain an optimum sampling rate and sample number for the measurement of mean velocities and higher order statistics such as the rms velocity, skewness and kurtosis. Sufficient samples are required in order to capture the component of the fluid flow that is required. The user must be aware that the ADV is capable of recording vast amounts of data and that beyond a certain threshold there will be negligible improvement to results. High sampling rates and long time periods merely result in large quantities of data which may not provide any beneficial advantages. The user must be aware of the type of flow that is being measured. The probability density function (pdf) of the data should be examined to verify if the flow is homogeneous, isotropic or shear flow. This is indicated by the shape of the distribution (ie skewed or Gaussian).

Prior to physical measurements in the model preliminary ADV tests were undertaken in an effort to answer the questions posed above. For this purpose, two flow situations were chosen. Position 1 was located on the centreline of the main channel, 1.0m downstream of the entrance to the model. The depth of the probe sampling volume was 47mm from the bed. The flow entering the model was 58 l/s and the flow depth was 195mm. This gave a Reynolds number of:

$$Re = \frac{\rho.v.D}{\mu} \qquad\qquad 4.6$$

Where

$\rho = $ Density of water $= 1000 \, kg \, / \, m^3$

$v = $ Average velocity of flow $= Q \, / \, A = 0.058 \, /(0.195 \times 0.6) = 0.496 \, m \, / \, s$

$D = $ Characteristic Dimension $=$ Depth $= 0.195m$

$\mu = $ Vis cos ity $= 1.2 \times 10^{-3} kg \, / \, ms$

Thus   Re = 80 600 at position 1

Position 2 was also located at the centreline of the main channel a distance of 2.0m downstream of the entrance to the model. However the depth of the probe sampling volume from the bed of the channel was 82 mm and the depth of flow was 395 mm. The flow entering the model was also 58 l/s. This corresponded to a Reynolds number of:

$$Re = \frac{1000 \times 0.245 \times 0.395}{1.2 \times 10^{-3}} = 80\,645 \text{ at position 2.}$$

Data were recorded using a range of sampling rates and time periods at these two sampling positions to accumulate blocks of data ranging from 50 to 20 000 samples. The data was "block averaged" using WinADV and the corresponding data was analysed using Microsoft Excel. The following sections present the results of these tests.

4.5.2 The Measurement of Mean Velocities

Figures 4.36 and 4.37 show the results of the sample number tests for the measurement of mean velocity in the x direction at positions 1 and 2 respectively.
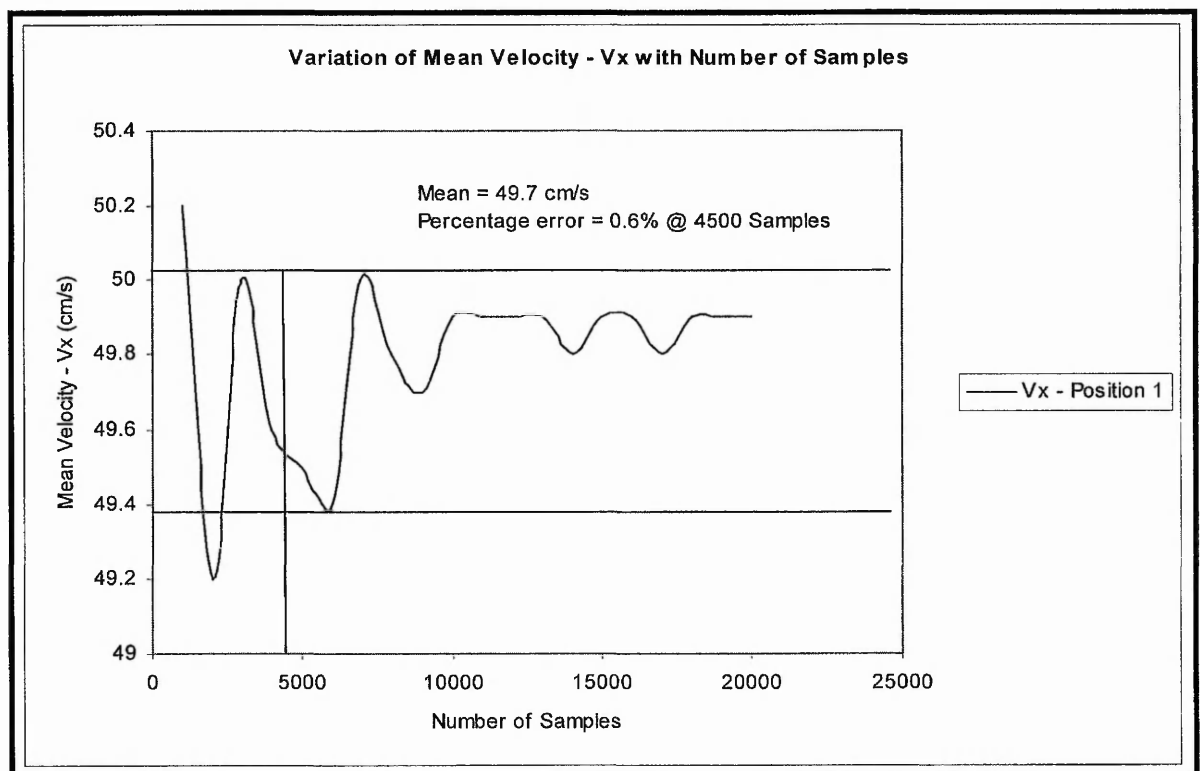
Figure 4.36   Variation of mean velocity in the x direction with number of samples at position 1.

Variation of Mean Velocity - Vx with Number of Samples

Mean = 19.2 cm/s
Percentage Error = 1% @ 4500 Samples
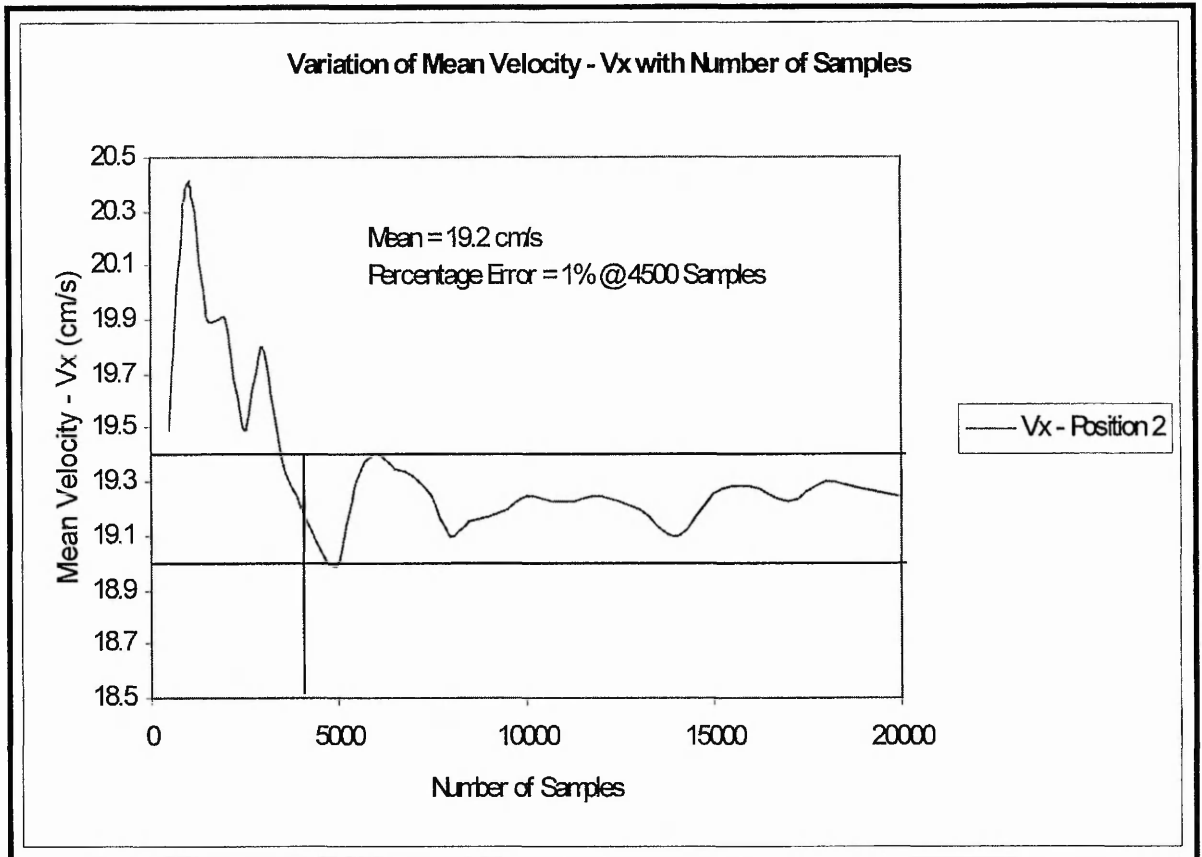
Vx - Position 2

Figure 4.37   Variation of mean velocity in the x direction with number of samples at position 2.

Figure 4.36 shows the variation of the mean velocity in the x direction with the number of samples recorded. Each point plotted on the graph represents an average value for velocity at the corresponding number of samples taken. It can be observed that with increasing sample numbers the value of the mean velocity converged. The purpose of these tests was to ascertain a sample number that would capture data with the required uncertainty but at a reasonable time period. Therefore a compromise between sample time period and uncertainty was required. The graph shows that at a sample number of 4500 a mean velocity of 49.7 cm/s was obtained. The uncertainty error bounds at this sample number corresponds to a percentage error of 0.6%. This was a satisfactory error for the purposes of this study.

Similarly Figure 4.37 shows the results at position 2. It can be observed that at a sample number of 4500 a mean velocity in the x direction of 19.2 cm/s was obtained. The error bounds corresponded to an uncertainty error of 1%. This again was considered acceptable for the purposes of this study. A sample number of 4500 represented a time period of test of 180 seconds at a sampling rate of 25 Hz. This

was considered to be a reasonable time period for data capture at each measurement position. Sample time periods in excess of 180 seconds had a negligible effect upon the accuracy of the mean velocities measured and simply resulted in excessive quantities of data.

Analyses of the y and z components were subsequently undertaken. Figure 4.38 and 4.39 show the corresponding results for positions 1 and 2 respectively.
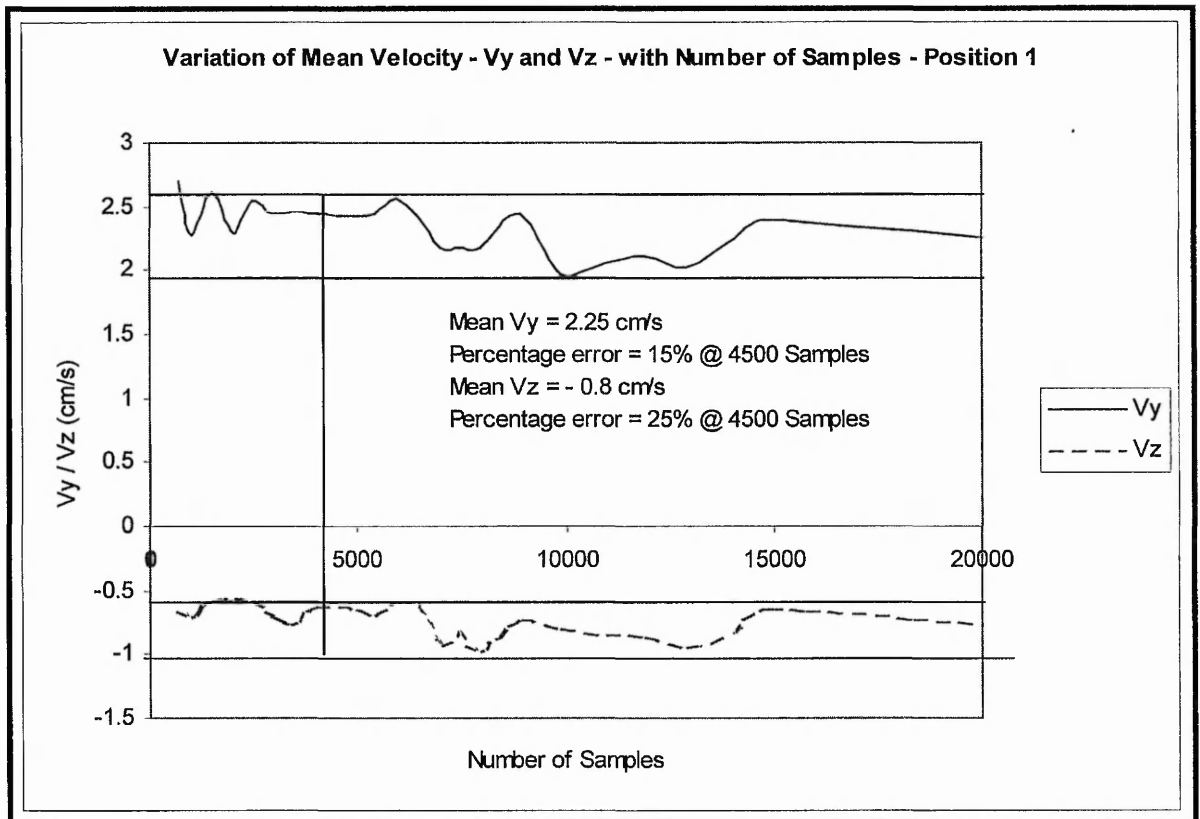
Figure 4.38   Sample number test for Vy and Vz at position 1.

Figure 4.38 shows that the percentage errors at 4500 samples for Vy and Vz were 15% and 25% respectively. The increase in observed errors were due to the turbulent fluctuations of the flow. The flow at positions 1 and 2 was predominantly in the x direction and therefore it was expected that the fluctuations in the y and z directions would have a more onerous effect upon the observed accuracies of these components. It should also be noticed from this graph that the percentage error did not improve significantly with increased sample numbers up to 20 000 samples.

Similar results were obtained at position 2.
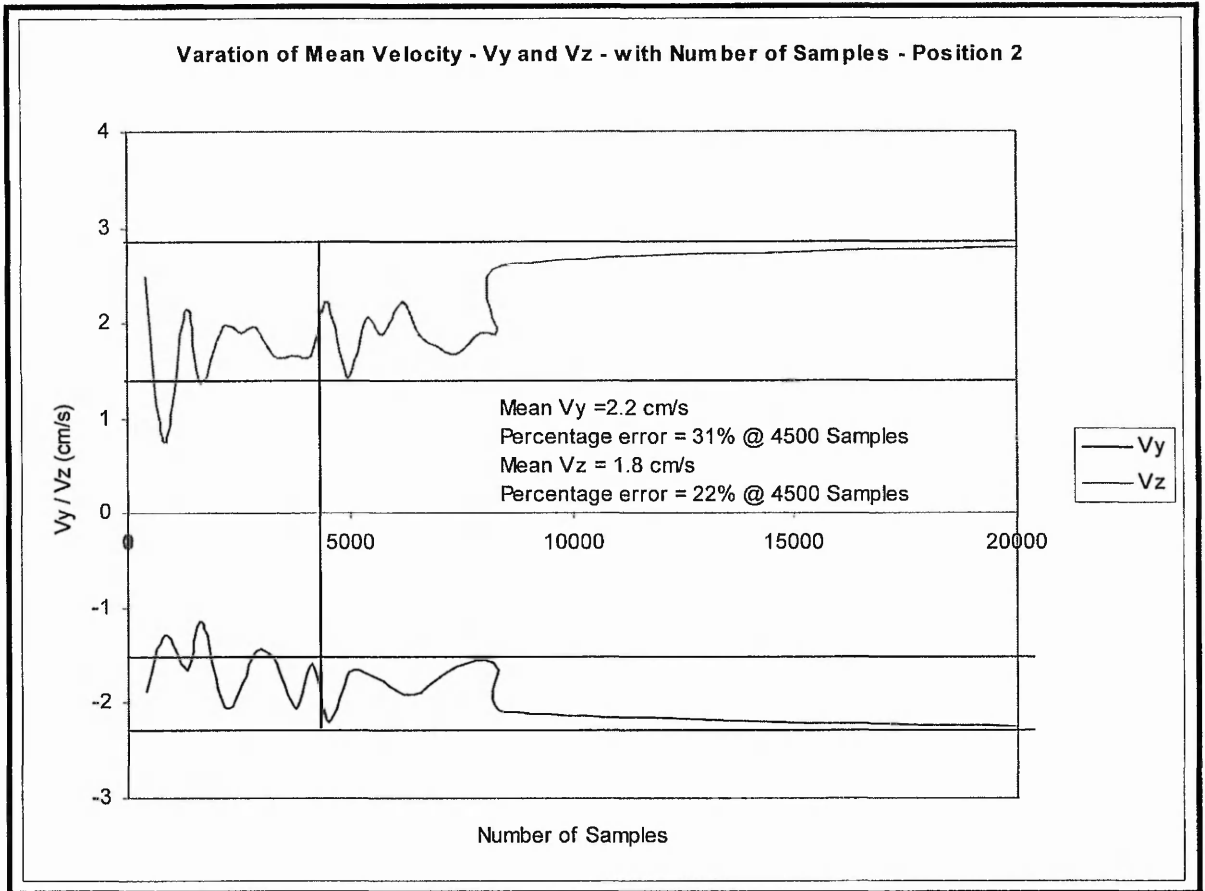
Figure 4.39   Sample number tests for Vy and Vz at position 2.

4.5.3   The Measurement of Turbulence Parameters

At this point the type of flow and the nature of the turbulence being measured was considered. The mechanism of turbulent motion is of such a complex nature that at present it is not possible to formulate a general model on which to base the analysis. Thus the problem is approached from a rigorous statistical theory into which simplifying assumptions are introduced which allow the solution of the variables of interest. Turbulence can be represented with a crude model. The eddies range in size from the smallest to the largest. The boundaries of the domain influence only the large eddies and transfer energy to or from them. The larger eddies transfer energy to the smaller eddies until the energy is transferred to the smallest eddies. The smallest eddies lose their energy by viscous dissipation.

There are basically three principle types of turbulence; *homogeneous, isotropic turbulence* and *turbulent shear flow.* Homogeneous turbulence implies that the

velocity fluctuations in the system are random and that the average turbulent characteristics are independent of the position in the fluid i.e. invariant to axis translation. Also it is assumed that velocity fluctuations are independent of the axis of reference i.e. invariant to axis rotation and reflection. This leads to isotropic turbulence which is always homogeneous. The difference therefore between the two can be explained in terms of the rms velocity fluctuations:

$$u_x' = \sqrt{\overline{u_x^2}} \ , \ u_y' = \sqrt{\overline{u_y^2}} \ , \ u_z' = \sqrt{\overline{u_z^2}} \qquad\qquad 4.7$$

In homogeneous turbulence the rms values can all be different but each value must be constant over the entire turbulent field. In isotropic turbulence, spherical symmetry requries that the fluctuations be independent of the direction of reference or that all the rms are equal:

$$\sqrt{\overline{u_x^2}} = \sqrt{\overline{u_y^2}} = \sqrt{\overline{u_z^2}} \ \ \text{or} \ \ u_x' = u_y' = u_z' \qquad\qquad 4.8$$

In isotropic homogeneous flows there are no shearing stresses and no gradients of the mean velocity. Isotropic turbulence is a constant space system and thus the statistical quantities can vary only with time. Such a state of motion cannot easily be observed in experiments. Therefore the area of turbulent study which is of much greater interest to the hydraulic engineer is turbulent shear flow.

Turbulent shear flow is the modification of completely homogeneous flow to allow for shear stresses. Usually one or two of the Reynolds shearing stresses is zero. Turbulent shear flow may also be subdivided into flows that are nearly homogeneous in the direction of flow and those that are not homogeneous in the direction of flow. Nearly homogeneous flows are usually bounded such as in pipe flow. Inhomogeneous shear flows are unrestricted systems such as jets. One type of flow that has both characteristics depending on the location of study is boundary layer flow. The area near the wall is nearly homogeneous in the direction of flow and the flow near the boundary between the boundary layer and the ideal flow is inhomogeneous.

Clearly for isotropic, homogeneous flows smaller sample numbers are required to capture the time-averaged values of turbulence. However in the case under investigation here the nature of the flow was certainly turbulent shear flow with anisotropic rms values and hence much larger sample numbers are required to capture the turbulent parameters. Turbulent shear flow is generally the type of flow that is encountered in natural systems such as rivers and oceans. In this type of flow there exists a turbulent energy balance between the boundaries and the upper limits of the flow. In this system diffusion of kinetic energy occurs away from the boundary and diffusion of pressure energy occurs towards the boundary as shown by Figure 4.41.

Examination of the pdf confirmed the presence of turbulent shear flow with a gaussian probability density function (pdf) observed in every case investigated. A typical pdf of the measurements is shown by Figure 4.41.

Sample number tests were subsequently undertaken on the second order statistic parameter of the rms velocity. WinADV computes the rms from the sample standard deviation. For example, the rms turbulence for the x velocity component is:

$$\text{rms}[v_x'] = \sqrt{\overline{(v_x')^2}} = \sqrt{\frac{\sum v_x^2 - (\sum v_x)^2 / n}{n-1}} \qquad 4.9$$

Where   n = Number of samples.
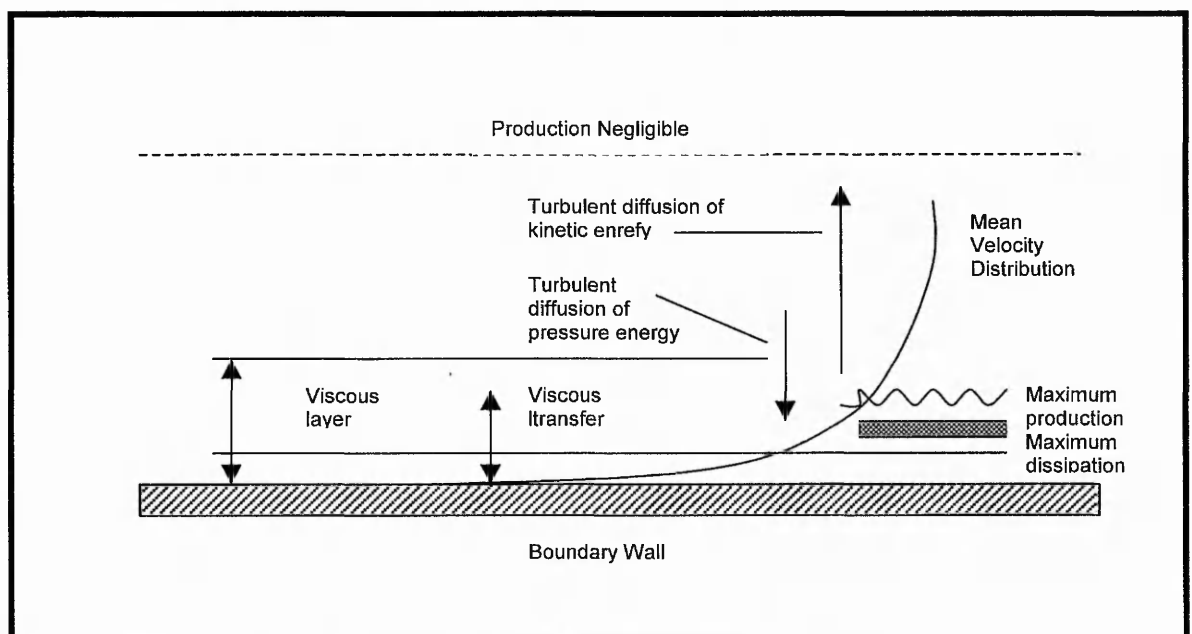
Figure 4.41   Turbulent Energy Transfer
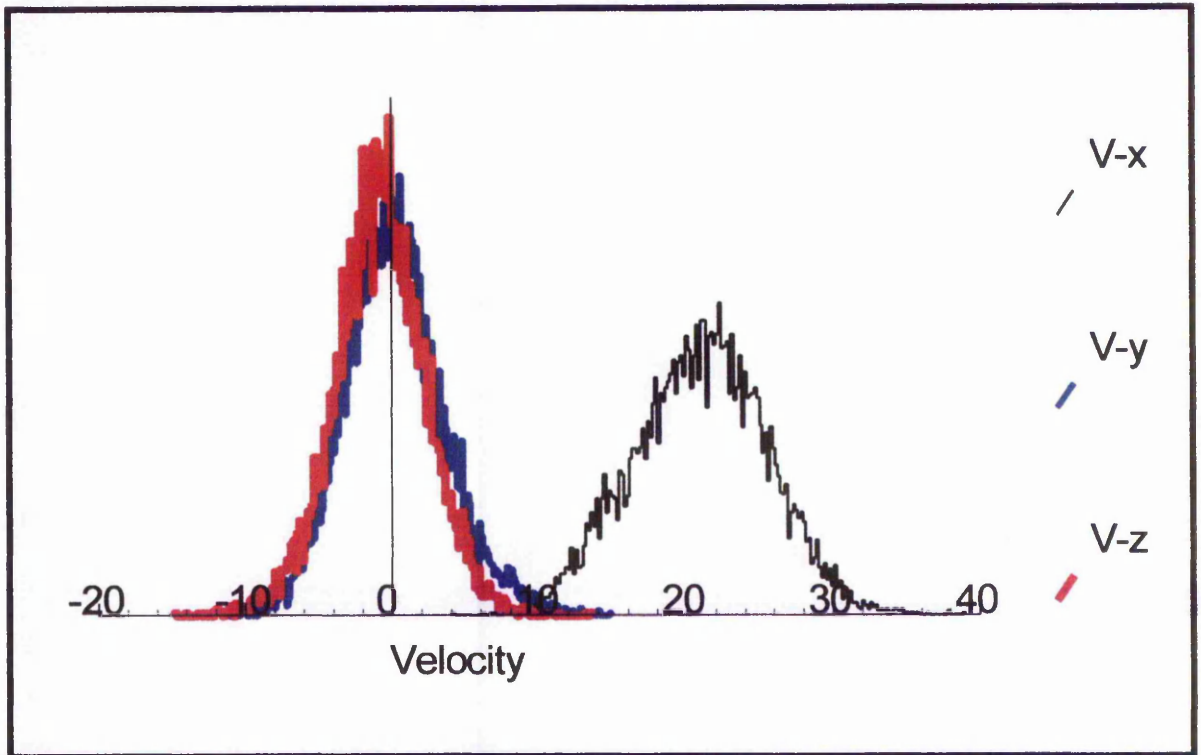
Figure 4.41   Typical pdf for sample number tests.

Figure 4.42 and 4.43 show the sample number tests for the rms velocity in the x direction at positions 1 and 2 respectively.
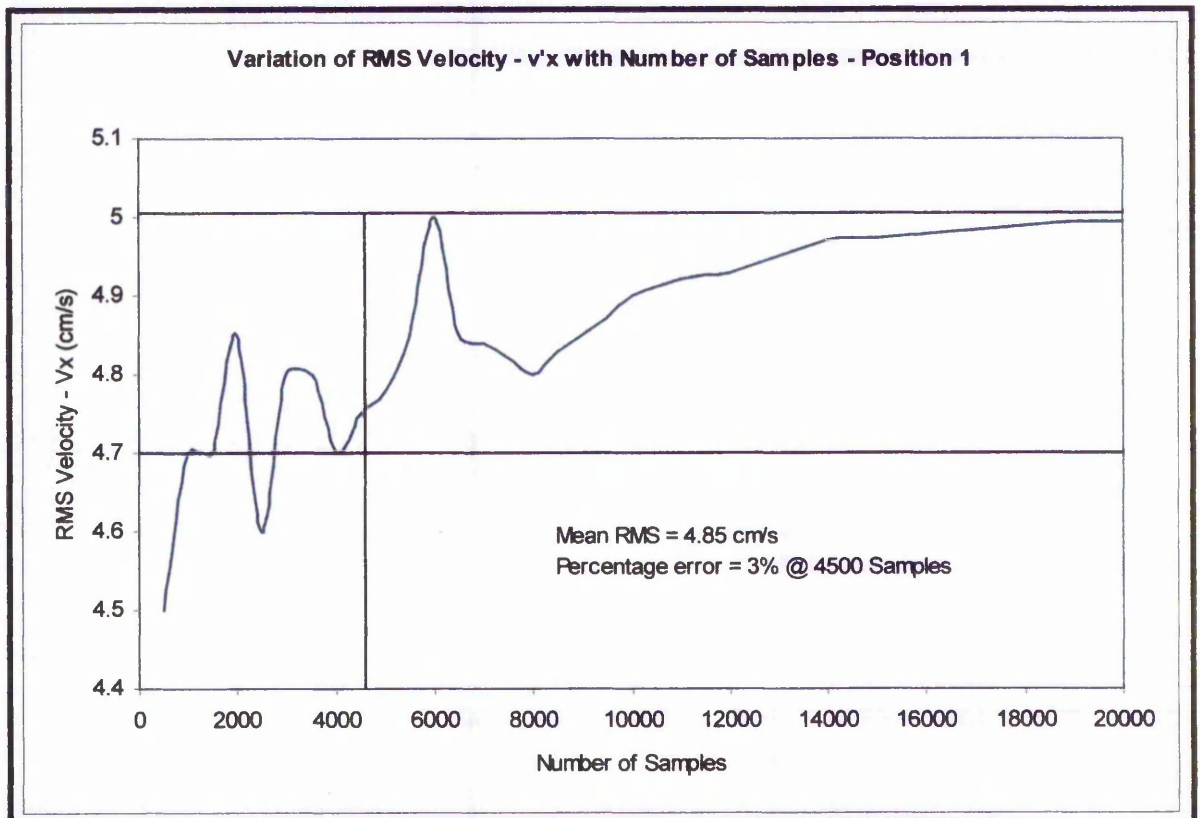
Figure 4.42   Sample number test for rms velocity (Vx) at position 1.
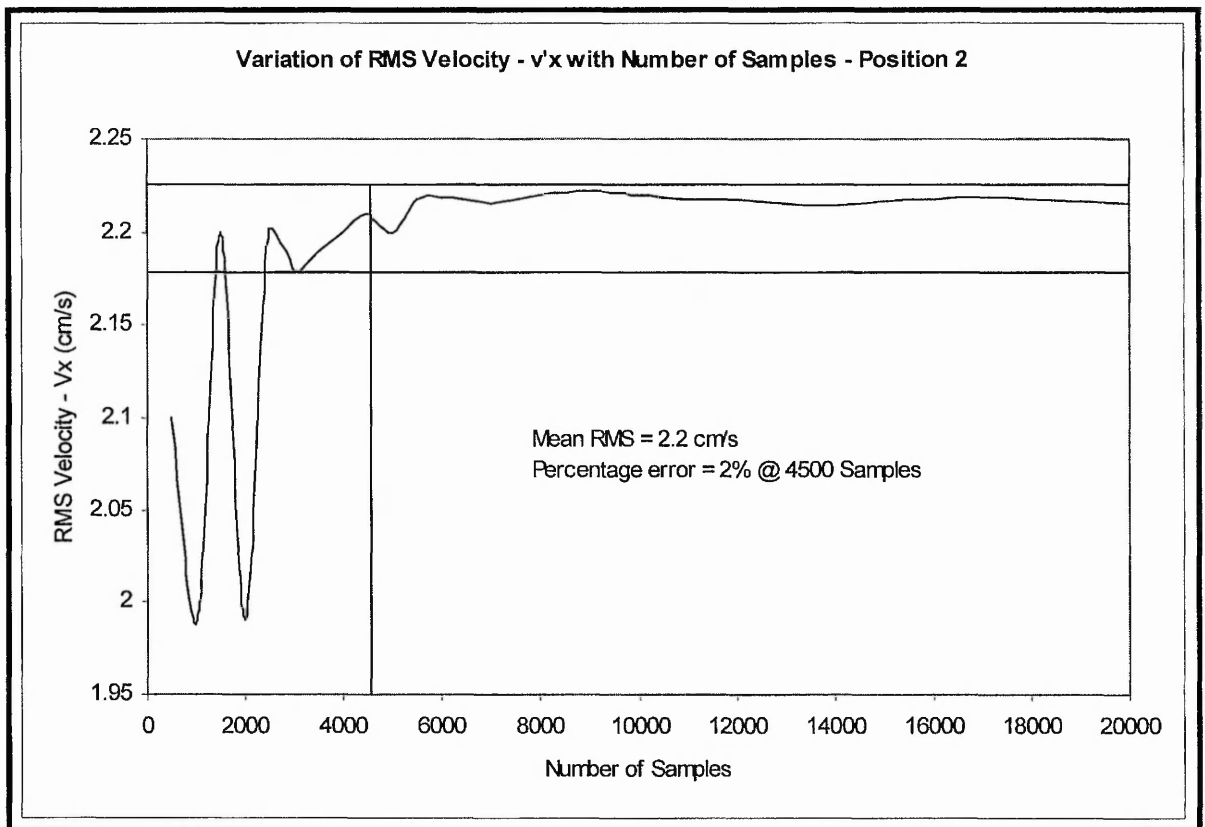
Figure 4.43   Sample number test for rms velocity (Vx) at position 2.

Figure 4.42 and 4.43 show that the rms velocity was generally lower at sample numbers less than 4500. At a sample number of 4500 the rms in the x direction was measured to an uncertainty of between 2 – 3%. It should also be noted that the turbulence intensity measured was similar at positions 1and 2. The turbulent intensity measured at position 1 was 9.8% compared to a turbulent intensity of 11.5% at position 2. A sample number of 4500 was therefore considered reasonable for the capture of second order turbulence parameters in this application.

Third and fourth order statistics were finally investigated. The effect of sample number on the skewness (third order) and kurtosis (fourth order) was tested.

Skewness is an indicator of non-symmetrical distributions of data. A skewness of zero indicates a distribution that is symmetric about the mean. A positive skewness indicates a distribution with an asymmetric tail extending towards more positive values. A negative skewness indicates a distribution with an asymmetric tail extending towards more negative values. Skewness was calculated as follows (for the x direction):

$$\text{Skewness}_x = \left[\frac{n}{(n-1)(n-2)s^3}\right]\left(\sum V_x^3 - \frac{3}{n}\sum V_x \sum V_x^2 + \frac{2}{n^2}(\sum V_x)^3\right) \quad 4.10$$

where s is the standard deviation.

Figure 4.44 and 4.45 show examples of positive and negative skewness respectively.
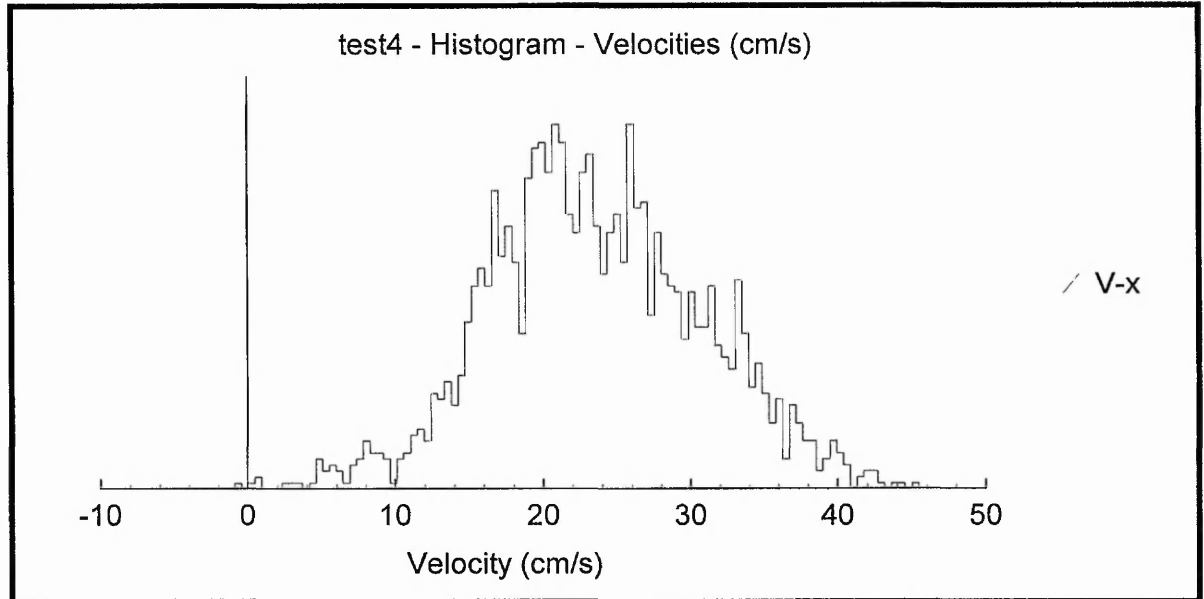
Figure 4.44   Slightly positive skewness with an asymmetric tail extending towards more positive values.
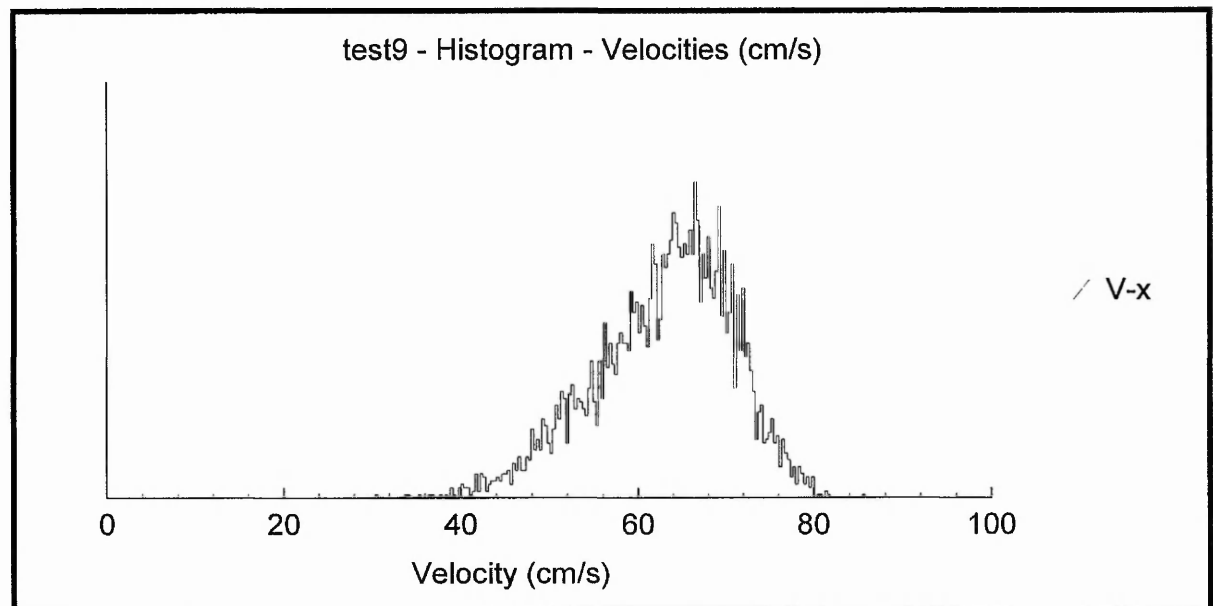
Figure 4.45   Negative skewness with an asymmetric tail extending towards more negative values.

The skewness coefficient calculated as shown previously is usually positive near the bed (0 < S < 1.0), negative in the intermediate region (-1.0 < S < 0) and positive again near the water surface (0 < S < 1.0). From a physical point of view, negative values of skewness coefficient in the flow region away from the bed and surface are determined by the transfer of turbulent kinetic energy from the bottom region upward.

Figure 4.46 shows a sample number tests for skewness at test position 1.
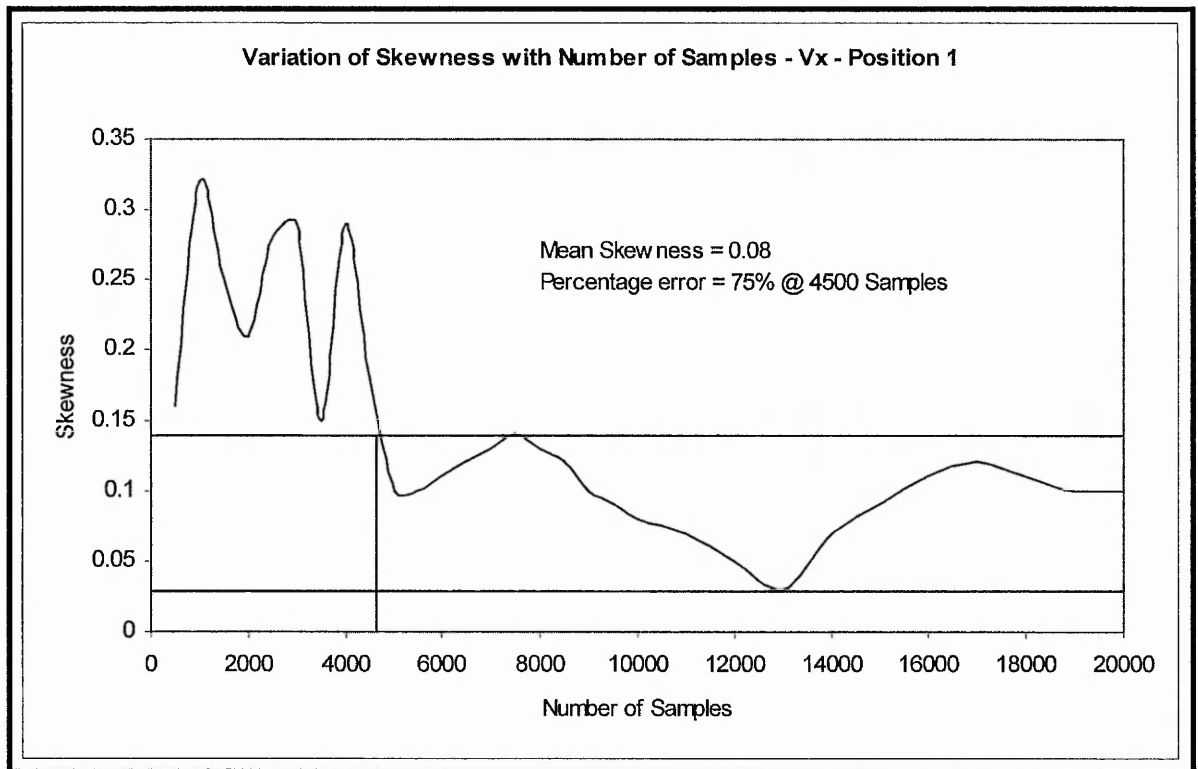
Figure 4.46   Sample number test for skewness in the x direction at position 1.

Figure 4.46 indicated that a sample number of 4500 was insufficient for the accurate collection of skewness data. In fact it was found that in excess of 20 000 samples (13.5 minute time period at 25 Hz sample rate) were required to reduce the accuracy of skewness calculations to less than 20%. Similar observations were found at position 2.   Therefore it was decided that skewness data capture would not be possible at all the measurement positions in the flow domain since the time requirements were excessive. Skewness measurements were subsequently taken during the physical modelling programme to investigate the nature of the flow but only at a few limited positions.

Kurtosis, the fourth order statistical parameter was finally investigated. In physical terms, Kurtosis gives and indication of the turbulent energy pulsation. Kurtosis did not usually exceed +/- 2 in the physical measurements taken using the ADV. In statistical terms, kurtosis characterises the relative peakedness or flatness of a distribution compared to the normal distribution. Positive kurtosis indicates a relatively peaked distribution. Negative kurtosis indicates a relatively flat distribution. Kurtosis was calculated (for the x direction) as follows:

$$\text{Kurtosis}_x = K_1\left(\sum V_x^4 - \frac{4}{n}\sum V_x \sum V_x^3 + \frac{6}{n^2}\left(\sum V_x\right)^2 \sum V_x^2 - \frac{3}{n^3}\left(\sum V_x\right)^4\right) - K_2 \quad 4.11$$

Where:

$$K_1 = \frac{n(n+1)}{(n-1)(n-2)(n-3)s^4}$$

$$K_2 = \frac{3(n-1)^2}{(n-2)(n-3)}$$

Figure 4.47 illustrates the statistical parameter, kurtosis.
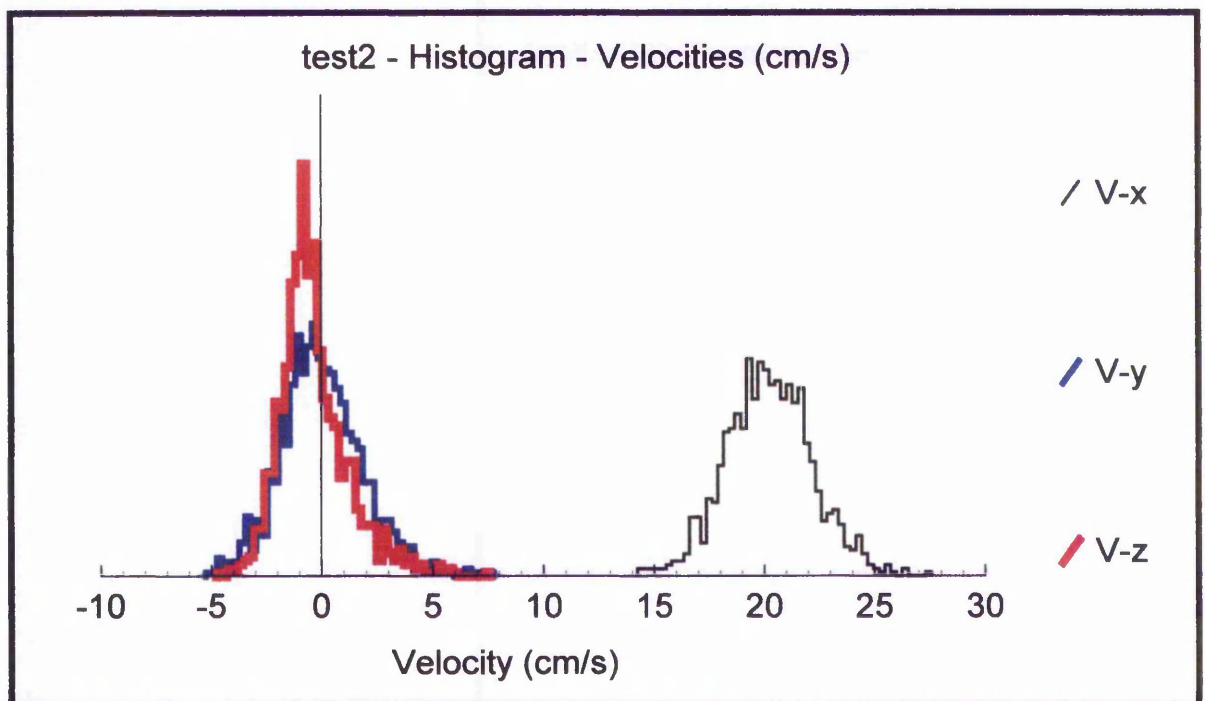
Figure 4.47   Graph to illustrate kurtosis.

Kurtosis values for Figure 4.474 were Vx = 0.21, Vy = 0.73, Vx = 1.96 and these values were represented by the flatness of the histograms shown in the graph. The

histogram for Vz was the most peaked and this distribution correspondingly had the highest kurtosis of 1.96. With reference to the sample number tests, Figure 4.48 shows the results of a kurtosis test undertaken at position 1.

Variation of Kurtosis - Vx - with Number of Samples - Position 1

Mean Kurtosis = 0.23
Percentage error = 117% @ 4500
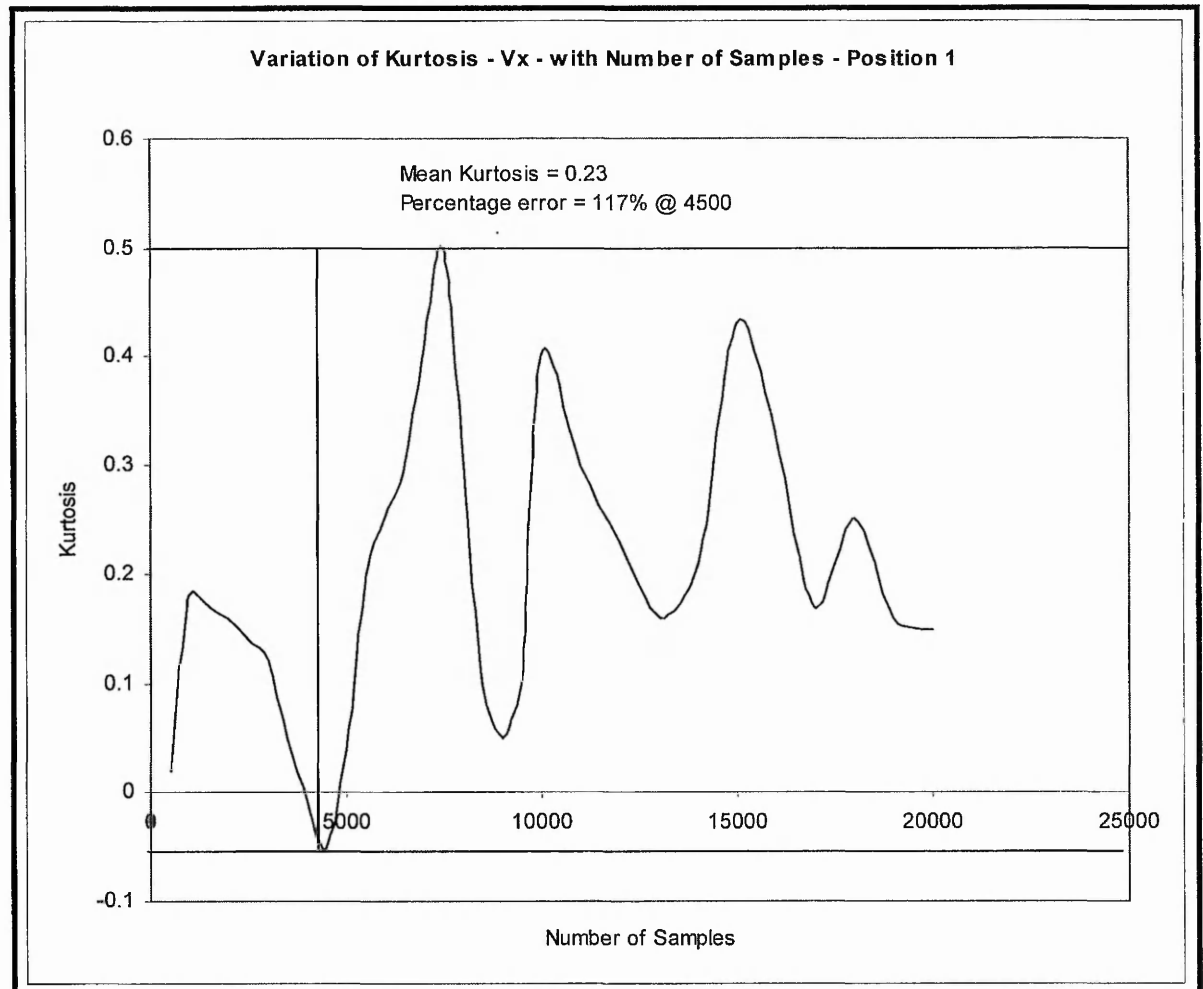
Figure 4.48   Sample number test for kurtosis in the x direction at position 1.

Figure 4.48 illustrates similar porperties to Figure 4.47 in which large errors in accuracy were obtained at a sample number of 4500. At this sample number an error in kurtosis of 117% was obtained. Clearly this was excessive and sample numbers in excess of 20 000 were required to substantially reduce this value. Again this excessive amount of data required long sample time periods and as such kurtosis was only measured at carefully selected locations.

4.5.4 Conclusions to Sample Number Tests

The following conclusions were made as a result of the sample number tests:

- A sample number of 4500 was selected for the measurement of mean velocities and rms velocities in the x, y and z directions in the physical model testing programme. This corresponded to a sample time period of 3 minutes at a sampling rate of 25 Hz.

- Uncertainties in the measurement of the mean velocities of approximately 1% in the x direction and up to 30% and 25% in the y and z directions respectively were recorded. These uncertainties in measurements were in addition to calibration errors previously presented of 2% in the x direction and approximately 1% in the y and z directions.

- Uncertainties in the measurement of rms velocities of less than 3% were recorded in the x direction. Uncertainties of rms velocities in the y and z directions were clearly much greater than this and, due to the large uncertainties identified in the measurement of mean velocities in these directions, were not quantified in this study.

- Sample number effects on skewness and kurtosis were examined and it was found that considerably more samples were required to successfully capture the required data to calculate these parameters. It was found that at least 20 000 samples were required to calculate skewness and kurtosis to an acceptable uncertainty error and therefore only a limited number of tests were undertaken to identify these parameters in the physical model programme.

- Generally the overall accuracy achieved using the ADV was acceptable since the physical measurements were more accurate than the computational predictions.

5

CFD VALIDATION

5.1   INTRODUCTION

The subject of this chapter is the validation of a computational model, SSIIM (Sediment Simulation at Intakes Including Multiblock option). The term *computational model* refers to software whose primary function is to model a certain class of physical systems and may include pre- and post-processing components and other necessary ancillary programmes. Validation applies primarily to the theoretical foundation and to the computational techniques that form the basis for the numerical and graphical results produced by the software. In the context of this chapter, validation of the model is viewed as the formulation and substantiation of explicit claims about applicability and accuracy of the computational results.

At this point it is important to make the definition between verification and validation, two terms that are frequently confused by researchers. Verification refers to a process of checking and ensuring the numerical solution produced by the code does approximate the solution to the set of governing equations. The primary means of achieving this purpose are grid refinement studies (Roache 1994) (de Vahl Davis 1983), *a posteriori* error estimations (Morton and Suli 1993), comparisons with analytical solutions and in some cases, comparisons with numerical benchmark solutions obtained using the same set of governing equations and similar or the same numerical approximation.

Validation means a process of testing an already verified computer code for its ability to accurately model the essential physics of a problem. This is normally established by comparison with benchmark experimental data or reliable and validated numerical results.

A succinct description of verification is "solving the equations right" and of validation "solving the right equations". The code author defines concisely what partial differential equations (PDEs) are being solved and demonstrates that they are solved correctly; this is verification. Only a calculation (or range of calculations within a code) can be validated.

Previously, there have been only two independent validation investigations carried out using SSIIM (Alfredson *et al.* 1997), (Seed 1997). Alfredson *et al.* Compared the output from SSIIM to the output from two other computational models. However, only a small proportion of the capabilities of SSIIM were tested. The validation carried out by Seed was much more comprehensive, however no tests of the multiblock capabilities of SSIIM were carried out. In addition neither of the previous validation exercises made comparisons of the turbulent kinetic energy results obtained. It was therefore considered that an independent validation of the code was required. Two papers have been written based on the validation exercise and these are contained in Appendix D of this thesis (Bowles *et al.* 1998, 1998).

This chapter therefore documents the results of a validation exercise on SSIIM, although certain elements of verification are also presented. Grid convergence studies were undertaken using SSIIM and this should strictly be classified as verification. Numerous verification papers have been presented by the author of the code (Olsen 1991), (Olsen 1994), (Olsen and Stokseth 1995) and therefore verification is not specifically covered by this thesis.

5.2   MODEL OVERVIEW

SSIIM was designed for use in river, environmental, hydraulic and sedimentation engineering. The program solves the Navier Stokes equations with the k-epsilon turbulence model on a three dimensional, non-orthogonal, structured grid. A control volume is used for the discretisation, together with the power law scheme or the second order upwind scheme. The SIMPLE method is used for the solution of pressure coupling. This gives the velocity field in the geometry. The velocities are used when solving the convection diffusion equations for different sediment

problems. This gives the sediment deposition pattern (Note: in this study the sediment transport capabilities of SSIIM were not used or tested).

The model has a user interface with capabilities of presenting graphical plots of velocity vectors and scalar variables. The plots show a two dimensional view of the three dimensional grid. Three plots showing the geometry from above, in cross section and in longitudinal profiles are available. In addition it is possible to simulate particle animation for visualisation purposes.

The model includes several utilities which makes it easier to give input data. The most commonly used data can be given in dialogue boxes. Several of the modules in the program can be run simultaneously. There is an interactive graphical grid editor with elliptic and transfinite interpolation. The shape of the grid and some of the input data can be changed during the calculations. This is useful for convergence purposes and also for optimising the geometry with respect to the flow field.

5.2.1 Model Development

Brief details of the computational code SSIIM were given in chapter 1, however at this point it is appropriate to give a more detailed description of the code.

The code was originally developed by Dr N. R. B. Olsen (Olsen 1991) during his Doctorate at the Division of Hydraulic Engineering at the Norwegian Institute of Technology. It was called Sediment Simulation at Intakes (SSII) and was developed for the Personal Computer (PC) rather than a larger UNIX workstation for example, due to lack of funding. Due to the long computational times that were required it was written for a mutli tasking operating system. At that time the only operating system available for the PC which was capable of multi tasking was OS/2 which was produced by IBM. SSII (and the later SSIIM) are multi threaded. This means that several of the program modules can run simultaneously. A typical example is that the graphics modules can be run simultaneously with the numerical computation modules. This means that the user can see the values of the variables while the calculations are running. In addition, other functions of the PC can be used such as word processing since this uses only a fraction of the computational power of the PC. The disadvantage with SSII was that a structured grid was used and it was only

possible to have one block for an outblocked region which represented an obstruction in the geometry.

An improvement which was subsequently made was a multi-block model with general out blocking possibilities and this later version was called SSIIM, which was first released in 1993. Since 1993 several minor improvements have been made with some bug corrections. The most significant improvement was the 3D graphics capabilities added to SSIIM, using Open GL graphics (a graphics library supplied by IBM and available with the latest versions of OS/2). SSIIM was used for the study outlined by this thesis from May 1996. Regular correspondence was undertaken with the author of the code, Dr Olsen, and numerous bugs have been found in the duration of the study which have subsequently been rectified by Dr Olsen. SSIIM is presently available as Freeware and can be downloaded from the Internet. The latest version of SSIIM is Version 2.12[1998]. SSIIM was operated under OS/2 Version 4 Warp. This version contained the Open GL graphics required for 3D visualisation techniques. It was initially installed on a Pentium 133Mhz PC with 32Mb RAM. Due to time limitations and the excessive computational times experienced this was subsequently upgraded to a Pentium II 333Mhz processor with 132Mb RAM. This increased the convergence times of a typical model by a factor of 10.

5.2.2 Grid Generation

One of the fundamental principles of Computational Fluid Dynamics (CFD) is to divide the fluid geometry into elements or cells and solve an equation for each cell. Grids can be classified according to several characteristics; shape, orthogonality, structure, blocks, position of variable and grid movements.

The shape of the cells is usually triangular or quadrilateral in 2D and tetrahedral or hexahedral in 3D. The orthogonality of the grid is determined by the angle between crossing grid lines. If the angle is 90 degrees, the grid is orthogonal. If it is not 90 degrees the grid is non-orthogonal and this is the case with grids used by SSIIM. Figure 1.17, chapter 1 shows orthogonal and non-orthogonal grids. Grids can be structured or unstructured. Often a structured grid is used in finite element methods. However, this is not always the case. Figure 1.18, chapter 1 shows a structured and an unstructured grid. In a structured grid it is possible to make a 2D array by indexing

the grid cells. If this is not possible the grid is unstructured. Structured grid were used by SSIIM in this study although recently SSIIM has been modified to accept unstructured grids.

There are also classifications according to where in the grid the variable is calculated. To improve stability, some models calculate pressure and velocity in different positions. This is called a staggered grid. A non-staggered grid is used when all the variables are calculated in the same location, most often at the centre of each cell. These terms are most often used in the control volume terminology. In finite element methods the variables are most often calculated at grid intersections and sometimes also in the centre of each cell. Figure 5.1 shows the locations of the calculation points. P denotes a point where pressure is calculated and U denotes a point where velocity is calculated. SSIIM uses a non-staggered grid.
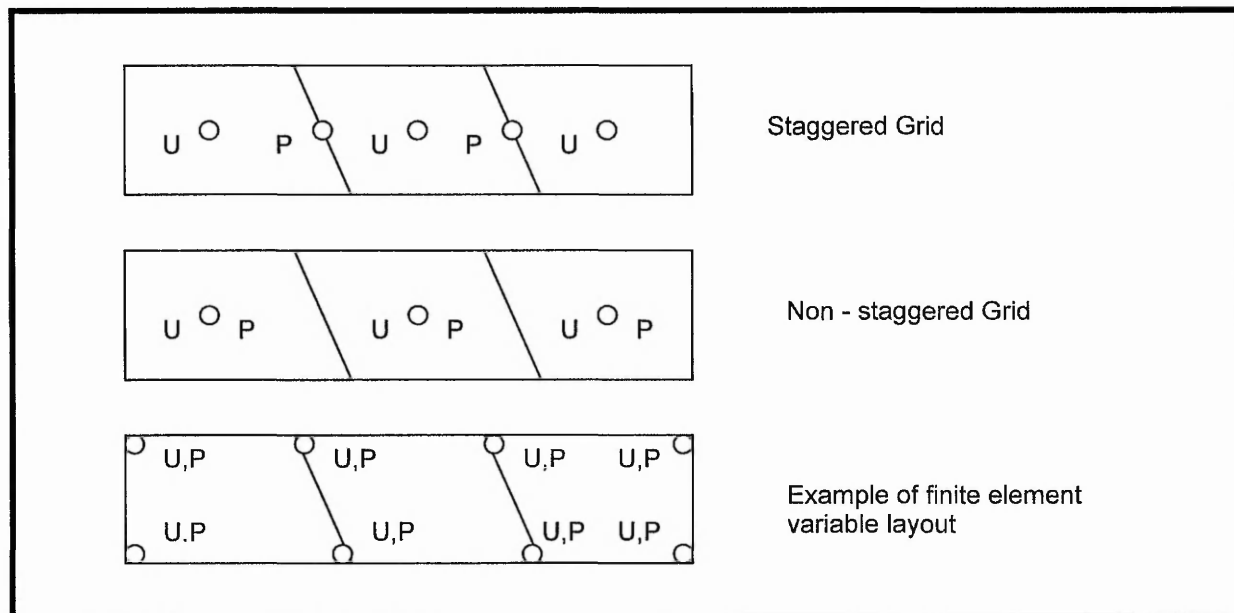
Figure 5.1   Grid variable classification.

An adaptive grid moves according to the calculated flow field or the physics of the problem. When the water surface or the bed moves during a time step, it is possible to make the grid move accordingly using adaptive grid techniques. Adaptive grids are used by SSIIM for sediment deposition or scour and are used to model changes in the free water surface for example when calculating a flood wave.

The numbering system for grid lines and cells used in SSIIM is as follows. In a structured grid there will always be one more grid line than grid cells in any given

direction. Because boundary conditions are also needed, there will be a grid cell with zero thickness at the walls. The number of this cell is 1. The number of the first cell inside the grid is therefore 2. The variable in the centre of the first grid cell has the identifier (2,2). The variables on the boundary are only used as boundary conditions. The variables in the corners: (1,1), (1,5), (5,1), (5,5) are not used in any calculations. Figure 5.2 shows these numbering systems.

(1.4	(2.4	(3.4	(4.4
(1.3	(2.3	(3.3	(4.3
(1.2	(2.2	(3.2	(4.2
(1.1	(2.1	(3.2	(4.1

Numbering of Grid Lines

(1.5 (2.5	(3.5	(4.5 (5.5
(1.4 (2.4	(3.4	(4.4 (5.4
(1.3 (2.3	(3.3	(4.3 (5.3
(1.2 (2.2	(3.2	(4.2 (5.2
(1.1 (2.1	(3.1	(4.1 (5.1

Numbering of Grid Cell Calculation
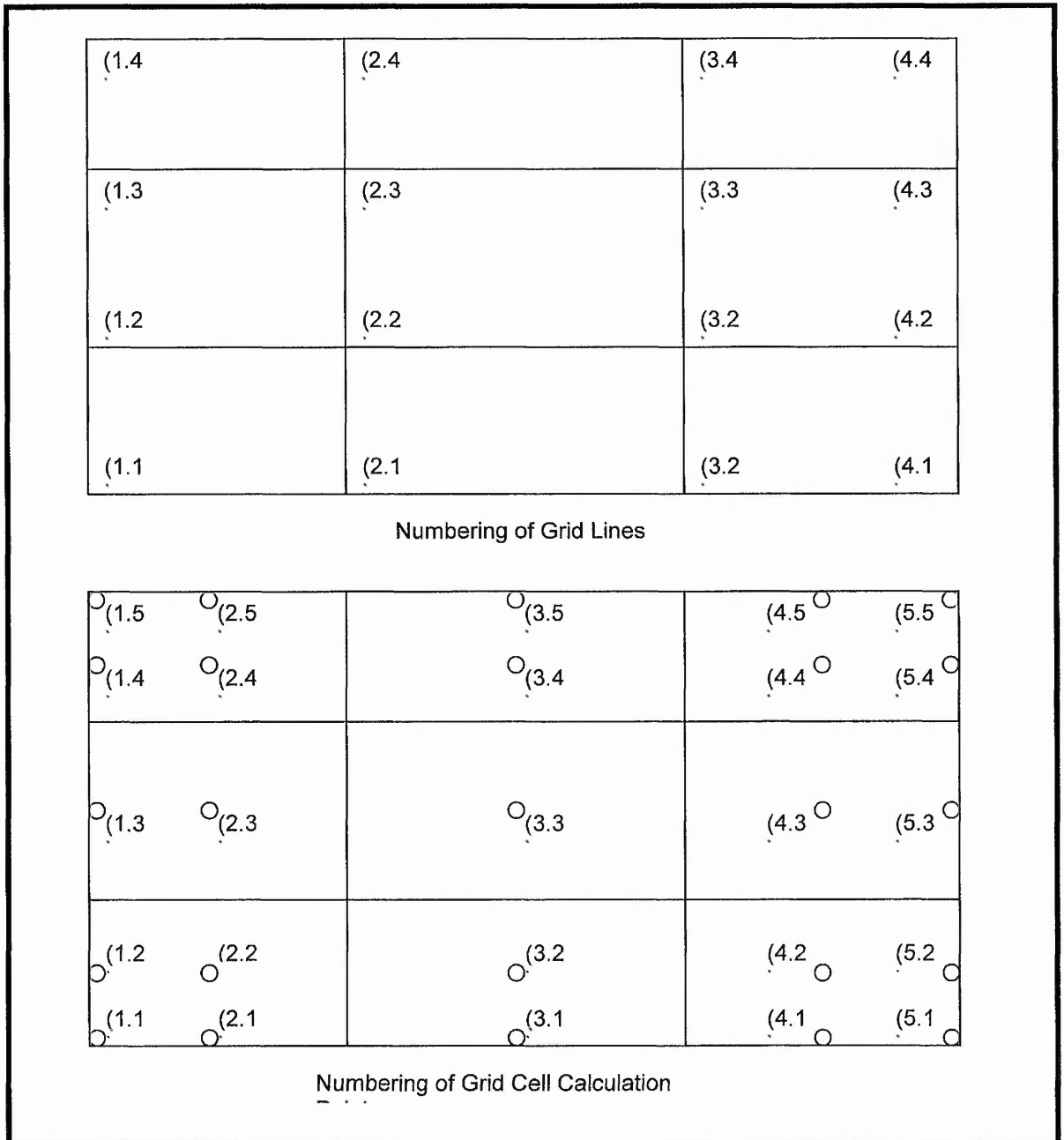
Figure 5.2   Grid cell reference system in SSIIM.

When constructing grids for finite volume calculations it is important to consider the shape of the cells that are created. Three characteristics of the grid should be considered:

- Non-orthogonality
- Aspect ratio
- Expansion ratio

The non-orthogonality of the intersections of the grid lines is the deviation from 90 degrees. If the angle of the grid line intersection is less than 45 degrees or greater than 135 degrees, the grid is classed as very non-orthogonal and this should be avoided. Low orthogonality of the grid leads to more rapid convergence and usually better accuracy.

Aspect ratio can be considered with reference to figure 5.3.
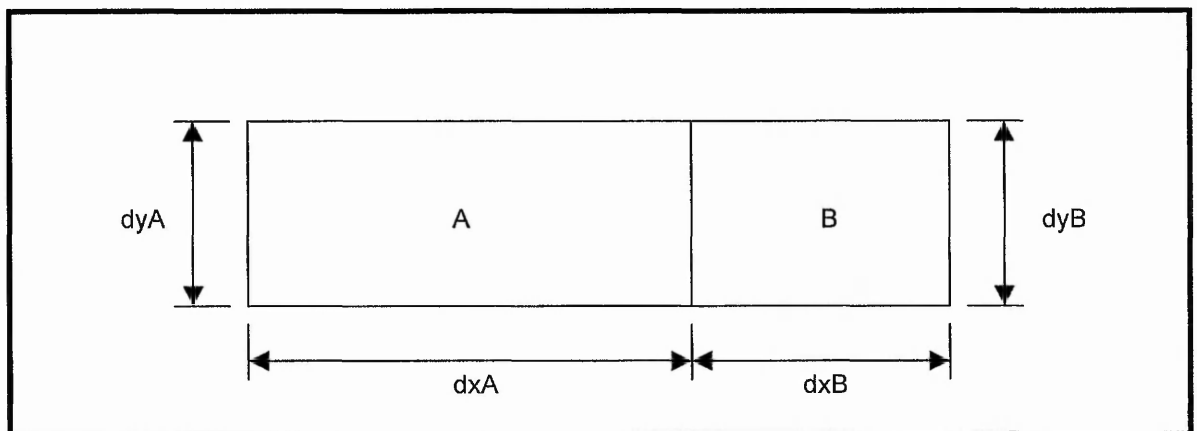
Figure 5.3   Grid cells.

Figure 5.3 shows two grid cells, A and B of width dxA and dxB and height dyA and dyB respectively.

The expansion ratio is the ratio of the width of the adjacent cells, dxA / dxB.

The aspect ratio is the ratio of the width to height of a cell, dxA / dyA and dxB / dyB.

Large expansion and aspect ratios create convergence problems and inaccuracies. Typical aspect ratios should not exceed 2-3 if the flow direction is parallel to the

longest side of the cell. Aspect ratios of 10 – 50 give extremely slow convergence times. Typical expansion ratios should not exceed 1.2.

Occasionally, upon examination of the results when using SSIIM, gross errors were obtained. This was usually due to poor grid generation in terms of aspect and expansion ratios. Manipulation of the grid to with reference to these parameters usually improved the rogue results considerably. These problems were generally experienced at the beginning of analysis when a new grid was constructed.

SSIIM includes algorithms to assist in the construction of computational grid. These include facilities such as elliptic and transfinite grid generators. However, with experience of the code it was found that these methods of grid generation were not suitable for the grids that were constructed for the purposes of this study. It was found that the best method was to draw the geometry and construct the grid lines "by eye". The grid drawn on graph paper was then digitised to obtain the co-ordinates of the grid intersections. The co-ordinates were input into the code using the grid co-ordinate file of SSIIM, which is called the Koordina File. This is essentially an ASCII type file which contains details of the grid intersections and the geometry of the domain in the following data ranges; Node Reference I, Node Reference J, Node Reference K, X Co-ordinate, Y Co-ordinate, Z Co-ordinate. The grids were constructed with the following important considerations:

- The grid lines should follow the assumed stream lines as much as possible.
- The grid line intersections should be as orthogonal as possible.
- The grid aspect ratio should not be too great.
- The grid expansion ratio should not be too great.
- There should be higher grid densities in areas with high velocity gradients.

Three examples of grids used in this study are given by Figure 5.4. These represent grids for intake angles of 15, 30 and 45 degrees.

Outblocking was used in construction of the grids. An outblocked region is a part of the grid where the water is not allowed to flow and in the case of this study outblocked regions were used to define the inlet piers of the intake structure. The

outblocked region is specified in the Control file and this will be covered later in this chapter.
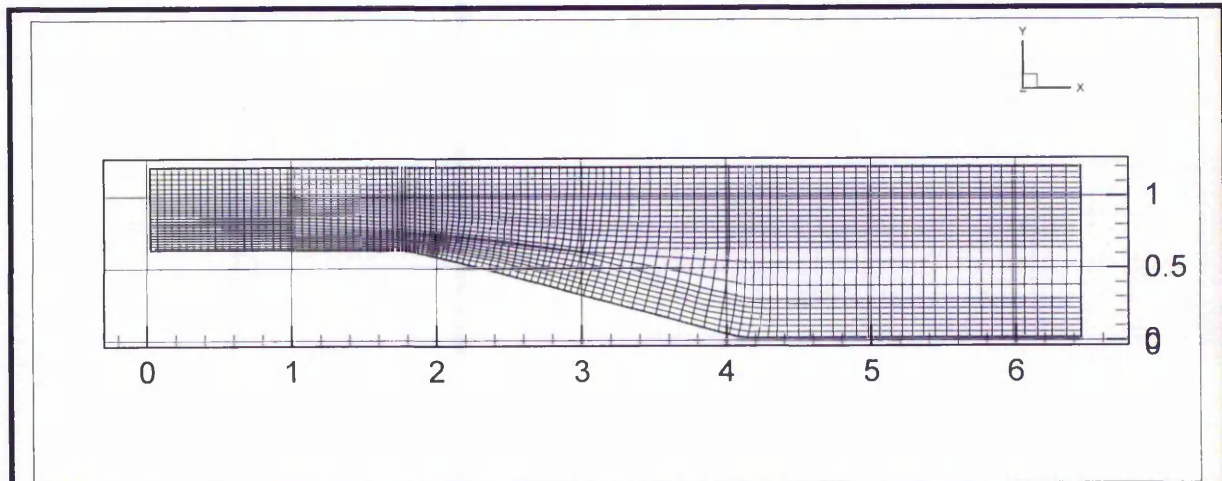
Computational grid for 15 degree intake.
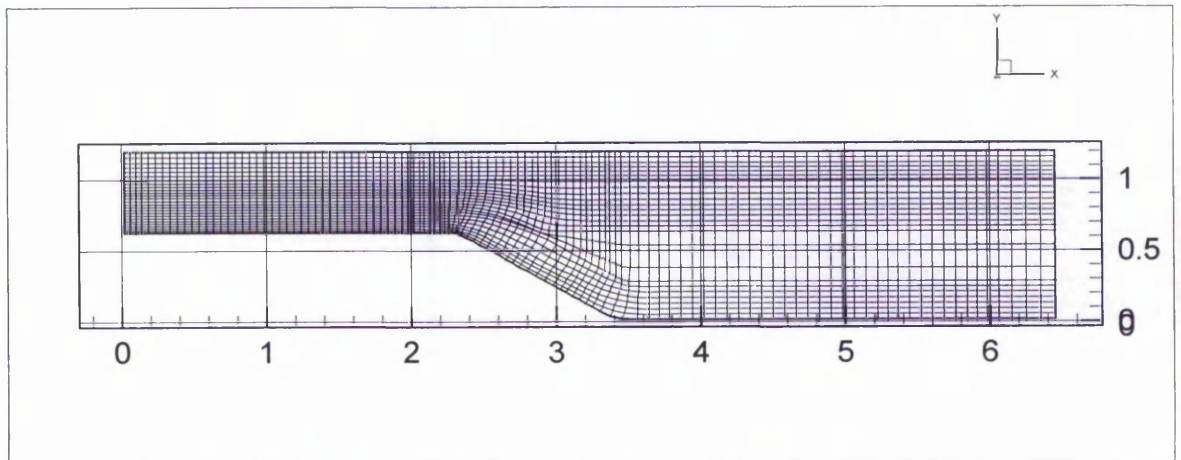
Computational grid for 30 degree intake.
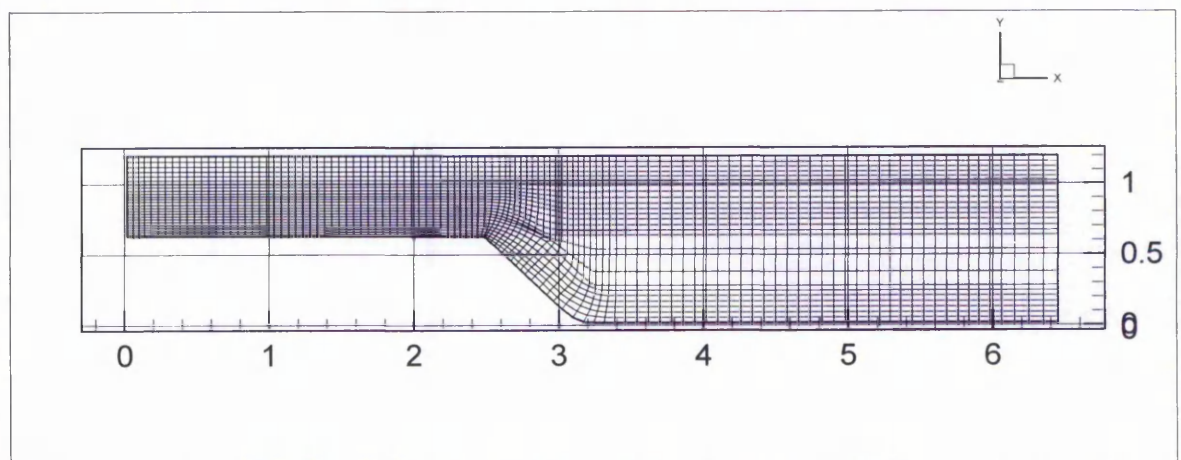
Computational grid for 45 degree intake.

Figure 5.4   Sample computational grids used in the study

Figure 5.5 shows a 3D view of grid which was constructed for a typical 15 degree intake analysis. This illustrates more clearly the construction of the grid.
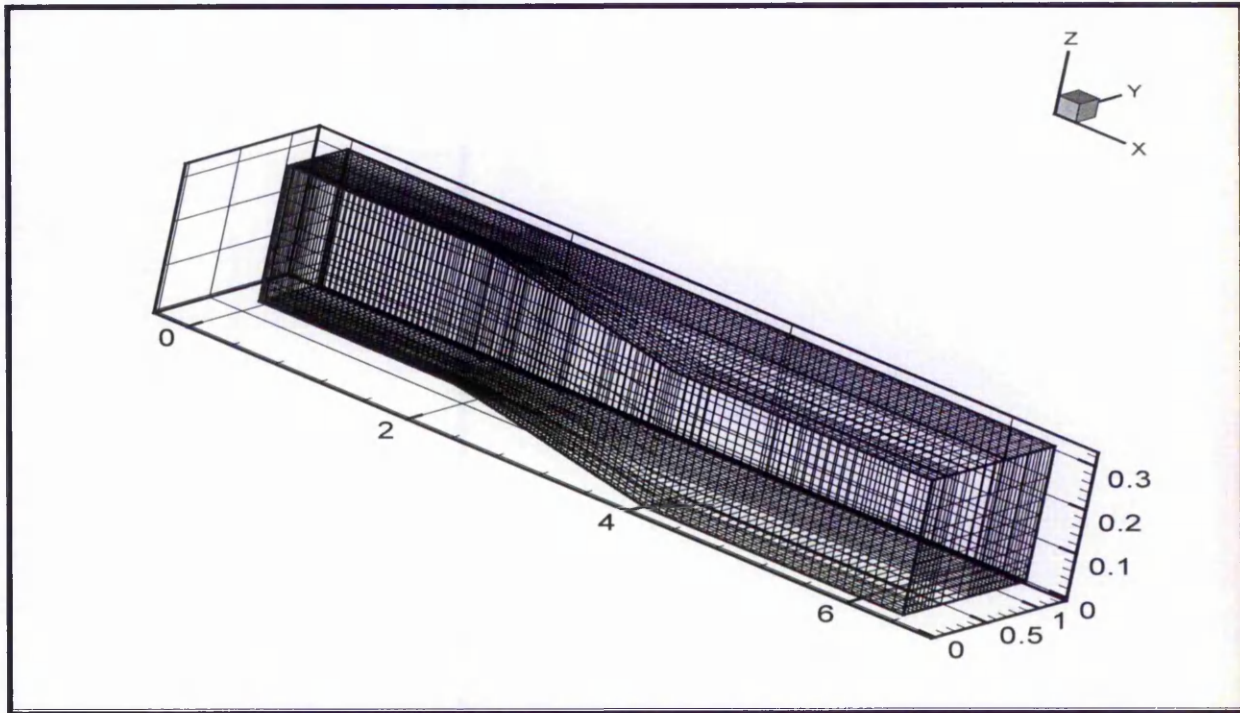
Figure 5.5   A 3D view of a grid which represented a 15 degree intake.

Seven computational grids were tested during the validation studies ranging from grids containing 3,192 cells up to 48,816 cells. These grids incorporated four different combinations of cells in the vertical direction and three different combinations of cells in the horizontal direction.

SSIIM has a grid function called Multiblock. This function is particularly useful for constructing grids for domains with branching channels. However it was found that the Multiblock option was not suitable for this study since the proportion of the flow entering the branching channel must be specified prior to computational analyses i.e. the value of the flow split ratio was required. Calculation of the flow split ratio was initially an objective of the study and a standard grid was considered to be most appropriate. In addition the validation study (which is detailed later in this chapter) highlighted that the improvements to the results were negligible when using a Multiblock grid. An example of a Multiblock grid is shown by Figure 5.6. Notice that the grid basically consists of two independent grids connected at the appropriate position. Multiblock grids are most suited to complicated river bifurcations where outblocking is difficult.
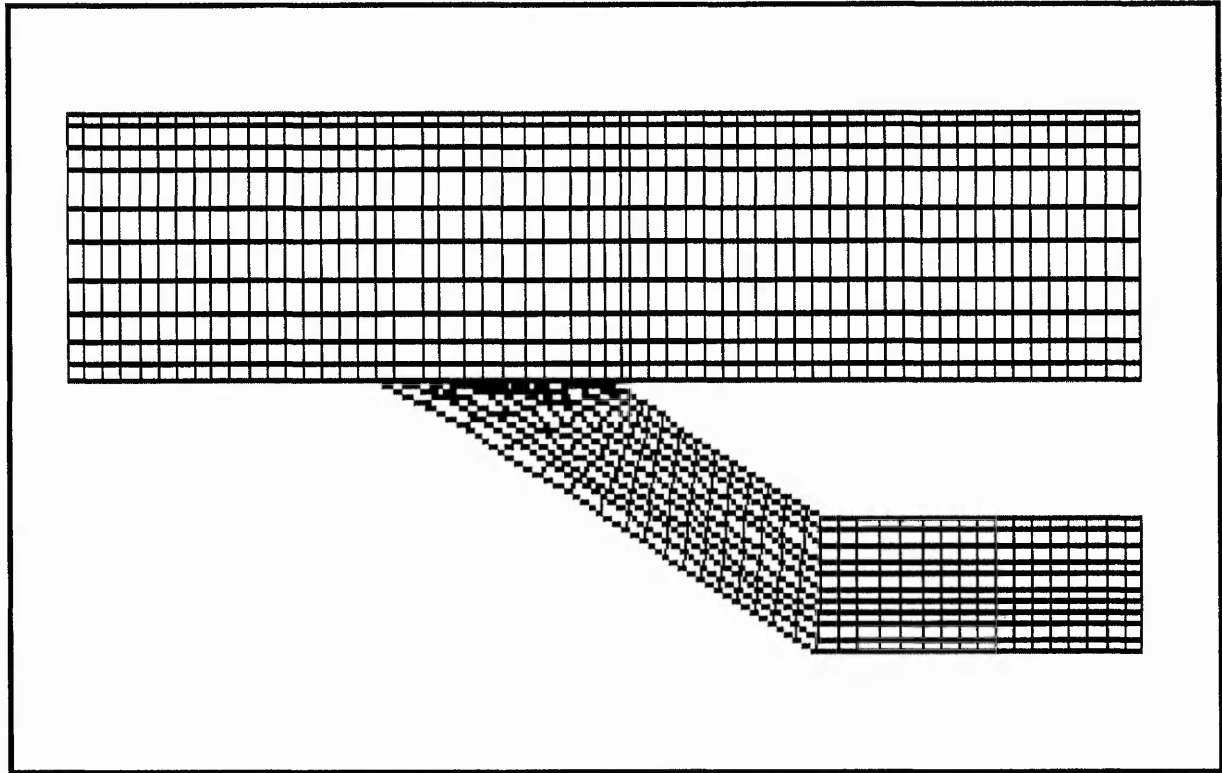
Figure 5.6   A Multiblock grid.

5.2.3 Calculation of Water Velocity

The main equations of fluid flow are the Navier Stokes equations. The equations were derived on the basis of equilibrium forces on a small volume of water in laminar flow and were subsequently modified for turbulent flow creating Reynolds' averaged versions of the equations. Thus the Navier Stokes equations for turbulent flow in a general 3D geometry for non-compressible and constant density flow can be modelled as:

$$U_j \frac{\partial U_i}{\partial x_j} = \frac{1}{\rho} \cdot \frac{\partial}{\partial x_j}(-P\delta_{ij} - \rho.\overline{u_i.u_j}) \qquad\qquad 5.1$$

Where:

U = Velocity, P = Pressure, δ_{ij} = Kronecker delta = 1 if i = j and 0 if i ≠ j and $\overline{u_i.u_j}$ = Reynolds stress term.

The term on the left side of the equation is a convection term. The first term on the right side is a pressure term and the second term is the Reynolds stress term. To evaluate the Reynolds stress term a turbulence model is required. It is often modelled using a Boussinesq approximation:

$$-\rho.\overline{u_i.u_j} = \rho.\nu_T\left(\frac{\partial U_i}{\partial x_j} + \frac{\partial U_j}{\partial x_i}\right) - \frac{2}{3}.\rho.k.\delta_{ij} \qquad\qquad 5.2$$

k, the turbulent kinetic energy and ν_T is the turbulent eddy viscosity which is modelled in SSIIM using the k - ε turbulence model of Launder and Spalding (1974) and is dealt with later in this section.

Inserting the equation for the Reynolds Stress into the Navier Stokes equation gives:

$$U_j\frac{\partial U_i}{\partial x_j} = \frac{1}{\rho}.\frac{\partial}{\partial x_j}\left(-(P + \frac{2}{3}k).\delta_{ij} + \nu_T.\frac{\partial U_i}{\partial x_j} + \nu_T.\frac{\partial U_j}{\partial x_i}\right) \qquad 5.3$$

On the right side of the equation there is now a pressure / kinetic energy term, a diffusion term and a stress term. The stress term is usually neglected since it has little effect on the solution for many cases. The kinetic energy is usually very small and is negligible when compared to pressure. The solution of the convection and diffusion terms using discretisation methods and numerical algorithms in SSIIM is dealt with in section 5.2.4. The pressure term is presently solved using many different algorithms but in SSIIM the SIMPLE and SIMPLEC algorithms are used. Modifications and improvements have been made in recent years to the SIMPLE algorithm but these are currently not included in SSIIM. A description of the SIMPLE and SIMPLEC algorithms can be found in Versteeg and Malalasekera (1995).

The k - ε Turbulence Model
The k - ε model uses the following formula to calculate the turbulent eddy viscosity:

$$\nu_T = c_\mu\frac{k^2}{\varepsilon} \qquad\qquad 5.4$$

The turbulent kinetic energy (see also chapter 4), k is defined as:

$$k \equiv \frac{1}{2}\overline{u_i.u_j} \qquad\qquad 5.5$$

k is modelled as:

$$U_j\left(\frac{\partial k}{\partial x_j}\right) = \frac{\partial}{\partial x_j}\left(\frac{v_T}{\sigma_k}.\frac{\partial k}{\partial x_j}\right) + P_k - \varepsilon \qquad\qquad 5.6$$

P_k is defined as:

$$P_k = v_T.\frac{\partial U_i}{\partial x_j}.\left(\frac{\partial U_j}{\partial x_i} + \frac{\partial U_i}{\partial x_j}\right) \qquad\qquad 5.7$$

ε is modelled as:

$$U_j\frac{\partial \varepsilon}{\partial x_j} = \frac{\partial}{\partial x_j}.\left(\frac{v_T}{\sigma_\varepsilon}.\frac{\partial \varepsilon}{\partial x_j}\right) + C_{\varepsilon1}.\frac{\varepsilon}{k}.P_k - C_{\varepsilon2}.\frac{\varepsilon^2}{k} \qquad\qquad 5.8$$

Empirical constants contained in the preceding equations were derived by Launder and Spalding as a results of numerous tests and the values of the constants are defined as follows:

$$c_\mu = 0.09,\ C_{\varepsilon1} = 1.44,\ C_{\varepsilon2} = 1.92,\ \sigma_k = 1.0,\ \sigma_\varepsilon = 1.3. \qquad\qquad 5.9$$

The main advantages of the k - ε turbulence model over the numerous other turbulence models that are presently available today are that the constants are almost universal. This means that the model can be used on a number of different flow situations without calibration. It is also reasonably robust and it is the most validated turbulence model presently in use. However it can be seen from the previous equations that the eddy viscosity is isotropic (turbulence is modelled as an average of the three directions of motion, x, y and z). Schall (1977) did a study where the eddy viscosity was measured in a laboratory flume in three directions. This work showed that the eddy viscosity was considerably greater in the vertical direction than

in the cross stream direction. The k - ε model therefore tends to over predict turbulence and other models which take account of anisotropic turbulence would give better results. The reader is referred to Abbott and Basco (1989) for further details on turbulence modelling.

5.2.4 Discretisation Methods

The discretisation method used by SSIIM is the control finite volume approach. There are also two other discretisation methods; the finite element and the finite difference method which are commonly used in computational analyses. The finite difference and finite element method, however, are more commonly used in structural analyses.

The finite volume approach was originally developed as an adaptation of the finite difference approach. It consist of the following steps:

- Integration of the governing equations of fluid flow over all the (finite) control volumes of the solution domain.
- Discretisation which involves the substitution of a variety of finite difference type approximations for the terms in the integrated equation representing flow processes such as convection, diffusion and source terms.
- Solution of the algebraic equations by an iterative method.

The Power Law scheme (POW) and the Second Order Upwind scheme (SOU), Pantakar 1980), are implemented in SSIIM and the choice of these parameters is at the discretion of the user, dependent upon the nature of the problem being investigated. The relative merits of the SOU and POW are discussed in section 5.4.3.

5.2.5 Boundary Conditions

Boundary conditions must be entered into SSIIM prior to calculations commencing. In some cases this is undertaken automatically by SSIIM based upon flow, depth, and roughness of the walls. Boundary conditions can be divided into four main types; inflow, outflow, water surface and bed/wall.

Inflow

There are essentially two types of boundary conditions which can be applied to inflows:

- Zero gradient
- Dirichlet

Zero gradient boundary conditions means that the derivative of the variable at the boundary is zero. With an iterative solution the boundary value is set equal to the value at the cell closest to the boundary for each iteration. A zero gradient boundary condition is a type of Neumann boundary condition. A Neumann boundary condition is defined as gradient prescribed on the boundary.

Dirichlet boundary conditions mean that the value of a variable is given at the boundary. This is the type of boundary condition used by SSIIM for inflow and bed/wall boundaries. Therefore at the inlet, velocities are easily calculated using the flow and depth entering the domain in combination with standard, theoretical velocity profiles. Physical studies have shown that the velocity profile in the turbulent boundary layer is approximated closely over a wide range of Reynolds numbers by the equation:

$$\frac{V}{U_0} = \left(\frac{y}{\delta}\right)^7$$

5.10

Where:

V = Local velocity, U_0 = Depth averaged velocity, y= Depth from bed of localised velocity and δ = Boundary layer thickness.

If the turbulent boundary layer is assumed to develop at the leading edge of the entrance to the domain:

$$\delta_x = 0.37.x.\left(\frac{\nu}{U_0.x}\right)^{\frac{1}{5}} = \frac{0.37.x}{Re_x^{\frac{1}{5}}}$$

5.11

Where:

δ_x = Boundary layer thickness a distance x downstream form the inlet to the domain, v = Kinematic viscosity, Re = Reynolds Number.

In addition it is also possible to enter measured velocities using a file called INNFLOW. For some validation cases this method was used. It is usually more difficult, however, to enter turbulence. A method used by SSIIM to specify the turbulence is by using a simple turbulence model which gives the eddy viscosity:

$$\Gamma = \alpha..U_*.H \qquad\qquad 5.12$$

Where:

U_* = Shear Velocity, H = Water Depth, α = Empirical cons tan t = 0.11(Keefer, 1971).

Given the depth averaged velocity it is also possible to estimate the shear stress at the entrance bed:

$$\tau_* = 0.0225.\rho.U_0^2.\left(\frac{v}{U_0.\delta_x}\right)^{\frac{1}{4}} \qquad\qquad 5.13$$

The turbulent kinetic energy k, at the inflow bed is determined by the following equation:

$$k = \frac{\tau_*}{\rho.\sqrt{c_\mu}} \qquad\qquad 5.14$$

Where:

c_μ = Empirical constant = 0.09

The above equation assumes turbulence equilibrium at the bed cell.

The value of the dissipation of turbulent kinetic energy ε, is given by the turbulence model developed by Launder and Spalding (1974):

$$v_T = c_\mu \frac{k^2}{\varepsilon} \qquad\qquad 5.15$$

Where:

v_T = Turbulent eddy viscosity.

Outflow

Zero gradient boundary conditions are used by SSIIM at outflow boundaries for all the variables.

Water Surface

Zero gradient boundary conditions are used for the dissipation of turbulent kinetic energy, ε and turbulent kinetic energy, k are set to zero in SSIIM. Symmetry boundary conditions are used for water velocity. This basically means that zero gradient boundary conditions are used for the velocity in the horizontal directions. The vertical velocity is set so that there is zero flux across the water surface. This boundary condition is a major shortfall of the code and the problems this caused are discussed in greater detail in the concluding chapter.

Bed / Wall

The flux through the bed or walls is zero and therefore no boundary conditions are given in SSIIM. However, the flow gradients towards the walls are very steep and it would require a substantial number of cells to dissolve the gradient significantly. This would result in a dramatic increase in computational time and be unecenomical. Instead a method called the wall laws is used by SSIIM. The wall law is applied by integration over the cell closest to the bed. A modification to the wall law for rough boundaries is used by SSIIM (Schlichting, 1980):

$$\frac{U}{u_*} = \frac{1}{\kappa}\ln\left(\frac{30.y}{k_s}\right) \qquad 5.16$$

Where:

U = Velocity, u_* = Shear velocity, κ = Von Karman's coefficient = 0.4, k_s = roughness and y = Distance from the wall to the centre of the cell nearest to the boundary.

The wall law is used for both velocities and the turbulence parameters.

5.2.6 Stability and Convergence

There are a number of factors that assist in the convergence of numerical models such as SSIIM. The choice of the discretisation methods (described previously) employed can effect convergence dependent upon the flow situation. There are also some other numerical methods used to improve convergence and these are described in the following sections.

Relaxation

The iterative procedure involved when solving the equations basically involves the improvement of a guessed velocity field. For each iteration a new guess is made. For example consider iterations at i-1 and i. The obvious choice for the value to be used at i+1 is the variable obtained at i. However, by introducing a relaxation coefficient r, the variable used is:

$$V = r * V_i + (1 - r) * V_{i-1}$$
                                                                 5.17

The relaxation coefficient is normally between 0 and 1. Relaxation gives slower convergence speed towards the final solution but with less instability. If the solution diverges or does not converge because of instability it is normal to reduce the relaxation coefficient.

Multigrid and Block Correction

The purpose of the multigrid method is to accelerate convergence of the solution. The main principle of the method is to divide the grid into several coarser sub-grids. The solution is first iterated once on the fine grid, then iterated once on the coarse grid and this is repeated until convergence is achieved. Transformation functions are used to evaluate the variables of one grid from another using extrapolation and interpolation. If the finest grid has an excessively large amount of cells it is possible to have mutliple grids with varying quantities of cells. A modification of the multigrid method is block correction. For a 2D grid the method treats the cells as shown by Figure 5.7.
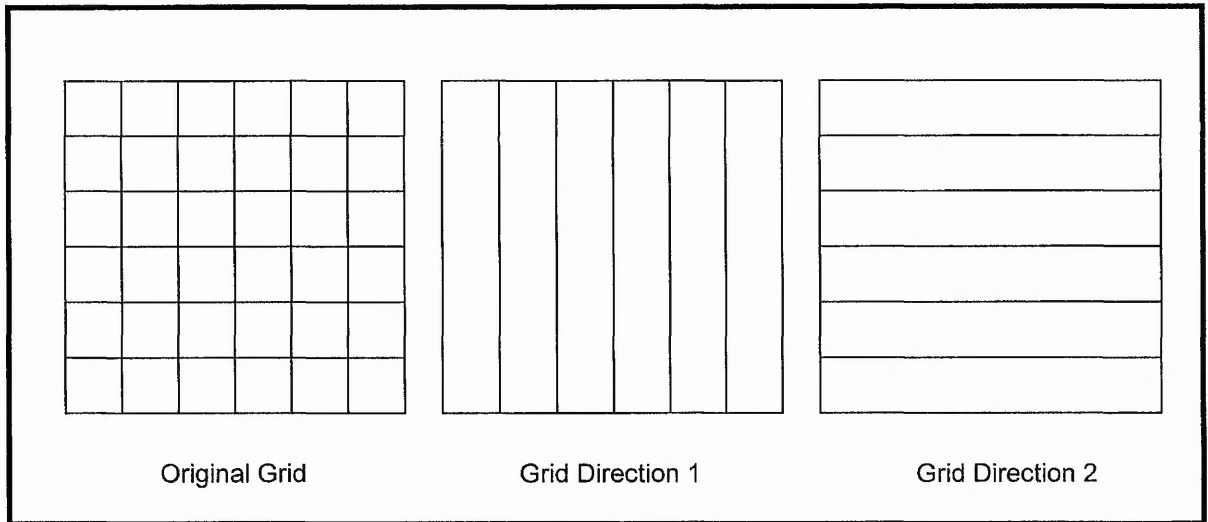
Figure 5.7   Block correction.

The iterations are started on the original grid. Then all the variables are summed in a slice of the grid so that a 1D grid emerges. This is solved and the result is used to correct the original values. This is repeated in all directions shown in Figure 5.11 with two coarse grids.

The Rhie and Chow interpolation

When using a non-staggered grid all the variables are calculated in the centre of the cells (see 5.2.2). This can cause oscillations in the solution and instabilities. The staggered grid was developed to prevent this from happening. With a staggered grid the pressure is calculated between the centres of the grid cells which can cause problems especially with non-orthogonal grids. The Rhie and Chow interpolation was developed to avoid instabilities while still using a non-staggered grid. The interpolation gives the velocity on the cell surface. The basic idea of the Rhie and Chow (1983) interpolation is to use information about pressure gradients in staggered and non-staggered positions. The interpolation formula is:

$$U = U_l + \frac{A^2}{a_p}\left(\overline{\frac{\partial P}{\partial i}} - \frac{\partial P}{\partial i}\right) \qquad 5.18$$

Where U is the interpolated velocity on the cell surface, which is multiplied by the cell surface area to give the flux on the cell surface. U_1 is the linearly interpolated velocity at the cell surface. A is the area, a_p is a coefficient in the discretised Navier Stokes equations, P is the pressure and i is the direction normal to the cell surface. The

overbar in the term $\dfrac{\overline{\partial P}}{\partial i}$ means that the pressure is calculated in staggered positions; the pressure is first linearly interpolated to the grid cell surface and then the difference between these values are used.

5.2.7 User Interface

This section gives details of the structure of the graphical user interface (GUI) of SSIIM. Figure 5.18 shows a flow diagram to represent the component parts of SSIIM. Note only the facilities used in this study are included in this chapter i.e. no sediment transport capabilities of SSIIM are listed here.
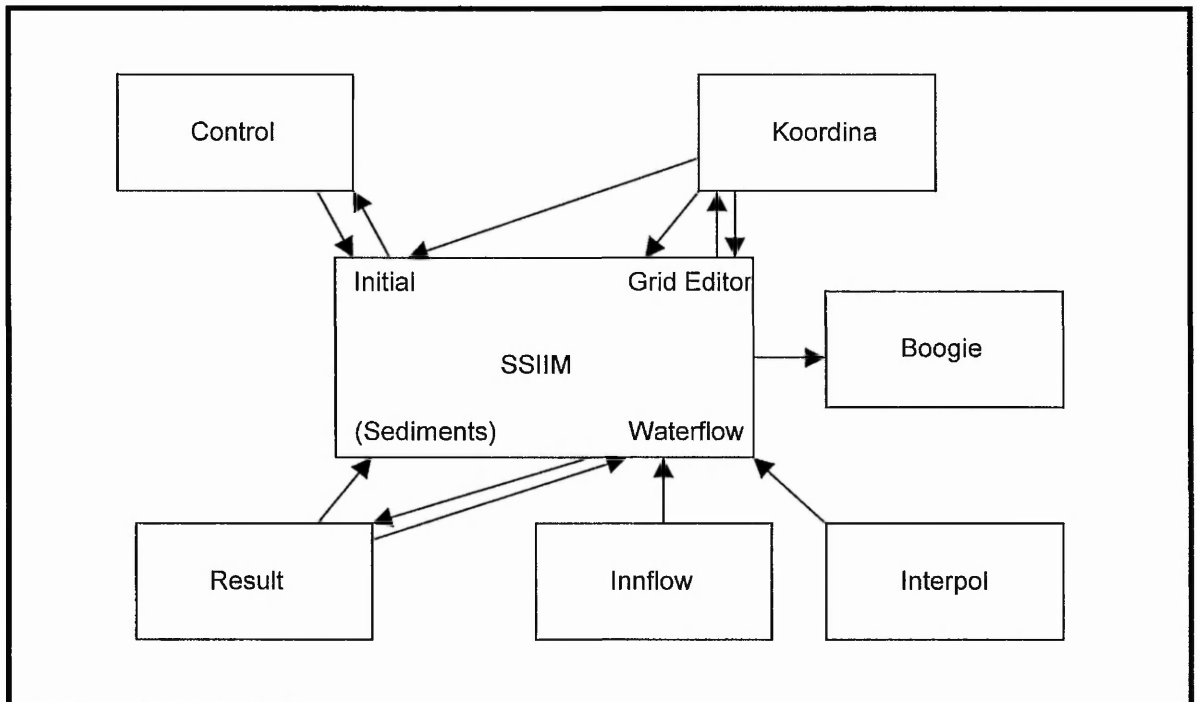
Figure 5.18   Structure of SSIIM graphical user interface.

The two main files are the Control file and the Koordina file. All the files are ASCII files and can be created using a standard text editor.

The Control File

The control file gives most of the parameters required by the model except the grid. SSIIM reads each character of the data field and stops if a capital T, F, G, I, S, N, B or W is encountered. Then the data set is read depending on the letter. A data set is defined as one or more numbers or letters that the program uses. This can for

example be the water discharge or the Manning's friction coefficient. It is possible to use lower case letters between data sets and it is possible to have more than one data set on each line. Not all data sets are required but some are. Default values are given when a non-required data set is missing. If an error is found a message is written to the Boogie file and the program is terminated. A list is given here for the main data sets used in this study.

T   Title field.

F 1   Debugging option. If the character that follows is a D a more extensive output is given in the Boogie file. If the character C follows the coefficients of the discretised equations is printed to the Boogie file.

F 7   Run options. If the following capital letters are included this means:

D: Double the number of grid cells in the streamwise direction in comparison to what is given in the Koordina file. Each cell is divided into two equal parts. When this option is used for the whole geometry the number of grid lines in the streamwise direction (on the G 1 data set) must be multiplied by 2 and 1 must be subtracted.

J: Double the number of grid cells in the cross stream direction. The same procedure as above applies.

F 15   An integer that determines how the wall laws will be used in the cells which border both the wall and the bed. A value of 0 will make the program use wall laws on both walls. A value of 1 will make the program only use wall laws on the bed.

F 24   Turbulence model. An integer is read which corresponds to the following model:

0: Standard $k - \varepsilon$ model (default).

1: Standard Renormalisation Group (RNG) turbulence model.

2: LES RNG model.

3: Constant eddy viscosity model.

G 1   x number, y number and z number. There are four numbers that show the number of grid lines in the streamwise, cross-streamwise and vertical direction. This data must be present in the Control file. The program reads these values and allocates space for the arrays accordingly.

G 3   Vertical distribution of grid cells. This data set gives the percentage of the total depth of each of the grid lines in the vertical direction.

G 7 This data set specifies the water inflow on the geometry sides, bed or surface. It was used when needed in this study to specify the flow split ratio in the intake model i.e. to instruct SSIIM of the flow entering the inlet channel and main channel. Each surface is given on G 7 data set and it is possible to have up to 19 G 7 data sets. On each data set, seven integers and four floats are read. The names of these variables are:

G 7 Type, side, a1, a2, b1, b2, parallel, update, discharge, Xdir, Ydir, Zdir.

Each variable is explained as follows:

Type: 1: Outflow, 0: Inflow

Side: 1: Plane i=1, -1: plane i= x number (cross streamwise plane)

                2: Plane j=1, -2: plane j= y number (streamwise plane)

                3: Plane k=1, -3: plane k= z number (horizontal plane)

a1, a2, b1, b2: four integers are given that determine the limits of the surface.

Parallel: direction of the flow:

                0: normal to the surface

                1: parallel to the grid lines normal to the surface

                2: direction is specified (vector directions).

Update: 0 for not update, 1 for update.

Discharge: discharge in m^3/s. The sign of the discharge must correspond to the direction of the desired flow velocity.

Xdir: Direction vector in x direction.

Ydir: Direction vector in y direction.

Zdir: Direction vector in z direction.

G 8 Values for initial velocities. Up to 19 G 8 data sets can be used. Six integers are read first to specify the volume that is being set, then three floats are read which define the velocities in the three directions.

G 8   i1   i2   j1   j2   k1   k2   U   V   W

G 13 Outblocking option that is used when a region of the gemoetry is blocked out by a solid object. This data set was used in this study to represent the inlet pier of the model. An integer is read first which determines which sides the wall laws will be applied on. The following options are possible:

0:      No wall laws are specified.

1:      Wall laws are used on both sides of the block.

2:      Wall laws are used on the sides and top of the block.

3:      Wall laws are used on the sides, the top and bottom of the block.

Six integers are then read which define the block; i1, i2, j1, j2, k1, k2. Up to 19 G 13 data sets can be used.

W 1 Manning's number, discharge and downstream waterlevel. This data set must be present in the Control file. The parameters here are used to generate the water level profile for the subsequent calculations using a standard backwater calculation.

K 1 Number of iterations for the flow procedure and the number that determines the minimum iterations between updates of the water surface. Two integers are read with defaults of 40000 50000.

K 2 Two integers are read that indicate if laws of the wall are being used. The first integer applies to the side walls. The second integer applies to the surface. 0 is used for wall laws and 1 for the free surface. Wall laws are always used for the bed, if not changed by the W 4 data set. Default: 0 1.

K 3 Relaxation Factors. Six floarts. For the three velocity equations, the pressure correction equation and the k and ε equations. Default: 0.8 0.8 0.8 0.8 0.2 0.5 0.5.

An example of a typical Control file used in this study is shown by Figure 5.9.

```
T   CU35*                    title field
F 7 D J
F 33 1 1
F 43 1
F 53 20 20 1 1
G 1 113 27 11 1      grid and array sizes
G 3 0.000000 4.850 9.722 14.583 19.443 30 40 50.02 60 78.506 100.000
vertical grid distribution
G 7 0 1 2 27 2 11 0 0 0.035 1.0 0 0
G 7 1 -1 2 9 2 11 0 0 0.0117 1.0 0 0
G 7 1 -1 12 27 2 11 0 0 0.0233 1.0 0 0
G 13 1 67 113 10 11 2 11
W 1 111.111 0.035 0.375
W 2 3 1 50 113
K 1 40000 60000
K 2 0
```

Figure 5.9   A typical Control file.

The Koordina file

The Koordina file is the input file where the bed of the geometry is described. The grid can be made using a map, a spreadsheet or the Grid Editor. In this study the geometry was drawn by hand, the grid lines were constructed on the drawing and

then the co-ordinates of the grid line intersections were digitised from the drawing. The format of the data is given as follows:

i   j   x   y   z

The Results file

This file contains the results from the water flow calculations. The file is written when the prescribed number of iterations have been calculated or when the solution has converged. The results are velocities in three dimensions, k, ε, pressure and the fluxes on all the walls of the cells. Figure 5.10 shows an example of a Results file from SSIIM.

```
Results from SSIIM - flow, iter = 1058
Residuals: 0.000715 0.000071 0.000012 0.000132 0.000196 0.000981
Roughness : 0.000164
C 113 27 11
 i  j  k    u     v     w    k    e    f1   f2   f3   p
F 67 25  2 1.05638461e-01 4.13467460e-04 -8.30524777e-07 9.36272140e-
05 4.09233890e-05 7.21486116e-02 2.97867015e-04 -3.84131623e-07
3.65249152e+00
F 67 25  3 1.06194685e-01 4.06282178e-04 3.92157711e-07 7.78065762e-
05 2.62999087e-05 7.28551765e-02 2.92103559e-04 3.09790533e-06
3.65259133e+00
F 67 25  4 1.06764602e-01 3.92779655e-04 2.85380129e-06 6.91369410e-
05 1.84570407e-05 7.30775586e-02 2.81445864e-04 8.48556856e-06
3.65258556e+00
F 67 25  5 1.07340475e-01 3.75134904e-04 6.18602337e-06 6.46152779e-
05 1.41227217e-05 7.34527131e-02 2.68717958e-04 1.54595845e-05
3.65248227e+00
F 67 25  6 1.08252001e-01 3.43373367e-04 1.17553215e-05 6.13013917e-
05 1.02975855e-05 1.60896636e-01 5.36738913e-04 3.20688330e-05
3.65226917e+00
F 67 25  7 1.09403256e-01 3.00730064e-04 2.23060032e-05 6.11176838e-
05 8.53886098e-06 1.54011914e-01 4.43250623e-04 5.15014360e-05
3.65225048e+00
```

Figure 5.10   A Results file.

The first line gives the residuals, the roughness and the grid size. Then each line gives the nine values for one cell. The three indices for the cell are given first followed by the three velocities and the k and ε values. These are followed by the fluxes in the three directions and finally the pressure.

The Boogie file

The Boogie file shows a print out of the intermediate results from the calculations. It also shows parameters such as average water velocity, shear stress and water depth

in the initialisation. If errors occur an explanation is written to this file before the program stops. Initially the memory allocation is given followed by a table which shows the cross sectional area, hydraulic radius, average velocity and water level at the cross sections that have been used for initialising the water surface.

There follows a sequence of two lines for each iteration of the model. The first line of each iteration is defined by the word "Iter" followed by a number which shows the number of the iteration. Then the residuals for the six equations are given. The x, y and z velocities residuals are given first followed by the pressure and the k and ε residuals. All these must be less than 10^{-3} for the model to converge.

The second line starts with the word "Cont" and a floating point value. This is the sum of all the water inflow and outflow in the geometry. This should be a very low value, typically less than 10^{-7}. If a larger value is given the boundary conditions should be checked. The word "DefMax" is then written. This is followed by the residual for the cell with the largest continuity defect. The indexes for the cell are then written with the velocities in the three directions. Figure 5.11 shows a typical Boogie file.

```
       Multi-block version of SSIIM
       In kread

       Transient inner iterations: 1
       In osiio1: IONo = 3
       TurbulenceModel = 0
       In initial - arrays

       End of initial - arrays
       Have allocated   21.68 Mbytes

        In initial - velocity

       Loop1,iter,area,radius,velocity,waterlevel: 4 2.640131e-01 3.750123e-
       01 1.325692e-01 3.750131e-01
       Loop1,iter,area,radius,velocity,waterlevel: 4 2.250151e-01 3.750252e-
       01 1.555451e-01 3.750261e-01
       Waterlevel = 0.375000 meters for cross-section i = 112
       Waterlevel = 0.375001 meters for cross-section i = 111
       Waterlevel = 0.375001 meters for cross-section i = 110
       Waterlevel = 0.375001 meters for cross-section i = 109
```

Figure 5.11   A Boogie file.

The Innflow file

This file is used to read the velocities in three directions for the upstream boundary condition. SSIIM searches for this file and uses the data contained in the file if it

exists. If the file does not exist a warning message is written to the Boogie file and SSIIM assumes a theoretical velocity profile.

On each line the velocities in a cells of the upstream section are given. First the character E is written. Then the indexes j and k (horizontal and vertical) are given. Finally the velocity components in the x, y and z directions are given. The file does not have to contain values for all the nodes. The normal initialisation procedures are applied first then the Innflow file is read. The nodes that are not present in the Innflow file will keep the values from before the file was read.

The Interpol and Interres files

This file contains details stipulating any required velocity profiles. Co-ordinates for the locations where profiles are wanted are given in this file. When the "write results" routine is activated in SSIIM, a search for the Interpol file is undertaken. If the file is not found, it will proceed normally and write the Result file. If the Interpol file is found, the program will not write to the Result file but will write the interpolated velocity profiles to a file named Interres.

The Verify file

This file is used as an input for the Verify Profile graphics option. The user can present calculated velocity profiles with measured values. Up to 20 vertical profiles in a section of the geometry can be shown. The horizontal location of the profiles are determined by the user so this method of presentation can be used for both cross sections, longitudinal sections or other user defined sections. Each profile is identified with a P. Then the x and y co-ordinates of the profile follow. The co-ordinates are given in the same system as the grid or the Koordina file. After the co-ordinates an integer is read which represents how many points are measured in the profile. Up to 20 measurements can be given. On the following lines the data is given. Two floats are given on each line. The first is the vertical co-ordinate where the data is recorded. The second float is the velocity data.

5.2.8 Presentation Graphics

There are eight graphics modules in SSIIM for the presentation of results. These can be invoked at any time during the calculation to observe convergence or after the completion of the calculations. More than one module can run simultaneously. The modules are choices under the graphics option of the main menu.

Map presents the geometry viewed in plan. Velocity vector, pressure, k and ε plots can be chosen. It is also possible to plot the grid and change between different vertical levels. *Contour Map* presents the variables as contours viewed in plan. *Colour Map* presents the variables with colours and density patterns for each cell depending on the value in the cell viewed in plan. *Longitudinal Profile* presents a longitudinal profile of the geometry. Graphs with different parameters as a function of depth along the longitudinal profile can be displayed. It is also possible to view the grid or the velocity vectors and change between different profiles. *Cross Section* presents a cross section of the profile. It is only possible to show a velocity vector profile. It is possible to change between different cross sections. *Verify Profile* presents calculated profiles of velocity at locations specified by the user. It also presents user given data in the same plot. *Three dimensional* presents the bed and geometry in a 2D graphic of a 3D view and *Animation* shows particle animation through the geometry for visualisation purposes only.

5.3   PHYSICAL MODELLING

The validation of SSIIM consisted of two main parts; physical modelling and computational modelling. The validation was undertaken using the 15 degree intake model configuration. Measurements of velocities were carried out using the Acoustic Doppler Velocimeter (ADV). The calibration of the ADV had previously been checked and the results of the calibration exercise were presented in Chapter 4. It was found that velocities could be measured to an accuracy of +/- 2% in the x direction but only to an accuracy of +/- 30% in the y and z directions, based upon a sample time period of 3 minutes at a sampling rate of 25Hz.

Forty three measurement points on each of three levels through the depth of the flow were taken. These were taken near the bed (3.84cm from the bed), near the middle (19.76cm from the bed) and near the surface (31.01cm from the bed). In addition, profiles were measured at ten points in the model at positions of interest as follows. Three profiles were measured at the inlet to the model, three profiles were measured at 1.0m downstream of the inlet and four profiles were measured at other points in the flow designated by points A1 to A4 shown in Figure 5.12. A1 was positioned at x = 2000mm, y = 580mm, A2 is positioned at x = 3000mm, y = 520mm, A3 is positioned at x = 4000mm, y = 200mm, and A4 is positioned at x = 4000mm, y = 100mm. I1, I2 and I3 designate the positions of the inlet velocity profiles that were measured. The positions of the three profiles 1000mm downstream of the inlet are not shown for clarity. A flow of 57l/s and a flow depth of 395mm were set constant in the model. The Froude Number of the model was 0.12 and the Reynolds Number was 40,158 where:

$$\text{Froude Number, } Fr = \frac{V}{\sqrt{g.D_m}} \qquad 5.18$$

D_m = Hydraulic mean depth

V = Average velocity

g = Acceleration due to gravity.

$$\text{Reynolds Number} = \frac{\rho.V.D_m}{\mu} \qquad 5.19$$

ρ = Density of water

μ = Dynamic viscosity of water

Figure 5.12   Measurement positions for validation study

5.3.1 Validation of Flow Measurement

Flow in the model was measured using three methods; an orifice plate in the inlet pipe connected to an electronic manometer, two sharp crested weirs positioned at the outlets to the main and inlet channel and the velocity area method (Wilson 1994) from the velocity measurements taken using the ADV. Further details of these measurement methods were detailed in Chapter 4. The flow passing down the main and inlet channel was also calculated using the results of analyses undertaken using SSIIM. Five total flows were used for this study in the physical model ranging from 22.8l/s to 68.3l/s. Table 5.1 summarises the results of this preliminary study.

Weir Inlet (l/s)	Weir Main (l/s)	Weir Inlet / Main	ADV Inlet (l/s)	ADV Main (l/s)	ADV Inlet / Main	SSIIM Inlet (l/s)	SSIIM Main (l/s)	SSIIM Inlet / Main
6.7	13.4	0.50	8.2	13.0	0.62	5.6	15.8	0.36
10.9	21.8	0.50	12.7	21.1	0.60	9.7	24.4	0.40
15.6	29.6	0.53	16.6	28.5	0.58	14.8	33.3	0.44
19.9	37.6	0.53	19.8	34.1	0.58	16.6	41.1	0.41
21.1	43.3	0.49	25.0	42.8	0.58	18.5	46.4	0.40

Table 5.1   Results of flow validation.

In addition Table 5.2 shows a comparison of the total flows as calculated above with the total flow measured by the orifice plate.

Orifice (l/s)	Weirs (l/s)	ADV (l/s)	SSIIM (l/s)	Average (l/s)	Standard Deviation (l/s)	% Error Average – Orifice
22.8	20.1	21.2	21.4	21.3	0.9	6
35.0	32.7	33.8	34.1	33.8	0.7	3
47.3	45.1	45.2	48.0	46.6	1.2	1
58.9	57.5	53.9	57.7	57.0	1.8	3
68.3	64.4	67.8	64.9	66.4	1.8	3

Table 5.2   Comparison of flows with the orifice plate for the flow validation.

Table 5.1 shows a comparison of the flows measured in the model between various methods of flow measurement. It can be seen that there is reasonably good agreement between the methods. An average flow split ratio, Qr of 0.5 was obtained using the results of all the methods. Table 5.2 shows a comparison of the measurement methods with the measurements taken using the orifice plate in the inlet pipe to the model. It should be noted that the flow calculated using SSIIM was closest to the measurements taken using the orifice. Percentage errors between the methods of flow measurement and the measurements taken using the orifice were generally around 3% although in one case the error was 6%.

5.4   COMPUTATIONAL MODELLING

5.4.1 Boundary Conditions
Inflow Boundary

Two computational models were used to test the effects of altering the boundary conditions. One model assumed fully developed velocity profiles based on theory using the flow and depth entering the model. The other model used velocity profiles measured at the inlet to the physical model using the ADV (at positions I1 to I3 – see Figures 5.12 and 5.13). The results of these two tests are summarised by Tables 5.3 and 5.4, test numbers 1 and 2. These tables show the computational tests carried out and the corresponding parameters used, in conjunction with a comparison of results in terms of percentage errors between the calculated and measured values of velocity. Percentage errors are shown in the x and y directions at the four points A1 to A4 at two levels in the

Table 5.3. Summary table showing comparisons of percentage errors between measured and calculated velocities in the x - direction

Test No.	Time Taken	Memory	Iterations	Grid	Manning's 'n'	Inlet Conditions	Numerical Schemes	Matrix Solution	A1 a %	A1b %	A2a %	A2b %	A3 a %	A3 b %	A4a %	A4b %
1	1hr 50	4.53	5334	57x14x8	0.009	Theory	POW	GS	-4	-18	-16	-75	27	-11	18	-21
2	2hrs	4.53	695	57x14x8	0.009	Measured	POW	GS	-17	-34	-30	-101	19	-27	9	-37
3	1hr 55	4.53	603	57x14x8	0.012	Measured	POW	GS	-21	-36	-33	-100	17	-28	6	-39
4	1hr 20	2.99	444	57x14x4	0.009	Measured	POW	GS	-21	-41	-33	-150	7	-48	5	-72
5	5hr 30	6.06	730	57x14x12	0.009	Measured	POW	GS	-19	-58	-32	-116	16	-38	6	50
6	7hrs	7.60	1433	57x14x16	0.009	Measured	POW	GS	-21	-55	-35	-112	15	-36	5	-48
7	18hrs	15.84	789	113x27x8	0.009	Measured	POW	GS	-19	-38	11	-37	19	-26	9	-37
8	4hrs	4.53	538	57x14x8	0.009	Measured	SOU/POW	GS	-16	-34	-102	-204	8	-48	13	-33
9	5hrs	4.53	730	57x14x8	0.009	Measured	POW/SOU	GS	-17	-34	-30	-101	19	-27	9	-37
10	21hrs	4.53	11414	57x14x8	0.009	Measured	POW	TDMA	-17	-34	-30	-101	19	-27	9	-37
11*	3hrs	4.53	384	57x14x8	0.009	Measured	POW	GS	-17	-34	-30	-101	19	-27	9	-37
12	4hrs	4.53	503	57x14x8	0.009	Measured	SOU	GS	-17	-34	-102	-204	8	-48	14	-33
13**	5hr 30	5.98	747	96x11x8	0.009	Measured	POW	GS	4	-21	55	23	62	36	63	40
14	41hrs	26.60	841	113x27x16	0.012	Measured	SOU/POW	GS	-21	-63	6	-45	19	-23	-3	-46

Table 5.4. Summary table showing comparison of percentage errors between measured and calculated velocities in the y - direction

Test No.	Time Taken	Memory	Iteration	Grid	Manning's 'n'	Inlet Conditions	Numerical Scheme	Matrix Solution	A1a %	A1b %	A2a %	A2b %	A3a %	A3b %	A4a %	A4b %
1	1hr 50	4.53	5334	57x14x8	0.009	Theory	POW	GS	-108	-169	-36	-117	-5	-86	-76	-260
2	2hrs	4.53	695	57x14x8	0.009	Measured	POW	GS	-132	-203	-53	-148	-18	-115	-95	-321
3	1hr 55	4.53	603	57x14x8	0.012	Measured	POW	GS	-140	-209	-55	-147	-20	-113	-101	-315
4	1hr 20	2.99	444	57x14x4	0.009	Measured	POW	GS	-144	-220	-59	-203	-36	-146	-63	-432
5	5hr 30	6.06	730	57x14x12	0.009	Measured	POW	GS	-138	-202	-55	-161	-26	-137	-118	-410
6	7hrs	7.60	1433	57x14x16	0.009	Measured	POW	GS	-123	-188	-46	-102	1	-77	-183	-250
7	18hrs	15.84	789	113x27x8	0.009	Measured	POW	GS	-136	-207	-1	-60	-29	-135	-27	-210
8	4hrs	4.53	538	57x14x8	0.009	Measured	SOU/POW	GS	-130	-199	- 108	-223	-32	-141	-91	-321
9	5hrs	4.53	730	57x14x8	0.009	Measured	POW/SOU	GS	-132	-203	-53	-148	-18	-115	-95	-321
10	21hrs	4.53	11414	57x14x8	0.009	Measured	POW	TDMA	-132	-203	-53	-148	-18	-115	-95	-321
11*	3hrs	4.53	384	57x14x8	0.009	Measured	POW	GS	-132	-202	-	-148	-18	-115	-95	-321
12	4hrs	4.53	503	57x14x8	0.009	Measured	SOU	GS	-130	-200	108	-223	-32	-141	-92	-321
13**	5hr 30	5.98	747	96x11x8	0.009	Measured	POW	GS	-91	-169	49	12	74	44	82	45
14	41hrs	26.60	841	113x27x16	0.012	Measured	SOU/POW	GS	-160	-88	-7	-6	-1	-95	-14	-188

11*   Free water surface update

13** Multiblock grid analysis

depth of the flow. The lower case "a" following the position code represents the percentage error at a depth of 104mm from the bed. The lower case "b" represents the percentage error at a depth of 263mm from the bed.
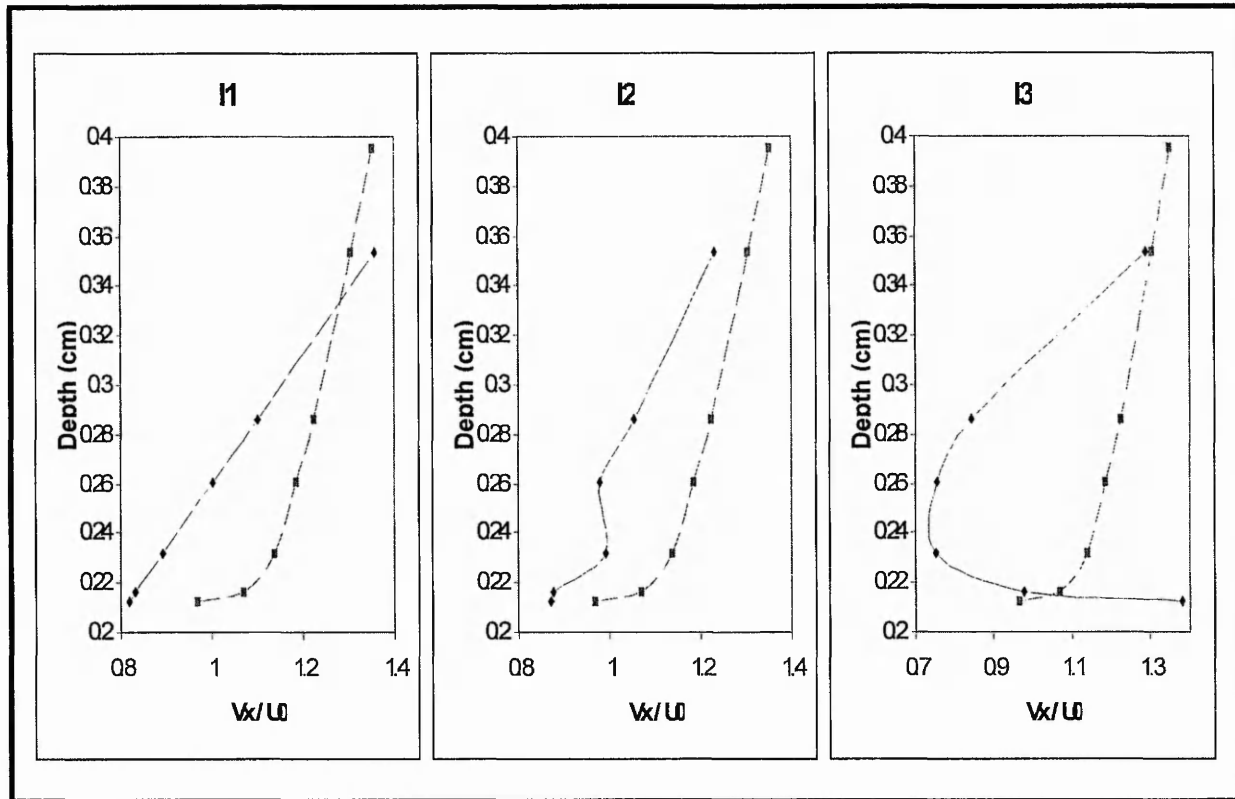
Figure 5.13   Graphs showing the measured and theoretical velocity profiles at I1, I2 and I3. Dotted line represents the theoretical velocity distribution.

The theoretical velocity distribution is based on the widely accepted velocity profile in a turbulent boundary layer (Featherstone and Nalluri 1995) which is approximated closely over a wide range of Reynolds Numbers by the equation:

$$\frac{V}{U_0} = \left(\frac{y}{\delta}\right)^{\frac{1}{7}}$$

5.20

Where:

U_0 = Depth averaged velocity

y = Depth from bed

δ = Boundary layer thickness

$$\delta = 0.37 . \left(\frac{\nu}{U_0 . x}\right)^{\frac{1}{5}}$$

5.21

Where: ν = Kinematic viscosity

Figure 5.13 shows that the measured velocity profiles at the inlet differed from the theoretical velocity distribution and therefore the comparison of analyses using theoretical and measured boundary conditions at the inlet was valid.

Figure 5.14 shows a comparison of the velocity profiles in the x direction at points A1, A2, A3 and A4 for both inlet conditions. Figure 5.15 shows a comparison of the velocity profiles in the y direction and Figure 5.16 shows a comparison of the turbulent kinetic energy with the same inlet conditions and at the same points.

Figure 5.14 shows qualitatively that generally at positions A1and A2, SSIIM under predicted the velocity in the x direction (Vx). Prediction improved nearer the bed. At positions A3 and A4 SSIIM over predicted the velocity in Vx to a depth from the bed of approximately 18cm then under predicted the velocity to the surface of the flow. It can also be noted that generally a slightly improved correlation was obtained between measured and predicted velocities when a theoretical inflow boundary condition based upon the flow and depth entering the model was used. This was in comparison to the measured inflow boundary condition at positions I1, I2 and I3. In this stage of the validation only the inflow boundary conditions were changed between the two analyses (Test 1 and 2, Tables 5.3 and 5.4). The grid used was 57 x 14 x 8 (stream wise, cross stream and vertical), Manning's 'n' was 0.009 and the POW discretisation and the Gauss Seidel (GS) matrix solution schemes were used.

Table 5.3 shows that quantitatively, the theoretical inflow boundary condition gave improved correlation. For example at position A1 near the bed, a percentage error of 4% between the SSIIM solution and the measured values of Vx was obtained using the theoretical inflow boundary condition as opposed to 17% when the measured inflow boundary condition was used. This trend can be observed throughout Tables 5.3 and 5.4 for tests 1 and 2.

In terms of velocity in the y direction (Vy) as shown by Figure 5.15 and Table 5.4, generally SSIIM under predicts the Vy at points A1 to A4 for both inflow boundary conditions. The differences obtained between the two inflow boundary conditions are not as pronounced as in Vx but the same trend still applies. Predictions by SSIIM in Vy or Vz were not as successful as in Vx with errors frequently in excess of 100%. This was a trend that was observed throughout the validation exercise.

Figure 5.14 Velocity in the x direction for measured and theoretical inflow boundary. (Purple dotted line = Measured, Solid blue line = Calculated).
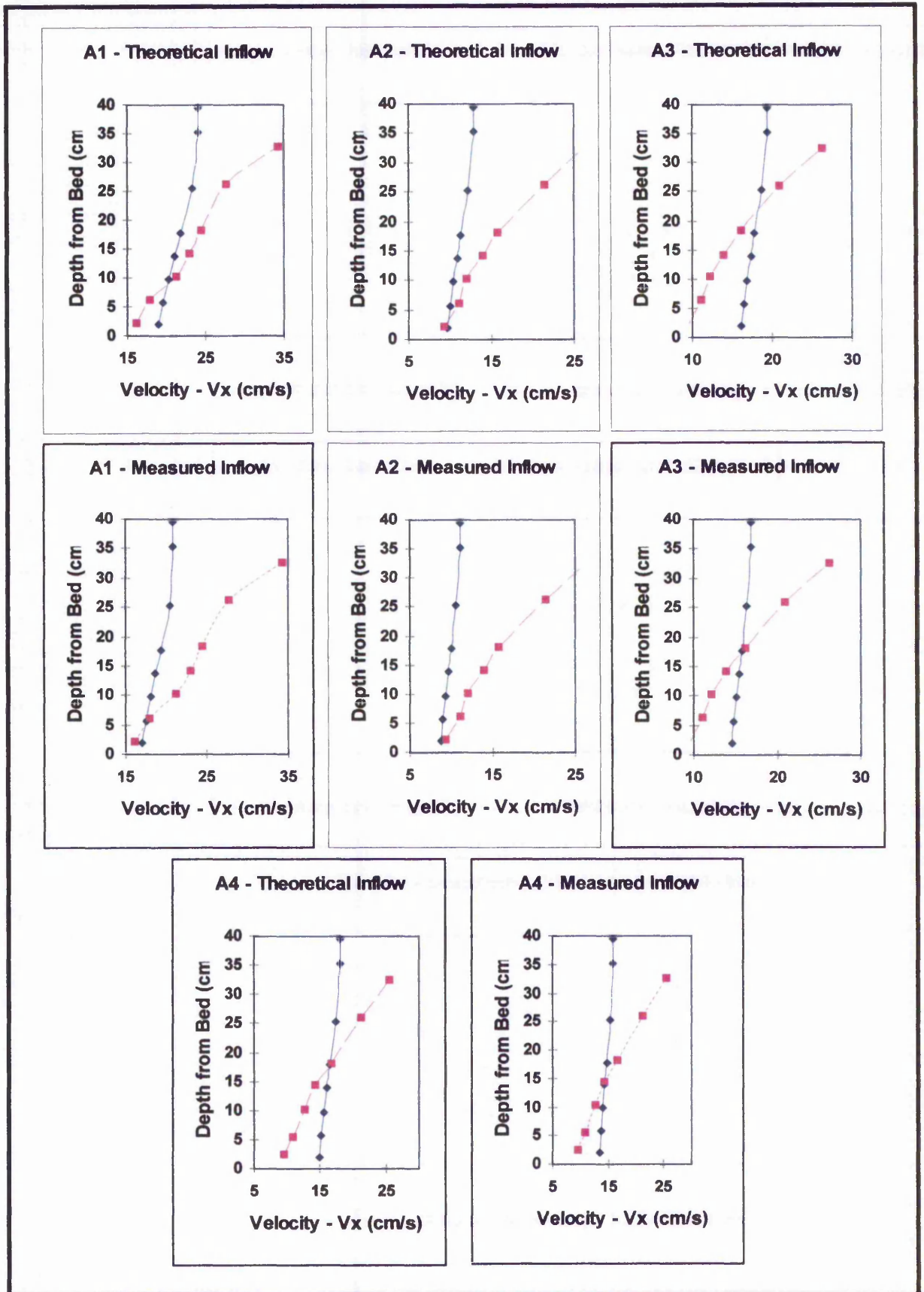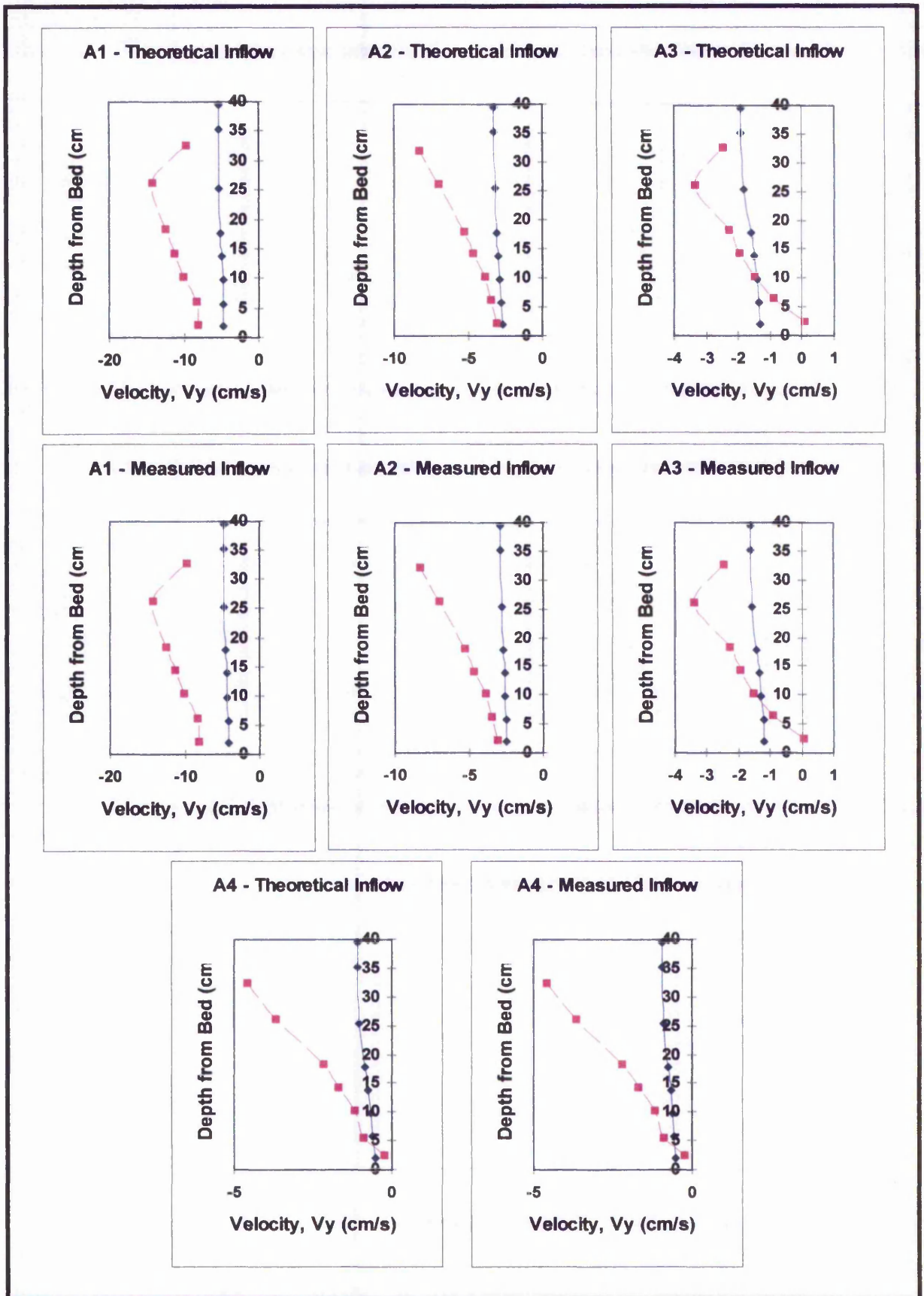
Figure 5.15   Velocity in the y direction for measured and theoretical inflow boundary. (Purple dotted line = Measured, Solid blue line = Calculated).
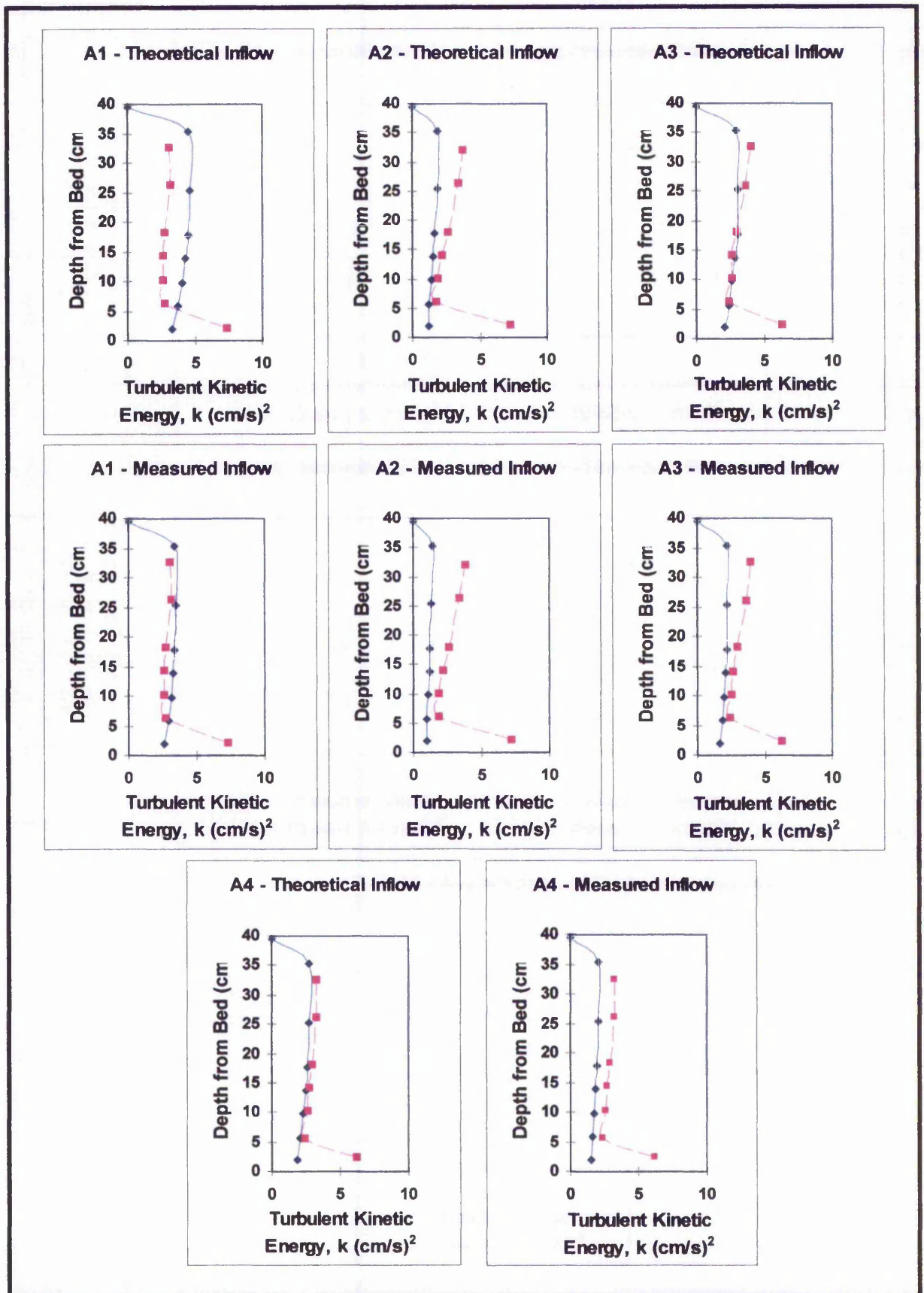
Figure 5.16 Turbulent kinetic energy for measured and theoretical inflow boundary. (Purple dotted line = Measured, Solid blue line = Calculated).

Figure 5.16 shows the prediction of the turbulent kinetic energy (TKE) measured using the ADV and predicted using SSIIM for both inflow boundary conditions. TKE was calculated as:

$$TKE = \frac{1}{2}(u'^2 + v'^2 + w'^2)$$ 5.22

Where:

u' = the RMS velocity x direction.

v = y direction

w = z direction

In can be observed that qualitatively, a good agreement was obtained at all positions and for both boundary conditions. However it should be noted that the ADV appeared to measure large TKE near the bed of the channel which was not predicted by SSIIM. Note also that it was not possible to measure quantities near to the surface of the flow using the ADV due to the orientation of the probe and the position of the sampling volume (55mm below the head of the probe). Quantitatively, TKE was generally predicted to better than 12% with the measured values. It appeared from the results that the inflow boundary condition had little effect on the values of TKE that were predicted using SSIIM.

Manning's Friction Coefficient 'n'

The Manning's formula was presented in 1889 by Robert Manning for calculating the flow in channels and is defined as:

$$Q = \frac{1}{n} \cdot \frac{A^{\frac{5}{3}}}{P^{\frac{2}{3}}} \cdot S_0^{\frac{1}{2}}$$ 5.23

Where:

n = Manning's friction coefficient

A = Cross sectional area of channel

P = Wetted perimeter of channel

S = Slope of channel

Q = Flow in channel.

Manning's formula is simple and it provides reasonably accurate results for a large range of natural and artificial channels, given that the flow is in the rough turbulent zone and that an accurate assessment of 'n' has been made. Values of n have been derived practically and empirically over many years and Table 5.5 gives typical values.

Channel Type	Surface material and alignment	'n'
River	Earth, straight	0.02 – 0.025
	Earth, meandering	0.03 – 0.05
	Gravel (75 – 150mm), straight	0.03 – 0.04
	Gravel (75 – 150mm), winding or braided	0.04 – 0.08
Unlined Canals	Earth, straight	0.018 – 0.025
	Rock, straight	0.025 – 0.045
Lined Canals	Concrete	0.012 – 0.017
Models	Mortar	0.011 – 0.013
	Perspex	0.009

Table 5.5   Typical values of Manning's 'n'.

The effect of the roughness of the model was tested by changing the Manning's n. The physical model was constructed using plastic coated wood ply sheeting for the base and inlet pier and plastic moulded panels for the side walls. It was therefore considered reasonable to use a Manning's 'n' of 0.009 in the computational model. A comparison Manning's 'n' of 0.012 (suitable for a concrete channel) was also tested in the computational model. These results are summarised in Tables 5.3 and 5.4 (tests 2 and 3). Figure 5.17 shows a selection of graphs from these two analyses.

Figure 5.17 shows a comparison between the results using a Manning's 'n' of 0.012 (test 3) and 0.009 (test 2). In every other detail the models were identical; Flow = 57 l/s, Depth = 395mm, Grid = 57 x 14 x 8, POW and GS schemes and measured boundary inflow conditions were used. The graphs of velocity in Vx at position A1 indicate that a slightly improved correlation was obtained when using a Manning's 'n' of 0.009 as opposed to 0.012 was used. A depth averaged Vx = 18cm/s was obtained using n = 0.012 as opposed to Vx = 22cm/s when using n = 0.009 which fell closer to the measured velocity profile. This trend was also observed at positions A2, A3 and A4.

In terms of Vy and Vz at positions A1 to A4 negligible improvements to the results were observed. These results are represented by graphs of Vy at A3 and Vz at A4 shown by Figure 5.17. Similarly, profiles of TKE at A2 shown by Figure 5.23 exhibit

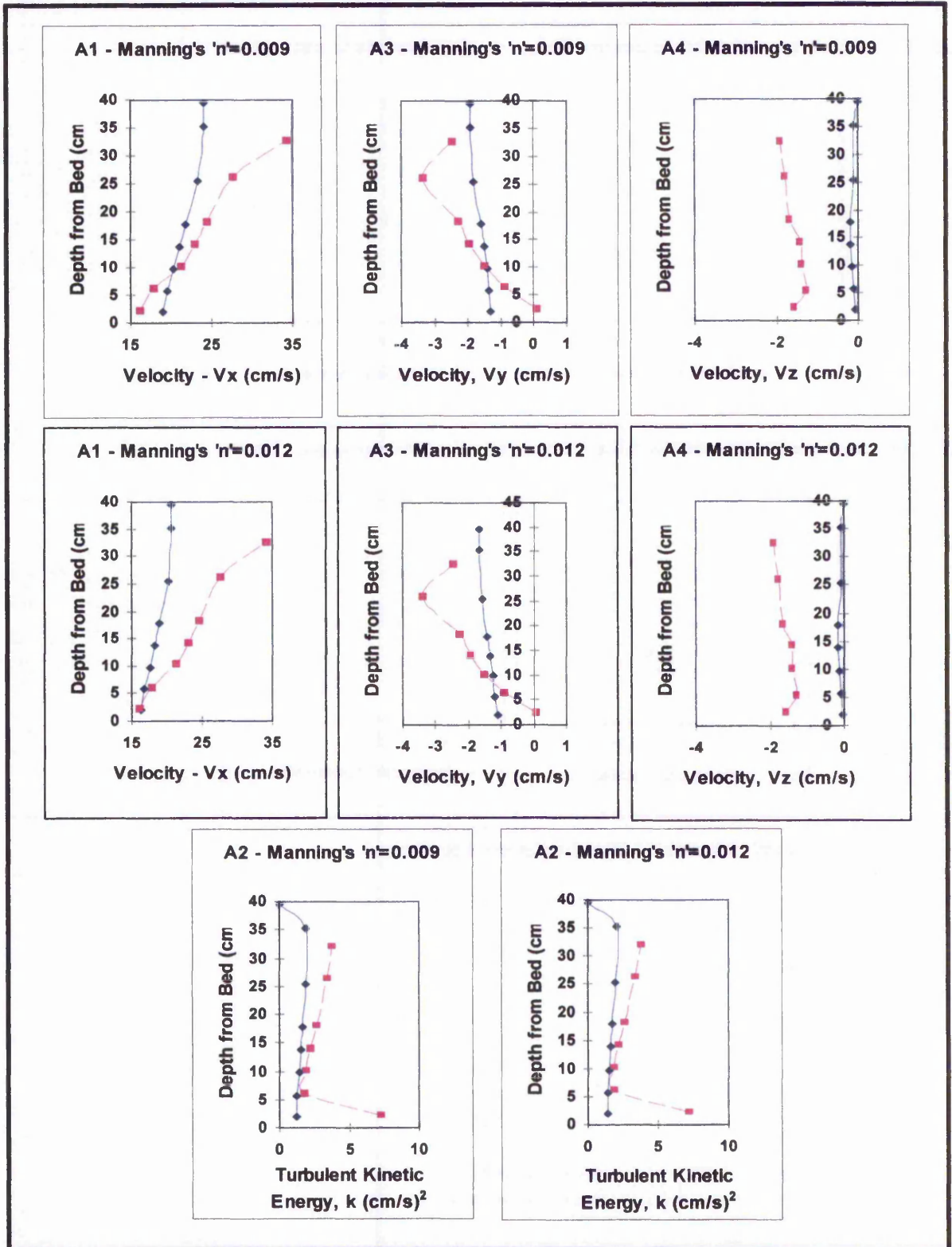**Figure 5.17   A selection of graphs from the Manning's 'n' analyses.**
(Purple dotted line = Measured, Solid blue = Calculated).

again that there were negligible differences between the results. Based upon the results obtained for Vx is was assumed that a Manning's 'n' of 0.009, corresponding to the friction coefficient for perspex, was more appropriate than 0.012, corresponding to the friction coefficient for concrete. This value of 0.009 was used in all subsequent validation tests.

5.4.2 Grid Dependency

Grid dependency was investigated in three ways. A comparison between the results of a Multiblock grid analysis of 91 x 11 x 8 and a standard grid analysis of 113 x 27 x 8 was undertaken (Tables 5.3 and 5.4, tests 13 and 7 respectively). A comparison between 4 computational grids of identical cells in the horizontal plane but with four variations of layers in the vertical plane were undertaken. These combinations comprised of 4 (test 4), 8 (test 2), 12 (test 5) and 16 (test 6) layers to assess the effects on results with increased density of grid cells in the vertical direction. Finally a Richardson's Extrapolation exercise was undertaken on four grids where the number of grid cells was doubled in the horizontal and vertical planes. Doubling the grid cells in the horizontal direction were represented by test 6 (57 x 14 x 16) and test 14 (113 x 27 x 16). Doubling the grid cells in the vertical direction were represented by test 3 (57 x 14 x 8) and test 6 (57 x 14 x 16).

Multiblock vs Standard Grid

The structure of the Multiblock grid and its advantages have been discussed earlier in this chapter. An analysis using the Multiblock grid was compared to a standard grid analysis. The results are presented in Tables 5.3 and 5.4. Figure 5.18 also shows graphical outputs from these analyses. At positions A1 to A4 the Multiblock grid over predicts Vx, to a lesser extent at A1 but to a greater extent at A2, A3 and A4. Quantitatively the over prediction by the Multiblock grid at A2, A3 and A4 is approximately 60%. However the over prediction at A1 is around 11%. The prediction using the standard grid is significantly closer to the measured values of Vx.

In Vy again the predicted values at A1 correlate closely between the Multiblock grid and the standard grid but at A2, A3 and A4 the agreement exhibits similar errors as in Vx. Generally the standard grid performed better than the Multblock grid in terms of prediction of the measured values. The profile at A4 is not shown in this instance.
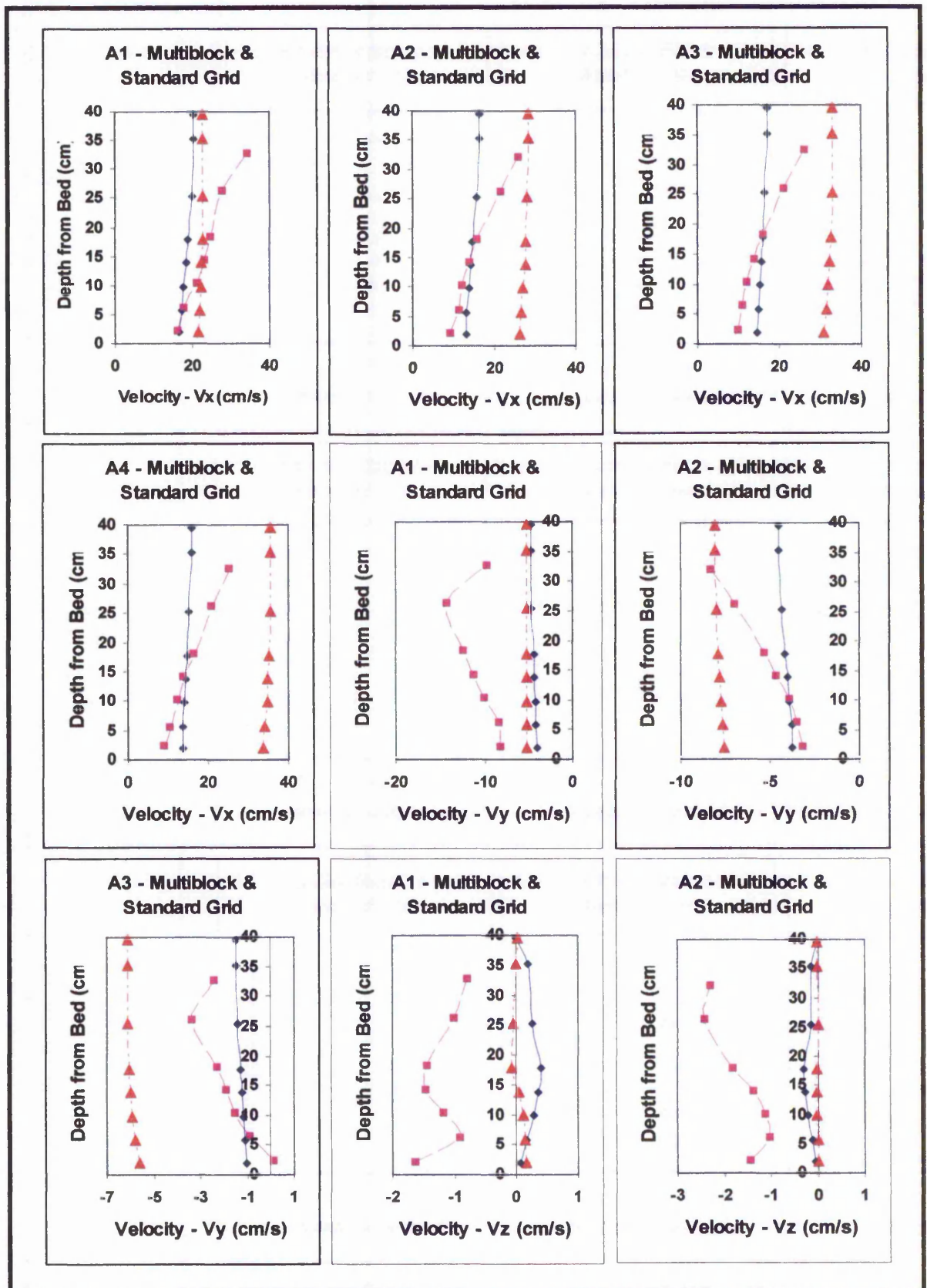
Figure 5.18 A selection of graphs from the Multiblock analyses. (Blue solid line = calculated standard grid, red dotted line, triangular symbols = calculated Multiblock grid)

because it exhibited similar features.

In Vz both the Multiblock grid and the standard grid failed to predict accurately the measured values of Vz in the physical model. However, apart from at A1 the standard grid predicted the measured values of Vz more closely.

For this validation test only the type of grid was changed. No other parameters were altered and therefore it can be concluded that the standard grid performed more accurately than the Multiblock grid. In addition, the proportion of the flow entering the inlet channel must be specified when using the Multiblock grid. This flow was calculated based on the mean flow in the inlet channel calculated from ten analyses using the standard grid. However, the convergence time using the Multiblock grid was considerably reduced to 5 hours 30 minutes in contrast to 18 hours using the standard grid. This was one of the main advantages of using the Multiblock grid. It was therefore decided to use the standard grid in all subsequent analyses, due to the improved accuracies obtained.

Layers of cells in the vertical plane

Figure 5.19 shows the results in terms of percentage errors between the predicted velocities (in Vx) using SSIIM and the measured velocities at two levels in the flow at positions A1 to A4 with increased number of layers in the z direction.
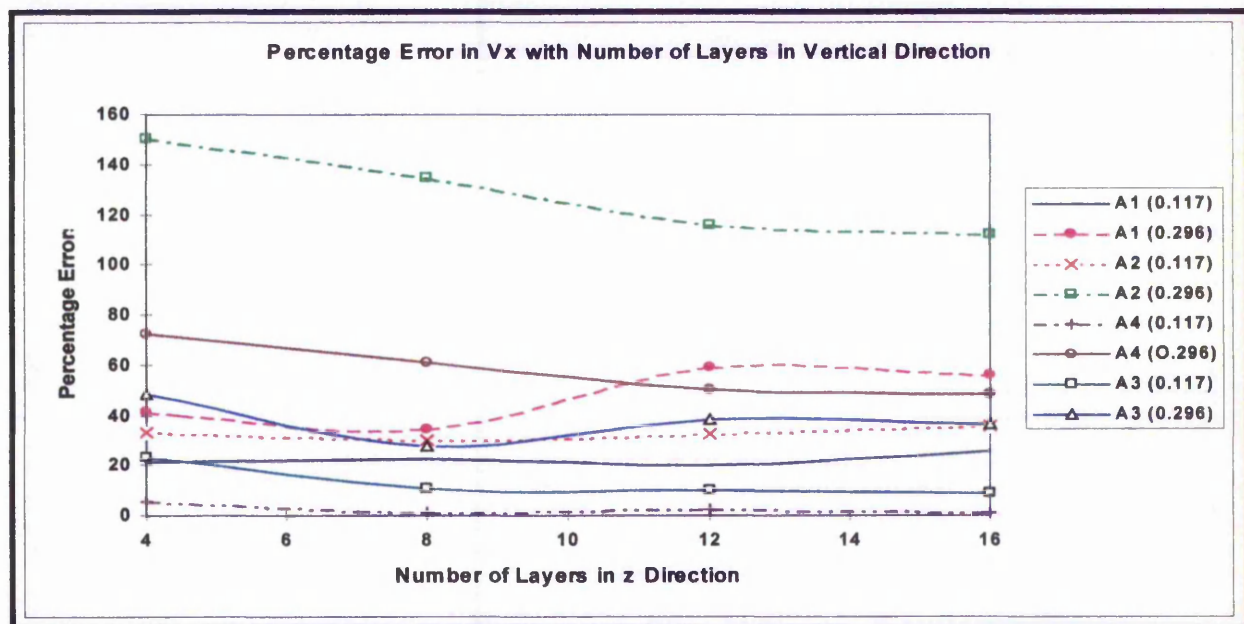
Figure 5.19   Percentage error in Vx with number of layers in the vertical direction.

The numbers in parentheses next to the measurement positions in the legend represent the depth in metres from the bed. It can be seen that the general trend was an improvement in terms of percentage errors with increased layers in the vertical direction.

Richardson's Extrapolation

Richardson's Extrapolation, also known as h^2 extrapolation, the deferred approach to the limit and iterated extrapolation, was first used by Richardson in 1910 and later modified in 1927. The discrete solutions to a variable f are assumed to have a series representation, in the grid spacing h, of:

$$f = f\ (exact) + g_1\,h + g_2\,h^2 + g_3\,h^3 + \dots\dots \qquad 5.24$$

Where:

g = Functions of the variable

h = Grid spacings

From this basic principle Richardson error estimators have been derived in order to approximate the uncertainty in numerical simulations based upon the grid spacings of the domain (Roache 1997). Thus, the Richardson error estimator for a fine grid solution f_1, by comparing this solution to that of a coarse grid, f_2 and can be defined as:

$$E_1^{FINE} = \frac{\varepsilon}{1-r^P} \qquad 5.25$$

The coarse grid Richardson error estimator approximates the error in a coarse grid solution, f_2, by comparing the solution to that of a fine grid, f_1 and can be defined as:

$$E_2^{COARSE} = \frac{r^P \varepsilon}{1-r^P} \qquad 5.26$$

Where:

$\varepsilon = f_2 - f_1$

f_2 = a coarse grid numerical solution obtained with a grid spacing of h_2

f_1 = a coarse grid numerical solution obtained with a grid spacing of h_1

r = refinement factor between the coarse and fine grid ($r = h_2\,/\,h_1 > 1$)

p = formal order of accuracy of the algorithm.

P is usually 1 or 2 depending on whether a first order or second order accurate algorithm is used. However, Roache states that P should be calculated from the solutions obtained from three different grid solutions of constant r using the following formula:

$$P = \ln\left(\frac{f_3 - f_2}{f_2 - f_1}\right) / \ln(r) \qquad\qquad 5.27$$

Where:

f_1 = solution from the finest grid

f_3 = solution from the coarsest grid.

For the purposes of grid convergence studies three tests were used to quantify P and the numerical uncertainty in Vx with increasing numbers of layers in the vertical direction; test 4 = 57 x 14 x 4 grid, test 2 = 57 x 14 x 8 grid and test 6 = 57 x 14 x 16. Here the grid refinement ratio, r, in the vertical direction was 2. Subsequently a grid convergence study was undertaken on two further tests to quantify the numerical uncertainty in Vy with grid doubling (r=2); test 2 = 57 x 14 x 8 grid and test 14 = 113 x 27 x 16. Analyses were undertaken at 5 levels in the vertical profile at positions A1, A2, A3 and A4. A sample calculation is shown as follows:

At position A1, depth from bed = 0.296m, Vx:

f_1 = test 14 – Vx = 0.199 m/s

f_2 = test 2 – Vx = 0.206 m/s

f_3 = test 4 – Vx = 0.195 m/s

$$P = \ln\left(\frac{f_3 - f_2}{f_2 - f_1}\right) / \ln(r)$$

5.28

$$P = \ln\left(\frac{0.195 - 0.206}{0.206 - 0.199}\right) / \ln(2)$$

P = 0.652 (1st order accurate)

$$E_1^{FINE} = \frac{\varepsilon}{1 - r^P} \quad \text{using tests 2 and 6}$$

$$E_1^{FINE} = \frac{(0.206 - 0.199)}{1 - 2^{0.652}}$$

$$E_1^{FINE} = -0.012 = 1.2\%$$

$$E_2^{COARSE} = \frac{2^{0.652} \times 0.007}{1 - 2^{0.652}}$$

$$E_2^{COARSE} = -0.019 = 1.9\%$$

Tabulated results of the grid convergence study at A1 to A4 are shown by Tables 5.6 and 5.7.

Position	Depth (m)	f_1 (cm/s)	f_2 (cm/s)	f_3 (cm/s)	P	E_1^{FINE} (%)	E_2^{COARSE} (%)
A1	0.020	0.163	0.170	0.164	0.22	-4.20	-4.90
A1	0.100	0.174	0.181	0.175	0.22	-4.20	-4.90
A1	0.200	0.187	0.197	0.184	0.38	-3.33	-4.33
A1	0.296	0.199	0.206	0.195	0.65	-1.23	-1.93
A1	0.395	0.205	0.208	0.195	2.11	-0.09	-0.39
A2	0.020	0.083	0.087	0.085	1.00	-0.40	-0.80
A2	0.100	0.088	0.092	0.090	1.00	-0.40	-0.80
A2	0.200	0.097	0.101	0.096	0.32	-1.60	-2.00
A2	0.296	0.103	0.108	0.103	0.1	-6.96	-7.47
A2	0.395	0.107	0.110	0.103	1.22	-0.23	-0.53
A3	0.020	0.138	0.145	0.139	0.22	-4.20	-4.90
A3	0.100	0.144	0.151	0.143	0.19	-4.90	-5.60
A3	0.200	0.152	0.160	0.150	0.32	-3.20	-4.00
A3	0.296	0.160	0.166	0.158	0.41	-1.80	-2.40
A3	0.395	0.163	0.169	0.158	0.88	-0.72	-1.32
A4	0.020	0.129	0.135	0.130	0.26	-3.00	-3.60
A4	0.100	0.135	0.140	0.135	0.10	-6.97	-7.47
A4	0.200	0.142	0.149	0.140	0.36	-2.45	-3.15
A4	0.296	0.149	0.155	0.147	0.42	-1.80	-2.40
A4	0.395	0.151	0.158	0.147	0.66	-1.23	-1.93

Table 5.6   Grid convergence results using tests 4, 2 and 6 with r = 2.

Table 5.6 shows that a range of values of P were obtained from 0.1 to 2.11. However, according to Barron and Latypov (1995) it is reasonable to calculate the average value of P, here equal to 0.55 (<1) then the algorithm can be assumed to be first order accurate. In subsequent analyses, P = 1. The table also gives the calculated uncertainties in Vx of the coarse and fine grid.

Position	Depth (m)	f_1 (cm/s)	f_2 (cm/s)	P	E_1^{FINE} (%)	E_2^{COARSE} (%)
A1	0.020	0.127	0.170	1	-4.30	-8.60
A1	0.100	0.173	0.181	1	-0.70	-1.40
A1	0.200	0.182	0.197	1	-1.50	-3.00
A1	0.296	0.192	0.206	1	-1.40	-2.80
A1	0.395	0.197	0.208	1	-1.10	-2.20
A2	0.020	0.063	0.087	1	-2.44	-4.88
A2	0.100	0.125	0.092	1	-3.30	-6.60
A2	0.200	0.145	0.101	1	-4.40	-8.80
A2	0.296	0.153	0.108	1	-4.50	-9.00
A2	0.395	0.158	0.110	1	-4.82	-9.64
A3	0.020	0.117	0.145	1	-2.80	-5.60
A3	0.100	0.146	0.151	1	-0.50	-1.00
A3	0.200	0.168	0.160	1	-0.80	-1.60
A3	0.296	0.178	0.166	1	-1.20	-2.40
A3	0.395	0.183	0.169	1	-1.45	-2.90
A4	0.020	0.104	0.135	1	-3.10	-6.20
A4	0.100	0.122	0.140	1	-1.82	-3.64
A4	0.200	0.142	0.149	1	-0.72	-1.44
A4	0.296	0.152	0.155	1	-0.30	-0.60
A4	0.395	0.158	0.158	1	0	0

Table 5.7   Grid convergence results using tests 2 and 14, r = 2, P = 1.

The results shown by Table 5.7 can be further illustrated by Figure 5.20 which shows the graphs of the uncertainty in the coarse and fine grids at positions A1 to A4 using the computational grids of tests 2 and 14.
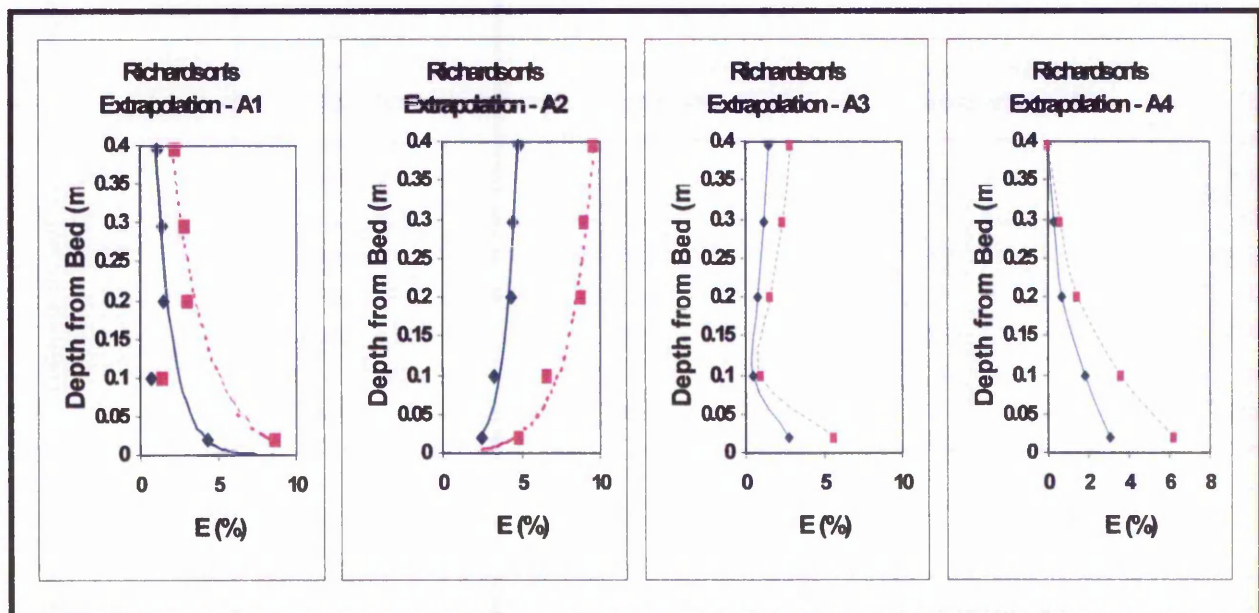

Figure 5.20   Graphs of Uncertainty in Vx from Richardson's Extrapolation at A1 to A4. (Blue solid line = fine grid, purple dotted line = coarse grid).

The graphs contained in Figure 5.25 show that at positions A1 to A4 the fine grid of 113 x 27 x 16 cells had the lowest uncertainty error. The uncertainty error of the grid was a minimum of approximately 1.2% at A4 and a maximum of approximately 4% at A2. The uncertainty error in the coarse grid was a minimum of approximately 3% at A3 and a maximum of approximately 8% at A2. Notice also that the value of the error varies with depth from the bed.

The value of ε derived in the formulae for Richardson's extrapolation, may be accepted as an error band provided that all grid convergence studies are performed using the same grid refinement ratio, r and the methods are of the same order, P. This is a very restrictive condition which is not always possible to implement. One way to overcome this difficulty is to 'scale' the error estimates obtained from grid refinement studies performed with arbitrary values of r and P to values of these error estimates corresponding to some 'reference' values of r and P. Reference values of r=2 and P=2 are suggested by Roache (1997). Using this principle Roach derived the Grid Convergence Index (GCI) where:

$$GCI = \frac{3 \, |\varepsilon|}{r^P - 1}$$

5.29

which is effectively the same as $3 \times E_1^{FINE}$. The GCI effectively imparts a factor of safety of 3 onto the error. Using Roach's GCI therefore and applying it to the fine grid the following error estimators were found for the grid convergence studies:

Position	Mean E_1^{FINE} (%)	GCI
A1	1.8	5.4
A2	3.9	11.7
A3	1.4	4.2
A4	1.2	3.6

5.4.3 Numerical Schemes

POW and SOU

Two of the numerical schemes that were tested in the validation analyses were the SOU and POW schemes (see section 5.2.4). In the POW scheme, ϕ_e (the east face

of the cell where the variable is being calculated) is determined using the upwind scheme ($\phi_e = \phi_E$ i.e. the value at the eastern node for the flow into the cell and $\phi_e = \phi_P$ for flow out of the cell) but the diffusive flux is reduced by a factor which is dependent on the Peclet number. The Peclet number is the ratio of convection to diffusion representing the relative significance of these two parameters. At high Peclet numbers, convection predominates and diffusive flux is zero. High Peclet numbers were present in the model for these analyses. The POW scheme is therefore accurate and stable where the flow is aligned to the grid. The POW scheme is a first order accurate scheme.

However the POW scheme is highly susceptible to false diffusion. False diffusion is numerical diffusion which increases with the size of the grid and occurs where the flow is not aligned to the grid. The effects of false diffusion may be reduced by refining the grid but the computational time and memory requirements are considerably increased. Alternatively, false diffusion can be reduced by using the SOU scheme in which ϕ_e is determined from the linear extrapolation of the two cells upwind of the face (e). Thus for flow out of the cell $\phi_e = \phi_P + 1/2\,(\phi_P - \phi_W)$ and for flow into the cell $\phi_e = \phi_E + 1/2\,(\phi_E - \phi_{EE})$ where ϕ_{EE} is the value of ϕ two cells to the east of the current cell. However, the SOU scheme is less stable than the POW scheme and more computationally intensive for the same grid size. Thus where the flow is aligned to the grid, the POW scheme is preferred.

Therefore the SOU scheme should give improved results in regions of recirculation such as positions A1 or A2. The SOU scheme is also second order accurate which should result in more accurate results. Tests were conducted using SOU, POW and two mixed schemes where SOU was used for the solution of velocity, POW was used for the solution of pressure and k and ε and vice versa (tests 12, 2, 8 and 9 respectively, Tables 5.3 and 5.4).

Figure 5.21 shows the variation in Vx and Vy with the various numerical schemes. It is shown that at position A1 the choice of numerical scheme appears to have little effect upon the results obtained in Vx, with all the results, irrespective of numerical scheme, lying on the same profile. This is perhaps as expected, since A1 lies in a

position in the domain where the flow is aligned with the grid. Also high velocity gradients were not measured in this region and there was no recirculation evident.
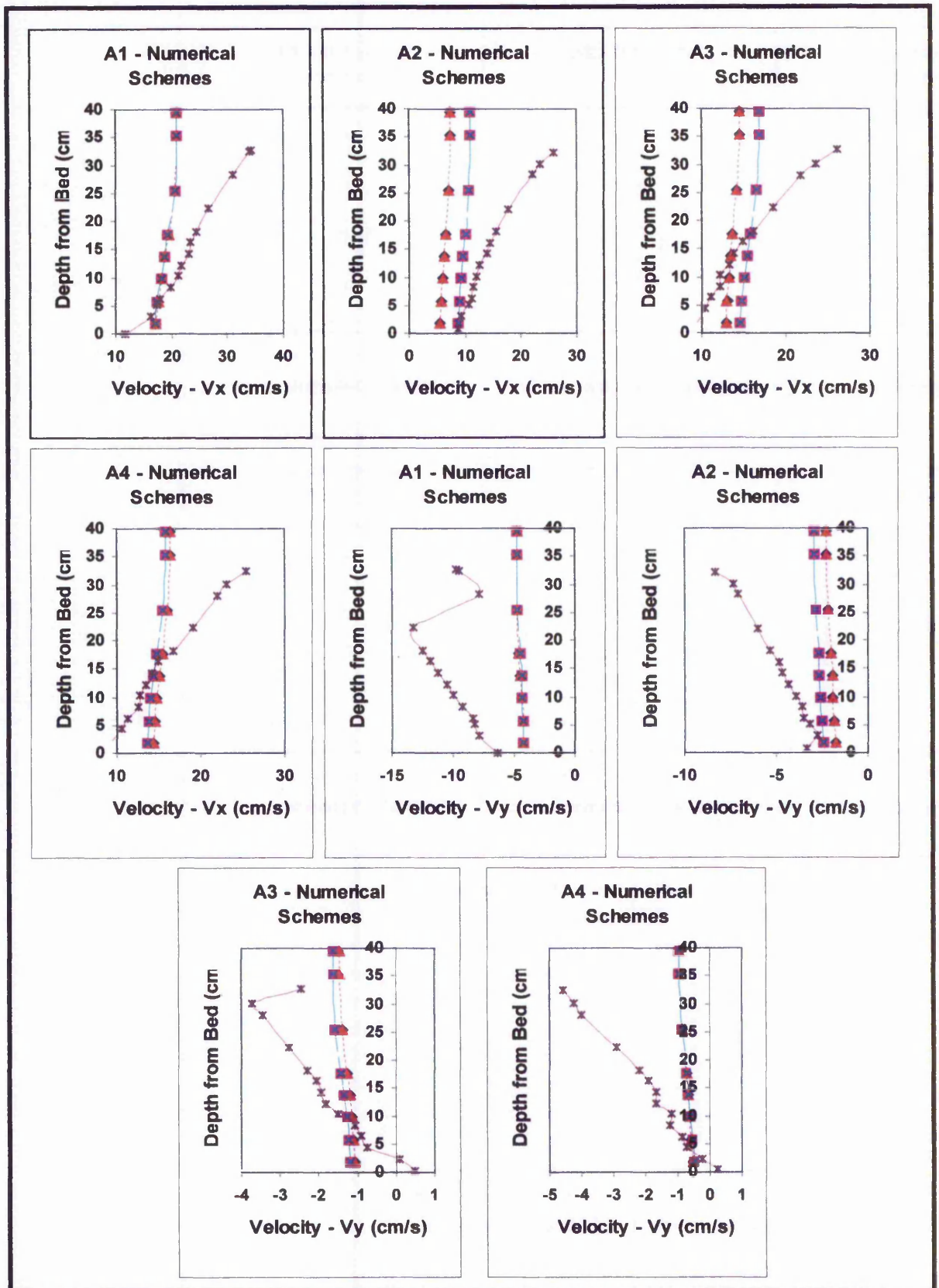

Figure 5.21 Graphs to show the variation in Vx and Vy with numerical schemes.

(Dk blue diamond = POW, purple square = SOU, red triangle = POW/SOU, light blue cross = SOU/POW.)

However points at which re-circulation was likely to occur and in an area of high velocity gradients at points A2 and A3 the results were different. It is shown in Figure 5.26 that the SOU schemes (light blue crosses = SOU / POW and purple squares = SOU) predicted Vx more successfully than the POW schemes. The SOU scheme generally predicted velocities in Vx approximately 60% more accurately at A2 and 25% more accurately at position A3. At A4 the numerical scheme selected, again appears to have a negligible effect on the results obtained. At A4 the flow structure was less complex than A2 and A3 and the flow was aligned to the grid more closely. It should also be noted that with all the numerical schemes the results under predicted the measured results.

In terms of Vy, similar characteristics to Vx were observed. At A1 the choice of numerical scheme appeared to have had a negligible influence on the results obtained. At A2 and A3 improved results were again observed when the SOU scheme was used to predict velocity in preference to the POW scheme. The improvement in accuracy when using the SOU scheme approximated to 45% and 20% at A2 and A3 respectively. At A4 the choice of numerical scheme had a negligible effect upon results. In similarity with Vx the numerical schemes under predicted Vy in comparison with the measured values at every point. Tables 5.3 and 5.4 quantify this under prediction.

Figure 5.22 shows turbulent kinetic energy, k, profiles at positions A1 to A4 with the numerical schemes adopted. The results at A1 show that the choice of numerical scheme has a negligible effect upon the results obtained although a close agreement between the measured and predicted values of k was obtained for all the numerical schemes used. At A2, A3 and A4 extremely close agreement was obtained when the POW scheme (purple squares and light blue crosses in Figure 5.22) was used for the prediction of k. The SOU scheme under predicted k at A2 and over predicted k at A3 and A4.

Thus the trend observed was that the mixed scheme of SOU for velocities and POW for k and ε achieves the lowest percentage errors. This is in agreement with another validation study undertaken using SSIIM by Seed (1997).
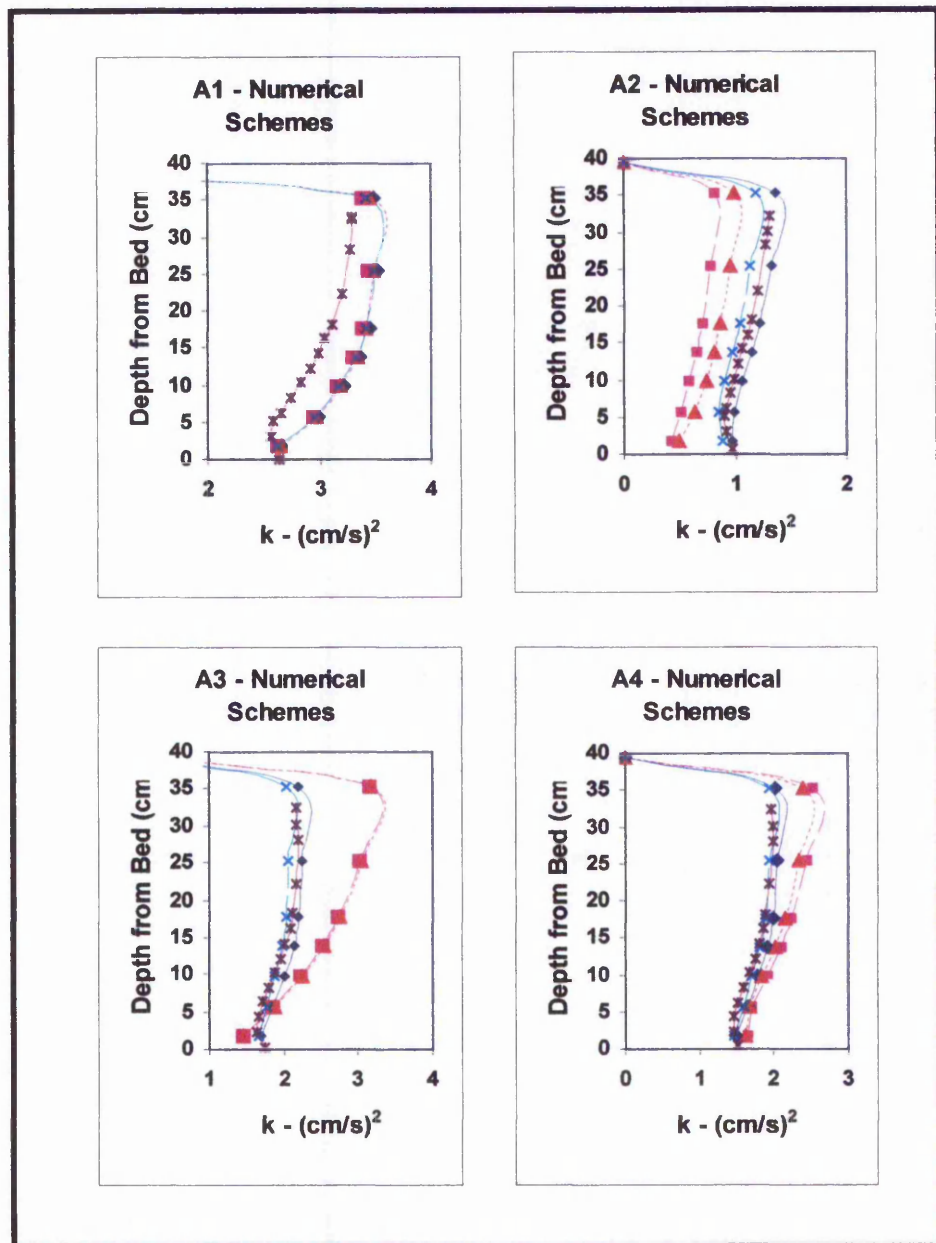
Figure 5.22   Graphs to show the variation in turbulent kinetic energy, k with the numerical schemes.

(Dk blue diamond = POW, purple square = SOU, red triangle = POW / SOU, light blue cross = SOU / POW).

SIMPLE and SIMPLEC

Two options are available in SSIIM for the solution of the pressure – velocity coupling. These are the SIMPLE and SIMPLEC algorithms. The SIMPLE family of algorithms is based on using a relationship between velocity and pressure corrections. This relationship is derived from the momentum equation. In these

methods an assumed pressure field is used to determine a predicted velocity field. The above relationship, combined with the continuity equation is used to calculate corrections for the velocity and pressure fields. The system of equations is then solved iteratively. SIMPLE is used by default in SSIIM but problems in which convergence is limited by pressure – velocity coupling can converge more quickly using SIMPLEC. This method has been found to be successful by other researchers. Seed, however, found that the convergence rates were mostly limited by other factors, particularly the convergence of k and ε. Thus he used the more robust scheme, SIMPLE in his validation study.

In this validation study it was found that SIMPLEC caused the solutions to diverge in all cases, despite altering the relaxation factors. Therefore only the SIMPLE scheme was used for all the cases in this validation.

Matrix Solution Method

At this stage it is appropriate to summarise the iterative procedure that SSIIM uses to solve the equations of fluid flow. The numerical scheme reduces the nonlinear, simultaneous, differential equations of fluid flow to a set of simultaneous matrix equations. The matrix equations are solved by an iterative scheme which starts from arbitrary initial conditions, except at boundaries, and converges to a solution after performing a number of iterations. The main steps can be summarised as follows:

- The u, v, w momentum equations are each solved in turn using current values for pressure, in order to update the velocity field.
- The 'pressure correction' equation is then solved using the SIMPLE or SIMPLEC equations to obtain the corrections to the pressure and velocity fields.
- The k and ε equations are solved using the updated velocity field.
- The water surface is updated if required.
- The above steps are repeated until convergence is reached (i.e when all the equations are solved to sufficient accuracy).

Within the above iterative procedure, SSIIM also uses iterative techniques to obtain an approximate solution to each of the matrix equations. In large systems, solving equations iteratively requires less effort than solving them directly. One technique used by SSIIM is the line by line solution technique, known as the Line Gauss Seidel

(LGS) method. In LGS, the equations are solved simultaneously for each line of cells, where a line is a complete row or column of cells. During the solution of a line, the neighbouring lines are treated as correct and kept constant. The solution of all lines in the x, y and z directions is referred to as a 'sweep' of the solver. SSIIM provides the facility to specify the number of sweeps performed for each equation. The default number of sweeps is set at 5 for the pressure correction equation and 1 for the other equations. However, the facility for altering the number of sweeps was not tested as part of this validation study.

Another technique used by SSIIM is the Tri-diagonal matrix algorithm (TDMA) developed by Thomas (1949). The TDMA is actually a direct method for one-dimensional situations but it can be applied iteratively in a line by line fashion, to solve multi-dimensional problems and is widely used in CFD programs. It is computationally inexpensive and has the advantage that it requires the minimum amount of storage. For further details on LGS and TDMA see Versteeg and Malalasekera (1995).

For thirteen of the tests conducted as part of this study, the LGS algorithm was used. For comparison, one test was conducted using the TDMA. Theoretically the results should be identical but it was considered necessary to confirm this. Test 10 in Table 5.3 and 5.4 using the TDMA shows the differences with an almost identical test 2 but which uses the LGS algorithm. The results in terms of the variables were confirmed to be identical but the convergence time using the TDMA was vastly extended from the convergence time using LGS. The TDMA solution took approximately eight times longer to converge using 11414 iterations as opposed to 695 iterations when the LGS algorithm was used. This is in contradiction to the theory that the TDMA is computationally inexpensive and this extension in convergence time may be due to a 'bug' in SSIIM.

Relaxation Factors

Due to the non-linearity of the equations being solved, it is not generally possible to obtain a solution by fully substituting the 'improved' values for each variable which have been generated by the approximate solution of the matrix equations. Convergence can be achieved by under relaxation which reduces the difference between the old and new values of the variable from successive iterations. Thus:

$$\phi_{NEW} = \phi_{OLD} + (\delta\phi \times R) \hspace{3cm} 5.30$$

Where:

ϕ = Variable

$\delta\phi$ = Computed change of the var iable

R = Relaxation factor.

In SSIIM the default values for the relaxation factors are 0.8 for the velocities, 0.2 for pressure and 0.5 for turbulence (k and ε). In the validation tests described here, it was necessary to reduce the relaxation factors to 0.5 for the velocities, 0.1 for pressure and 0.3 for turbulence. In one test (10), when the TDMA was used, it was necessary to further reduce these factors to 0.3, 0.1 and 0.1 respectively deduced iteratively, to achieve convergence. In tests conducted after the validation study was completed (chapters 7 and 8) it was necessary to reduce the relaxation factors still further to 0.1, 0.02 and 0.1. In general, lower relaxation factors gave less instabilities during convergence, but resulted in slower convergence. Higher relaxation factors gave more rapid convergence if there were no instabilities. Sometimes the relaxation factors may be changed during the calculations. If the solution diverges after the first few iterations, it is possible to set the relaxation factors very low and then increase them for the subsequent iterations. It was found, however, during this validation study that the process of setting relaxation factors was often an iterative process.

Block Correction

SSIIM provides an optional block correction procedure for accelerating the convergence of the POW scheme. The block correction technique (Pantakar 1980), speeds up convergence by applying a quasi one dimensional correction to the current solution field in order to satisfy global conservation. The global conservation disappears as the local convergence is achieved throughout the domain. Theo one dimensional grid is made by summing the values in the other two directions. Then an iteration is performed on the one dimensional grid and a correction applied to all points in each layer. This is repeated in all three directions. Further details of block correction were given earlier in this chapter in the model overview (section 5.2).

Block correction usually gives greater stability and better convergence. It reduces long wavelength errors in the direction where they are applied but may introduce

large short wavelength errors. In particular problems occurred when the geometry was blocked out, which was typically the case when modelling the inlet pier. The initial tests showed that although block correction gave accelerated convergence during the early part of the solution, subsequently the solution would oscillate and usually diverge. This could only be avoided by examining the convergence and adjusting parameters leading to the solution, carefully throughout the duration of the run. Several of the runs were undertaken overnight and obviously constant attendance was not possible. Block correction was therefore not used in the validation study. Block correction should not alter the results, merely reduce convergence times.

Water Surface

There were three options available in SSIIM for the solution of the free water surface. The free surface was modelled using a 'rigid lid' approach where the vertical accelerations cause variations in surface pressure. The initial position of the surface is determined by a standard step, backwater calculation.

For a more accurate representation of the surface, it was possible to adjust the position of the surface so that the surface is located where the pressure equates to zero. The effect of this adjustment was to slightly modify the height of the water column in the cells nearest to the surface and thus modify the strength of the velocities. The significance of this was dependent on the square of the Froude number. For this validation study the Froude number was 0.12 and hence the effect of the water surface update was negligible, shown by the results of test 11 (Tables 5.3 and 5.4). In addition the inclusion of the water surface update significantly increased convergence times.

The third option available for the solution of the free water surface was a surface update including an allowance for gravity. A solution using this third option could not be obtained and therefore this option was not used in subsequent validation studies.

5.4.4 Model Convergence

Tables 5.3 and 5.4 list the convergence times of the 14 computational tests undertaken and the iterations taken to reach convergence. The criteria used by SSIIM to signify convergence are when all the residuals to the calculated variables,

Vx, Vy, Vz, pessure, k and ε are below a certain level. Thus the residuals of a numerical scheme are a measure of how close the model is to convergence. At any node, the residual is the difference between the old and new values. When using
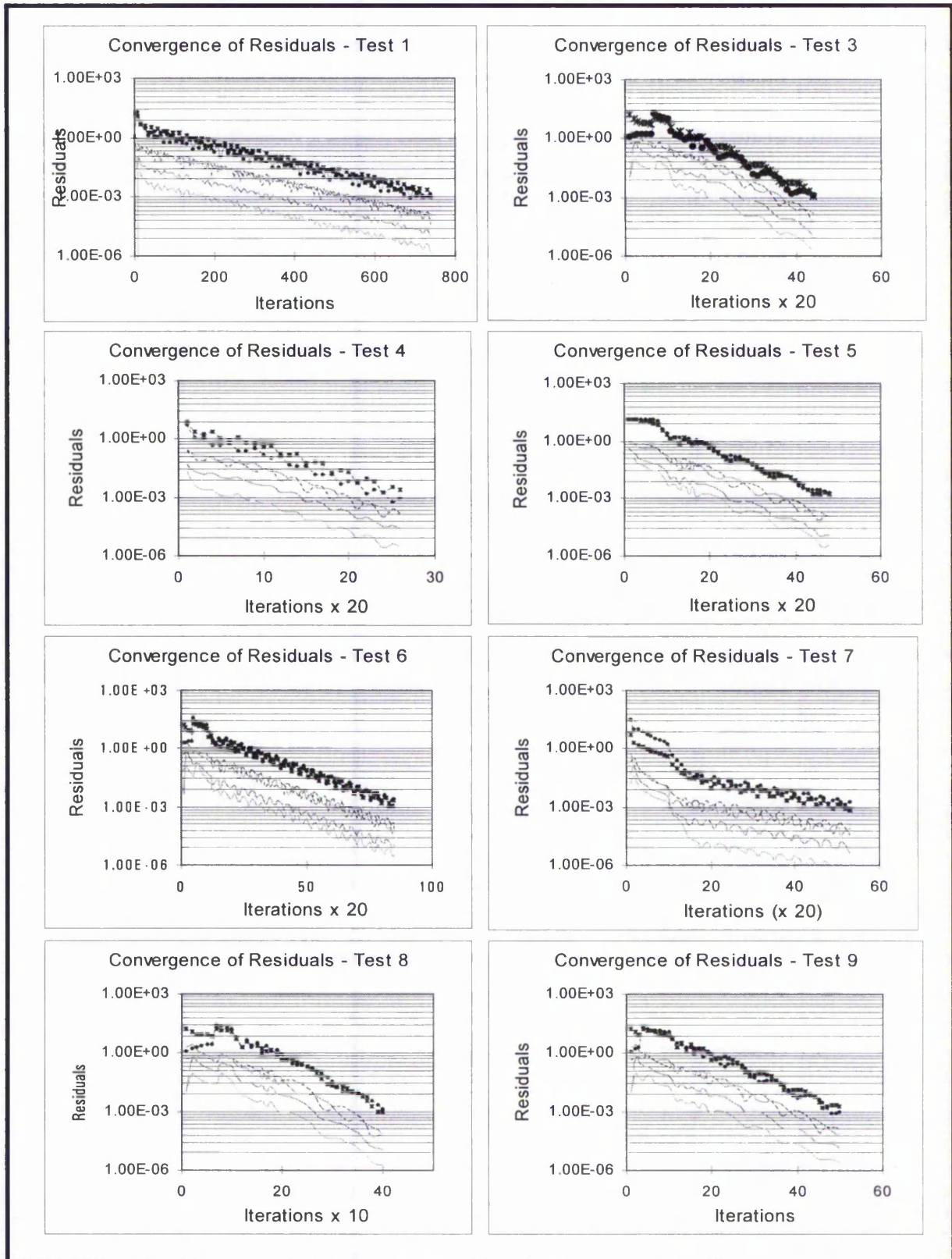

Figure 5.23   Convergence graphs for tests 1, 3, 4, 5, 6, 7, 8 and 9.

residuals to test for convergence an average residual is used and this is normalised with reference to the characteristic flux entering the domain. The convergence criterion for SSIIM is that all the normalised residuals are less than 10^{-3}. After the first 10 – 20 iterations the residuals should decrease steadily. A plot of the log of the residuals against the number of iterations should decrease approximately linearly if convergence is to be reached after an acceptable time. Figure 5.23 shows a selection of convergence graphs from the study. Other possibilities are:

- The model diverges.
- The residuals fall and rise.
- The residuals fall monotonically but one or more of the residuals falls very slowly.

The reasons for non-convergence were usually that the grid was too coarse or uneven, an unstable flow pattern, or a numerical method (such as block correction) that should not be applied. A slower but more stable reduction in residuals was achieved by reducing the relaxation factors. This was done in increments of 0.05 or 0.1 and was applied to the equations that had non-convergent residuals, typically the k and ε equations.

With reference to the graphs of Figure 5.23 it should be noted that oscillations in the convergence of the residuals occurred in every test, although there was a general linear trend to the decrease in residuals with the number of iterations. The order of convergence in nearly every case was Vz, Vy, Vx, pressure, ε and k, in terms of the first variable to converge. The rate of convergence of Vz and Vy was reasonably closely correlated with the convergence of pressure and Vx very closely correlated. Similarly the convergence of k and ε were also closely correlated. Increasing the cells (doubling) in the horizontal plane appeared to increase the rate of convergence considerably near the start of the simulation (test 7) but invariably the total time to convergence exceeded that of a grid with fewer cells (test 6).

The mixed schemes of SOU/POW and POW/SOU appeared to increase convergence times with the POW/SOU scheme taking more iterations (SOU/POW = SOU for Vx, Vy and Vz, POW for k and ε). In addition more instabilities in the solution were observed at the beginning of the simulation when these two mixed

schemes were used. The SOU scheme is second order accurate, using more neighbouring cells in the computational algorithm and the POW scheme is first order accurate using fewer cells in the computational algorithm. This explains the extended convergence time experienced when using the SOU scheme (see test 11 – POW and test 12 - SOU).

5.5 UNCERTAINTY ANALYSES

The previous sections have given details of the various validation and verification studies that were undertaken using SSIIM. This section summarises the results of this chapter and combines the results with the results and findings of chapter 4, ADV calibration. Recently, a new approach to CFD validation has been developed that gives proper consideration to experimental and simulation uncertainties. The summary given by this section follows this approach of Coleman and Stern (1997).

5.5.1 Uncertainties in Data and in Simulation

Uncertainty in experimental data comes from both bias (systematic) and precision (random) sources. However, the uncertainty is transformed into a fixed quantity (a bias) once the value of the data point is recorded and reported. Uncertainties associated with predictions from simulations can be divided into two broad categories: (1) Numerical uncertainties and (2) modelling uncertainties. Numerical uncertainty includes uncertainties due to the numerical solution of the mathematical equations (discretisation, iterative and grid non-convergence, non-conservation of mass, momentum and energy etc.) Modelling uncertainty includes uncertainties due to assumptions and approximations in the mathematical representation of the physical process (geometry, mathematical equation, free surface boundary conditions, turbulence models etc.) and also uncertainties due to the incorporation of previous experimental data into the model (fluid properties and constants).

The overall process leading to validation and simulation uncertainty estimation can be categorised as documentation, verification and validation. Verification involves estimation of numerical uncertainty through parametric, convergence and order of

accuracy studies. Validation involves estimation of the difference (error) between the simulation's prediction and the truth.

CFD Code Validation

The comparison error E can be defined as:

$$E = D - S \qquad\qquad 5.31$$

Where:

D is the experimentally determined value of the variable.

S is the simulation determined value of the variable.

The comparison error E is the resultant of all the errors associated with the experimental data and the simulation. Coleman and Stern state that the simulation uncertainty can be represented as:

$$U_S^2 = U_{SN}^2 + U_{SPD}^2 + U_{SMA}^2 \qquad\qquad 5.32$$

Where U_{SN} is the simulation numerical uncertainty, U_{SPD} is the simulation modelling uncertainty arising from previous experimental data and U_{SMA} is the simulation modelling uncertainty arising from modelling assumptions. U_{SMA} cannot be estimated thus it is better to define validation uncertainty U_V as the combination of all uncertainties than can be estimated:

$$U_V^2 = U_E^2 - U_{SMA}^2 = U_D^2 + U_{SN}^2 + U_{SPD}^2 \qquad\qquad 5.33$$

If $|E|$ is less than U_V then the combination of all the errors in D and S is smaller than the estimated validation uncertainty and validation has been achieved at the U_V level. Also U_{SPD} is assumed negligible relative to other uncertainties.

Determination of the simulation numerical uncertainty, U_{SN} can be defined as:

$$U_{SN}^2 = U_{SI}^2 + U_{SG}^2 + U_{SAD}^2 \qquad\qquad 5.34$$

Where:

U_{SI} = Uncertainty for iterative convergence

U_{SG} = Uncertainty for grid convergence

U_{SAD} = Uncertainty for artificial dissipation.

U_{SI} is based on the evaluation of the iteration records for the variables. The level of iterative convergence is determined by the numbers of orders of magnitude reduction and magnitude in the residuals. The value of U_{SI} can therefore be based on an assumption that its value is approximately a half of the difference between the maximum and minimum value of the variable during the iteration procedure.

U_{SG} is based on Richardson's extrapolation error estimates for grid convergence which were outlined in section 5.4.2.

U_{SAD}, the uncertainty for artificial dissipation can be determined by:

$$U_{SAD} = \frac{(\phi_1 - \phi_2)}{\phi_1} \qquad\qquad 5.35$$

Where:

ϕ represents the variable at a node for a fine grid (subscript 1) and a coarse grid (subscript 2).

Uncertainty in Experimental Data

Chapter 4, ADV calibration, gave details of the uncertainties in the experimental data when using the ADV. It was stated that uncertainties in the measurement of mean velocities of 1% in the x direction and up to 30% and 25% in the y and z directions respectively were obtained. These uncertainties were in addition to calibration errors of 2% in the x direction and 1% in the y and z directions. These errors can be combined to give U_D the uncertainty in the experimental data:

$$U_D^2 = U_{DM}^2 + U_{DC}^2 \qquad\qquad 5.36$$

Thus:

$$U_D Vx = \sqrt{1^2 + 2^2} = 2.2\%$$
$$U_D Vy = \sqrt{30^2 + 1^2} = 30.0\%$$
$$U_D Vz = \sqrt{25^2 + 1^2} = 25.0\%$$

5.5.2 Results of Uncertainty Analysis

Uncertainty analyses were undertaken using the simulation of test 14 since this was the arrangement that gave the most accurate results during the previous analyses that have been described in the preceding sections. The study was undertaken using the theory of Coleman and Stern, initially with reference to the velocity in the x direction at positions A1, A2, A3 and A4. Table 5.8 shows the results of the coefficients of this study.

Pt.	z cm	D cm/s	S cm/s	E %	U_v %	U_d %	U_{sn} %	U_{si} %	U_{sg} %	F1 cm/s	F2 m/s	U_{sad} %
A1	0.02	16.3	12.7	22.1	34.3	2.2	34.3	3.1	4.3	12.7	17.0	-33.9
A1	0.10	20.6	17.3	16.0	6.0	2.2	5.6	3.1	0.7	17.3	18.1	-4.6
A1	0.20	25.6	18.2	28.9	9.2	2.2	8.9	3.1	1.5	18.2	19.7	-8.2
A1	0.29	32.2	19.2	40.4	8.3	2.2	8.0	3.1	1.4	19.2	20.6	-7.3
A1	0.39	34.0	19.7	42.1	6.8	2.2	6.5	3.1	1.1	19.7	20.8	-5.6
A2	0.02	9.2	6.3	31.5	38.4	2.2	38.3	3.1	2.4	6.3	8.7	-38.1
A2	0.10	11.8	12.5	-5.9	26.9	2.2	26.8	3.1	3.3	12.5	9.2	26.4
A2	0.20	15.8	14.5	8.2	30.9	2.2	30.8	3.1	4.4	14.5	10.1	30.3
A2	0.29	22.2	15.3	31.1	29.9	2.2	29.9	3.1	4.5	15.3	10.8	29.4
A2	0.39	23.4	15.8	32.5	30.9	2.2	30.9	3.1	4.8	15.8	11.0	30.3
A3	0.02	9.2	11.7	-27.2	24.4	2.2	24.3	3.1	2.8	11.7	14.5	-23.9
A3	0.10	12.2	14.6	-19.7	5.1	2.2	4.6	3.1	0.5	14.6	15.1	-3.4
A3	0.20	17.0	16.8	1.2	6.1	2.2	5.7	3.1	0.8	16.8	16.0	4.8
A3	0.29	21.8	17.8	18.3	7.8	2.2	7.5	3.1	1.2	17.8	16.6	6.7
A3	0.39	23.4	18.3	21.8	8.7	2.2	8.4	3.1	1.5	18.3	16.9	7.7
A4	0.02	8.6	10.4	-20.9	30.2	2.2	30.1	3.1	3.1	10.4	13.5	-29.8
A4	0.10	12.6	12.2	3.2	15.3	2.2	15.2	3.1	1.8	12.2	14.0	-14.8
A4	0.20	16.6	14.2	14.5	6.3	2.2	5.9	3.1	0.7	14.2	14.9	-4.9
A4	0.29	22.0	15.2	30.9	4.3	2.2	3.7	3.1	0.3	15.2	15.5	-1.9
A4	0.39	23.2	15.8	31.9	3.8	2.2	3.1	3.1	0	15.8	15.8	0

Table 5.8   Coefficients of Uncertainty analyses for test 14.

It was stated previously that for the validation to be achieved $|E| < U_v$. It can be observed from Table 5.8 that in several cases this does not occur. It appears from the table that validation is usually achieved to the bottom half of the flow but greater uncertainties are reported in the upper half of the flow. This is shown more clearly by graphs of the measured error and the uncertainty in the validation with depth at positions A1, A2, A3 and A4 in Figure 5.24. The graphs confirm that, according to the theory of Coleman and Stern, validation was not achieved towards the surface of the

flow despite the fact that the finest grid tested was used with the most appropriate computational parameters for the type of flow being investigated.
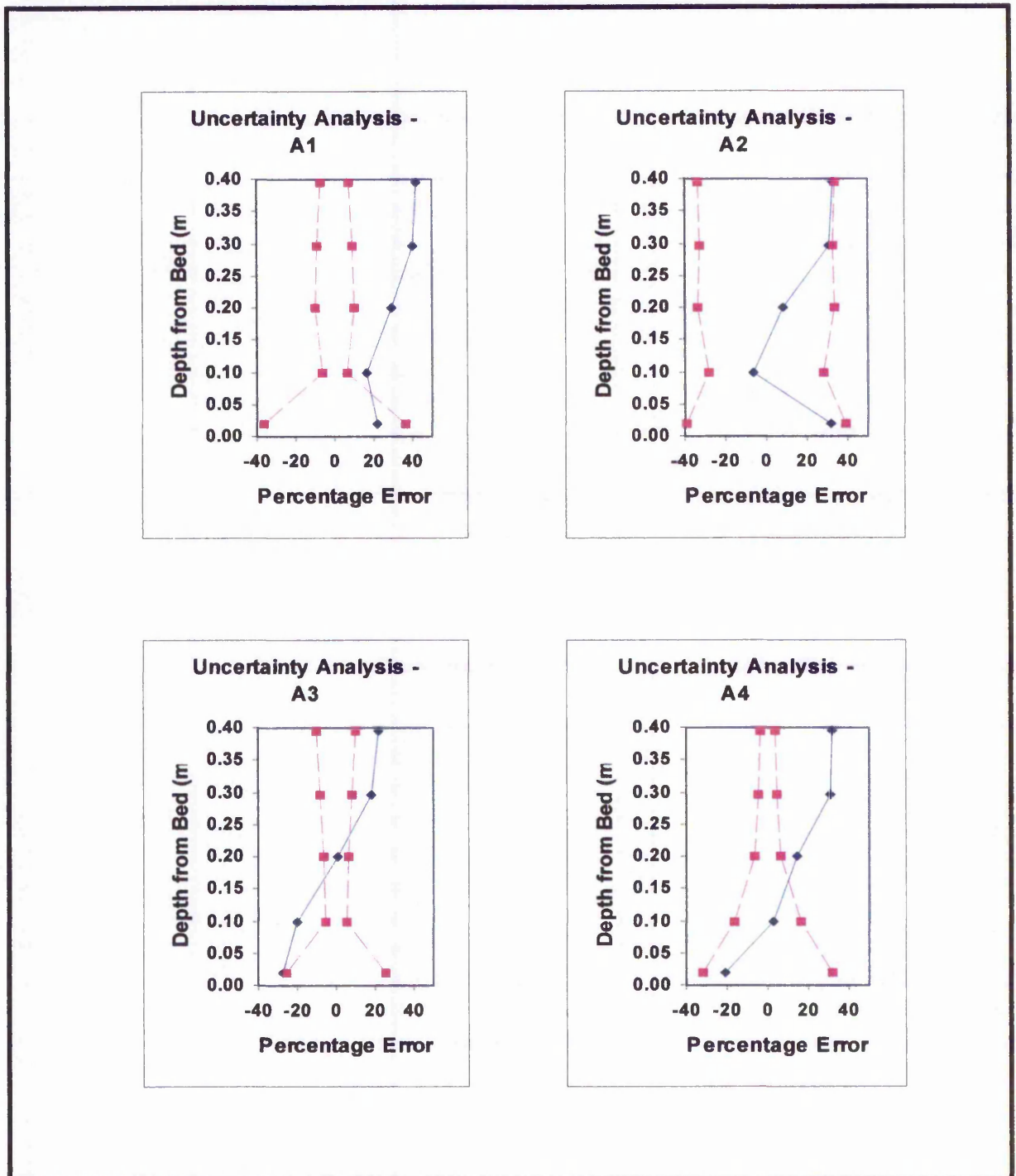

Figure 5.24   Measured error and validation uncertainty with depth at A1, A2, A3 and A4.

(Blue solid line = measured error, purple dotted line = validation uncertainty).

It is interesting to note that validation was achieved most successfully at position A2 where the flow was particularly complex, just downstream of the nosing of the inlet pier. At this position the measured error lay within the uncertainty error bounds +/- U_V.

5.6 CONCLUSIONS

The study described by this chapter has rigorously investigated the parameters used by SSIIM for the calculation of a complex hydraulic problem. Simulations from SSIIM have been compared with data obtained from laboratory experiments for a 15 degree intake arrangement. Three dimensional experimental and numerical data has been collected for over 14 test cases.

In general the accuracy of the numerical predictions was in excess of the accuracy of the physical measurements. Thus the accuracy of the physical measurements established in Chapter 4 was acceptable for the validation of the numerical code. The following observations and general recommendations can be made on how SSIIM should be used to investigate the flow structure at an intake of this arrangement.

- Simulations where the inlet velocity boundary condition was specified gave profoundly different results to using an assumed, fully developed, theoretical inlet velocity boundary condition. The reasons why a better correlation with experimentally measured data should be achieved when the inlet conditions were not specifically given, is impossible to explain within the constraints of this study. However, in such a complex problem as the intake structure which was used for this study, it is obvious that the validation would not be valid without specifying the inlet conditions. The flow entering the model was not fully developed and therefore this assumption should not be used.

- The study has shown that it is important to calibrate the model for the friction at the boundary. A Manning's 'n' of 0.009 is a representative value for a smooth walled physical model which was used in this study.

- Grid dependency is a major consideration for any computational modelling. The study using SSIIM has shown that the accuracy in prediction of the flow using the computational model should be offset against the large increase in computational time which will occur with an increase in the number of cells. The horizontal grid was refined in regions of highly varying flow such as in areas of re-circulation or high velocity gradients.

- The multiblock option provided by SSIIM has been shown to be a successful tool, but preliminary analyses are required in order to specify the proportions of the flow entering the main and inlet channel that are required by this facility. The over prediction by the multiblock grid was approximately 60% in Vx as opposed to approximately 12% when using the standard grid with the greatest number of grid cells.

- The number of layers required in the vertical direction depended on the features that gave rise to depth varying flow. However the general trend observed was that an improvement in percentage error was observed with increasing layers in the vertical direction up to a maximum of 16 layers.

- A Richardson's extrapolation study on the grid showed that the uncertainty due to grid refinement ranged from 4.9% to 0%. This was developed to use the Grid Convergence Index (GCI) to give a maximum uncertainty of 11.7% due to the grid.

- The POW numerical scheme is approximately 30% faster than the SOU numerical scheme and usually more stable but less accurate where the grid is coarse and the flow is not aligned to the grid. The SOU scheme can create undershoots qhich may cause instabilities in the k and ε equations. A very coarse grid may generate excessively oscillating solutions, delaying or preventing convergence. It is advised that the SOU scheme should be used for momentum equations since it imporves the accuracy for flow which is not aligned to the grid and it may reduce computational time. The POW scheme is recommended for the turbulence equations because of its greater stability. However the use of the SOU scheme can cause negative values of k and ε which can cause the solution procedure to fail.

- The SOU scheme predicted improvements in velocities to the POW scheme from 25% to 60% in Vx. In Vy improvements ranged from 45% to 20%. Negligible improvements were observed in k.

- Block correction, a numerical method which accelerates convergence of the POW scheme, was not tested because it caused the solution procedure to fail where there were blocked out regions of the domain. The SIMPLEC algorithm was not tested for similar reasons.

- Relaxation factors were difficult to determine. If they were chosen too small, solution times were increased unnecessarily but if they were chosen too high the model oscillated and failed to converge. The importance of the correct selection and the need to adjust the relaxation factors based upon the experience of the user was a major drawback of SSIIM.

- The matrices generated by the numerical schemes should be solved using the Gauss-Seidel option offered by SSIIM. The TDMA option does not alter or improve the results and it increases the computational time required considerably.

- Two of the three options for the solution of the free water surface were tested in this study. Improvements to the results by use of the unsteady update option was dependent on the Froude number of the model. It only gave a significant effect where the Froude number was large (considerably larger than 0.12, the Froude number for the model that was investigated).

- Velocities were predicted to an accuracy of less than 30% in Vx. Greater inaccuracies were reported for Vy and Vz but this was not considered as onerous since the qualitative direction of the velocity vectors was reasonable. In addition the experimentally measured values of Vy and Vz had large uncertainties. These results should be compared to the accuracy of the physical measurements. Chapter 4 described that the ADV measured velocities in Vx to an accuracy of 7% an in Vy to an accuracy of 2%.

- Isotropic turbulence in terms of turbulent kinetic energy, k was predicted to an accuracy of less than 12% with generally remarkably good agreement with measured data.

- The uncertainty of the validation, which combined both the experimental data and the simulation prediction, ranged from 34% to 5% when using the most appropriate grid and numerical parameters.

SSIIM was scrutinised closely by this validation study and perhaps placed under too extreme conditions. It was designed primarily for river engineering purposes. For the purposes of this study, SSIIM has been compared to a scaled physical model in a hydraulics laboratory under much more favourable conditions than one would expect to find in a prototype situation. Predictions in general in the x direction were acceptable and it may be considered that predictions in the y and z directions were unacceptable. However, the qualitative direction of the velocity vectors was predicted reasonably well and this was considered to be extremely important for subsequent analyses. The validation was successful in many cases according to the theory of Coleman and Stern. However, near to the surface of the flow validation was not fully achieved but in terms of available computational capacity, duration of tests and acceptable accuracy the most appropriate model was eventually selected.

The recommendations in the use of SSIIM were derived from experience, published works and private correspondence with Dr Nils Olsen, the author of SSIIM. The following table summarises briefly the influence of the various parameters available in SSIIM.

Item	For Accuracy	For stability	For speed
Resolution	Increase	Sufficient to resolve shear layers	Decrease
Numerical scheme	SOU (with recirculation)	POW	POW
Block correction	No influence	Avoid	Use with caution
Relaxation factors	No influence	Reduce	Increase

6

MODELLING OF INTAKE FLOWS

6.1   INTRODUCTION

This chapter is concerned with the investigation of the flow structure at a smooth walled, rectangular cross section intake structure where the ratio of intake channel width to main channel width was 0.5. The smooth walled nature of the model was a limitation of the investigation. Nevertheless the flow features described by the investigation are similar to the flow features described by a rough walled model. The investigation involves the numerical model that was described in Chapter 5, SSIIM. It also involves physical modelling with three dimensional, point velocity measurements being recorded using the Acoustic Doppler Velocimeter as described in Chapter 4. A variety of other techniques were used to measure the flow in the physical model and for visualisation of the flow structure both in the numerical and physical model. The objectives of this chapter are to provide the design engineer / researcher with a better understanding of the flow regime at a typical intake structure where the intake angle varies from 15 to 45 degrees and the flow split ratio varies from 0.5 to 3.0. In addition prediction methods are developed and described to quantify certain parameters of the flow structure. The sections covered by this chapter can be summarised as follows.

- Measurement and prediction of the dividing streamplane.
- Measurement and prediction of the flow diversion rate for an uncontrolled flow split
- Velocity vector visualisation.

- Velocity vector profile plots.

- Streamline pattern visualisation.

- Measurement and prediction of the maximum turbulent kinetic energy in the flow domain.

6.2   PREDICTION AND MEASUREMENT OF THE POSITION OF THE DIVIDING STREAMPLANE

6.2.1 Introduction

Prediction and measurement of the position of the dividing streamline in open channel diversions has been investigated by numerous researchers in recent years and these studies have been outlined in Chapter 2. The previous studies have mainly focussed on two-dimensional measurements. Three-dimensional predictions have been undertaken using computational fluid dynamics techniques but these have concentrated on ninety degree intake angles.

The location and prediction of the position of the three-dimensional streamline or the "streamplane" is important for several applications. The position of the streamplane is an important parameter in the quantification of the flow diversion rate and is involved with the determination of contraction losses (Hager 1984). The shape of the dividing streamplane and the rate of curvature of the plane as the flow passes into the intake, affects the energy losses at the intake to a considerable degree. Sediment transport engineers also have considerable interest in the location of the dividing streamplane since the position of the streamplane affects the quantities of sediments transported from the bed into the intake. Biomedical researchers have in recent years, tried to identify the position of the dividing streamplane occurring in blood flow at human arterial bifurcations.

Streamlines were constructed for the test cases using the commonly accepted theory presented in many hydraulic textbooks. A streamline is a line which is tangential to the velocity vectors of a connected series of fluid particles. The streamline is thus a line representing the direction of flow of the series of particles at a given instant. Because the streamline is always tangential to the flow, it follows that there is no flow across a streamline. For further details on the construction of streamlines the reader is referred to Chadwick and Morfett (1994). The investigations into the position and

nature of the dividing streamplane undertaken as part of this study are presented in the following sections.

6.2.2 Depth Variation of Dividing Streamplane

Neary and Odgaard (1993) presented the depth varying ratios of the dividing streamline for a 90 degree intake angle near the bed and near the surface of the flow. They found that the degree of three dimensionality was affected by the main channel roughness but was independent of the velocity ratio, U_2 / U_1, where U_1 is the bulk channel velocity at the main channel inlet and U_2 is the bulk channel velocity at the branch channel exit. A similar analysis was undertaken in this study but on intake angles of 15, 30 and 45 degrees. However only a smooth bed was used and thus the effects of bed roughness were not investigated.

The distance that the dividing streamplane extended into the main channel 1.0m upstream of the intake entrance was predicted and measured for intake angles of 15 and 30 degrees. A comparison of the predicted results with Neary and Odgaard's smooth bed predicted results is shown by Figure 6.1. It was found that the position of the dividing streamplane 1.0m upstream of the intake entrance was independent of intake angle and the velocity ratio.
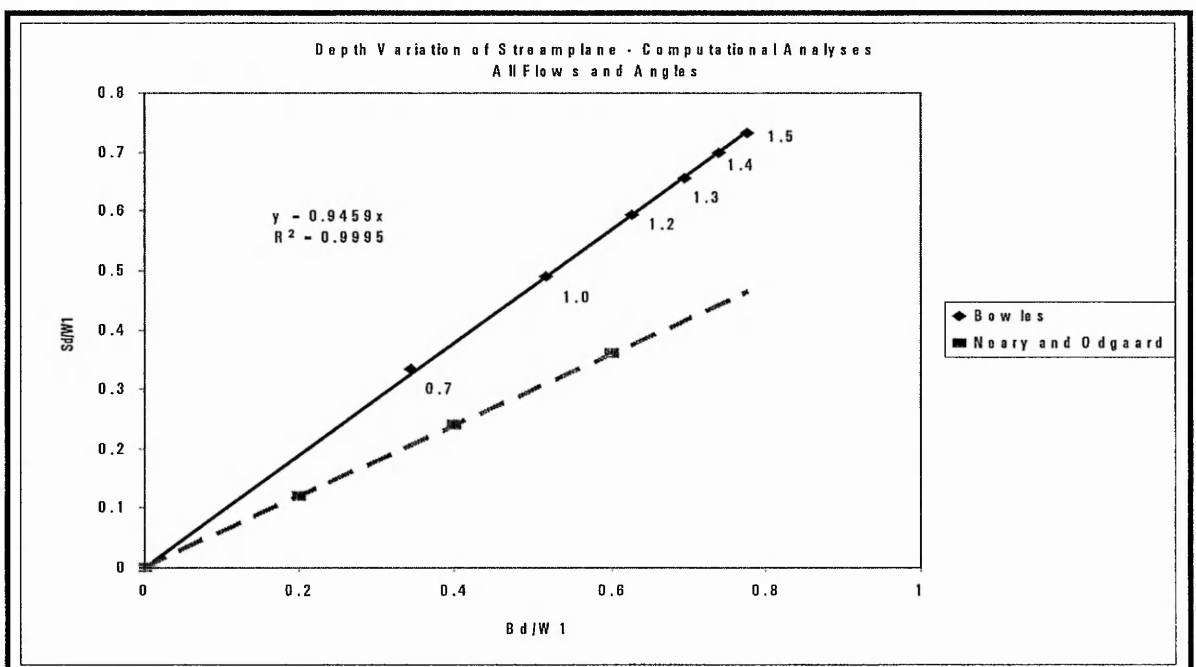
Figure 6.1   Predicted depth variation of dividing streamline based upon intake angles of 15, 30 and 45 degrees.

The symbols Sd, Bd and W1 represent the dimensions shown by Figure 6.2. The numbers next to the prediction of Bowles (unpublished) represent the velocity ratio. Depth variation ratios of Sd / Bd = 0.9 were obtained by this study as opposed to Sd / Bd = 0.6 which was obtained by Neary and Odgaard. However it must be noted that the study of Neary and Odgaard was undertaken using a 90 degree intake angle. Neary and Odgaard also took their measurements only 0.152m upstream of the intake entrance and it will be shown later in this section that it was unlikely that the streamline was parallel to the main channel at this proximity to the entrance.
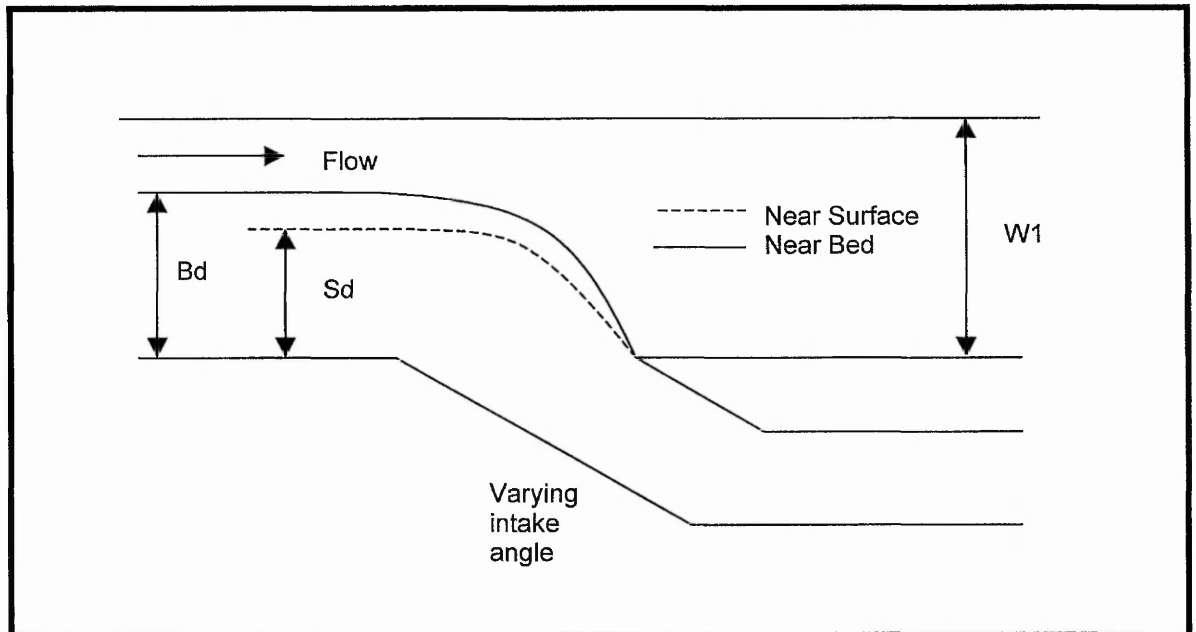
Figure 6.2   Symbol definition sketch for depth variation of dividing streamline.

A comparison of the predicted position of the dividing streamplane with the measured position is shown by Figure 6.3. It can be observed that a reasonable agreement was obtained although a significant proportion of the results lie between the predictions derived by this study and the predictions of Neary and Odgaard. It was found that the measured streamline position was extremely difficult to ascertain since the shape of the streamline tended to be much more irregular using the measured results than when the predicted results were used. This problem is highlighted further later in this section. The irregularities in the measured streamlines undoubtedly caused errors in the graph shown by Figure 6.3. The results also indicated that the dividing streamline at the bed extended further into the main channel than at the surface of the flow. This was a phenomenon that was repeatedly observed throughout all the streamplane tests.
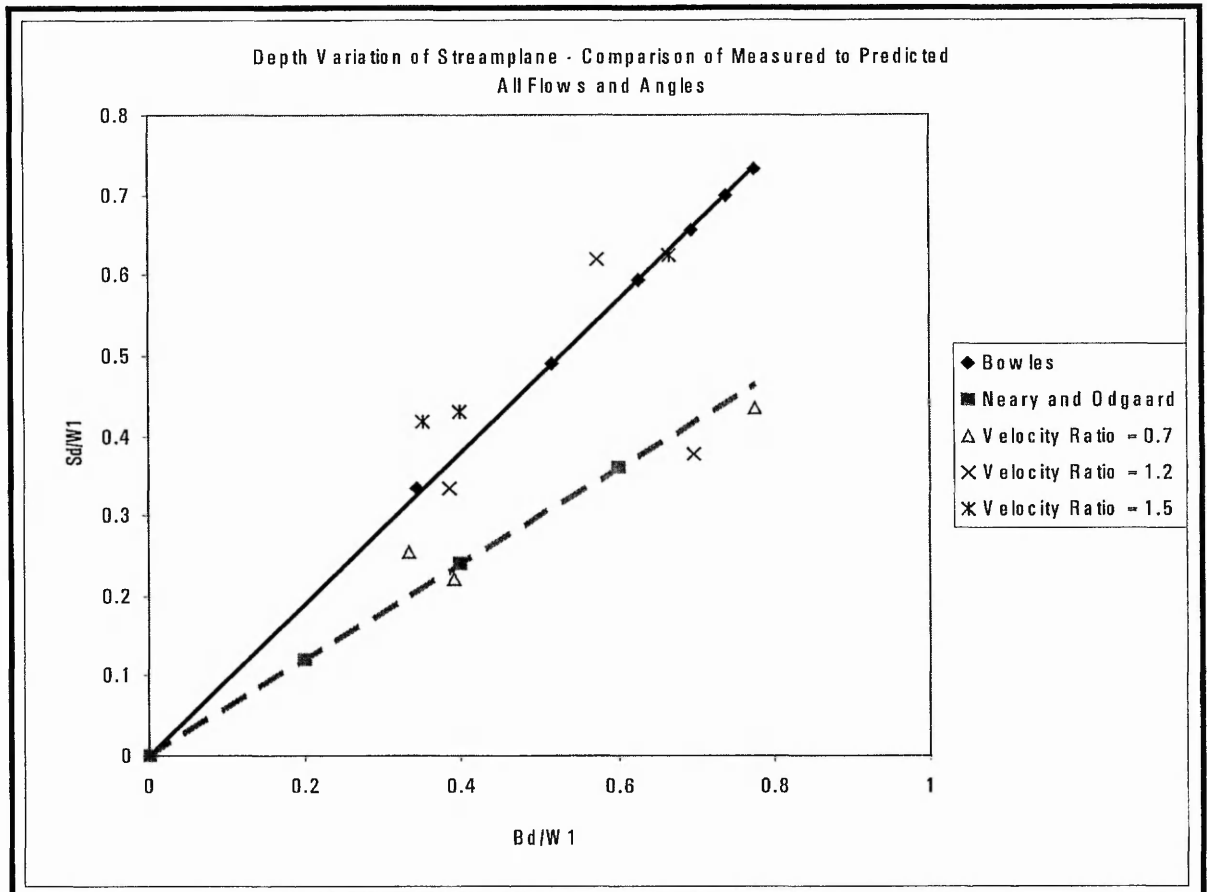
Figure 6.3   Predicted compared to measured depth variation of dividing streamline based upon intake angles of 15, 30 and 45 degrees.

6.2.3 Variation of position of dividing streamplane with flow split ratio, Qr.

The previous section highlighted that the position of the dividing streamline with depth was independent of the intake angle, and the velocity ratio (or Reynolds number ratio) for a smooth bed intake. The study was developed to investigate the effect of the flow split ratio Qr upon the position of the dividing streamplane. For the purposes of this study the flow split ratio, Qr, is defined as the ratio of the flow entering the intake to the flow passing through the main channel downstream of the intake. The convention for past research has been that Qr was the ratio of the flow entering the intake to the flow upstream of the intake in the main channel. However the author of this study considered that for the purposes of hydroelectric engineering it was more useful to present directly, the ratio of the flow extracted from the main channel to the flow left remaining in the main channel. Thus a Qr = 3.0 represents a flow in the intake channel of three times that left remaining in the main channel. The flow split ratio for this study is clarified by Figure 6.4.
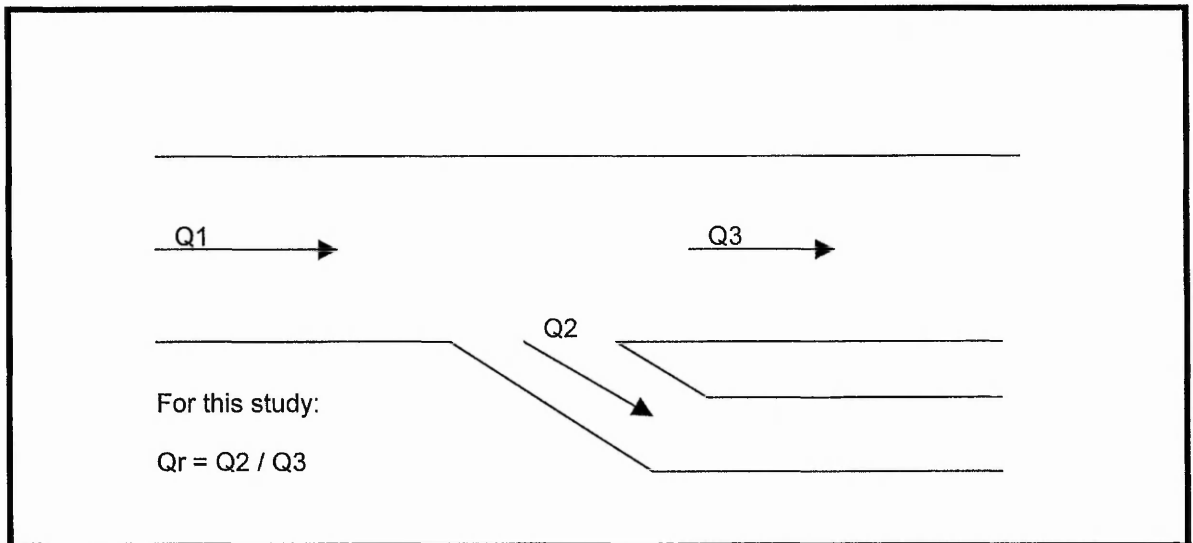
Figure 6.4   Convention for the flow split ratio, Qr, for the purposes of this study.

Where reference is made to the results of past researchers the flow split ratio has been converted to the appropriate ratio.

Thus the predicted position of the dividing streamline near the bed, near the middle and near the surface of the flow with the flow split ratio, Qr, can be defined graphically as shown by Figure 6.5. The position of the dividing streamline was predicted 1m upstream of the entrance of the intake for intake angles of 15, 30 and 45 degrees and Qr = 0.5, 1.0, 1.5, 2.0, 2.5 and 3.0. Figure 6.5 shows the parabolic relationship that existed between the distance from the edge of the channel of the streamline and Qr. It can also be observed from the graph that the difference in position of the streamline with depth was independent of the intake angle which reiterates the findings of the previous section. It should also be noted that the depth variation of the streamplane increases with increasing flow split ratio, Qr. At low values of Qr (e.g. Qr = 0.5), i.e. low draw-off rates from the main channel, the position of the dividing streamline varies little with depth.

Figure 6.5 shows that the dividing streamplane extends further into the main channel as Qr increases and the dividing streamline near the bed extends into the main channel further than near the surface so that the intake channel captures more flow near the bed, where there is less streamwise inertia.
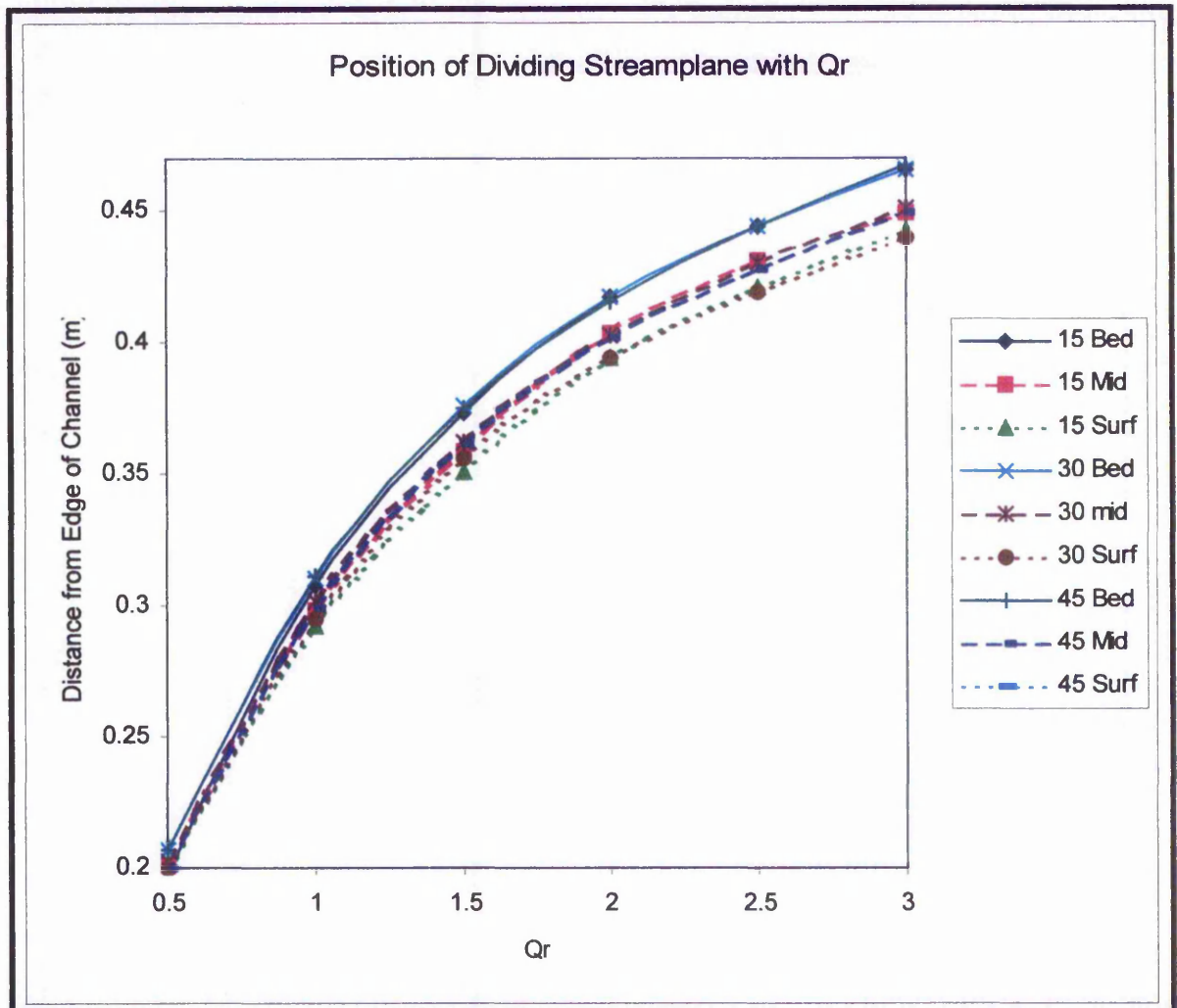
Figure 6.5   Position of dividing streamline with the flow split ratio and the intake angle.

The numbers in the legend of Figure 6.5 refer to the intake angle of the prediction.

6.2.4 Qualitative investigation into the shape of the dividing streamline.

The previous two sections have described the studies that were undertaken to determine the position of the dividing streamplane with depth 1.0m upstream of the entrance to the intake for intake angles of 15, 30 and 45 degrees. The study was subsequently developed to study the shape of the dividing streamline with intake angle, flow and flow split ratio. Streamline plots were produced and samples are shown by Figures 6.6 to 6.8. The streamlines were plotted based on the three-dimensional velocity data obtained from the numerical model near the bed of the flow domain. Figures 6.6, 6.7 and 6.8 show streamline plots for intake angles of 15, 30 and 45 degrees respectively at a flow of 35l/s and flow split ratios of 0.5, 1.0, 1.5, 2.0,
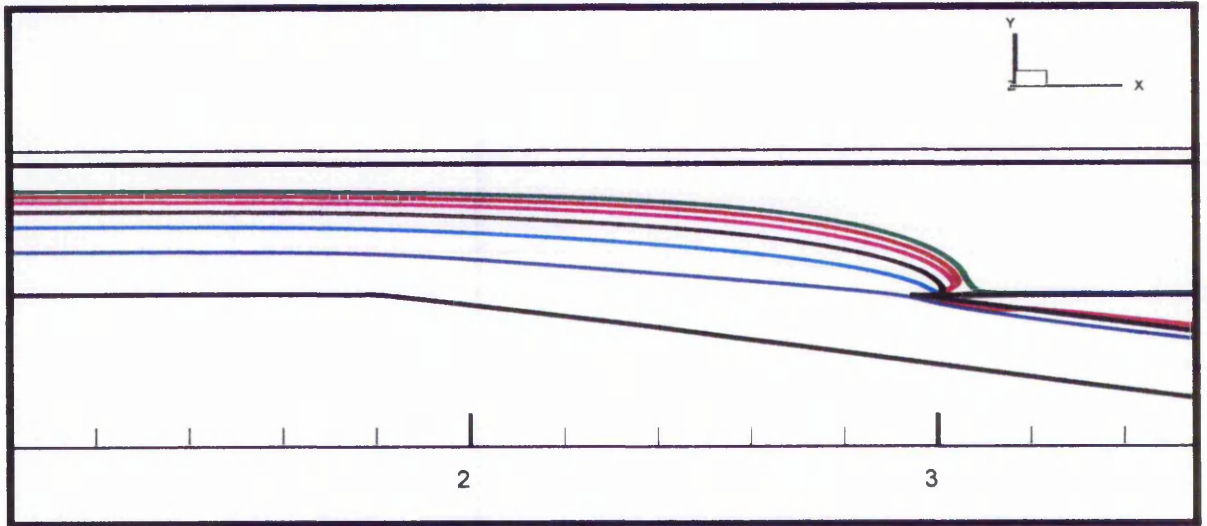
Figure 6.6   Dividing streamplane for 15 degree intake, flow = 35l/s, Qr = 0.5 to 3.0.
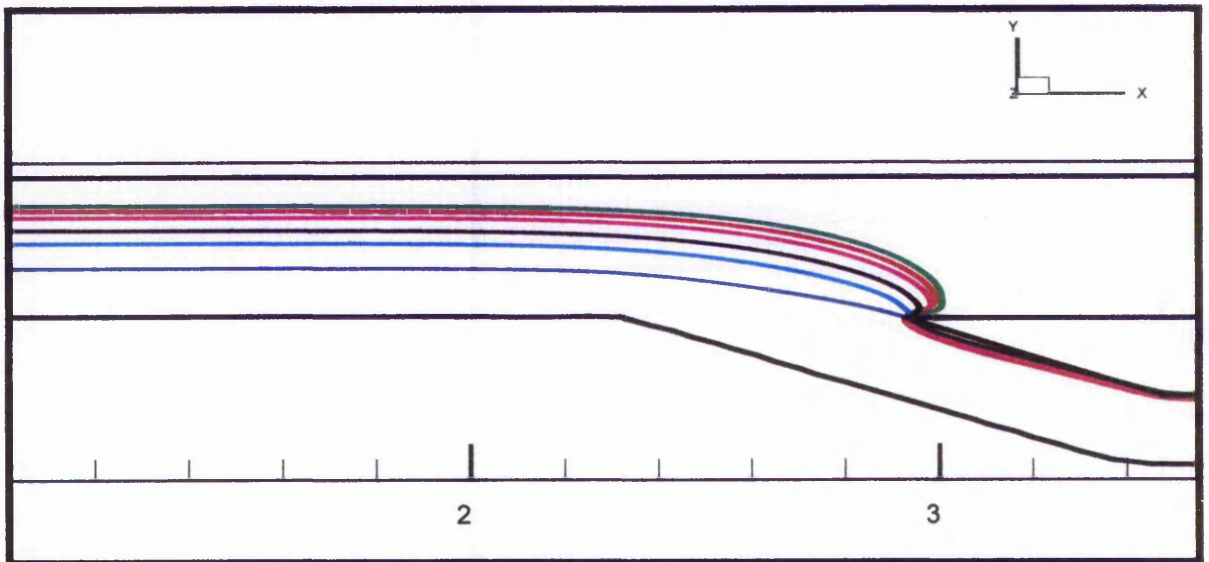
Figure 6.7   Dividing streamplane for 30 degree intake, flow = 35l/s, Qr = 0.5 to 3.0.
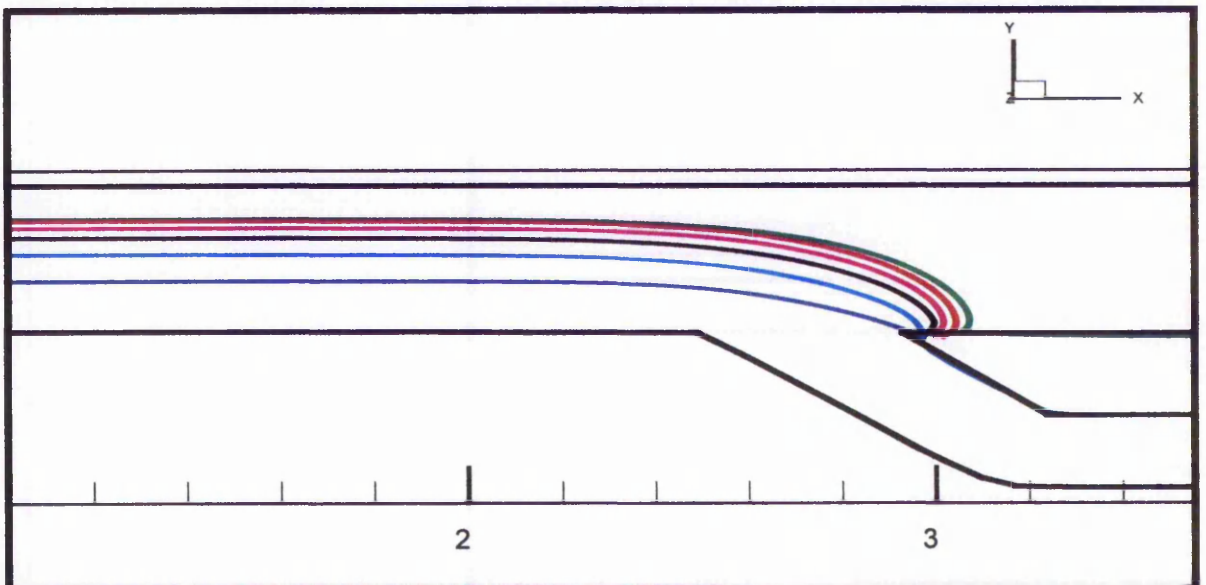
Figure 6.8   Dividing streamplane for 45 degree intake, flow = 35l/s, Qr = 0.5 to 3.0.

2.5 and 3.0. The colour coding to the plots was as follows: dark blue = Qr – 0.5, light blue = Qr – 1.0, black = Qr – 1.5, purple = Qr – 2.0, red = Qr – 2.5, green = Qr – 3.0. Several interesting features can be observed from these plots:

- The radius of curvature of the streamlines decreased with increased intake angles indicating that the flow turned through a greater angle in the vicinity of the entrance to the intake, with increased intake angle resulting in increased energy losses.

- The shape of the streamlines with flow split ratio, Qr, appeared qualitatively to be independent of the flow (and hence Reynolds number).

- The spread of the position of the streamlines appeared qualitatively, to be closer for a 15 degree intake angle, with the spread increasing with an increase in intake angle.

- The foci of the streamlines appeared to extend further downstream of the "nosing" of the intake pier with increased intake angle.

- Flow reversal occurred to a greater extent with a 45 degree intake just downstream of the nosing of the pier.

The results presented by these analyses gave a reasonably good qualitative representation of the nature of the streamplane at the intake. However a closer quantitative examination was required and the results are presented in the following section.

6.2.5 Quantitative investigation into the shape of the dividing streamplane.

A closer examination was considered necessary to identify the effect of the Reynolds number on the shape of the dividing streamplane at the intake. For this purpose the predicted position of the dividing streamline was plotted for flows of 35, 47 and 58l/s with intake angles of 15, 30 and 45 degrees. Figure 6.9 shows the results of this analysis. At this stage the flow split ratio, Qr, was constant at 0.5.
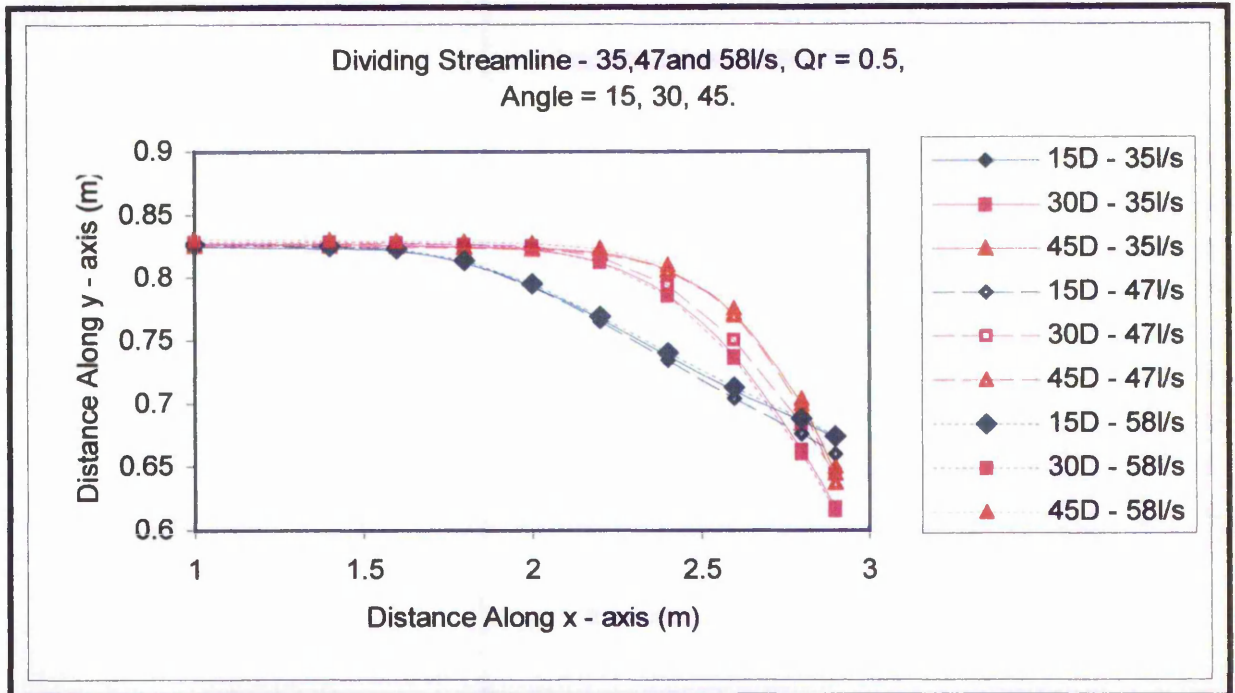
Figure 6.9   Shape of the dividing streamline with flow.

Figure 6.9 shows that there was a negligible deviation in the position of the dividing stream line with an increased flow for the respective intake angles. The small errors that can be observed by Figure 6.9 are probably due to inconsistencies in the numerical model. The results shown by Figure 6.9 confirmed the qualitative assessments made previously that the flow and hence Reynolds number, had little effect upon the shape of the dividing streamplane but that the shape was affected by the intake angle. The analyses presented by this figure were predicted near the middle of the flow domain.

The next stage of the study investigated quantitatively, the shape of the dividing streamplane with intake angle and flow split ratio. For the purposes of this stage of the study the mean dividing streamline near the bed was plotted based on the predicted results for flows of 35 and 47l/s. Figure 6.10 shows these results.
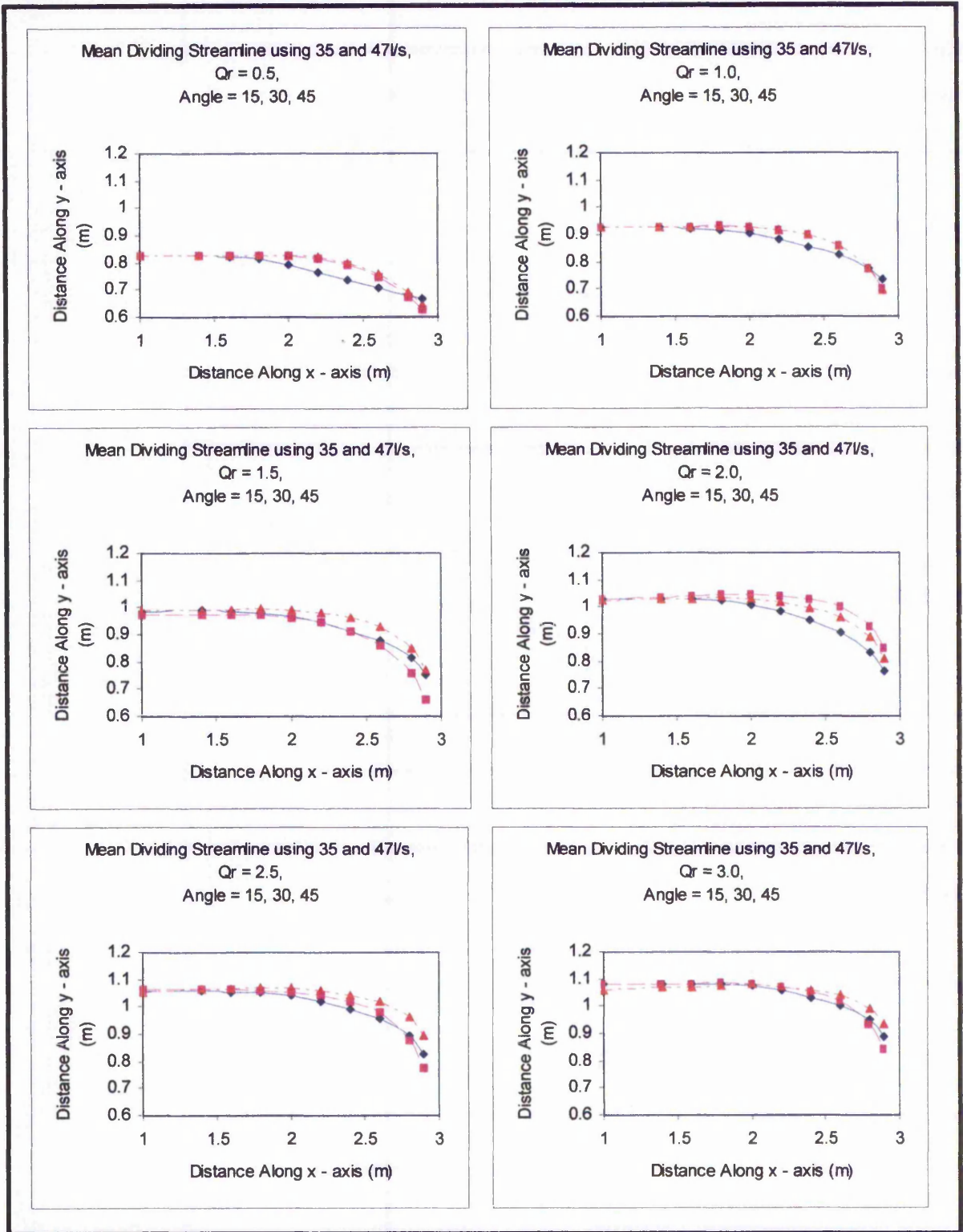
Figure 6.10 Position of dividing streamline with intake angle based on average flow. (Blue diamonds = 15 degree, purple squares = 30 degree, red triangles = 45 degree).

The graphs shown by Figure 6.10 illustrated that the radius of curvature of the dividing streamline appeared to decrease with increased intake angle but also that the radius of curvature decreased with increased flow split ratio. Another trend indicated was that the dividing streamline for a 45 degree intake appeared to extend further into the main channel than for the 30 or 15 degree intake. Clearly the flow into the intake for the 15 degree intake angle also represented the smoothest transition of flow with the least radius of curvature of the streamline. This would suggest that energy losses should be a minimum with a 15 degree intake angle. This will be discussed in greater detail in subsequent sections.

The previous figures have shown the predicted shapes of the dividing streamline at one level through the flow domain. Consideration was then given to the three-dimensionality of the dividing streamplane. It has been presented that the position and shape of the dividing streamplane was independent of the flow / Reynolds number. Therefore the depth variation studies used one flow of 47l/s. This flow was chosen since numerous physical measurements were available for validation of the predictions not only for the 15 degree intake but also for the 30 degree intake. Analyses were undertaken for the shape of the dividing streamplane near the bed, near the middle and near the surface of the flow domain. Figure 6.11 shows the results of the prediction for intake angles of 15, 30 and 45 degrees at flow split ratios of 0.5, 1.5 and 3.0.

Figure 6.11 exhibited similar trends to those that were presented in previous sections. The streamline at the bed extended further into the main channel than at the surface and the extension of the streamline into the main channel generally increased with increased intake angle. The radius of curvature of the streamline reduced with increased intake angle and flow split ratio.
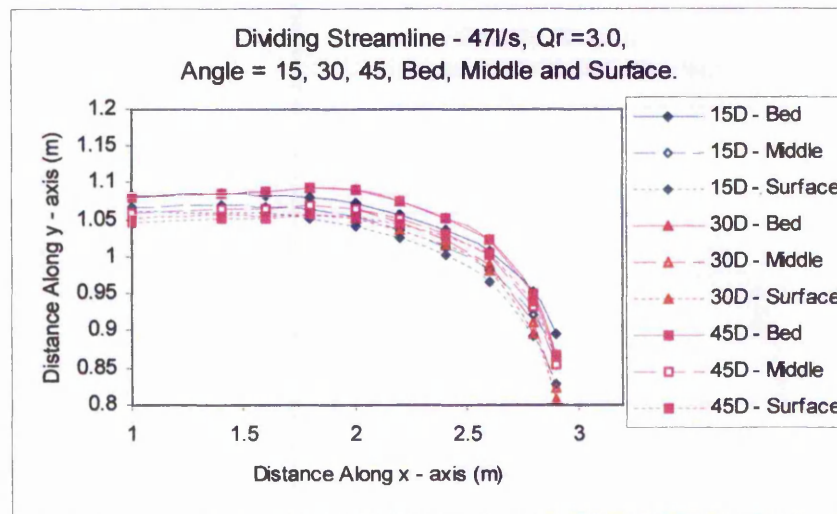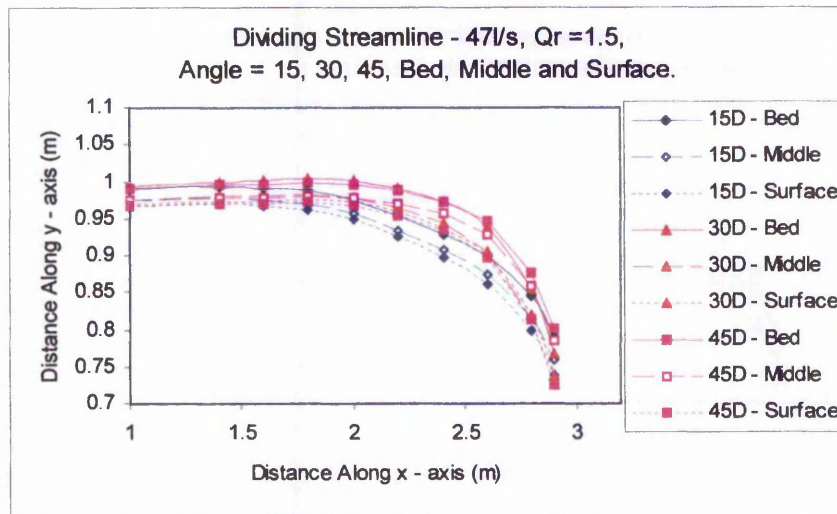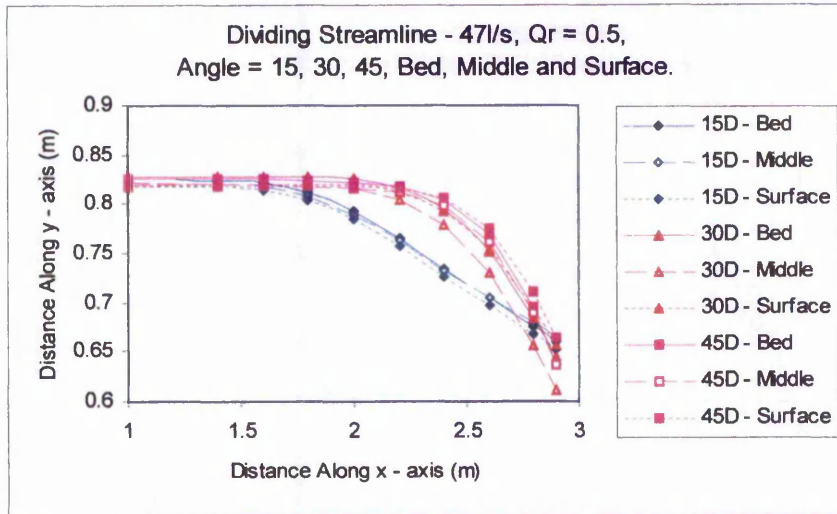
Figure 6.11   Predicted position and shape of dividing streamplane near the bed, middle and surface for Qr = 0.5, 1.5 and 3, with intake angles of 15, 30 and 45 degrees.

6.2.6 Families of Curves for the Prediction of the Shape and Position of the Dividing Streamplane.

From the previous analyses, families of curves were constructed which summarised the prediction of the shape and position of the three dimensional dividing streamplane for intake angles of 15, 30 and 45 degrees and flow split ratios of 0.5, 1.5 and 3.0. These are shown by Figure 6.12, 6.13 and 6.14 respectively. It should be noted that only the upper and lower bands of the streamplane are shown, i.e. the surface and the bed streamplane. From these graphs the position and shape of the dividing streamplane for any flow split ratio between 0.5 and 3.0 can be interpolated. Similarly for intake angles between 15 and 45 degrees. It can be observed from these figures that the distance from the edge of the channel to the position of the dividing streamplane has been normalised by the total width of the main channel (for this study 0.6m). Thus, the graphs can apply to any width of main channel since the position and shape is not affected by the flow passing down the channel, only by the flow split ratio and the intake angle.

It should also be noted from the figures that the boundaries of the dividing streamplane generally increased with increased flow split ratio and in agreement with previous findings the radius of curvature decreased with increased flow split ratio and intake angle. The curves indicated by the figures can also be represented by equations with the most accurate representation consisting of a 6th order polynomial equation as shown by Tables 6.1, 6.2 and 6.3. The 6th order polynomial equations are of the form:

$$Y = A\,x^6 + B\,x^5 + D\,x^4 + E\,x^3 + F\,x^2 + G\,x + C$$

Where y is the position of the streamline in the cross stream direction and x is the position upstream of the nosing of the intake pier (or the focus) in the streamwise direction.

The hypotheses described here were tested against physical data. The dividing streamline was plotted based on the three-dimensional velocity data measured in the physical model. Physical models of 15 and 30 degrees intake angles were used. Main channel flows of 35, 47 and 58 l/s and flow split ratios of 0.5, 1.5 and 3.0 were

used for the 15 degree intake angle model. A main channel flow of 47 l/s and flow split ratios of 0.5, 1.5 and 3.0 were used for the 30 degree intake angle model.

Qr	Z	Coeff. x^6	x^5	x^4	x^3	x^2	x	C
0.5	Bed	-0.069	-0.470	-1.155	-1.213	-0.559	-0.347	0.051
0.5	Middle	-0.062	-0.425	-1.050	-1.094	-0.484	-0.306	0.061
0.5	Surface	-0.068	-0.466	-1.153	-1.223	-0.580	-0.360	0.369
1.5	Bed	-0.288	-1.837	-4.569	-5.615	-3.693	-1.477	0.220
1.5	Middle	-0.258	-1.663	-4.183	-5.222	-3.533	-1.493	0.165
1.5	Surface	-0.276	-1.773	-4.446	-5.533	-3.738	-1.585	0.126
3.0	Bed	-0.296	-1.875	-4.642	-5.729	-3.835	-1.537	0.392
3.0	Middle	-0.278	-1.772	-4.425	-5.527	-3.774	-1.569	0.338
3.0	Surface	-0.108	-0.812	-2.433	-3.720	-3.179	-1.620	0.274

Table 6.1   Coefficients of polynomial expression to predict dividing streamplane at a 15 degree intake.

Qr	Z	Coeff. x^6	x^5	x^4	x^3	x^2	x	C
0.5	Bed	0.052	0.374	0.965	0.968	-0.045	-0.707	0.005
0.5	Middle	0.057	0.405	1.044	1.050	-0.044	-0.777	0.052
0.5	Surface	0.063	0.441	1.146	1.216	0.155	-0.595	0.032
1.5	Bed	-0.335	-2.163	-5.545	-7.279	-5.365	-2.296	0.145
1.5	Middle	-0.341	-2.194	-5.596	-7.310	-5.379	-2.340	0.074
1.5	Surface	-0.281	-1.805	-4.599	-6.029	-4.509	-2.035	0.109
3.0	Bed	-0.550	-3.438	-8.389	-10.190	-6.646	-2.436	0.307
3.0	Middle	-0.553	-3.460	-8.451	-10.285	-6.749	-2.526	0.227
3.0	Surface	-0.438	-2.814	-7.109	-9.065	-6.320	-2.152	0.200

Table 6.2   Coefficients of polynomial expression to predict dividing streamplane at a 30 degree intake.

Qr	Z	Coeff. x^6	x^5	x^4	x^3	x^2	x	C
0.5	Bed	0.038	0.170	0.091	-0.698	-1.536	-1.246	0.029
0.5	Middle	0.066	0.357	0.570	-0.084	-1.128	-1.118	0.026
0.5	Surface	0.073	0.396	0.674	0.067	-0.974	-0.995	0.025
1.5	Bed	-0.323	-2.082	-5.316	-6.929	-5.016	-2.063	0.210
1.5	Middle	-0.288	-1.864	-4.791	-6.323	-4.674	-1.979	0.188
1.5	Surface	-0.350	-2.249	-5.734	-7.473	-5.451	-2.322	0.074
3.0	Bed	-0.550	-3.438	-8.389	-10.190	-6.646	-2.436	0.307
3.0	Middle	-0.467	-2.908	-7.077	-8.616	-5.701	-2.172	0.296
3.0	Surface	-0.465	-2.933	-7.249	-8.974	-5.993	-2.217	0.310

Table 6.3   Coefficients of polynomial expression to predict dividing streamplane at a 45 degree intake.
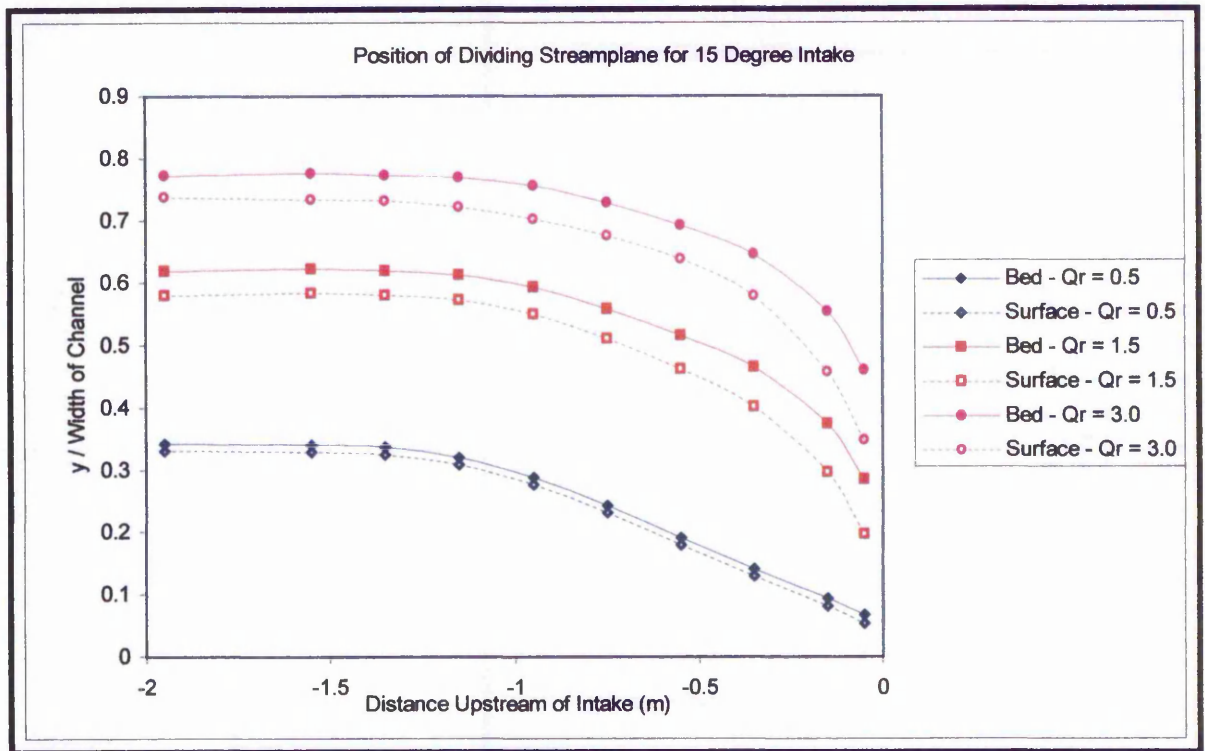
Figure 6.12   Family of curves to predict dividing streamplane for 15 degree intake.
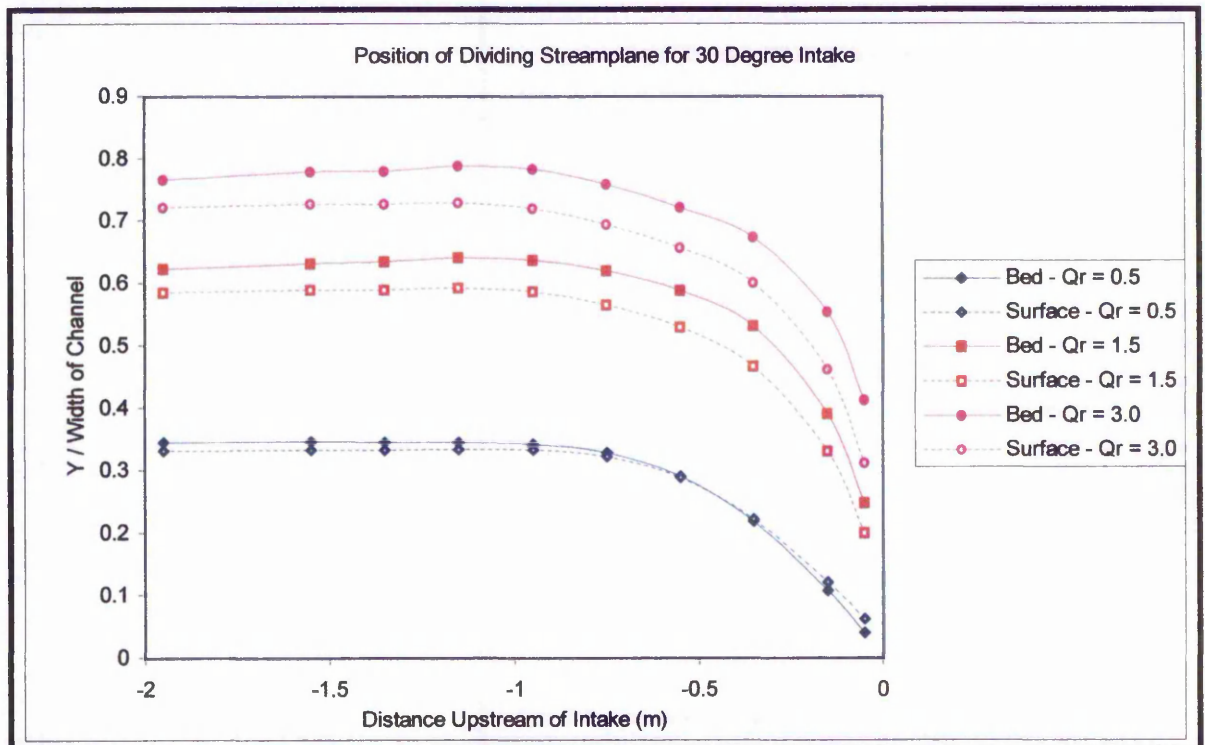

Figure 6.13   Family of curves to predict dividing streamplane for 30 degree intake.
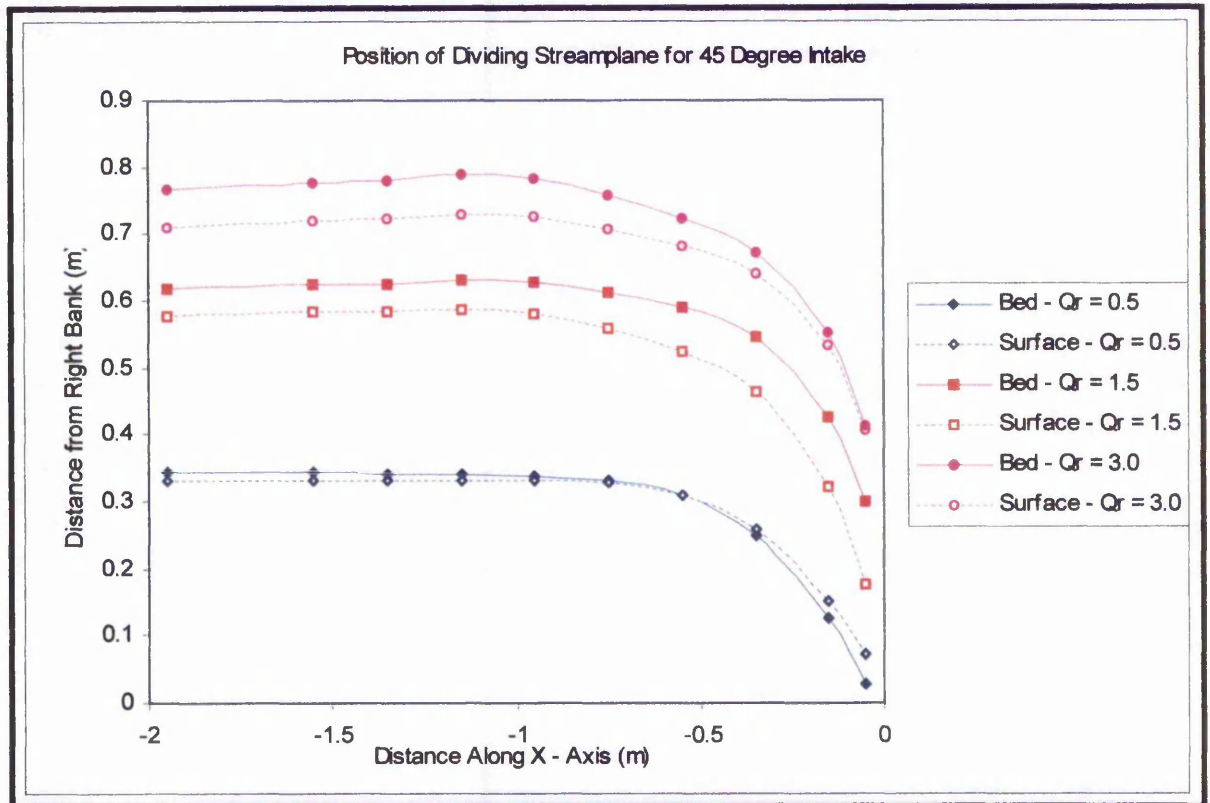
Position of Dividing Streamplane for 45 Degree Intake

Legend:
- Bed - Qr = 0.5
- Surface - Qr = 0.5
- Bed - Qr = 1.5
- Surface - Qr = 1.5
- Bed - Qr = 3.0
- Surface - Qr = 3.0

X-axis: Distance Along X - Axis (m)
Y-axis: Distance from Right Bank (m)

Figure 6.14   Family of curves to predict dividing streamplane for 45 degree intake.

Figures 6.15, 6.16 and 6.17 show the comparison of the predicted streamline with the measured streamline for a 15 degree intake angle and Figures 6.18, 6.19 and 6.20 show the respective results for an intake angle of 30 degrees.

Figure 6.15, shows the comparison between the predicted and measured dividing streamline indicating good agreement, with the majority of the measurements lying within +/- 10% of the predicted position and shape. Larger errors were experienced with the measurements taken near the surface for a flow of 35l/s and near the middle for a flow of 47l/s.

Figure 6.16 shows reasonable agreement between the predicted and measured dividing streamplane, with approximately half of the measurements lying within +/- 30% of the predicted position and shape. It was interesting to note that although errors in excess of 30% were recorded with regard to the position of the streamline, the shape of the streamline was predicted very well. The predicted position of the streamline constituted an over prediction of the measured in nearly every instance.
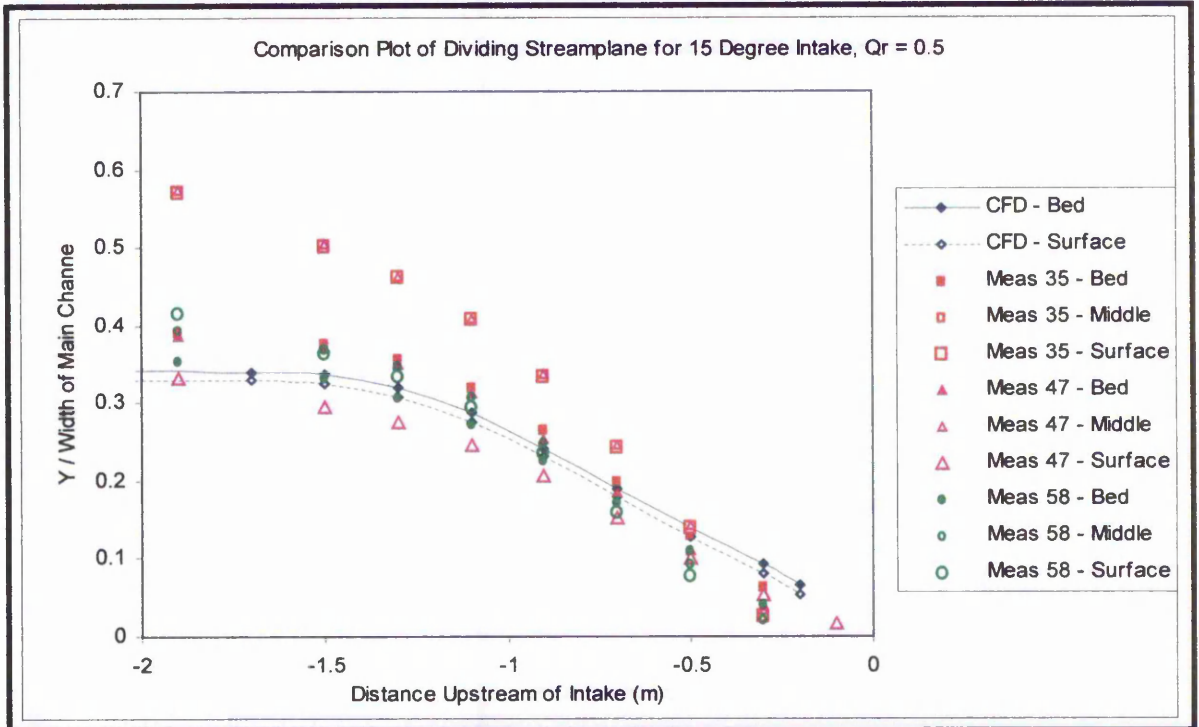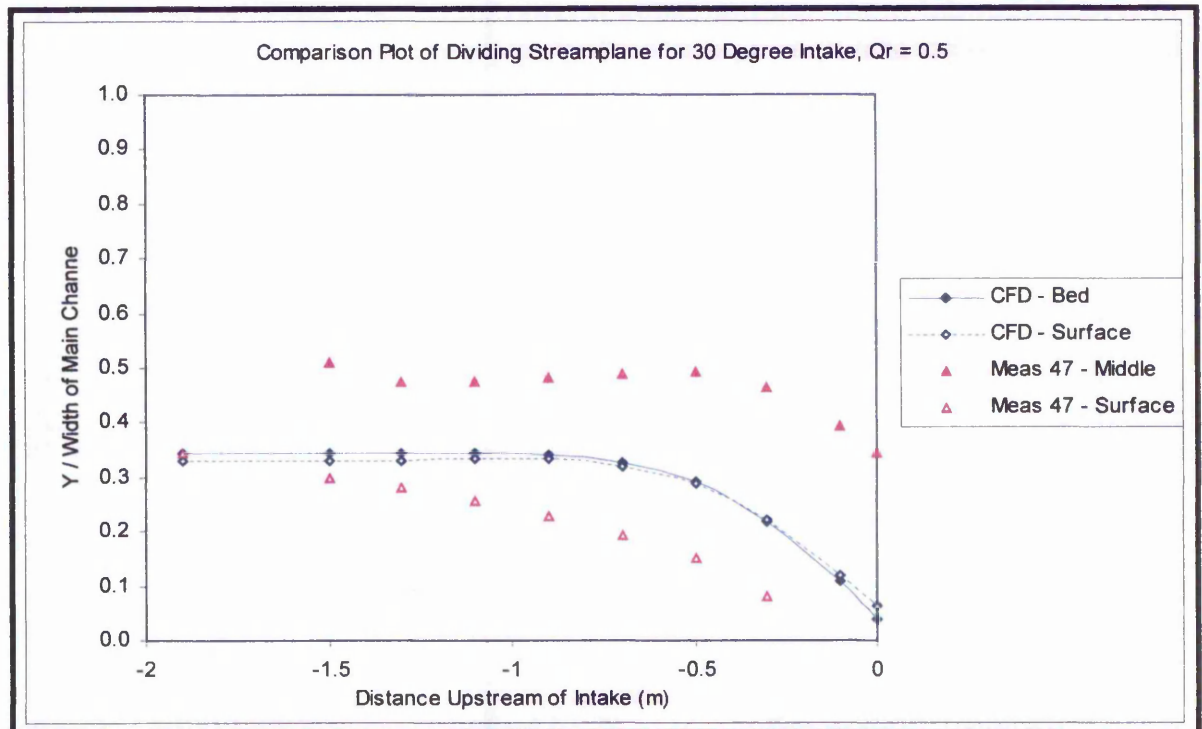
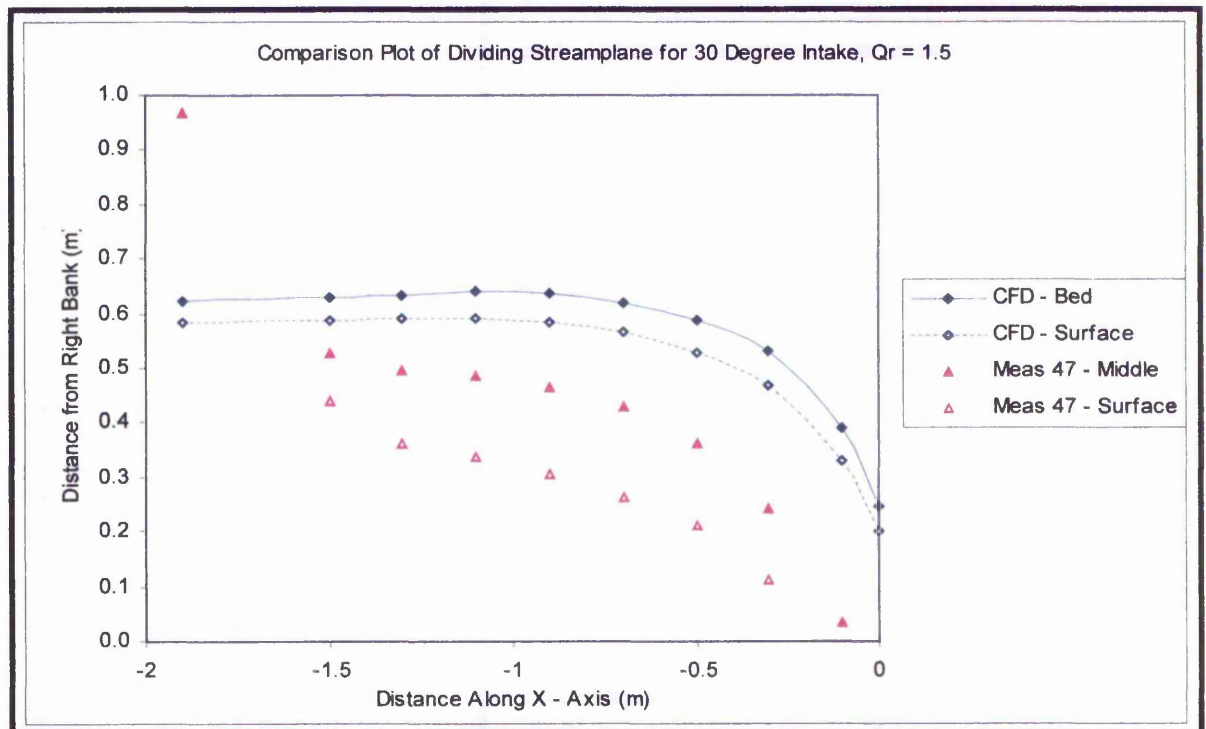Figure 6.15   Comparison of predicted to measured dividing streamline, 15 degrees, Qr = 0.5.
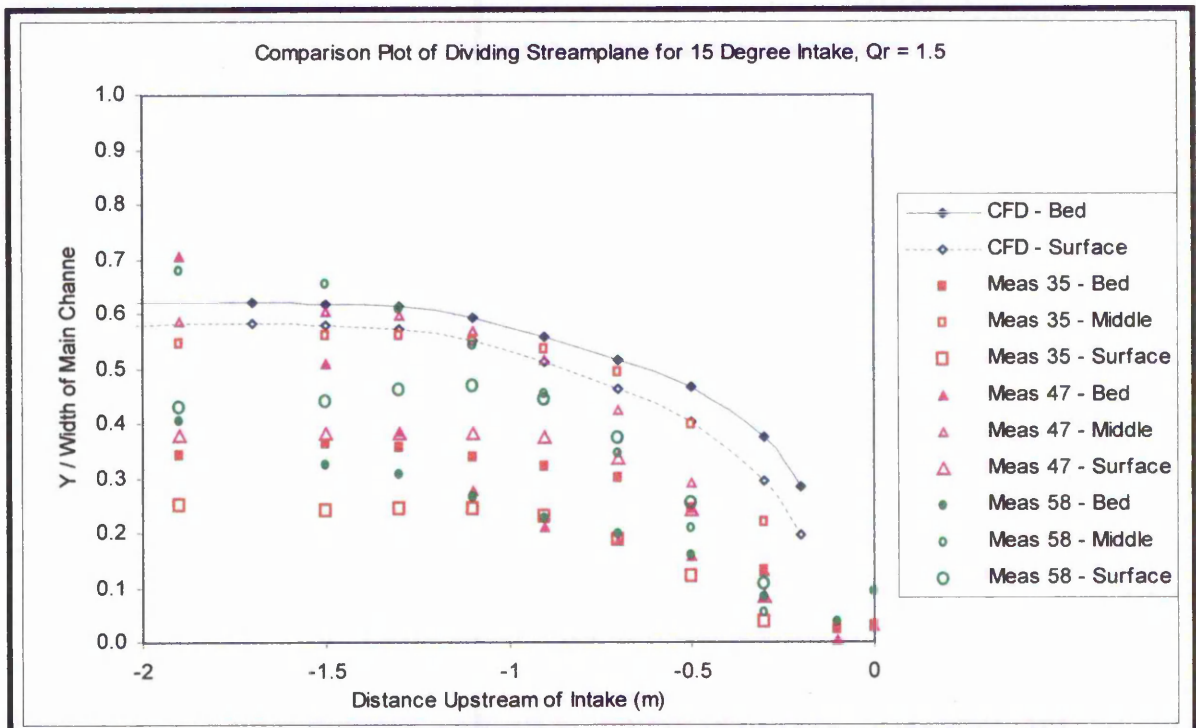
Figure 6.16   Comparison of predicted to measured dividing streamline, 15 degrees, Qr = 1.5.
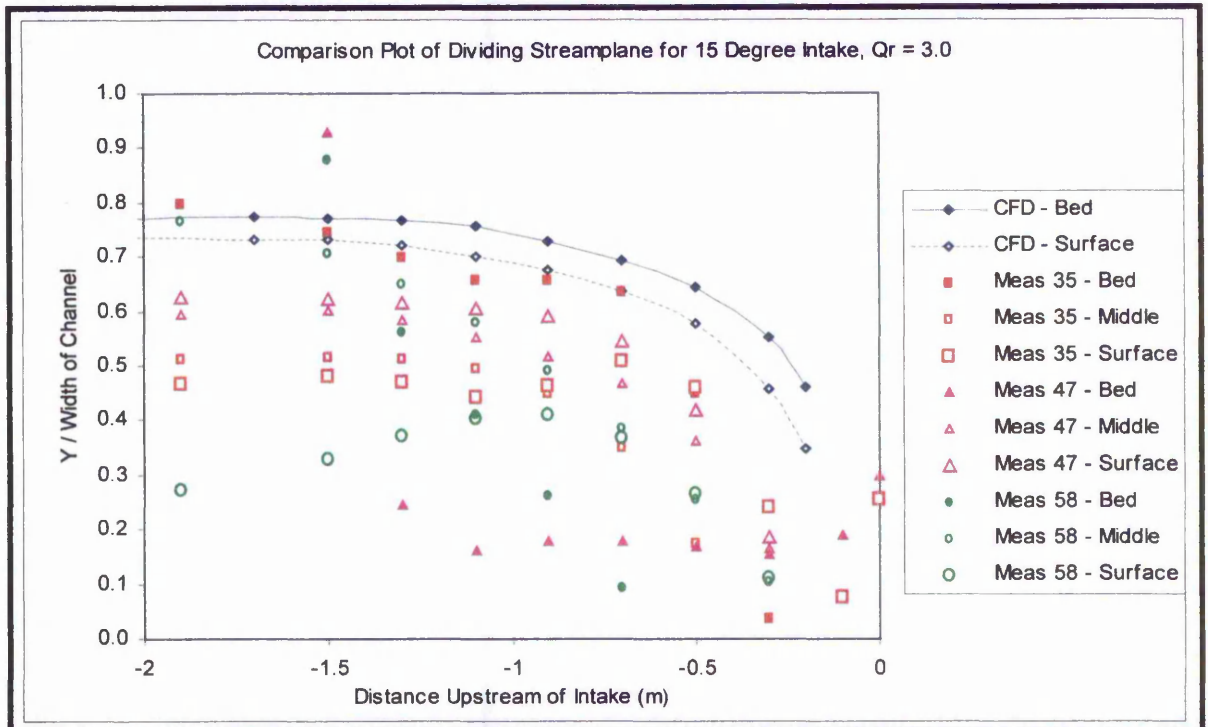
Figure 6.17   Comparison of predicted to measured dividing streamline, 15 degrees, Qr = 3.0.

Figure 6.17 shows similar results to Figure 6.16 with approximately 60% of the measurements lying within +/- 30% of the predicted results. Similarly the predicted dividing streamline generally extended further into the main channel than the measured dividing streamline.

Figure 6.18, 6.19 and 6.20 shows the comparisons between the predicted and measured dividing streamlines for a main channel flow of 47l/s and flow split ratios of 0.5, 1.5 and 3.0 respectively. It can be observed from these figures that the errors between the predicted and measured streamline are greater than for the 15 degree intake angle model. Similarily with the 15 degree intake angle studies, the predicted streamline extends further into the main channel than the measured for flow split ratios of 1.5 and 3.0. This is not the case for a flow split ratio of 0.5 as shown by Figure 6.18 which indicates that the streamline near the middle and the surface lie either side of the predicted positions. Errors of up to 60% were recorded between the measured and predicted positions of the divided streamline. It should be noted that the position of the measured dividing streamline near the bed is not shown in these figures. Large discrepancies in the streamline pattern between the measured and

predicted at the bed were observed and these could not be presented clearly using the graphical methods that have been used thus far.

Figure 6.18   Comparison of predicted and measured dividing streamline, Flow = 47l/s, Qr = 0.5.

Figure 6.19   Comparison of predicted and measured dividing streamline, Flow = 47l/s, Qr = 1.5.

Comparison Plot of Dividing Streamplane for 30 Degree Intake, Qr = 3.0
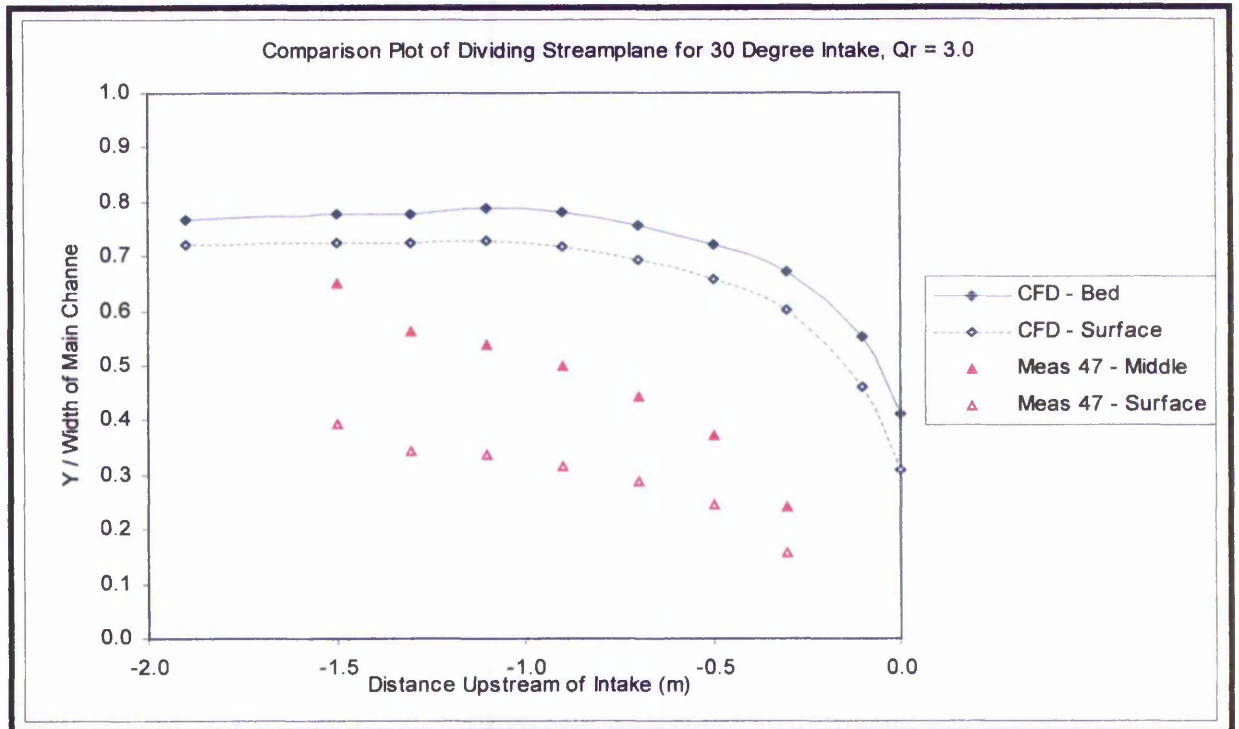
Figure 6.20 Comparison of predicted and measured dividing streamline, Flow = 47l/s, Qr = 3.0.

Figures 6.21 and 6.22 illustrate clearly the streamline patterns that were measured and predicted respectively, near the bed for the 30 degree intake angle model. Figure 6.21 showed some interesting features, particularly at a flow split ratio of 3.0. Here it can be seen that a definite vortex formed just inside the intake entrance near to the apex of the intake pier. This was not identified by the model prediction. Note also that at this high flow split ratio, flow is drawn both from the upstream and downstream portions of the main channel. Therefore, near the bed, the measurements indicate that no flow passes through the main channel downstream of the intake entrance. Clearly this was not predicted by the numerical model as shown by Figure 6.22. Notice also that although at a flow split ratio of 0.5 the streamline and velocity vector patterns compare closely between the measured and predicted, the radius of curvature and the extent of re-circulation is not predicted well at a flow split ratio of 1.5. Prediction of the streamline pattern was, however, significantly improved at greater elevations from the bed i.e. near the middle and surface.
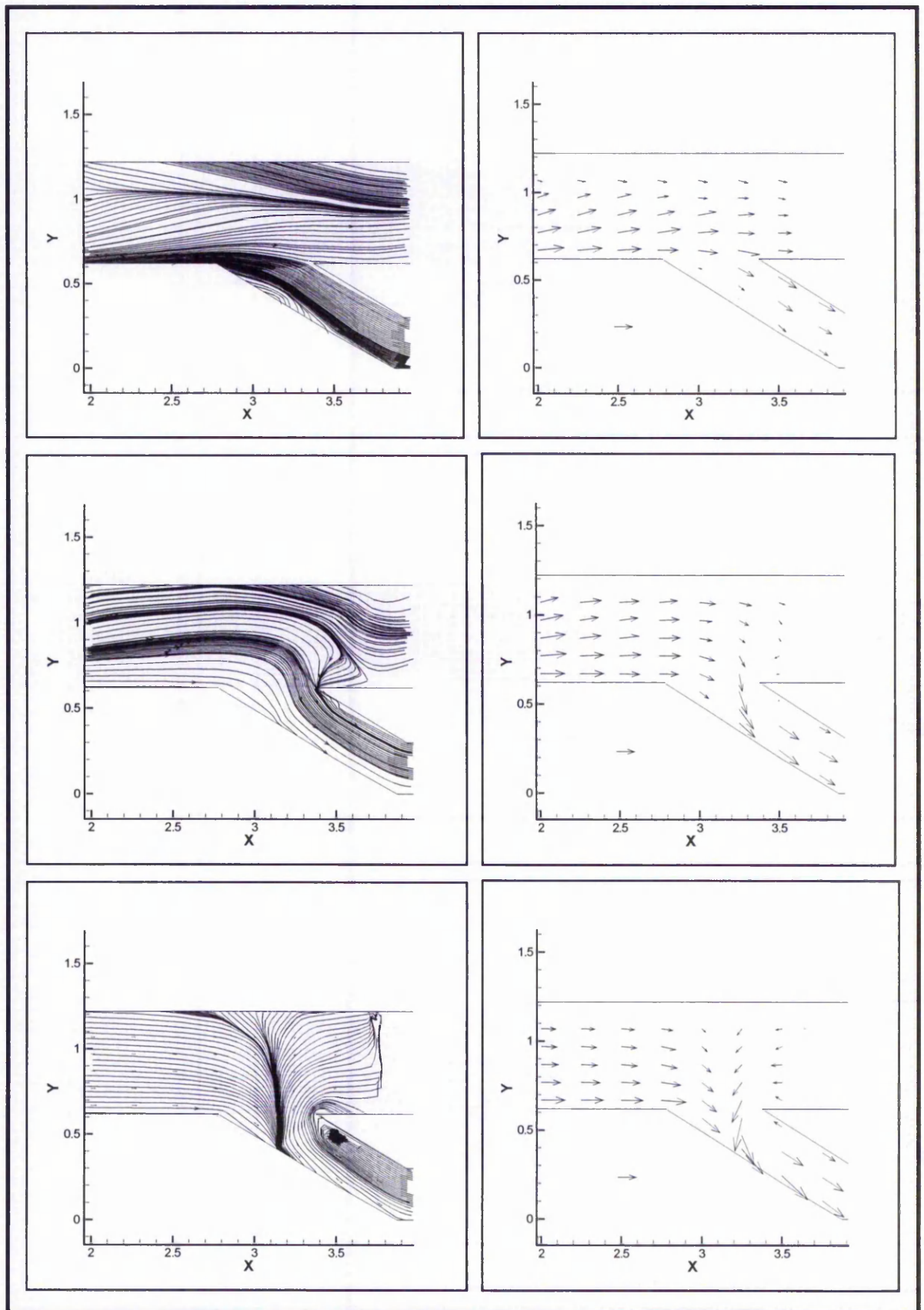
Figure 6.21   Measured streamline and vector plots at the bed for 30 degree intake, flow=47l/s, Qr = 0.5, 1.5 and 3.0.
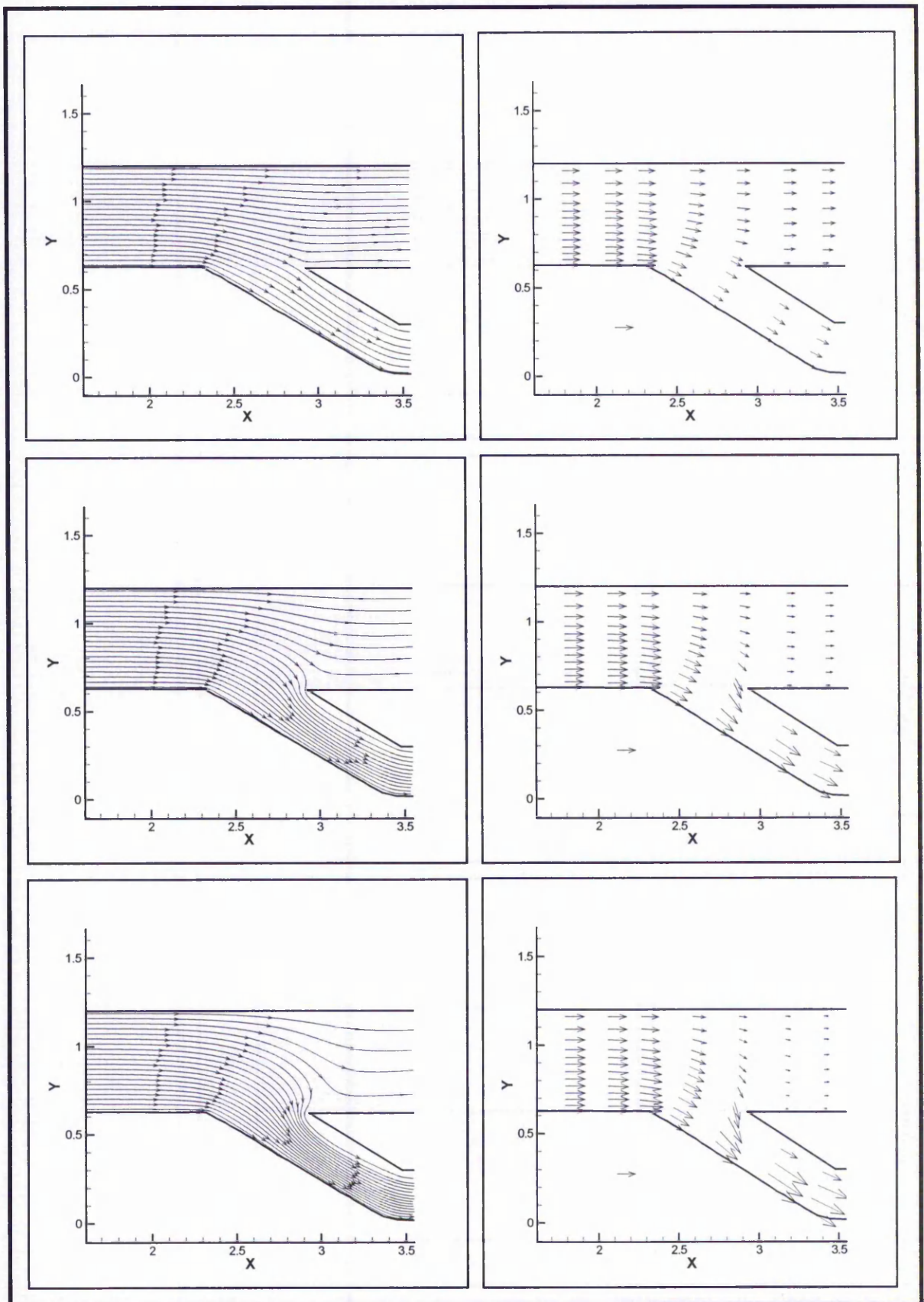
Figure 6.22   Predicted streamline and vector plots at the bed for 30 degree intake, flow=47l/s, Qr = 0.5, 1.5 and 3.0.

6.2.7 Conclusions from the Prediction of the Shape and Position of the Dividing Streamplane

The previous pages have illustrated the method that was developed for the hypothesis to predict the position and shape of the dividing streamplane for intake angles ranging from 15 to 45 degrees with flow split ratio, Qr ranging from 0.5 to 3.0. The following conclusions can be drawn from this study.

- The initial study of the depth variation of the dividing streamplane made comparisons with the findings of Neary and Odgaard. It was found that the position of the dividing streamplane upstream of the intake entrance was independent of intake angle and velocity ratio. Reasonable correlation was found between the results of this study and the results of Neary and Odgaard. The errors obtained can be attributed to the fact that Neary and Odgaard studied an intake angle of 90 degrees as opposed to intake angles of 45 degree and lower as used in this study. The initial study highlighted the phenomenon that the streamplane extended further into the main channel near the bed than near the surface due primarily to friction effects and the reduction in momentum near the bed.

- The comparison of the predicted results of the initial study to the measured results illustrated errors of less than 24% in terms of the position of the dividing streamline upstream of the entrance to the intake.

- The second part of the study investigated the position of the dividing streamplane with flow split ratio, Qr. This part of the study reinforced the previous findings and also illustrated that the depth variation of the streamplane increased with increasing flow split ratio. At low draw off rates from the main channel (e.g. Qr = 0.5), the position of the dividing streamplane varied little with depth. Quantitatively the streamplane varied by 9% in position at Qr = 3.0 in comparison to 0.2% at Qr = 0.5. This variation was due largely to inertia effects having a greater influence at larger flow split ratios.

- A qualitative investigation was subsequently undertaken into the shape of the dividing streamplane with intake angle, flow split ratio and total flow. It was found that the radius of curvature of the streamlines decreased with increased intake angles which resulted in increased energy losses. The shape of the streamlines appeared to be independent of the total flow. The spread of the positions of the dividing streamlines describing the streamplane appeared to be within a closer

range for a 15 degree intake with the range increasing with increased intake angle. The foci of the streamlines appeared to extend further downstream of the 'nosing' of the intake pier with increased intake angle. It was also observed that flow reversal occurred to a greater extent with a 45 degree intake just downstream of the nosing of the pier.

- The previous part of the study was extended to investigate the shape of the dividing streamplane quantitatively. This study confirmed the results of the previous study, showing that the shape of the streamplane was independent of the flow (and hence Reynolds number) but was dependent upon the intake angle and flow split ratio. The study also showed that the position of the dividing streamplane extended further into the main channel with large intake angles and the transition into the intake channel was smoother with an increased radius of curvature of the streamlines with lower intake angles. This suggested that energy losses were reduced with lower intake angles.

- Finally the investigation was developed to produce a family of curves that can be used to predict the shape and position of the dividing streamplane with intake angle and flow split ratio. The extension of the streamplane into the main channel was normalised by the width of the main channel so that the graphs can be used for any dimension of main channel where the ratio of intake channel to main channel is 0.5. This hypothesis for prediction was compared to physical measurements for the 15 and 30 degree intake angles with flow split ratios of 0.5, 1.5 and 3.0. The correlation obtained was reasonable with the majority of the measurements for a 15 degree intake angle, with $Qr = 0.5$ falling within +/- 10% of the predicted results. The correlation reduced to an error between measured and predicted results of +/- 30% with the higher flow split ratios of 1.5 and 3.0.

- Larger errors of up to 60% between the measured and predicted results were found with an intake angle of 30 degrees and these errors were explained with a closer comparison of the predicted and measured streamlines and velocity vectors. The comparison showed some significant areas of physically measured flow reversal which were not predicted using the computational model.

Thus this part of the study into the flow structure at an intake has developed a hypothesis for the prediction of the shape and position of the dividing streamplane for a smooth intake scenario with intake angles of 15 to 45 degrees and flow split ratios of 0.5 to 3.0.

6.3   PREDICTION OF THE FLOW SPLIT RATIO FOR AN UNCONTROLLED INTAKE.

6.3.1 Introduction.

In the previous section of the study for all the cases tested, the flow was controlled physically using the vertical sluice gate in the inlet channel and a weir in the main channel. The flow split ratio was defined during the computational modelling. A study was therefore undertaken to determine the flow split ratio of an uncontrolled intake with varying intake angle and total flow.

6.3.2 Predicted Flow Split Ratio.

A comparison was undertaken between the measured and predicted flow split ratio for intake angles of 15 and 30 degrees. The flow split ratio was measured in the physical model using sharp crested weirs of the same crest level, placed at the ends of the intake and main channels. The total flow in the physical model was measured using an orifice plate in the model delivery pipe. Figure 6.23 illustrates the results of these analyses showing the flow split ratio with total flow in the model. The general trend observed was that the proportion of the main channel flow entering the intake channel reduced with increased intake angle. This observation can be attributed to the fact that energy losses increased with increased intake angle, confirming the previous findings of the study into the dividing streamplane. Figure 6.23 also shows the comparison of the flow split ratio calculated using ADV measurements taken in the physical model for an intake angle of 15 degrees. In addition the predicted flow split ratio for an intake angle of 45 degrees is also shown for comparison purposes. An intake angle of 45 degrees was not physically modelled in this study.

Other observations that can be made from the results shown by Figure 6.23 are:
- The computational analyses under-predicted the flow split ratio in every test case, by a mean error of 9% from the measured results.
- The flow split ratio calculated from the ADV measurements was larger by a mean of 9% from the predicted results and 8% from the results measured using the weirs.

- The proportion of the main channel flow entering the intake channel for a 30 and 45 degree intake angle was approximately 11% and 15% less respectively than for a 15 degree intake angle.
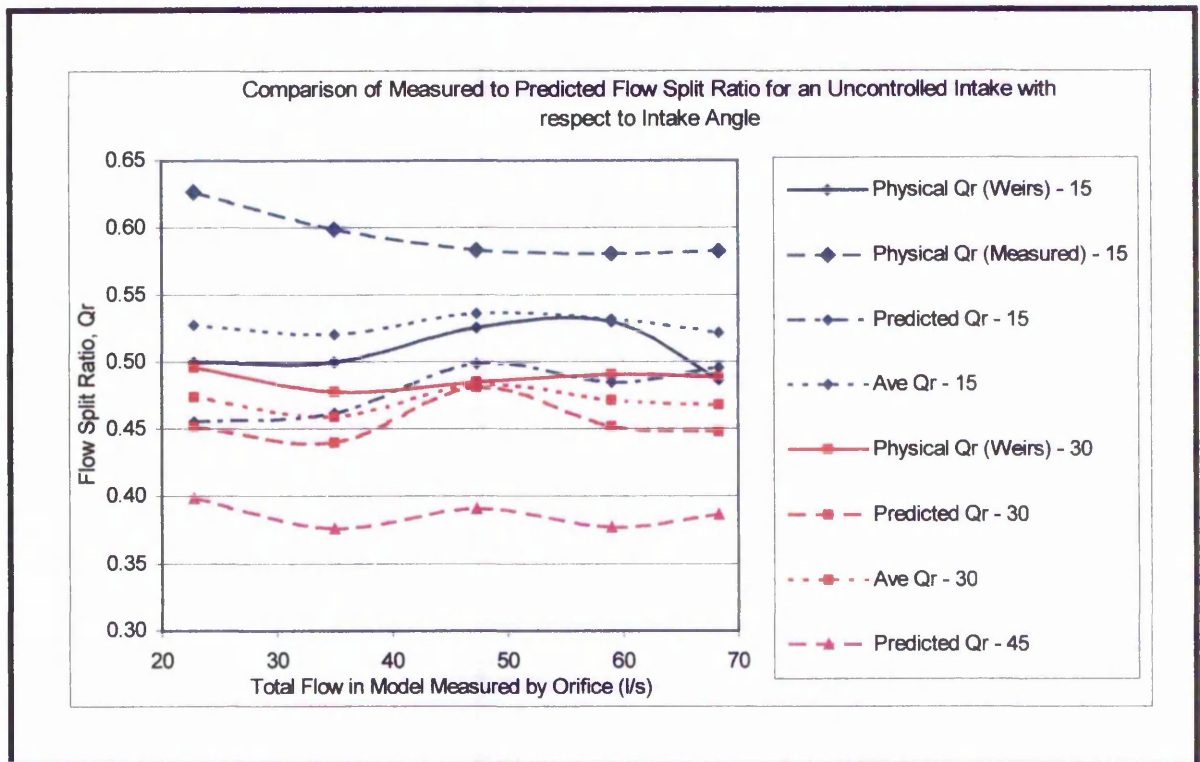

Figure 6.23   Comparison of the measured to predicted flow split ratio in an uncontrolled intake with intake angles of 15, 30 and 45 degrees.

6.4   VECTOR VISUALISATION

6.4.1 Introduction

Vector visualisation analyses were undertaken on a model with an intake angle of 15 degrees in order to identify in more detail the nature of the flow structure at the diversion. The figures that are presented here should be observed in conjunction with the previous studies. Comparison plots of two-dimensional velocity vectors were constructed for the measured and predicted results at total flows of 35 and 47 l/s.

6.4.2 Velocity Vector Comparison Plots

Figures 6.24 show comparison plots of velocity vectors at a 15 degree intake configuration with flows of 35 l/s and flow split ratios of 0.5 and 1.5. The figures also

show the variation with depth near the bed, near the middle and near the surface of the flow. The blue dotted vectors represent the measurements taken in the model using the ADV and the black solid vectors represent the predicted velocity vectors. In can be observed that generally the vectors calculated using the computational analyses under predicted the results of the physical measurements. Qualitatively the direction was generally well predicted, however a larger flow split ratios areas of re-circulation and flow reversal were measured which were not predicted by the computational model. For further details of the quantitative analysis the reader is referred back to Chapter 5, CFD Validation.

Reference to Figure 6.24 helps to explain some of the previous findings. The inability of the computational model to predict certain areas of flow reversal contributes to the under prediction of the flow split ratio described by section 6.3. Also the discrepancies observed in the prediction of the dividing streamplane can be better visualised using these figures.

Further quantitative analyses to explain previous results is illustrated in section 6.5.

6.5   VELOCITY VECTOR PROFILES

6.5.1 Introduction

The figures shown in this section illustrate the plan velocity profiles that were obtained for a comparison between the measured and predicted results. These figures help to clarify the results presented by previous sections.

6.5.2 Plan Velocity Profiles for a 15 Degree Intake Angle

Figure 6.25 shows comparison plan profiles of the resultant velocity that were obtained for an intake angle of 15 degrees with a total flow of 35 l/s and a flow split ratio of 0.5.
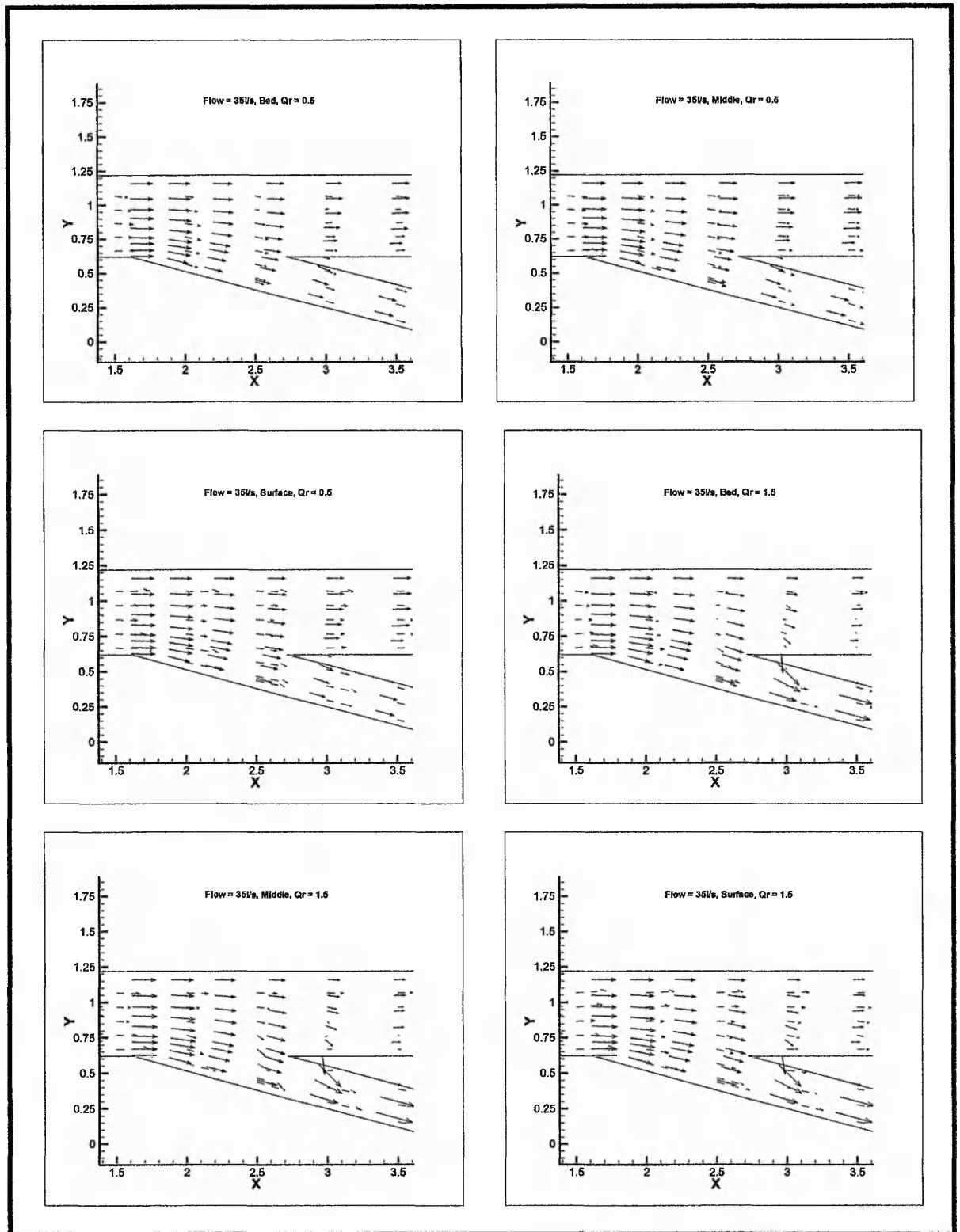
Figure 6.24   Velocity vector comparison plots for an intake angle of 15 degrees, flow = 35 l/s, Qr = 0.5 and 1.5.
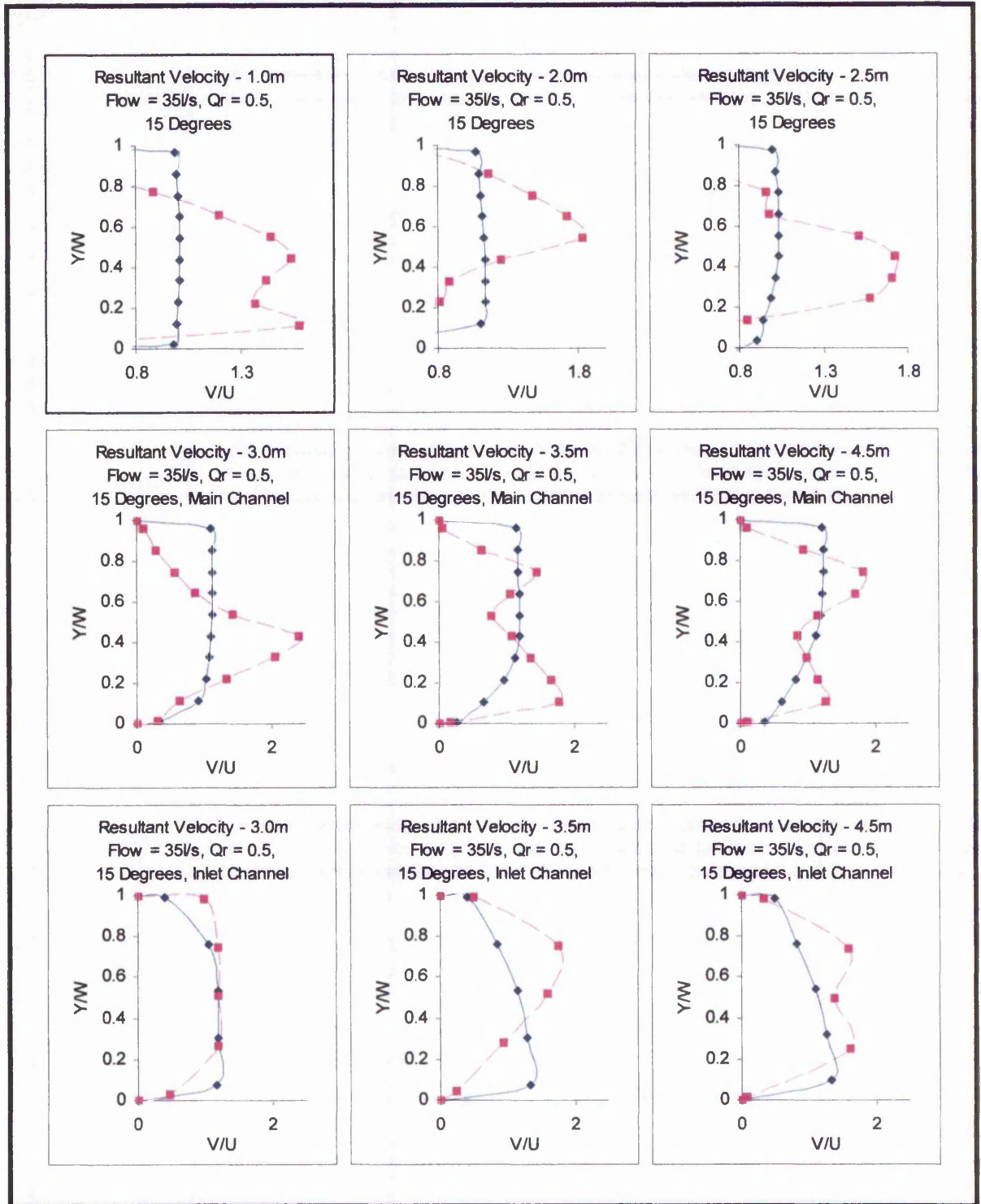
Figure 6.25   Plan resultant velocity, predicted compared to measured, near the bed, for 15 degree intake angle, flow = 35l/s, Qr = 0.5.

(Blue solid line = predicted, purple broken line = measured).

The number next to the title for each insert of the figure represents the chainage of the cross section in the model. The chainages referred to here are more clearly illustrated by Figure 6.26. The resultant velocity was normalised by the mean velocity

in the main and intake channel respectively. The cross stream dimension was also normalised by the total width of the main and inlet channels respectively.

It can be observed from Figure 6.25 that the computational model predicted the velocity poorly near the bed for a flow split ratio of 0.5, particularly in the main channel. Improvements were observed in the prediction of the velocities in the intake channel .
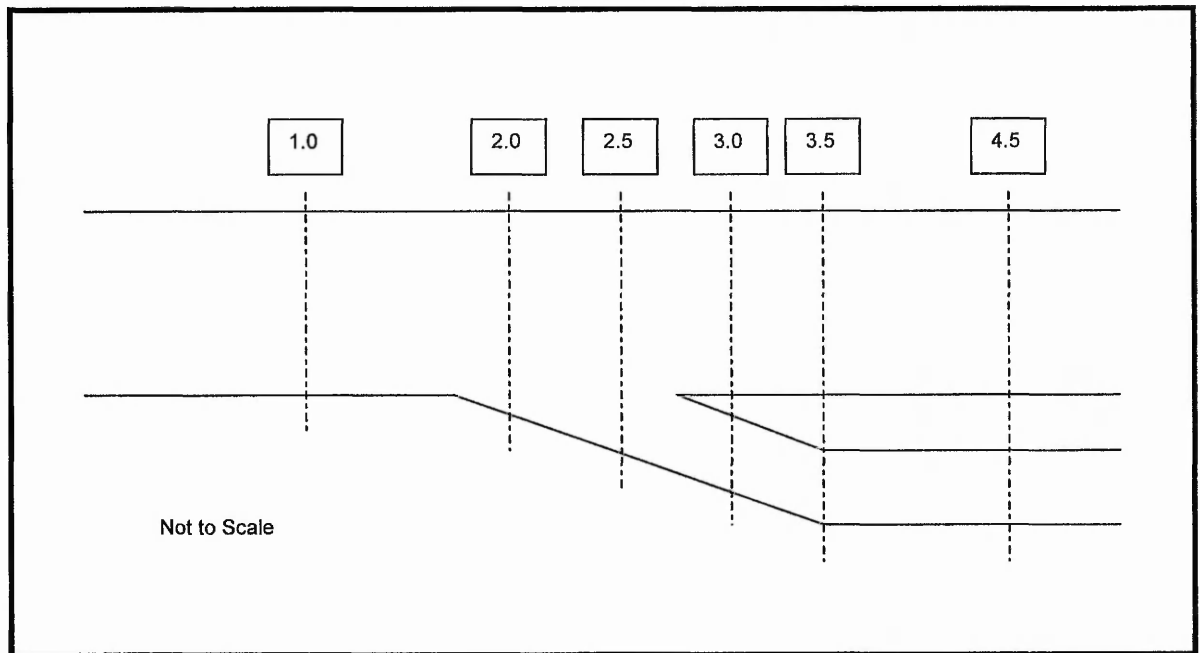
Figure 6.26   Velocity profile cross section locations for 15 degree intake.

The errors reduced near the middle and near the surface of the flow with the prediction again showing the lowest errors in the intake channel. The larger errors observed near the bed were caused for the same factors demonstrated previously by Figure 6.21 and 6.22. The computational model failed to identify accurately the flow structure near the bed. Due to friction effects at the bed, the flow pattern was considerably different to that observed away from the bed. These differences in the observed flow pattern would have been accentuated had a rough bed been examined.

Further improvements in the results were obtained for larger total flows and flow split ratios. Typical results are shown by Figure 6.27 which illustrates the results for a total flow of 47 l/s and a flow split ratio of 1.5. It can be seen that significant improvements in errors between the predicted and measured velocity profiles were obtained.

However the computational model was unable to predict the variation in the velocity in the cross stream direction that was measured in the physical model. This was mainly due to the fact that the computational model assumed fully developed flow
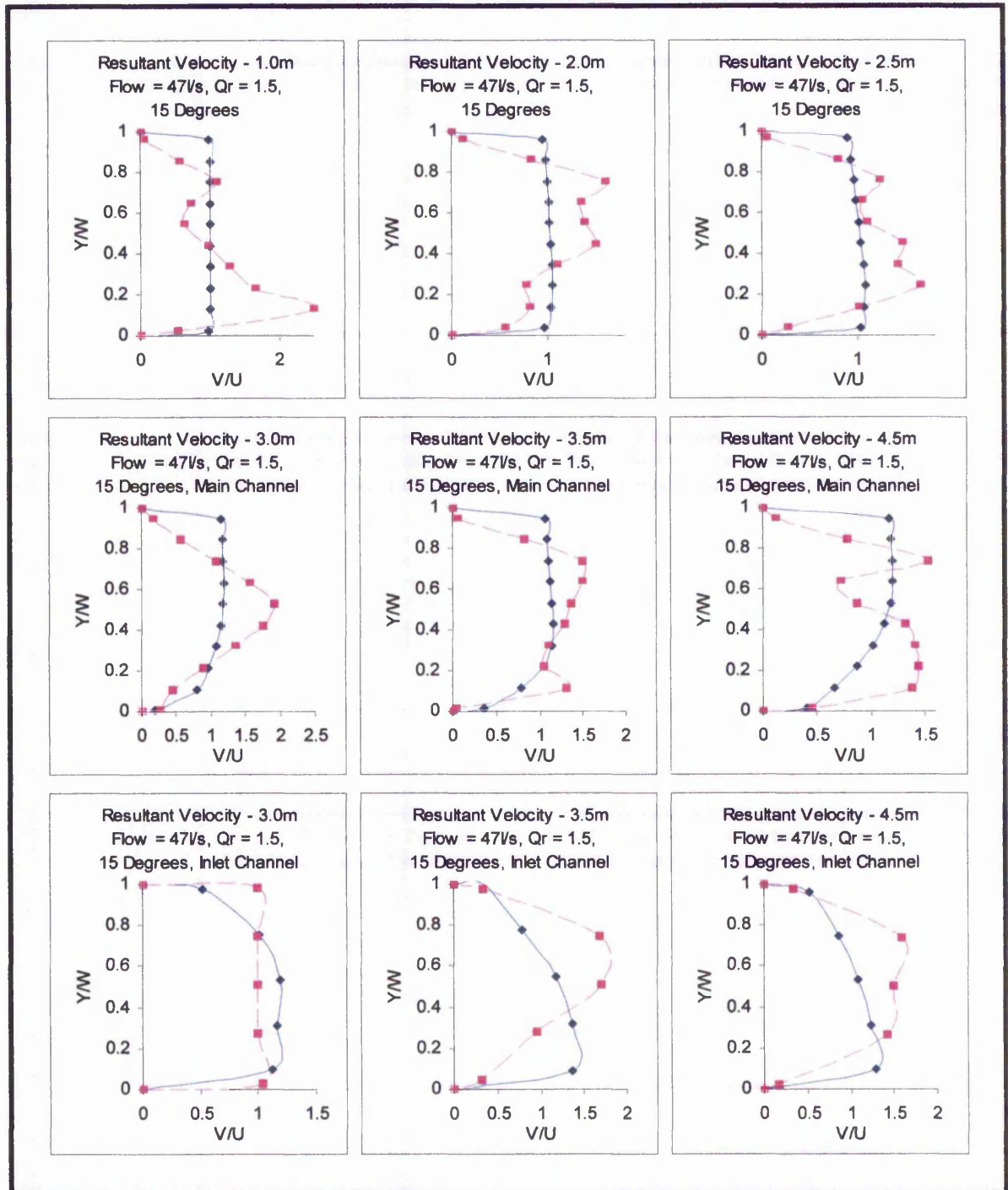
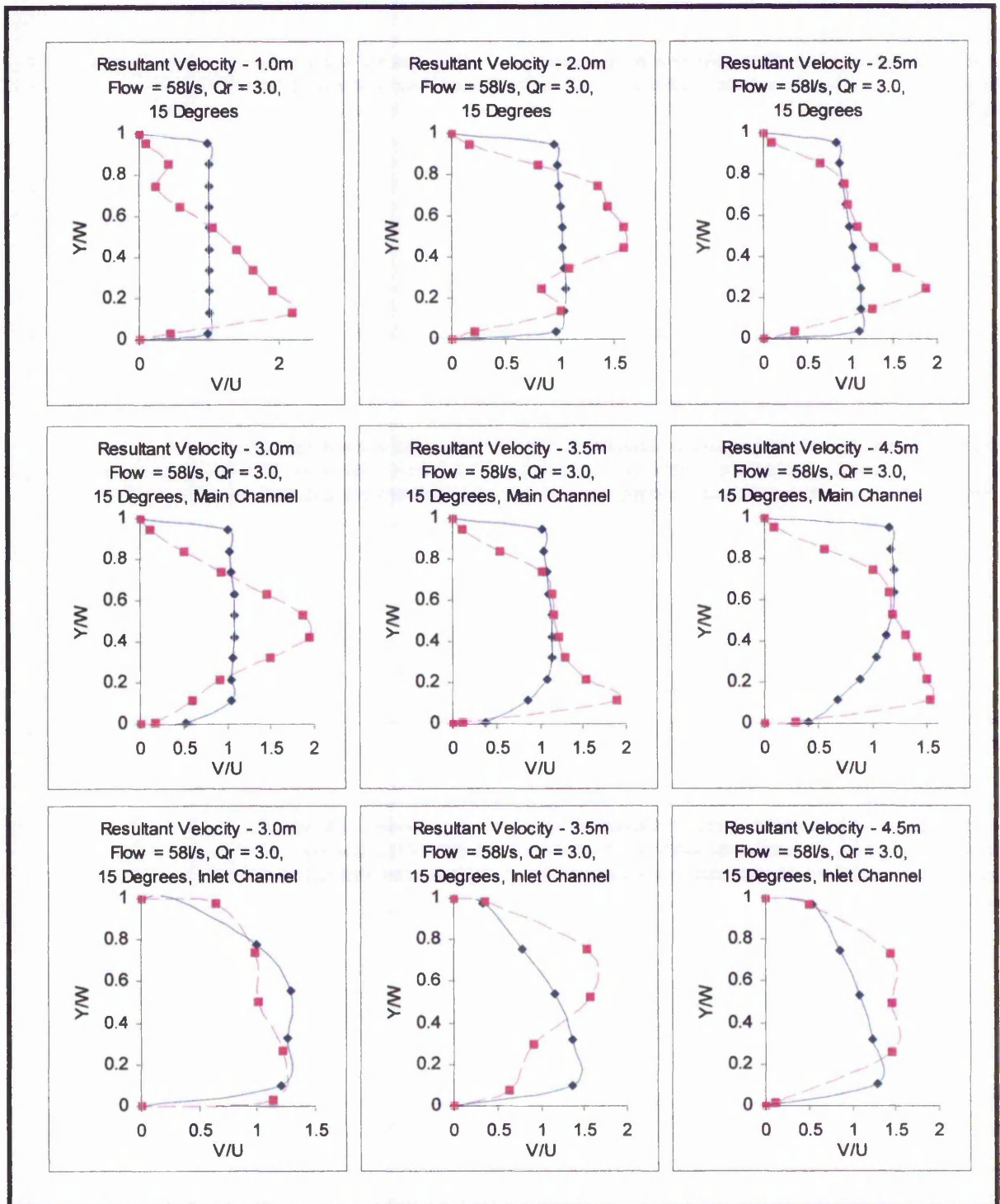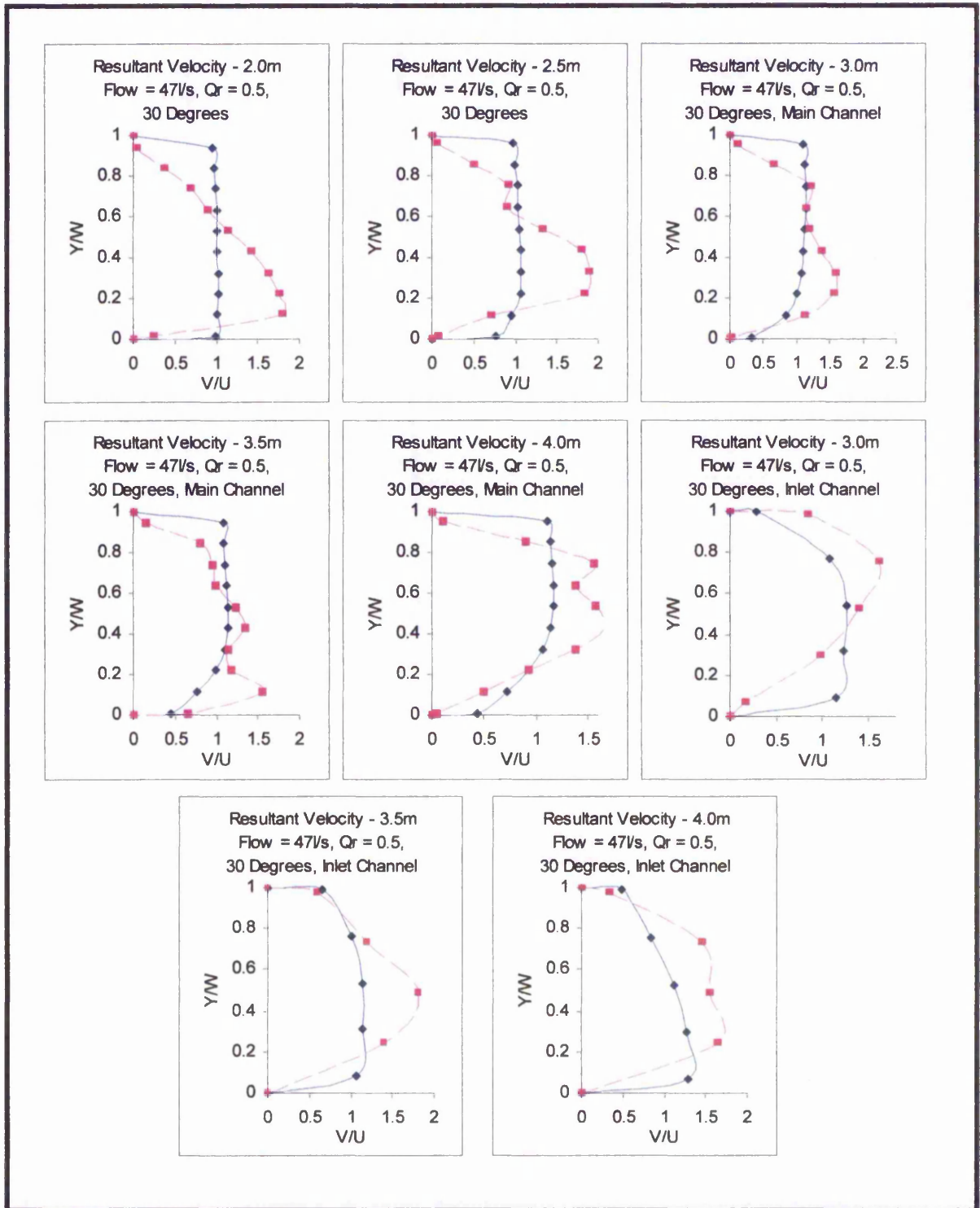Figure 6.27 Plan resultant velocity, predicted compared to measured, near the middle, for 15 degree intake angle, flow = 47l/s, Qr = 1.5.

whereas the flow in the physical model was not fully developed. Taking this fact into consideration in conjunction with the numerical and physical errors of validation and

calibration respectively (described in Chapters 4 and 5), it is reasonable to say that the results represented by the velocity profiles were acceptable.
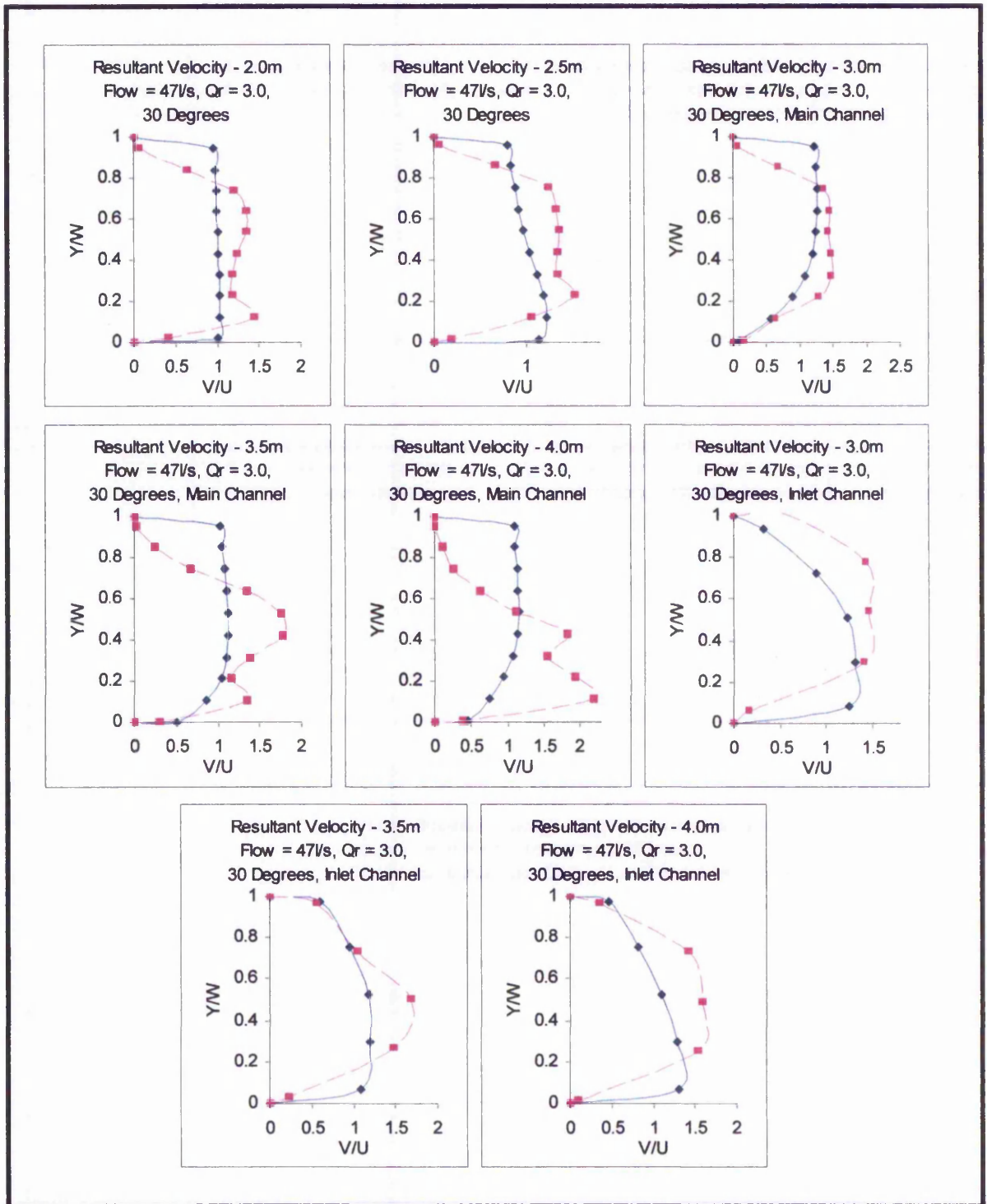

Figure 6.28 Plan resultant velocity, predicted compared to measured, near the surface, for 15 degree intake angle, flow = 58l/s, Qr = 3.0.

Further illustration of the results obtained for the 15 degree intake are shown by Figure 6.28 which shows the results near the surface for a total flow of 58 l/s and flow split ratio of 3.0.

6.5.3 Plan Velocity Profiles for a 30 Degree Intake Angle

Improved comparisons between predicted and measured velocity profiles were observed with an intake angle of 30 degrees. In similarity with the previous studies it was found that the computational model under predicted the measured velocity. However again a similar trend to the previous study was observed in which the largest errors were found near the bed.

Figure 6.29 shows a schematic representation of the location of the profile cross sections for the 30 degree intake angle.
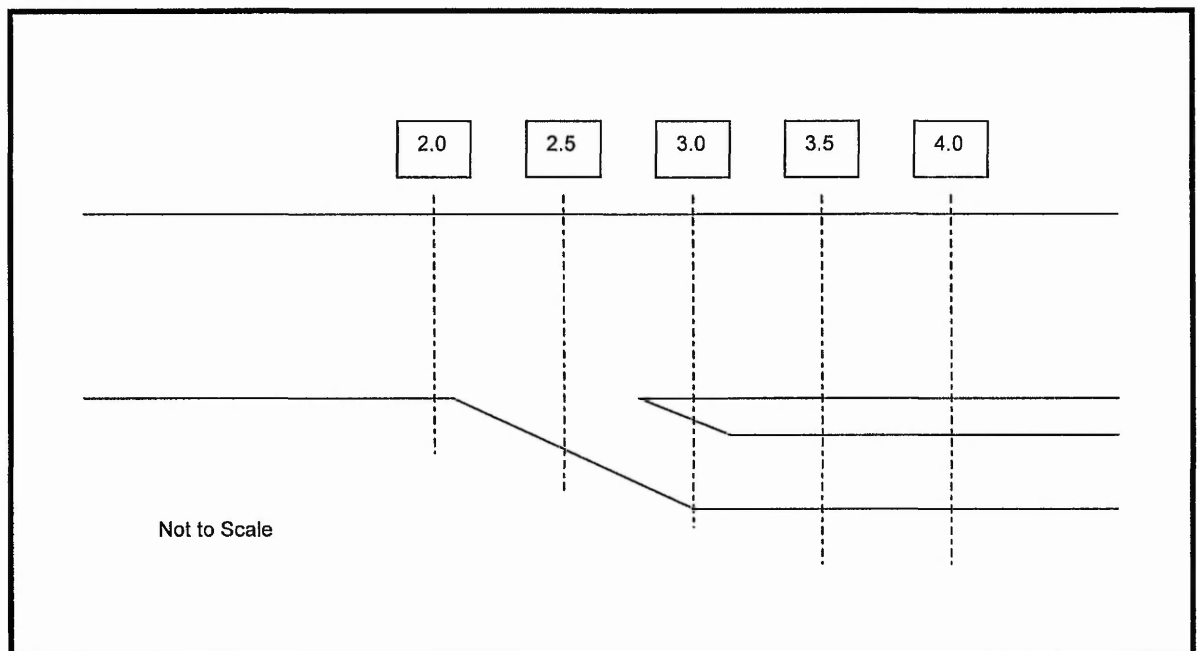
Figure 6.29   Velocity profile cross section locations for 30 degree intake.

Figure 6.30 shows the plan resultant velocity profiles for an intake angle of 30 degrees a total flow of 47 l/s and a flow split ratio of 0.5, near the bed. Similarly Figures 6.31 and 6.32 show velocity profiles for the same intake angle and total flow with flow split ratios of 1.5 and 3.0 near the middle and near the surface respectively.

Figure 6.30   Plan resultant velocity, predicted compared to measured, near the bed, for 30 degree intake angle, flow = 47l/s, Qr = 0.5.

Figure 6.32   Plan resultant velocity, predicted compared to measured, near the surface, for 30 degree intake angle, flow = 47l/s, Qr = 3.0.

6.6   PREDICTION OF THE MAXIMUM TURBULENT KINETIC ENERGY IN A FLOW DIVERSION

6.6.1 Introduction

Energy losses are an important associated factor when studying the effects of intake angle and flow split ratio upon the flow regime at the intake. The velocity distribution and streamline patterns, in conjunction with the findings of the previous sections described in this chapter, suggested that significant energy losses could be predicted using the computational model. Therefore a hypothesis was developed to predict the maximum turbulent kinetic energy (TKE) of the system by investigation of the distribution of the TKE through various scenarios of intake angle, flow split ratio and Reynolds number in the intake configuration. Comparisons of the predicted to measured TKE were also undertaken. Rigorous analyses were undertaken on the 15 degree intake configuration which are presented by the following section. The hypothesis developed was then applied to intake angles of 30 and 45 degrees and these results are described by the subsequent sections.

6.6.2 Maximum Turbulent Kinetic Energy with an Intake Angle of 15 Degrees and Total Flows of 22l/s, 35l/s, 47l/s, 58l/s and 68l/s.

A series of contour plots showing the distribution of TKE in the intake domain were generated and a sample is shown by Figure 6.33. Significant observations that were made from the contour plots focussed on the location of the maximum TKE, which was located to the left side of the intake channel near to the 'nosing' of the intake pier. This region represented the area of maximum re-circulation and turbulence and this was reflected by the levels of TKE in this region. A general observation that was observed from the contour plots and subsequent analyses was that the maximum TKE decreased with increased flow split ratio but the length and width of the zone of maximum TKE increased in size with increased flow split ratio. Quantitatively, Figure 6.34 summarises the results. This figure illustrates the variation of maximum TKE which increased with increased flow split ratio.
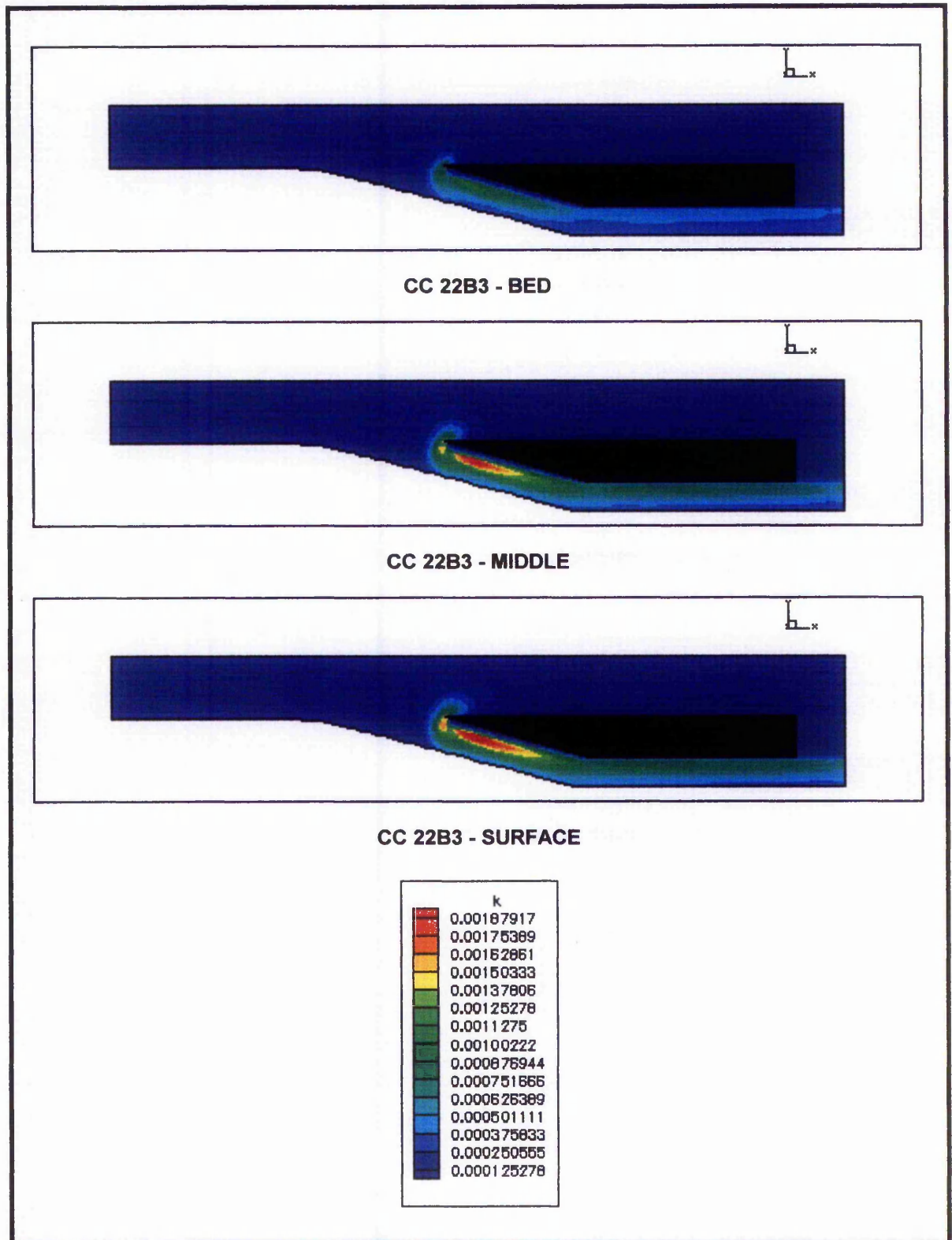
CC 22B3 - BED

CC 22B3 - MIDDLE

CC 22B3 - SURFACE

Figure 6.33   Contour plots of predicted turbulent kinetic energy, intake angle = 15 degrees, flow = 22 l/s, Qr = 2.5.
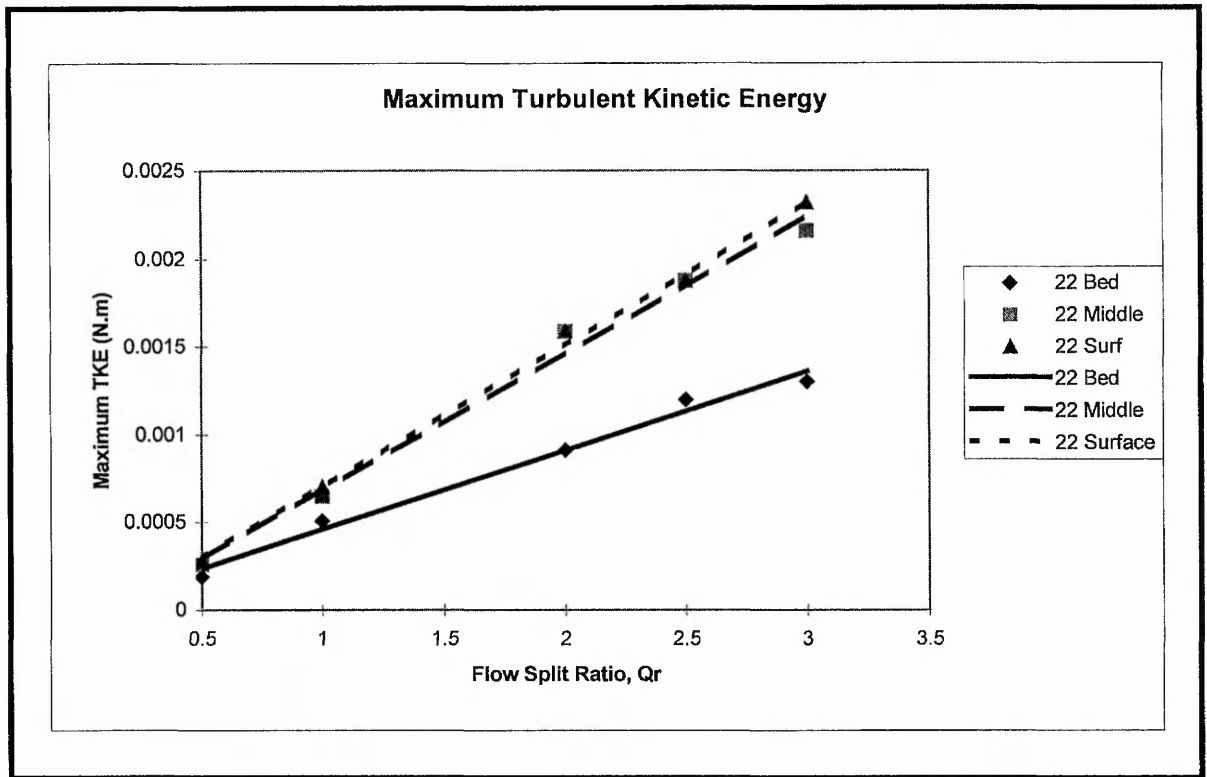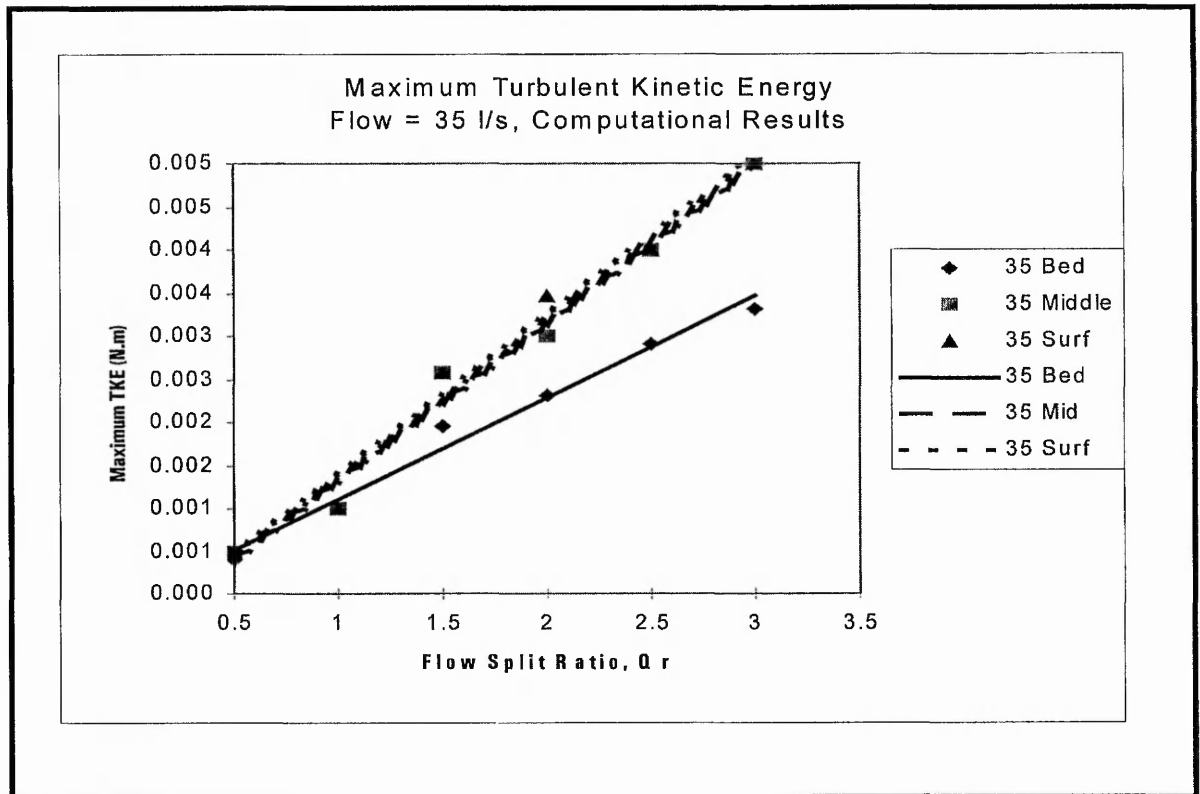
Figure 6.34   Graph to show the variation of the maximum turbulent kinetic energy with Qr, flow = 22 l/s, intake angle = 15.

Figure 6.34 indicated that there was a linear relationship between the maximum TKE and the flow split ratio. The maximum TKE was lowest near the bed and greatest near the surface of the flow. The maximum TKE near the middle and near the surface followed a similar linear relationship but the relationship at the bed was significantly different.

Further analyses of the relationship between maximum TKE, total flow (Reynolds number) and flow split ratio were undertaken for flows of 35l/s, 47l/s, 58l/s and 68l/s. The qualitative results shown by these figures are summarised by the graphical output shown in Figure 6.35 (15 degree, 35l/s), Figure 6.36 (15 degree, 47l/s), Figure 6.37 (15 degree, 58l/s) and Figure 6.38 (15 degree, 68l/s).

Similar results are shown by the summarising graph of Figure 6.35 to those of Figure 6.34. A linear relationship between maximum TKE and flow split ratio was observed and lower maximum TKE was observed near the bed. The relationship for maximum TKE near the middle and near the surface were again closely related. However the

Figure 6.35   Graph to show the variation of the maximum turbulent kinetic energy with Qr, flow = 35 l/s, intake angle = 15.

magnitude of the maximum TKE was greater for a total flow of 35l/s shown by the increase in gradient of the linear line in Figure 6.35.
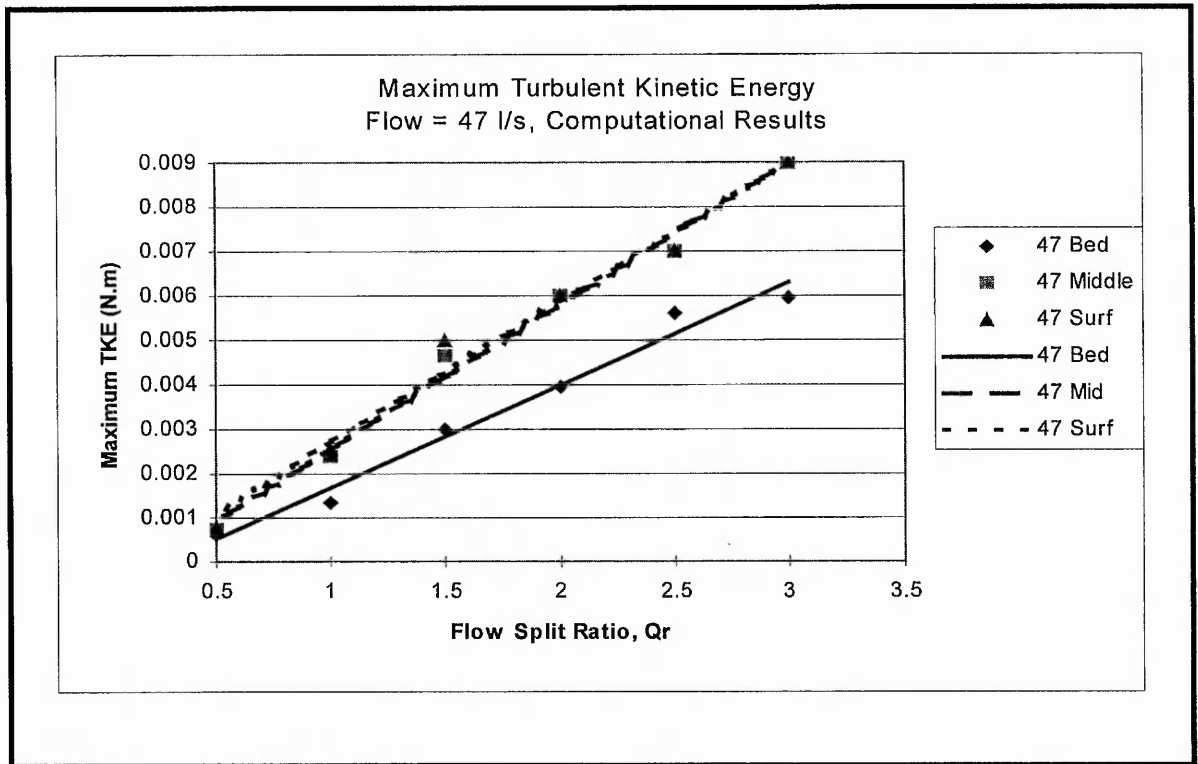
Figure 6.36   Graph to show the variation of the maximum turbulent kinetic energy with Qr, flow = 47 l/s, intake angle = 15.

Figure 6.36 summarises the results of the analysis of the maximum TKE for a flow of 47l/s. Similar results to the previous summarising graphs are observed but most notably the magnitude of the maximum TKE predicted was greater than for a flow of 35l/s.

Comparison was also made to the measured TKE and this is shown by Figures 6.37, 6.38 and 6.39 (Qr = 0.5, 1.5, 3.0 (15 degree, 35l/s), and Figure 6.40 (Qr = 3.0, 15 degree, 47l/s). Analyses undertaken on the measured TKE in the flow domain identified some interesting features. Although the distribution of the measured TKE was considerably different to the predicted TKE, the measured results identified an area of maximum TKE in a similar location to the predicted results. This was shown again to be near the entrance to the intake channel on the left side of the intake channel. However, the TKE was identified to be greater near the bed and this was clearly in disagreement to the predicted results. A possible explanation for this was due to the highly irregular flow pattern induced by turbulence that was measured and described in a previous section of this study.
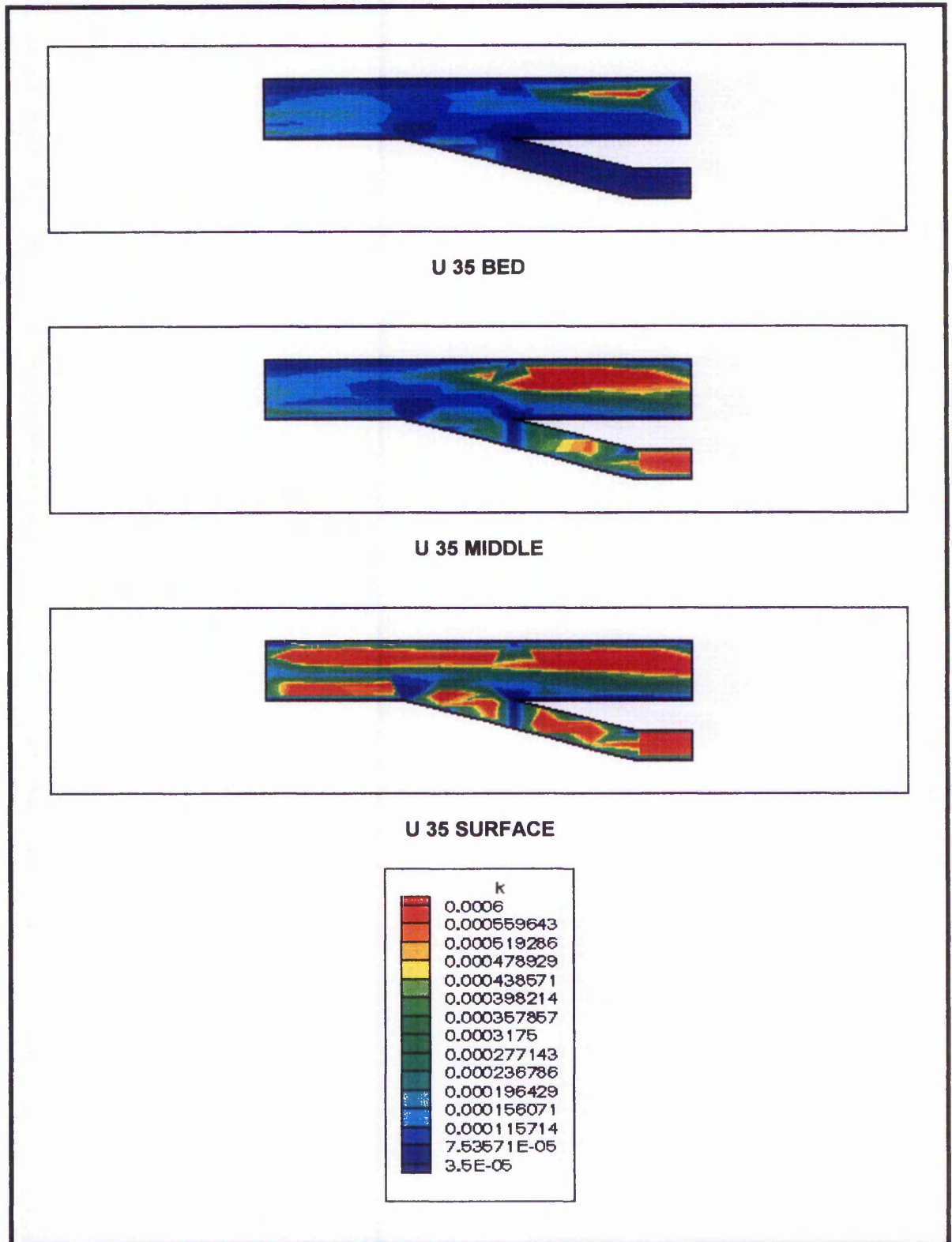
U 35 BED

U 35 MIDDLE

U 35 SURFACE

Figure 6.37   Contour plots of measured turbulent kinetic energy, intake angle = 15 degrees, flow = 35 l/s, Qr = 0.5.

C 35A - BED

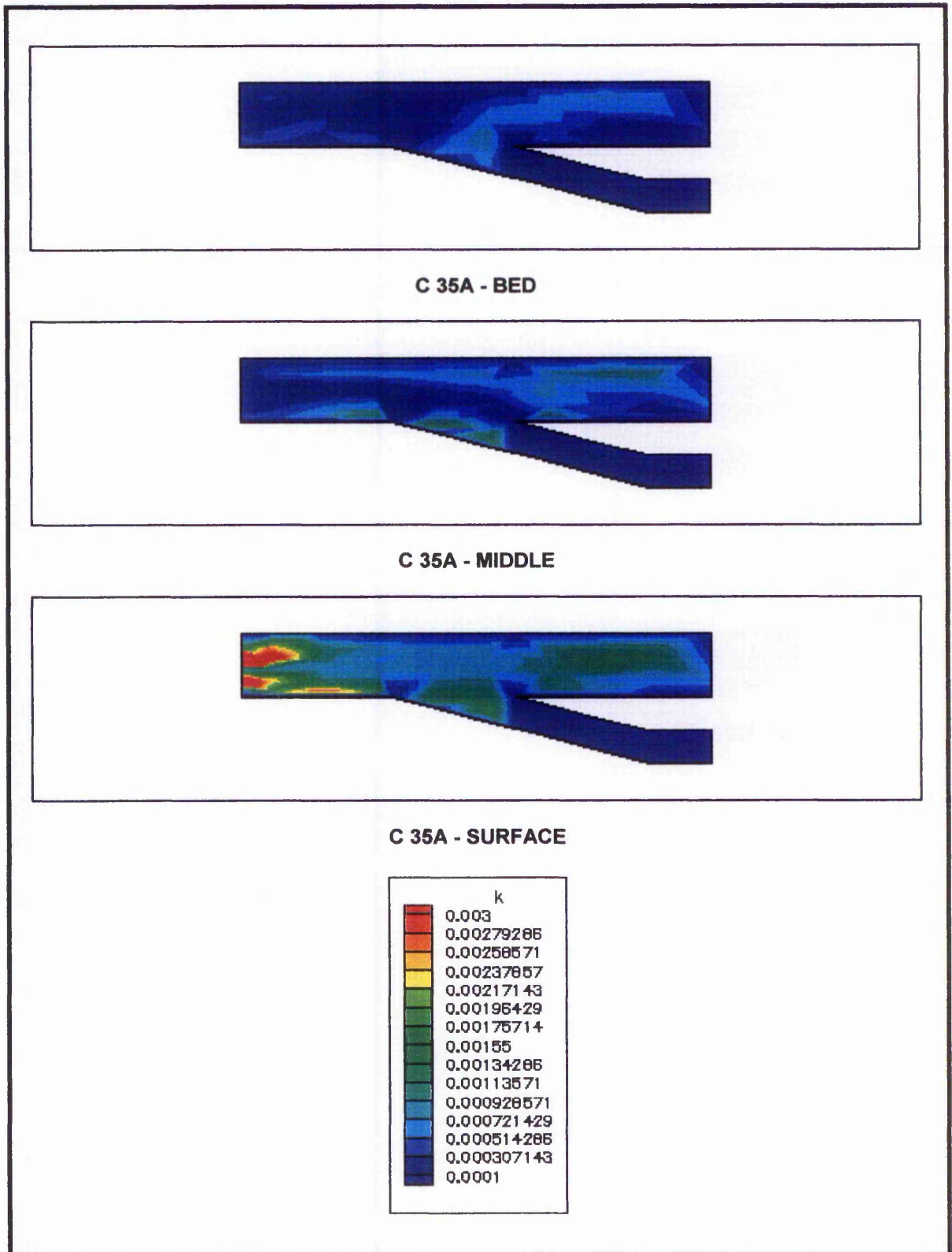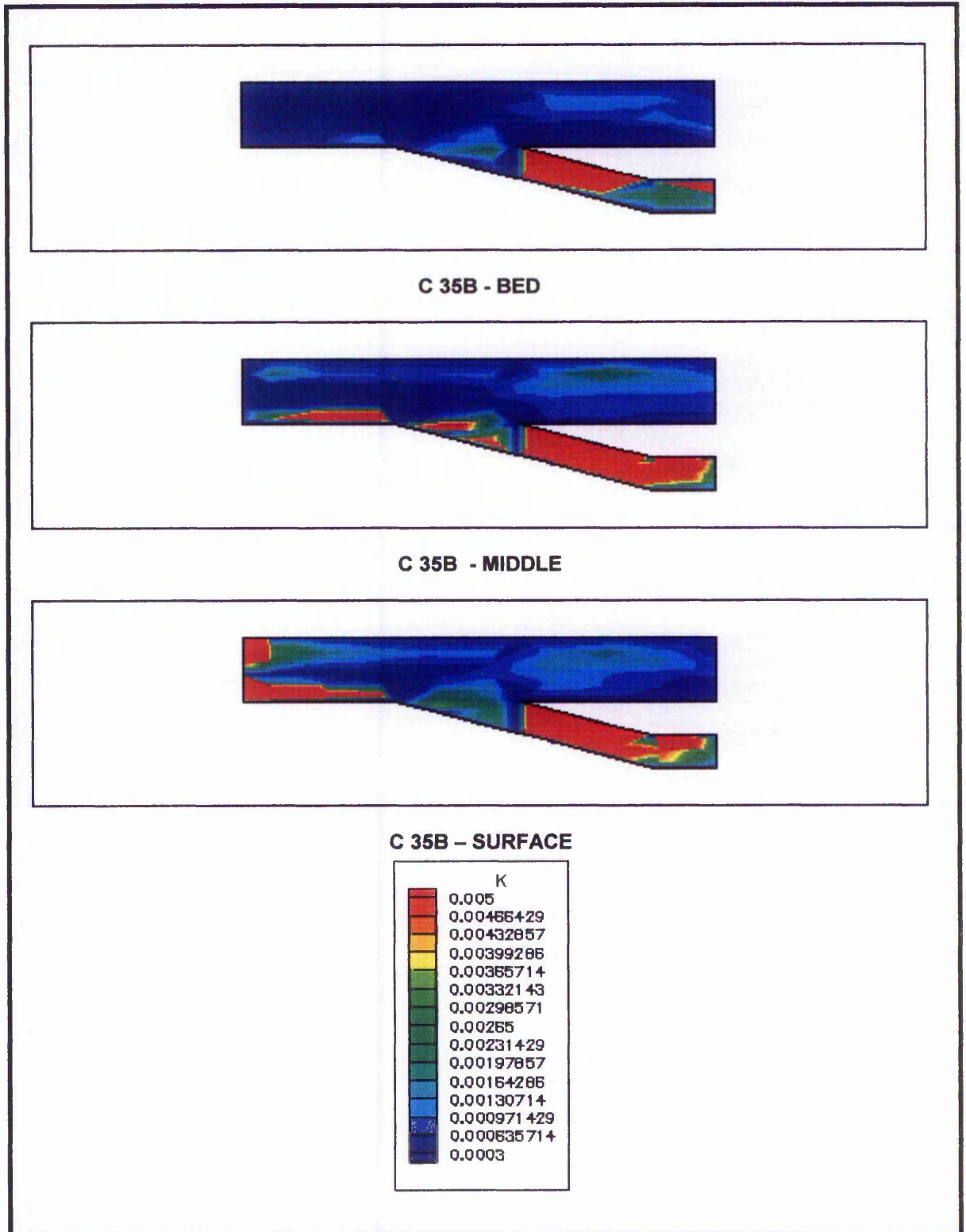**C 35A - MIDDLE**

C 35A - SURFACE

k
0.003
0.00279286
0.00258571
0.00237857
0.00217143
0.00196429
0.00175714
0.00155
0.00134286
0.00113571
0.000928571
0.000721429
0.000514286
0.000307143
0.0001

Figure 6.38   Contour plots of measured turbulent kinetic energy, intake angle = 15 degrees, flow = 35 l/s, Qr = 1.5.

C 35B - BED

C 35B - MIDDLE

C 35B – SURFACE

K
0.005
0.00466429
0.00432857
0.00399286
0.00365714
0.00332143
0.00298571
0.00265
0.00231429
0.00197857
0.00164286
0.00130714
0.000971429
0.000635714
0.0003

Figure 6.39   Contour plots of measured turbulent kinetic energy, intake angle = 15 degrees, flow = 35 l/s, Qr = 3.0.

C 47B - BED

C 47B - MIDDLE

C 47B - SURFACE
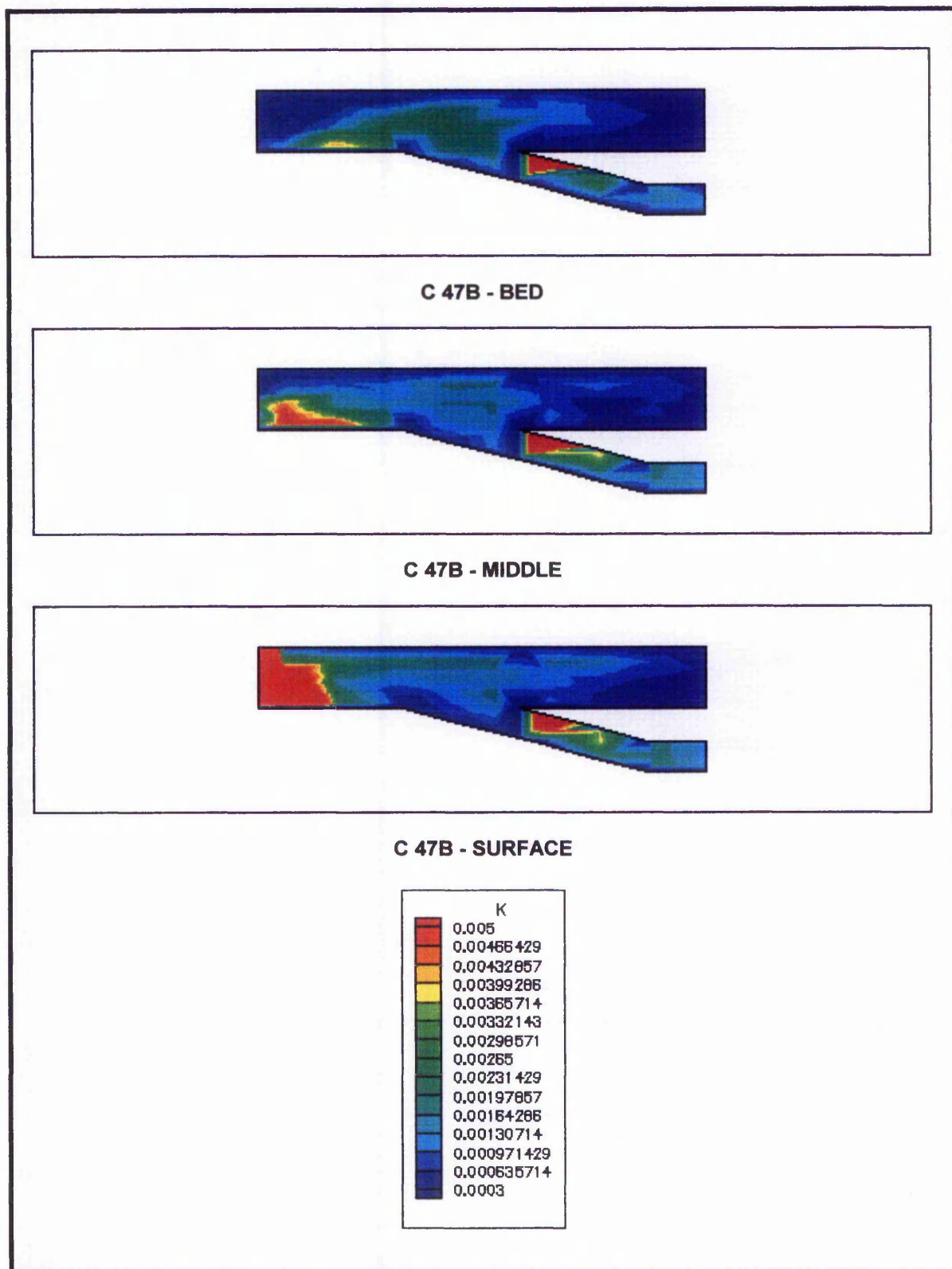
Figure 6.40   Contour plots of measured turbulent kinetic energy, intake angle = 15 degrees, flow = 47 l/s, Qr = 3.0.

Figure 6.40 shows the distribution of the measured TKE for a total flow of 47l/s. A maximum TKE of 0.006Nm was measured near the surface for this case which can be compared to a predicted maximum of 0.009Nm, an error of 33%. The general trend observed was that the maximum TKE was predicted with errors less than 30%. In addition the measured results of a total flow of 47l/s, correlated more successfully with the predicted in terms of location. Figure 6.40 clearly shows a zone of high TKE to the left of the intake channel, just downstream of the nosing of the intake pier. In all the visualisation studies for the TKE this zone was observed to contain the maximum TKE.

The following figures develop the observations to total flows of 58l/s and 68l/s.
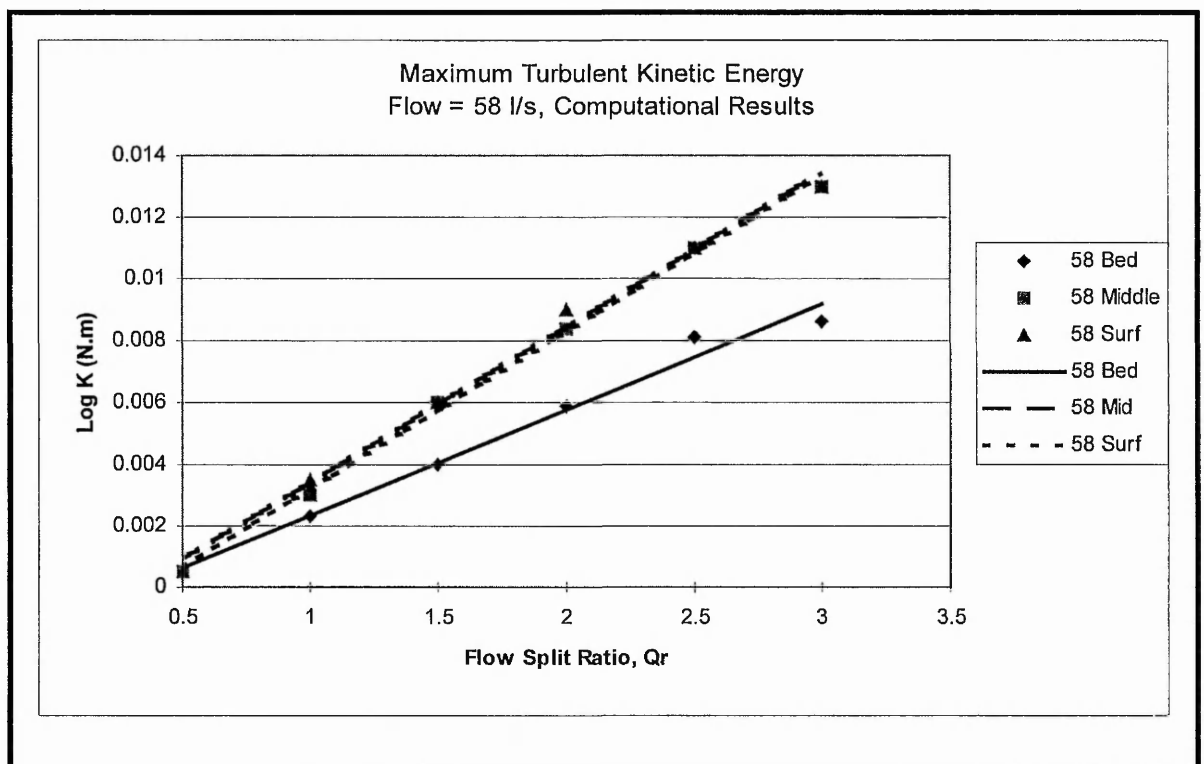
Figure 6.41   Graph to show the variation of the maximum turbulent kinetic energy with Qr, flow = 58 l/s, intake angle = 15.

The summarising graphs of Figures 6.41 and 6.42 again show similar trends to the previous findings with a linear relationship between maximum TKE and flow split ratio with the magnitude of the TKE also increasing with increased flow. The conclusions to all the results presented here was that the maximum TKE was a function of the flow and hence Reynolds number and the flow split ratio. Figure 6.43 brings all the findings of this study together in one graph showing the relationship of the maximum

TKE to flow and flow split ratio. Here it can be seen that the TKE increased with increased flow and flow split ratio.
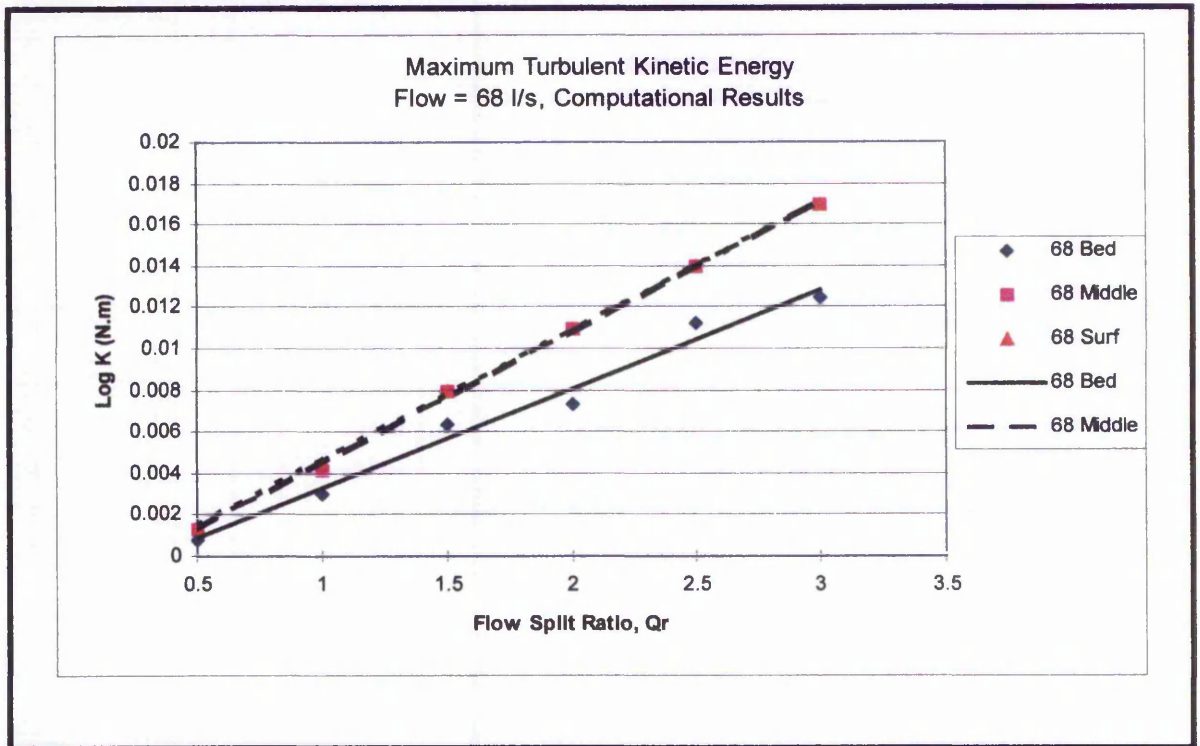

Figure 6.42   Graph to show the variation of the maximum turbulent kinetic energy with Qr, flow = 68 l/s, intake angle = 15.
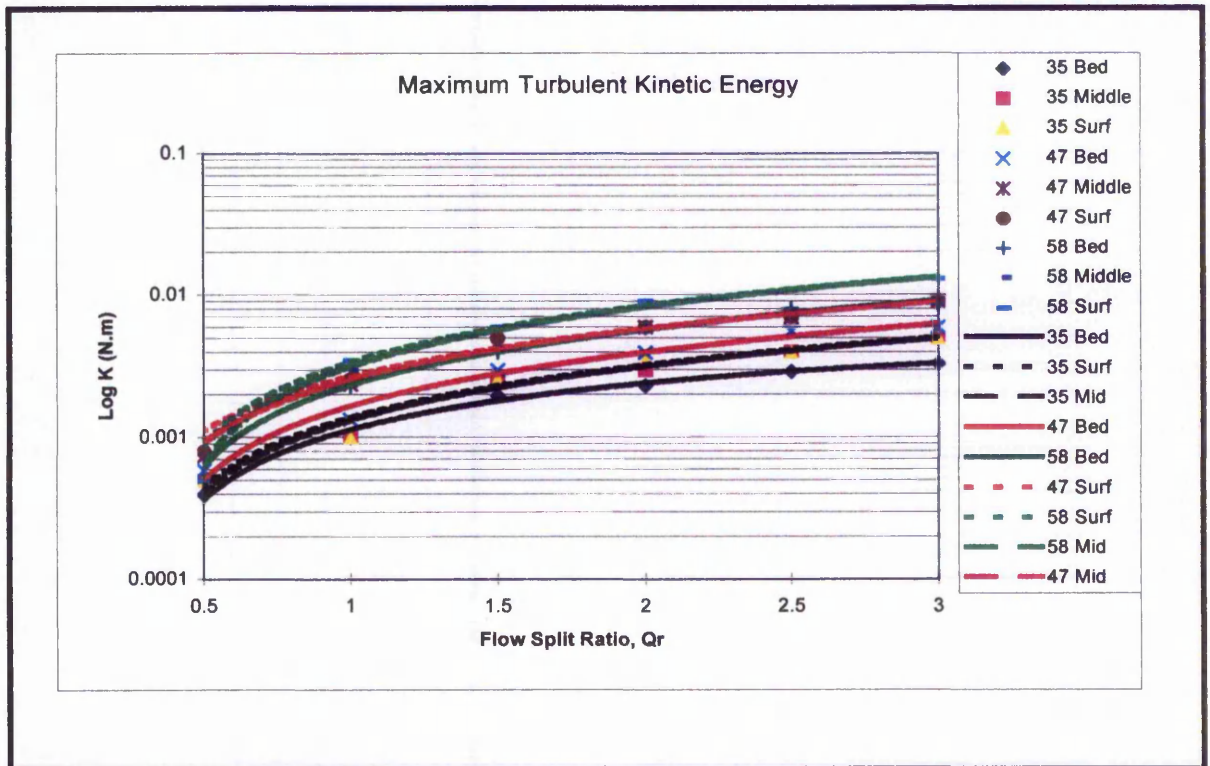

Figure 6.43   Variation of the maximum turbulent kinetic energy with flow and flow split ratio, intake angle = 15.

Tables 6.4, 6.5, 6.6 show the observed errors between the measured and predicted maximum TKE. Generally TKE was predicted to an error of less than 30% but occasionally gross errors were observed. These were probably due to abnormalities in the code or measurement errors in the physical model.

Qr	Computational	Physical	Difference	% Error (P from C)	Level
0.5	0.0004	0.0001	0.0003	300	Bed
0.5	0.0005	0.0005	0.0000	0	Middle
0.5	0.0006	0.0008	-0.0002	-25	Surface
1.5	0.0071	0.0082	-0.0011	-13	Bed
1.5	0.0026	0.0067	-0.0041	-61	Middle
1.5	0.0026	0.0033	-0.0007	-21	Surface
3.0	0.0033	0.0532	-0.0499	-94	Bed
3.0	0.0050	0.0058	-0.0008	-14	Middle
3.0	0.0050	0.0065	-0.0015	-23	Surface

Table 6.4 Comparison of the predicted to measured maximum turbulent kinetic energy in a 15 degree intake with a flow of 35 l/s.

Qr	Computational	Physical	Difference	% Error (P from C)	Level
0.5	0.0006	0.0002	0.0004	200	Bed
0.5	0.0007	0.0008	-0.0001	-12.5	Middle
0.5	0.0008	0.0018	-0.0010	-56	Surface
1.5	0.0030	0.0031	-0.0001	-3	Bed
1.5	0.0047	0.0041	0.0006	15	Middle
1.5	0.0050	0.0029	0.0021	72	Surface
3.0	0.0060	0.0047	0.0013	28	Bed
3.0	0.0090	0.0072	0.0018	25	Middle
3.0	0.0090	0.0091	0.0001	1	Surface

Table 6.5 Comparison of the predicted to measured maximum turbulent kinetic energy in a 15 degree intake with a flow of 47 l/s.

Qr	Computational	Physical	Difference	% Error (P from C)	Level
0.5	0.0005	0.0005	0.0000	0	Bed
0.5	0.0005	0.0009	-0.0004	-44	Middle
0.5	0.0005	0.0006	-0.0001	-17	Surface
1.5	0.0040	0.0026	0.0014	53	Bed
1.5	0.0060	0.0080	-0.0020	-25	Middle
1.5	0.0060	0.0065	-0.0005	-8	Surface
3.0	0.0086	0.0099	-0.0013	-13	Bed
3.0	0.0130	0.0059	0.0071	120	Middle
3.0	0.0130	0.0149	-0.0019	-13	Surface

Table 6.6 Comparison of the predicted to measured maximum turbulent kinetic energy in a 15 degree intake with a flow of 58 l/s.

Having completed the investigation into the maximum TKE for a 15 degree intake, a hypothesis was developed to enable the prediction of the maximum TKE as a function of the total flow, the flow split ratio and the intake angle. This hypothesis was

designed to be applied to any channel ratio of 0.5 (intake channel / main channel) with a smooth bed. The term smooth bed would typically apply to a concrete channel in a prototype situation. The hypothesis was based on the fact that a linear relationship existed between the maximum TKE and the flow split ratio and the total flow. Thus a relatively simple analyses of the regression equations obtained from the previous studies resulted in a linear equation of the general form:

$$\text{Maximum TKE} = (m \times Qr) - C \qquad\qquad 6.1$$

Where:

M is a coefficient interpolated from Figure 6.44.

Qr = Flow split ratio.

C is a constant interpolated from Figure 6.44.
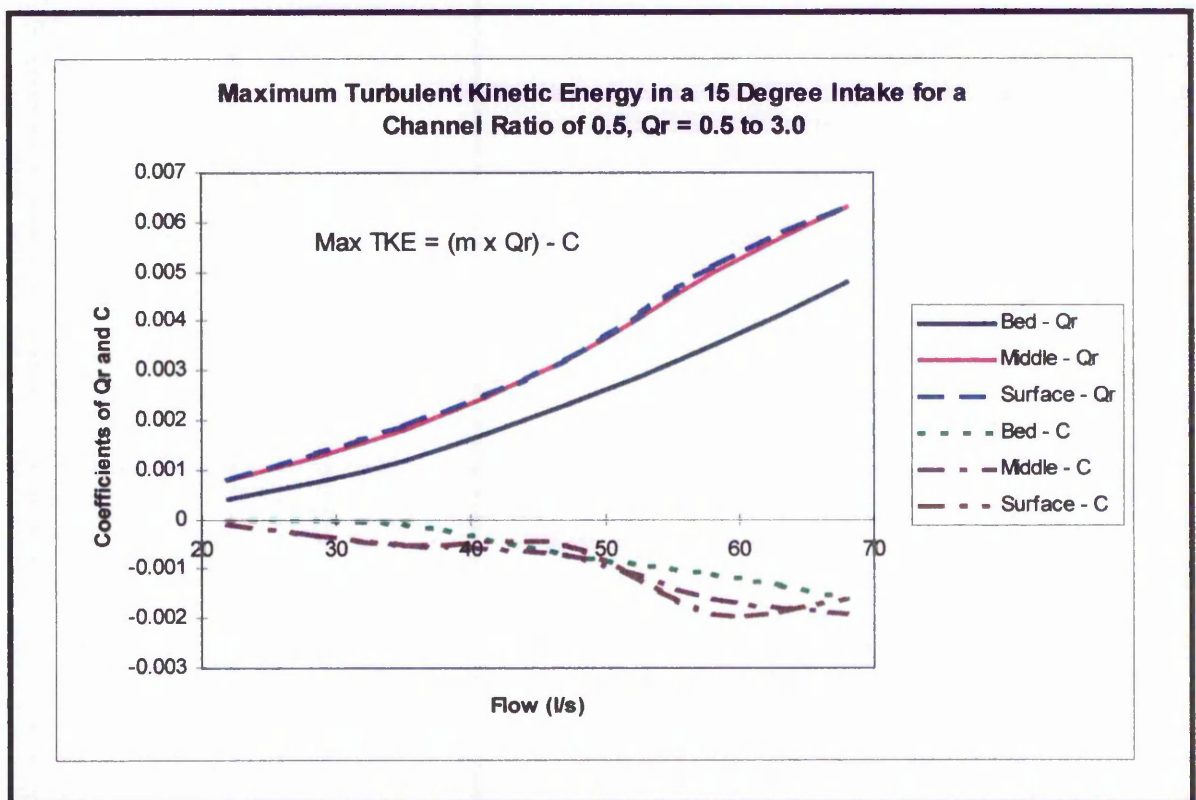
Figure 6.44   Prediction graph for the maximum turbulent kinetic energy in a 15 degree intake for a channel ratio of 0.5, Qr = 0.5 to 3.0.

The correlation to the measured results that were undertaken previously showed that the above hypothesis could be used to predict the maximum TKE to an uncertainty of less than 30%, with the prediction being conservative.

This hypothesis was developed for intake angles of 30 and 45 degrees as described by the following sections.

6.7.4 Maximum Turbulent Kinetic Energy with an Intake Angle of 30 Degrees

Similar analyses to the analyses undertaken previously were applied to an intake angle of 30 degrees. For clarity and to save repetition, only a selection of the graphical output are presented here. Figures 6.45 show contour plots of the maximum TKE for an intake angle of 30 degrees with a flow split ratio of 0.5 with a total flow of 35l/s. These plots show some characteristics that were typical of the results obtained from these analyses.

The contour plots obtained from the study of the 30 degree intake should be compared to those obtained from the study of the 15 degree intake. It can be seen that there were subtle differences between the location of the maximum TKE in the predictive models for the 15 and 30 degree intake. A zone of high TKE was observed on the nosing of the intake pier for the 30 degree intake which was independent of the zone of high TKE to the left side of the intake channel. With increased flow split ratio and hence increased velocities entering the intake channel, these two zones eventually merged to become one larger zone. This effect was observed to a greater extent with the 45 degree predictive model.

Figures 6.46, 6.47 and 6.48 summarise the predicted results of the analyses for the 30 degree intake. These figures show similar trends to those observed for the 15 degree intake. The application of the previously defined hypothesis resulted in the graphical plot shown by Figure 6.49 which provides the coefficients and constants that are required for the prediction of the maximum TKE.

C35G1 - BED

C35G1 – MIDDLE

C35G1 - SURFACE
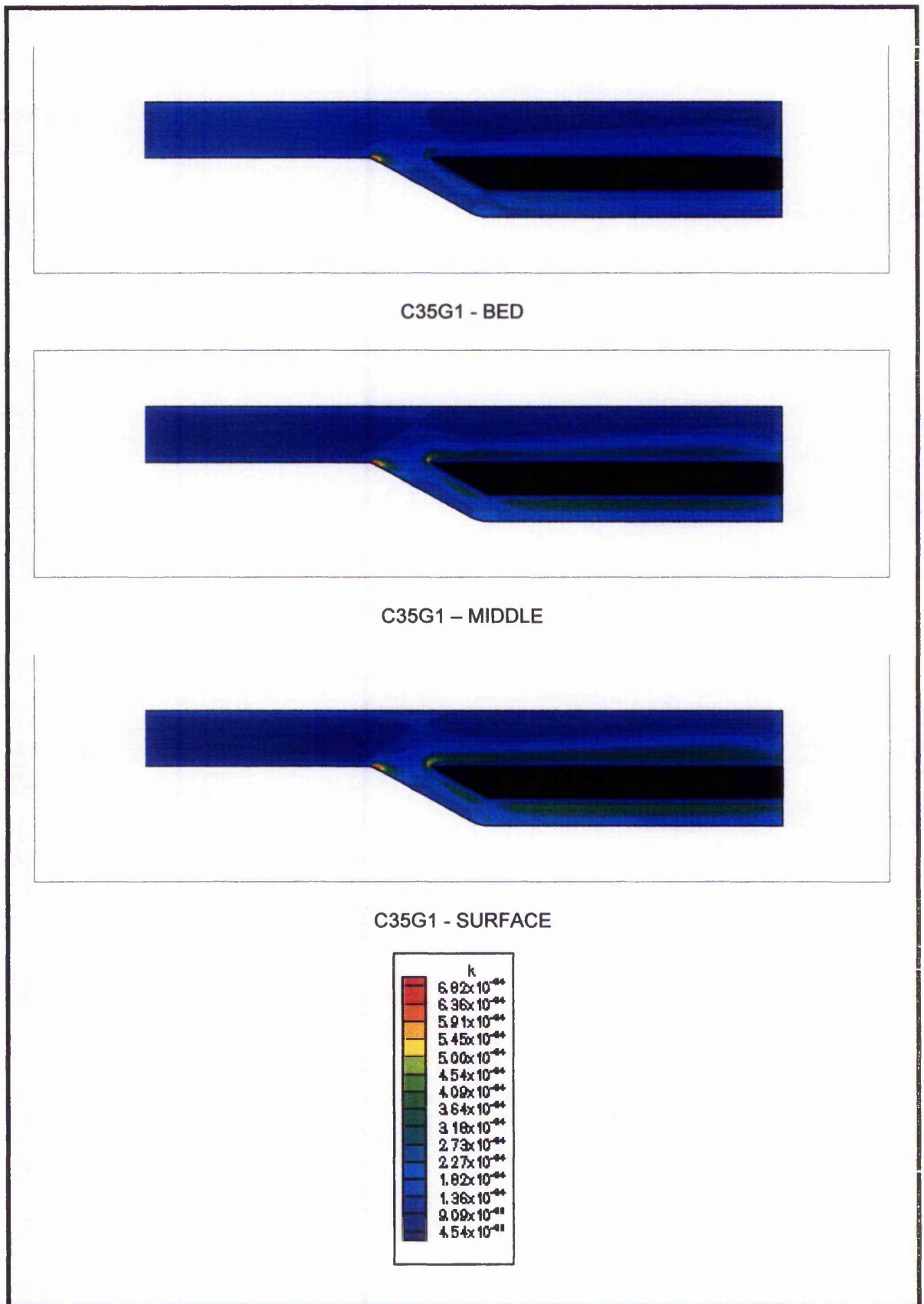
Figure 6.45   Contour plots of predicted turbulent kinetic energy, intake angle = 30 degrees, flow = 35 l/s, Qr = 0.5.
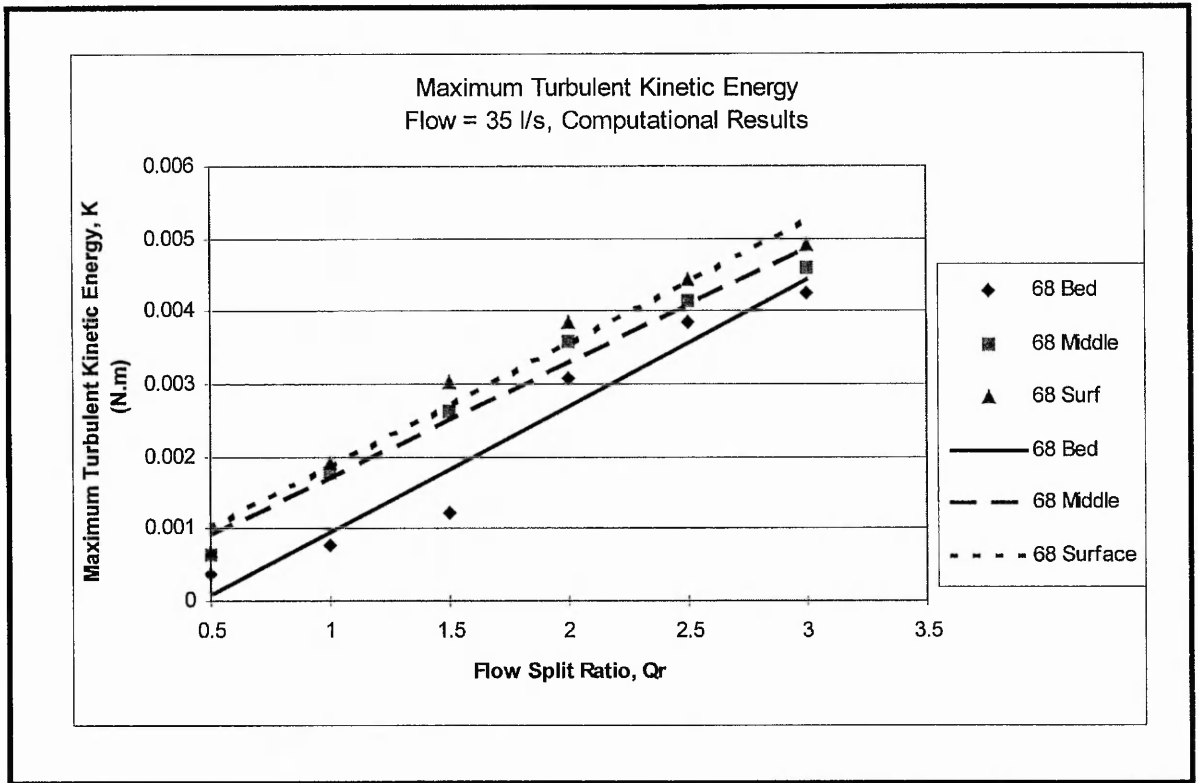
Figure 6.46   Graph to show the variation of the maximum turbulent kinetic energy with Qr, flow = 35 l/s, intake angle = 30.
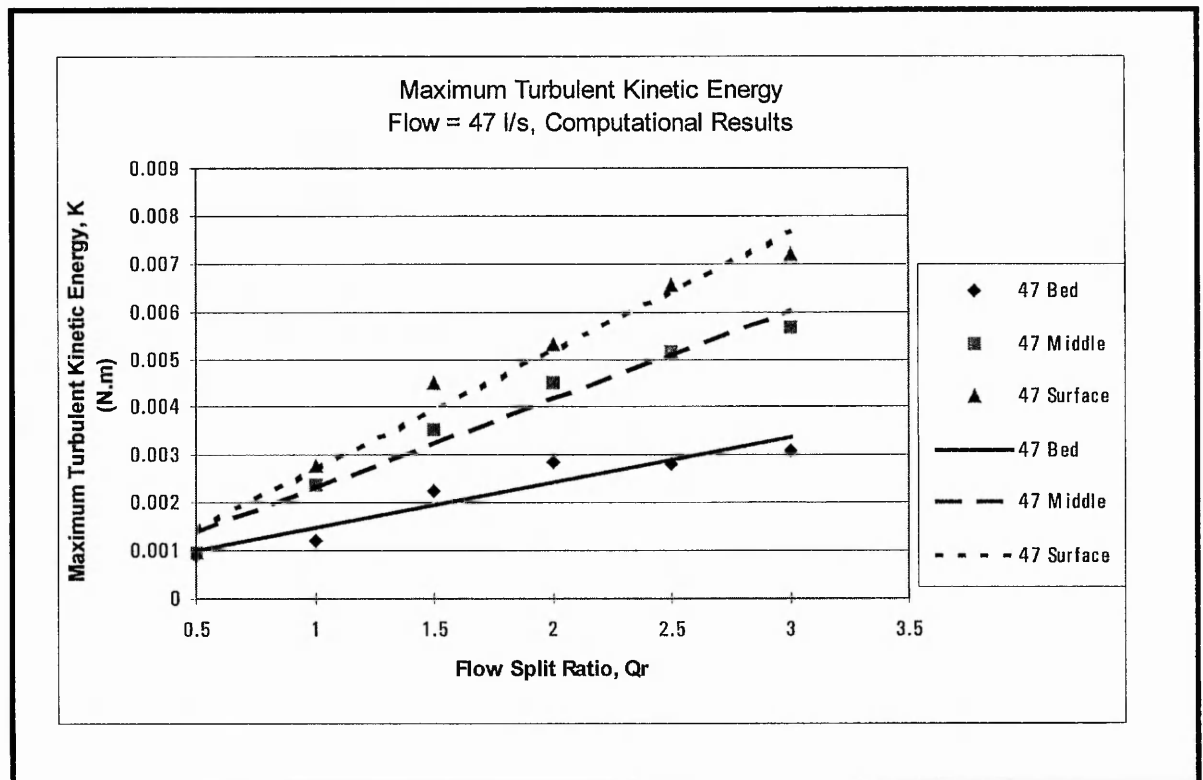

Figure 6.47   Graph to show the variation of the maximum turbulent kinetic energy with Qr, flow = 47 l/s, intake angle = 30.
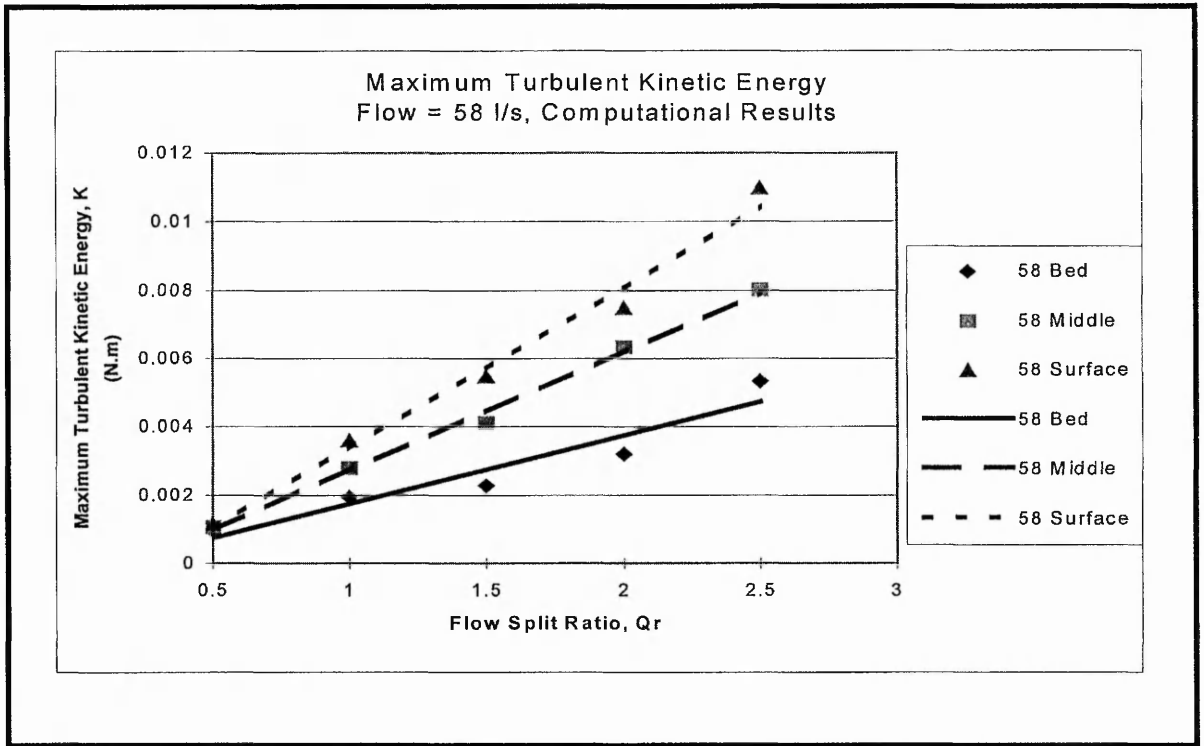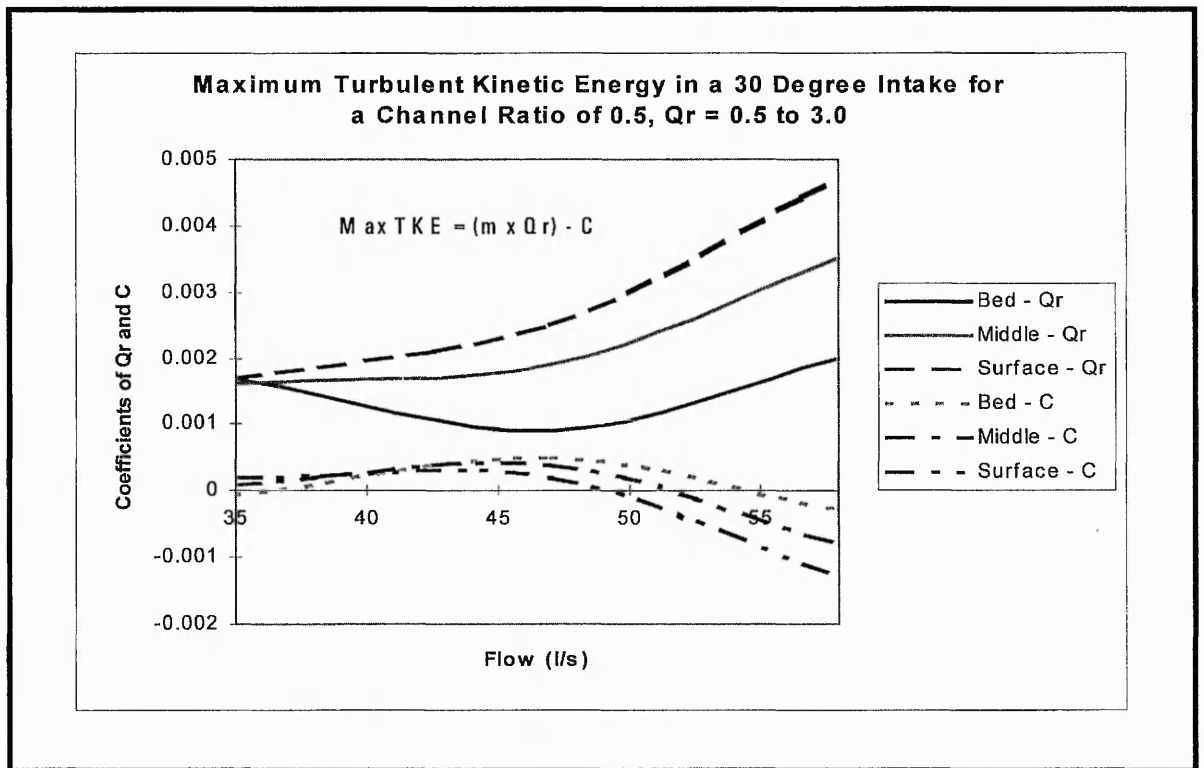
Figure 6.48   Graph to show the variation of the maximum turbulent kinetic energy with Qr, flow = 58 l/s, intake angle = 30.

Figure 6.49   Prediction graph for the maximum turbulent kinetic energy in a 30 degree intake for a channel ratio of 0.5, Qr = 0.5 to 3.0.

It is interesting to note that the shape of the predictive curves shown by Figure 6.49 were similar to the predictive curves obtained for the 15 degree intake analyses. However, the overall magnitude of the TKE predicted for the 30 degree intake was less than the TKE predicted for the 15 degree intake at the locations identified previously. An explanation for this was due to the increased effect of the re-circulation region just down stream of the nosing of the intake pier, with an increase in intake angle. Velocities in this region reduced with an increase in intake angle. This naturally resulted in a lower TKE predicted in this area.

6.7.5 Maximum Turbulent Kinetic Energy with and Intake of 45 Degrees

The final set of graphs in this section shown by Figures 6.50, 6.51 and 6.52 illustrate the corresponding graphs for the prediction of the maximum TKE which were used to develop the summary predictive graph shown by Figure 6.53. For simplicity the contour plots are not presented here because they displayed similar trends to the previous analyses. It can be observed from Figure 6.53 that the overall magnitude of TKE was lower for the 45 degree intake than for the 30 degree intake. This was due to identical reasons described in the previous section i.e. the increased effect of the re-circulation on reducing velocities in this zone.
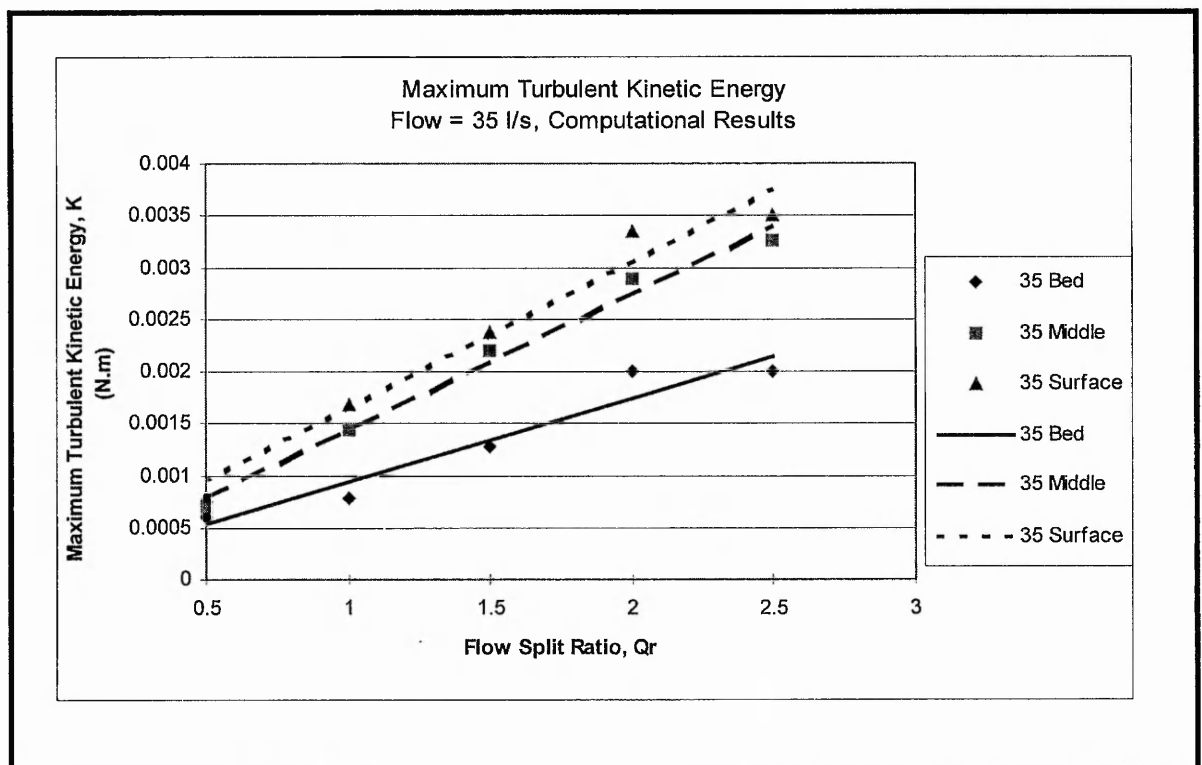

Figure 6.50   Graph to show the variation of the maximum turbulent kinetic energy with Qr, flow = 35 l/s, intake angle = 45.
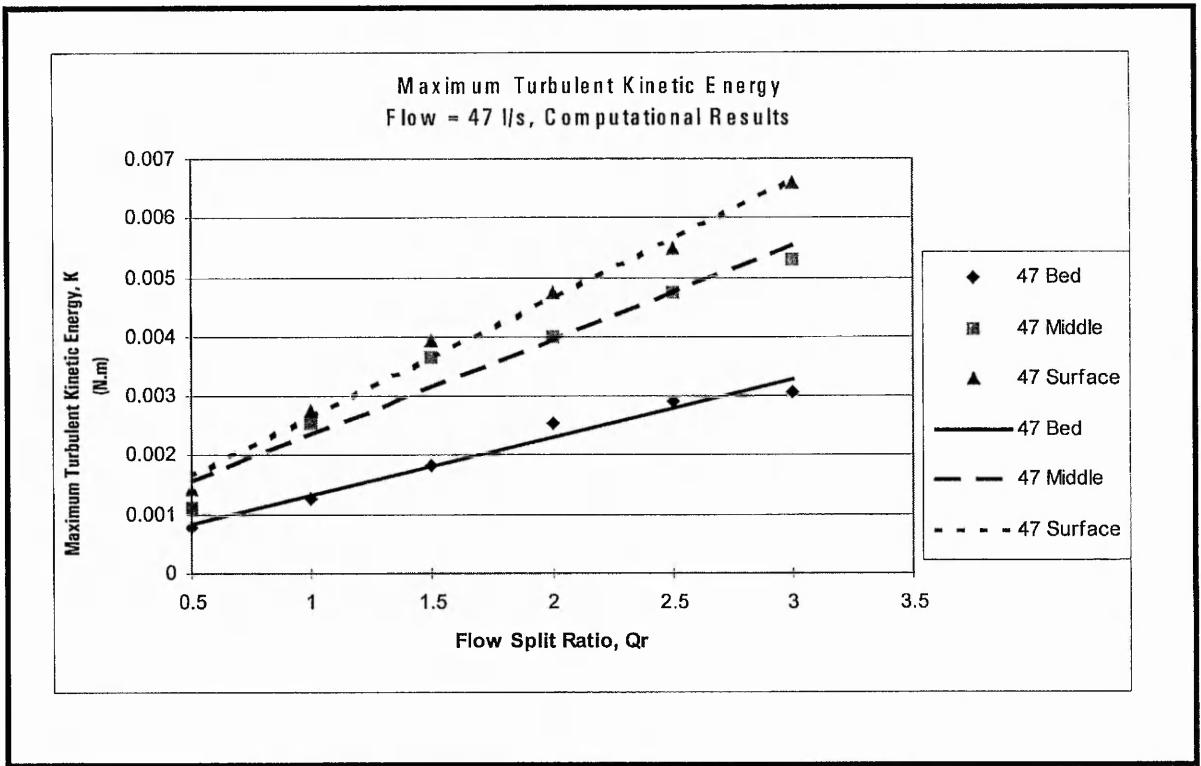
Figure 6.51   Graph to show the variation of the maximum turbulent kinetic energy with Qr, flow = 47 l/s, intake angle = 45.
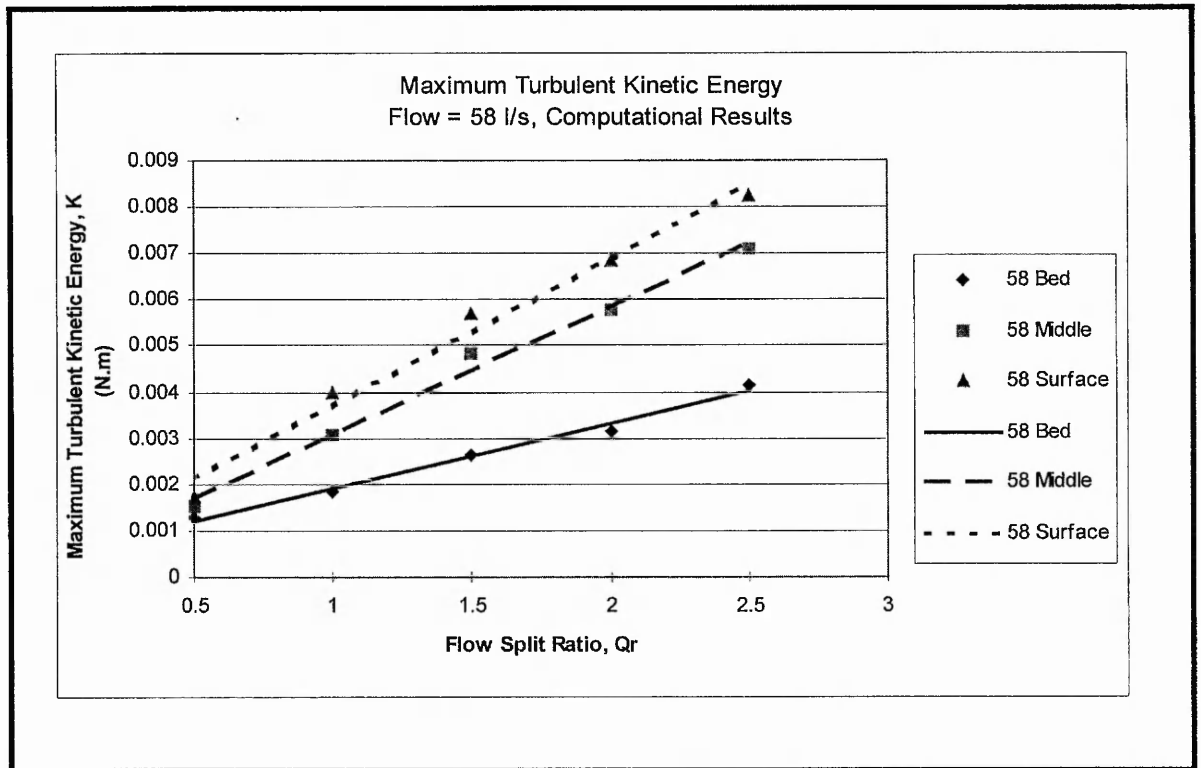

Figure 6.52   Graph to show the variation of the maximum turbulent kinetic energy with Qr, flow = 58 l/s, intake angle = 45.
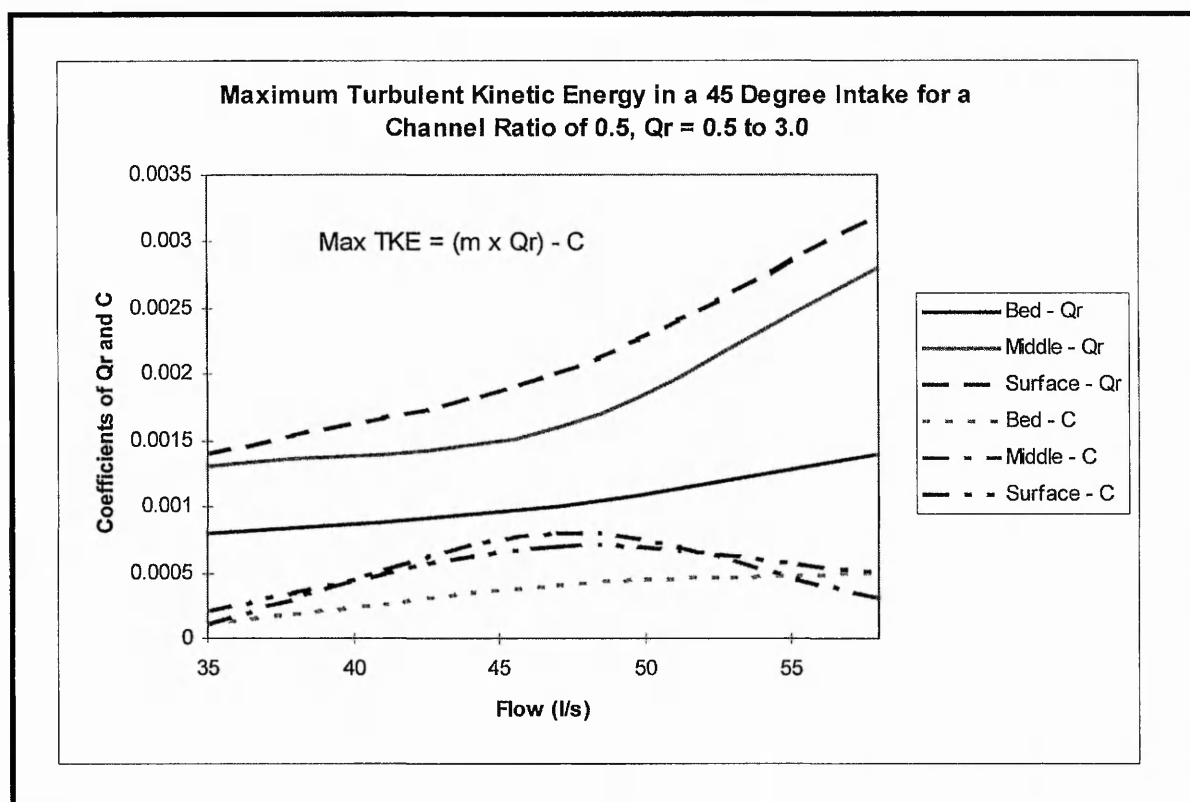
Figure 6.53 Prediction graph for the maximum turbulent kinetic energy in a 30 degree intake for a channel ratio of 0.5, Qr = 0.5 to 3.0.

6.7.6 Conclusions from the Prediction of the Maximum Turbulent Kinetic Energy

The preceding pages of this section have described how analyses were undertaken to test the hypotheses for the prediction of the maximum TKE for intake domains of intake angles of 15, 30 and 45 degrees. The resulting output was a corresponding family of curves which can be used to predict the maximum TKE in similar domain scenarios. Comparison of predicted results with measured results has indicated that the prediction was on the whole, successful to an accuracy of better than 30%. It is generally accepted that the k-ε model rarely gives predictions to an accuracy of less than 30% and therefore the results obtained from this study can be considered to be reasonable.

However, it must be noted that under the limitations of this study, these hypotheses have not been extended to prototype situations where their application would be most useful for design engineers. This matter is discussed further in Chapter 7, Recommendations for Future Research.

6.8 VISUALISATION OF THE FLOW STRUCTURE AT A DIVERSION

6.8.1 Introduction

Finally, to conclude this chapter, it was considered relevant to present the results of some flow visualisation studies that were undertaken in the physical model. Analyses of the resulting flow patterns helped in the understanding of the phenomena presented by this chapter. Flow visualisation studies were conducted in a 15 and 30 degree intake model at total flows of 22l/s, 35l/s, 47l/s, 58l/s and 68l/s. Flow split ratios of 0.5, 1.5 and 3.0 were also used in the investigation. Photographic images were taken at two locations in the flow domain, just upstream of the entrance to the intake and at the re-circulation region downstream of the intake pier apex, identified by the previous studies. Visualisation of the flow structure was facilitated using a red clothing dye and methylene blue mixed in a water based solution. The red dye was injected near to the surface of the flow domain and the blue dye was injected near to the bed of the flow domain. Figures 6.55, 6.56, 6.57 and 6.58 illustrate the results that were obtained. Figure 6.54 shows the orientation of the camera for these figures.
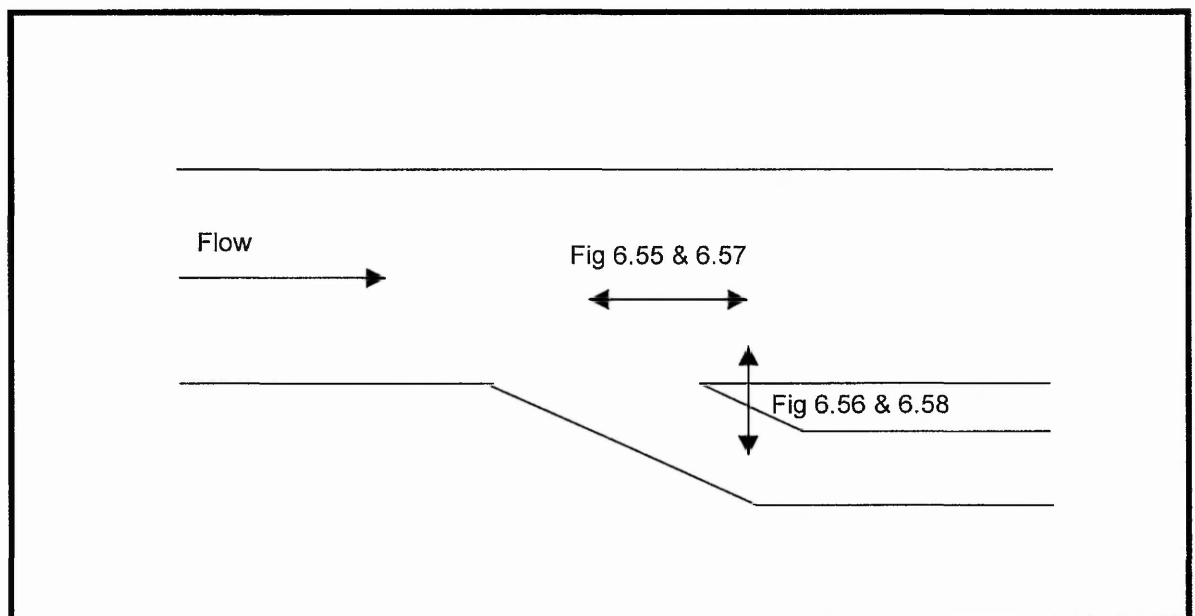

Figure 6.54   Orientation of camera for flow visualisation figures.

6.8.2 General Observations

Flow visualisation proved to be an invaluable qualitative tool used to understand the flow structure at a flow diversion. The observations made from analyses of the images confirmed many of the findings described in this chapter. The main observations drawn from the following images can be summarised as follows.

- Dispersion of the dyes increased with increased flows and hence Reynolds number. This was caused by a resulting increase in turbulence.

- Generally, the red dye (near the surface) was drawn towards the intake channel to a greater extent than the blue dye (near the bed). This confirms a finding of the analytical analyses that the dividing streamline near the bed extended further into the main channel than near the surface. The reduction in streamwise inertia between the bed and surface was clearly shown by these images.

- The re-circulation region was clearly identified by the images located near the apex of the intake pier. At low flow split ratios and total flows the development of the re-circulation region can just be seen to form. The length and width of this region was shown to increase with increasing flow and flow split ratio.
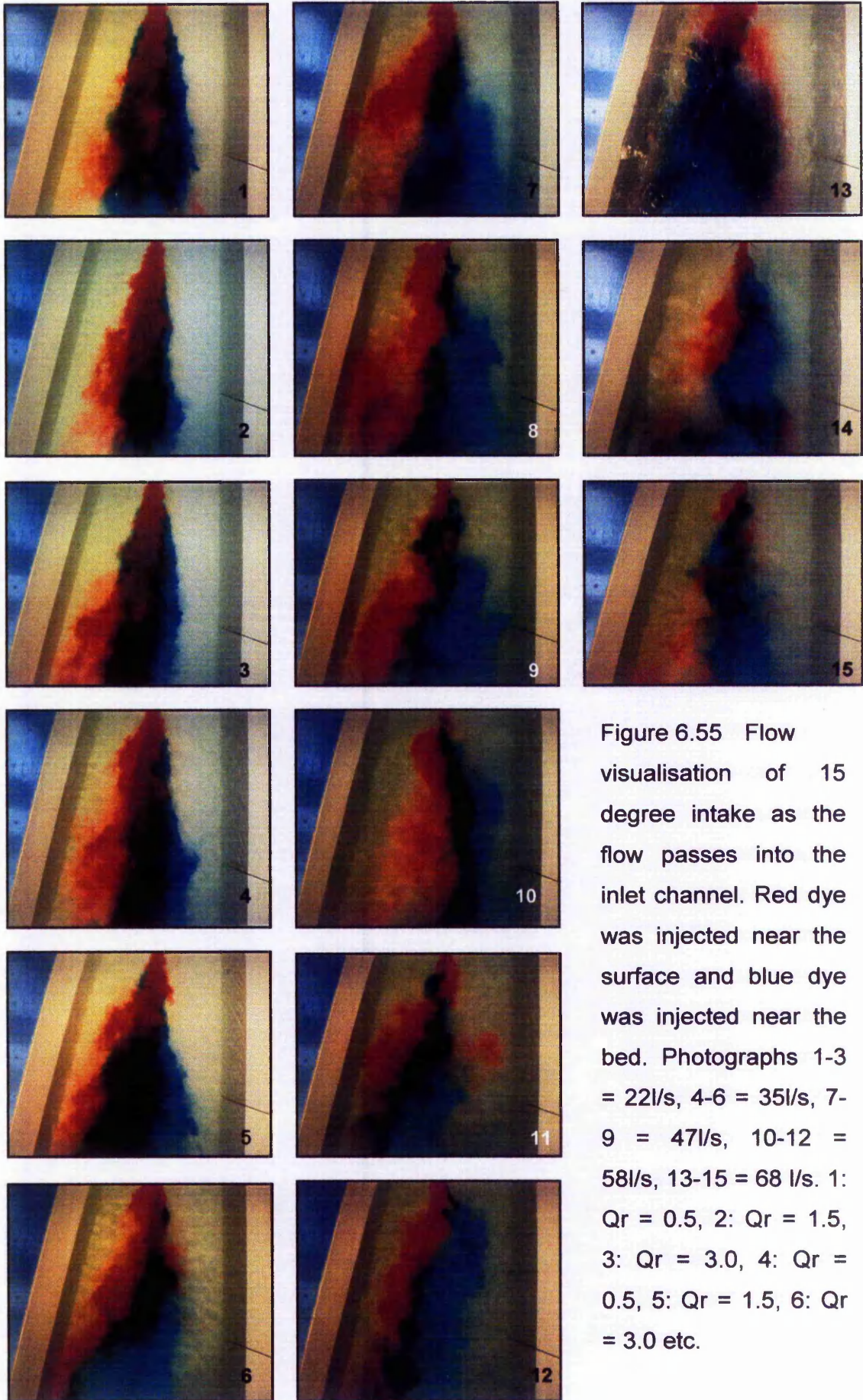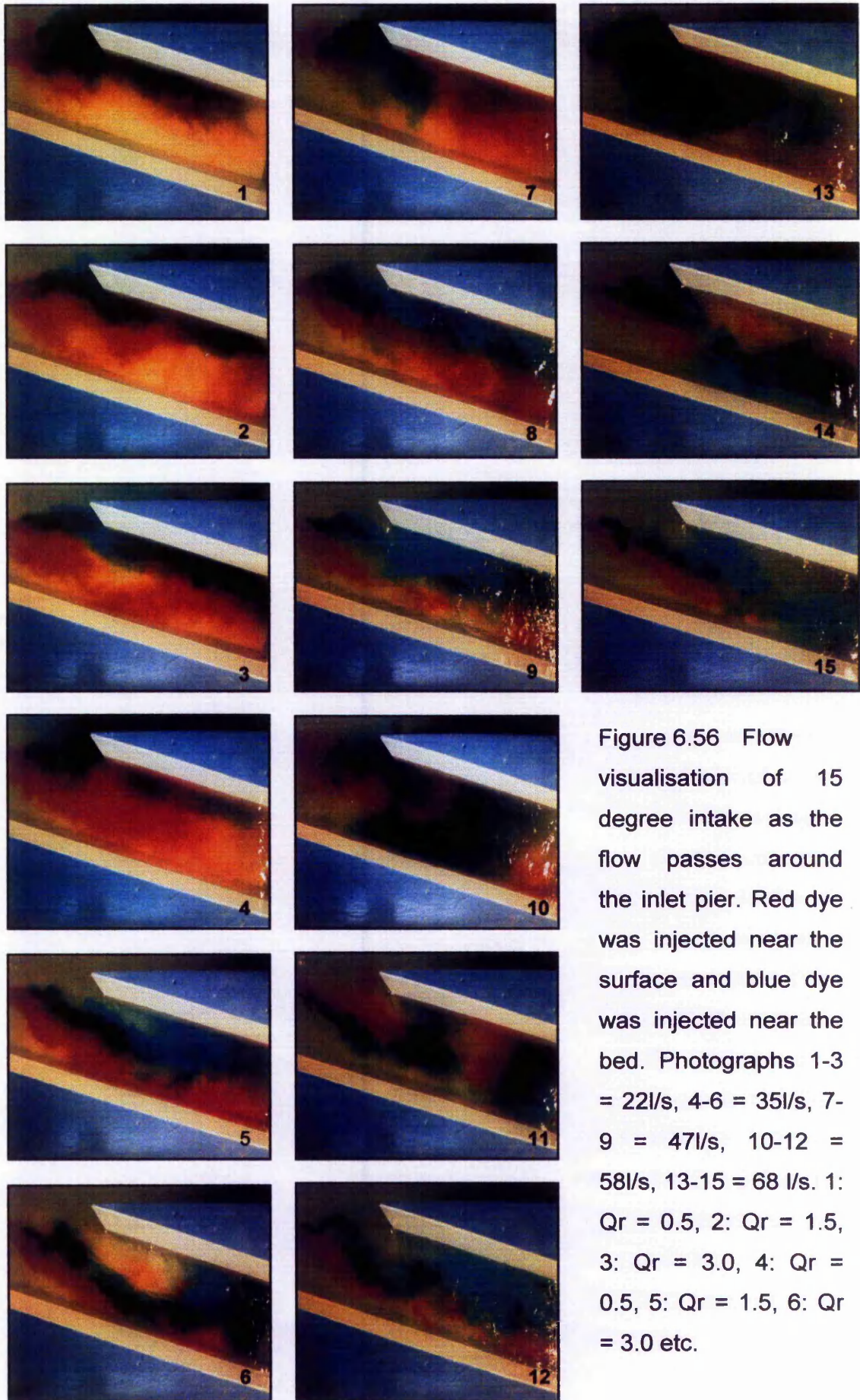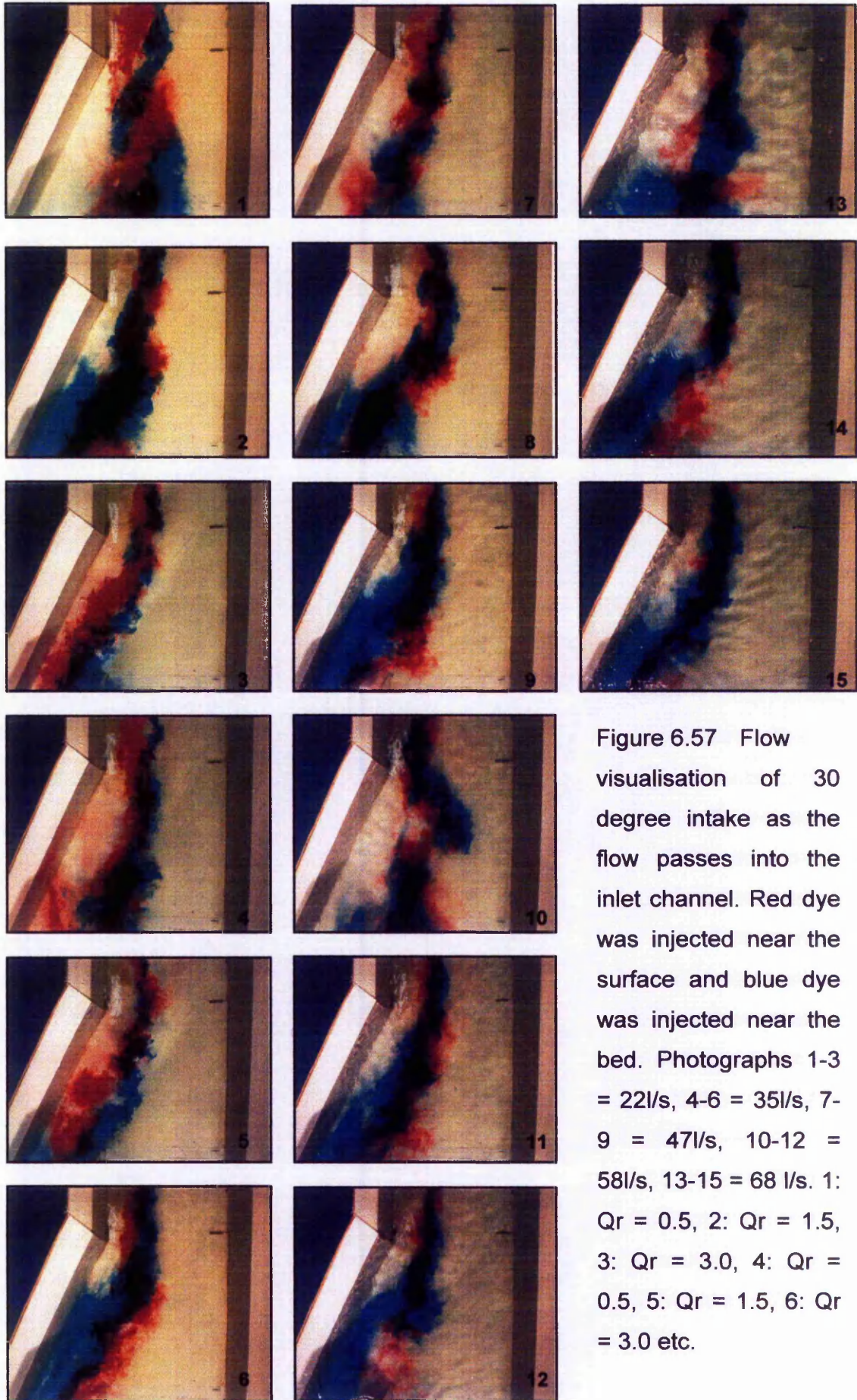
Figure 6.55 Flow visualisation of 15 degree intake as the flow passes into the inlet channel. Red dye was injected near the surface and blue dye was injected near the bed. Photographs 1-3 = 22l/s, 4-6 = 35l/s, 7-9 = 47l/s, 10-12 = 58l/s, 13-15 = 68 l/s. 1: Qr = 0.5, 2: Qr = 1.5, 3: Qr = 3.0, 4: Qr = 0.5, 5: Qr = 1.5, 6: Qr = 3.0 etc.

Figure 6.56   Flow visualisation of 15 degree intake as the flow passes around the inlet pier. Red dye was injected near the surface and blue dye was injected near the bed. Photographs 1-3 = 22l/s, 4-6 = 35l/s, 7-9 = 47l/s, 10-12 = 58l/s, 13-15 = 68 l/s. 1: Qr = 0.5, 2: Qr = 1.5, 3: Qr = 3.0, 4: Qr = 0.5, 5: Qr = 1.5, 6: Qr = 3.0 etc.

Figure 6.57 Flow visualisation of 30 degree intake as the flow passes into the inlet channel. Red dye was injected near the surface and blue dye was injected near the bed. Photographs 1-3 = 22l/s, 4-6 = 35l/s, 7-9 = 47l/s, 10-12 = 58l/s, 13-15 = 68 l/s. 1: Qr = 0.5, 2: Qr = 1.5, 3: Qr = 3.0, 4: Qr = 0.5, 5: Qr = 1.5, 6: Qr = 3.0 etc.

Figure 6.58 Flow visualisation of 30 degree intake as the flow passes around the inlet pier. Red dye was injected near the surface and blue dye was injected near the bed. Photographs 1-3 = 22l/s, 4-6 = 35l/s, 7-9 = 47l/s, 10-12 = 58l/s, 13-15 = 68 l/s. 1: Qr = 0.5, 2: Qr = 1.5, 3: Qr = 3.0, 4: Qr = 0.5, 5: Qr = 1.5, 6: Qr = 3.0 etc.

6.9 CONCLUSIONS OF THE MODELLING OF INTAKE FLOWS

6.9.1 Introduction

This chapter has described the detailed, extensive investigations that were undertaken in an attempt to more fully understand the phenomena associated with the flow structure at diversion structures. It is hoped that the findings will be useful to research engineers involved with the study of associated subjects. Probably the most important point to not out of this study is the association of the physical modelling to the computational modelling. Computational modelling is not yet in a position to be trusted implicitly. Validation of numerical predictions must be undertaken. The accuracy of the physical modelling was initially ascertained and it has been shown that the errors obtained were generally less than the computational predictions as therefore suitable for validation. It is appropriate at this point to summarise the findings of this chapter.

6.9.2 Prediction of the Dividing Streamplane

The ratio of Sd / Bd (Sd = position of dividing streamline near surface, Bd = similarly near the bed) was predicted to be a linear relationship of 0.9 for intake angles of 15 to 45 degrees in comparison to the findings of Neary of 0.6 for a 90 degree intake angle.

- The position of the dividing streamline with depth was independent of the intake angle and velocity ratio (main / intake channel).
- The depth variation of the dividing streamline increased with increased flow split ratio.
- The streamline near the bed extended further into the main channel than near the surface due to the decrease in streamwise inertia near the bed.
- The radius of curvature of the dividing streamplane reduced with increased intake angle.
- The shape of the dividing streamplane was independent of the flow.
- Flow reversal and areas of particularly high velocity gradient were predicted and measured at an intake angle of 45 degrees.

- Families of curves were constructed to predict the position of the dividing streamplane which were found to be independent of flow but dependent upon flow split ratio and intake angle. Thus the curves can be used for any quantity of flow with intake angles between 15 and 45 degrees and flow split ratios between 0.5 and 3.0. The curves, however, only apply to smooth beds and channel ratios of 0.5 (inlet / main).

- Comparisons of predicted results with measured results indicated errors of +/- 15% for a 15 degree intake and +/- 30% with a 30 degree intake.

- The shape of the dividing streamplane was predicted successfully but the numerical model generally over-predicted the position.

6.9.3 Calculation of the Flow Diversion Rate for an Uncontrolled Flow Split

- This study showed that the proportion of the main channel flow entering the intake channel decreased with increased intake angle. The probable cause of this was due to energy losses which increased with increased intake angle.

- Predicted uncontrolled flow split ratios of approximately 0.53, 0.47 and 0.39 were obtained for intake angles of 15, 30 and 45 degrees respectively. Reasonably good agreement was obtained with physical measurements.

6.9.4 Vector Visualisation

- The numerical model generally under predicted the magnitude of velocity. Further details of this are also given in Chapter 5, CFD Validation.

- The direction of the velocity vectors was satisfactorily predicted apart from areas of re-circulation or high velocity gradients.

- The numerical model failed to predict some of the areas of flow reversal, particularly near the bed and at high flow split ratios. This was probably due to the turbulence model used in the numerical model, the k-epsilon model, which although commonly used in engineering is notoriously poor at prediction near boundaries.

- This study provided a valuable qualitative assessment of the flow structure.

6.9.5 Vector Profile Plots

- In general the numerical model performed reasonably well in prediction of the velocities.

- The main problems experienced were caused by the fully developed flow that was assumed in the predictive methods as opposed to the undeveloped flow that was actually measured in the physical model.

- The velocity profiles were more successfully predicted in the 30 degree model than the 15 degree model. There was no clear explanation for this but this could possibly have been due to improved quality of measured data obtained for the 30 degree physical model, which correlated more closely to the predicted results.

6.9.6 Prediction of the Maximum Turbulent Kinetic Energy

- The tke was observed to increase with increased flow split ratio and increased total flow, primarily due to the larger velocities that were measured and predicted in such scenarios. This increase showed a linear relationship.

- Tke was generally predicted to an error of less than 30% with the measured tke.

- Families of curves were produced which can be used to predict the maximum tke in intakes of 15 to 45 degrees, flows up to 68l/s and flow split ratios of up to 3.0.

- Subtle differences were observed in the position of the zone of maximum tke for intake angles of 15, 30 and 45 degrees.

- The maximum tke reduced with increased intake angle but the size of the zone increased in terms of width and length. This indicated an increase in the re-circulation zone near the apex of the intake pier. This zone of maximum tke resulted in contraction losses which although not quantified under the constraints of this study caused a reduction of the volumetric flow into the intake channel.

7

CONCLUSIONS

7.1   SUMMARY

It is appropriate at this point to give a summary of the subjects that this thesis has covered.

Chapter 1 gave a brief introduction into the subject of diversion flows. It introduced the associated problems such as sedimentation, fish passage and the effects to navigation at intakes with particular reference to small scale, low head, run-of-the-river hydropower plants. The main subjects of this thesis, the flow structure and associated energy losses at a generalised intake were also introduced. This chapter also introduced the techniques that were used to validate the computational model used, to calibrate the measurement equipment and introduced the physical model in which these measurements were taken.

Chapter 2 outlined the previous research that has been undertaken in the field of diversion flows, including field and laboratory investigations, biomedical observations, theoretical and numerical model descriptions. The chapter illustrated that much research has been undertaken to study the flow structure at diversions both physically and theoretically, particularly for 90 degree intake angles. It was clear from the literature survey undertaken that few comparisons with numerical model predictions have been undertaken and that those that have, mainly focussed on 90 degree intake angles.

The literature survey indicated that there was a need for a three dimensional investigation of the flow structure at a flow diversion. One and two dimensional model descriptions of the flow structure at diversions are relatively common, particularly

theoretical and physical studies. Numerical three dimensional studies at flow diversions were noticeably rare with the only notable exception being that of Neary. However, Neary's investigations were limited to 90 degree intake angles and were focussed on the application of sedimentation at intake structures. No record was located of three dimensional numerical investigations with physical validation for the flow structure at diversions ranging from 15 to 45 degrees. It was therefore considered that any addition to the knowledge and description of such flows was of benefit to the hydraulic research community.

Chapter 3 described the physical model that was used during the investigation for validation of numerical predictions and for flow visualisation purposes. The measurement techniques used in the model were discussed and their calibration described. The problems associated with the model were also described. It was found that the flow entering the model was highly turbulent with areas of extremely high velocity gradients and re-circulation regions. The flow entering the model was not therefore fully developed. Methods to improve the uniformity of the flow entering the model were described. A combination of a honeycomb material in conjunction with a synthetic horse-hair material was found to diffuse and straighten the flow most successfully. The resulting flow structure at the entrance to the model was described and although still not fully developed, could be modelled numerically.

Chapter 4 described the need to calibrate the primary measurement equipment used in the physical modelling. The ADV is a relatively new technology having only been developed for professional use in 1994. The research programme covered by this thesis commenced in 1995 and it was considered vital to confirm the claims in uncertainty of the measurements made by the manufacturers.

Numerous rigorous validation tests were undertaken from which a simple validation test was described. Although the accuracy of this simple test would not highlight small inadequacies of the ADV it would, as proven, identify serious malfunctioning of the probe. This simple test, which can be undertaken in a small laboratory flume, evolved from more complex tests undertaken at two of the Country's leading towing tank facilities, HR Wallingford and Southampton Institute. Initial gross errors were found to exist within the ADV hardware which would not otherwise have been identified had a validation exercise not been carried out. After rectifying these

problems the manufacturer's uncertainty claims of +/-0.25%+/-0.25cm/s in the measurement of three dimensional fluid flow velocities was tested. It was found that rarely could the ADV perform to this level of uncertainty although under many conditions it came close. However the level of uncertainty of the ADV measurements was lower than those expected from the numerical model and were therefore acceptable for the purposes of this study. The uncertainty of the measurements in the x-direction was 2% and 1% in the y-direction. Uncertainties were considerably larger in the z-direction at approximately 20%. However, the relative magnitude of the velocity in z-direction was significantly low that the effect of these uncertainties was assumed to be negligible.

Effects on the uncertainty in the measurements as a result of pitch and yaw, salinity and temperature of the fluid measured were also tested and presented. Finally a measurement regime for the ADV, in terms of sample number and time period for the flow situations to be investigated, was tested and presented.

At the time that the calibration programme commenced on the ADV, no other calibration tests had been undertaken independently of the manufacturer. Recently Snyder of the University of Surrey, has also undertaken calibration tests with similar results.

Chapter 5 documented the measures that were undertaken to validate the numerical model. The numerical model used in the investigation, SSIIM, was described in detail, including a description of the governing equations and the discretisation methods it utilised for the solution of the flow field. SSIIM, written by Olsen of Norway has not previously been validated independently. It was found that the numerical model gave satisfactory prediction in some comparisons with physical measurements but was lacking in areas of high velocity gradients and flow reversal. This was mainly due to the inadequacies of the turbulence closure model that SSIIM adopts, the k-ε turbulence model.

Grid dependency studies were undertaken using Richardson's extrapolation techniques and also those techniques of Roach, including the use of the Grid Convergence Index. The effects of the roughness coefficient were tested and it was found that the roughness had a considerable effect upon the velocity field that was

predicted. The numerical discretisation schemes, POW and SOU were tested and it was found that the POW was approximately 30% faster in terms of CPU time than the SOU scheme and usually more stable but less accurate where the grid was coarse and the flow was not aligned to the grid. It was found most beneficial to use the SOU scheme for the solution of the momentum equations and the POW scheme for the solution of the turbulence equations.

Relaxation factors used in the iterative solution procedure were tested and it was found that this was the most difficult problem to analyse. The choice of the most appropriate relaxation factors to use for a particular flow situation was either a matter of experience or involved an iterative 'trial and error' procedure.

Velocities were predicted to an accuracy of less than 30% in the x-direction. Greater inaccuracies were reported in the y- and z-directions but this was not considered as onerous since the qualitative direction of the velocity vectors was reasonable. Isotropic turbulence in terms of turbulent kinetic energy, k was predicted to an accuracy of less than 12% with generally remarkably good agreement with measured data.

The uncertainty of the validation which combined with both the experimental data and the simulation prediction, ranged from 34% to 5% when using the most appropriate grid and numerical parameters.

Finally *Chapter 6* described the application of the numerical and the physical modelling to the examination of the flow structure at a 15, 30 and 45 degree intake angle. Prediction of the three dimensional dividing streamplane was undertaken and this was compared to the measured dividing streamplane in the physical model. The results of this study were similar to those of Neary's investigation. It was found that the position of the dividing streamplane with depth was independent of intake angle and velocity ratio (intake/main channel). The streamline near the bed of the main channel extended further into the main channel than near the surface due to the decrease in streamwise inertia near the bed. The radius of curvature of the streamplane entering the intake channel decreased with increased intake angle due to the increase in streamwise inertia entering the intake channel as the intake angle

increased. Areas of high velocity gradient and re-circulation were predicted at an intake angle of 45 degrees.

Families of predictive graphs for the position and shape of the dividing streamplane were constructed which were independent of the flow but dependent on the flow split ratio and the angle of the intake. This was significant because the graphs could be used on any diversion situation with 'smooth' (i.e. concrete), rectangular cross section channels with channel width ratios of 0.5 (intake/main). The accuracy of the prediction when compared to physical measurements was approximately 15% and 30% for intake angles of 15 and 30 degrees respectively.

The flow split was successfully predicted for an uncontrolled intake. The proportion of flow entering the intake reduced with increased intake angle due to energy losses which occurred at the entrance to the intake channel.

Vector visualisation and plotting of velocity profiles was undertaken which showed that the numerical model generally under predicted the magnitude of the velocity in comparison to the physical measurements. It also showed that the numerical model did not perform well in areas of excessively high turbulence or areas of high velocity gradients and flow reversal.

Investigation of the streamline patterns plotted from the numerical prediction and the physical measurements showed some interesting results. It indicated that higher velocities were predicted and measured on the outside of the bend of the intake channel (which was as expected). The velocity distribution across the intake channel was more uniform for a 15 degree intake than for a 30 or 45 degree intake angle. This suggested that lower intake angles are more suitable for hydropower installations since a uniform velocity distribution is preferable for such applications.

Finally in chapter 6, a study was undertaken into the distribution of the maximum turbulent kinetic energy (TKE) with intake angle and flow split ratio. It was found that the maximum TKE increased with increased flow split ratio and hence increased velocities in the intake channel. The TKE was generally predicted to less than 30% of the measured value. From this study, families of predictive graphs were derived which were subsequently compared to physical measurements of TKE. The

maximum TKE reduced with increased intake angle but the size of the zone of maximum TKE increase in terms of length and width. The zone of maximum TKE usually occurred just downstream of the apex of the intake pier. This zone also represented an area of high re-circulation which was observed during flow visualisation studies and the previous parametric analyses. High TKE and re-circulation are closely linked and represent areas of significant energy losses in the diversion system. The zone of maximum TKE and re-circulation resulted in contraction losses causing a reduction in volumetric flow passing into the intake channel. However the significance of these contraction losses were not quantified as part of this investigation.

7.2   CONCLUSIONS

The investigation detailed by this thesis leads to the following conclusions that can be made on the use of physical and numerical modelling to predict the complex mechanics of turbulent flows through diversions:

7.2.1 Physical Modelling

Physical modelling continues to provide a valuable tool by which hydraulic phenomena can be studied. Confidence in numerical modelling has not currently reached a level to which the hydraulic engineer has complete confidence in the results that are obtained. The need to validate numerical models is an extremely important requirement and physical modelling facilitates the necessary data capture that fulfils validation.

Physical model design is an important consideration. Attention must be paid to the choice of scaling laws; Froude or Reynolds scaling. Where gravitational forces predominate in the modelling of hydraulic structures such as intake configurations, it is appropriate to use the Froude scaling laws. Care was taken in the design of the physical model used in this investigation to choose dimensions that realistically represented a potential prototype.

Physical modelling is an expensive tool in terms of construction costs and operator hours. Investigations which incorporate physical modelling should be carefully designed to produce methodologies which concisely and clearly focus on the important parameters that are required. This investigation involved approximately 3000 hours of laboratory time. This does not take into consideration the time taken to develop the methodology for the physical model in other laboratory flumes, that was undertaken prior to the construction of the physical model. The physical modelling time requirement can be compared to the numerical CPU time that was required to analyse identical model scenarios, which was approximately one third of the time required for physical modelling.

7.2.2 ADV Calibration

Methods of flow measurement should be carefully considered and the relative accuracy of each of the methods should be ascertained in the selection process. Calibration of the flow measurement apparatus is essential for each investigation. It is also prudent to use several different methods such that results obtained using different methods can be correlated. For each of the methods used in this investigation, careful calibration techniques were used to guaranty the validity of the measurements taken. The calibration of the Acoustic Doppler Velocimeter underlines the requirement for calibration with significant implications. Initially the errors that were identified in the early stages of this investigation were acknowledged sceptically by the manufacturers of the ADV. However, the UK sales agents for the ADV, HR Wallingford Equipment Sales, provided every possibly opportunity and assistance in the independent calibration of the ADV. For this they must be commended. The results of the calibration were periodically presented to members of the research community and the results were subsequently verified by the manufacturer. In addition Snyder of the University of Surrey undertook similar calibration which compared closely to the calibration described in this thesis. It is probable that the errors initially experienced with the ADV purchased by Nottingham Trent University, were not typical of the majority of approximately 500 ADVs (number obtained from private correspondence with Nortek, Norway and Sontek, USA) that are currently in use around the World to date. With repair to the ADV probe hardware and factory re-calibration of the ADV by the manufacturers, the accuracy of the ADV was improved to an accuracy acceptable for most applications.

However, it is the opinion of the author of this thesis, that the manufacturer's claim to the accuracy of the ADV is slightly optimistic. In support of the ADV, it is a robust, relatively accurate, simple to use and importantly, relatively inexpensive. Typically laser Doppler Anemometry (LDA), the only other presently available method that can measure three dimensional fluid flow velocities, can take hours to prepare for point measurements as opposed to the ADV which may only take minutes to prepare for point measurements. In addition the cost of purchase of LDA is typically ten times that of the ADV. Finally, the ADV can be used in the field as opposed to LDA which is most suited to laboratory investigations.

7.2.3 CFD Validation

CFD is a relatively new technology in hydraulic engineering. It has been widely used in other disciplines for many years such as the aeronautic or automobile industries. It is these disciplines that have developed rigorous verification and validation techniques that should be applied to numerical models that are used in hydraulic engineering. It is important to distinguish between verification and validation of a numerical code. Verification, in simplistic terms, is the quantification of the uncertainty involved with the use of the numerical algorithms and equations. A phrase to elucidate this is 'solving the equations right'. Validation, in simplistic terms, is the quantification of the uncertainty involved with the use of the numerical code when applied to specific flow situations. Similarly, a phrase to elucidate this is 'solving the right equations'. Theoretically, verification need only be applied to a numerical code once, but validation should be undertaken for each independent application of the numerical code to different flow situations. The term verification and validation are frequently confused.

The numerical model used in this investigation, SSIIM, performed reasonably well under the extremely close scrutiny that was applied to its validation. SSIIM was not specifically written to laboratory model applications, rather prototype studies constructed to a considerably larger scale or river studies. Therefore the errors obtained by this investigation were reasonable considering the demands that were placed on the numerical code.

The merits of the turbulence closure model used by SSIIM, the k-ε turbulence model, have been highlighted by the investigation. It has been widely used in numerical modelling of turbulent flows for the last 20 years since its conception in the 1970's. However, in recent years improvements have been made to this basic model with developments such as the k-ω turbulence model. Roughness effects, unlike other two equation turbulence models, are simulated through the ω boundary condition at the surface (for further details see Wilcox, 1994). Hence, it is perhaps the best suited near-wall closure presently available for simulating complex three dimensional flows with roughness effects. Despite the fact that a theoretically smooth bed model was modelled here, the k-ε model clearly modelled the flows near the bed with the greatest inaccuracies. This was illustrated to the greatest effect with comparisons of the flow patterns obtained near the bed. Frequently the predicted velocity field near the bed was considerably different to the measured flow field.

The latest developments such as Direct Numerical Simulation or Large Eddy Simulation would undoubtedly have provided improved results. However, these methods are expensive in terms of computational hardware and CPU time.

The solution of the free water surface undertaken by SSIIM is by use of a standard backwater analysis. The resulting profile is then fixed (also termed the 'rigid lid' approach). This approach is most suitable for straight channel cases, where the pressure profile can be directly converted into a water slope profile. However, this assumption means that a gravity term is not included in the equations and therefore does not represent accurately what is happening physically. Use of this approach was undoubtedly a contributing factor in the inaccuracies obtained, particularly at higher flow split ratios and intake angles, where flow reversal caused more significant changes to the water surface.

The preceding paragraphs discuss the conclusions to the primary causes of the inaccuracy that was experienced when using SSIIM for the investigation of the flow structure at a flow diversion. Further recommendations are made in the next section about how SSIIM should be best used to predict this flow structure.

7.2.4 Modelling of Intake Flows

The need to elucidate on the three dimensional nature of intake flows was identified by the Literature Review (Chapter 2). An attempt was made to satisfy this during the modelling of intake flows undertaken as part of this investigation. It was found that the flow structure at a generalised intake such as the one modelled in this investigation, was extremely complex and this complexity increased with increased intake angle and flow split ratio. The exact complexity of the flow in areas of flow reversal was not fully explained mainly due to the inability of the numerical code to correctly predict the flow structure in these regions. These regions occurred predominantly near to and just downstream of the apex to the intake pier. The length and width if this region increased with increased velocity occurring with greater flow split ratios. An increase in the diversion angle also accentuated this region of complex flow structure.

However, a significant contribution has been made to the understanding and the prediction of the dividing streamplane at intake angles varying from 15 to 45 degrees. A hypothesis to predict the dividing streamplane was developed and successfully tested using physical measurements. The resulting family of graphs can be applied with a certain amount of confidence, to idealised diversion situations where the geometry is rectangular and smooth and the ratio of the intake to main channel width is 0.5.

Furthermore descriptions of the flow structure and pattern at a flow diversion have been undertaken with comparisons of predicted streamline patterns, velocity profiles and TKE profiles to similar physical measurements. In addition, flow visualisation in the physical model by means of a novel method for dye injection has enabled a further understanding of the complex three dimensional nature of these flows.

In undertaking the study the following recommendations can be given when applying a three dimensional numerical model such as SSIIM to diversion flows.:

- The horizontal and vertical mesh should be refined in regions of highly varying flow, particularly near the apex of the intake pier.
- Sensitivity tests and grid convergence / dependency test should be undertaken.

- The numerical scheme SOU is recommended for the momentum equations since it improves accuracy for flow that is not aligned to the grid and may reduce CPU time.

- The numerical scheme POW is recommended for the turbulence equations because of its greater stability. The use of the SOU scheme can cause negative values of k and ε which may cause the solution procedure to fail.

- Relaxation factors are extremely difficult to determine and their selection is primarily based upon experience. If they are chosen too small, solution times are increased unnecessarily but if they are chosen too high the model may oscillate and fail to converge. The need to select relaxation factors is a disadvantage with the use of SSIIM.

- A minimum computational hardware requirement of Pentium II processor, 333Mhz clock speed, with preferably 128Mbytes of RAM is recommended when using PC based numerical codes such as SSIIM. In the initial stages of the numerical investigation a Pentium processor, 133 MHz clock speed with 32Mbytes of RAM was used. It was calculated that this PC achieved convergence of independent numerical models, a factor of 10 times slower than the improved specification PC that was subsequently used for the investigation.

- SSIIM presently uses the IBM O/S 2 Warp Version 4 operating system and this is a major drawback when processing analyses. Results must be transferred from O/S 2 to the Windows operating system for more thorough analyses. The graphical outputs incorporated into SSIIM are limited and for the purposes of analyses and presentation of results, a data processing and visualisation package called Tecplot, manufactured by Amtec of Washington D.C., USA was used. The author of SSIIM intends to modify SSIIM for Windows and improve the graphical options in the near future.

Although the capabilities of SSIIM to predict the velocity field in fluid flow were rigorously tested, the sediment transport capabilities of the code were not tested.

The potential for CFD codes such as SSIIM for predicting fluid flow is promising but there is still a considerable need for further developments before such codes are trusted implicitly without the need for validation and verification for every application. The advantage of conducting numerical model studies in conjunction with experimental investigations has been clearly demonstrated. Numerical predictions

were also useful in determining where refinement of the experimental measurement grid was required to resolve regions of high velocity gradients and areas of flow reversal.

The scope of this investigation was restricted simply due to the nature of trying to undertake a numerical and experimental investigation simultaneously. Major improvements can be made to the analyses and predictive descriptions presented by this thesis.

7.3   RECOMMENDATIONS

This investigation has covered a large area of work in many areas which could be further investigated. The following recommendations for future work can therefore be made.

7.3.1 Numerical Modelling

There are numerous areas where the numerical model can be improved to predict the complex flow structure that has been described in this thesis more successfully:

- Algorithms could be added to the numerical model to analyse more complicated physics of diversion flows. These include such things as a deformable free surface. The 'rigid lid' approach (Taylor, 1944) was used by SSIIM in this investigation. The results could be improved, particularly at higher Froude numbers that are encountered at higher flow split ratios and intake angles. At lower flow split ratios and lower velocities the free water surface effects were minimal but for extreme conditions, backwater effects and hydraulic jumps can form and would have significant effects on the flow features studied here. Hydrostatic assumptions would perhaps have improved the results at more extreme cases as would the Volume-of-Fluid (VOF) method. The VOF method requires a certain layer of air to be modelled above the water surface in order to correctly ascertain the position of the free water surface.

- It has been shown that rarely could the k-ε turbulence model exactly the secondary velocities present in areas of flow reversal. A mixing length model would not have predicted this either but a Reynolds stress model could show these relevant patterns. In addition both the k-ε model (used in this investigation) and the k-ω model (which it was suggested previously in this chapter may have produced improved results) model turbulence isotropically. Modelling anisotropic turbulence would probably improve the turbulent flow predictions by producing less skewed velocity profiles. Therefore Large Eddy simulations or Direct Numerical simulations, would have far improved results in spite of their demands on CPU time and hardware costs.

- A 'smooth' bed was modelled under the constraints of this investigation. It would be interesting to model a 'rough' bed as this would represent a prototype situation more closely. It would also be interesting to investigate the interaction of stress driven secondary circulation cells with skew induced ones which are more onerous with rough beds.

- Finite Element meshes provide a very flexible way to create complicated grids and it is therefore suitable for hydraulic applications where contours and bathymetry can be quite irregular. Since the Finite Volume (used by SSIIM in this investigation) and the Finite Difference method use quadrilateral elements, the grid construction process is not as flexible especially if the sotfware package has strong restrictions on non-orthogonality. The author of SSIIM is currently trying to address this problem with the introduction of multiblock and multigrid techniques. However, for the purposes of this study these methods were not sufficiently developed to be used here with confidence. Such methods would improve predictions particularly around the intake pier. Use of multigrid techniques would also improve the models efficiency with convergence acceleration techniques.

- Selection methods for relaxation factors in SSIIM could be considerably improved. Presently the selection process is rather *ad hoc* and a considerable amount of research could be devoted to ascertaining relaxation factors for specific flow and geometric situations.

- The sediment transport capabilities of SSIIM should be validated independently of the author as this subject was not tested as part of this investigation.

7.3.2 Modelling of Intake Flows

The investigation has made considerable contributions to knowledge in terms of the investigation and prediction of the flow structure at intake angles between 15 and 45 degrees. Advancements to this knowledge could follow these recommendations:

- The investigation only considered a channel ratio of 0.5 (intake / main). Many other combinations obviously occur in river and lateral intake geometry. Thus modelling more realistic intake geometry would be beneficial to knowledge. This includes cross sectional geometry other than plane rectangular as used by the simplified approach adopted in this investigation. Similarly, as mentioned previously, scenarios such as rough bed geometry, more representative of river situations, should be modelled. Bed forms would also have a significant effect upon the near bed limiting streamline and the shear stress distribution. Significant areas of scour may occur in areas of high velocity gradients or re-circulation and deposition may occur in stagnation zones. These phenomena have been identified and predicted to a certain degree by the physical and numerical modelling respectively. Adaptations, therefore, to the numerical model to account for a deformable bed would also provide more realistic results.

- A significant contribution to knowledge of the dividing streamplane has been made by the predictive graphs that have been constructed. This predictive hypothesis could be further simplified and tested in prototype situations in order that it could be applied with more engineering confidence in the design process.

- The intake pier geometry investigated here is an idealised situation and could be modified to represent a more realistic geometry. Rarely would a sharp edged intake pier apex be encountered in practice. The pier would more likely be curved or parabolic and this would have a significant effect upon the flow structure and secondary circulation cells observed.

- The flow control methods used in this investigation were again simplified. It was intended to examine the flow structure with a diversion weir in place just downstream of the intake pier but due to time constraints this was not possible. It would be interesting to study this situation which would represent a more realistic intake for small scale, run-of-the-river, low head hydropower.

- Numerical predictions of the maximum turbulent kinetic energy could be improved. The results obtained by this investigation were subject specific and it

would be interesting to apply the methodology developed here to produce a more general hypothesis which could be applied and tested to other intake configurations.

- Physical modelling is an extremely expensive technique in terms of time demands and a considerable amount of further research could be conducted to collect valuable data.

- Finally, sediment transport and exclusion problems could be studied as these are an important consideration in the design of intake structures and are closely related to the flow structure that has been described by this investigation.

ACKNOWLEDGEMENTS

Finally and most importantly, I would like to thank my family and friends for their assistance, encouragement and their patience during this prolonged period of study.

REFERENCES

Abdel, A. I. B., 1949. Treatment of heavy silt canals, Report to *the Second International Congress of Irrigation*, Cairo, Egypt.

Alfredson, K., Marchand, W., Bakken, T. H. and Harley, A., 1997. Application and comparison of computer models for quantifying impacts of river regulation on fish habitat. *HYDROPOWER '97*, Norway.

Avery, P. (ed)., 1989. *Sediment control at intakes*, BHRA Fluid Engineering Centre, Cranfield, England.

Barron, R. M. and Latypov, A. M., 1995. Survey of current verification and validation methodologies and resources for CFD, *Proc. 3rd Annual Conference of the CFD Society of Canada,* Vol. 1, 327-334.

Bharadvaj, B. K., Mabon, R. F. and Giddens, D. P., 1982. Steady flow in a model of the human carotid bifurcation. Part 1 – Flow visualisation, *J. Biomechanics*, Vol.15, No. 5, 349-362.

Bondurant, D. C. and Thomas, A. R., 1952. Discussion of Diversion from alluvial channels by C. Lidner, *Trans.*, ASCE, 78(D-112), 1-7.

Bowles, C. B. 1996. The use of the Acoustic Doppler Velocimeter for the measurement of mean velocities, Unpublished paper presented at *1st UK ADV Users Meeting,* HR Wallingford, Oxon, UK.

Bowles, C. B., 1997. Experiences with the Acoustic Doppler Velocimeter, Unpublished paper presented at *2nd UK ADV Users Meeting,* HR Wallingford, Oxon, UK.

Bowles, C. B., Daffern, C. and Ashforth-Frost, S., 1997. The independent calibration of the Acoustic Doppler Velocimeter, Presented at 27th IAHR Int. Congress, San Francisco, California, 8pp.

Bowles, C. B., Daffern, C. and Ashforth-Frost, S., 1998. An investigation into the flow field at a generalised intake structure using SSIIM, a 3D numerical model. *ASCE Water Resources Congress,* Memphis, USA.

Bowles, C. B., Daffern, C. and Ashforth-Frost, S., 1998. The independent calibration of SSIIM, a 3D numerical model. *Hydroinformatics '98,* Copenhagen, Denmark.

British Standards, 1980. BS 3680: Part 3A, BSI, London.
British Standards, 1981. BS 3680: Part 4A, BSI, London.1
British Standards, 1992. BS1042: Section 1.1, BSI, London.

Cabelka, J., 1950. Hydro Electric Station Design, *The Electrician*, June, 1181 – 1186.

Cabrera, R. and Lohrmann, A., 1994. Small scale laboratory flow measurements with the ADV-1, *Proc. Oceans '93,* Vol. 2, 404-407.

Chadwick, A. and Morfett, J., 1994. *Hydraulics in Civil and Environmental Engineering*, 2nd edition, E. and F.N. Spon, London.

Cho, Y. I., Back, L. H. and Crawford, D. W., 1985. Experimental investigation of branch flow ratio, angle and Reynolds Number effects on the pressure and flow fields in arterial branch models, *J. Biomechanical Engrg.,* Vol. 107, 257-267.

Chow, V. T., 1959. *Open Channel Hydraulics*, McGraw-Hill, London.

Cioc, D. 1962. Some problems of river hydraulics, in *Hydraulic Studies*, Vol IV, ISCH, Bucharest.

Coleman, H. W. and Stern, F., 1997. Uncertainties and CFD code validation, *J. of Fluids Engineering,* Vol. 119, 795-803.

De Valt Davies, G., 1983. Natural convection of air in a square cavity: a benchmark numerical solution. *Int. J. for Numerical Methods in Fluids,* 3(3), 249-264.

Department of Trade and Industry, 1994. *The Non Fossil Fuel Obligation,* Announcement of Second Tranche, DTI, London.

Gardel, A. and Rechsteiner, J. F., 1970. Energy losses in circular branches, *Bulletin Technique de la Suisse Romande,* No. 25.

Hager, W. H., 1984. An approximate treatment of flow in branches and bends, *Proceedings of the Institution of Mechanical Engineers,* 198C (4), 63-69.

Hamill, L., 1995. *Understanding Hydraulics,* Macmillan, London.

Issa, R. I. And Oliveira, P. J., 1994. Numerical predictions of phase separation in two phase flow through T-junctions, *Computers in Fluids,* 23(2), 347-372.

Ito, H. and Imai, K., 1973. Energy losses at 90 degree pipe junctions, Proc. ASCE., *J. Hydr. Div.,* 99, HY9, 1353-1368.

Karino, T., Kwong, H. H. M. and Goldsmith, H. L., 1979. Particle flow behaviour in models of branching vessels: I. Vortices in 90 degree T-junctions, *Biorheology,* Vol. 16, 231-248.

Keefer, T. N., 1971. The relation of turbulence to diffusion in open channel flow. PhD Dissertation, Colorado State University, USA.

Kent, A., 1956. *Flow Measurement,* Leagrave Press Ltd., London, 2nd edition.

Kraus, N. C., Lohrmann, A., and Cabrera, R., 1994. New acoustic meter for measuring 3D laboratory flows, *J. of Hydraulic Engineering,* Vol. 120, No. 3.

Lakshmana, R. N. S. , Sridharan, K. and Baig, M. Y. A., 1968. Experimental study of the division of flow in an open channel, *Australasian Conference on Hydraulics and Fluid Mechanics*, Sydney, 139-142.

Law , S. W. and Reynolds, A. J., 1966. Dividing flow in an open channel, *J. Hydraulic Division*, Proc. of the ASCE, 92(HY2), 207-231.

Lee, D. and Chiu, J. J., 1992. Computation of physiological bifurcation flows using a patched grid, *Computers in Fluids*, Vol. 21, No. 4, 519-535.

Leipsch, D., Moravic, S., Rastogi, A. K. and Vlachos, N. S., 1982. Measurement and calculations of laminar flow in a ninety degree bifurcation, *Biomechanics,* 15, 473-485.

Leonard, B. P., 1979. A stable and accurate convective modelling procedure based on quadratic upstream interpolation, *Comput. Methods Appl. Mech. Eng.,* Vol. 19, 59-98.

Levi, I. I., 1947. Hydraulic design of intakes with minimal entrance losses, *Izvestiia VNIIG*, Vol. 34.

Lhermitte, R. and Serafin, R., 1984. Pulse to pulse coherent Doppler signal processing techniques, *J. Atmos. And Oceanic Technol.,* Vol. 1, 293-308.

Linder, C. P., 1952. Diversions from alluvial streams, *Proc.for the ASCE*, Vol. 79 (112), 1-25.

Lohrmann, A., Cabrera, R. and Kraus, N. C., 1994. Acoustic Doppler Velocimeter for laboratory use, *Proc. Fundamentals and Advancements in Hydraulic Measurements and Experimentation,* Hydraulics Division ASCE.

Miller, D. S., 1979. New data on flow losses in piping systems, *Waserwirtchaft,* 69, 163-166.

Miller, K. S. and Rochwarger, M. M., 1972. A covariance approach to spectral moment estimation, *IEEE Trans. Inform. Theory*, IT-18, 588-596.

Morton, K. W. and Suli, E., 1993. A posterior and a priori error analysis of finite volume methods. Technical Report NA-93/05, NAGp, Oxford Computing Laboratory, UK.

Neary, V. S., 1992. Flow structure at an open channel diversion. M. S. Thesis, Civil and Environmental Engineering, The University of Iowa, Iowa City, Iowa.

Neary, V. S. and Odgaard, A. J., 1993. Three dimensional flow structure at open channel diversions, *J. Hydr. Engrg.,* 119 (11), 1224-1230.

Neary, V. S., Barkdoll, B. and Odgaard, A. J., 1994. Sand bar formation in side diversion channels, *Proc. National Conference*, Hydraulics Division, ASCE, Buffalo, New York., 1171-1175.

Neary, V. S., Barkdoll, B. and Odgaard, A. J., 1994. Sand bar formation in side diversion channels. *Proc. National Conference,* Hydraulics Division, New *York.,* 1171-1175.

Neary, V. S., Sotiropoulos, F. and Odgaard, A. J., 1995. Predicting 3-D flows a lateral water intakes, *Proc. Waterpower '95,* ASCE San Francisco, USA.

Nortek, 1996. Frequently Asked Questions, compiled by HR Wallingford Equipment Sales, Oxfordshire, UK.

Novak, P. and Cabelka, J., 1989. *Models in Hydraulic Engineering, Physical Principles and Design Applications*, Pitman, London.

Ofitserov, A., 1952. *Intake Hydraulics*, Gosstroizdat, Moscow.

Olsen, N. R. B., 1991. A numerical model for simulation of sediment movements in water intakes. Dr. Ing. Dissertation, The Norwegian Institute of Technology, Trondheim, Norway.

Olsen, N. R. B., 1994. A 3 dimensional numerical model for the simulation of water and sediment flow. *HYDROSOFT-94*, Porto Carras, Greece.

Olsen, N. R. B., 1995. Three dimensional numerical modelling of water flow in a river with large bed roughness, *IAHR J. Hydraulic Research,* Vol. 33, No. 4.

Pantakar, S. V., 1980. *Numerical heat transfer and fluid flow.* Hemisphere Publishing Corporation, Taylor and Francis Group, New York, USA.

Popp, M. and Sallet, D. W., 1983. Experimental investigation of one and two phase flow through a T-junction, *International Conference on the Modelling of Multiphase Flow*, Coventry, England, 67-88.

Ramamurthy, A. S. and Satish, M. G., 1988. Division of flow in short open channel branches, *J. Hydr. Engrg.,* 114(4), 428-438.

Ramamurthy, A. S. and Satish, M. G., 1990. Dividing flow in open channels, *J. Hydr. Engrg.,* 116(3), 449-454.

Ramirez, R., 1985. *The F. F. T., Fundamentals and concepts*, Prentice Hall, London.

Razvan, E., 1989. *River intakes and diversion dams*, Elsevier Science, Oxford, England.

Roache, P. J., 1994. Perspective: A method for uniform reporting of grid refinement studies. *ASME J. Fluids Engineering,* 116, 405-413, September.

Schlichting, H. 1979. *Boundary Layer Theory.* McGraw Hill, New York.

Seed, D. J., 1997. River training and channel protection; Validation of a 3D numerical model. HR Wallingford Technical Report, SR 480, Construction Sponsorship Directorate, HR Wallingford, Oxfordshire, UK.

Snyder, W. H., 1997. Evaluation of Acoustic Doppler Velocimeter in a stratified towing tank, Internal report No. ME-FD/97.73, Environmental Research Centre, University of Surrey.

Sotiropoulos, F. and Patel, V. C., 1992. Flow in curved ducts of various cross section, IIHR Report No. 358, University of Iowa, USA.

Spalding, D. B., 1972. A novel finite difference formulation for differential expressions involving both first and second order derivatives. *Int. J. Numerical Methods Engineering*, Vol. 4, 551-562.

Sridharan, L., 1966. Division of flow in open channels, MSc thesis presented to the Indian Institute of Science, Bangalore, India.

Taylor, E. H., 1944). Flow characteristics at rectangular open channel junctions, *Trans*. ASCE, No 109, 893-912.

Thomas, L. H., 1949. Elliptic problems in linear difference equations over a network. Watson Scientific Computing Laboratory Report, Columbia University, New York, USA.

Vanoni, V. A., 1975. *Sedimentation Engineering*, ASCE, New York, USA.

Versteeg, H. K. and Malalasekera, W., 1995. *An introduction to computational fluid dynamics*. Longman Scientific and Technical, London, UK.

Wilcox, D. C., 1994. Simulation of transition with two equation turbulence model, *AIAA J.*, Vol. 32, No. 2.

Yildiz, D. and Kuzum, L., 1994. Turning up the power, *International Water Power & Dam Construction*, Small Hydro Supplement, September, xx- xxvi.

Zrnic, D. S., 1997. Spectral moment estimates from correlated pulse pairs, *IEEE Trans. Aerosp. and Electron. Syst.*, AES-13, 344-354.

APPENDIX A

Drawings of Physical Model

CB/1/11/96

CB/2/11/96

TRAVERSING SYSTEM FOR INTAKE MODEL

DETAIL A

SCALE 1:20

- 200
- 50
- 100 Carriage
- 75 Wall of Tank
- 32 Stainless Steel Tube
- ON ADV TROLLEY
- with 20 Bars

For further details of Carriage arrangement see Detail A
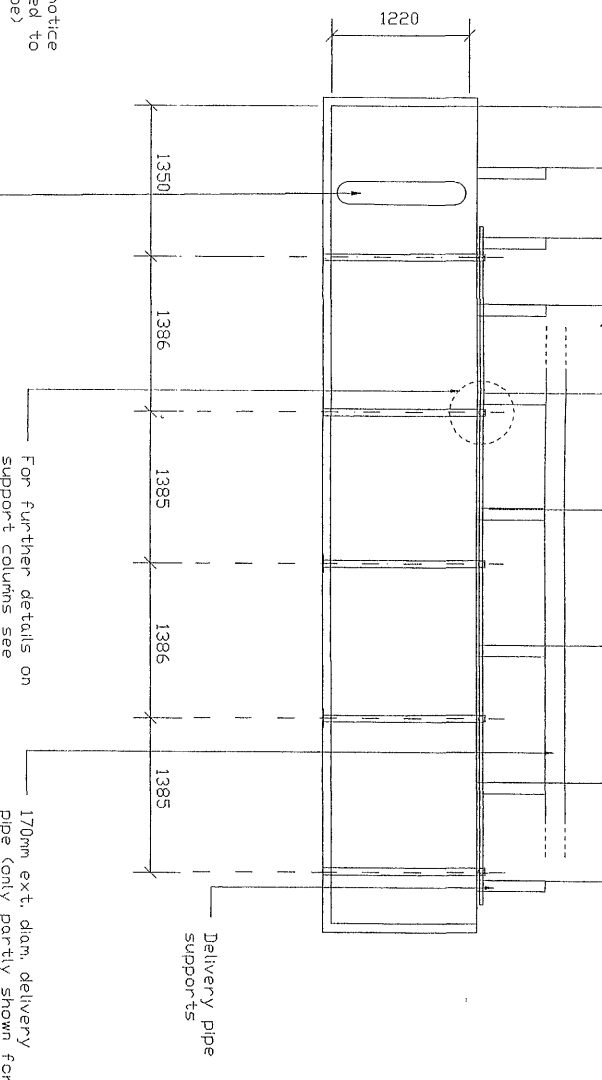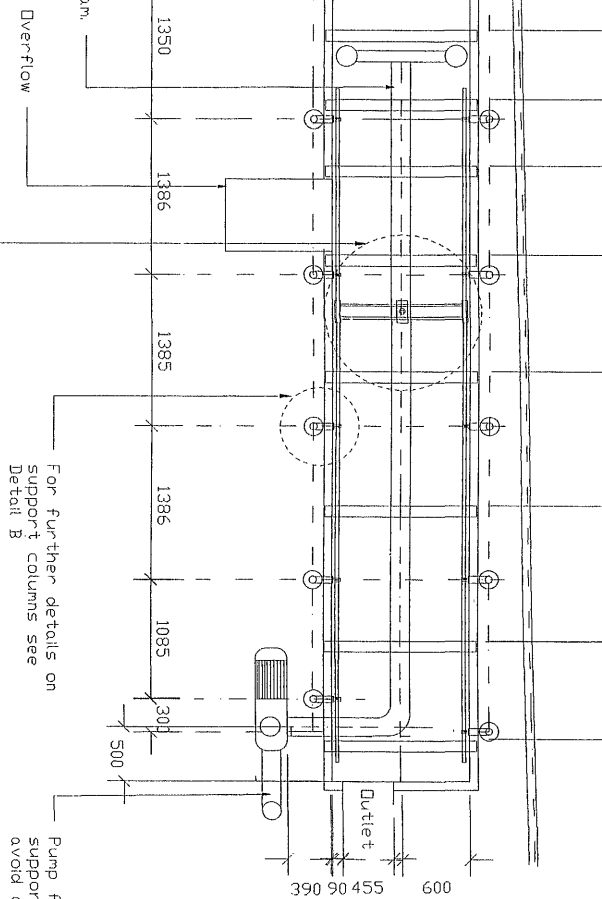
DETAIL B

PLAN ON BASEPLATE OF COLUMN

SCALE 1:10

- 95
- 60
- 20
- 60
- 32
- 20
- 150

For further details on support columns see Detail B

DETAIL C

SECTION THROUGH TRAVERSING COLUMN

SCALE 1:20

- 1245
- Varies to suit existing floor levels

For further details see Detail D

For further details on support columns see Detail C

Inlet to tank

DETAIL D

SECTION SHOWING COLUMN WITH TROLLEY

SCALE 1:10

- Support column
- 30
- 65
- 25
- Wall of tank
- 20 mm diam. trolley rail
- 32 mm diam. stainless steel rail

Overflow

Pump for tank (notice support re-aligned to avoid delivery pipe)

- 1350
- 1386
- 1385
- 1386
- 1085
- 300
- 500
- Outlet
- 390 90 455 600

- 1220
- 1350
- 1386
- 1385
- 1386
- 1385

170mm ext. diam. delivery pipe (only partly shown for clarity)

Delivery pipe supports

PHYSICAL MODEL OF INTAKE STRUCTURE

DRAWN BY C. BOWLES
DATE NOVEMBER '96

DETAIL A

2313
1194
15
300
300 320 600

DETAIL D

DWS PHASE INLET CONFIGURATION

Inlet Channel

350

Tilting Tailgate (see Section B-B)

SECTION B-B THROUGH INLET CHANNEL

2313
1829
750
450

Tilting Tailgate

V-Notch Weir

DETAIL B

620
2313
519
1074
30
300
554
640
300 320 600

DETAIL E

620
2313
695
620
45
300
320
874
300 320 600

350
150

DETAIL E SHOWS PHASE TWO OF THE INLET CONFIGURATION
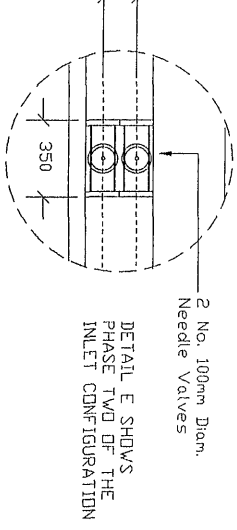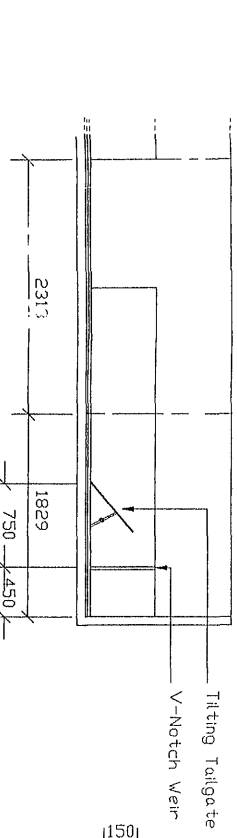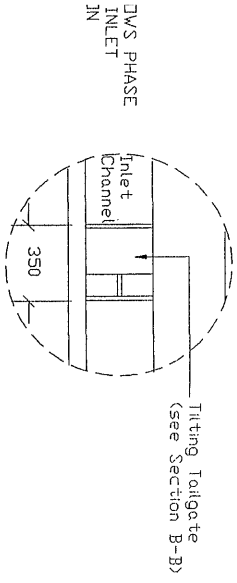
2 No. 100mm Diam. Needle Valves

150mm Honeycomb (or similar) Flow Straightener

Main Channel

B

Inlet Channel

15

Existing Round Crested Weir Modified to fit in Main Channel

See Details A to C

Overflow

50mm Diffusing Mesh (Geotextile or Similar)

See Detail D and E

150
415 50 150
3200
450
2313
1829
350 400 450
90 455 600

Outlet

B

A

B

DETAIL C

620
2313
1829
450
150
100 150
3200
450
995
250
Varies 424 to 1119

Honeycomb Flow Straightener and Diffuser

Overflow

Inlet Channel

Round Crested Weir

Base formed with 22mm Wysaform sheets

Inlet Structure formed in High Density Polystyrene Foam fastened to second base sheet of 22mm Wysaform Sheet

Upper Limit of Channel

V-Notch Weir

APPENDIX B

Drawings of fabrication details for ADV mounting apparatus

CB/1/11/96 (1)

feed into burette from pump

Clamping arrangement to allow movement of the burette in vertical and horizontal directions.

WATER LEVEL

Varies

45 12 34

650 - 734 - 741

Plate to be fabricated to bolt onto existing bracket of carriage

Mounting fitting for ADV onto plate to be able to rotate about a fixed point.

ADV probe to be able to tilt from the vertical through 15 and 30 degrees.

84

91

30

64

32

Existing mounting of bracket onto carriage.

Bracing to bracket

Existing bracket

Bolt holes to be slotted to facilitate plumbing of the ADV mounting plate with carriage bracket.

56

88

15 32 42

250

SCALE	1:50, D&E 1:25	PRELIM. FABRICATION DETAILS FOR TOWING TANK TEST	DRAWN BY	C. BOWLES
DRWG No	CB/1/11/96 (1)		DATE	FEBRUARY '97

APPENDIX C

Simple calibration check of the ADV

THE NOTTINGHAM TRENT UNIVERSITY

DEPARTMENT OF CIVIL
& STRUCTURAL ENGINEERING

C. B. Bowles, B Eng (Hons), DiplWEM
E-Mail :- Chris.Bowles@ntu.ac.uk

A SIMPLE PROCEDURE TO CHECK THE CALIBRATION OF THE ACOUSTIC DOPPLER VELOCIMETER

1.0   Introduction

The following text gives an outline of a towing tank method developed by C. Bowles of the Department of Civil and Structural Engineering, Nottingham Trent University, to check the calibration of the ADV.

2.0   ADVCHECK

ADVCHECK, the software incorporated into the ADV system, should be used regularly. Reference to the ADV manual will give an indication of the interpretation of the graphical output.

3.0   Standard Calibration Issues

Standard calibration issues should be checked such as :-

Bent probe arms.
Accurate speed of sound corrections.
Correct probe configuration file.

4.0   Towing Tank Test

A small laboratory flume can be used for this test, although obviously the longer the flume, the more averaging data will be available and hence the more accurate the results. I used an Armfield flume 11.0m long by 300mm wide by 400mm deep. The following procedure can be used to check the calibration of the ADV.

1. Close off the downstream end of the flume using a vertical gate or similar.

2. Fill the flume with water to a suitable depth.

3. Attach the ADV to a carriage running along the top of the flume. Most flumes have such a carriage for measuring water surface profiles and depths. Align the x component receiver (red painted probe arm) in the streamwise direction.

4. Allow the water to stabilise for a period of time (say 5 to 10 minutes). Stabilisation can be checked by running the ADV in the still water and observing the graphical output. Carry out a test run by pushing the carriage holding the ADV through the flume whilst the ADV is measuring, to assess SNR. If SNR's obtained are consistently less than 8 dB, seeding of the water will be required.

5. Place two reference marks on the glass wall of the tank at a suitable upstream and downstream limit (I used a distance of 10.0m).

6. With the aid of an assistant, initiate the measurements using the ADV. Using a stopwatch measure the time taken to push the ADV through the flume over the predetermined reference distance. Try to keep the movement of the carriage along the flume as constant as possible. You will see from the ADV graphical velocity trace that it is quite easy to get a reasonably constant velocity.

7. Calculate the mean velocity of the carriage from distance travelled by ADV / time taken. Compare this to the mean velocity measured by the ADV. This can be easily obtained using WinADV (US Bureau of Reclamation). Filter out any data with a SNR < 8dB. The velocity in the x direction should be used. The mean values in the y and z directions should be negligible if the water in the flume has been allowed to stabilise sufficiently.

8. Carry out similar tests by rotating the ADV through 90 degrees in the horizontal to test the y component and rotate through the vertical to test the z component.

9. Obviously the more tests undertaken at a range of different velocities the better will be the interpretation of the calibration of the ADV.

10. Graphical plots of Carriage Velocity with Velocity measured by the ADV can be produced to assess the linearity and accuracy of the calibration. Similarly percentage errors should be calculated to assess if the ADV is measuring to a sufficient accuracy for your application.

11. It is reasonable to estimate that this simple method will calculate the accuracy of the ADV to a tolerance of approximately +/- 2-3%.

Chris Bowles, September 1997.

APPENDIX D

Published Papers

THE USE OF THE ACOUSTIC DOPPLER VELOCIMETER FOR THE MEASUREMENT OF MEAN VELOCITIES

C. B. Bowles, C. D. Daffern and S. Ashforth Frost
Department of Civil and Structural Engineering,
Nottingham Trent University, Nottingham, England, U.K.

ABSTRACT

An Acoustic Doppler Velocimeter (A.D.V.) manufactured by SonTek Inc. of San Diego, California, U.S.A., was purchased from the U.K. agents, HR Wallingford Limited of Oxfordshire, England in March 1996, by the Department of Civil and Structural Engineering at The Nottingham Trent University. The ADV is a high precision instrument that measures velocity of fluid flow in three components. It uses acoustic sensing techniques to measure flow in a remote sampling volume and the measured flow is undisturbed by the presence of the probe. This paper describes a methodology for ascertaining a suitable time period and sampling rate dependent upon the regime of the flow being measured.

INTRODUCTION

The field version of the Acoustic Doppler Velocimeter (ADV) was purchased by the Department of Civil and Structural Engineering of the Nottingham Trent University (TNTU) from HR Wallingford Limited (HRW) of Oxfordshire England. HRW are the U.K. agents for SonTek Inc., of San Diego, California, U.S.A. SonTek Inc. were the original manufacturers of the ADV and there is now a sister company, Nortek, based in Norway.

The ADV is claimed by the manufacturers, to be a high precision instrument that measures velocities in three components. The ADV uses acoustic sensing techniques based upon the Doppler Principle (Lohrmann et al. 1994) to measure flow in a remote sampling volume. The measured

flow is undisturbed by the presence of the probe. The instrument consists of three modules: the measuring probe, the conditioning probe and the processing module which contains low noise electronics enclosed in a waterproof housing.

Figure 1. The ADV, consisting of probe, conditioning module and processing module, (from Lohrmann et al. 1994).

The acoustic sensor consists of one transmit transducer and three receive transducers. The receive transducers are mounted on short arms around the transmit transducer at 120^0 azimuth intervals. The acoustic beams are orientated so that the receive beams intercept the transmit beam at a point located approximately 55mm below the sensor. The intersection of these four beams, together with the width of the transmit pulse, define the sampling volume. The volume is 3-9mm long and approximately 6mm in diameter. The ADV samples instantaneous velocities at a sampling rate of up to 25 Hertz, from which the associated software calculates the mean velocities in the x, y and z directions.

Sampling rates of 5, 10 and 25 Hertz with sample time periods ranging from 5 seconds to 10 minutes have been examined.

SAMPLE TIME PERIOD AND SAMPLING RATE TESTS

A methodology for a test was developed in order to ascertain the correct sampling rate and time period for a specific application. The application was that of a small Armfield flume, the dimensions of which are given in figure 1. The depth of the flow in the channel was 110mm with a mean flow of 6.5 l/s passing down the flume, with typical mean velocities of 10 cm/s. The ADV probe was set at a location in the flume of 200 mm offset from the right hand wall of the flume at a sample volume depth of 13 mm from the bed of the flume. The probe was fixed at streamwise distance of 2250 mm from the inlet sump of the channel.
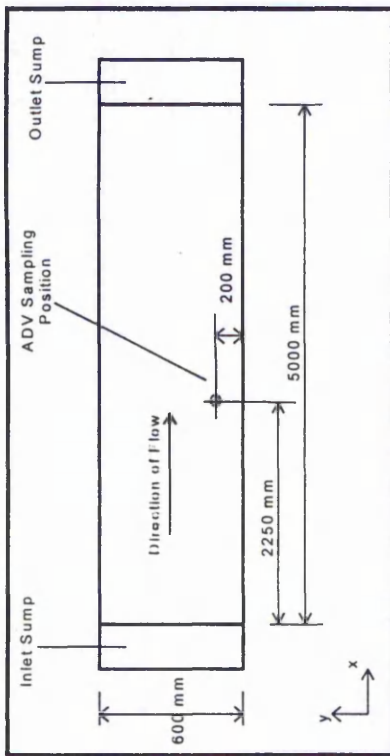
Figure 2 illustrates the variation in the velocity in the x-direction with increasing sample time periods over 5, 10 and 25 Hertz sampling rates. It is seen that after a sample time period of 5 minutes (300 seconds), the magnitude of the x-component of velocity for 5, 10 and 25 Hertz sampling rates ranges from 10.2 cm/s to 10.5 cm/s. This is a difference of 0.3 cm/s, which is further reduced with sample time periods in excess of 5 minutes. Similar behaviour occurs for the y and z components of the velocity.
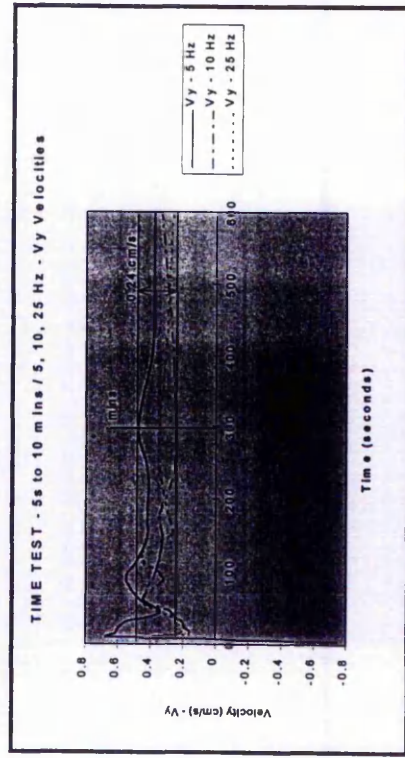
Figure 4. Variation of the y-component of velocity with sampling rate and sample time period.
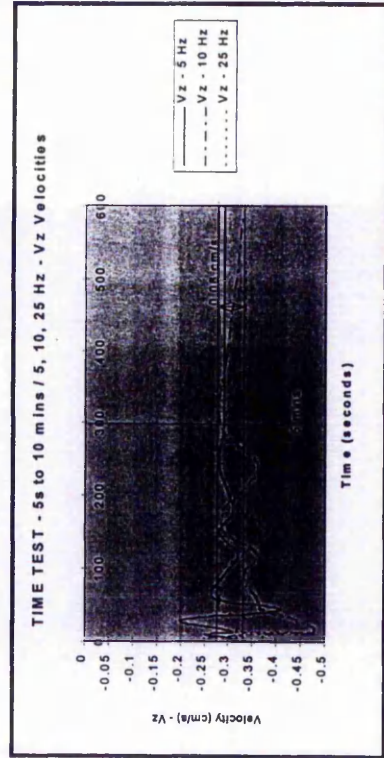
Figure 5. Variation of the z-component of velocity with sampling rate and sample time period.

Figure 2. Configuration of the ADV probe in the flume.

A series of fourty two tests were carried out at this location with sample time periods of 5, 10, 15, 30, 45, 60, 90, 120, 150, 180, 240, 300, 420 and 600 seconds and sampling rates of 5, 10 and 25 Hertz. A period of flow stabilisation was required in the flume as a results of phenomena which were discovered using the ADV previously. Measurements taken using the ADV indicated that the flow in the flume varied cyclically for a period of up to 2 hours after which time the flow in the flume became stable.

The results of the test indicates that the velocities in the x, y and z directions (see figure 1 for component directions) appear to reduce with time.

Figure 3. Variation of the x-component of velocity with sampling rate and sample time period.

The sample rate appears to have little effect upon the mean velocities that are obtained. Further examination of this can be undertaken by examining the standard deviation from the mean velocities. The standard deviation of the mean velocity over the three sampling rates used is as shown in figure 6.
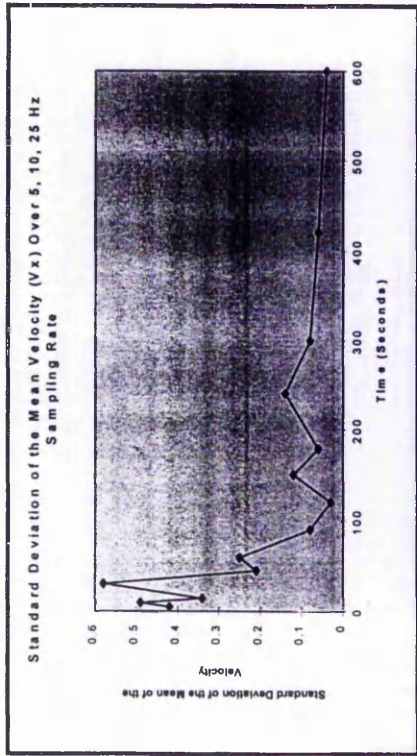
Figure 6. Standard deviation of the mean velocity in the x-direction with time, over 5, 10 and 25 Hertz sampling rates.

With regard to figure 4, the standard deviation of the mean velocity over the three sampling rates reduces rapidly with time. Initially, a standard deviation of 0.42 cm/s is obtained at a sample time period of 5 seconds. However, with a sample time period of 5 minutes, the value for the standard deviation has reduced to 0.08 cm/s which is a reduction of 80%. The reduction in the standard deviation between sample time periods of 5 minutes and 10 minutes is from 0.08 cm/s to 0.04 cm/s. This represents a further reduction in the standard deviation of only 10% from the initial value, at a sample time period of 5 seconds. Thus, sample time periods in excess of 5 minutes will have a negligible effect upon the accuracy of the mean velocities obtained for this particular application. Similarly the results indicate that, for the purposes of the measurement of mean velocity components, the choice of sampling rate beyond a time period of 5 minutes is also negligible. The results in the y and z components illustrate similar behaviour.

CONCLUSIONS

The tests discussed in this paper have highlighted that preliminary tests are necessary when using the ADV, in order to ascertain appropriate sampling rates and sampling time periods. The choice of these two parameters will vary depending on the flow conditions. It is critical to identify a minimum sample time period, beyond which there is negligible improvement to the results obtained.

Similarly it is important to consider the sampling rate. In highly turbulent flow conditions, it may be necessary to use a sampling rate of 25 Hertz, to ensure the capture of the required data for the calculation of turbulent intensities. In addition, under less turbulent flow conditions, there may be little or no advantage to be gained by using high sampling rates. High sampling rates and long time periods merely result in large quantities of data.

ACKNOWLEDGMENTS

Mr I Shepherd, Equipment Sales Manager, HR Wallingford Ltd., Howbery Park, Wallingford, Oxon. OX10 8BA, U.K. for assistance with the interpretation of the data.

Mr A Lohrmann, Nortek AS, Bruksveien 17, N-1390 Vollen, Norway for assistance in the interpretation of the data.

REFERENCES

Lohrmann, A., Cabrera, R. & Kraus, N.C. (1994), **Acoustic Doppler Velocimeter for Laboratory Use**, Proceedings of Fundamentals and Advancements in Hydraulic Measurements and Experimentation, Hydraulics Division ASCE.

SonTek, Inc (1995), **ADV Software Manual**, Version 2.3 Reference Manual, San Diego, California.

Wahl, T. (1996), **WinADV Post Processing Software**, Water Resources Research Laboratory, U.S. Bureau of Reclamation, Denver, Colorado.

Presented at :- The 27th IAHR International Congress,
San Francisco, U.S.A., August 1997.

C. B. Bowles Page 1

THE INDEPENDENT CALIBRATION OF THE ACOUSTIC DOPPLER VELOCIMETER

C. B. Bowles, C. D. Daffern, Department of Civil and Structural Engineering, S.Ashforth-Frost, Department of Mechanical and Manufacturing Engineering, Nottingham Trent University, Nottingham, England, U.K.

ABSTRACT

The Acoustic Doppler Velocimeter is a relatively new high precision instrument that measures mean velocity and higher order statistics of fluid flow in three directions. It uses acoustic sensing techniques to measure the velocity characteristics of seeding particle suspended in and following, the mean bulk flow as they pass through a remote sampling volume. It is non-intrusive and direction sensitive. It is a simple, inexpensive yet valuable diagnostic technique especially in large scale modelling of fluid flow. This paper presents an independent calibration of the Velocimeter in the range 10 cm/s to 100 cm/s. The ADV tested was found to have mean errors of 7 % in the x component with mean errors of 2 % in the y component with respect to the measurement of mean velocities.

INTRODUCTION

The field version of the Acoustic Doppler Velocimeter (ADV) was purchased by the Department of Civil and Structural Engineering of The Nottingham Trent University (TNTU) from HR Wallingford Limited (HRW) of Oxfordshire, England. HRW are the U.K. agents for SonTek Inc., of San Diego, California, U.S.A. SonTek Inc. were the original manufacturers of the ADV and there is now a sister company, Nortek, based in Norway.

The ADV is claimed by the manufacturers, to be a high precision instrument that measures velocities in three components. The ADV uses

acoustic sensing techniques based upon the Doppler Principle (Lohrmann *et al.* 1994) to measure flow in a remote sampling volume. The measured flow is undisturbed by the presence of the probe. The instrument consists of three modules: the measuring probe, the conditioning probe and the processing module which contains low noise electronics enclosed in a waterproof housing.

Figure 1. The ADV, consisting of probe, conditioning module and processing module, (from Lohrmann *et al.* 1994).

The acoustic sensor consists of one transmit transducer and three receive transducers. The receive transducers are mounted on short arms around the transmit transducer at 120^0 azimuth intervals. The acoustic beams are orientated so that the receive beams intercept the transmit beam at a point located approximately 55mm below the sensor. The intersection of these four beams, together with the width of the transmit pulse, define the sampling volume. The volume is 3-9mm long and approximately 6mm in diameter.The ADV is able to record instantaneous velocities at a sampling rate of up to 25 Hertz.

Three sets of calibration test have been carried out. The first was carried out in an Armfield flume in the Hydraulics Laboratory of the Department of Civil and Structural Engineering at TNTU, the second in the Towing Tank at HRW and the third in the Towing Tank at Southampton Institute. For all of the tests, seeding was required to the tanks since there was insufficient particulate matter present in the tanks. Towing Tank tests have previously been carried out with the ADV by the manufacturers (Lohrmann *et al.*, 1994), (Cabrera and Lohrmann, 1994) but it was considered that an independent check was required prior to the ADV being used in laboratory model measurements.

TOWING TANK TESTS

HYDRAULICS LABORATORY, NOTTINGHAM TRENT UNIVERSITY

A relatively simple Towing Tank test was carried out in the Armfield flume in the Hydraulics Laboratory at TNTU. The flume is 11 metres long by 300mm wide by 400mm deep. The ADV was attached to a carriage running along rails on the top of the flume. Clean tap water was introduced to the flume by high pressure hose. An initial test was carried out in the flume to investigate if seeding was required. The ADV was pushed manually through the flume following a period of stabilisation of the water in the flume. Average Signal to Noise Ratios (SNR) of 2-3 dB were obtained. SNR gives an indication of the quality of the Doppler signal received by the probe. The manufacturers quote a minimum SNR of 5 dB for the measurement of mean velocities. A methodology for seeding was therefore required.

A series of seeding tests were carried out in the flume. A burette was used to introduce the seeding material upstream of the ADV probe. Seeding material of varying concentrations was delivered to the burette at varying rates via gravity. The seeding was tested with two positions of the burette in relation to the ADV probe in the streamwise direction and vertically in relation to the probe. PVC powder in suspension with water was used for the seeding material.

The tests indicated that the most suitable arrangement for seeding was PVC powder in suspension with water at a concentration of 15 g/l, a delivery rate of 1.5 ml/s with the seeding burette positioned at 670mm in front of the ADV probe with the tip of the burette operating at an elevation of 10mm above the sampling position.

Towing Tank tests were subsequently carried out in the flume by recording the time taken for the carriage holding the ADV, to travel a pre-determined distance, to enable the velocity of the carriage to be calculated. The velocity of the carriage was then compared to the velocities measured by the ADV presented in table 1.

ADV - Vx (cm/s)	Velocity of Carriage (cm/s)	Carriage - ADV (cm/s)	% Error	SNR (dB)
17.76	20.2	2.44	12.08	24.2
11.21	13.3	2.09	15.71	12.2
27.06	27.7	0.64	2.31	25.6
27.67	26.2	-1.47	-5.61	24.8
23.21	23.1	-0.11	-0.48	20.8
13.07	15.7	2.63	16.75	12.9
31.53	35.3	3.77	10.68	33.0
17.79	19.3	1.51	7.82	12.8
16.42	16.6	0.18	1.08	27.1
22.17	24.7	2.53	10.24	14.7
40.27	38.9	-1.37	-3.52	20.2
16.05	19.1	3.05	15.97	23.2
23.87	24.3	0.43	- 1.77	27.6
43.83	39.9	-3.93	-9.85	24.9
12.81	14.7	1.89	12.86	34.5
12.94	14.4	1.46	10.14	22.4
38.17	38.2	0.03	0.08	27.0

Table 1. Table showing the errors between the carriage velocities and the velocities measured by the ADV.

In all cases the SNR measured was adequate but the resulting errors caused concern.

TEST AT HR WALLINGFORD LIMITED, OXFORDSHIRE

A Towing Tank test was undertaken at a facility at HRW. This Towing Tank is 78 metres long by 2m wide by 2m deep. A carriage holding the ADV runs along the top of the tank at a known velocity. It was necessary to fabricate a mounting attachment for the ADV and it was also necessary to modify the seeding arrangement.

Figure 3. Towing Tank at HRW.

A series of tests were undertaken over the period of a day and the results measured by the ADV were compared to the known velocity of the carriage. The results of the test are shown in figure 4 below.

Test No.	ADV Vx	ADV Vy	ADV Vz	ADV Resultant Velocity	Carriage Velocity	Carriage - Resultant	% Error	SNR
	(cm/s)	(cm/s)	(cm/s)	(cm/s)	(cm/s)	(cm/s)		(dB)
1	3.42	2.13	1.15	4.19	5	0.81	16.20	7.66
1c	3.99	0.90	1.28	4.29	5	0.71	14.28	14.19
2a	4.19	0.91	1.15	4.44	5	0.56	11.22	16.34
2b	4.02	0.92	1.05	4.26	5	0.74	14.89	14.64
2c	2.58	3.33	0.62	4.26	5	0.74	14.84	13.1
2c	2.88	2.73	0.70	4.03	5	0.97	19.41	12.31
3b	6.06	5.79	0.16	8.38	10	1.62	16.17	20.6
3c	6.48	5.33	0.47	8.40	10	1.60	15.96	19.91
3c	7.91	2.63	1.04	8.40	10	1.60	16.00	20.75
3d	6.69	4.56	1.11	8.17	10	1.83	18.28	19.83
4	18.28	1.70	0.85	18.38	20	1.62	8.11	17.19
5	17.56	2.89	0.75	17.81	20	2.19	10.94	19.13
6	22.60	9.46	0.24	24.50	30	5.50	18.33	16.6
7	25.22	4.70	0.95	25.67	30	4.33	14.43	20.33
8	23.41	7.86	0.49	24.70	30	5.30	17.67	13.89
9	23.96	6.76	0.64	24.90	30	5.10	16.99	20.25
10	27.47	0.21	1.27	27.50	30	2.50	8.33	25.12
11	43.85	5.40	0.19	44.18	50	5.82	11.64	12.59
12	45.67	2.54	0.33	45.74	50	4.26	8.52	14.42
13	42.08	8.57	0.55	42.95	50	7.05	14.11	13.38
14	42.62	7.92	1.03	43.36	50	6.64	13.28	13.18
15	41.69	9.66	1.33	42.82	50	7.18	14.37	12.59
16	44.75	23.23	2.86	50.50	60	9.50	15.83	12.11
16	48.19	14.13	1.62	50.24	60	9.76	16.26	12.11
17	49.55	11.72	1.32	50.93	60	9.07	15.11	12.12
18	51.73	8.72	1.04	52.47	60	7.53	12.55	12.32
19	50.08	11.58	1.52	51.42	60	8.58	14.29	11.21
20	49.25	12.44	1.43	50.82	60	9.18	15.31	13.53

Figure 4 showing the results of the Towing Tank test at HRW.

It can be observed that although the SNR in all cases was adequate the resulting errors were unacceptable. The ADV probe was subsequently returned to the U.K. agents HRW, for checking.

TEST AT SOUTHAMPTON INSTITUTE

The ADV was checked by HRW and returned. A further test was then carried out at Southampton Institute. Although the facility at Southampton is slightly smaller than the facility at HRW, the principle of the tests were identical. The results of the test can be illustrated by the following graphs.
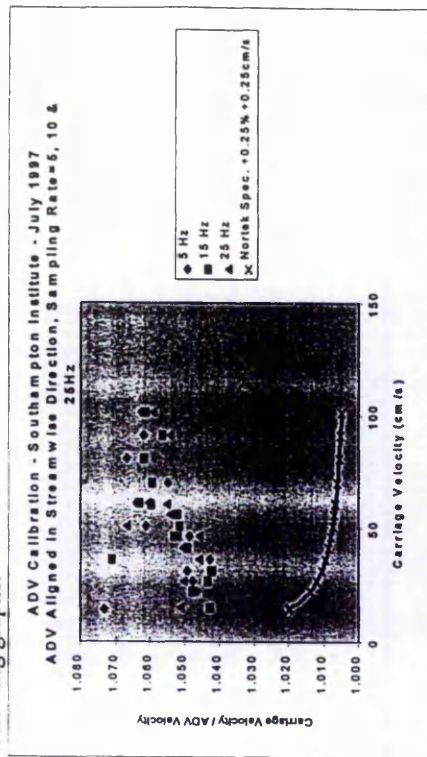
Figure 5 showing the results of the test with the ADV aligned in the x-direction (streamwise).
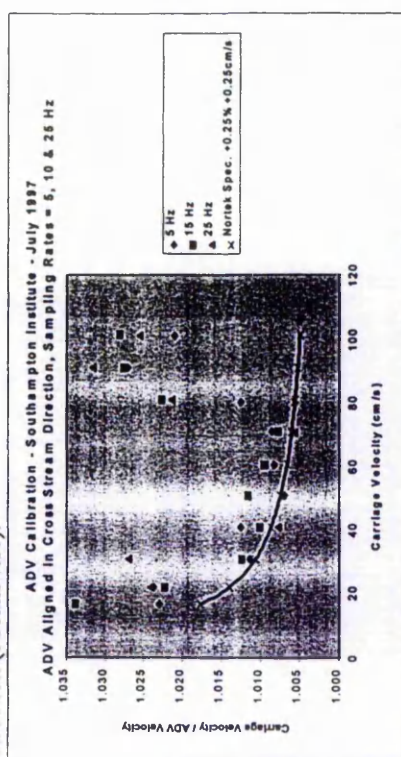
Figure 6 showing the results of the test with the ADV rotated through 90⁰.

The above graphs show the results of the Towing Tank tests in comparison to the accuracy claimed by Lohrmann et al (1994) (labeled as Nortek Spec.) of +/-0.25% +/-0.25cm/s. It has been shown clearly that

for this particular ADV, the mean velocity measurements are more accurate in the y component (average 2% error) than in the x component (average 7%). However in nearly every case the velocities measured fall outside the accuracy quoted by the manufacturer. The accuracy shown by this test is an improvement on the previous tests when it was clear that the ADV was not functioning correctly.

CONCLUSIONS

It has been shown how the ADV can be independently calibrated in the laboratory and the tests described have indicated how essential it is to check the factory calibration. It is not necessary to use large scale facilities such as those at HRW or Southampton, because a simple test can be undertaken in a small scale laboratory flume as described at the start of this paper. Such a basic test will give an indication as to the accuracy of the ADV. The tests have shown how it is possible to obtain calibration data which can then be used to calculate correction factors which can be applied to measured mean velocities in the laboratory.

The tests have highlighted the importance of checking the operation of the ADV at regular intervals using the built in checking systems. A programme called ADFCHECK is incorporated into the operating software (SonTek, 1995) which will identify any damage or malfunctioning of the ADV. This program was used to confirm that the ADV was malfunctioning for the first two tests described by this paper. Calibration issues such as bent probe arms, accurate speed of sound corrections and correct probe configuration files should also be checked.

Other factors which should be checked when undertaking Towing Tank tests are patches in the seeding. At low SNR(less than 8 dB) the ADV will underestimate the velocity. To ensure that mean velocities are not contaminated by inaccurate velocity measurements data with SNR<8dB should be filtered out (this may be done using a package called WinADV written by Wahl, 1996). In addition, the fluid motion in the Towing Tank should be allowed to settle between each testrun.

ACKNOWLEDGMENTS

Mr I Shepherd, Equipment Sales Manager, HR Wallingford Ltd., Howbery Park, Wallingford, Oxon. OX10 8BA, U.K. for assistance with the Towing Tank test at HRW.

Mr S Delzell, Maritime Faculty, Southampton Institute, Southampton, U.K. for assistance with the Towing Tank test at Southampton.

Mr A Lohrmann, Nortek AS, Bruksveien 17, N-1390 Vollen, Norway for assistance in the interpretation of the results.

REFERENCES

Lohrmann, A., Cabrera, R. & Kraus, N.C. (1994), **Acoustic Doppler Velocimeter for Laboratory Use**, Proceedings of Fundamentals and Advancements in Hydraulic Measurements and Experimentation, Hydraulics Division ASCE.

SonTek, Inc (1995), **ADV Software Manual, Version 2.3 Reference Manual**, San Diego, California.

Wahl, T. (1996), **WinADV Post Processing Software**, Water Resources Research Laboratory, U.S. Bureau of Reclamation, Denver, Colorado.

The independent validation of SSIIM, a 3D numerical model

C.B. Bowles & C. Daffern
Department of Civil and Structural Engineering, Nottingham Trent University, UK

S. Ashforth-Frost
Department of Mechanical and Manufacturing Engineering, Nottingham Trent University, UK

ABSTRACT: This paper presents the results of an independent validation of a computational fluid dynamics code written specifically for river engineering. The code which has been investigated is SSIIM, (Simulation of Sediment Movements in Water Intakes with Multiblock option). The paper presents results of a comparison between the flow field of a generalised intake structure investigated by physical modelling and by computational modelling using SSIIM. The intake structure is typical of many inlets used for hydropower plants, irrigation or navigation. Generally the results are reasonable with the most appropriate computational model predicting velocity vectors showing agreement varying between 1% and 35% with the physical measurements. Poorer results are obtained nearer the surface of the flow. Turbulent Kinetic Energy is predicted well with the best accuracies of about 12%.

1 INTRODUCTION

SSIIM is an acronym which stands for Simulation of Sediment Movements in Water Intakes with Multiblock option. The code was written by Olsen (1994) of the Norwegian Institute of Technology, Trondheim, Norway and was intended for use in river, environmental, hydraulic and sedimentation engineering. Previously, there have been only two independent validation investigations carried out (Alfredson et al. 1997), (Seed 1997). Alfredson et al. compared the output from SSIIM to the output from two other computational models. However, only a small proportion of the capabilities of SSIIM were tested. The validation carried out by Seed was much more comprehensive, however no tests of the multiblock capabilities of SSIIM were carried out. In addition both of the previous validation exercises made no comparison of the turbulent kinetic energy results obtained. SSIIM is presently being used as part of a study into the energy losses associated with run-of-the-river hydropower intake structures (Bowles 1998) and it was considered that an independent validation of the code was required.

A physical model of a generalised intake structure has been constructed in the hydraulics laboratory of the Department of Civil and Structural Engineering at Nottingham Trent University. Physical measurements of velocity have been taken in the model using an Acoustic Doppler Velocimeter (ADV) (Cabrera and Lohrmann 1996). Numerous computational models have been used which comprise a parametric study comparing the results to the physical measurements taken using the ADV. Comparison tables, velocity profiles and vector plots are presented at points of interest around the structure, particularly at points of separation and flow reversal. A comparison study of turbulent kinetic energy is also presented.

2 PHYSICAL MODELLING

Figure 1 shows a diagram of the physical model. Measurement of velocities were undertaken using an ADV. Previously the calibration of the ADV had been checked (Bowles et al. 1997) and subsequently adjustments were made to the ADV by the manufacturers, Sontek Inc., of San Diego, California. It was found that velocities could be measured to an accuracy of +/- 2%. Fourty three measurement points on each of three levels through the depth of flow were taken, near the bed (3.84cm from the bed), near the middle (19.76cm from the bed) and near the surface (31.01cm from the bed). In addition profiles were measured at ten points in the model at positions of interest. Three profiles were measured at the inlet to the model, three profiles were measured at 1.0m
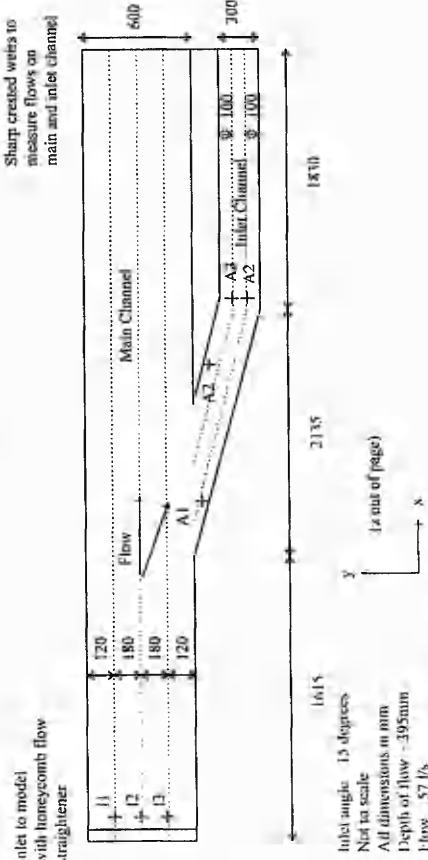
Figure 1 Plan of model and measurement positions

inlet to model with honeycomb flow straightener

Sharp crested weirs to measure flows on main and inlet channel

Flow | Main Channel

120 | 180 | 180 | 120

600 | 300

1615 | 2135 | 1815

I1 I2 I3 — A4 — Inlet Channel Ø 100 — A2 — Ø 100 — A1

Inlet angle 15 degrees
Not to scale
All dimensions in mm
Depth of flow -395mm
Flow .57 l/s

(x out of page)

---

downstream of the inlet and four profiles were measured at other points in the flow designated by points A1 to A4. Further clarification of these positions is shown in figure 1. Positions A1 to A4 have the following coordinates :- A1 is positioned at x = 2000mm, y = 580mm, A2 is positioned at x = 3000mm, y = 520mm, A3 is positioned at x = 4000mm, y = 200mm and A4 is positioned at x = 4000mm, y = 100mm. I1, I2 and I3 designate the positions of the inlet velocity profiles. The position of the three profiles 1000mm downstream of the inlet are not shown in figure 1 for clarity. A flow of 57 l/s and a flow depth of 395mm was set constant in the model. The Froude Number of the model was 0.12 and the Reynolds Number was 40,158. Flow in the model was measured using three methods; an orifice plate in the inlet pipe connected to an electronic manometer, two sharp crested weirs positioned at the outlets of the main channel and the inlet channel and the velocity - area method (Wilson 1994) from the velocity measurements taken using the ADV.

3 COMPUTATIONAL MODELLING

SSIIM solves the Navier - Stokes equations with the k - epsilon turbulence model (Rodi 1980) on a three dimensional structured grid, which is non - orthogonal in plan but regular in the vertical direction. The latest version of SSIIM has been modified to use a non - structured grid but this was not tested as part of this validation exercise. A control volume method is used with cell centred nodes. Two numerical schemes are available for discretisation; the Power - Law scheme (POW) (Pantakar

1980) and the Second Order Upwind scheme (SOU) (Pantakar 1980). The option of the methods SIMPLE (Pantakar & Spalding 1972) or SIMPLEC (Van Doormal & Raithby 1984) are available to use pressure coupling to generate corrections to the (incomplete) solutions to the momentum equations. The matrix equations that are generated are solved using the Gauss - Seidel method (Versteeg & Malalasekera 1995) with an option for block correction. An alternative solution to the matrix solutions is offered by the Tri Diagonal Matrix Algebra option (TDMA) (Thomas 1949). Wall laws for rough boundaries (Schlichting 1979) are used to model the boundary conditions. This gives the velocity field in the geometry which can be used when solving the convection - diffusion equations for sediment transport.

The code has a graphical user interface which presents plots of velocity vectors and scalar variables. There is an interactive graphical grid editor with elliptic and transfinite interpolation facilities (Olsen 1996). It is possible to view the geometry in three dimensions and it is possible to simulate particle animation for visualisation purposes. The grid and some of the input data can be changed during the calculation which can be useful for convergence purposes and also when optimising the geometry with respect to the flow field. The code is written to operate on IBM compatible personal computers using the operating system O/S 2 Warp Version 4 or higher.

Seven computational grids were used in the analyses; 3192, 6384, 9576, 12768, 24408 cells, an 8184 celled multiblock grid arrangement and a 48816 celled prototype model tested using the most successful parameters identified by the study.

Figure 2. Sample computational grid of 57 x 14 grid cells in plan.

Figure 1 Sample Multiblock computational grid of 97 x 11 grid cells in plan.

These grids incorporated four different combinations of cells in the vertical direction and three different combinations of cells in the horizontal direction. Two sample computational grids are shown in figures 2 and 3.

4 COMPARISON OF RESULTS

4.1 Boundary Conditions

Two computational models were used to test the effects of altering the boundary conditions. One model used assumed fully developed velocity profiles based on theory using the flow entering the model. The other model used velocity profiles measured at the inlet to the physical model using the ADV. The results of these two models are summarised by figure 4 (test1 and test 2). Tables 1 and 2 lists the computational tests carried out and the corresponding parameters used, in conjunction with a comparison of the results in terms of percentage errors between the calculated and measured values of velocity. Percentage errors are shown in the x and y directions at the four points A1 to A4 at two levels in the depth of flow. The lower case 'a' following the position code represents the percentage error at a depth of 104mm from the bed. The lower case 'b' represents the percentage error at a depth of 263mm from the bed.

Tables 1 and 2 shows the trend that smaller percentage errors are achieved using a theoretical, fully developed velocity profile at the inlet than when using the actual measured values of velocity at the inlet.

The flow into the model was held constant at 57 l/s. For the Multiblock analyses however, the proportion of the flow entering the inlet channel must be specified. This flow in the inlet channel calculated from ten analyses using the standard grid. The flow

---

entering the inlet channel was calculated to be 17.6 l/s.

The effects of the roughness of the model were tested by changing the Manning's friction coefficient. The physical model was constructed using plastic coated wood ply sheeting for the base and inlet pier and plastic moulded panels for the side walls. It was therefore considered reasonable to use a Manning's 'n' of 0.009 in the computational model. A comparison Manning's 'n' of 0.012 (suitable for concrete) was also tested in the comparison model. These results are summarised in tables 1 and 2 (tests 2 and 3). The trend shown here is that a Manning's 'n' of 0.009 gives smaller percentage errors than a Manning's 'n' of 0.012. This would suggest that the assumption to use a value of 0.009 was valid.

4.2 Grid Dependency

The combinations of grids used in the analyses have been highlighted in section 3. A comparison of the results between the Multiblock grid tested and the five other grids can be observed in tables 1 and 2 (test 2, 4, 5 and 6). Figure 4 shows the results in terms of percentage errors between the computed velocities (in the x direction) and the measured velocities at two levels in the flow at the positions A1 to A4 with increased number of layers in the z direction.

The numbers in parenthesis next to the measurement position in the legend represent the depth in metres from the bed. It can be seen that the general trend is an improvement in terms of percentage error with increased layers in the z direction.

The results of test 13 listed in tables 1 and 2 show the percentage errors between measured and calculated velocities for the multiblock grid analysed using SSIIM. In the multiblock analyses, SSIIM analyses the domain as two separate blocks of computational cells. In all the other tests, only one block of cells is analysed in the domain with
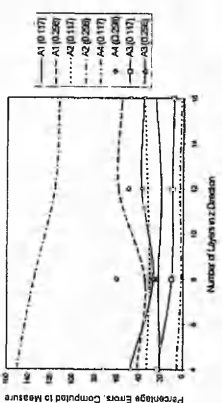

Figure 4. Reduction in percentage errors between measured and computed velocities (Vx) with number of layers in the z direction.

for turbulence (k and ε). In all the tests conducted it was necessary to reduce these values to 0.5 for the velocities, 0.1 for pressure and 0.3 for turbulence, to achieve convergence. In one case, (test 10), using the TDMA solution for the matrices produced by the numerical algorithms described previously, it was necessary to further reduce these factors (0.3, 0.1 and 0.1 respectively) to achieve convergence. Tables 1 and 2 shows that there is no significant advantage to using the TDMA solution over the Gauss - Seidel solution (test 11), with respect to percentage errors in the velocity. With respect to computational time, the TDMA solution takes 8 times longer to converge than the Gauss - Seidel solution.

4.4 Solution of the free water surface

There are presently three options available in SSIIM for the solution to the free water surface. The free surface is modelled as a 'rigid lid' and vertical accelerations cause variations in surface pressure. The initial position of the surface is determined by a standard step, backwater calculation. For a more accurate representation of the surface, it is possible to adjust the position of the surface so that the surface is located where the pressure is zero. The effect of this adjustment is to slightly modify the height of the water column in the cells nearest the surface and thus modify the strength of the velocities. The significance of this effect is dependent on the square of the Froude number. For this validation exercise the Froude number was 0.12 and hence the effect of the water surface update was negligible, shown by the results of test 11 in tables 1 and 2. In addition the inclusion of water surface update reduced the speed of convergence.

The third option available for the solution to the free water surface, surface update with gravity, caused the model to crash and was not therefore tested in this study.

4.5 Convergence

Table 1 lists the convergence times of the 14 computational tests undertaken and the iterations taken to reach convergence. The criteria used by SSIIM to signify convergence are when all the residuals to the calculated variables, Vx, Vy, Vz, Pressure, k and epsilon are less than a factor of 10^{-3}. It can be seen from table 1 that convergence time is not directly proportional to the number of iterations. Each complete iteration takes a different period of time dependent upon the geometry of the grid and the numerical scheme used. For example test 2 and test 10 are identical geometries but the Gauss-Seidel solution to the matrices is used for test 2 as

opproval to the TDMA solution which is used for test 10. In consequence test 2 took 2 hours to converge whereas test 10 took 21 hours to converge. Figure 7 shows a typical convergence graph of log residual with number of iterations. This graph represents the convergence of test 4 but the nature of the convergence is typical of the analyses for this intake example.

Figure 7. Convergence graph for test 4.

4.6 Modelling of prototype

Tables 1 and 2 show a summary of the percentage errors obtained between a range of measured and calculated velocities in the x and y directions. It can be seen that particularly in the y direction, there are some excessively large percentage errors, in many instances well over 100%. In the x - direction the percentage errors are improved mainly because the difference between the measured and calculated velocity is smaller in comparison with the magnitude of the velocity. This therefore gives a misleading impression of the accuracy of SSIIM. It was therefore decided to undertake an analyses (test 14) using a computational grid of 113x27x16 (48816 cells), a numerical scheme using POW for the velocities and SOU for k and epsilon and with the dimensions, depth and flow of the model scaled at 1 to 25 using the Froude Law (Novak 1996). The resulting flow was 175 m³/s and the depth of flow was 9.8m. The widths of the inlet channel and main channel were 7.5m and 15.0m respectively. The results of this computational analysis were compared to the measured velocities and turbulence parameters scaled at 1 to 25 using the Froude Law.

It can be seen from tables 1 and 2 that test 14 gave improved results, particularly in the y - direction. However, computational time was greatly increased with the model taking 41 hours to converge. The machine used for this study was a personal computer, with a Pentium 200 processor with 32 Mb of RAM. The computational time could be reduced with increased provision of RAM.

Figure 8 shows a comparison velocity profile in the x - direction at position A3 for test 14. It can be seen that a good correlation is obtained between the physically measured data and the computationally obtained data.
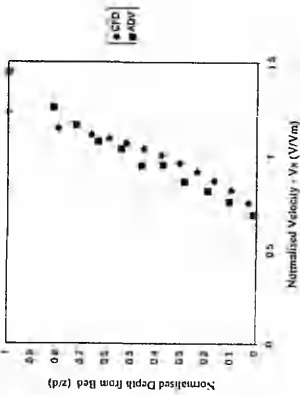
Figure 8. Velocity profile, test4, position A3 in the x - direction.

Further analyses of the data obtained from test 14 can be presented by figure 9 which shows a velocity profile in the y - direction at position A2.

tween measured and calculated velocities in the y - direction.

5 CONCLUSIONS

The study described by this paper has rigorously investigated the parameters used by SSIIM for the calculation of a complex hydraulic problem. Initially the results of a boundary condition study were presented. It was shown that specifying the velocities at the inlet to the model could give profoundly different results to using an assumed, fully developed, theoretical inlet velocity profile. The reasons why a better correlation with physically measured data should be achieved when the inlet conditions were not specifically given, is impossible to explain within the constraints of this study. However, in such a complex problem as the intake structure which was used for this study, it is obvious that such a study would not be valid without specifying the inlet conditions. The flow entering the model was not fully developed and therefore this assumption should not be used.

The study has shown that it is important to calibrate the model for the friction at the boundary. A Manning's 'n' of 0.009 is a representative value for a smooth walled physical model which was used in this study.

Grid dependency is a major consideration for any computational modelling. The study with SSIIM has shown that accuracy in prediction of the flow using the computational model should be offset against the large increase in computational time which will occur with an increase in the number of cells. Tables 1 and 2 give the reader an indication of the computational time required using the computer specified. The multiblock option provided by SSIIM has been shown to be a successful tool, but preliminary analyses are required in order to specify the proportions of flow that are required by this facility.

The POW numerical scheme is approximately 30% faster than the SOU numerical scheme and usually more stable but less accurate where the grid is coarse and the flow is not aligned to the grid. The SOU scheme can create undershoots which may cause instability in the k and epsilon equations. A very coarse grid may generate excessively oscillating solutions, delaying or preventing convergence. It is advised that the SOU scheme should be used for the momentum equations since it improves the accuracy for flow which is not aligned to the grid and it may reduce computational time. The POW scheme is recommended for the turbulence equations because of its greater stability. However, the use of the SOU scheme can
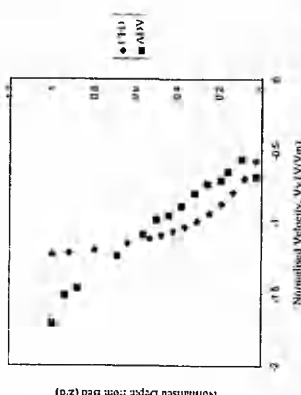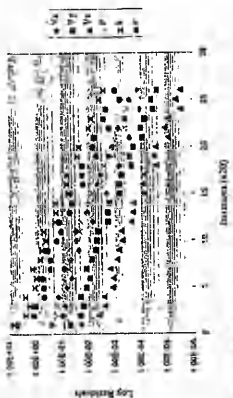
Figure 9. Velocity profile, test 14, position A2, in the y - direction.

Figure 9 shows that the percentage error between the measured and calculated velocity in the y - direction increases near the surface of the flow. This is typical of many of the models that were computed using SSIIM for this study. However, the correlation through the rest of the depth of flow is acceptable with a mean of less than 20% error be-

cause negative values of k and epsilon which can cause the solution procedure to fail.

Block correction, a numerical method which accelerates convergence of the POW scheme, was not tested because it causes the solution procedure to fail where there are out blocked regions of the flow. The SIMPLEC algorithm was not tested for similar reasons.

The matrices generated by the numerical schemes should be solved using the Gauss - Seidel option offered by SSIIM. The TDMA option does not improve the results and it increases the computational time required considerably.

Two out of the three options for the solution of the free water surface were tested in this study. Improvements to the results by use of the unsteady updip option is dependent on the Froude number of the model. It will only have a significant effect where the Froude number is large (considerably larger than 0.12 for the model used in this study).

SSIIM has been scrutinised closely by this study and perhaps placed under too extreme conditions. It is designed primarily for river engineering purposes. For the purposes of this study, SSIIM has been compared to a scaled physical model in a hydraulics laboratory under much more favourable conditions than one would expect to find in a prototype situation. For this reason, test 14 was carried out in order to compare SSIIM to a hypothetical prototype situation. In this case SSIIM performed satisfactorily, predicting velocities to better than 30% in the x - direction and turbulent kinetic energy to better than 12%. SSIIM also predicted the qualitative direction of the velocity vectors reasonably well although in terms of percentage errors the results may appear to be poor.

This validation study has provided valuable physical data which may be used for further validation studies for 3D computational models. A copy of the tabulated physical data may be obtained from the authors. (Bowles, Dalfern, Ashforth - Frost, January 1998)

REFERENCES

Alfredson, K., Marchand, W., Bakken, T. H. & Harby, A. 1997. Application and comparison of computer models for quantifying impacts of river regulation on fish habitat. *HYDROPOWER '97*.

Bowles, C. B., 1998. The use of computational fluid dynamics for the design of small scale hydropower intake structures. *Study notes towards the fulfilment of a Doctor of Philosophy*.

Bowles, C. B., Dalfern, C. & Ashforth - Frost, S. 1997. The independent calibration of the acoustic doppler velocimeter. Presented at *27th Biennial Congress of the IAHR*, San Francisco.

Lohrmann, A., Cabrera, R. & Kraus, N. C. 1994. The acoustic doppler velocimeter for laboratory use. *Proceedings of Fundamentals and Advancements in Hydraulic Measurement and Experimentation*. Hydraulics Division of the ASCE.

Novak, P. 1996. *Hydraulic Structures*. London : E. & F. N. Spon.

Olsen, N. R. B. 1991. A numerical model for simulation of sediment movements in water intakes. *Dr. Ing. Dissertation*. The Norwegian Institute of Technology, Trondheim.

Olsen, N. R. B. 1996. *SSIIM - A three dimensional numerical model for simulation of sediment movements in water intakes with multiblock option*. Users Manual, Version 1.4. The Norwegian Institute of Technology, Trondheim.

Patankar, S. V. 1980. *Numerical Heat Transfer and Fluid Flow*. New York : McGraw Hill.

Patankar, S. V. & Spalding, D. B. 1972. A calculation procedure for heat, mass and momentum transfer in three dimensional parabolic flows. *Int. J. Heat Mass Transfer*. Vol. 15, p. 1787.

Rodi, W. 1980. Turbulence models and their application in hydraulics. *IAHR State - of - the - art paper*.

Steed, D. I. 1997. River training and channel protection; Validation of a 3D numerical model. *HR Wallingford Technical Report SR 480*, Construction Sponsorship Directorate.

Thomas, L. H. 1949. Elliptic problems in linear difference equations over a network. *Watson Sci. Comput. Lab. Report*, Columbia University, New York.

Wilson, E. M. 1994. *Engineering hydrology*. 4th Edition. London : Macmillan Press.

Schlichting, H. 1979. *Boundary layer theory*. New York : McGraw Hill.

Van Doormal, J. P. & Raithby, G. D. 1984. Enhancements of the SIMPLE method for predicting incompressible fluid flows. *Numer. Heat Transfer*, Vol. 7, pp 147 - 163.

Versteeg, H. K. & Malalasekera, W. 1995. *An Introduction to computational fluid dynamics*. London : Longman Scientific & Technical.